Pre-eruptive conditions, crustal processes, and magmatic timescales recorded in products of Calbuco and Osorno volcanoes, Southern Andes

Eduardo Esteban Morgado Bravo

Submitted in accordance with the requirements for the degree of

Doctor of Philosophy

The University of Leeds

School of Earth and Environment

August 2019

Declaration

The candidate confirms that this work submitted is his own, except where work which has formed part of jointly authored publications has been included. The contribution of the candidate and other authors to this work is explicitly indicated below. The candidate confirms that appropriate credit is given within the thesis where the reference has been made to the work of others.

The work in Chapter 2 of this thesis was published in Bulletin of Volcanology as follows:

Morgado, E., Morgan, D.J., Harvey, J., Parada M.Á., Castruccio, A., Brahm, R., Gutiérrez, F., Georgiev, B., Hammond, S.J. (2019). *Localised heating and intensive magmatic conditions prior to the 22–23 April 2015 Calbuco volcano eruption (Southern Chile).*

The idea of this paper was developed by myself and the co-authors, and methodology was developed by myself and DJM using the published literature. The fall deposits were collected by myself and the co-authors during fieldwork in Calbuco volcano (Southern Chile). I obtained the mineral chemistry and performed all calculations. I produced all the figures of the article, except the last figure, with was developed together with the illustrator Katerina Nicolau del Roure. I wrote this manuscript, which was improved by suggestions and comments from all the co-authors, two anonymous reviewers, and Editors of Bulletin of Volcanology. The article and Supplementary Material can be found here: https://doi.org/10.1007/s00445-019-1280-2.

The work in Chapter 3 of this thesis was published in Contributions to Mineralogy and Petrology as:

Morgado, E., Morgan, D.J., Castruccio, A., Ebmeier, S.K., Parada, M.Á., Brahm, R., Harvey, J., Gutiérrez, F., Walshaw, R. (2019). *Old magma and a new, intrusive trigger: using diffusion chronometry to understand the rapid-onset Calbuco eruption, April 2015 (Southern Chile).*

The idea of this manuscript was developed by myself and DJM, and methodology was developed by myself using the published literature using the samples collected in Calbuco volcano (Southern Chile). I obtained the mineral chemistry with the assistance of RW and performed all calculations. I produced all the figures of the article and wrote the manuscript, which was improved by suggestions and comments from all the co-authors, two anonymous reviewers, and Editors of Contributions to Mineralogy and Petrology. The article and Supplementary Material can be found here: https://doi.org/10.1007/s00410-019-1596-0.

The work in Chapter 4 of this thesis is a manuscript to be submitted to Journal of Petrology as follows:

Morgado, E., Morgan, D.J., Harvey, J., Castruccio, A., Brahm, R., McGee, L.E., Georgiev, B., Parada, M.Á. (in prep.). *Pre-eruptive conditions of the 1835 eruption of Osorno: a combined mineralogical, geochemical, and numerical approach.*

The idea of this manuscript was developed by myself and the co-authors, and methodology was developed by myself using the published literature using the samples collected in Osorno volcano (Southern Chile). I obtained the mineral chemistry with the assistance of R. Walshaw and performed all calculations. I produced all the figures and wrote this manuscript, which

was improved by suggestions and comments from all the co-authors. The isotopic data from Osorno and Calbuco were obtained by JH and BG.

Acknowledgments

PhD is an adventure, one I wanted to live even when I did not know what it really meant. I really believe I chose the correct university to do it, mainly because I met people who lived this experience with me as I lived their experiences with them. After this adventure, I know much better who I am and what I want. I can say that even if I am the only one who is going to be awarded a PhD, certainly this is a collective achievement: it has been me, crossing the jungle and the desert with the help of many (some of them anonymous) hands. This is a humble recognition to some of these people who gave me a hand along this beautiful adventure.

Many thanks to my supervisors: Dan J. Morgan and Jason Harvey. Although they were critic reviewers of my work, they always heard and respected my points of view, which was significant to my self-confidence as a proto-scientist. To Miguel Ángel Parada, co-supervisor who encouraged me to take this trip and was my host when I visited the University of Chile. To Angelo Castruccio, who went with me to the field and was always available to discuss different topics: science and life in general. To Susanna Ebmeier, who was always available to discuss and encouraging me to research. To Richard Walshaw, who helped me during long sessions using the EPMA.

Thanks to all the people from Office 8.512, the best office to work. Special thanks (and sorry!) to all those who helped me with my *grammatical things*, and were always available to read what I wrote: Claire “the amazing” Harnett, Patrick “the chosen one” Sugden, and Ruth Amey. Fruitful discussions and company of *my sestra querida* and housemate Lubka Tomanikova are greatly acknowledged. Thanks also to those who were at the University and Volcano Group: Rodrigo, Chris, Edna, Ita, Dinko, Kev, Josh, Sam, Amicia, Locko, Dave, Delia, Fiona, Katie, Ben, Tim, Tom, Rachel, among others. Many, many thanks to all the

people I have met in Leeds, which always heard my problems, especially to Alberto, Jesús, Natalia, Julio, Rodrigo, Vishnu, Laura, Victoria, Nicole, Mario, Claudio, among others.

To follow my dream in this adventure, I have been away from the most important people to me: my family. I thank Eduardo, Liliana, Loreto and Benjamín. They always gave me support on my decision of following my dream and studying a PhD, even when it means to be far away from home for several years.

Abstract

The Southern Volcanic Zone (SVZ) of the Andes is an active volcanic chain generated by the subduction of the Nazca Plate below the South American Plate. The SVZ has been subdivided into four segments, based on tectonic setting. One of those four subdivisions is the Central Southern Volcanic Zone (CSVZ), where the most active volcanoes of the SVZ are located: Villarrica, Llaima, Calbuco, Puyehue-Cordón Caulle, Osorno, and Mocho-Choshuenco. In recent years, some of these volcanoes have erupted (e.g. Villarrica in 2015, Llaima in 2008, Puyehue-Cordón Caulle in 2011–2012) and those eruptions have been captured by volcano monitoring. By contrast, other active volcanoes have erupted for the last time before monitoring instruments were installed in the neighbouring areas (e.g. Osorno in 1835 and Mocho-Choshuenco in 1864). Petrological studies are useful to assess previous eruptions and, as a consequence, can be used in volcano monitoring and forecasting. The present study is focused on the most recent eruptions of Calbuco and Osorno stratovolcanoes.

In April 2015, an unpredicted rapid-onset eruption occurred at Calbuco Volcano in the Southern Andes of Chile. This event consisted of two, sub-Plinian eruptions separated by a few hours. I identify an upper-crustal reservoir using available geophysical data combined with amphibole geobarometry. Based on textural features, I conclude the presence of a mush zone within this reservoir. From the collected samples, whole-rock chemistry and an array of geothermometers of silicate phases (amphibole, amphibole-plagioclase, two-pyroxenes) gave similar conditions for all samples possessing ~40 crystal volume, with the exception of the sample Cal-160 (~60 % crystal volume), which is slightly more evolved and yields lower temperatures for all silicate-phase geothermometers. In addition, I performed Fe-Ti oxides thermometry, which gave lower temperatures than those silicate-phase based. Comparing temperatures calculated by pairs of ilmenite-titanomagnetite core compositions with those

calculated using rim compositions, I observe a late-stage temperature increase of between 70ºC and 200ºC in sample Cal-160, which represents the bottom of the crystal mush and the magma reservoir. I suggest this recognised heating triggered the eruption requiring the involvement of a hot, presumably mafic magma injection at the base of a shallow, crystal-rich reservoir, though the mafic magma was not itself erupted.

I determine timescales of pre-eruptive heating at the partially-solidified chamber base (represented by sample Cal-160) and constrain the magma residence time for the bulk of the carrier magma (represented by the rest of the collected samples). The ilmenite-titanomagnetite pairs from sample Cal-160 yielded magmatic timescales of < 4 days, interpreted as time between the triggering and the eruption. These short magmatic timescales explain why the April 2015 Calbuco eruption showed precursors of only a few hours. By contrast, the ilmenite-titanomagnetite pairs of other samples (distinct from Cal-160) yielded magmatic timescales of > one year, which represent resident, eruptible magmas in the middle of the reservoir at stable temperatures and oxygen fugacity. This portion of the magma reservoir did not interact with any magma recharge immediately prior to or during the eruption, indicating the eruption was triggered before the thermal homogenisation of the magma reservoir beneath Calbuco volcano.

During 1835, two eruptive events occurred; the first during January-February and the second during November-December. The erupted products of both events are lavas and tephra fall deposits of basaltic-andesite composition (52.4–52.9 SiO_2 wt%) with of crystallinity ranging from 23 to 45 vol% comprising: olivine, plagioclase, clinopyroxene, and Cr-spinel. Using the erupted products, I calculated pre-eruptive conditions: temperature of ~1,140ºC (via olivine-augite and Ca-in-olivine thermometry), oxygen fugacity of ΔQFM +0.3 (via Cr-spinel-melt oxybarometry and numerical modelling), dissolved water content up to ~1.5 wt% (via numerical modelling), and depths of up to 4.5 km (numerical modelling). Based on textural

features, I conclude the presence of a mush zone within this reservoir, which underwent partial disaggregation prior both eruptive events. The studied eruption presents the same eruptive features, mineral assemblage, and composition as the historical products from Osorno volcano, in consequence, it can be used to assess other previous eruptive events and future behaviour.

In addition, comparison of products from the neighbour stratovolcanoes Calbuco, Osorno and La Picada was performed using trace elements (fluid mobile/immobile and rare earth elements) and $^{87}Sr/^{86}Sr$ and $^{143}Nd/^{144}Nd$ isotope ratios. These analyses display higher both slab-derived fluid input and partial melting degree in the mantle beneath stratovolcanoes (Osorno, Calbuco, and La Picada) than in small eruptive centres (represented by La Viguería cones). Although the most significant signature comes from the mantle source, these results suggest also the minor influence of crustal assimilation. Finally, implications of this study are argued, comparing with other volcanic system from the CSVZ at 39º30'S latitude, which exhibit some similarities.

Contents

Chapter 4

Chapter 5

Chapter 6

List of Figures

List of Tables

Nomenclature

List of acronyms

ASTER	Advanced Spaceborne Thermal Emission and Reflection
AVZ	Austral Volcanic Zone
BSE	Backscattered Electron
CSVZ	Central Southern Volcanic Zone
CVZ	Central Volcanic Zone
DRE	Dense Rock Equivalent
EDS	Energy Dispersive Spectrometer
EPMA	Electron Probe Micro Analysis
GDEM	Global Digital Elevation Model
InSAR	Intereferometric Synthetic-Aperture Radar
LOFZ	Liquiñe-Ofqui Fault Zone
LP	Long period
NNO	Nickel-Nickel Oxide buffer
NSVZ	Northern Southern Volcanic Zone
NVZ	Northern Volcanic Zone
OVDAS	Observatorio Volcanológico de los Andes del Sur
PDC	Pyroclastic Density Current
QFM	Quartz Fayalite Magnetite buffer
REE	Rare-earth element
SEM	Scanning Electron Microscope
SERNAGEOMIN	Servicio Nacional de Geología y Minería
SSVZ	Southern Southern Volcanic Zone
SVZ	Southern Volcanic Zone
TAS	Total alkalis versus silica

TSVZ	Transitional Southern Volcanic Zone
USGS	United States Geological Survey
UTC	Coordinated Universal Time
VEI	Volcanic explosivity index
VT	Volcano-tectonic
WDS	Wavelength Dispersive Spectrometer

List of symbols

fO_2	Oxygen fugacity	(Pa)
T	Temperature	(K)
R	Ideal gas constant	($J\ K^{-1}\ mol^{-1}$)
E	Activation energy	($J\ mol^{-1}$)
ε	Uncertainty	(-)
K_D	Partition coefficient	(-)

Chapter 1

1. Introduction

This work is focused on identifying pre-eruptive physical intensive conditions, timescales and regional features of magmas erupted during the last eruptions of two of the most active volcanoes from the Central Southern Volcanic Zone of the Andes: Calbuco (April 2015) and Osorno (1835). The study is approached utilising detailed chemical composition, textural features of the phenocrysts, whole-rock major and trace element chemistry, and isotope chemistry. This thesis benefits from previous studies of volcanoes of the region, presented from geophysical (e.g. Van Eaton et al., 2016; Delgado et al., 2017; Nikkhoo et al., 2017), geochemical (e.g. Tagiri et al., 1993; López-Escobar et al., 1995a; 1995b; Hickey-Vargas et al., 1995), and structural (Cembrano and Lara, 2009) point of views.

This thesis gives information of pre-eruptive conditions to understand the last eruptions of Calbuco and Osorno volcano, which can be used to take actions related to hazard mitigation and public policies of the studied volcanoes as well as other neighbour volcanic centres (e.g. La Picada volcano, La Viguería small eruptive centre). The main objective of this thesis is to answer the following questions:

1. What are the physical intensive conditions of the magmas from the last eruptions of Calbuco and Osorno volcanoes?
2. Is there any crystal mush within the magma chambers beneath those volcanoes? What is the influence on eruptive features of that?
3. What are the pre-eruptive timescales of those volcanoes? How could be related to geophysical observations?
4. What are the conditions of magma generation, fluid supply and crustal contamination of the region?

Those main questions are addressed in the five chapters of this thesis. This chapter introduces the context and outstanding problems in the Central Southern Volcanic Zone of the Andes. Chapter 1 also provides an introduction to the techniques and methods used later in the thesis to achieve the objectives. Chapter 2 (published as Morgado et al., 2019a) focuses on determining the pre-eruptive physical intensive conditions of the April 2015 Calbuco eruption products, recognising the presence of a crustal mush within a magma reservoir in the upper crust, and and the involvement of a new, hotter magma input as the eruption trigger. Chapter 3 (published as Morgado et al., 2019b) expands on the previous study, presenting Fe-Ti diffusion chronometry in ilmenite-titanomagnetite contact pairs to calculate the timescales from heating (triggered by the new, hotter magma input recognised in Chapter 2) to eruption and also comparing and coupling the modelled pre-eruptive timescales with geophysical published data. Chapter 4 (being prepared for submission to Journal of Petrology) focuses on the pre-eruptive physical intensive conditions of the 1835 Osorno eruption products, distinguishing the presence of a crustal mush within an upper crustal magma reservoir and concludes by presenting a regional magmatic model considering fluid supply and crustal contamination. Finally, Chapter 5 presents a summary and discussion of the key findings and compares the findings with other volcanic systems of similar eruptive features, in both the Andes and further afield.

1.1. Why study Central Southern Volcanic Zone of the Andes?

The Andean volcanoes are classified in four distinct segments (Stern et al., 2007; Fig. 1.1): Northern Volcanic Zone (NVZ, 2–5ºN), Central Volcanic Zone (CVZ, 14–28ºS), Southern Volcanic Zone (SVZ, 33-46°S), and Austral Volcanic Zone (AVZ, 49–55ºS). These zones are separated by areas where arc volcanism does not exist (Stern et al., 2007): Peruvian flat-slab segment (between NVZ and CVZ), Pampean flat-slab segment (between CVZ and SVZ), and Chile Rise (between SVZ and AVZ). This thesis focuses on volcanoes from the SVZ of the Andes, which is an active volcanic chain generated as a consequence of the subduction of the Nazca plate below the South American plate.

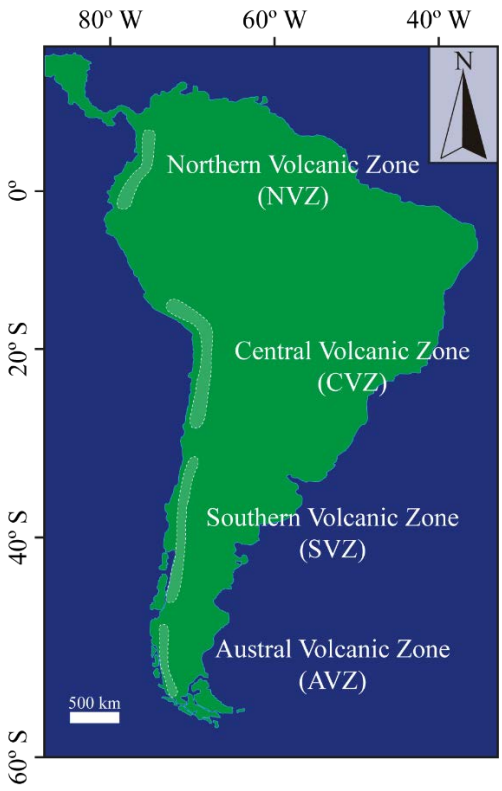

Figure 1.1. *Location of the different volcanic zones of the Andes with respect to South America.*

On the basis of tectonic setting, geochemical and petrologic considerations the SVZ itself has been sub-divided into four segments (Tormey et al., 1991; López-Escobar et al., 1995a; Stern, 2004; Stern et al., 2007): Northern (NSVZ, 33.3-34.4ºS), Transitional (TSVZ, 34.4-37ºS),

Central (CSVZ, 37-42ºS; Fig. 1.2), and Southern (SSVZ, 42-46ºS). The largest crustal structure of the SVZ is the ~1200 km long NS dextral strike-slip Liquiñe-Ofqui Fault Zone (LOFZ; Cembrano et al., 1996; 2000). Most of the large stratovolcanoes of the SVZ are not built over the LOFZ, but most of them are located within 50 km of it.

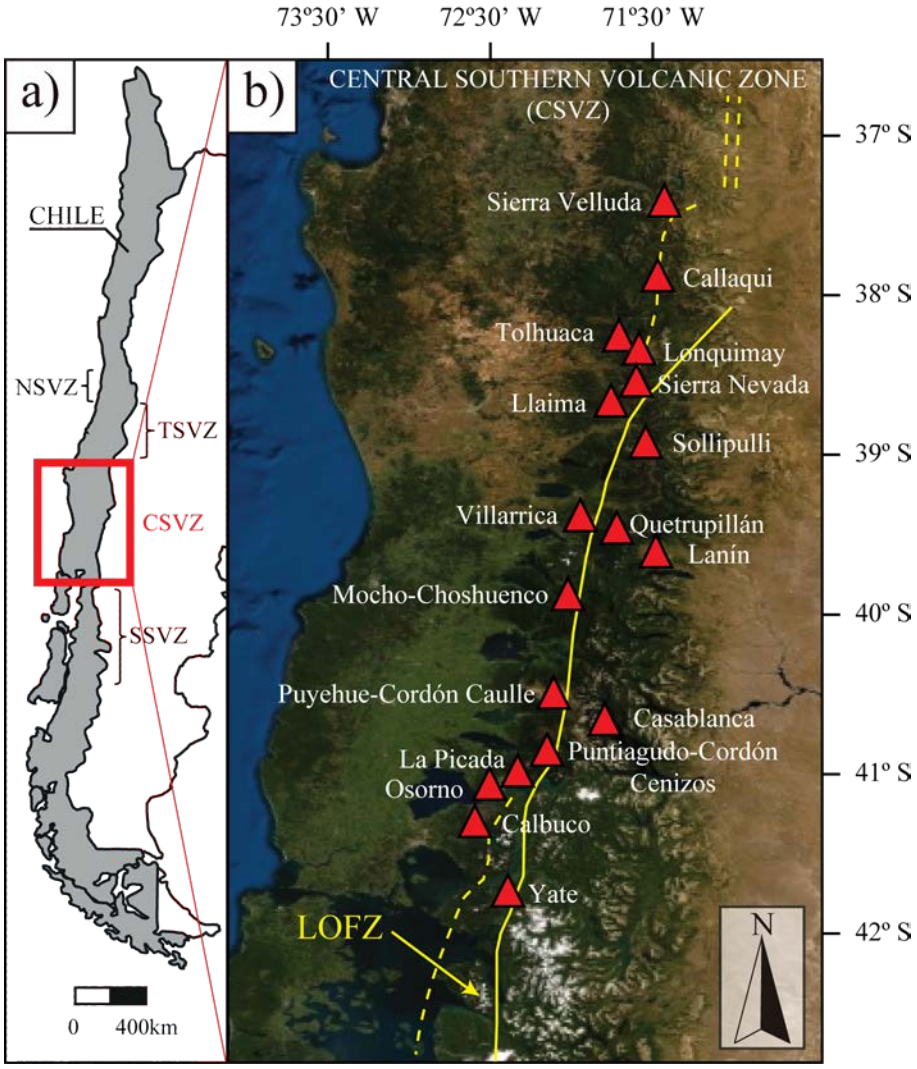

Figure 1.2. *a) Location of the four subdivisions of the Southern Volcanic Zone with respect to* Central b) Central Southern Volcanic Zone and the l*ocation of both stratovolcanoes and the Liquiñe-Ofqui Fault Zone (LOFZ). The location of the LOFZ (solid and dashed lines) was inferred from Cembrano et al. (1996) and Cembrano and Lara (2009).*

In the CSVZ, south of 39º S, Cembrano and Lara (2009) proposed structural models beneath volcanoes from the region depending on the volcano alignments:

- NE-trending volcanic alignments (e.g., La Picada-Puntiagudo-Cordón Cenizos; Moreno et al., 2010; Vander Auwera et al., 2019; Fig. 1.2) are proposed to be related to tension cracks, which may reach the surface and then build either a stratovolcano or an elongated cluster of minor eruptive centres, depending on the balance between strain rate and magma input (cf. Takada, 1994).
- NW-trending alignments (e.g., Villarrica, Morgado et al., 2015; Pizarro et al., 2019; Puyehue-Cordón Caulle, Lara et al., 2004, 2006), in which volcanoes are built on top of west-northest-striking, pre-Andean, oblique-slip faults.
- Small eruptive centres built over the LOFZ master fault (e.g., Caburgua-Huelemolle small eruptive centres; Hickey-Vargas et al., 1989, 2002; Morgado et al., 2015, 2017; Mcgee et al., 2017; Cayutué-La Viguería group; López-Escobar et al., 1995b). The melts erupted from small eruptive centres, are considered to ascend rapidly through the crust and do not interact with it extensively (e.g. McGee and Smith, 2016; Hickey-Vargas et al., 2016a; Smith and Németh, 2017), this volcanism is usually related to extensional domains (e.g. Nakamura, 1977; Takada, 1994; Piochi et al., 2005).

In this model (see Fig. 1.3), Cembrano and Lara (2009) relate the trace element compositions (Cr vs. Rb) of the magmas from CSVZ (and SVZ in general), to crustal residence times (see Fig. 1.3), however, they do not calculate those timescales. The calculation of pre-eruptive timescales beneath volcanoes of the CSVZ is still an ongoing task. Stratovolcanoes, which are not related to any major structures (e.g. Calbuco volcano; López-Escobar et al., 1995; Sellés and Moreno, 2010) are not mentioned in the model of Cembrano and Lara (2009).

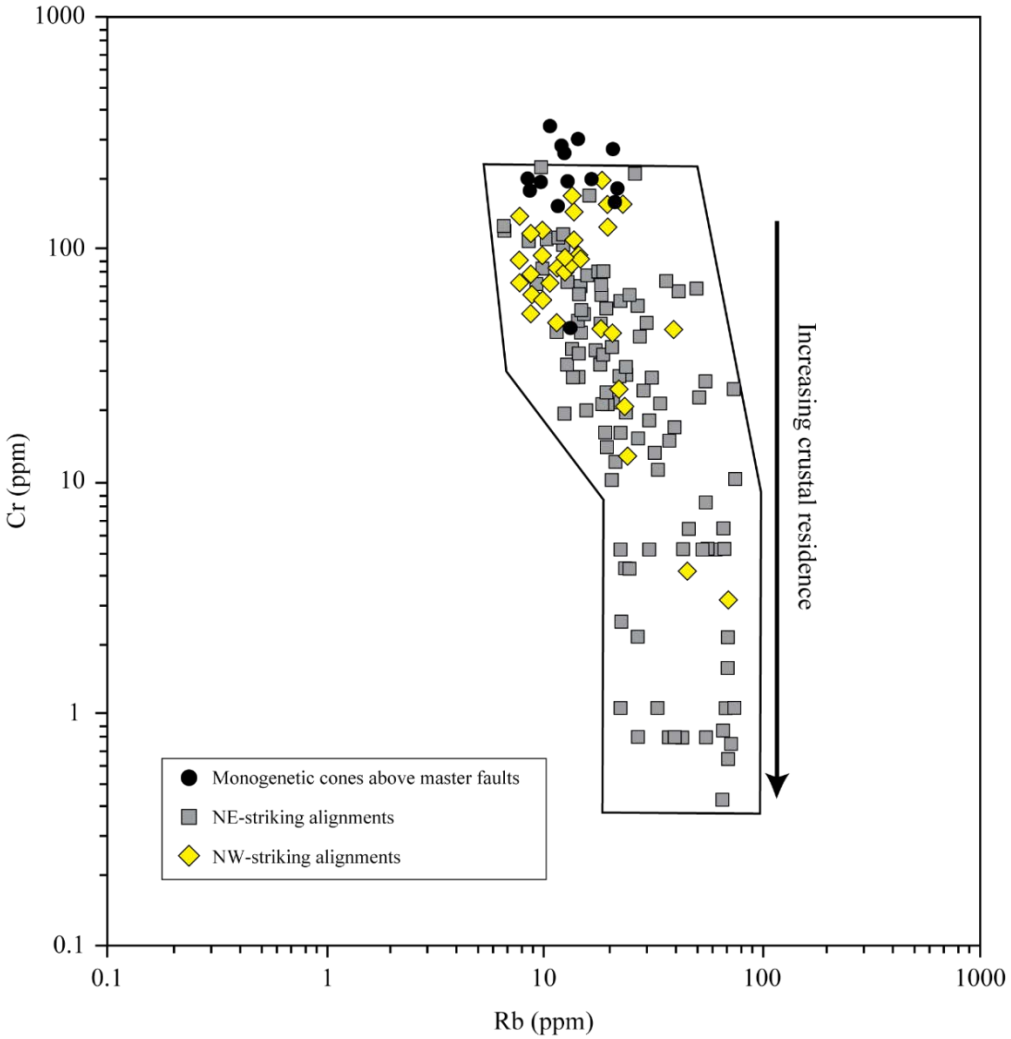

Figure 1.3. *Cr versus Rb from different volcanic systems from the SVZ. The authors suggest the crustal magmatic residence increases while Cr content in the studied products is decreasing. The shortest magmatic timescales would correspond to small eruptive centres built over LOFZ master fault, longer magmatic timescales would correspond to volcanoes in NW-striking alignments, and the longest would correspond to the products of volcanoes built over NE-striking alignments. Modified from Cembrano and Lara (2009).*

The CSVZ includes some of the most dangerous volcanoes among 90 active volcanic systems of the Chilean Andes (Lara et al., 2011, Table 1.1). All these active volcanoes are monitored by OVDAS-SERNAGEOMIN, but some of them do not have not yet been examined in detail in terms of petrology, magmatic physical intensive conditions, and magmatic timescales. This thesis proposes to study those aspects of the products from the last eruptions of Calbuco and Osorno volcanoes.

Table 1.1. The most hazadous volcanoes from the Central Southern Volcanic Zone

Volcano	Hazard ranking	Last eruption	Reference
Villarrica	1	2015	Romero et al., 2018; Pizarro et al., 2019
Llaima	2	2008	Bouvet de Maissoneuve et al., 2012
Calbuco	3	2015	Castruccio et al., 2016
Puyehue-Cordón Caulle	5	2011	Jay et al., 2014
Osorno	6	1835	Lara et al., 2012
Mocho-Choshuenco	7	1864	Moreno and Lara, 2007

1.2. Volcanic hazards in the Central Southern Volcanic Zone

Volcanoes are potentially dangerous depending on how explosive the eruptions are and how close they are to population centres (e.g. Gudmundsson, 2010; Donovan et al., 2017). To reduce the hazard and risk of potentially disastrous eruptive events, volcano monitoring uses several approaches (seismology, ground deformation, gas chemistry, etc.) to assess the real-time state of volcanoes and to monitor any changes in those states. Through the integration and evaluation of information given by volcano monitoring tools, volcano observatories are in charge of the indication of the state of volcanic alert (Fig. 1.4).

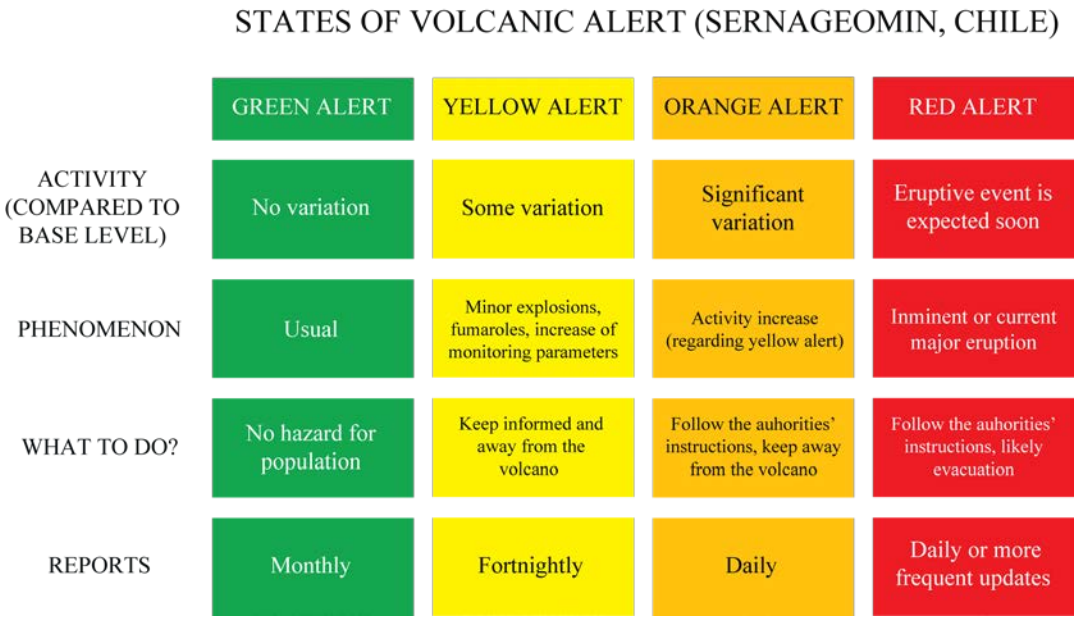

Figure 1.4. *States of volcanic alert in Chile, published by the Southern Andes Volcano Observatory (OVDAS) from the National Geological Survey (SERNAGEOMIN) (available at sernageomin.cl/abc).*

In some cases, volcano monitoring has not been able to give a timely forecast of rapid-onset eruptions (e.g. El Reventador Volcano in 2002, Hall et al., 2004; Calbuco volcano in 2015; Romero et al., 2016; Castruccio et al., 2016) and in other cases volcanoes have not been monitored during an eruptive event (Chaitén in 2008, Lara, 2008; Osorno in 1835, Lara et al., 2012), due to the monitoring instruments have been installed after the last eruptions. In both cases, an understanding of the past eruptive behaviour is necessary as a guide for future eruptive behaviour of a specific volcano. Materials produced during previous eruptions are studied to constrain fundamental properties such as temperature, pressure, and oxygen fugacity.

How disastrous an eruptive event can be is usually related to the magma composition and volatile content of the erupted material: more siliceous and volatile-rich magmas are typically more hazardous than those less siliceous and volatile-poor magmas. Beneath active volcanoes, there are certain places where the magma is stored and differentiation processes can occur: magma chambers. Moreover, studying zoning patterns in crystals from erupted material, we can calculate the timescales of magmatic processes (differentiation, heating, crustal residence, etc.). All this petrological information can be coupled with volcano monitoring to reduce the volcanic hazard (e,g, Peccerillo et al., 2006).

The study of Calbuco and Osorno volcanoes, in CSVZ, is significant for volcanic hazard mitigation because they are active volcanoes located close to population centres (Table 1.2; Fig. 1.5).

Table 1.2. Population centres close to Calbuco and Osorno volcanoes.

Population centre	Population*	Distance to Calbuco volcano (km)	Distance to Osorno volcano (km)
Puerto Varas	44,578	30	45
Puerto Montt	245,902	32	52
Alerce	72,500	24	43
Las Cascadas	700	30	12
Cochamó	4,023	30	43
Ensenada	1,623	12	12
Correntoso	~250	12	40

* Data from Chilean Census 2017

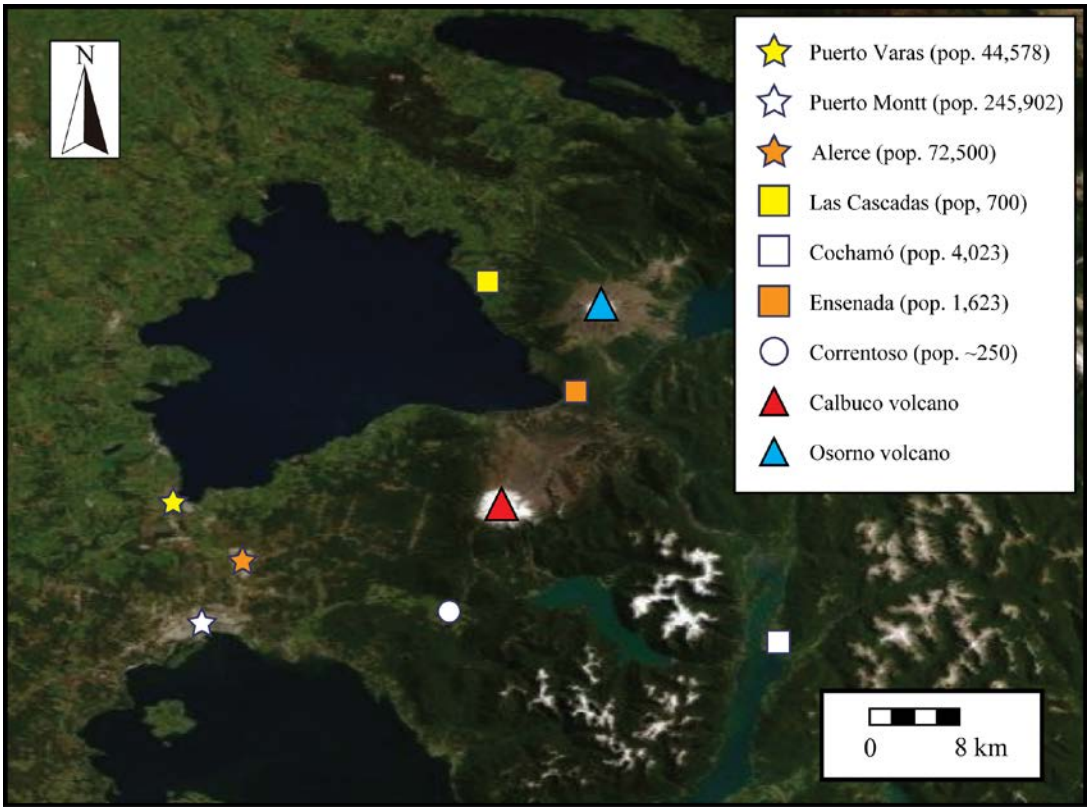

Figure 1.5. *Location of the main population centres (Puerto Varas, Puerto Montt, Alerce, Las Cascadas, Cochamó, Ensenada, and Correntoso) close to Calbuco and Osorno volcanoes. Population data from the Chilean Census 2017. The ASTER image was obtained via the ArcGIS software ®.*

1.3. Why study the April 2015 Calbuco eruption?

Calbuco volcano (41º19'S, 72º36'W) is a Late Pleistocene to Holocene composite stratovolcano, situated ~20 km west of the LOFZ, but not directly related to any major regional structure (Fig. 1.6; Sellés and Moreno, 2011). Calbuco has been catalogued as the third most hazardous Chilean volcanic system (Fig. 1.1; Lara et al., 2011; SERNAGEOMIN, 2017). The Calbuco products have been divided into four geological units, three of them pre-historic (units Calbuco 1, 2, and 3) and one historical unit, Calbuco 4. The historically erupted products comprise lava flows (basaltic to basaltic andesite with rare dacite), andesitic to dacitic domes (Fig. 1.7) and layers of pyroclastic tephras, block and ash flows, and deposits from hot and cold lahars (López-Escobar et al. 1992, 1995a, b; Petit-Breuilh 1999; Moreno et al. 2006; Stern et al. 2007; Castruccio et al. 2010; Sellés and Moreno 2011; Watt et al. 2011; Daga et al. 2014). The last eruption occurred in April 2015. For the last Calbuco eruption, OVDAS-SERNAGEOMIN, the volcano observatory in charge of Calbuco volcano monitoring, only announced a red alert at the moment of the onset of the eruption, before that, the volcano was in green alert (see Fig. 1.4). None of the published articles studying the Calbuco 2015 eruption have given detailed petrological information or an explanation on how the pre-eruptive timescales can be related to this rapid eruption.

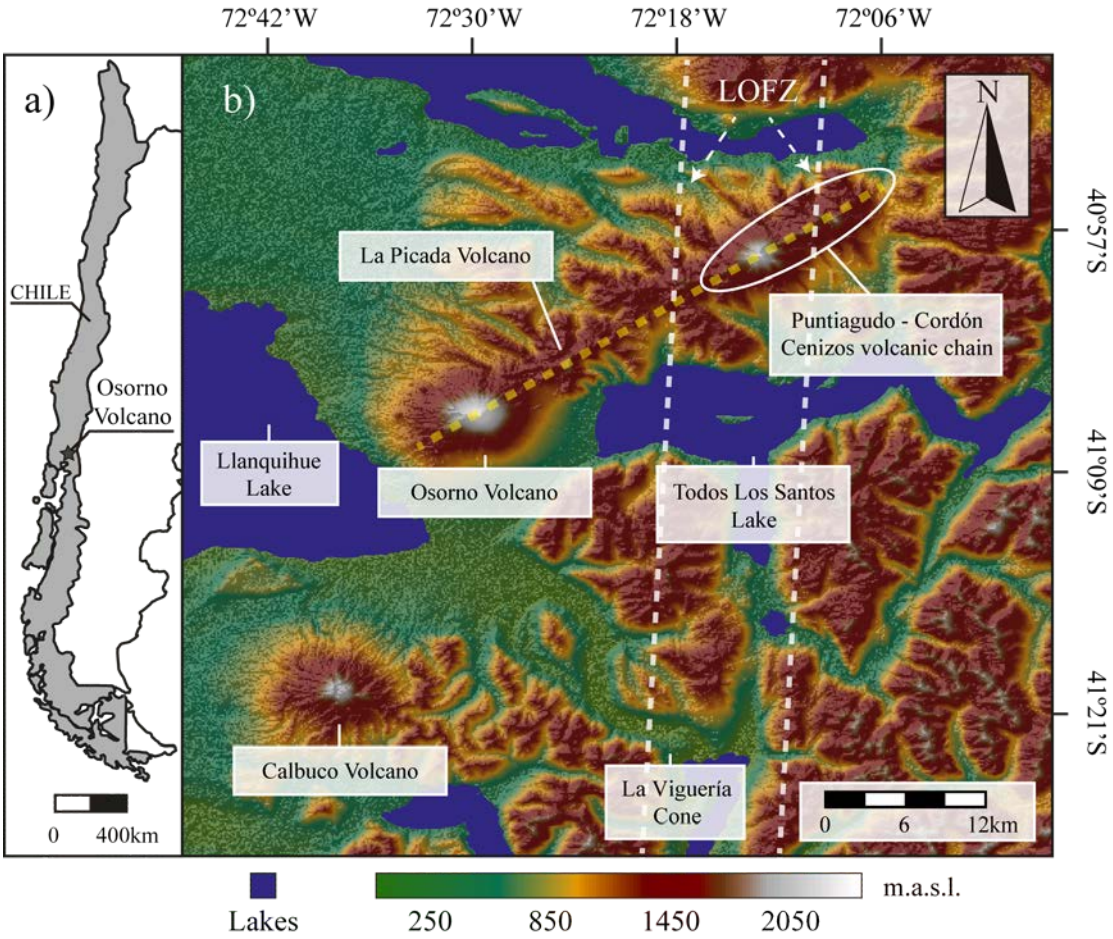

Figure 1.6. *a) Location of the studied region regarding Chile. b) Position of Osorno, La Picada, Puntiagudo, and Calbuco volcanoes and Cordón Cenizos volcanic chain, La Viguería cone, and the Liquiñe-Ofqui Fault Zone (LOFZ, white dashed line). The alignment Osorno, La Picada, Puntiagudo and Cordón Cenizos is represented by a yellow, dashed line. The advanced Spaceborne thermal Emission and Reflection Radiometer (ASTER) Global Digital Elevation Model (GDEM) image was obtained via EarthExplorer, USGS (http://earthexplorer.usgs.gov)*

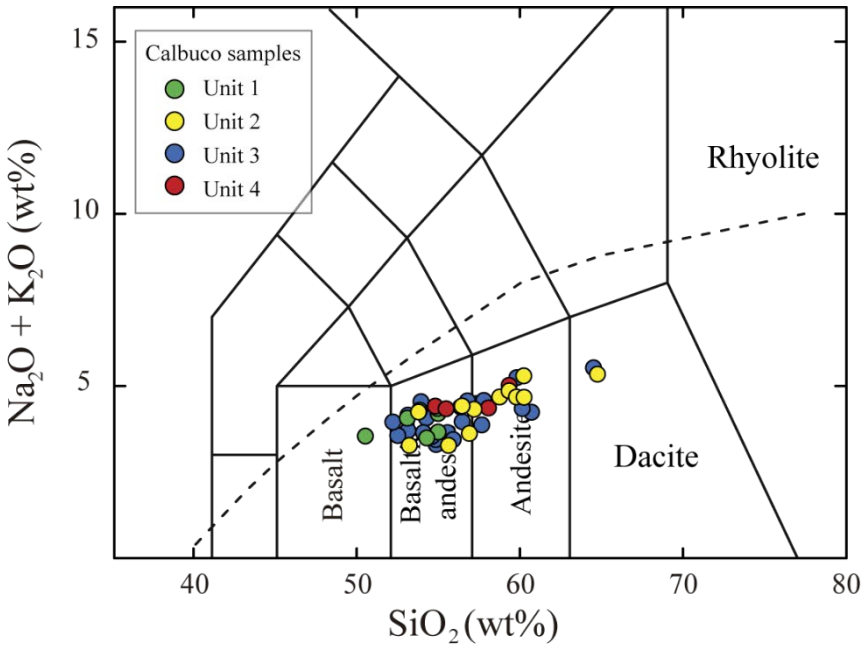

Figure 1.7. *Total alkali versus silica (Le Bas et al., 1986) plots of Calbuco products of all volcanic units. Data taken from López-Escobar et al. (1995a), Sellés and Moreno (2011), and references therein.*

During the 22–23 April 2015, two sub-Plinian eruptive events occurred at Calbuco volcano (Fig. 1.8). The first eruptive pulse started on 22 April at 20:50 UTC, it lasted two hours and, five hours after the end of the first eruptive pulse (Valderrama et al., 2015), the second pulse started at 4:00 UTC and it lasted six hours (SERNAGEOMIN 2015a, b, c, d). Valderrama et al. (2015) reported precursory activity occurring between 1 January and 21 April 2015. 142 volcano-tectonic events (VT, associated with fracturing of the wall rock) and five long-period events (LP, associated with the collapse of gas bubbles in rising magma or fluid movement). During 22 April, SERNAGEOMIN (2015e) reported a seismic swarm of 140 VT starting 3 h before the eruption onset and also the first LP events of the day occurred at 19:34 UTC (1.5 h before the eruption onset, SERNAGEOMIN 2015f).

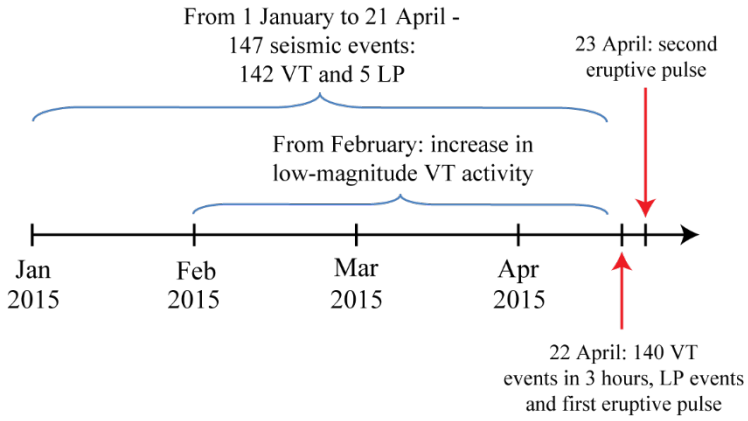

Figure 1.8. *Schematic timeline of the sequence of seismic activity before the 22-23 April 2015 Calbuco eruption.*

Although a lack of significant deformation was reported, Delgado et al. (2017) documented syn-eruptive deflation via interferometric synthetic-aperture radar (InSAR) during the first eruptive pulse, which agrees with the tiltmeter information (Valderrama et al., 2015). There are articles suggesting the location (8–11 km depth) and shape (prolate spheroid) of the reservoir beneath Calbuco (Delgado et al., 2017; Nikhoo et al., 2017) using InSAR to constrain this geometry. In consequence, there is a lack of information related to physical intensive conditions and triggering mechanisms of the April 2015 eruption from a petrological point of view.

The April 2015 Calbuco (Fig. 1.9) eruption is an excellent opportunity to study magmatic physical intensive conditions and magmatic timescales to be compared with the geophysical studies (tiltmeter, seismometer, InSAR). In addition, as Calbuco is not considered to be related to any alignments or LOFZ, it is not a member of any group described by theoretical model of Cembrano and Lara (2009), which can be used to compare with other volcanoes located in other geological settings (such as, Puyehue-Cordón Caulle, Lara et al., 2006; Villarrica, Hickey-Vargas et al., 1989; Moreno and Clavero, 2006).

Figure 1.9. *Picture of Calbuco volcano during the first eruptive pulse of the April 2015 sub-Plinian eruption (picture courtesy of Marcela Vollmer).*

1.4. Why study the 1835 Osorno eruption?

Osorno (41º06`S, 72º20`W, CSVZ) is a Mid-Pleistocene composite stratovolcano (Moreno et al., 2010) situated ~13 km west of the LOFZ and ~20 km NNE of Calbuco volcano. Osorno volcano is the southernmost member of an NE volcano alignment including Osorno, La Picada, Puntiagudo, and Cordón Cenizos volcanic chain (Fig. 1.6). In general, its postglacial activity (~ 12,000 years BP; Clapperton, 1993) has been confined to summit crater eruptions, but parasitic cones and dacitic domes are also significant modes of activity (Moreno et al., 2010). The Osorno products have been classified (Moreno, 1974; Moreno et al., 1979) into four geological units, three of them pre-historic (units Osorno 1, 2, and 3) and one historical

unit, Osorno 4. Erupted material compositions can be seen as represented in the figure 1.10. The last eruption of Osorno volcano occurred in 1835.

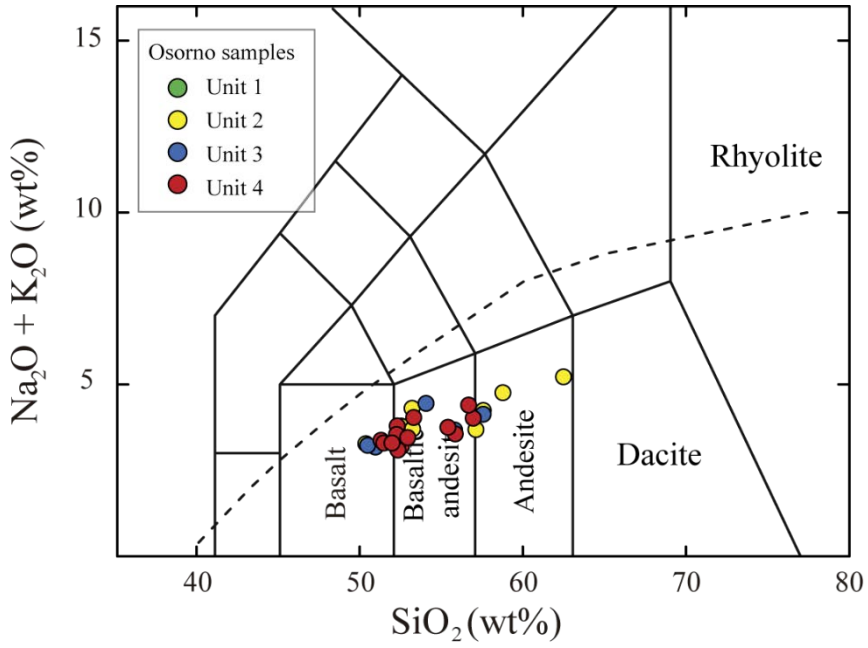

Figure 1.10. *Total alkali versus silica (Le Bas et al., 1986) plots of Osorno products of all volcanic units. Data taken from Tagiri et al. (1993) and Moreno et al. (2010).*

Charles Darwin (1839a; 1840) described two eruption stages of Osorno volcano during 1835 (Fig. 1.11). He described a "smoke" release in November 1834 (Darwin, 1839b), but the first stage of the 1835 Osorno eruption started on 19 January and it was still erupting on 18 February, two days before the earthquake of Concepción (M_w 8.0-8.3; Watt et al., 2009) that affected much of Southern Chile (Darwin, 1840). According to Darwin (1840), a second stage of eruptive activity occurred starting on 11 November 1835, resuming lava emission from the same vents as the first stage (Lara et al., 2012). During 5 December a fissure eruption occurred and for succeeding fortnight, ashes were erupted (Darwin, 1840). The 5 January 1836, the volcano was still erupting (Gillis, 1855).

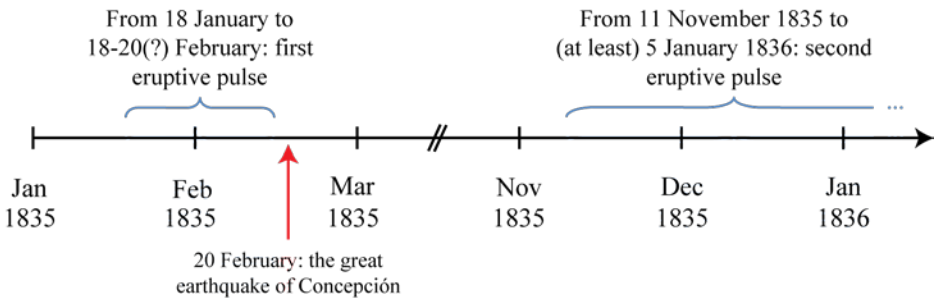

Figure 1.11. *Schematic timeline of the sequence of the 1835 Osorno eruptive activity before the 22-23 April 2015 eruption.*

The 1835 Osorno eruption is an opportunity to study the typical volcanic products of the Unit 4, which have a SiO_2 wt% range of 51.3–56.9 (including the 1835 eruption) and the same mineral assemblage: plagioclase, olivine, and clinopyroxene (Tagiri et al., 1993; López-Escobar et al., 1995b; Moreno et al., 2010). Before the 1835 eruption, the eruptive frequency was ~30 years, but Osorno volcano has not erupted since then. Since 2016, Osorno volcano has shown seismic activity over the base level (including LP events) and, during 2018, a period of seven months of yellow alert was announced by OVDAS-SERNAGEOMIN (Fig. 1.12). This recent activity highlights the need for having pre-eruptive information on the last Osorno eruption, which occurred before the volcano monitoring was established around Osorno. Although the reports of these volcano-tectonic events recognise a shallow seismic source at 2.6–3.9 km depth, it is not clear it corresponds to a magma reservoir (SERNAGEOMIN, 2017; 2018a, b; 2019).

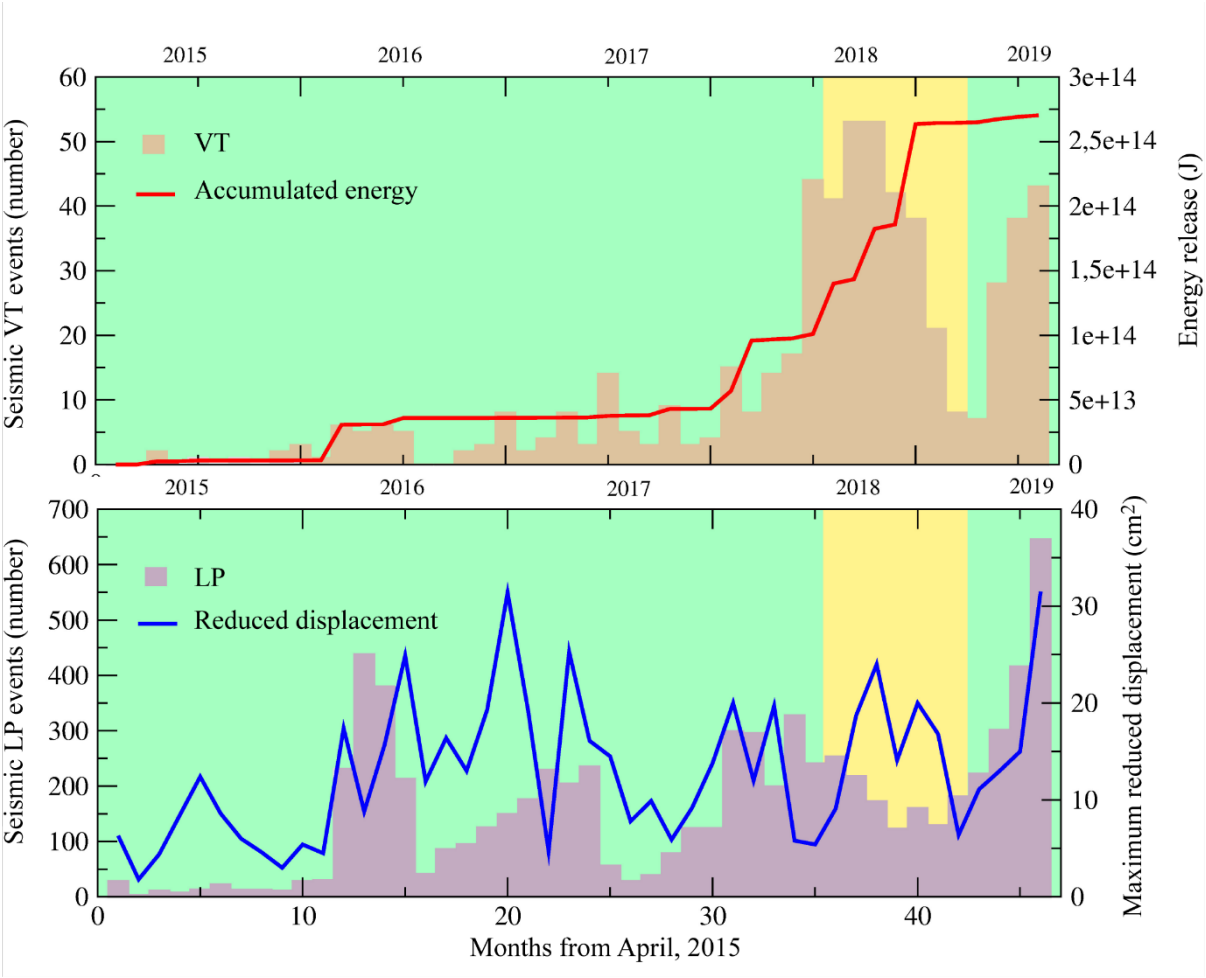

Figure 1.12. *Summary of the seismic activity detected beneath Osorno volcano in the period from April 2015 to February 2019. An increase of volcano-tectonic (VT) activity has been recorded since 2016. LP represents long-period events. Background colour represents the alert level of the region. A period of yellow alert of around seven months was announced during 2018 (Image modified from the reports of OVDAS-SERNAGEOMIN, 2019).*

1.5. Crystal mush paradigm

The crystal mush paradigm has transformed our understanding of how conventional models of crustal magmatic reservoirs are understood (e.g. Cashman and Giordano, 2014; Jackson et al., 2019; Lissenberg et al., 2019). The conventional model considered melt was the phase dominating the modal proportion within magma chambers (cf. Bachmann and Bergantz, 2004; Hildreth, 2004). Textural features and geochemical evidence indicate that voluminous silicic magma reservoirs are controlled by fractional crystallisation processes leading higher

crystal contents (e.g. Hildreth, 1981; 2004; Bacon and Druitt, 1988; Marsh, 1996; Bachmann and Bergantz, 2003).

According to the mush paradigm (Fig. 1.13), within the continental crust, magma reservoirs are considered to be represented by both *magma chambers*, these being defined as continuous, melt-rich, lenticular regions where the magma is fluid and eruptible and within which magma crystallinity is < 45 vol.%, and *crystal mushes*, i.e. a body with a rigid crystal framework and crystallinity > 45% (Marsh 1989, 1996; Hildreth 2004; Bachmann and Bergantz 2008). Crystallinities > 45 vol.% are associated with rheological properties which impede convection processes (e.g. Bachmann and Bergantz 2004, 2008; Huber et al. 2010; Burgisser and Bergantz 2011; Parmigiani et al. 2014). These reservoirs exist as shallow magma reservoirs (≤ 10 km depth) and may evolve over long cooling periods to become plutons (e.g. Koyaguchi and Kaneko 1999; Claiborne et al. 2010; Cooper and Kent 2014; Molina et al. 2015; Szymanowski et al. 2017; Cooper et al. 2017).

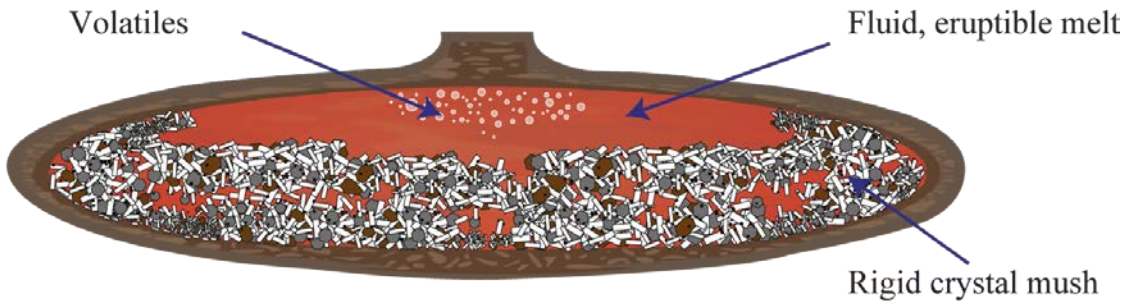

Figure 1.13. *Schematic illustration of a theoretical magma reservoir, including rigid crystal mush, fluid eruptible melt and exsolved volatiles.*

Although the existence of crystal mushes within magma reservoirs is an established paradigm for magmatic systems of felsic magmatic composition and calderas (e.g. La Picana caldera system, Chile, Lindsay et al., 2001; Fish Canyon tuff, U.S., Bachmann and Bergantz, 2003, 2004; Bishop tuff, U.S., Hildreth, 2004; Hildreth and Wilson, 2007), crystal mushes have also, in recent years, been documented in smaller and more mafic magma reservoirs (e.g.

Laki volcano, Passmore et al., 2012; Kīlauea volcano, Rae et al., 2016). In addition, beneath volcanoes of the Southern Volcanic Zone (SVZ) of the Andes, crystal-mushes have been recognised in volcanic products of widely varying compositions: Quizapu (andesitic and dacitic compositions, Ruprecht et al., 2012); Quetrupillán (trachydacite composition, Brahm et al., 2018); Llaima (basaltic andesite composition, Bouvet de Maisonneuve et al., 2012). For other active volcanoes of the SVZ (e.g. Calbuco and Osorno volcanoes) the existence (or not) of a crystal mush beneath them has to be determined, as well as the influence of that crystal mush on fractionation, mobilisation, and eruption triggering processes.

1.6. Objectives

CSVZ is the most active sub-division of the SVZ of Andean volcanism. All the active volcanoes of the CSVZ are monitored by OVDAS-SERNAGEOMIN, but some of them have not petrological studies on the historical eruptions, such as Calbuco and Osorno volcanoes. Studying the last eruptions of Calbuco (2015) and Osorno (1835) volcanoes gives an opportunity to learn about the pre-eruptive processes occurring beneath the volcanic systems from CSVZ of the Chilean Andes. The objectives of this thesis are:

1. Obtain pre-eruptive physical intensive conditions of magma (temperature, pressure, oxygen fugacity, and water content dissolved).
2. Recognise the existence or absence of a crystal mush within magma reservoirs and determine how it influences the magmatic systems.
3. Calculate magmatic timescales via diffusion modelling.
4. Generate a regional magmatic model, including slab-derived fluid supply and possible crustal contamination, at the latitude of Calbuco and Osorno volcanoes.

Finally, this petrological and geochemical model will be combined with volcano monitoring information to generate a holistic model of the studied volcanoes and pre-eruptive processes at that latitude. To achieve these objectives, the following specific tasks were carried out:

1. Collect several samples in the field (Calbuco and Osorno deposits). From those samples, thin sections were prepared, details in Chapters 2 and 4.
2. Recognise and describe magmatic textural features in Calbuco and Osorno samples in optical microscope and Scanning Electron Microscope (SEM), details in Chapters 2 and 4.
3. Obtain the chemistry of the whole-rock and the solid phases found in the volcanic products: crystals and melts. To obtain mineral chemistry we use Electron Probe Micro Analysis (EPMA), details in Chapters 2, 3, and 4.
4. Determine the equilibrium (or disequilibrium) conditions between the solid phases, details in Chapters 2, 3, and 4.
5. Calculate physical intensive conditions depending on the solid phases in equilibrium, details in Chapters 2, and 4.
6. Calculate magmatic timescales via diffusion chronometry in those solid phases exhibiting (partial or absolute) chemical disequilibrium. Study new perspectives of diffusion chronometry, details in Chapters 3, and 4.
7. Compare the physical intensive conditions and magmatic timescales with the volcano monitoring reports.
8. Assess fluid supply via major and trace elements coupled with Sr and Nd isotopic ratios from whole-rock chemistry of several volcanic systems at similar latitude (Calbuco volcano, Osorno volcano, La Picada volcano, and La Viguería monogenetic cone; Fig. 1.6).

1.7. Magmatic physical intensive variables calculation

A key concept in being able to calculate physical intensive variables (P, T, etc.) is the concept of thermodynamic equilibrium of the phases considered in a particular assemblage of crystals and melt (e.g., Aranovich and Podlesskii, 1983; Köhler and Brey, 1990; Powell and Holland, 1994; Putirka, 2008; Ghiorso and Evans, 2008). The concept of thermodynamic equilibrium is based on the definition of chemical potential. If we consider a homogeneous system with different species, where n1, n2, n3, etc. are the number of moles of those species.

Then, if we define a function G of these mole numbers in addition to entropy (S) and volume (V), so the fundamental relation must be written as (Ganguly, 2007):

$$G = G(S, V, n_1, n_2, \dots) \qquad (Eq.\ 1.1)$$

Then, the total derivative of G is then:

$$\partial G = \left(\frac{\partial G}{\partial S}\right)_{V,n_i} dS + \left(\frac{\partial G}{\partial V}\right)_{S,n_i} dV + \left(\frac{\partial G}{\partial n_1}\right)_{V,S,n_{i\neq 1}} dn_1 + \cdots \qquad (Eq.\ 1.2)$$

The partial derivative of G with respect to n_i is called the chemical potential of the component i and is represented by μ_i. Then, the bigger μ_i, the faster the energy changes with the concentration of the component *i* (Fig. 1.14).

If we consider now two homogeneous systems, which are permeable to the transfer or diffusion of one component *i* , when the chemical potentials of the two systems are the same, that system is in thermodynamic equilibrium Gibbs (1876). It means, there must be no net diffusion of component *i* through the boundary in between these two systems. Then, the various μ are uniform, and we can define partition coefficients as ratios of two values of μ. The methods developed to calculate physical intensive conditions in rock-forming mineral

assemblages and melts are calibrated under equilibrium conditions (Powell and Holland, 1994).

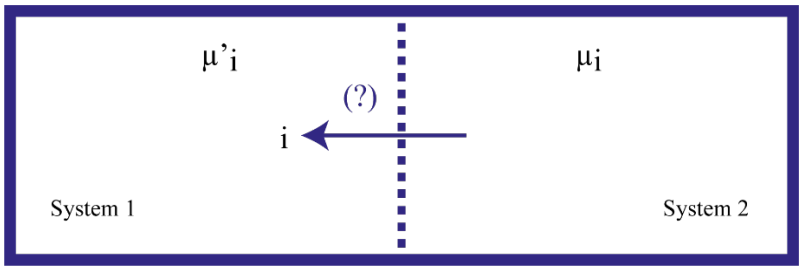

Figure 1.14. *Two systems sharing a boundary, which could allow transference of the element i. That element transfer occurs from system 2 to system 1 if* $\mu_i > \mu_i'$. *The standard consideration in igneous petrology is that if chemical potentials are equal, then partitioning is set up (Image modified from Ganguly, 2007).*

For example, the olivine-augite thermometer calibrated by Loucks (1996) is based on the equilibrium of olivine and augite regarding Fe and Mg, or $\mu_{Fe}^{olivine} = \mu_{Fe}^{augite}$ or $\mu_{Mg}^{olivine} = \mu_{Mg}^{augite}$. In other assemblages (for example systems A and B, with elements a, b, c,...), in which bulk equilibrium is considered as:

$$\mu_{a,b,c\ldots}^{A} = \mu_{a,b,c\ldots}^{B} \qquad (Eq.\,1.3)$$

In cases when the chemical potential of two (or more) systems are not equal, then there is diffusive (and usually reactive) element transfer or exchange (Lasaga, 1979; 1983; Loomis, 1983).

1.8. Diffusion chronometry

Atomic diffusion is the motion of a particle relative to the position of others in a determined region (Onsager, 1945; Watson and Baxter, 2007). An atom in a rational lattice can move to an interstitial site, exchange location with other atom, or occupy a contiguous vacant site in the lattice to move through diffusion (Borg and Dienes, 1988; Watson and Baxter, 2007). Such vacant sites are called point defects and they are formed when an ion is removed from its position in the crystal structure, then the crystal is locally charge-imbalanced, the charge is compensated by other reaction (e.g. Grove et al., 1984; Costa and Chakraborty, 2008). Intrinsic diffusion occurs when diffusion is controlled by vacancies stimulated thermally, is related to a high activation energy of diffusion, in which diffusivity depends on physical intensive variables and not on chemical potential (Borg and Dienes, 1988; Chakraborty, 2008). By contrast, extrinsic diffusion occurs at lower temperatures, when activation energies are relatively low (compared to intrinsic diffusion in specific minerals and elements) and diffusivity depends on physical intensive variables and chemical potential defines direction of diffusion (see Fig. 1.14.; Borg and Dienes, 1988; Chakraborty, 2008). There are two dominant types of intrinsic defects to keep the electroneutrality (e.g. Lasaga, 1998; Costa and Morgan, 2011; Fig. 1.15):

- Schottky defect: in different lattice-sites, there are cation and anion vacancies, they are charge-compensated, which may migrate maintaining the electric neutrality of the crystal.

- Frenkel defect: there is the same number of interstitial atoms and vacancies of one ion in the crystal. They are formed if a cation (or anion) is in an interstitial site leaving a cationic (or anionic) vacancy behind.

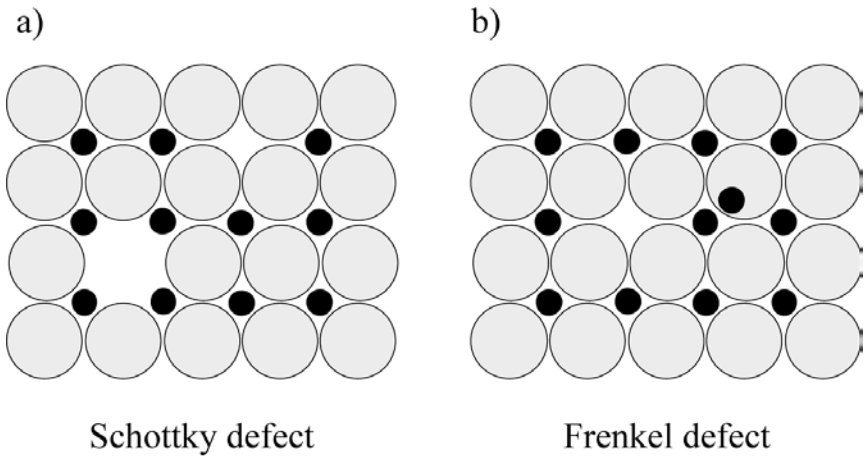

Figure 1.15. *Example of point defects in crystals. a) Schottky defects correspond to charge-compensated vacancies in different sites of the crystal and it maintains the electronic neutrality. b) Frenkel defects correspond to locate an ion in a position different from the original (usually an interstitial position), creating vacancy. Image modified from Costa and Morgan (2011).*

As a consequence of the third law of thermodynamics, it is not possible to find perfect crystals at temperatures over 0 K. A crystal with defects reduces its free energy and it is stabilised compared to a perfect, idealised crystal (Chakraborty, 2008). In addition to the vacancies considered above, point defects can also include available lattice positions, interstitial atoms (i.e., atoms which does not correspond to the lattice), and trace elements (impurities) occupying lattice positions (Borg and Dienes, 1988). The existence of point defects and the consequent existence of vacancies enabled via charge balance or structural balancing allows diffusion to occur in all solid materials (even if they occur at low temperature). Diffusion in the solid state is ubiquitous (though often almost infinitely slow at room temperature), this allows us to use it to estimate timescales of magmatic processes (Chakraborty, 2008; see Chapter 3). The existence of chemical zoning in minerals means there are significant variations in the composition, and hence the chemical potential, of a certain mineral phase. This zoning is due to substantial changes in physical intensive variables (e.g. temperature, pressure, oxygen fugacity) of the magma during crystal growth and the internal difference chemical potential homogenise the crystal composition after a

certain amount of time (e.g. Costa et al 2008; Costa and Morgan, 2011). The compositional flux depends on the gradient of the potential as well as the material in which diffusion occurs (Costa and Morgan, 2011) and is described by the Fick's first law (Equation 1.4):

$$J = -D_i^a \frac{\partial C}{\partial x} \qquad (Eq.\ 1.4)$$

where J is the flux (mol $m^{-2}\ s^{-1}$), D is the diffusivity of the phase "*a*" and the element "*i*", C is the concentration of the studied element "*i*", and x is distance.

There are three scenarios for elemental diffusion in minerals and their related timescales (Chakraborty, 2008; Costa et al 2008): (1) the timescale is relatively short and there is no distinguishable evolution of the system, (2) the degree of evolution of the system is time-dependent and it could be used to determine timescales, and (3) the timescales is too long, then the system has reached equilibrium and it is no longer time-dependent (Fig. 1.16). In the second case, we can establish a link between diffusive processes and timescales via the diffusion equations (Borg and Dienes, 1988). The approach which describes this connection is the one dimension diffusion time-dependent equation, known as Fick's second law (Equation 1.5):

$$\frac{\partial C_i(x,t)}{\partial t} = \frac{\partial}{\partial x}\left(D_i^a \frac{\partial C(c,t)}{\partial x}\right) \qquad (Eq.\ 1.5)$$

where C is concentration of the studied element "*i*", t is time, *x* is distance, and D is the diffusivity of the phase "*a*" and the element "*i*".

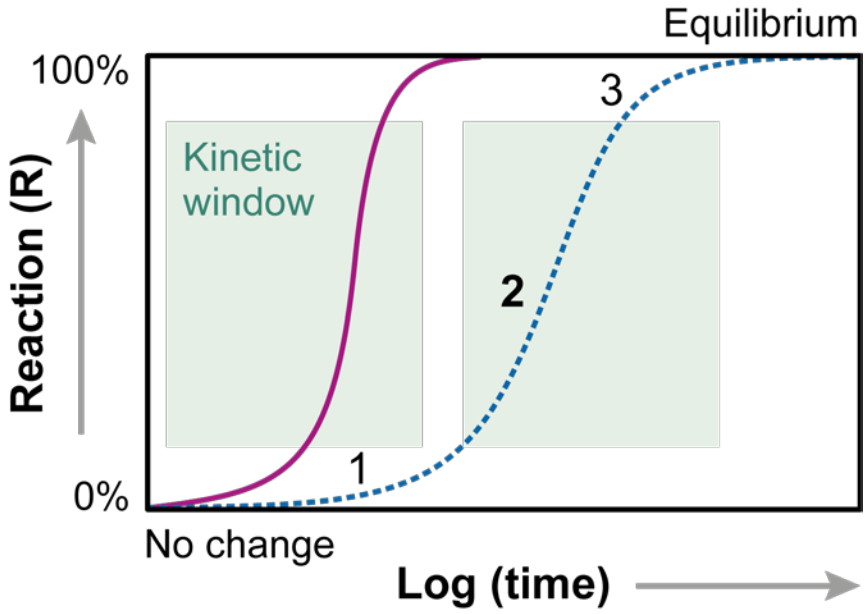

Figure 1.16. *A diagram to illustrate the evolution of a system from a first state (reaction, R=0%), which changes together with a reaction and depending on time, to an equilibrium state (reaction, R=100%). Each curve represents different diffusivities (directly related to the kinetics of the reaction), which is decreasing from the purple solid line (which reach the equilibrium state in a shorter timescale) to the blue dashed-line (which reach the equilibrium state in a longer timescale). The number represent the three scenarios for elemental diffusion: 1) Short timescale, no distinguishable evolution. 2) The system could be used to determine timescales. 3) The system reached the equilibrium or a largely-equilibrated state. Image modified from Chakraborty (2008).*

Diffusion chronometry can yield a wide range of timescales, from few days to years, depending on the mineral phase and the elements studied (e.g. Devine et al. 2003; Morgan et al. 2004; Turner and Costa, 2007; Costa and Morgan, 2011; Morgado et al. 2017).

1.9. Electron microscopy and microprobe analysis

1.9.1. Scanning electron microscope (SEM)

Scanning electron microscopes (SEMs) are used for imaging (secondary backscatter electrons) and determination of solid phase (minerals and glasses). The SEM (Fig. 1.17) is based on electron bombardment of solid materials and is composed of a filament to provide and stable beam of electron, condenser lenses and apertures to focus the beam, and detectors for electrons emitted from the studied specimen (Fig.1.17).

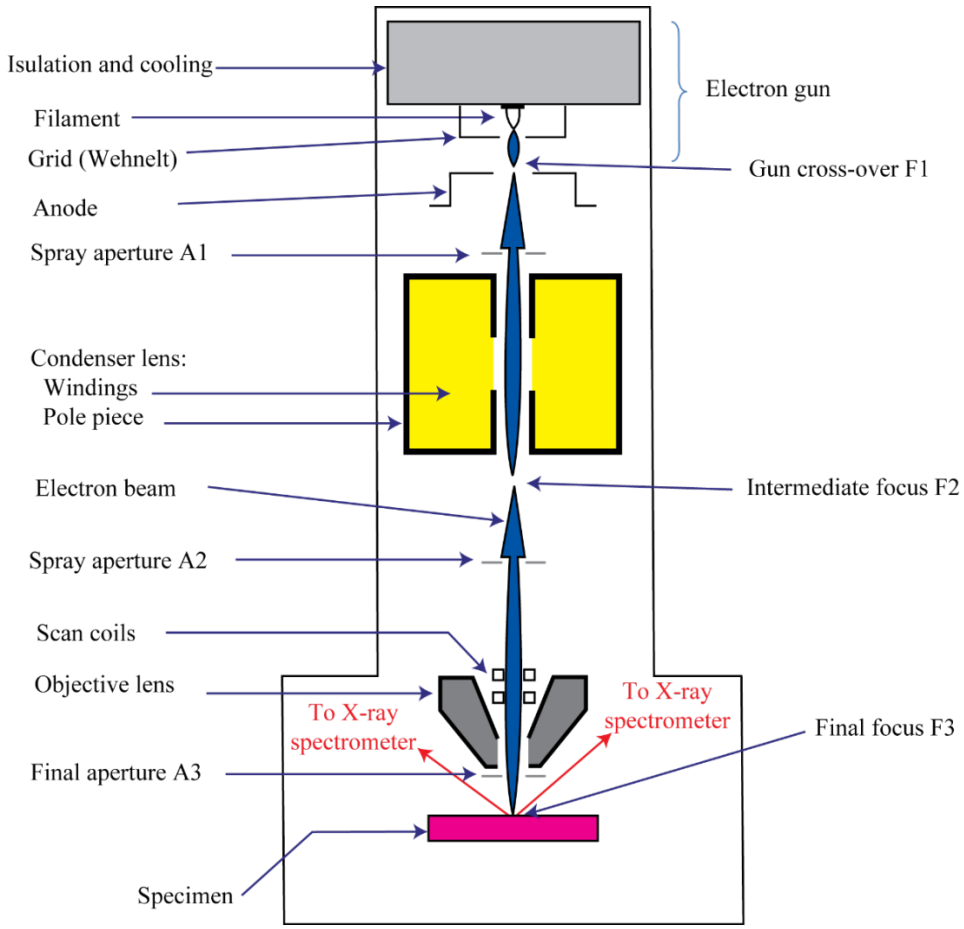

Figure 1.17. *Schematic cross-section of a typical Electron MicroProbe column. The electron gun is at the top of the instrument and the studied bombarded specimen is at the bottom (Modified from Gill, 1997).*

1.9.2. Secondary and backscattered electrons

When an electron beam strikes solid materials, the electrons are slowed mainly by inelastic interactions with atomic electrons. There is a probability of an incident electron being deflected by an angle greater than 90º and emerge from the surface of the target. Electrons can also emerge through multiple deflections of smaller angle (Fig. 1.18; Reed, 1975; 2005). The fraction of incident electrons emerging from the surface in this way is known as backscattering coefficient (η) and is strongly dependent on atomic number. With increasing Z leading to an increase in the probability of high angle deflection (Fig. 1.19), but it is independent from the incident electron energy.

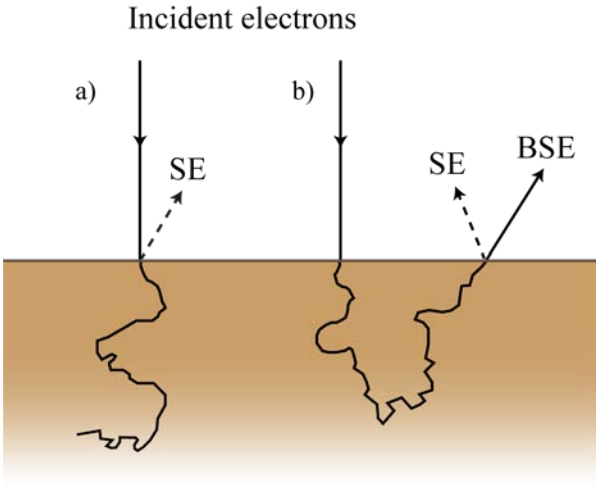

Figure 1.18. *Schematic image representing how secondary and backscattered electrons are ejected from the solid material. Figure a) shows incident electrons producing secondary electrons, figure b) represents how backscattered electrons are produced and how they can produce secondary electrons (Image modified from Reed, 2005).*

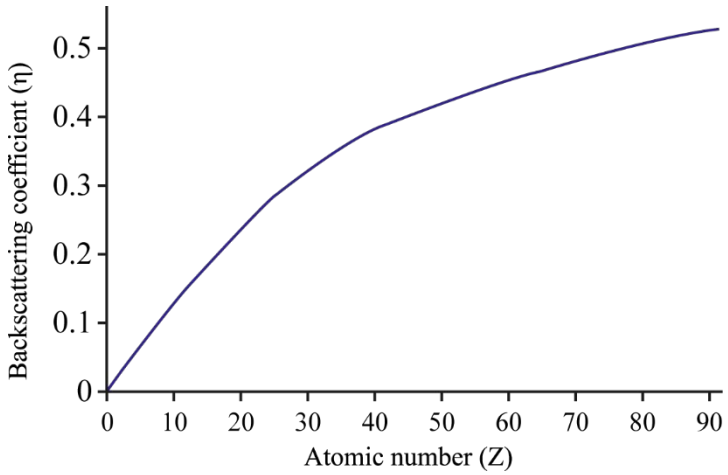

Figure 1.19. *Backscattering coefficient (η) versus atomic number (Image modified from Reed, 1975).*

The energy of the backscattered electrons are relatively high and it allows to create greyscales images representing densities (Fig. 1.20), which are very useful as a proxy of composition and to observe mineral textures (Reed, 2005).

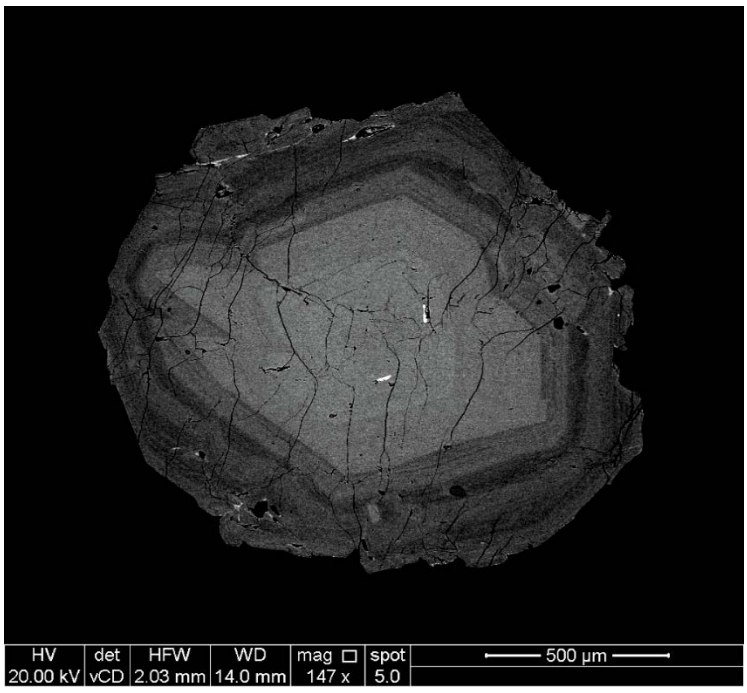

Figure 1.20. *Backscatter electron (BSE) image of a plagioclase crystal from a 2015 Calbuco eruption product. Greyscale false-colours represent density variations within the grain: brighter colours (at the core of the grain) represent higher density than outer parts of the grain, represented darker tones. Black sections represent vesicles and cracks (minimum density of the picture).*

Other electrons, which are ejected at relatively lower energy are called secondary electrons, they can be released due to both incident and backscattered electrons (Fig. 1.18). Because of their low energy, the only electrons that can leave the solid material are those within a few nanometres from the surface. The number of ejected secondary electrons produced per incident electron is known as secondary electron coefficient (δ), which does not depend on the atomic number (Reed, 1975). The emitted signals allow to create images representing surface topography (Fig. 1.21). After electron bombardment, another consequence is the emission of X-rays, which are produced via two different mechanisms: the continuous X-ray spectrum and characteristic X-ray spectra.

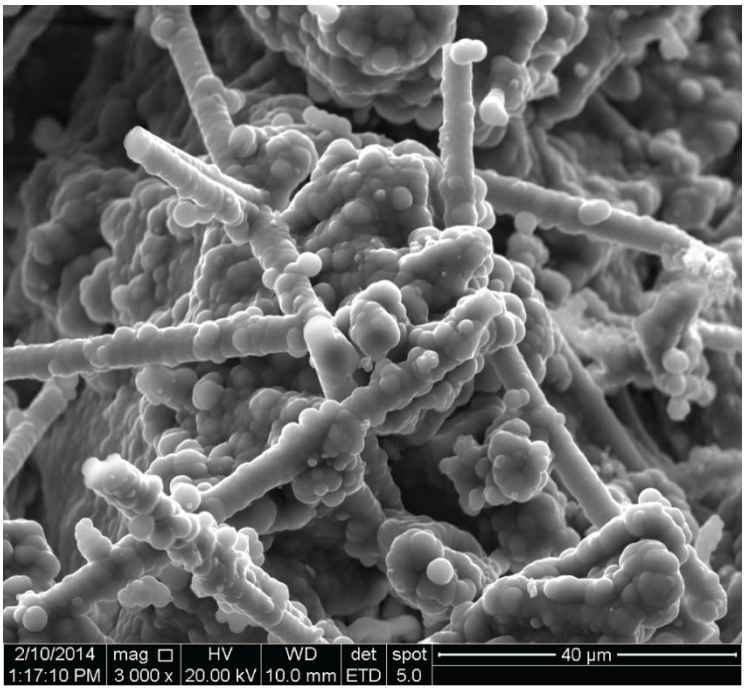

Figure 1.21. *Secondary electron image showing morphology and microtextures of Opal A from Puchuldiza geothermal field, Chile (Image courtesy of Camilo Sánchez-Yáñez).*

1.9.3. X-ray spectra: continuous and characteristic

Continuous X-ray spectrum

Continuous X-ray spectrum. When an electron passes through an electric field and it is close to an atomic nucleus, can be deflected from its original path and its energy decreases. As a consequence, an X-ray photon is emitted with maximum energy equals to the initial electron energy. The result is a continuous X-ray spectrum (Fig. 1.22), usually called Bremsstrahlung curve, which limits the detectability of the characteristic lines of the elements existent.

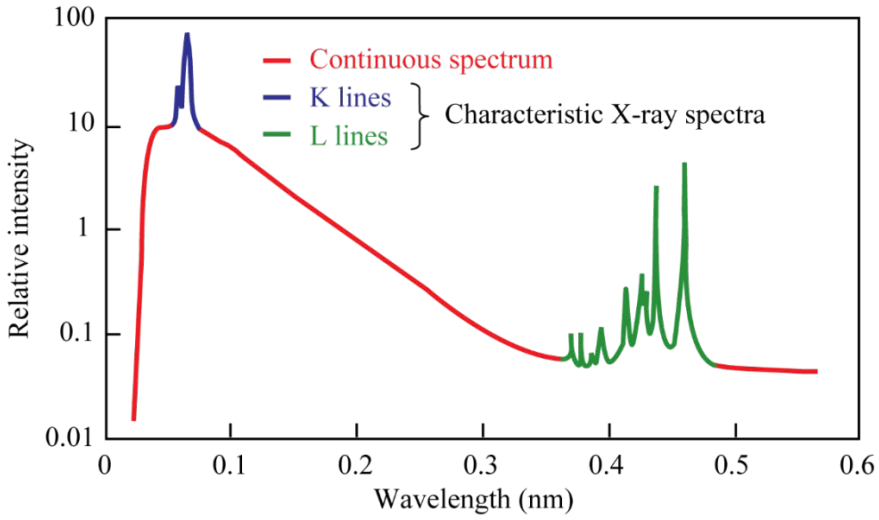

Figure 1.22. *Example of X-ray spectra showing characteristic lines and the continuous X-ray spectrum superimposed. The energy decreases when wavelength increases, then K lines are related to higher energy than L lines (modified from Gill, 1997).*

Characteristic X-ray spectra

In the case of characteristic X-rays, X-rays are generated by the release of energy when an electron decays from an outer shell to an inner shell of an ion's electron orbitals. These have a defined set of energies, as a function of the charge, ionic radius and electronic configuration of the ion (Fig. 1.22). This transition follows after an electron bombardment, which could release an internal electron. Inner orbits are designated K (energy level = 1), L (energy level = 2), M (energy level = 3), etc. increasing the distance from the nucleus (Fig. 1.23) and also

decreasing energy (e.g., Bertin, 1975, Goldstein et al., 1975; Reed, 1975; Reed, 2005). The constituent elements and their concentrations maybe identified (see Fig. 1.22).

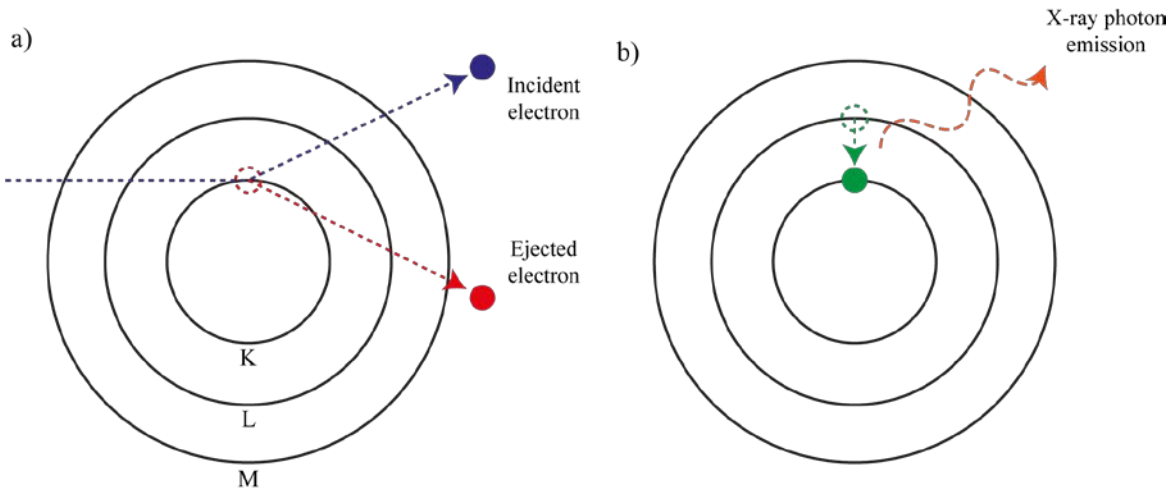

Figure 1.23. *Schematic diagram of inner atomic electron energy levels. In a) is represented an incident electron ejecting other from an inner orbit. Characteristic X-rays is shown in b), generated by electron transitions between these energy levels (Image modified from Reed, 1975).*

Energy dispersive X-ray spectrometers (EDS) are usually attached to SEMs. The X-ray electromagnetic emission spectrum of energy emitted is characteristic for any single element and it allows to get a qualitative analysis rapidly, producing a plot of intensity versus X-ray photon energy (Fig. 1.22). In the charts given by the SEM, the X-ray continuous spectrum (Bremsstrahlung curve) is subtracted, allowing to see only characteristic spectra (Fig. 1.24). The objective of EDS is to find out the elements present in any mineral phases, very often it allows mineral recognition.

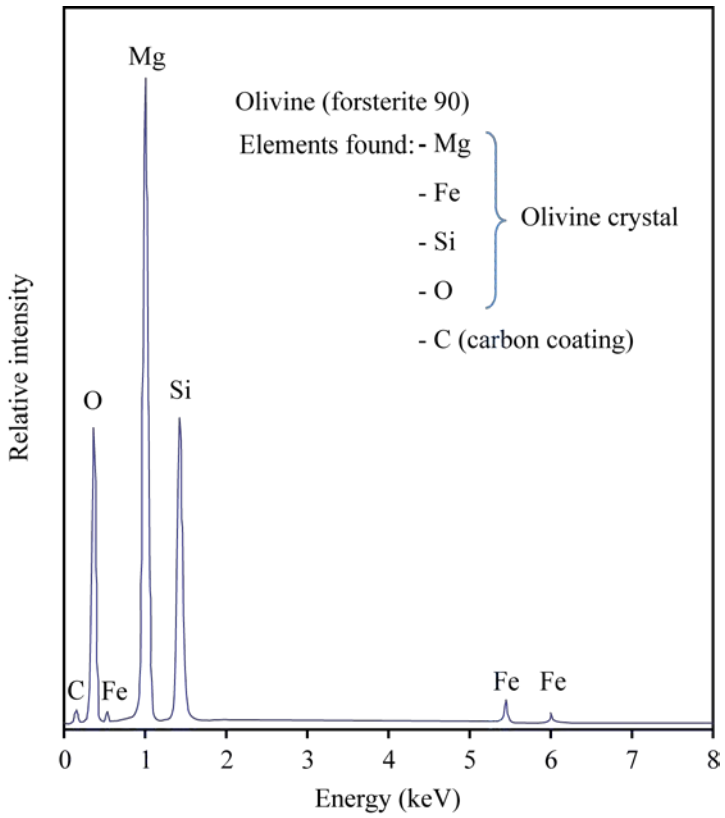

Figure 1.24. *Typical energy dispersive X-ray spectrum for an olivine grain (forsterite 90). The peaks of Mg, Fe, Si, and O correspond to the measured olivine grain, whereas the C correspond to the carbon coating, which is usually covering the mineral surface enabling or improving imaging of samples.*

EPMA works similarly to SEM, based on electron bombardment, but the latter have several crystals of wavelength dispersive spectrometers (WDS) fitted and together with EDS are usually attached allowing full quantitative analyses. WDS uses Bragg reflection by crystals in an attached spectrometer, which is calibrated with one wavelength (Fig. 1.25). The WDS and secondary standards (solids of known composition) are normally attached to EPMA and used for quantitative analyses (e.g., Wittry, 1962; Smith, 1965; Sweatman and Long, 1969). In a focusing spectrometer the X-ray source, the diffracting crystal and the detector lie on the hypothetical circumference called the Rowland circle (Fig. 1.25).

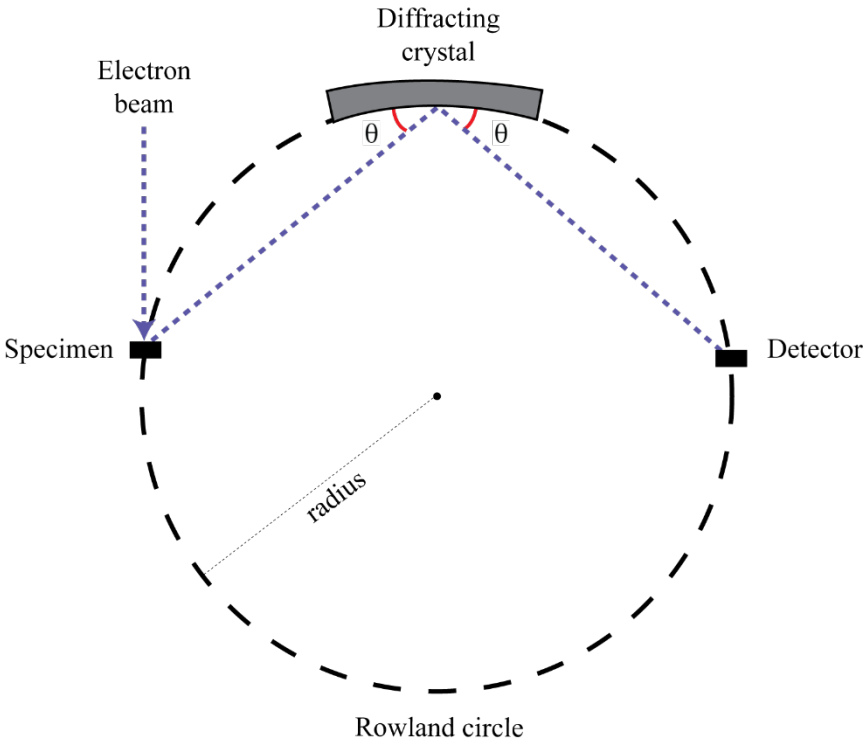

Figure 1.25. *Rowland circle geometry, a constant Bragg angle is obtained when the specimen, diffracting crystal, and detector lie on a circumference. Image modified from Reed (1975).*

The X-rays emitted from the specimen (as a consequence of electron bombardment) go to a diffracting crystal, composed of consecutive atomic layers separated by interplanar spacing. The difference between X-ray path length before (ABC) and after reflection by the diffracting crystal (A'B'C') to determined wavelength works as a filter of wavelengths (Fig. 1.26) depending on the distance between the interplanar spacing (atomic layers separated by a distance "d", Fig. 1.26) of the diffracting crystal in certain angle of incidence and reflection (Bragg's angle). This relation is given by Bragg's law, according to the following equation 1.6:

$$n\lambda = 2d\sin(\theta) \qquad (Eq.\,1.6)$$

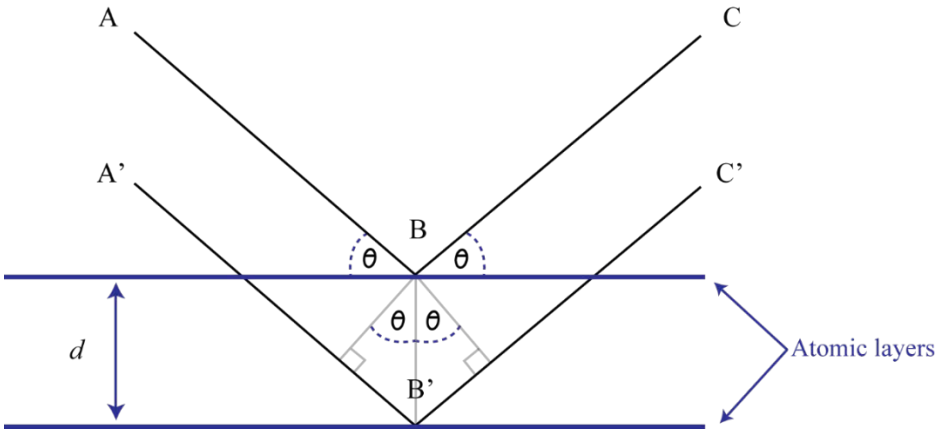

Figure 1.26. *Representation of Bragg reflection. Diffracted rays are in phase if distance A'B'C' differs from ABC by an integer number of wavelengths (modified from Reed, 1975).*

where *n* is the order of reflection (always an integer number), λ is wavelength, d is the interplanar spacing. Only the most intense reflections are used for WDS analysis, which are related to n=1 (i.e. first order of reflection). If the reflection is equals to one, the wavelength range is restricted, in consequence, diffracting crystals with different interplanar spacing values in order to cover the whole range of wavelengths of interest (Table 1.3; Fig. 1.27).

Table 1.3. Crystals used in WDS.*

Crystal name	2d (A)
LiF	4.026
PET	8.742
TAP	25.9

* Reed, 1975

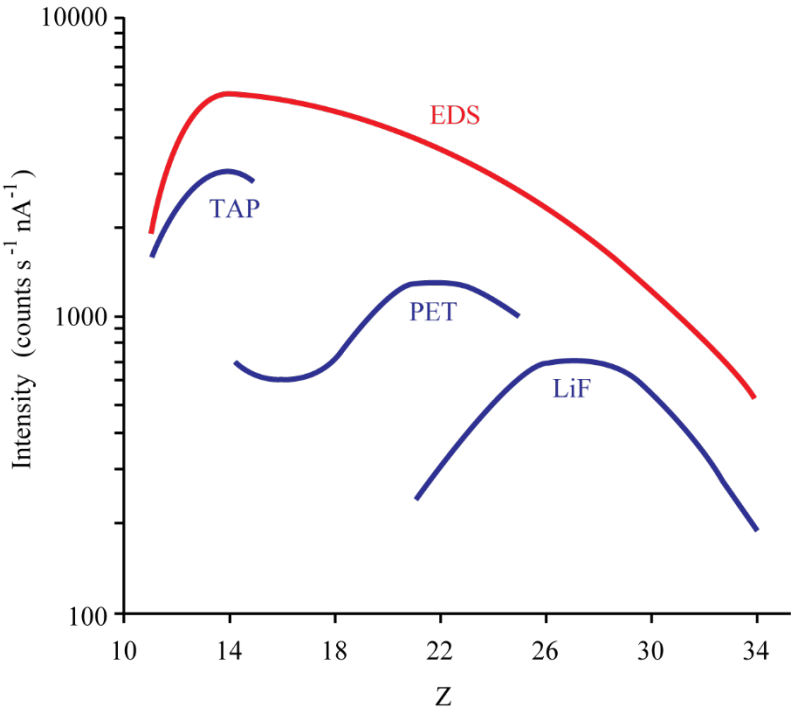

Figure 1.27. *Intensities of Kα line for pure elements (represented by the atomic number, Z) as recorded by an ED spectrometer and WD spectrometer with different crystals (TAP, PET, and LiF) at accelerating voltage of 20kV (Image modified from Reed, 1975).*

1.10. References

Bachmann, O, Bergantz, GW (2003) Rejuvenation of the Fish Canyon magma body: A window into the evolution of large-volume silicic magma systems. Geology 31(9): 789-792.

Bachmann, O, Bergantz, GW (2004) On the Origin of Crystal-poor Rhyolites: Extracted from a Batholithic Crystal Mushes. J Petrol 45(8), 1565-1582.

Bachmann, O, Bergantz, G (2008). The magma reservoirs that feed supereruptions. Elements, 4(1), 17-21. https://doi.org/10.2113/GSELEMENTS.4.1.17

Bacon, CR, Druitt, TH (1988) Compositional evolution of the zoned calcalkaline magma chamber of Mount Mazama, Crater Lake, Oregon. Contrib Mineral Petrol 98(2): 224-256.

Bertin, EP (1975) Principles and Practice of X-ray Spectrometric Analysis. Plenum Press, New York.

Borg, RJ, Dienes GJ (1988) An Introduction to Solid State Diffusion. Academic Press.

Bouvet De Maisonneuve, C, Dungan, MA, Bachmann, O, Burgisser, A (2012) Insights into shallow magma storage and crystallization at Volcán Llaima (Andean southern volcanic zone, Chile). J Volcanol Geot Res 211: 76-91.

Brahm, R, Parada, MA, Morgado, E, Contreras, C, McGee, L (2018) Origin of trachyte lavas of the Quetrupillán Volcanic Complex, Chile (39º30'S): Examples of residual melts in rejuvenated crystalline mush reservoir. J Volcanol Geotherm Res 357, 163-176. http://doi.org/10.1016/j.jvolgeores.2018.04.020

Burgisser, A, Bergantz, GW (2011) A rapid mechanism to remobilize and homogenize highly crystalline magma bodies. Nature, 471, 212-216. http://dx.doi.org/10.1038/nature09799

Cashman, KV, Giordano, G (2014) Calderas and magma reservoirs. J Volcanol Geoth Res 288: 28-45.

Castruccio, A, Clavero, J, Rivera, A (2010) Comparative study of lahars generated by the 1961 and 1971 eruptions of Calbuco and Villarrica volcanoes, Southern Andes of Chile. J Volcanol Geotherm Res 190(3–4), 297–311. http://doi.org/10.1016/j.jvolgeores.2009.12.005

Castruccio, A, Clavero, J, Segura, A, Samaniego, P, Roche, O, Le Pennec, J, Droguett, B (2016). Eruptive parameters and dynamics of the April 2015 sub-Plinian eruptions of Calbuco volcano (Southern Chile). Bull Volcanol 327: 469-483. http://dx.doi.org/10.1007/s00445-016-1058-8

Cembrano, J, Hervé, F, Lavenu, A (1996) The Liquiñe Ofqui fault zone: a long-lived intra-arc fault system in southern Chile. Tectonophysics 259(1-3): 55-66.

Cembrano, J, Lara, L (2009) The link between volcanism and tectonics in the southern volcanic zone of the Chilean Andes: a review. Tectonophysics 471(1-2): 96-113.

Cembrano, J., Schermer, E., Lavenu, A., Sanhueza, A. (2000). Contrasting nature of deformation along an intra-arc shear zone, the Liquiñe–Ofqui fault zone, southern Chilean Andes. Tectonophysics 319(2): 129-149.

Censo Chile, Instituto Nacional de Estadísticas (2017) http://www.censo2017.cl Accessed March 2019.

Chakraborty, S (2008). Diffusion in solid silicates: a tool to track timescales of processes comes of age. Annu Rev Earth Pl Sc 36: 153-190.

Claiborne, LL, Miller, CF, Flanagan, DM, Clynne, MA, Wooden, JL (2010) Zircon reveals protracted magma storage and recycling beneath Mount St. Helens. Geology 38(11), 1011-1014. https://doi.org/10.1130/G31285.1

Cooper, GF, Morgan, DJ, Wilson, CJ (2017). Rapid assembly and rejuvenation of a large silicic magmatic system: Insights from mineral diffusive profiles in the Kidnappers and Rocky Hill deposits, New Zealand. Earth Planet Sc Lett, 473, 1-13. https://doi.org/10.1016/j.epsl.2017.05.036

Cooper, KM, Kent, AJ (2014). Rapid remobilization of magmatic crystals kept in cold storage. Nature, 506(7489), 480. https://doi.org/10.1038/nature12991

Costa, F, Chakraborty, S (2008) The effect of water on Si and O diffusion rates in olivine and implications for transport properties and processes in the upper mantle. Phys Earth Planet Inter 166(1-2): 11-29.

Costa, F Dungan, M (2005). Short time scales of magmatic assimilation from diffusion modeling of multiple elements in olivine. Geology 33(10): 837-840.

Costa, F, Morgan, D (2011). Time constraints from chemical equilibration in magmatic crystals. Timescales of magmatic processes: from core to atmosphere. Wiley, Chichester: 125-159.

Costa, F, Dohmen, R, Chakraborty, S (2008) Time scales of magmatic processes from modeling the zoning patterns of crystals. Rev Mineral Geochem 69(1): 545-594.

Darwin, CR (1839a) Journal of Researches into the Geology and Natural History of the various countries visited by H.H.S. Beagle. London: Henry Colburn, 629 p.

Daga, R, Ribeiro Guevara, S, Poire, DG, Arribére, M (2014) Characterization of tephras dispersed by the recent eruptions of volcanoes Calbuco (1961), Chaitén (2008) and Cordón Caulle Complex (1960 and 2011), in Northern Patagonia. J S Am Earth Sci *49*, 1–14. http://doi.org/10.1016/j.jsames.2013.10.006

Clapperton, C (1993) Quaternary geology and geomorphology of South America. Elsevier Science Publishers, Amsterdam.

Darwin, CR (1839b) Narrative of the surveying voyages of His Majesty's Ships Adventure and Beagle between the years 1826 and 1836, describing their examination of the southern shores of South America, and the Beagle's circumnavigation of the globe. Journal and remarks. 1832-1836. London: Henry Colburn.

Darwin, CR (1840) On the connexion of certain volcanic phenomena in South America; and on the formation of mountain chains and volcanos, as the effect of the same powers by which continents are elevated. Transactions of the Geological Society of London 5 (3), 601-631.

Delgado, F, Pritchard, ME, Ebmeier, S, González, P, Lara, L (2017) Recent unrest (2002-2015) imaged by space geodesy at the highest risk Chilean volcanoes: Villarrica, Llaima, and Calbuco (Southern Andes). J Volcanol Geotherm Res 344, 270-288.

Devine, JD, Rutherford, MJ, Norton, GE, Young, SR (2003) Magma storage region processes inferred from geochemistry of Fe–Ti oxides in andesitic magma, Soufriere Hills Volcano, Montserrat, WI. J Petrol 44(8): 1375-1400.

Donovan, A, Eiser, JR, Sparks, RSJ (2017) Expert opinion and probabilistic volcanic risk assessment. J Risk Res 20(6): 693-710.

Gill, R (1997) Modern Analytical Geochemistry: an introduction to quantitative chemical analysis techniques for Earth, environmental and materials scientists. Routledge.

Goldstein, J, Newbury, D, Joy, D, Lyman, C, Echlin PEL, Sawyer, L, Michael J (2003) Scanning electron microscopy and X-ray microanalysis. New York Springer.

Grove, TL, Baker, MB, Kinzler, RJ (1984) Coupled CaAl-NaSi diffusion in plagioclase feldspar: Experiments and applications to cooling rate speedometry. Geochim Cosmochim Acta 48(10): 2113-2121.

Gudmundsson, G (2011) Respiratory health effects of volcanic ash with special reference to Iceland. A review. Clin Respir J 5(1): 2-9.

Hall, M, Ramón, P, Mothes, P, LePennec, JL, Garcia, A, Samaniego, P, Yepes, H (2004). Rev Geol Chile 31(2): 349-358.

Hickey-Vargas, R, Abdollahi, MJ, Parada, MÁ, López-Escobar, L, Frey, FA (1995) Crustal xenoliths from Calbuco Volcano, Andean Southern Volcanic Zone: implications for crustal composition and magma-crust interaction Contrib Mineral Petrol 119(4), 331-344.

Hickey-Vargas, R, Moreno, H, Escobar, LL, Frey, FA (1989) Geochemical variations in Andean basaltic and silicic lavas from the Villarrica-Lanin volcanic chain (39.5 S): an evaluation of source heterogeneity, fractional crystallization and crustal assimilation. Contrib Mineral Petrol 103(3): 361-386.

Hildreth, W (1981) Gradients in silicic magma chambers: implications for lithospheric magmatism. J Geophys Res: Solid Earth 86(B11): 10153-10192.

Hildreth, W (2004) Volcanological perspectives on Long Valley, Mammoth Mountain, and Mono Craters: several contiguous but discrete systems. J Volcanol Geotherm Res 136(3), 169-198. https://doi.org/10.1016/j.jvolgeores.2004.05.019

Hildreth, W., & Wilson, C. J. (2007). Compositional zoning of the Bishop Tuff. J Petrol 48(5): 951-999.

Huber, C, Bachmann, O, Dufek, J (2010a) The limitations of melting on the reactivation of silicic mushes. J Volcanol Geotherm Res 195(2), 97-105. https://doi.org/10.1016/j.jvolgeores.2010.06.006

Kahl, M, Chakraborty, S, Costa, F, Pompilio, M (2011) Dynamic plumbing system beneath volcanoes revealed by kinetic modeling, and the connection to monitoring data: An example from Mt. Etna. Earth Planet Sc Lett 308(1-2): 11-22.

Kahl, M, Chakraborty, S, Costa, F, Pompilio, M, Liuzzo, M, Viccaro, M (2013) Compositionally zoned crystals and real-time degassing data reveal changes in magma transfer dynamics during the 2006 summit eruptive episodes of Mt. Etna. Bull Volcanol 75(2): 692.

Koyaguchi, T, Kaneko, K (1999) A two-stage thermal evolution model of magmas in continental crust. J Petrol 40(2), 241-254. https://doi.org/10.1093/petroj/40.2.241

Jackson, MD, Blundy, J, Sparks, RSJ (2018) Chemical differentiation, cold storage and remobilization of magma in the Earth's crust. Nature 564(7736): 405.

Lara, LE (2009) The 2008 eruption of the Chaitén Volcano, Chile: a preliminary report. Andean Geology 36(1), 125-129.

Lara, LE, Lavenu, A, Cembrano, J, Rodríguez, C (2006) Structural controls of volcanism in transversal chains: resheared faults and neotectonics in the Cordón Caulle–Puyehue area (40.5 S), Southern Andes. J Volcanol Geoth Res 158(1-2): 70-86.

Lara, LE, Orozco, G, Amigo, A, Silva, C (2011). Peligros Volcánicos de Chile, Servicio Nacional de Geología y Minería, Carta Geológica de Chile, Serie Geología Ambiental.13: 34. Mapa escala 1:2.000.000. Santiago.

Lara, LE, Orozco, G, Piña-Gauthier, M (2012) The 1835 AD fissure eruption at Osorno volcano, Southern Andes: Tectonic control by the intraarc stress field instead of remote megathrust-related dynamic strain. Tectonophysics 530, 102-110.

Lasaga, AC (1998) Kinetic theory in the earth sciences. Princeton university press.

Lindsay JM, Schmidt AK, Trumbull RB, De Silva SL, Siebel W, Emmermann R (2001) Magmatic evolution of the La Pacana Caldera system, Central Andes, Chile: compositional variation of two cogenetic, large-volume felsic ignimbrites. J Petrol 42:459-486

Lissenberg, CJ, MacLeod, CJ, Bennett, EN (2019) Consequences of a crystal mush-dominated magma plumbing system: a mid-ocean ridge perspective. Philos Trans Royal Soc A 377(2139): 20180014.

López-Escobar, L, Cembrano, J, Moreno, H (1995a) Geochemistry and tectonics of the Chilean Southern Andes basaltic Quaternary volcanism (37-46º S). Rev Geol Chile 22 (2), 219-234.

López-Escobar, L, Parada, MÁ, Hickey-Vargas, R, Frey, FA, Kempton, PD, Moreno, H (1995b). Calbuco Volcano and minor eruptive centers distributed along the Liquiñe-Ofqui Fault Zone, Chile (41º-42º S): contrasting origin of andesitic and basaltic magma in the Southern Volcanic Zone of the Andes. Contrib Mineral Pet. 119:345-36. http://dx.doi.org/10.1007/BF00286934

López-Escobar, L, Parada, MÁ, Moreno, H, Frey, FA, Hickey-Vargas, RL (1992) A contribution to the petrogenesis of Osorno and Calbuco volcanoes, Southern Andes (41º00'-41º30' S): comparative study. Rev Geol Chile 19(2), 211-226.

Marsh, BD (1989) Magma chambers. Annu Rev Earth Pl Sc 17(1), 439-472. http://dx.doi.org/10.1146/annurev.ea.17.050189.002255

Marsh, BD (1996) Solidification fronts and magmatic evolution. Mineral Mag 60(1), 5-40. http://doi.org/10.1180/minmag.1996.060.398.03

Martin, VM, Morgan, DJ, Jerram, DA, Caddick, MJ, Prior, DJ, Davidson, JP (2008) Bang! Month-scale eruption triggering at Santorini volcano. Science 321(5893): 1178-1178.

Molina, PG, Parada, MÁ, Gutiérrez, FJ, Ma, C, Li, J, Yuanyuan, L, Reich, M, Aravena, Á (2015) Protracted late magmatic stage of the Caleu pluton (central Chile) as a consequence of heat redistribution by diking: Insights from zircon data and thermal modeling. Lithos 227, 255-268. https://doi.org/10.1016/j.lithos.2015.04.008

Moreno, H (1974) Airplane flight over active volcanoes central-south Chile. In Intemational Symposium on Andean and Antarctic Volcanology Problems, Intemational Association Volean and Chemistry of the Earth Interior (IAVCEI), Departamento de Geología, Universidad de Chile, Guide Book.

Moreno, H, Clavero, J (2006) Geología del volcán Villarrica, Regiones de la Araucanía y de los Lagos. Servicio Nacional de Geología y Minería. Carta Geológica de Chile, Serie Geología Básica 98(1).

Moreno, H., Lara, L., Orozco, G. (2010). Geología del volcán Osorno. Servicio Nacional de Geología y Minería, Carta Geológica de Chile, Serie Geológica Básica, No. 126, Mapa escala 1:50000.

Moreno, H, Naranjo, JA, Clavero, J (2006). Generación de lahares calientes en el volcán Calbuco, Andes del sur de Chile (41,3ºS). In Congreso Geológico Chileno, no. 11, actas 512-513, Antofagasta.

Moreno, H, Naranjo, JA, López-Escobar, L (1979) Geología y Petrología de la cadena volcánica OsornoPuntiagudo, Andes del Sur, Latitud 41°-10'S. In Congreso Geológico Chileno, No. 2, Actas, Vol. 3: El 09- E131. Arica.

Morgado, E, Parada, MÁ, Morgan, DJ, Gutiérrez, F, Castruccio, A, Contreras, C (2017) Transient shallow reservoirs beneath small eruptive centres: Constraints from Mg-Fe interdiffusion in olivine. J Volcanol Geotherm Res 347: 327-336.

Morgan, DJ, Blake, S, Rogers, NW, DeVivo, B, Rolandi, G, Macdonald, R, Hawkesworth, CJ (2004) Time scales of crystal residence and magma chamber volume from modelling of diffusion profiles in phenocrysts: Vesuvius 1944. Earth Planet Sc Lett 222(3-4): 933-946.

Nakamura, M (1995) Residence time and crystallization history of nickeliferous olivine phenocrysts from the northern Yatsugatake volcanoes, Central Japan: Application of a growth and diffusion model in the system Mg-Fe-Ni. J Volcanol Geotherm Res 66(1-4): 81-100.

Nikkhoo, M, Walter, TR, Lundgren, PR, Prats-Iraola, P (2016) Compound dislocation models (CDMs) for volcano deformation analyses. Geophys J Int 208:877-894. https://doi.org/10.1093/gji/ggw427

Parmigiani, A, Huber, C, Bachmann, O (2014) Mush microphysics and the reactivation of crystal-rich magma reservoirs. J. of Geophys. Res Solid Earth 119(8), 6308-6322. http://doi.org/10.1002/2014JB011124

Passmore, E, Maclennan, J, Fitton, G, Thordarson, T (2012) Mush disaggregation in basaltic magma chambers: evidence from the AD 1783 Laki eruption. J Petrol 53(12), 2593-2623. https://doi.org/10.1093/petrology/egs061

Peccerillo, A, Frezzotti, ML, De Astis, G, Ventura, G (2006) Modeling the magma plumbing system of Vulcano (Aeolian Islands, Italy) by integrated fluid-inclusion geobarometry, petrology, and geophysics. Geology 34(1): 17-20.

Petit-Breuilh, ME (1999) Cronología eruptiva histórica de los volcanes Osorno y Calbuco, Andes del Sur (41º-41º30'S). Boletín no. 53. Servicio Nacional de Geología y Minería, 46 p.

Onsager, L (1945). Theories and problems of liquid diffusion. Ann N Y Acad Sci 46(5): 241-265.

Rae, AS, Edmonds, M, Maclennan, J, Morgan, D, Houghton,B, Hartley, ME, Sides, I (2016) Time scales of magma transport and mixing at Kīlauea Volcano, Hawai'i. Geology 44(6): 463-466.

Reed, SJB (1975) Electron Microprobe Analysis. Cambridge University Press.

Reed, SJB (2005) Electron Microprobe Analysis and Scanning Electron Microscopy in Geology. Cambridge University Press.

Romero, JE, Morgavi, D, Arzilli, F, Daga, R, Caselli, A, Reckziegel, F, Viramonte, J (2016) Eruption dynamics of the 22 – 23 April 2015 Calbuco Volcano (Southern Chile): Analyses of tephra fall deposits. J Volcanol Geotherm Res 317, 15–29.

Saunders, K, Blundy, J, Dohmen, R, Cashman, K (2012) Linking petrology and seismology at an active volcano. Science 336(6084): 1023-1027.

Ruprecht, P, Bergantz, GW, Cooper, KM, Hildreth, W (2012) The crustal magma storage system of Volcán Quizapu, Chile, and the effects of magma mixing on magma diversity. J Petrology 53(4): 801-840.

Sellés, D, Moreno, H (2011) Geología del Volcán Calbuco, Región de Los Lagos. Carta Geológica de Chile. Serie Geológica Básica, No. 130. Escala 1:50.000.

SERNAGEOMIN (2015a) Reporte especial de actividad volcánica (REAV) - Región de los Lagos, 2015, abril 22 – 18:00.

SERNAGEOMIN (2015b) Reporte especial de actividad volcánica (REAV) - Región de los Lagos, 2015, abril 22 – 20:45.

SERNAGEOMIN (2015c) Reporte especial de actividad volcánica (REAV) - Región de los Lagos, 2015, abril 23 – 10:30

SERNAGEOMIN (2015d) Reporte especial de actividad volcánica (REAV) - Región de los Lagos, 2015, abril 23 – 01:10

SERNAGEOMIN (2015e) Reporte especial de actividad volcánica (REAV) - Región de los Lagos, 2015, abril 22 – 22:30.

SERNAGEOMIN (2015f) Reporte especial de actividad volcánica (REAV) - Región de los Lagos, 2015, abril 22 – 17:30

SERNAGEOMIN (2017) Reporte especial de actividad volcánica (REAV) — Región de los Lagos, volcán Osorno 2017, Diciembre 19 —18:30 (local time).

SERNAGEOMIN (2018a) Reporte especial de actividad volcánica (REAV) — Región de los Lagos, volcán Osorno 2018, Abril 14 —14:30 (local time).

SERNAGEOMIN (2018b) Reporte especial de actividad volcánica (REAV) — Región de los Lagos, volcán Osorno 2018, Junio 23 —11:00 (local time).

SERNAGEOMIN (2019) Reporte de actividad volcánica (RAV) — Región de los Lagos, volcán Osorno, Febrero 2019.

Smith, JV (1965) X-ray emission microanalysis of rock-forming minerals I: experimental techniques. J Geol 73: 830-864.

Stern, CR, Moreno, H, López-Escobar, L, Clavero, J, Lara, L, Naranjo, JA, Parada, MÁ, Skewes, MA (2007) Chilean Volcanoes. In: Geology of Chile, Moreno, T, Gibbons, W (Eds). The Geological Scoiety London: 147-178.

Stern, CR (2004) Active Andean volcanism: its geologic and tectonic setting. Rev Geol Chile 31(2): 161-206.

Sweatman, TR, Long, VP (1969) Quantitative Electron-probe Microanalysis of Rock-forming Minerals. J Petrol 10: 332-379.

Szymanowski, D, Wotzlaw, JF, Ellis, BS, Bachmann, O, Guillong, M, von Quadt, A (2017) Protracted near-solidus storage and pre-eruptive rejuvenation of large magma reservoirs. Nat Geosci. http://doi.org/10.1038/NGEO3020

Tagiri, M, Moreno, H, López-Escobar, L, Notsu, K (1993) Two magma types of the high-alumina basalt series of Osorno Volcano, Southern Andes (41°06′ S)-plagioclase dilution effect. J Mineral, Petrol Econ Geol 88(7): 359-371.

Tormey, DR, Hickey-Vargas, R, Frey, FA, López-Escobar, L (1991) Recent lavas from the Andean volcanic front (33 to 42 S); interpretations of along-arc compositional variations. Andean magmatism and its tectonic setting: Geol Soc Am Spec 265: 57-77.

Turner, S, Costa, F (2007). Measuring timescales of magmatic evolution. Elements 3(4): 267-272.

Valderrama, Ó, Franco, L, Gil-Cruz, F (2015) Erupción intempestiva del volcán Calbuco, Abril 2015, XIV Congreso Geológico Chileno, III, p. 91-93.

Van Eaton, AR, Amigo, Á, Bertin, D, Mastin, LG, Giacosa, RE, González, J, Valderrama, Ó, Fontijn, K, Behnke, SA (2016) Volcanic lightning and plume behavior reveal evolving hazards during the April 2015 eruption of Calbuco volcano, Chile. Geophys Res Lett 43(7): 3563-3571.

Watson, EB, Baxter, EF (2007) Diffusion in solid-Earth systems. Earth Planet Sc Lett 253(3-4): 307-327.

Watt, S. F., Pyle, D. M., Mather, T.A. (2009). The influence of great earthquakes on volcanic eruption rate along the Chilean subduction zone. Earth and Planetary Science Letters 277(3-4), 399-407.

Watt, SF, Pyle, DM, Naranjo, JA, Rosqvist, G, Mella, M, Mather, TA, Moreno, H (2011) Holocene tephrochronology of the Hualaihue region (Andean southern volcanic zone, ~42ºS), southern Chile. Quatern Int 246(1), 324-343. http://doi.org/10.1016/j.quaint.2011.05.029

Wittry, DB (1962) Fluorescence by characteristic radiation in electron-probe microanalysis. USCEC Rep 84-204. Univ Calif.

Chapter 2

2. Localised heating and magmatic intensive conditions prior to the 22-23 April 2015 Calbuco volcano eruption (Southern Chile)

Eduardo Morgado [1, 2*], Daniel J. Morgan[1], Jason Harvey[1], Miguel-Ángel Parada[2, 3], Angelo Castruccio[2, 3], Raimundo Brahm[2, 3, 4], Francisco Gutiérrez [5], Bogomil Georgiev[1], Samantha J. Hammond[6]

[1] Institute of Geophysics and Tectonics, School of Earth and Environment, University of Leeds, Leeds LS2 9JT, UK.

[2] Centro de Excelencia en Geotermia de los Andes (CEGA-FONDAP 15090013), Chile.

[3] Departamento de Geología, Facultad de Ciencias Físicas y Matemáticas, Universidad de Chile, Chile.

[4] Volcanic Risk Solutions, Institute of Agriculture and Environment, Massey University, Palmerston North 4442, New Zealand.

[5] GeoExpedition, Las Barrancas 25, Pirque, Santiago 9480000, Chile.

[6] Environment, Earth & Ecosystems, The Open University, Milton Keynes, MK7 6AA, UK.

Citation: **Morgado, E.**, Morgan, D.J., Harvey, J., Parada, M.Á., Castruccio, A., Brahm, R., Gutiérrez, F., Georgiev, B., Hammond, S.J., 2019.Localised heating and intensive magmatic conditions of the 22-23 April 2015 Calbuco volcano eruption. Bulletin of Volcanology, v. 81, 24. DOI: 10.1007/s00445-019-1280-2

2.1. Abstract

Calbuco volcano is a Late-Pleistocene composite stratovolcano and member of the Southern Volcanic Zone of the Chilean Andes (41º19'S, 72º36'W). It lies ~20 km west of the Liquiñe-Ofqui Fault Zone, but is not located directly upon any major regional structures. During April 2015, a sub-Plinian eruption occurred, with a bulk erupted volume of ~0.3-0.6 km^3 (~0.1-0.2 km^3 DRE). The eruption was a rapid-onset event that produced highly-crystalline products (from 40 to 60 volume %) including the mineral phases: plagioclase, clinopyroxene, orthopyroxene, amphibole, olivine, apatite, ilmenite, titanomagnetite, and chalcopyrite. An upper-crustal reservoir is inferred using available geophysical data combined with amphibole geobarometry. Consideration of textural features, including high crystallinity, complex mineral zonation, crystal clots, and interstitial glass between crystals from clots suggests the presence of a mush zone within this reservoir.

From the nine collected samples, whole-rock chemistry and an array of geothermometers (amphibole, amphibole-plagioclase, two-pyroxenes, and Fe-Ti oxides) gave similar results for all samples possessing ~40 volume % of crystals, with the exception of the sample Cal-160 (~60 volume % crystallinity), which is slightly more evolved and yields lower temperatures for all geothermometers. By comparing temperatures calculated in sample Cal-160 using pairs of ilmenite-titanomagnetite core compositions with those calculated using rim compositions we observe a late-stage temperature increase of between 70 ºC and 200 ºC. We suggest that this local-scale heating event was at least partly responsible for triggering the eruption.

Our data suggest that the bulk of the erupted magma was derived from a relatively uniform (970–1,000ºC), crystal-rich magma mass. Sample Cal-160 was derived from a cooler environment (910–970 ºC), where it was subjected to pre-eruptive heating to

temperatures considerably higher than those observed in associated, erupted magmas (up to 1,070 ºC). This requires the involvement of a hot, presumably mafic magma injection at the base of a shallow, crystal-rich reservoir, though the mafic magma was not itself erupted. The localised nature of interaction and rapidity of eruption onset have implications for potential future hazards at Calbuco volcano.

2.2. Introduction

Within the continental crust, magma reservoirs are considered to be represented by both *magma chambers*, these being defined as continuous, melt-rich, lenticular regions where the magma is fluid and eruptible and within which magma crystallinity is < 45 vol %, and *crystal mushes*, i.e., a body with a rigid crystal framework and crystallinity > 45% (Marsh 1989, 1996; Hildreth 2004; Bachmann and Bergantz 2008). Crystallinities > 45 vol % are associated with rheological properties which impede convection processes (e.g., Bachmann and Bergantz 2004, 2008; Huber et al. 2010a; Burgisser and Bergantz 2011; Parmigiani et al. 2014). These reservoirs exist as shallow magma reservoirs (≤ 10 km depth) and may evolve over long cooling periods to become plutons (e.g., Koyaguchi and Kaneko 1999; Claiborne et al. 2010; Cooper and Kent, 2014; Molina et al. 2015; Szymanowski et al. 2017; Cooper et al., 2017).

Sample mineralogy and whole-rock chemistry are usually studied together in order to understand magma reservoirs. Mineral compositions, however, yield diverse information regarding crystallisation conditions, crystal re-equilibration and timescales; which depend upon the diffusion kinetics of their constituent elements. For example, major elements of Fe-Ti oxides show much higher interdiffusivity (Aragon et al. 1984; Aggarwal and Dieckmann 2002a, b) than those of silicate phases (e.g., plagioclase, Grove et al. 1984; clinopyroxene, Müller et al. 2013; orthopyroxene, Ganguly and Tazzoli 1994; Dohmen et al. 2016; and olivine, Dohmen and Chakraborty 2007a, b).

Therefore, Fe-Ti oxides equilibrate much faster than silicate phases, typically recording magma eruption temperatures. By contrast, the silicates can provide information on earlier stages of the magmatic history with little re-equilibration. This study reports whole-rock chemistry, mineral chemistry, textural features and calculations of pre-eruptive intensive conditions (geothermometry, geobarometry, and oxybarometry) derived from fall deposits of the sub-Plinian eruption of Calbuco volcano (Southern Chile), which occurred on 22-23 April 2015. In doing so we recognise and quantify a local-scale heating event prior to the eruption, which we interpret to represent an input of new, hot magma beneath an inferred shallow magma reservoir including a mush zone with limited mixing or interaction between the overlying reservoir and the new magma input.

2.3. Geological setting

2.3.1. Calbuco volcano

Calbuco volcano (41º19'S, 72º36'W) is a Late Pleistocene-Holocene composite stratovolcano (López-Escobar et al. 1992) of the Central Southern Volcanic Zone of the Andes. Its summit is 2003 meters above sea level and the basal area of the volcano is 150 km^2 (Sellés and Moreno 2011). Calbuco has been catalogued as the third most dangerous Chilean volcanic system (Lara et al. 2011; SERNAGEOMIN, 2017). It is located ~20 km west of the Liquiñe-Ofqui Fault Zone (LOFZ; Fig. 2.1), a major dextral, transpressive strike-slip structure of the Southern Volcanic Zone (Cembrano et al., 1996; 2000). According to Sellés and Moreno (2011), however, Calbuco volcano is not itself located directly upon any major regional structure. The basement of the area is comprised of late Palaeozoic metamorphic rocks from the Sotomó-Chaiquenes (Thiele et al. 1985) and Lenga (SERNAGEOMIN-BRGM 1995) metamorphic complexes and later plutonic rocks, which are members of the Miocene plutonic belt of the Northern

Patagonian Batholith (López-Escobar et al. 1992; Adriasola et al. 2006). The Calbuco volcanic edifice immediately overlies Early Pleistocene volcanic sequences (the Hueñuhueñu and Reloncaví strata; López-Escobar et al. 1995b).

The construction of the Calbuco edifice is ~300 ka old (Sellés and Moreno 2011) and is characterised by alternations between lava flows (basaltic to basaltic andesitic with rare dacite), andesitic to dacitic domes, and layers of pyroclastic tephras, block and ash flows, and deposits from hot and cold lahars (López-Escobar et al. 1992; 1995a, b; Petit-Breuilh 1999; Moreno et al. 2006; Stern et al. 2007; Castruccio et al. 2010; Sellés and Moreno 2011; Watt et al. 2011; Daga et al. 2014). The dominantly andesitic composition of its products (with high Sr isotope ratios and low Nd isotope ratios; López-Escobar et al., 1995b), combined with the presence of crustal xenoliths and magmatic amphibole phenocrysts, make this volcano notably more evolved by comparison to other nearby volcanic complexes such as Osorno volcano (Parada 1990; López-Escobar et al. 1992; 1995a, b; Hickey-Vargas et al. 1995). The long-term evolution of the products of Calbuco volcano has been divided into four units (Lahsen et al. 1985; López-Escobar et al. 1992, 1995b; Sellés and Moreno 2011); details of the three prehistoric units (Calbuco 1, 2, and 3) are shown in the Table 2.1 and details of the historical unit (Calbuco 4) are shown in Table 2.2.

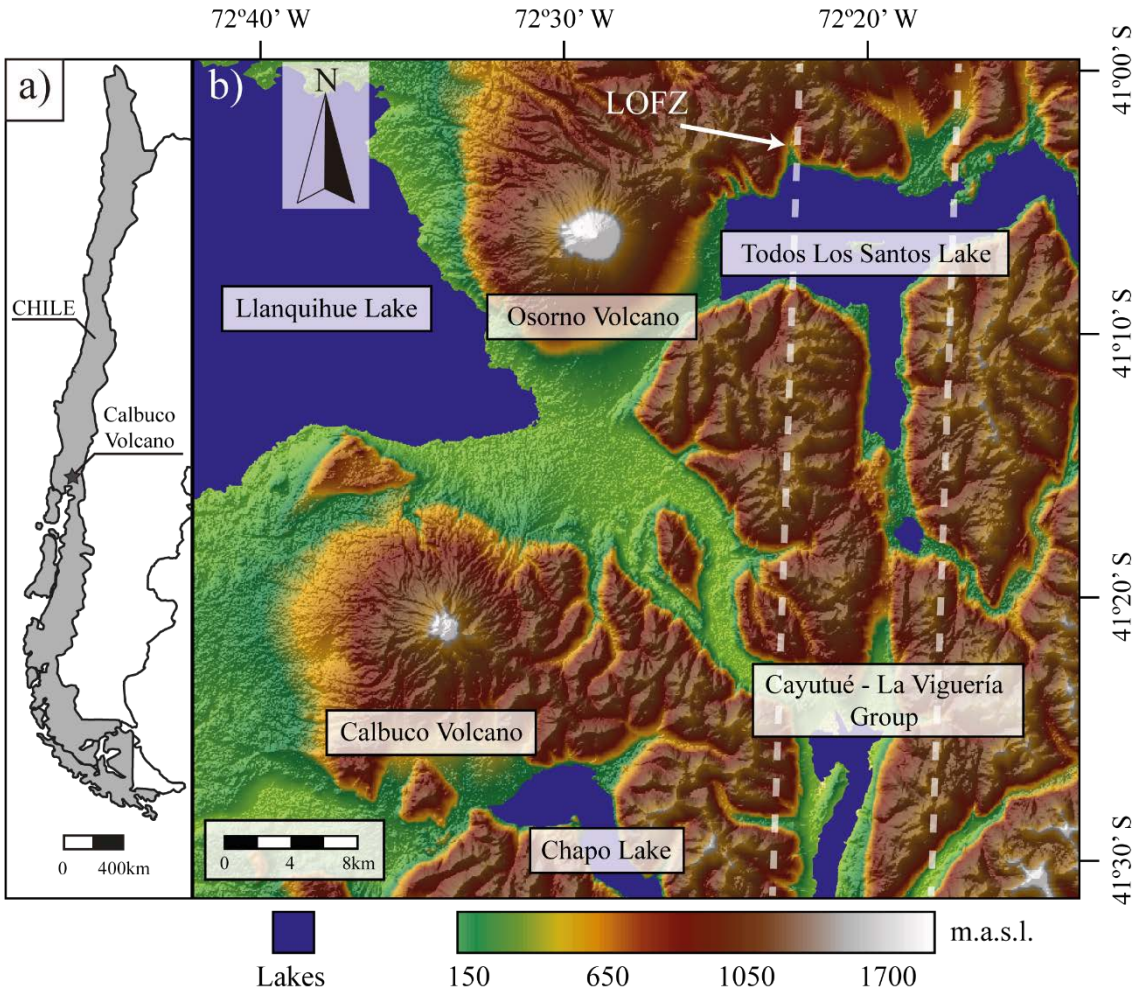

Figure 2.1. *a) Location of Calbuco volcano with respect to Chile, and b) regional map of Calbuco volcano on shaded relief/Digital Elevation Model. Calbuco is located between Llanquihue and Chapo lakes, ~20 km west from the Liquiñe-Ofqui Fault Zone (LOFZ, dashed white line). The Advanced Spaceborne Thermal Emission and Reflection Radiometer (ASTER) Global Digital Elevation Model (GDEM) image was obtained via EarthExplorer, USGS (http://earthexplorer.usgs.gov).*

Table 2.1. Main features of the different prehistorical units of Calbuco volcano.

Unit	Description	Mineralogy**
Calbuco 1 (340-110ka)	Unit composed mainly of andesite-basalt and scarce basalt lavas (50-56.6 wt% SiO_2) interbedded with volcanoclastic deposits. The deposits lie in disconformity over plutonic and metamorphic basement as well as volcanic and volcaniclastic deposits (Estratos de Hueñuhueñu, 1.4 Ma; Lahsen, 1985). Sellés and Moreno (2011) have recognized gabbro and pyroxenite xenoliths.	Plagioclase, clinopyroxene, orthopyroxene, olivine*, amphibole
Calbuco 2 (110-14.5ka)	Unit composed mainly of andesitic lavas (56-61 wt% SiO_2) interbedded with pyroclastic flows, fall deposits, and laharic breccias. Occasionally can be found andesitic dome lavas, pyroclastic deposits, and volcanic avalanches (Sellés and Moreno, 2011).	Plagioclase, clinopyroxene, orthopyroxene, olivine*
Calbuco 3 (~14ka -1893 AD)	Unit composed of lavas (mainly of andesitic composition), pyroclastic rocks, and laharic breccias. Most of the samples have andesite-basaltic and andesitic composition (55-60 wt% SiO_2). Scarce dacites (64.5 wt% SiO_2) also have been recognized (Sellés and Moreno, 2011).	Plagioclase, clinopyroxene, orthopyroxene, olivine*

* All the olivines were surrounded by a pyroxene crown.
** According to Sellés and Moreno (2011).

Table 2.2. Main features of the historical products of Calbuco volcano.

Year of the eruption	Description	Mineralogy
1893	A violent eruption started on February 1893 and finished during the last months of 1895 (Petit-Breuilh, 1999). During October 1893, was the paroxysmal stage, when the eruptive column reached ~9 km height (VEI 3 estimated; Fischer, 1893; Petit-Breuilh, 1999)	-
1911	During 1911 and 1912 gas and ashes were erupted (Petit-Breuilh, 1999)	-
1917	During April 1971 an eruption occurred with a lava flow, dome-cone, and some lahars were associated. The lava flow had andesitic composition (59.3 wt% SiO_2) and gabbroic and troctolitic clots were found (Sellés and Moreno, 2011).	Plagioclase, orthopyroxene, amphibole, opaque
1929	During January 1929, 2.5 km long (from the crater to NE direction) and 0.5 km long (from the crater to SE direction) andesitic lavas (55.5 wt% SiO_2). Some crystal mush xenolith of amphibole gabbros have been recognized (Sellés and Moreno, 2011). Lahars were generated during the eruption flowing towards northwest (Petit-Breuilh, 1999).	Plagioclase, pyroxenes, olivine*, amphiboles
1961	During February 1961, 4.6 km long (NE direction) and 1.7 km long (SE direction) andesitic lavas were erupted. As consequence, some lahars and hot lahars were generated (Klohn, 1963; Moreno et al., 2006; Castruccio et al, 2010). According to the morphological features of glassy particles, this eruption is associated to magma/water interactions (Daga et al., 2014). Also granulitic, gabbroic and noritic clots have been recognized (Hickey-Vargas et al., 1995; Moreno and Sellés, 2011).	Plagioclase, clinopyroxene, orthopyroxene, olivine*, amphibole, quartz

* All the olivines were surrounded by a pyroxene crown
- No information available

2.3.2. The April 2015 Calbuco eruption

During 22-23 April 2015, two sub-Plinian eruptive events occurred at Calbuco volcano. The first eruptive pulse started on 22 April at 17:50 local time (20:50 UTC) and the second started on 23 April at 01:00 local time (04:00 UTC) (SERNAGEOMIN, 2015a, b, c, d). These pulses produced eruptive columns with heights exceeding 15 km (SERNAGEOMIN 2015e; Romero et al. 2016, Van Eaton et al. 2016). Van Eaton et al. (2016) reported pyroclastic density currents (PDCs) at the end of the first eruptive pulse, with the largest PDCs occurring at the onset of the second eruptive pulse. During the entire eruption sequence, primary and secondary lahars were generated on the S, N and NE flanks and no lava flows were emitted (Castruccio et al. 2016).

Several authors have estimated the bulk erupted volume during the eruption: 0.27 km^3 (0.11–0.13 km^3 dense rock equivalent, DRE; Romero et al., 2016), 0.56 ± 0.28 km^3 (0.18 ± 0.09 km^3 DRE; Van Eaton et al. 2016), 0.38 ± 0.1 km^3 (0.15 km^3 DRE; Castruccio et al. 2016), and 0.37-0.6 km^3 (Delgado et al. 2017). The eruption had a volcanic explosivity index (VEI) of four, based on the estimated bulk volumes (Romero et al. 2016; Van Eaton et al. 2016). Most of the products were erupted during the first pulse (Romero et al. 2016).

In terms of precursory activity, Valderrama et al. (2015) reported 147 seismic events occurring from 1 January to 21 April 2015, of which 142 were volcano-tectonic (VT, related to fracturing of the wall rock) and five were long-period (LP, related to collapse of gas bubbles in rising magma or fluid movement events). From February 2015, there was an increase in low-magnitude VT seismic activity and later, during 22 April, a seismic swarm of 140 VT events was recognised starting just three hours before the eruption onset (SERNAGEOMIN 2015f). The first LP events were registered at 16:34 local time (19:34 UTC, ~1.5 hours before the eruption) and during the second pulse

there was an increase in the number of VT seismic events (SERNAGEOMIN 2015g). Although no deformation was recognised up to 1.5 days before the eruption, deflation was documented during the eruption (Delgado et al. 2017), which agrees with the contemporary tiltmeter information (Valderrama et al. 2015). According to Delgado et al. (2017) the deformation source models are consistent with a deflation between 8 and 11 km depth. The consequences of the eruption were not only local, where chemical-climate interaction modelling suggests that the 2015 Calbuco eruption led to an increase in the areal extent of the Southern ozone hole by 4.5×10^{6} km^{2} (Ivy et al. 2017). Although on 30 April there was another eruptive pulse, this was a steam-driven eruption with little participation of fresh magma. The plume reached < 5 km above the vent with dispersion towards the SE (SERNAGEOMIN 2015g; Van Eaton et al. 2016). The registered deformation during this eruptive event was negligible (Delgado et al. 2017).

2.4. Analytical Procedures

2.4.1. Geochemistry

Nine samples (four lapilli-sized pyroclasts from fall deposits and five bombs from pyroclastic density current deposits) were collected from the products of the 2015 Calbuco eruption deposits from seven locations (Fig. 2.2). Whole-rock compositions of three lapilli and four bomb samples were analysed via XRF (for major elements) at Acme Analytical Labs (Vancouver, Canada) using OREAS-184 and SY-4 standards for all the major elements, and CCU-1D, and OREAS-700 standards for FeO. Accuracy for major elements in all standards is better than 3 % (relative) except for TiO_2 in SY-4 which is 4.5 % (relative) and P_2O_5 in OREAS-184 and SY-4 which are 14 % and 17 % (relative), respectively. Trace element compositions were analysed via ICP-MS at the Open University (Milton Keynes, UK) using the BHVO-2, JB-2, and AGV-1 standards. The reproducibility of analyses was better than 8 % (relative; 2σ) and accuracy in the trace elements in JB-2 (n = 5), BHVO-2 (n = 2) and AGV-1 (n = 2) is better than 10 %, except in Ni (21 % in AGV-1) and Pb (13 % in BHVO-2).

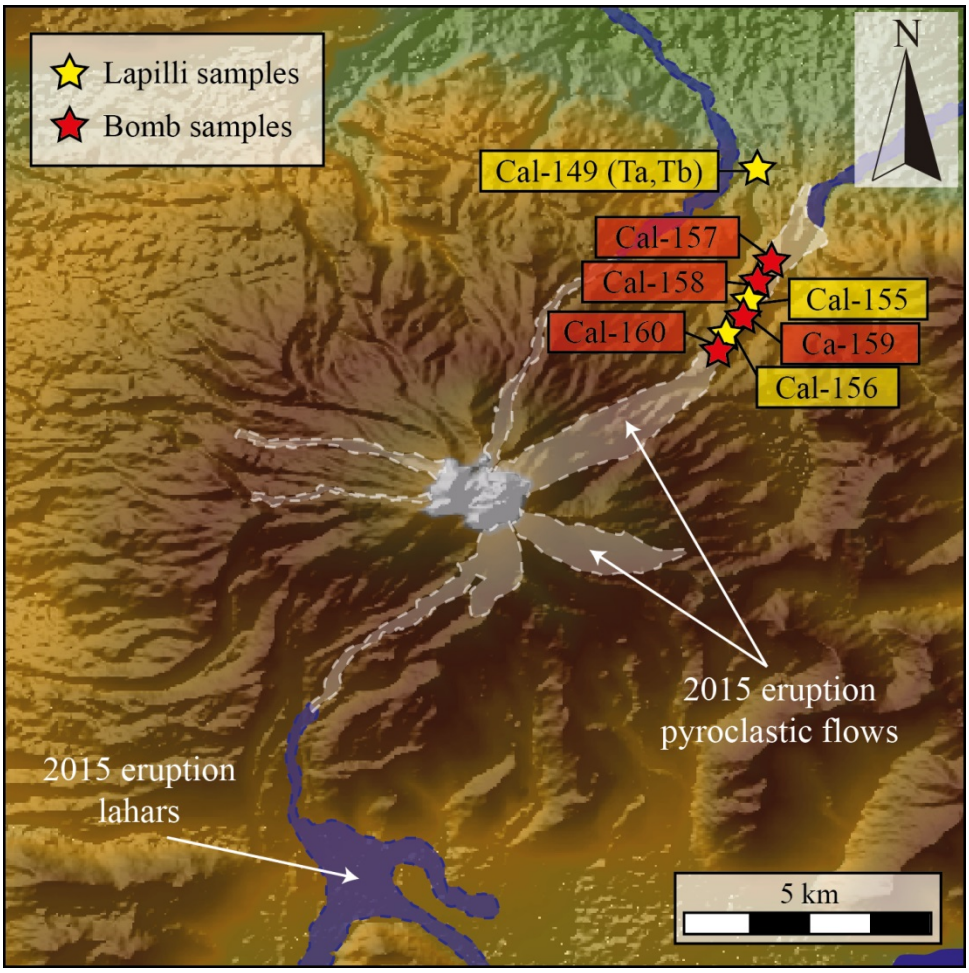

Figure 2.2. *Location of samples (lapilli and bombs) from the 2015 Calbuco eruption on shaded relief/Digital Elevation Model. Location of pyroclastic density currents (white) and lahars (blue) are based on Castruccio et al. (2016). The ASTER–GDEM Image obtained via EarthExplorer, USGS (http://earthexplorer.usgs.gov).*

The mineral chemistry analyses of amphibole, plagioclase, pyroxene, Fe-Ti oxide, and olivine were measured using an electron microprobe (JEOL JXA8230) at Leeds Electron Microscopy and Spectroscopy Centre at the University of Leeds (Leeds, UK). Counting time is distributed equally between on-peak and background measurements, using the following conditions:

Amphiboles. Major and minor element concentrations (Si, Ti, Al, Fe, Mn, Mg, Ca, Na, K, Cr, Cl, and F) were measured in the cores amphibole grains. The analytical conditions consisted of an accelerating potential of 20 keV and focused beam for all the elements. An electron beam current of 15 nA was used for Si, Ti, Al, Fe, Mn, Mg, Ca,

Na, K, and Cr, whereas a current of 100 nA was used for F and Cl. Counting times were 30 s for Ti, Al, Cr, Fe, Mn, Mg, Ca, and Na; 40 s for Si, 100 s for F, and 80 s for Cl. Values of Fe^{3+} were obtained following the formulation of Leake et al. (1997).

Plagioclases. Compositional profiles (spacing ~4–8 μm) of major (Si, Al, Ca, Na, and K) and minor (Ti, Fe, Mg, Sr, and Ba) element concentrations were obtained in plagioclase phenocrysts. The analytical conditions consisted of an accelerating potential of 20 keV and electron beam current of 10 nA for major elements and 40 nA for minor elements with a defocused beam (2 to 5 μm) in order to reduce volatile alkali loss. Counting times for major elements were 32 s, 240 s for Ti, Fe, and Ba, and 480 s for Mg and Sr.

Clinopyroxenes and orthopyroxenes. Concentrations of major (Si, Mg, Fe, and Ca), minor and trace (Ti, Al, Mn, Cr, Ni) elements were obtained in pyroxene phenocryst cores and rims. The analytical conditions consisted of an accelerating potential of 20 keV and electron beam current of 30 nA with a focused beam. Counting times for major elements were 60 s and 80 s for minor and trace elements. Values of Fe^{3+} were obtained following the formulation of Putirka (2008).

Fe-Ti oxides. Compositional profiles (spacing ~2–3 μm) of major (Ti, Fe, and O) and minor and trace (Al, Mg, Ca, Mn, V, Cr, Zn, Ni, Co, and Si) elements were measured in titanomagnetite and ilmenite. The analytical conditions consisted of an accelerating potential of 15 keV and electron beam current of 30 nA with a focused beam. Counting times for all the elements were 60 s except for O, in which counting times were 260 s. Values of Fe^{3+} were obtained following the formulations of Droop (1987) for ilmenite grains and Stormer (1983) for titanomagnetites.

Olivines. Concentrations of major (Si, Mg, and Fe), minor and trace (Al, Ni, Mn, Ca) elements were obtained in the core of olivine phenocryst. Analyses were taken away from grain boundaries in order to avoid secondary fluorescence issues during the acquisition of Ca concentrations (cf. Dalton and Lane, 1996). The analytical conditions consisted of an accelerating potential of 20 keV and electron beam current of 30 nA for Si, Fe, Mg, and Mn and 100 nA for Al, Ni, and Ca, all with a focused beam. Counting times for all the elements but Ca were 40 s and 400 s for Ca.

2.4.2. Geothermobarometry

Amphiboles. The methods of Ridolfi et al. (2010) and Ridolfi and Renzulli (2012) are used to calculate intensive conditions (T, P, and fO_2) independently in 109 amphibole cores from both Cal-149Ta (light-brown lapilli) and Cal-160 (white bomb) samples.

Amphibole-plagioclases. The Holland and Blundy (1994) thermometry is applied using core compositions of 16 plagioclase-amphibole pairs, where equilibrium is assumed because the plagioclase crystals are found as inclusions in amphibole phenocrysts.

Clinopyroxene-orthopyroxenes: Two-pyroxene thermobarometry (Putirka 2008) is used with 35 ortho- and clinopyroxene pairs that passed the test for equilibrium according to the Putirka (2008) chemical filter across the nine samples.

Fe-Ti oxides: The Ghiorso and Evans (2008) thermoxybarometer is applied to compositions of crystal cores and close (~2 µm to the interface) to ilmenite-titanomagnetite grain boundaries.

Olivine: The Ca-in-olivine thermometer of Shejwalkar and Coogan (2013) is applied to core composition data from 16 olivine phenocrysts in crystal clots, where equilibrium with the surrounding crystal phases (plagioclase, clinopyroxene and orthopyroxene) is assumed due to textural relation and chemical filters (cf. Grove et al., 1997). Nine

calculated temperatures were discarded, due to the low forsterite content (Fo_{61-68}) of the crystals considering Fo_{70} as the lower limit of the calibration of the thermometer (Shejwalkar and Coogan 2013).

The error propagation of geothermo- and geobarometers is carried out considering both internal uncertainties (associated with the experimental method) and external uncertainties (associated with precision and accuracy electron microprobe analyses). In later parts of this work, MELTS modelling uses the intensive physical variables derived from the thermobarometry (see *Intensive variable conditions* section).

2.5. Descriptions and compositions of the samples

According to Castruccio et al. (2016) the fall deposits of the 22-23 April eruptions are made up of four sub-units: the lower layer (unit 0) corresponds to the first event and is composed mainly of light-brown, highly-vesicular basaltic andesite scoria and up to 10 vol% of lithics. Layers 1, 2 and 3 correspond to the second (largest) event and there is a transition in the dominant clast type present in the deposits, from light-brown scoria in layer 1 to dark-brown, dense juveniles with the same composition within layer 3. Samples Cal-149Ta, Cal-155 and Cal-156 correspond to layer 1, the sample Cal-149Tb corresponds to layer 3, samples Cal-157, Cal-158, and Cal-159 correspond to scoriaceous bombs from PDCs, and sample Cal-160 corresponds to a distinctive, white bomb with darker zones extracted from a PDC deposit.

All samples are porphyric, with ~35 to 65 vol% of phenocrysts. Dominant mineral phases present in all the samples are plagioclase, orthopyroxene, and clinopyroxene. Minor phases include amphibole (only in Cal-149Ta and Cal-160), olivine (in all samples except Cal-160), titanomagnetite, ilmenite, apatite, and chalcopyrite. All the mineral phases are present as clots of crystals and isolated crystals. The samples exhibit

crystallinities of ~40 vol% except for Cal-160, which shows a higher crystallinity of ~60 vol% (Table 2.3). The samples show a large range of vesicularities: from 15 to 60 vol% and the highest values correspond to light-brown lapilli (samples Cal-149Ta, Cal-155, Cal-156) from 42 to 60 vol% (see details in Table 2.3). The crystallinity percentages and quantification of the main petrographic of the collected products of the April 2015 Calbuco eruption were obtained by image processing techniques via "Background Extraction" of pseudo-coloured images through the freeware JMicrovision.

All the samples correspond to calc-alkaline basaltic-andesites (55.6-56.9 SiO_2 wt%; Fig 2.3a). The Mg# (Mg# = molar $Mg/(Mg+Fe^{2+})$) values are from 0.56 to 0.59. The maximum SiO_2 content (56.9 wt%) and the minimum Mg# (0.56) correspond to the Sample Cal-160 (Table 2.4; Fig. 2.3). All samples show similar rare earth elements (REE) patterns, with a narrow range of La_N/Yb_N (2-2.4); only the sample Cal-155 shows a slight positive Eu anomaly (see Online Resource 1). The spider diagram of the studied samples shows similar trends in all samples and display positive Rb, Pb, and Sr anomalies and negative Nb, P, and Ti anomalies, which are typical of magmas from arc settings (Fig. 2.3c).

Table 2.3. Main features of the samples analysed from Calbuco's April 2015 eruption.

Section name (Cal-)	149Ta	149Tb	155	156	157a	157b	158	159	160
Description	LL	DL	LL	LL	DB	DB	DB	DB	WB
Vesicles (total %)	59.8	15.4	42.3	51.4	32.9	49.7	41.1	37.2	25.4
Groundmass (total %)	22.3	52.9	38	31.5	37	28.9	35.8	39.6	27.1
Plagioclases (total %)	12	23.1	14.7	12.9	18.1	14.2	16.1	15.7	35.2
Pyroxenes (total %)	3.8	7.1	3.7	3.9	11.1	5.8	5.4	6.3	9.7
Amphiboles (total %)	1.2	-	-	-	-	-	-	>0.1	>0.1
Olivine (total %)	-	0.1	0.1	>0.1	0.1	>0.1	0.1	>0.1	-
Oxides (total%)	0.9	1.4	1.2	0.3	0.9	1.4	1.5	1.2	2.5
Crystallinity (%)**	44.5	37.5	34.1	35.2	44.9	42.5	39.2	36.9	63.7

LL= Light-brown lapilli; DL= Dark lapilli; DB= Dark bomb; WB= White bomb

** Percentage not considering vesicles

Table 2.4. Whole-rock analyses of samples from the 2015 Calbuco eruption.

	Detection limit	Cal-149A	Cal-149B	Cal-155	Cal-157	Cal-158	Cal-159	Cal-160
		Lapilli	Lapilli	Lapilli	Bomb	Bomb	Bomb	Bomb
SiO_2	0.01 (%)	56.2	56.2	55.6	55.7	55.8	55.7	56.9
Al_2O_3	0.01 (%)	18.8	18.7	18.9	18.8	18.9	18.7	18.6
TiO_2	0.01 (%)	0.93	0.92	0.87	0.92	0.93	0.94	0.82
FeO	0.2 (%)	4.99	4.99	5.69	5.27	5.55	5.27	5.41
Fe_2O_3	0.01 (%)	2.87	2.77	2.22	2.6	2.41	2.71	2.17
MnO	0.01 (%)	0.16	0.16	0.17	0.17	0.17	0.15	0.16
MgO	0.01 (%)	3.93	3.9	4.27	4.14	4.2	4.25	3.81
CaO	0.01 (%)	8.04	7.96	8.21	8.16	8.14	8.12	7.63
Na_2O	0.01 (%)	3.77	3.78	3.45	3.65	3.65	3.65	3.67
K_2O	0.01 (%)	0.62	0.64	0.53	0.61	0.61	0.61	0.67
P_2O_5	0.01 (%)	0.17	0.16	0.15	0.16	0.16	0.16	0.16
LOI		-0.3	-0.3	-0.2	-0.3	-0.3	-0.3	-0.1
TOTAL		100.48	100.18	100.06	100.18	100.52	100.26	99.99
Li	0.03 (ppm)	15.12	15.65	14.85	14.83	14.17	14.69	16.87
Sc	0.05 (ppm)	21.75	22.82	21.43	23.23	22.76	24.04	19.91
V	0.07 (ppm)	181.7	183.7	185.3	189.3	188.6	197.1	170.1
Co	0.01 (ppm)	40.9	38.86	43.27	38.36	38.29	34.86	34.81
Ni	0.32 (ppm)	10.01	10.81	11.73	12.92	15.72	12.88	11
Cu	0.66 (ppm)	44.19	45.37	24.05	50.56	47.5	45.99	36.92
Cr	0.01 (ppm)	12.9	14.92	15.08	18.19	17.41	16.98	15.84
Zn	2.207 (ppm)	79.84	75.96	79.41	76.31	78.27	81.24	81.82
Tl	0.04 (ppm)	0.115	0.111	0.117	0.094	0.091	0.088	0.135
Rb	0.01 (ppm)	16.48	16.37	14.27	15.92	15.17	15.83	18.35
Ba	0.5 (ppm)	152.1	151.6	131.4	146	139.7	145.3	164
Th	0.001 (ppm)	1.1	1.03	0.88	1.02	0.97	1.01	1.2
U	0.001 (ppm)	0.31	0.31	0.259	0.304	0.287	0.296	0.35
Nb	0.003 (ppm)	5	3	3	5	3	3	3
La	0.001 (ppm)	6.42	6.44	5.55	6.19	5.89	6.11	6.9
Ce	0.002 (ppm)	17	17	14	16	16	16	17
Pb	0.14 (ppm)	4.99	4.67	6.57	4.02	4.25	4.39	4.96
Pr	0.005 (ppm)	2.391	2.411	1.95	2.301	2.194	2.287	2.45
Sr	0.02 (ppm)	347	355	375	350	335	352	353
Nd	0.001 (ppm)	11.79	11.82	9.44	11.35	10.8	11.27	11.81
Zr	0.06 (ppm)	88.5	87.26	68.32	83.8	79.55	83.97	89.78

Table 2.4. (continued)

	Detection limit	Cal-149A	Cal-149B	Cal-155	Cal-157	Cal-158	Cal-159	Cal-160
		Lapilli	Lapilli	Lapilli	Bomb	Bomb	Bomb	Bomb
Sm	0.001 (ppm)	3.271	3.259	2.478	3.143	3.012	3.155	3.111
Eu	0.001 (ppm)	1.03	1.083	0.957	1.019	0.993	1.003	1.026
Gd	0.001 (ppm)	3.52	3.453	2.626	3.355	3.225	3.369	3.278
Tb	0.001 (ppm)	0.583	0.584	0.436	0.562	0.546	0.571	0.546
Dy	0.001 (ppm)	3.576	3.577	2.648	3.439	3.308	3.452	3.338
Ho	0.001 (ppm)	0.784	0.776	0.581	0.752	0.723	0.756	0.726
Er	0.01 (ppm)	2.221	2.204	1.651	2.121	2.047	2.131	2.062
Y	0.01 (ppm)	22.48	23.16	17.13	22.06	20.9	22.18	21.27
Yb	0.01 (ppm)	2.187	2.3	1.719	2.171	2.056	2.114	2.047
Lu	0.002 (ppm)	0.333	0.335	0.254	0.322	0.311	0.326	0.316

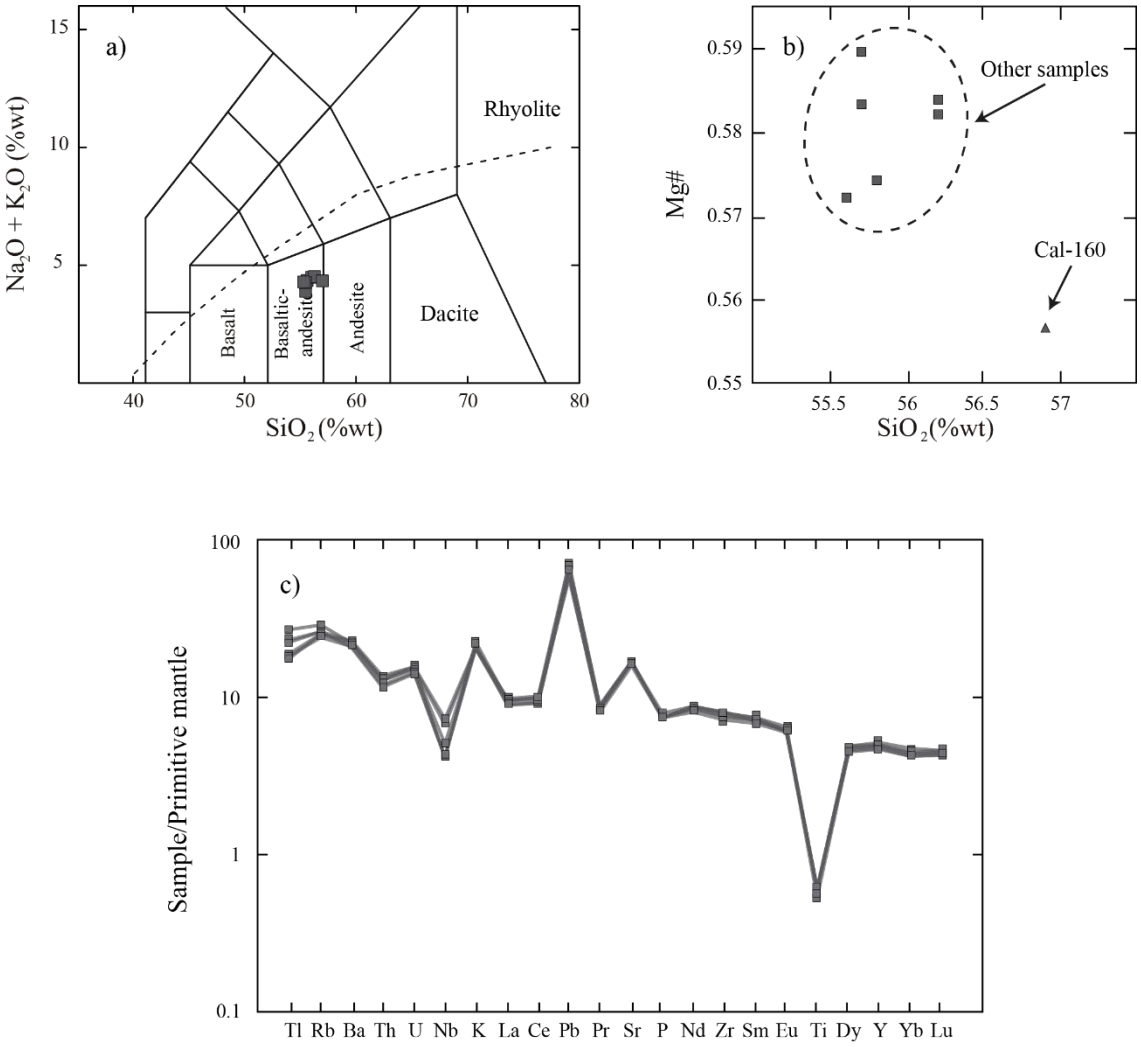

Figure 2.3. *a) Total alkali vs. silica (Le Bas et al. 1986) plots of the Calbuco 2015 volcanic products. Boundary dashed-line between alkaline and subalkaline rocks is taken from Irvine and Baragar (1971); b) Variation diagram of SiO_2 (wt%) vs. Mg# (details in Table 4), where sample Cal-160 shows the highest Mg# and the lowest SiO_2 wt%; c) Primitive mantle-normalised (Sun and McDonough, 1989) spider diagram. Details of major and trace element concentrations are available in Table 4.*

2.6. Mineral chemistry and petrography

Plagioclase. Plagioclase phenocrysts are 0.1–2.0 mm in size and can be found as isolated crystals and as members of cumulocrysts and glomerocrysts (together with pyroxene, olivine, titanomagnetite, apatite, amphibole, and scarce sulphides). Most of the plagioclase phenocrysts display zonation patterns with distinct cores and rims, with the exception of some crystals found as inclusions in amphibole and pyroxene crystals.

Two compositional types are identified in plagioclase phenocrysts: Zone 1 corresponds to compositions of An_{80-92} (Fig. 2.4; Fig. 2.5), which is restricted to phenocryst cores. Zone 2 corresponds to compositions of An_{46-79} (Fig. 2.4), mainly located on phenocryst rims, where oscillatory zonation is ubiquitous (Fig. 2.6). According to the presence/absence of these zones, plagioclase crystals have been classified into two groups:

- Group 1: Crystal core shapes are euhedral to subhedral, resorption features and patchy zonation are not recognised. Core compositions correspond to Zone 1 compositions. The rims have variable thickness (from 20 to 280 μm) and their compositions correspond to Zone 2 compositions.
- Group 2: These plagioclase crystals show oscillatory zoning within Zone 2 compositional range. Resorption and sieve texture as well as patchy zoning are very common.

Plagioclase grains found as inclusions in amphibole have compositions in the range An_{50-89}.

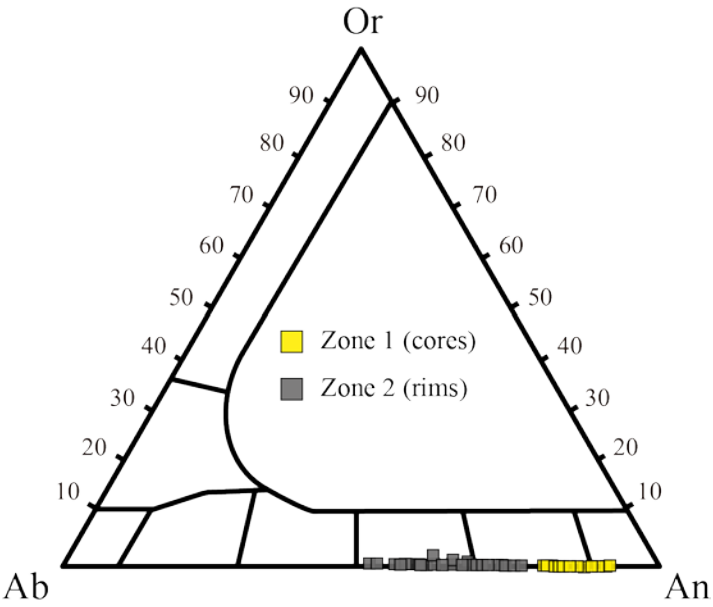

Figure 2.4. *Plagioclase compositions of the studied samples. Zone 1 represents core compositions of the Group 1, whereas zone 2 represents rim compositions of the Group 1 and the whole-crystal composition of Group 2.*

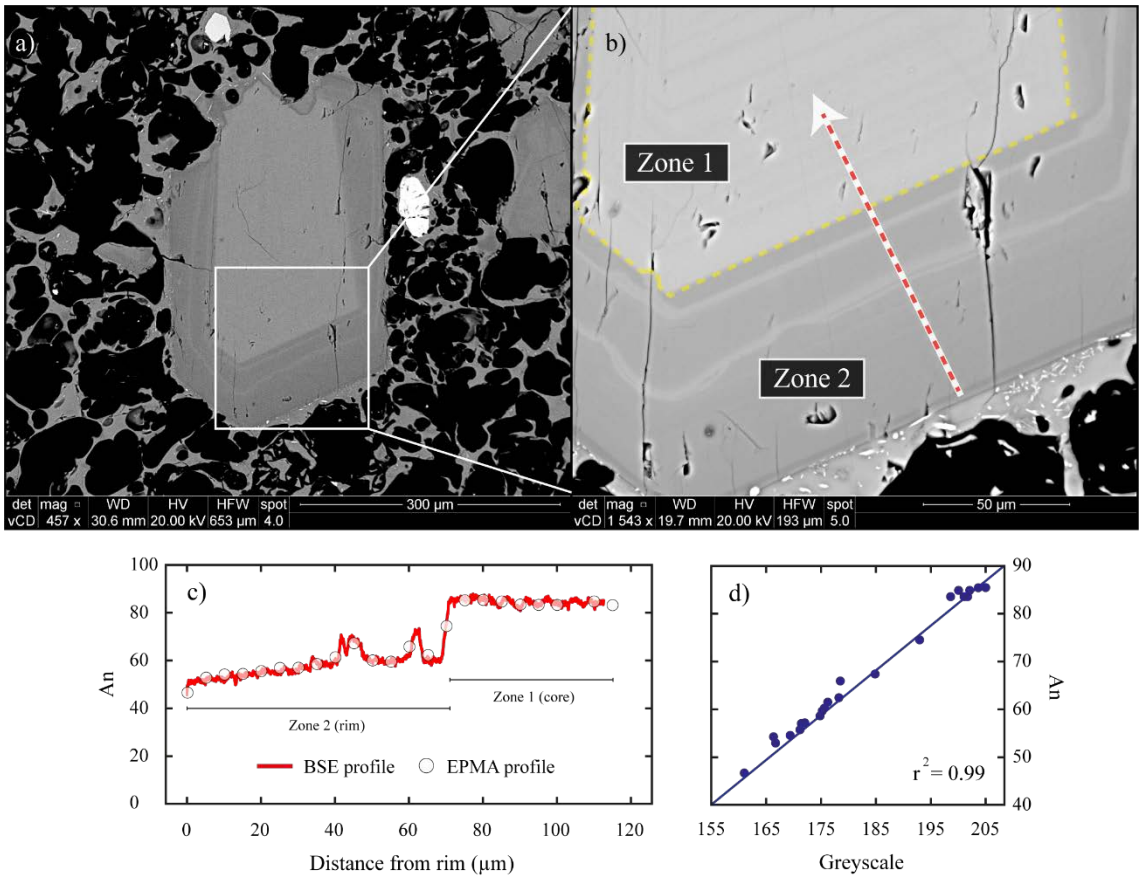

Figure 2.5. *a) Backscatter electron (BSE) image of a plagioclase crystal representative of the Group 1. Brighter greyscale colours are correlated to higher density. b) The arrow represents the profile measured by electron microprobe (EPMA) and its direction. c) Anorthite profile composition (An = 100×Ca/(Ca+Na+K); elements in mols) by EPMA of the measured profile (circles) coupled with the n (BSE) profile based on greyscale values calibrated with the composition measured by electron microprobe (solid line). d) Relation and coefficient of determination (r^2) between BSE profile and the measured anorthite content (An). Group 1 plagioclases have compositions corresponding to Zone 1 (*$An_{80\text{-}92}$*) in the core and Zone 2 (*$An_{46\text{-}79}$*) in the rims. "An"* represents the composition of plagioclases, because in all crystals the K content is fairly constant (see Fig. 2.4).

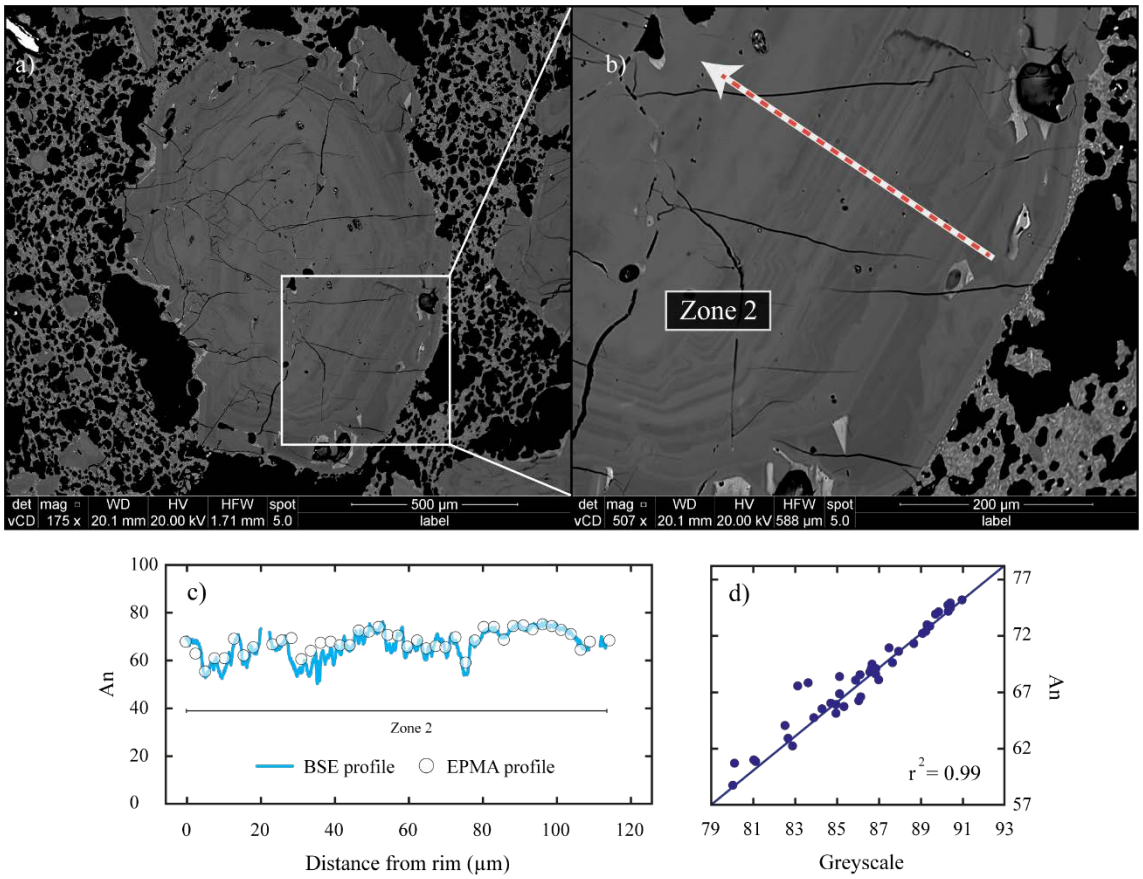

Figure 2.6. *a) Backscatter electron (BSE) image of a plagioclase crystal representative of the Group 2. Brighter greyscale colours are correlated to higher density. b) The arrow represents the profile measured by electron microprobe (EPMA) and its direction. Anorthite profile composition (An = 100×Ca/(Ca+Na+K); elements in mols) by EPMA of the measured profile (circles) coupled with the backscatter electron (BSE) profile based on greyscale values calibrated with the composition measured by electron microprobe (solid line). d) Relation and coefficient of determination (r^2) between BSE profile and the measured anorthite content (An). Group 2 plagioclases have compositions corresponding to Zone 2 (An_{46-79}). "An"* is representing the composition of plagioclases, because in all crystals the K content is fairly constant (see Fig. 2.4*).*

Amphibole. Amphibole phenocrysts are found only in Cal-149Ta (fall deposit, layer 1) and Cal-160 (white bomb from PDC). All Cal-149Ta amphiboles of Cal-149Ta are pargasites (after Leake et al., 1997; Mg#: 0.64-0.74; Si apfu: 6.3–6.5; Fig. 2.7) and can be found as isolated crystals and glomerocrysts (together with plagioclase, pyroxene, titanomagnetite, olivine, ilmenite, and apatite). All amphibole phenocrysts are euhedral and usually contain plagioclase inclusions. In sample Cal-160, 70 % of the amphiboles are edenite ($NaCa_2Mg_5(AlSi_7)O_{22}(OH)_2$) (after Leake et al., 1997; Mg#: 0.65-0.77; Si apfu: 6.5-6.6; Fig. 2.8), and 30 % are pargasites ($NaCa_2(Mg,Fe)_4Al(Al_2Si_6)O_{22}(OH)_2$) (after Leake et al., 1997; Mg#: 0.71-0.77; Si apfu: 6.2–6.5). In contrast to Cal-149Ta, amphiboles in Cal-160 are anhedral and are found as members of glomerocrysts (together with plagioclase, pyroxene, titanomagnetite, olivine, ilmenite, and apatite).

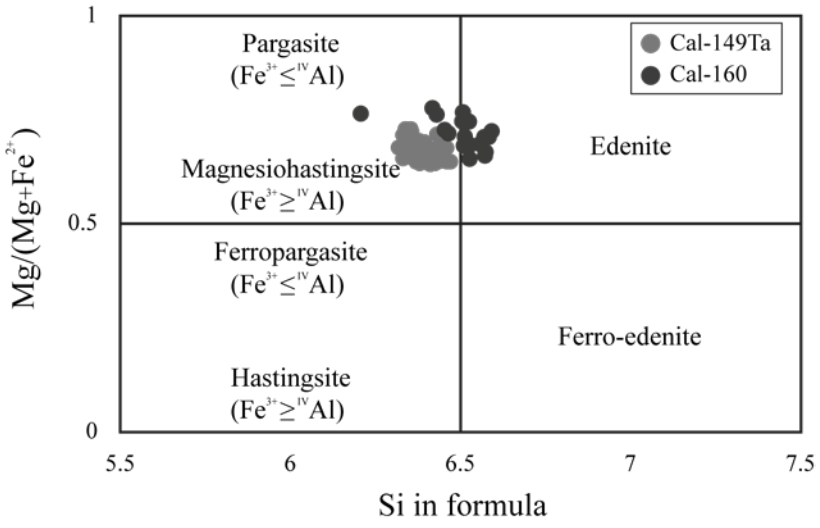

Figure 2.7. *Amphibole compositions and classification (after Leake et al. 1997) of samples Cal-149Ta (grey circles) and Cal-160 (dark circles). All amphiboles of the sample Cal-149Ta correspond to pargasites; whereas amphiboles of sample Cal-160 correspond to 70% edenites and 30% pargasites.*

Fe-Ti oxides. Ilmenite grains are scarce and have composition of X_{ilm} (i.e., the cation atomic proportion of Ti) = 0.77–0.85 (i.e., X_{hmt}, the cationic proportion of Fe^{2+} = 0.15–0.23). They occur as both inclusions and in contact with titanomagnetites. Titanomagnetites can be classified into two groups: high-Ti, with a relatively high ulvöspinel component (X_{usp}: 0.42–0.46; X_{mgt}: 0.54–0.58) and low-Ti (X_{usp}: 0.10–0.17; X_{mgt}: 0.83–0.9). They appear as isolated crystals or in clots of crystals together with amphibole, plagioclase, pyroxene, olivine, ilmenite, and apatite.

Pyroxenes. Pyroxenes are found both as isolated grains and as members of clots of crystals together with amphibole, plagioclase, pyroxene, olivine, ilmenite, titanomagnetite, apatite, and chalcopyrite (see Online Resource 2). All the pyroxene crystals exhibit slight reverse and oscillatory zoning. Clinopyroxene crystals exhibit reverse zoning, from $En_{43-47}Fe_{9-15}Wo_{40-44}$ (Fig. 2.8) composition in the cores to $En_{44-46}Fe_{10-12}Wo_{43-45}$ composition in the rims (Fig. 2.8; Fig. 2.9); oscillatory zoning with compositions of $En_{43-46}Fe_{10-13}Wo_{42-45}$ (Fig. 2.8; Fig. 2.9) have also been observed. Orthopyroxenes exhibit reverse zoning from $En_{67-69}Fe_{29-31}Wo_{2-3}$ composition in the cores to $En_{69-71}Fe_{26-28}Wo_{2-3}$ composition in the rims (Fig. 2.9); oscillatory zoning with compositions of $En_{69-72}Fe_{24-27}Wo_{2-4}$ (Fig. 2.8; Fig. 2.9) have also been recognised.

Olivine. Olivine grains are found surrounded by pyroxene and titanomagnetite crystals (see example images on Online Resource 2). Their composition of Fo_{60-75} (Fig. 2.8) is fairly homogeneous for each crystal, thus no zonation patterns are recognised. Olivine crystals are found in all the samples except Cal-160 (Table 2.3).

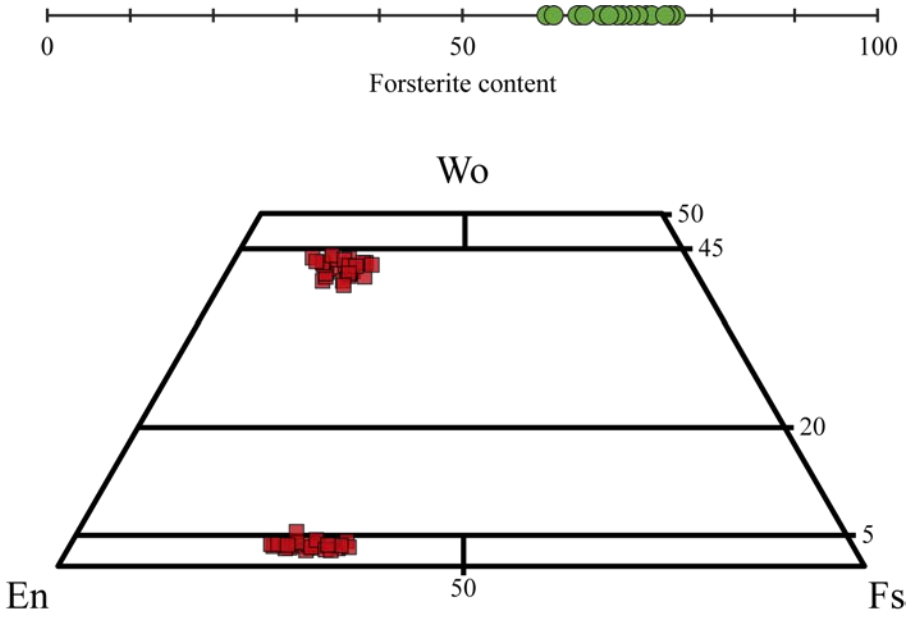

Figure 2.8. *Olivine (found in all samples except Cal-160) and pyroxene (clino- and orthopyroxene, found in all samples, including Cal-160) compositions of the analysed samples.*

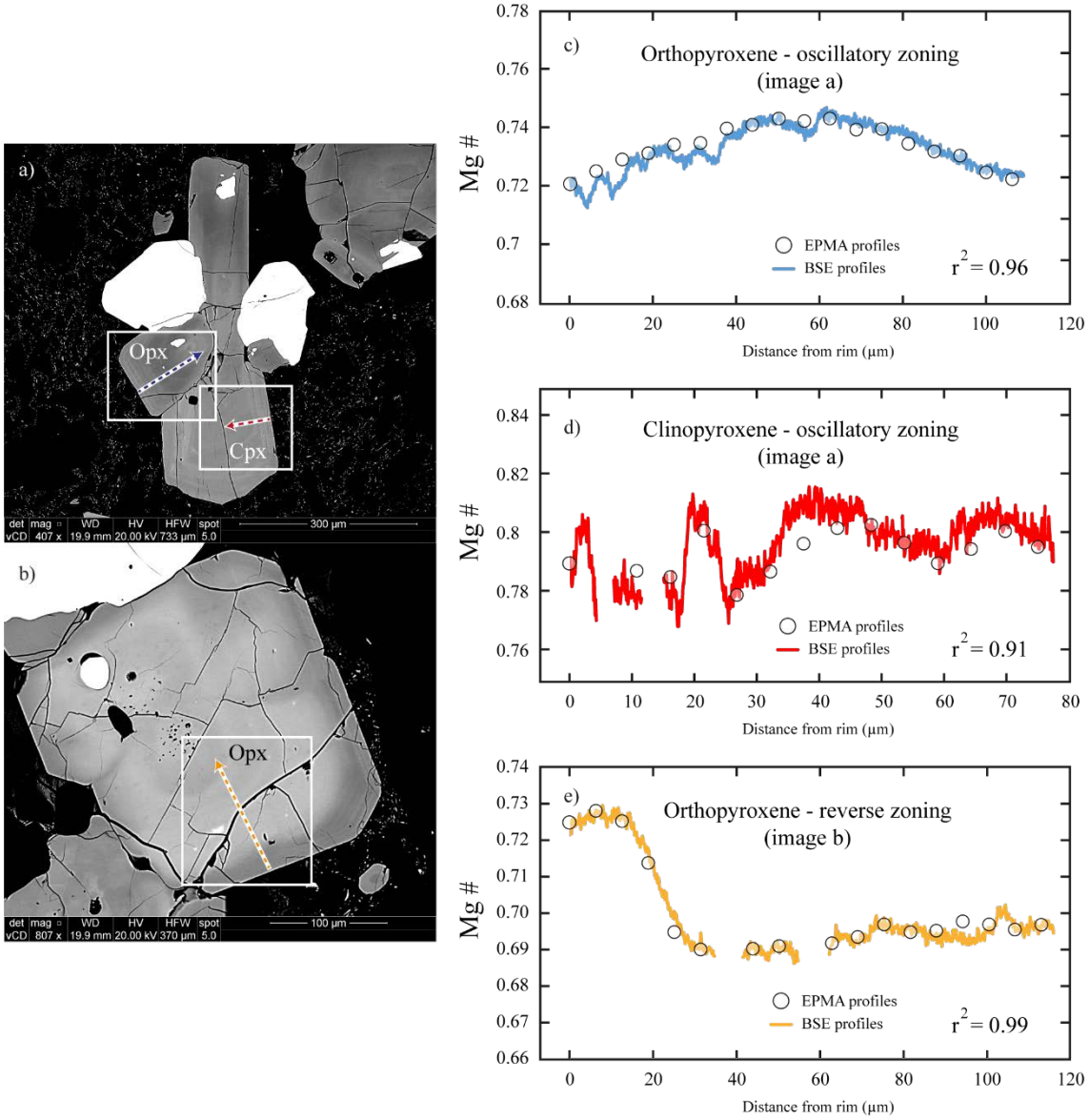

Figure 2.9. *a,b) Backscatter electron (BSE) images of clots of crystals where representative pyroxenes with oscillatory and reverse zonation patterns are found. Brighter greyscale colours are correlated to higher density. Arrows represent the measured profiles by electron microprobe (EPMA) and their directions. The orthopyroxene profile in a) is shown in c) and the clinopyroxene profile in a) is shown in d). The orthopyroxene profile in b) is shown in e). c,d,e) Mg# (Mg# = Mg/(Mg+Fe^{2+}); elements in moles) of the measured profile (circles) coupled with the backscatter electron (BSE) profile based on greyscale values calibrated with the composition measured by EPMA (solid line). The relation and coefficient of determination (r^2) between BSE profile and the Mg# measured content. Greyscale values represent Mg#* because the content of Ca within pyroxene crystals is fairly constant. *Mg#* represents the composition of pyroxenes, because in all crystals the Ca content is fairly constant (see Fig. 2.8).

2.7. Intensive variable conditions

2.7.1. Two-pyroxene thermobarometry

Mineral pairs measured in all samples except Cal-160 give temperatures of 958–1013 ± 56 ºC (Fig. 2.10; Table 2.5), with an average of 984 ºC (σ= 12 ºC), and pressures of 1.5–4.7 ± 3.2 kbar (Table 2.5), with an average of 3.3 kbar (σ= 0.8 kbar). The pairs measured in the sample Cal-160 give temperatures of 944–981 ± 56 ºC (Fig. 2.10; Table 2.6), with an average of 968 ºC (σ = 13 ºC), and pressures of 3.9–6.8 kbar ± 3.2 kbar (Table 2.6), with an average pressure of 5.7 kbar (σ= 1.3 kbar).

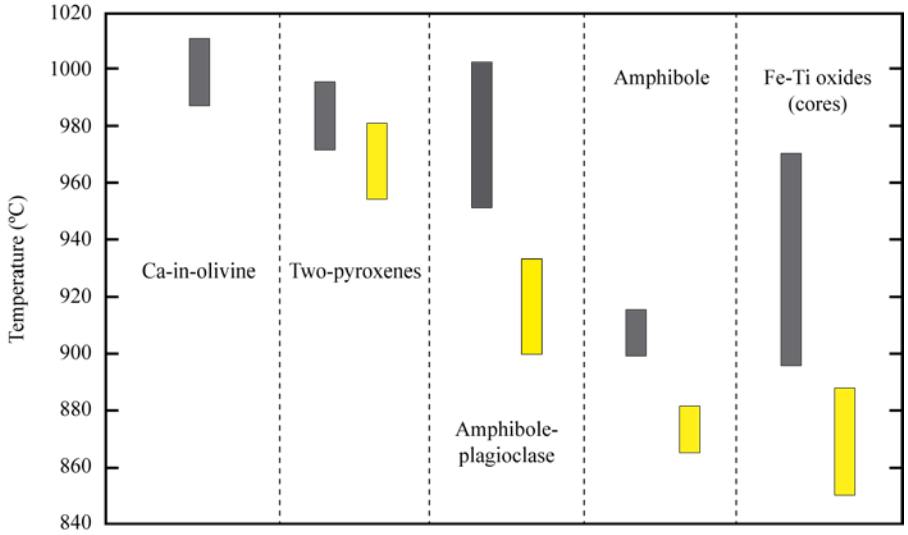

Figure 2.10. *Diagram showing the results of several thermometers (Ca-in-olivine, Shejwalkar and Coogan 2013; two-pyroxenes, Brey and Köhler 1990; Putirka 2008; amphibole-plagioclase, Holland and Blundy 1994; amphibole, Ridolfi and Renzulli 2012; Fe-Ti oxides (cores), Ghiorso and Evans 2008). Vertical bars represent values of average temperature ± one standard deviation of all the samples except Cal-160 (grey) and Cal-160 (yellow). Sample Cal-160 gave temperatures systematically lower than the others. Ca-in-olivine was not used in sample Cal-160 because olivine was not found.*

2.7.2. Amphibole thermobarometry and oxybarometry

Sample *Cal-149Ta* (light-brown lapilli): The thermometer of Ridolfi et al. (2010) gives temperatures of 894–922 ± 24 ºC (Fig. 2.10; Table 2.5), with an average temperature of 906 ºC (σ= 7 ºC), a range and average which is slightly lower than those obtained by

two-pyroxene thermometry. The pressure conditions obtained using the Ridolfi et al. (2010) barometer are 2–2.6 ± 0.3 kbar (Fig. 2.11; Table 2.5), with an average pressure of 2.3 kbar (σ= 0.1). The relative oxygen fugacity values given by the Ridolfi et al. (2010) oxygen-barometer are between 0.2 and 0.5 (± 0.4) ΔNNO units (Table 5), with an average of 0.3 ΔNNO (σ= 0.1). The Ridolfi and Renzulli (2012) thermometer yields temperatures of 882–910 ± 16 ºC (Fig. 2.10; Table 2.5), with an average temperature of 897 ºC (σ= 7 ºC). For the same amphiboles, pressures of 1.9–2.3 ± 0.4 kbar (Fig. 2.11; Table 2.5), with an average of 2.1 kbar (σ= 0.1 kbar) are obtained. The relative oxygen fugacities given by the Ridolfi and Renzulli (2012) oxygen-barometer are between -0.9 and -0.2 ΔNNO (Table 2.5), with an average of -0.6 ΔNNO (σ= 0.1).

Sample *Cal-160* (white bomb): Temperatures obtained by the thermometer of Ridolfi et al. (2010) are 862–886 ± 23 ºC (Fig. 2.10; Table 2.6), similar to Cal-149Ta amphibole temperatures, with an average of 874 ºC (σ= 7 ºC). The Ridolfi et al. (2010) barometer gave pressures between 1.6 and 2 ± 0.3 kbar (Fig. 2.11; Table 2.6) and an average pressure of 1.8 kbar (σ= 0.2 kbar). The relative oxygen fugacity values are between 0.2 and 0.5 ± 0.4 ΔNNO (Ridolfi et al. 2010; Table 2.6), with an average of 0.3 ΔNNO (σ= 0.1). The Ridolfi and Renzulli (2012) thermometer gives temperatures of 823–859 ± 23 ºC (Fig. 2.10; Table 2.6) with an average of 842 ºC (σ= 11 ºC). The same amphiboles gave pressures of 1.4–1.8 ± 0.4 kbar (Fig. 2.11; Table 2.6), with an average pressure of 1.6 kbar (σ= 0.1 kbar). According to the oxygen barometer of Ridolfi and Renzulli (2012) oxygen fugacity is between 0.4 and 0.8 ΔNNO (Table 2.6), with an average of 0.7 ΔNNO (σ= 0.1).

Table 2.5. Calculated intensive conditions, methods, and associated errors of the samples except Cal-160.

Method	References	T (ºC)	error (±)	Average (ºC)	Std. Dev. (σ)	P (kbar)	error (±)	Average (kbar)	Std. Dev. (σ)	fO_2 ΔNNO	error (±)
Two-pyroxenes	Putirka (2008)	958-1013	56	984	12	1.5-4.7	3.2	3.3	0.8	-	-
Amphibole	Ridolfi et al. (2010)	894-922	24	906	7	2-2.6	0.3	2.3	0.1	0.2-0.5	0.4
	Ridolfi and Renzulli (2012)	882-910	16	897	7	1.9-2.3	0.4	2.1	0.1	-0.9-0.2	-
Plagioclase-amphibole	Holland and Blundy (1994)	945-1018	42	977	26	-	-	-	-	-	-
Ca-in-olivine	Shejwalkar and Coogan (2013)	987-1019	22	997	13	-	-	-	-	-	-

Table 2.6. Calculated intensive conditions, methods, and associated errors of the sample Cal-160.

Method	References	T (ºC)	error (±)	Average (ºC)	Std. Dev. (σ)	P (kbar)	error (±)	Average (kbar)	Std. Dev. (σ)	fO_2 ΔNNO	error (±)
Two-pyroxenes	Putirka (2008)	944-981	56	968	13	3.9-6.8	3.2	5.7	1.3	-	-
Amphibole	Ridolfi et al. (2010)	862-886	23	874	7	1.6-2.0	0.3	1.8	0.2	0.2-0.5	0.4
	Ridolfi and Renzulli (2012)	823-859	23	842	11	1.4-1.8	0.4	1.6	0.1	0.4-0.8	-
Plagioclase-amphibole	Holland and Blundy (1994)	902-934	42	914	18	-	-	-	-	-	-

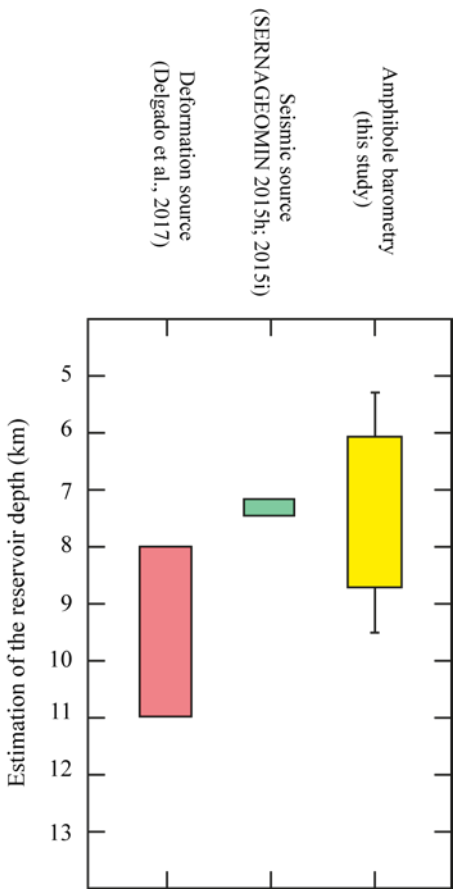

Figure 2.11. *Comparison of different methods that allow the estimation of the reservoir depth: amphibole barometry (yellow bar and including errors; this study), seismic source (green bar; SERNAGEOMIN 2015h, i), and deformation source (red bar; Delgado et al. 2017). The full barometry depth range is from 5.5 to 11 km (considering different pressure condition approaches) and corresponds to upper-to-middle crust conditions.*

2.7.3. Plagioclase-amphibole thermometry

Twelve pairs of amphibole-plagioclase in sample Cal-149Ta give equilibrium temperatures of 945-1,018 ± 42 ºC (Fig. 2.10; Table 2.5), with an average temperature of 977 ºC (σ= 26 ºC). Sample Cal-160 gives lower equilibrium temperatures of 902–934 ± 42 ºC (Fig. 2.10; Table 2.6) with an average temperature of 914 ºC (σ= 18 ºC). All these temperatures are higher than those obtained by the methods of Ridolfi et al. (2010) and Ridolfi and Renzulli (2012) based on single amphibole compositions.

2.7.4. Ilmenite-titanomagnetite thermometry and oxygen barometry

Ilmenite-titanomagnetite pairs are found only in samples Cal-149Tb (very scarcely), Cal-155 (very scarcely), and Cal-160 (common), and give temperature and oxygen fugacity values which all fell within the calibrated temperature and oxygen fugacity ranges of 800 to 1,300 °C, and -3 to +3 log units ΔNNO, respectively. The core compositions gave large ranges of both temperature (841–966 ± 22 °C; Fig. 2.10) and oxygen fugacity (0.2–0.75 ± 0.9 ΔNNO; Table 7); the rims give significantly different intensive conditions only in the sample Cal-160, with calculated temperatures ranging from 900 to 1,073 ºC (Fig. 2.10) and oxygen fugacities from 0.2 to 0.75 ΔNNO ± 0.1 ΔNNO (Table 2.7). Details of intensive conditions related to each ilmenite-titanomagnetite pair and associated errors are given below and included in Table 2.7.

Samples *Cal-149Tb* and *Cal-155*: Temperatures are calculated from four core compositions of ilmenites and associated titanomagnetites considering diverse measurements (details in Online Resource 3). Individual pairs of grains show fairly constant compositions and, consequently, similar temperatures and oxygen fugacities, but different temperatures are obtained in different samples (see Table 2.7). For the sample Cal-149Tb, the temperatures are 961–1,008 ± 22 ºC (average 982 ºC, σ = 23 ºC) and oxygen fugacities are 0.36–0.45 ΔNNO (average 0.41 ΔNNO, σ = 0.04); for sample Cal-155 temperatures are 902–922 ± 22 ºC (average 907 ºC, σ = 10 ºC) and oxygen fugacities are 0.17–0.23 ΔNNO (average 0.2 ΔNNO, σ = 0.13).

Sample *Cal-160*: In every crystal pair, compositions close to the boundary between these two mineral phases give considerably higher temperatures and slightly lower oxygen fugacity than core compositions (see Table 2.7). Cal-160 core temperatures are 841–894 ± 17 °C (average 870 ºC, σ = 18 ºC) with oxygen fugacities of 0.5–0.94 ± 0.09 ΔNNO (average 0.64 ΔNNO, σ = 0.18); whereas rim temperatures are 947–1,073 ± 23

°C (average 1,018 ºC, σ = 45 ºC) and oxygen fugacities are 0.21–0.75 ± 0.09 ΔNNO (average 0.48 ΔNNO, σ = 0.16).

2.7.5. Ca-in-olivine thermometry

Seven olivine cores give temperatures of 987–1,019 ± 22 ºC (Fig. 2.10; Table 2.5), with an average temperature of 997 ºC (σ = 13 ºC). These Ca-in-olivine temperatures are therefore consistent with those obtained using the two-pyroxenes, Fe-Ti oxides, and plagioclase-amphibole thermometers for the same samples.

2.7.6. MELTS modelling

The initial melt composition used in MELTS (Ghiorso and Sack, 1995) modelling corresponds to the anhydrous groundmass composition of sample Cal-159 (Table 4) because it shows the highest Mg# (0.59), possesses representative mineral assemblages and textural features observed in all April 2015 Calbuco products. The initial composition is calculated via an extraction of the modal composition of representative mineral phases from the whole-rock composition of the sample (Table 2.3). Details of the MELTS modelling results are available as Online Resource 4.

Zone 2 compositions of plagioclase phenocrysts (later rims and crystals) and the entire range of observed clinopyroxene and orthopyroxene compositions are reproduced by MELTS at conditions of 2–4% dissolved water, 2–6 kbar of pressure, temperatures from 900 to 1,060 °C and crystallinity of 16-35 wt%. Conversely, the Zone 1 composition of older plagioclase phenocryst cores and the remaining phases (notably amphibole, olivine and Fe-Ti oxides) are not reproduced. Crystallisation modelling of the products gives a range of solid phases between 16 and 35 wt%. This range does not consider other mineral phases that could not be reproduced by MELTS (amphibole, olivine,

ilmenite, titanomagnetite, and Zone 1 of plagioclase phenocrysts), which increases the crystallinity considerably (see details in Online Resource 4).

Table 2.7. Fe-Ti oxide core (pre-heating) and rim (during heating) intensive conditions rank ordered by core temperature.

Sample	Pair	Place	T (ºC)	Std. Dev.	Error	fO_2 (ΔNNO)	Std. Dev.	Error	Place	T (ºC)	Error	fO_2 (ΔNNO)	Error
160	Fig1_p2	core	841	6	12	0.94	0.05	0.04	rim	1041	14	0.55	0.04
160	Fig1_p1	core	841	7	12	0.91	0.03	0.04	rim	1067	17	0.5	0.05
160	Fig1_p3	core	846	4	12	0.9	0.02	0.04	rim	1005	15	0.56	0.05
160	Figh_p1	core	865	8	15	0.5	0.06	0.09	rim	1068	15	0.64	0.03
160	Figf_p1	core	868	11	16	0.49	0.03	0.09	rim	1073	23	0.21	0.09
160	Figf_p2	core	870	1	17	0.45	0.01	0.09	rim	947	19	0.27	0.09
160	Figb_p1	core	879	8	17	0.44	0.1	0.09	rim	952	18	0.32	0.09
160	Figex_p1	core	879	13	15	0.55	0.06	0.07	rim	1015	18	0.43	0.06
160	Fig13_p2	core	879	7	15	0.61	0.03	0.08	rim	1013	15	0.61	0.05
160	Fig17_p4	core	883	8	16	0.55	0.03	0.07	rim	963	17	0.47	0.08
160	Fig17_p2	core	892	6	15	0.59	0.03	0.07	rim	1048	14	0.75	0.03
160	Fig17_p1	core	894	14	15	0.66	0.08	0.07	rim	1029	19	0.4	0.07
155	Fig3_p1	core	903	17	20	0.21	0.11	0.12	rim	922	21	0.23	0.12
155	Fig24_p1	core	902	18	21	0.17	0.1	0.13	rim	900	22	0.2	0.13
149Tb	Fig14_p2	core	961	6	22	0.36	0.02	0.1	rim	1008	22	0.45	0.09
149Tb	Fig14_p1	core	966	6	22	0.39	0.03	0.1	rim	996	21	0.45	0.09

2.8. Discussion

All the April 2015 Calbuco samples studied here (including sample Cal-160) have characteristics typical of Calbuco's products documented previously for all the volcanic units by López-Escobar et al., 1995b; Moreno et al., 2006; Sellés and Moreno, 2011; Daga et al., 2014. These include whole-rock chemistry, mineral assemblage, and textural features (cf. Tables 2.1 and 2.2). Additionally, the trace-element data (Fig. 2.3c) show no significant differences in either elemental concentrations or distribution patterns across the whole sample suite (including Cal-160). Of the whole-rock chemistry of the April 2015 Calbuco eruption presented here (55.6–56.9 wt% SiO_2), the compositions are very similar to those reported for this eruption by Castruccio et al. (2016) for scoriaceous, pumiceous and dense juvenile products (54.5–58.1 wt% SiO_2). Further, the composition of the products analysed here are chemically within the range of older units (Unit 1: 50.5–60.3 wt% SiO_2, Unit 2: 57.1–61 wt% SiO_2, Unit 3: 54.3–64.5 wt% SiO_2; López-Escobar et al. 1995b; Sellés and Moreno 2011) and other deposits of Unit 4 (54.8–58.6 wt% SiO_2; López-Escobar et al. 1995b). The mineral assemblage has been fairly constant during the history of the volcano (Sellés and Moreno 2011), it being composed of plagioclase, clinopyroxene, orthopyroxene, amphibole, ilmenite, titanomagnetite, and olivine, (see Table 1) the latter always being surrounded by pyroxenes, plagioclase and Fe-Ti oxides.

2.8.1. Mush reservoir in the upper crust

The Calbuco volcanic products of 2015 possess several features that have been regarded as consistent with mush-zone magma storage, in the manner proposed by, for example, Hildreth (2004) and Bachmann and Bergantz (2006). These features include: high crystallinity (~40–60 vol%) of the volcanic products (cf. Hildreth, 2004; Bachmann and Bergantz, 2006), the presence of clots of crystals where interstitial glasses are locally well-preserved and

compositionally different from the outer glasses (e.g., Saunders et al., 2010; Passmore et al., 2012; Spera and Bohrson, 2018), and the presence of complex textural features that suggest episodes of re-equilibration (cf. Moore et al., 2014). Although only small compositional ranges are recognised here for Calbuco in plagioclase, pyroxene, and amphibole, the complex mineralogical textures commonly observed indicate a prolonged history of crystallisation and with changes in either temperature, pressure, melt composition, oxygen fugacity, or other intensive variables through a protracted period of time (see Fig. 2.5, 2.6, and 2.9).

Our assumption that at the Cal-159 groundmass is a reasonable proxy for the melt composition in equilibrium with the crystal mush, is supported by the MELTS modelling which can reproduce the compositions of the dominant crystal phases of plagioclase (Zone 2), ortho- and clino-pyroxene. Pressure ranges obtained via amphibole barometry (considering average and standard deviation pressures) suggest the location of the mush reservoir at shallow depth. The barometer calibrated by Ridolfi et al. (2010) gives pressures equivalent to 5.8–9.5 km depths; while the barometer calibrated by Ridolfi and Renzulli (2012) gives pressures equivalent to 5.1–8.4 km depths (each considering a crustal density of 2.8 g/cm^3; Fowler, 2005). These depth ranges have some degree of overlap with the source of co-eruptive subsidence located between 8 and 11 km depth by Delgado et al. (2017). In addition, the barometry results are consistent with the source related to the seismic swarm that occurred a few hours before the eruption, this being a VT event of depth between 7.1 and 7.4 km (SERNAGEOMIN, 2015h; 2015i). A summary of inferred depths for the reservoir that fed the eruption is given in Fig. 2.11. The shallow reservoir suggested in this figure would belong to upper crustal magma storage (Tašárová 2007). This is distinct from the crystallisation of crustal xenoliths at 6–8 kbar (equivalent to depths of 21 to 28 km) reported by Hickey-Vargas et al. (1995) based on amphibole barometry on samples of the 1961 eruption. These results suggest middle to lower crustal storage of the 1961 magma. In several

volcanic complexes of the Southern Andes mush magma reservoirs have been recognised in the upper crust (e.g., at Llaima, Bouvet de Maisonneuve et al., 2012 and Quetrupillán, Brahm et al., 2018). Shallow reservoirs in the Southern Volcanic Zone of the Andes have also been inferred via changes in rigidity of the upper crust (Morgado et al. 2017) and the compressive intra-arc tectonic setting (Cembrano and Lara 2009; Chaussard and Amelung 2012). Together these results suggest that a complex system of chambers extending from deep to shallow levels may be commonplace at Andean volcanoes.

2.8.2. Shape and heterogeneity of the reservoir

Delgado et al. (2017) have suggested a prolate, pressurised spheroid shape for the reservoir beneath Calbuco volcano via modelling of the co-eruptive subsidence signal. According to the time-dependent numerical modelling of an evolving magma chamber by Gutiérrez and Parada (2010), thermal heterogeneities are much more likely in stock-like than sill-shaped chambers. Considering long-term thermometry (via two-pyroxenes, amphibole-plagioclase, amphibole, and Ca-in-olivine geothermometers; see Tables 5 and 6), sample Cal-160 shows systematically lower temperatures than all other samples (Fig. 2.10). Fe-Ti oxides thermometry is commonly used to estimate immediately pre-eruptive temperatures (this being "short-term thermometry": Ruprecht and Bachmann 2010; Brahm et al. 2018), and here sample Cal-160 shows systematically lower temperatures for core-core equilibria of in-contact ilmenite-titanomagnetite pairs (see Table 7).

According to Gutiérrez and Parada (2010), in modelling of stock-like reservoirs, the highest temperatures related to crystallinities of between 30 and 40 vol% are found in the middle of the reservoir. This is a feature of all samples except Cal-160. Instead, lower temperatures related to crystallinities of ~60 vol% are found at the bottom of the reservoir, as is consistent with features of sample Cal-160. In addition, sample Cal-160 is slightly more evolved than all other samples (lower Mg# and higher SiO_2 wt%, see Fig. 2.3). This according to the

Gutiérrez and Parada (2010) modelling, is also consistent with the location of Cal-160 in the lower zone or at the borders of the magma chamber.

2.8.3. Local-scale heating

In-contact ilmenite-titanomagnetite pairs exchange elements (e.g., $Fe^{2+}+Ti^{4+} \leftrightarrow 2Fe^{3+}$; Ghiorso and Sack 1991) across the interface, which can be used as thermometer and oxygen barometer (Ghiorso and Evans 2008; Sauerzapf et al. 2008). As a consequence, such boundaries respond rapidly to changes in the intensive physical properties of temperature and/or oxygen fugacity within the reservoir (Lasaga 1983). Therefore, we can postulate that crystal core compositions may represent older, relatively long-term temperatures, whereas rim compositions give information of changes of temperature over a short timescale immediately before eruption.

Rim compositions (close to the interface of the crystal pairs) yield considerably higher temperatures than core compositions only in the sample Cal-160 (70 to 220 °C higher relative to crystal cores; Table 7). The remaining samples show similar Fe-Ti oxides temperatures for cores and rims, with no late heating stage. Additionally, the compositional zonations in orthopyroxene, clinopyroxene, and plagioclase phenocrysts (see Figs. 2.5, 2.6, and 2.9) are within the crystal clots as well as in contact with the groundmass, suggesting these zonings were inherited from the crystal mush development stage. This development period would not be associated with zoning due to an ionic exchange as response to the same heating as Fe-Ti oxides recorded, because the silicate phases have much lower ionic diffusivities and record older stages of the evolution of the system.

Sample Cal-160, is unique across the sampled deposits as being the only material that records evidence of heating. Its composition and crystallinity make it representative of the bottom of the mush reservoir. The heating that this sample records seems both localised and intense,

consistent with an input of hotter magma. Underlying recharge of hot magma has been suggested as a trigger for many eruptions of Southern Andean shallow reservoirs (e.g., Quizapu, Ruprecht and Bachmann 2010; Villarrica, Lohmar et al. 2012; Morgado et al., 2015). Some eruptions have also involved the presence of a mush zone (e.g., Llaima, Bouvet de Maisonneuve et al. 2012; Quetrupillán, Brahm et al. 2018). The nature and extent of magma mixing in such situations has been further proposed to influence eruptive style: Ruprecht and Bachmann (2010) suggested that increasing degrees of magma mixing (between felsic magma and a more mafic recharge) decreases the fragmentation efficiency and magma viscosity, and thus favours effusive eruptions. Restricted compositional interaction between the new magma influx and an overlying crystal mush could occur because of the mush acting (at least initially) as a rheological barrier (Huber et al. 2009; Kent et al. 2010) or because of the occurrence of a volatile layer between the hot magma and the crystal mush (Bachmann and Bergantz 2006; Huber et al. 2010b; Parmigiani et al. 2014; Schleicher and Bergantz 2017; Spera and Bohrson 2018). In this situation, only small magma volumes could be reheated, favouring explosive eruptions (cf. Couch et al. 2001; Ruprecht and Bachmann, 2010). Data presented here suggest that this was the case for the April 2015 Calbuco eruption. Our results are consistent with those from Castruccio et al. (2016) who, based on stratigraphy and whole-rock geochemistry, suggested that the April 2015 Calbuco eruption was triggered by either volatile exsolution or a moderate-sized magmatic intrusion of a new magma into the base of the reservoir with almost no mixing effects.

2.9. Conclusions

The 2015 Calbuco eruption is an example of a shallow, crystal-rich magma reservoir feeding a moderate-sized eruption (~0.3–0.6 km^3 erupted products, non-DRE). Based on textural and compositional criteria of nine representative samples, we conclude the existence of a mush reservoir, which amphibole barometry indicates to lie within the upper to middle crust (at 5.5–9.5 km depth), consistent with previous works (SERNAGEOMIN 2015h, i; Delgado et al. 2017).

A prolate spheroid shape of the reservoir has been inferred from previous studies and, based on detailed thermobarometry, crystallinity and the compositions of nine representative samples, we infer that all samples of this study (except Cal-160) are derived from the middle of a mush reservoir. Sample Cal-160 represents a portion of the rheologically rigid basal envelope. In addition, based on Fe-Ti oxide (ilmenite and titanomagnetite) thermometry and textural features of the crystal-clot-rich Cal-160 sample, we identify a localised heating event of 70–220 ºC, reaching potentially as high as 1070 °C. This mobilised magma represented by Cal-160, an event which we infer to be linked to eruption triggering (Fig. 2.12) and that would have affected only the magma reservoir at its highly crystalline (mush) base. The absence of a heating record in the remaining samples suggests that all other magma remained thermally and chemically unaffected by the trigger pulse during eruption. This emphasises the need for rapid warning systems to communicate hazards rapidly to the local population.

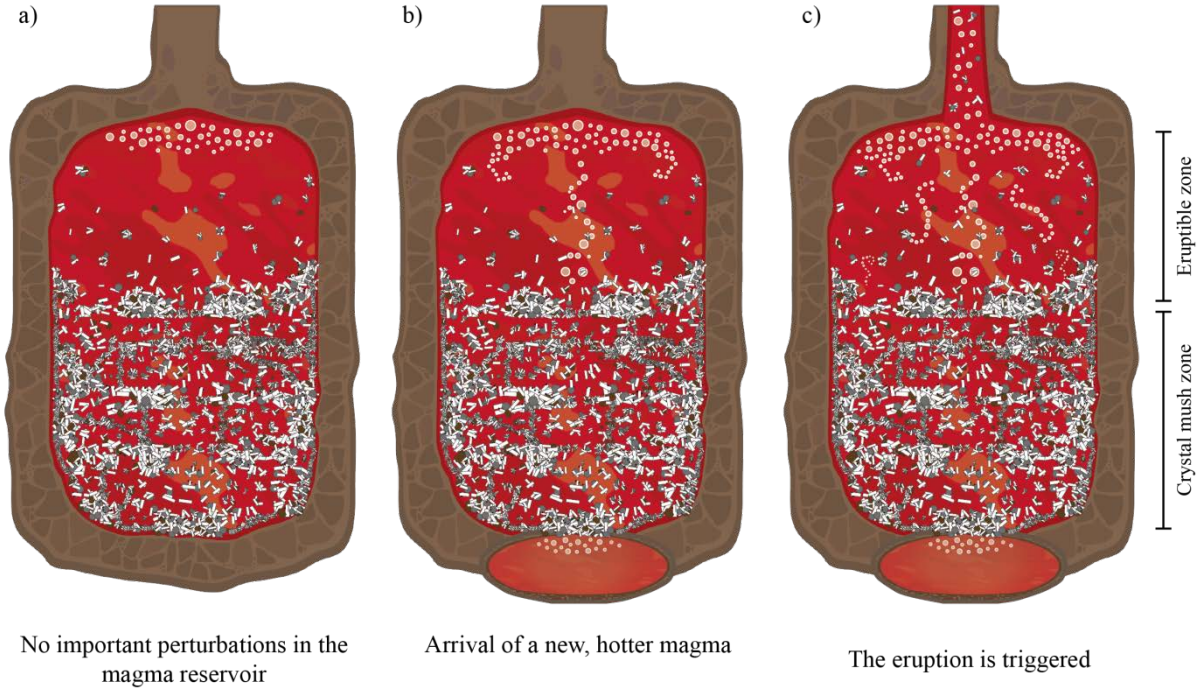

Figure 2.12. *Schematic representation of the shape, and evolution in time, of the magma reservoir beneath Calbuco volcano; a) represents the reservoir, including a mush zone at the bottom, before the input of new magma; b) represents the arrival of the new, hotter magma generating a local-scale heating; c) represents the moment of eruption triggering.*

2.10. Acknowledgements

We acknowledge the help in the field of Marcela Vollmer. We acknowledge Richard Walshaw for assistance with the EPMA, and Duncan Hedges who provided assistance with the SEM at the University of Leeds. Financial support through FONDAP project 15090013 (Centro de Excelencia en Geotermia de los Andes, CEGA), CONICYT MSc fellowship (22141497, RB) and CONICYT PhD fellowship (72160268, EM) are acknowledged. We would like to specially thank to Claire Harnett. We thank two anonymous reviewers for their detailed and constructive comments. Editorial handling and constructive comments of L. Pioli and A. Harris are greatly appreciated.

2.11. References

Adriasola, AC, Thomson, SN, Brix, MR, Hervé, F, Stöckhert, B (2006) Postmagmatic cooling and late Cenozoic denudation of the North Patagonian Batholith in the Los Lagos region of Chile, 41− 42 15′ S. Int J Earth Sci 95(3), 504-528. http://doi.org/10.1007/s00531-005-0027-9

Aggarwal, S, Dieckmann, R (2002a) Point defects and cat ion tracer diffusion in $(Ti_xFe_{1-x})_{3-\delta}O_4$. 1. Non-stoichiometry and point defects. Phys Chem Miner 29(10), 695-706. http://doi.org/10.1007/s00269-002-0282-2

Aggarwal, S, Dieckmann, R (2002b) Point defects and cation tracer diffusion in $(Ti_xFe_{1-x})_{3-\delta}O_4$. II. Cation tracer diffusion. Phys Chem Miner 29(10), 707-718. http://doi.org/10.1007/s00269-002-0284-0

Aragon, R, McCallister, RH, Harrison, HR (1984) Cation diffusion in titanomagnetites. Contrib Mineral Petr *85*(2), 174-185. http://doi.org/10.1007/BF00371707

Bachmann, O, Bergantz, GW (2004) On the Origin of Crystal-poor Rhyolites: Extracted from a Batholithic Crystal Mushes. J Petrol 45(8), 1565-1582. http://doi.org/10.1093/petrology/egh019

Bachmann, O, Bergantz, GW (2006) Gas percolation in upper-crustal silicic crystal mushes as a mechanism for upward heat advection and rejuvenation of near-solidus magma bodies. J Volcanol Geotherm Res 149(1), 85-102. https://doi.org/10.1016/j.jvolgeores.2005.06.002

Bachmann, O, Bergantz, G (2008). The magma reservoirs that feed supereruptions. Elements, 4(1), 17-21. https://doi.org/10.2113/GSELEMENTS.4.1.17

Bouvet De Maisonneuve, C, Dungan, MA, Bachmann, O, Burgisser, A (2012) Insights into shallow magma storage and crystallization at Volcán Llaima (Andean Southern Volcanic Zone, Chile). J Volcanol Geotherm Res *211*, 76-91. http://doi.org/10.1016/j.jvolgeores.2011.09.010

Brahm, R, Parada, MA, Morgado, E, Contreras, C, McGee, L (2018) Origin of trachyte lavas of the Quetrupillán Volcanic Complex, Chile (39º30'S): Examples of residual melts in rejuvenated crystalline mush reservoir. J Volcanol Geotherm Res 357, 163-176. http://doi.org/10.1016/j.jvolgeores.2018.04.020

Burgisser, A, Bergantz, GW (2011) A rapid mechanism to remobilize and homogenize highly crystalline magma bodies. Nature, 471, 212-216. http://dx.doi.org/10.1038/nature09799

Castruccio, A, Clavero, J, Rivera, A (2010) Comparative study of lahars generated by the 1961 and 1971 eruptions of Calbuco and Villarrica volcanoes, Southern Andes of Chile. J Volcanol Geotherm Res 190(3–4), 297–311. http://doi.org/10.1016/j.jvolgeores.2009.12.005

Castruccio, A, Clavero, J, Segura, A, Samaniego, P, Roche, O, Le Pennec, J, Droguett, B (2016). Eruptive parameters and dynamics of the April 2015 sub-Plinian eruptions of Calbuco volcano (Southern Chile). Bull Volcanol 327: 469-483. http://dx.doi.org/10.1007/s00445-016-1058-8

Cembrano, J, Hervé, F, Lavenu, A (1996) The Liquine Ofqui fault zone: a long-lived intra-arc fault system in southern Chile. Tectonophysics 259(1-3), 55-66. http://doi.org/10.1016/0040-1951(95)00066-6

Cembrano, J, Lara, L (2009) The link between volcanism and tectonics in the southern volcanic zone of the Chilean Andes: a review. Tectonophysics 471(1-2), 96-113. http://doi.org/10.1016/j.tecto.2009.02.038

Cembrano, J, Schermer, E, Lavenu, A, Sanhueza, A (2000) Contrasting nature of deformation along an intra-arc shear zone, the Liquiñe-Ofqui fault zone, southern Chilean Andes. Tectonophysics 319, 219-149. doi: http://doi.org/10.1016/S0040-1951(99)00321-2

Chaussard, E, Amelung, F (2012) Precursory inflation of shallow magma reservoirs at west Sunda volcanoes detected by InSAR. Geophys Res Lett 39(21). http://doi.org/10.1029/2012GL053817

Claiborne, LL, Miller, CF, Flanagan, DM, Clynne, MA, Wooden, JL (2010) Zircon reveals protracted magma storage and recycling beneath Mount St. Helens. Geology 38(11), 1011-1014. https://doi.org/10.1130/G31285.1

Cooper, GF, Morgan, DJ, Wilson, CJ (2017). Rapid assembly and rejuvenation of a large silicic magmatic system: Insights from mineral diffusive profiles in the Kidnappers and Rocky Hill deposits, New Zealand. Earth Planet Sc Lett, 473, 1-13. https://doi.org/10.1016/j.epsl.2017.05.036

Cooper, KM, Kent, AJ (2014). Rapid remobilization of magmatic crystals kept in cold storage. Nature, 506(7489), 480. https://doi.org/10.1038/nature12991

Daga, R, Ribeiro Guevara, S, Poire, DG, Arribére, M (2014) Characterization of tephras dispersed by the recent eruptions of volcanoes Calbuco (1961), Chaitén (2008) and Cordón Caulle Complex (1960 and 2011), in Northern Patagonia. J S Am Earth Sci *49*, 1–14. http://doi.org/10.1016/j.jsames.2013.10.006

Dalton, JA, Lane, SJ (1996). Electron microprobe analysis of Ca in olivine close to grain boundaries: the problem of secondary X-ray fluorescence. American Mineralogist, 81(1-2), 194-201. https://doi.org/10.2138/am-1996-1-224

Delgado, F, Pritchard, ME, Ebmeier, S, González, P, Lara, L (2017) Recent unrest (2002-2015) imaged by space geodesy at the highest risk Chilean volcanoes: Villarrica, Llaima, and Calbuco (Southern Andes). J Volcanol Geotherm Res 344, 270-288. http://dx.doi.org/10.1016/j.jvolgeores.2017.05.020

Dohmen, R, Chakraborty, S (2007a) Fe–Mg diffusion in olivine I: experimental determination between 700 and 1,200 ° C as a function of composition, crystal orientation and oxygen fugacity. Phys Chem Miner 34:389–407. http://dx.doi.org/10.1007/s00269-007-0157-7

Dohmen, R, Chakraborty, S (2007b) Fe–Mg diffusion in olivine II: point defect chemistry, change of diffusion mechanisms and a model for calculation of diffusion coefficients in natural olivine. Phys Chem Miner 34:409–430. http://dx.doi.org/10.1007/s00269-007-0158-6

Dohmen, R, Ter Heege, JH, Becker, HW, Chakraborty, S (2016). Fe-Mg interdiffusion in orthopyroxene. Am Mineral 101(10), 2210-2221. http://doi.org/10.2138/am-2016-5815

Droop, GTR (1987) A general equation for estimating Fe^{3+} concentrations in ferromagnesian silicates and oxides from microprobe analyses, using stoichiometric criteria. Mineral Mag 51, 431-435.

Fischer, O (1893) Erupción del volcán Calbuco. Anales de la Universidad de Chile LXXXV, 197-204. Santiago.

Fowler, CMR (2005). The solid Earth: an introduction to global geophysics. 2nd edition. Cambridge: Cambridge University Press.

Ganguly, J, Tazzoli, V (1994) Fe^{2+}-Mg interdiffusion in orthopyroxene: Retrieval from the data on intracrystalline exchange reaction. Am Mineral 79(9-10), 930-937.

Ghiorso, MS, Evans, BW (2008) Thermodynamics of rhombohedral oxide solid solutions and a revision of the Fe-Ti two-oxide geothermometer and oxygen-barometer. Am J Sci 308, 957–1039. http://dx.doi.org/10.2475/09.2008.01

Ghiorso, MS, Sack, O (1991) Fe-Ti oxide geothermometry: thermodynamic formulation and the estimation of intensive variables in silicic magmas. Contrib Mineral Petr 108(4), 485-510. http://doi.org/10.1007/BF00303452

Grove, TL, Baker, MB, Kinzler, RJ (1984) Coupled CaAl-NaSi diffusion in plagioclase feldspar: experiments and applications to cooling rate speedometry. Geochim Cosmochim Acta 48(10), 2113-2121. http://doi.org/10.1016/0016-7037(84)90391-0

Grove, TL, Donnelly-Nolan, JM, Housh, T (1997). Magmatic processes that generated the rhyolite of Glass Mountain, Medicine Lake volcano, N. California. Contributions to Mineralogy and Petrology, 127(3), 205-223.https://doi.org/10.1007/s004100050276

Gutiérrez, F, Parada, MÁ (2010) Numerical modeling of time-dependent fluid dynamics and differentiation of a shallow basaltic magma chamber. J Petrol 51(3), 731-762. http://doi.org/10.1093/petrology/egp101

Hickey-Vargas, R, Abdollahi, MJ, Parada, MA, López-Escobar, L, Frey, FA (1995) Crustal xenoliths from Calbuco Volcano, Andean Southern Volcanic Zone: implications for crustal composition and magma-crust interaction. Contrib Mineral Petr 119(4), 331–344. http://dx.doi.org/10.1007/BF00286933

Hildreth, W (2004) Volcanological perspectives on Long Valley, Mammoth Mountain, and Mono Craters: several contiguous but discrete systems. J Volcanol Geotherm Res *136*(3), 169-198. https://doi.org/10.1016/j.jvolgeores.2004.05.019

Holland, T, Blundy, J (1994) Non-ideal interactions in calcic amphiboles and their bearing on amphibole-plagioclase thermometry. Contrib Mineral Petrol 116(4), 433–447. http://dx.doi.org/10.1007/BF00310910

Huber, C, Bachmann, O, Dufek, J (2010a) The limitations of melting on the reactivation of silicic mushes. J Volcanol Geotherm Res *195*(2), 97-105. https://doi.org/10.1016/j.jvolgeores.2010.06.006

Huber, C, Bachmann, O, Manga, M (2009) Homogenization processes in silicic magma chambers by stirring and mushification (latent heat buffering). Earth Planet Sc Lett 283(1), 38-47. https://doi.org/10.1016/j.epsl.2009.03.029

Huber, C, Bachmann, O, Manga, M (2010b) Two competing effects of volatiles on heat transfer in crystal-rich magmas: thermal insulation vs defrosting. J Petrol 51(4), 847-867. https://doi.org/10.1093/petrology/egq003

Irvine, TNJ, Baragar, WRAF (1971) A guide to the chemical classification of the common volcanic rocks. Can. J. Earth Sci., 8 (5), 523–548. https://doi.org/10.1139/e71-055

Ivy, DJ, Solomon, S, Kinnison, D, Mills, MJ, Schmidt, A, Neely, RR (2017) The influence of the Calbuco eruption on the 2015 Antarctic ozone hole in a fully coupled chemistry-climate model. Geophys Res Lett 44, 1–6. http://dx.doi.org/10.1002/2016GL071925

Kent, AJ, Darr, C, Koleszar, AM, Salisbury, MJ, Cooper, KM (2010) Preferential eruption of andesitic magmas through recharge filtering. Nat. Geosci., 3(9), 631-636. http://doi.org/10.1038/ngeo924

Koyaguchi, T, Kaneko, K (1999) A two-stage thermal evolution model of magmas in continental crust. J Petrol 40(2), 241-254. https://doi.org/10.1093/petroj/40.2.241

Klohn, E (1963) The February 1961 eruption of Calbuco Volcano. B. Seismol. Soc. Am., 53(6), 1435-1436.

Lahsen, A, Moreno, H, Varela, J, Munizaga, F, López, L (1985) Geología y riesgo volcánico del volcán Calbuco y centros eruptivos menores. Proy Canutillar, ENDESA-Univ Chile, Informe Técnico, 215p.

Lara, LE, Orozco, G, Amigo, Á, Silva, C (2011) Peligros Volcánicos de Chile, Servicio Nacional de Geología y Minería, Carta Geológica de Chile, Serie Geología Ambiental. No. 13:34, Mapa escala 1:2.000.000. Santiago.

Lasaga, AC (1983) Geospeedometry: an extension of geothermometry. In: Saxena, S.K. (Ed.), Kinetics and Equilibrium in Mineral Reactions. In: Advances in Physical Geochemistry, vol. 3. Springer, New York, pp. 81–114.

Le Bas, ML, Maitre, RL, Streckeisen, A, Zanettin, B, IUGS Subcommission on the Systematics of Igneous Rocks (1986) A chemical classification of volcanic rocks based on the total alkali-silica diagram. J Petrol., 27(3), 745-750. https://doi.org/10.1093/petrology/27.3.745

Leake, BE, Woolley, AR, Arps, CES, Birch, WD, Gilbert, MC, Grice, JD, Hawthorne, FC, Kato, A, Kisch, HJ, Krivovichev, VG, Linthout, K, Laird, J, Mandarino, JA, Maresch, WV, Nickel, EH, Rock, NMS, Schumacher, JC, Smith, DC, Stephenson, NCN, Ungaretti, L, Whittaker, EJW, Youzhi, G (1997) Nomenclature of amphiboles: Report of the subcomittee on amphiboles of the International Mineralogical Association, Commission on new minerals and mineral names. Can Mineral 35, 219–246.

Lohmar, S, Parada, M, Gutiérrez, F, Robin, C, Gerbe, MC (2012) Mineralogical and numerical approaches to establish the pre-eruptive conditions of the mafic Lican Ignimbrite, Villarrica Volcano (Chilean Southern Andes). J Volcanol Geotherm Res *235*, 55-69. doi: http://doi.org/10.1016/j.jvolgeores.2012.05.006

López-Escobar, L, Cembrano, J, Moreno, H (1995a) Geochemistry and tectonics of the Chilean Southern Andes basaltic Quaternary volcanism (37-46º S). Rev Geol Chile 22 (2), 219-234.

López-Escobar, L, Parada, MÁ, Hickey-Vargas, R, Frey, FA, Kempton, PD, Moreno, H (1995b). Calbuco Volcano and minor eruptive centers distributed along the Liquiñe-Ofqui Fault Zone, Chile (41º-42º S): contrasting origin of andesitic and basaltic magma in the Southern Volcanic Zone of the Andes. Contrib Mineral Pet. 119:345-36. http://dx.doi.org/10.1007/BF00286934

López-Escobar, L, Parada, MÁ, Moreno, H, Frey, FA, Hickey-Vargas, RL (1992) A contribution to the petrogenesis of Osorno and Calbuco volcanoes, Southern Andes (41º00'-41º30' S): comparative study. Rev Geol Chile 19(2), 211-226.

Marsh, BD (1989) Magma chambers. Annu Rev Earth Pl Sc 17(1), 439-472. http://dx.doi.org/10.1146/annurev.ea.17.050189.002255

Marsh, BD (1996) Solidification fronts and magmatic evolution. Mineral Mag 60(1), 5-40. http://doi.org/10.1180/minmag.1996.060.398.03

Molina, PG, Parada, MÁ, Gutiérrez, FJ, Ma, C, Li, J, Yuanyuan, L, Reich, M, Aravena, Á (2015) Protracted late magmatic stage of the Caleu pluton (central Chile) as a consequence of heat redistribution by diking: Insights from zircon data and thermal modeling. Lithos *227*, 255-268. https://doi.org/10.1016/j.lithos.2015.04.008

Moore, A, Coogan, LA, Costa, F, Perfit, MR (2014) Primitive melt replenishment and crystal-mush disaggregation in the weeks preceding the 2005–2006 eruption 9° 50′ N, EPR. Earth Planet Sc Lett 403, 15-26. https://doi.org/10.1016/j.epsl.2014.06.015

Moreno, H, Naranjo, JA, Clavero, J (2006). Generación de lahares calientes en el volcán Calbuco, Andes del sur de Chile (41,3ºS). In Congreso Geológico Chileno, no. 11, actas 512-513, Antofagasta.

Morgado, E, Parada, MÁ, Contreras, C, Castruccio, A, Gutiérrez, F, McGee, L (2015) Contrasting records from mantle to surface of two nearby arc volcanic complexes: Caburgua-Huelemolle Small Eruptive Centers and Villarrica Volcano**.** J Volcanol. Geotherm Res 306:1-16. http://dx.doi.org/10.1016/j.jvolgeores.2015.09.023

Morgado, E, Parada, MÁ, Morgan, DJ, Gutiérrez, F, Castruccio, A, Contreras, C (2017) Transient shallow reservoirs beneath small eruptive centres: Constraints from Mg-Fe interdiffusion in olivine. J Volcanol Geotherm Res 347, 327-336. http://doi.org/10.1016/j.jvolgeores.2017.10.002

Müller, T, Dohmen, R, Becker, HW, Ter Heege, JH, Chakraborty, S (2013) Fe–Mg interdiffusion rates in clinopyroxene: experimental data and implications for Fe–Mg exchange geothermometers. Contrib Mineral Petr 166(6), 1563-1576. http://doi.org/10.1007/s00410-013-0941-y

Parada, MÁ (1990) Composición de fenocristales en lavas en volcán Calbuco y sus implicancias en la historia temprana de cristalización. Actas XI Congreso Geológico Argentino, 1: 101-104.

Parmigiani, A, Huber, C, Bachmann, O (2014) Mush microphysics and the reactivation of crystal-rich magma reservoirs. J. of Geophys. Res Solid Earth 119(8), 6308-6322. http://doi.org/10.1002/2014JB011124

Passmore, E, Maclennan, J, Fitton, G, Thordarson, T (2012) Mush disaggregation in basaltic magma chambers: evidence from the AD 1783 Laki eruption. J Petrol 53(12), 2593-2623. https://doi.org/10.1093/petrology/egs061

Petit-Breuilh, ME (1999) Cronología eruptiva histórica de los volcanes Osorno y Calbuco, Andes del Sur (41º-41º30'S). Boletín no. 53. Servicio Nacional de Geología y Minería, 46 p.

Putirka, KD (2008) Thermometers and Barometers for Volcanic Systems. Rev. Mineral. Geochem. 69(1), 61–120. http://dx.doi.org/10.2138/rmg.2008.69.3

Ridolfi, F, Renzulli, A (2012) Calcic amphiboles in calc-alkaline and alkaline magmas : thermobarometric and chemometric empirical equations valid up to 1,130 ° C and 2.2 GPa, Contrib Mineral Petrol 163: 877–895. http://dx.doi.org/10.1007/s00410-011-0704-6

Ridolfi, F, Renzulli, A, Puerini, M (2010) Stability and chemical equilibrium of amphibole in calc-alkaline magmas: an overview, new thermobarometric formulations and application to subduction-related volcanoes. Contrib Mineral Petrol 160(1), 45–66. http://dx.doi.org/10.1007/s00410-009-0465-7

Romero, JE, Morgavi, D, Arzilli, F, Daga, R, Caselli, A, Reckziegel, F, Viramonte, J (2016) Eruption dynamics of the 22 – 23 April 2015 Calbuco Volcano (Southern Chile): Analyses of tephra fall deposits. J Volcanol Geotherm Res 317, 15–29. http://dx.doi.org/10.1016/j.jvolgeores.2016.02.027

Ruprecht, P, Bachmann, O (2010) Pre-eruptive reheating during magma mixing at Quizapu volcano and the implications for the explosiveness of silicic arc volcanoes. Geology 38(10), 919-922. http://doi.org/10.1130/G31110.1

Sauerzapf, U, Lattard, D, Burchard, M, Engelmann, R (2008) The titanomagnetite–ilmenite equilibrium: new experimental data and thermo-oxybarometric application to the crystallization of basic to intermediate rocks. J Petrol 49(6), 1161-1185. http://doi.org/10.1093/petrology/egn021

Saunders, KE, Morgan, DJ, Baker, JA, Wysoczanski, RJ (2010) The magmatic evolution of the Whakamaru supereruption, New Zealand, constrained by a microanalytical study of plagioclase and quartz. J Petrol 51(12), 2465-2488. https://doi.org/10.1093/petrology/egq064

Schleicher, JM, Bergantz, GW (2017) The mechanics and temporal evolution of an open-system magmatic intrusion into a crystal-rich magma. J Petrol 58, 1059-1072. http://doi.org/10.1093/petrology/egx045

Sellés, D, Moreno, H (2011) Geología del Volcán Calbuco, Región de Los Lagos. Carta Geológica de Chile. Serie Geológica Básica, No. 130. Escala 1:50.000.

SERNAGEOMIN – BRGM (1995) Carta metalogénica X Región Sur, Chile. Servicio Nacional de Geología y Minería, Informe Registrado IR-95-05 (Inédito), 4 tomos, Santiago.

SERNAGEOMIN (2015a) Reporte especial de actividad volcánica (REAV) - Región de los Lagos, 2015, abril 22 – 18:00.

SERNAGEOMIN (2015b) Reporte especial de actividad volcánica (REAV) - Región de los Lagos, 2015, abril 22 – 20:45.

SERNAGEOMIN (2015c) Reporte especial de actividad volcánica (REAV) - Región de los Lagos, 2015, abril 23 – 10:30

SERNAGEOMIN (2015d) Reporte especial de actividad volcánica (REAV) - Región de los Lagos, 2015, abril 23 – 01:10

SERNAGEOMIN (2015e) Reporte especial de actividad volcánica (REAV) - Región de los Lagos, 2015, abril 22 – 22:30.

SERNAGEOMIN (2015f) Reporte especial de actividad volcánica (REAV) - Región de los Lagos, 2015, abril 22 – 17:30

SERNAGEOMIN (2015g) Reporte especial de actividad volcánica (REAV) - Región de los Lagos, 2015, abril 23 - 10.30.

SERNAGEOMIN (2015h) Reporte especial de actividad volcánica (REAV) - Región de los Lagos, 2015, abril 22.

SERNAGEOMIN (2015i) Reporte especial de actividad volcánica (REAV) - Región de los Lagos, 2015, abril – Volumen 4a.

SERNAGEOMIN (2017) Red Nacional de Vigilancia Volcánica, Volcán Calbuco. http://www.sernageomin.cl/volcan-calbuco/. Accesed 27 June 2018.

Shejwalkar, A, Coogan, LA (2013) Experimental calibration of the roles of temperature and composition in the Ca-in-olivine geothermometer at 0.1MPa. Lithos 177, 54–60. http://dx.doi.org/10.1016/j.lithos.2013.06.013

Spera, FJ, Bohrson, WA (2018) Rejuvenation of crustal magma mush: A tale of multiply nested processes and timescales. Am J Sci 318, 90-140. http://doi.org/10.2475/01.2018.05

Stern, CR, Moreno, H, López-Escobar, L, Clavero, JE, Lara, LE, Naranjo, JA, Parada, MÁ, Skewes, MA (2007) Chilean Volcanoes. In: Moreno, T., Gibbons, W. (eds) The Geology of Chile, Geological Society of London, London pp. 149-180.

Stormer, JC (1983) The effects of recalculation on estimates of temperature and oxygen fugacity from analyses of multicomponent iron-titanium oxides. Am Mineral 68, 586–594.

Sun, SS, McDonough, WS (1989) Chemical and isotopic systematics of oceanic basalts: implications for mantle composition and processes. Geological Society, London, Special Publications, 42(1), 313-345. https://doi.org/10.1144/GSL.SP.1989.042.01.19

Szymanowski, D, Wotzlaw, JF, Ellis, BS, Bachmann, O, Guillong, M, von Quadt, A (2017) Protracted near-solidus storage and pre-eruptive rejuvenation of large magma reservoirs. Nat Geosci. http://doi.org/10.1038/NGEO3020

Tašárová, ZA (2007) Towards understanding the lithospheric structure of the southern Chilean subduction zone (36°S-42°S) and its role in the gravity field. Geophys J Int 170(3), 995–1014. http://doi.org/10.1111/j.1365-246X.2007.03466.x

Thiele, R, Godoy, E, Parada, MÁ, Varela, J (1985) Estudio geológico-estructural regional y tectónico del drea Petrohué-Canutillar. Proyecto Petrohué-Canutillar, ENDESA-U. de Chile (Unpublished report).

Valderrama, Ó, Franco, L, Gil-Cruz, F (2015) Erupción intempestiva del volcán Calbuco, Abril 2015, XIV Congreso Geológico Chileno, III, p. 91-93.

Van Eaton, AR, Amigo, Á, Bertin, D, Mastin, LG, Giacosa, RE, González, J, Valderrama, Ó, Fontjin, K, Behnke, SA (2016) Volcanic lightning and plume behavior reveal evolving hazards during the April 2015 eruption of Calbuco volcano, Chile. Geophys Res Lett 43(7): 3563–3571. http://dx.doi.org/10.1002/2016GL068076

Watt, SF, Pyle, DM, Naranjo, JA, Rosqvist, G, Mella, M, Mather, TA, Moreno, H (2011) Holocene tephrochronology of the Hualaihue region (Andean southern volcanic zone, ~42ºS), southern Chile. Quatern Int 246(1), 324-343. http://doi.org/10.1016/j.quaint.2011.05.029

Chapter 3

3. Old magma and a new, intrusive trigger: using diffusion chronometry to understand the rapid-onset Calbuco eruption, April 2015 (Southern Chile)

Eduardo Morgado* [1,2], Daniel J. Morgan [1], Angelo Castruccio [2,3], Susanna K. Ebmeier[1], Miguel-Ángel Parada [2,3], Raimundo Brahm [4], Jason Harvey [1], Francisco Gutiérrez [5], Richard Walshaw [1]

[1] Institute of Geophysics and Tectonics, School of Earth and Environment, University of Leeds, Leeds LS2 9JT, UK

[2] Centro de Excelencia en Geotermia de los Andes (CEGA-FONDAP 15090013), Chile.

[3] Departamento de Geología, Facultad de Ciencias Físicas y Matemáticas, Universidad de Chile, Chile.

[4] Volcanic Risk Solutions, IAE, Massey University, Palmerston North 4442, New Zealand.

[5] GeoExpedition, Las Barrancas 25, Pirque, Santiago 9480000, Chile.

[*] Corresponding author at: Institute of Geophysics and Tectonics, School of Earth and Environment, University of Leeds, Leeds LS2 9JT, UK.

Citation: **Morgado, E.**, Morgan, D.J., Castruccio, A., Ebmeier, S.K., Parada, M.Á., Brahm, R., Harvey, J., Gutiérrez, F., Walshaw, R., 2019. Old magma and a new, intrusive trigger: using diffusion chronometry to understand the rapid-onset Calbuco eruption, April 2015 (Southern Chile). Contributions to Mineralogy and Petrology. DOI: 10.1007/s00410-019-1596-0

3.1. Abstract

In April 2015, an unpredicted rapid-onset eruption occurred at Calbuco Volcano, Southern Andes of Chile. This event consisted of two, sub-Plinian eruptions separated by a few hours. By analysis of Fe-Ti exchange between ilmenite and titanomagnetite crystals in samples of erupted material, we determine timescales of pre-eruptive heating experienced at the partially-solidified chamber base and constrain the magma residence time for the bulk of the carrier magma.

Analysis of the Fe-Ti oxide pairs from a sample retrieved from a pyroclastic density current (PDC) deposit (Cal-160), shows that it was affected by a significant heating event (recording 70 to 220 ºC of heating), while other collected samples did not record this late heating. This sample is interpreted to represent a piece of crystal mush located at the bottom of a prolate, ellipsoidal mush reservoir, mobilised < 4 days before the eruption by a triggering pulse of mafic magma considerably hotter than the typical magmatic temperature of the reservoir.

Another two fall deposit samples (lapillus, Cal-149Tb and Cal-155) of the eruption are interpreted to represent resident, eruptible magmas that did not interact with any magma recharge immediately prior to or during the eruption. We infer that these magmas had been at eruption temperature for some years based on their extensively equilibrated Fe-Ti oxides.

3.2. Introduction

Forecasting eruptions and tracking the evolution of magmatic systems are fundamental goals for volcanology. Before many eruptions, geochemical and geophysical time-series data are consistent with changes in magmatic conditions over months to years (e.g., Carapezza and Federico, 2000; Brenguier et al., 2008; Madonia et al., 2013; Delgado et al., 2014; Einarsson, 2018; Ebmeier et al., 2018). Some explosive eruptions, however, are preceded by unrest of only hours to days (e.g., El Reventador volcano in 2002, VEI 4, Hall et al., 2004; Rabaul

volcano in 1994, VEI 4, Roggensack et al., 1996; Chaitén volcano in 2008 (VEI ~5), Castro and Dingwell, 2009), although the certainty with which we can identify such events is limited by the availability and temporal resolution of monitoring data.

During April 2015, two sub-Plinian eruptive events (VEI 4, Romero et al., 2016; Van Eaton et al., 2016) occurred at Calbuco Volcano, Southern Chile, after ~54 years of quiescence (since the last major eruption, in 1961). Calbuco is a Late Pleistocene-Holocene composite stratovolcano (López-Escobar et al., 1992; Sellés and Moreno, 2011) located in the Central Southern Volcanic Zone of the Chilean Andes and is currently rated the third most hazardous of Chile's 90 active volcanoes (SERNAGEOMIN, 2016; 2017). The 2015 Calbuco eruption was notable for being preceded only by seismic unrest of very short duration. A two-hour long swarm of ~140 volcano-tectonic (VT) earthquakes began about three hours before the first eruptive event, while the first long-period (LP) seismicity began just 1.5 hours prior to the beginning of the first eruptive event (SERNAGEOMIN, 2015a; 2015b). Interferometric Synthetic Aperture Radar (InSAR) measurements demonstrate that no significant deformation occurred in the months leading up to eruption at least up until 36 hours before the eruption when the last pre-eruptive InSAR image was acquired (Delgado et al., 2017). Both subsequent satellite radar (Delgado et al., 2017; Nikkhoo et al., 2017) and tiltmeter measurements (Valderrama et al., 2015) captured co-eruptive subsidence during the first eruption consistent with a contracting source at depths of 8 to 11 km below the summit. Seven hours after the beginning of the first eruptive event (1.5 hours duration) a second eruptive event started, following further LP and hybrid seismicity (Valderrama et al., 2015). The eruption produced pyroclastic density current (PDC) and fall deposits with bulk compositions of basaltic andesites (54-56 wt% SiO_2) with scarce andesites (~58 wt% SiO_2; Castruccio et al., 2016). The mineral phases present are: plagioclase (two groups: An_{46-79} and An_{80-92}), clinopyroxene ($En_{43-47}Fs_{9-15}Wo_{40-45}$), orthopyroxene ($En_{67-71}Fs_{26-31}Wo_{2-3}$), amphibole

(edenite and pargasite), titanomagnetite (two groups: $Xusp_{0.10-0.17}$; $Xusp_{0.42-0.46}$), and ilmenite ($Xilm_{0.77–0.85}$) (Castruccio et al., 2016; Morgado et al., 2019). A recent study (Morgado et al., 2019) identified a heating event that affected a mush reservoir as a potential trigger of this rapid-onset eruption, based upon temperatures of up to 1070 ºC recorded in the rims of Fe-Ti oxide (ilmenite-titanomagnetite) crystal pairs (~120 ºC above the ambient magma) using the thermoxybarometer of Ghiorso and Evans (2008).

We collected nine samples from fall and PDC deposits; three of which contain scarce (< 0.1 vol%) titanomagnetite and ilmenite grains in contact with each other (Cal-149Tb, Cal-155, and Cal-160). Significant compositional zoning and exchange are only recorded at the interface of Fe-Ti oxide pairs in the highly-crystalline sample Cal-160 (~60% crystallinity, obtained via image processing of pseudo coloured images through the freeware Jmicrovision), erupted during the second eruptive stage (Fig. 3.1). This sample has been associated in earlier work with the base of the prolate spheroid shape (Delgado et al., 2017) of the magma reservoir based on considerations of differences in whole-rock chemistry, crystallinity, and recorded heating (Morgado et al., 2019). In the rest of the samples (~40% crystallinity, obtained via the same method as Cal-160), erupted during the first and second eruptive pulses, Fe-Ti oxide pairs exhibit relatively homogeneous compositional profiles and, therefore, do not record the same late-stage heating (Morgado et al., 2019). These samples were associated with middle levels of the mentioned reservoir, and represent a mobilised, eruptible magma. In this work we investigate the detailed timescales of heating in Cal-160 just before the eruption using Fe-Ti interdiffusion chronometry in ilmenite-titanomagnetite phenocryst pairs. In addition, we calculate minimum timescales of re-equilibration in ilmenite-titanomagnetite phenocryst pairs from samples Cal-149Tb and Cal-155, to better constrain the history of the erupted magma.

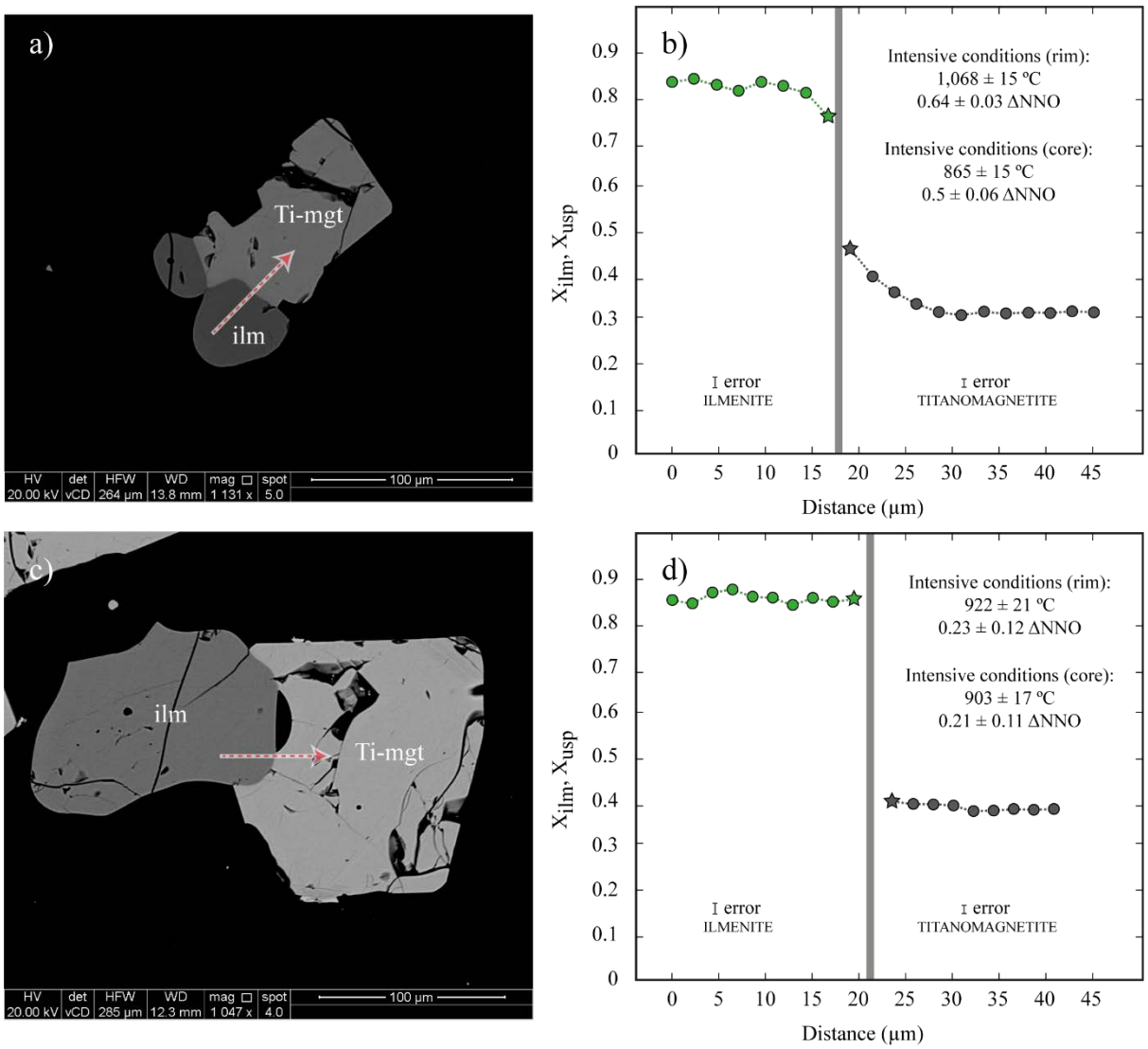

Figure 3.1. *a,c) Backscatter images of in-contact ilmenite-titanomagnetite pair from the sample Cal-160 (Fig. 3.1a) and from the sample Cal-155 (Fig. 3.1c), the arrows represent the direction of the profiles measured by Electron Probe Micro Analysis (EPMA); b,d) EPMA profile across in-contact ilmenite-titanomagnetite pairs from Figure 3.1a (Fig. 3.1b) and from Figure 3.1c (Fig. 3.1d). Core and rim (represented by the star) temperature and oxygen fugacity conditions were reported by Morgado et al. (2019), the associated errors come from measurement uncertainties.*

Diffusion chronometry has often been used to calculate magmatic timescales associated with mush reservoir processes (e.g., Nakamura, 1995; Martin et al., 2008; Hartley et al., 2016). The rapid interdiffusivity of Fe-Ti in ilmenite and titanomagnetite, in comparison to ionic diffusion in silicate mineral phases (Freer and Hauptman, 1978; Rutherford et al., 1993; Van Orman and Crispin, 2010) at the same intensive magmatic conditions (P,T, and fO_2), allows us to use Fe-Ti oxides to understand processes occurring shortly before eruptions (Nakamura, 1995; Coombs et al., 2000; Devine et al., 2003; Chertkoff and Gardner, 2004; Tomiya et al., 2013).

3.3. Thermometry and oxygen-barometry

Ilmenite solid solution (hematite and ilmenite end members, Fe_2O_3 and $FeTiO_3$ respectively) and titanomagnetite solid solution (magnetite and ulvöspinel end members, Fe_3O_4 and Fe_2TiO_4 respectively) are suitable for Fe-Ti thermometry and oxygen barometry when grains are in contact with each other. The thermometry models are based on the temperature-dependent exchange $Fe^{2+}+Ti^{4+} \leftrightarrow 2Fe^{3+}$ (e.g., Ghiorso and Sack, 1991; Ghiorso and Evans, 2008; Sauerzapf et al., 2008) according to the equation

$$Fe_2O_3\ (hematite) + Fe_2TiO_4\ (ulvöspinel) \leftrightarrow Fe_3O_4\ (magnetite) + FeTiO_3\ (ilmenite) \quad (1)$$

The oxygen barometer reported by Ghiorso and Evans (2008) is based on the redox equilibrium of hematite-magnetite with ulvöspinel buffer according to the equation:

$$6Fe_2O_3\ (hematite) \leftrightarrow 4Fe_3O_4\ (magnetite) + O_2\ (gas) \quad (2)$$

and the oxygen barometer reported by Sauerzapf et al. (2008) is based on the redox equilibrium of hematite-magnetite buffer according to the equation:

$$6FeTiO_3\ (ilmenite) + 2Fe_3O_4\ (magnetite)$$
$$\leftrightarrow 6Fe_2TiO_4\ (ulvöspinel) + O_2\ (gas) \quad (3)$$

All the methods used here to calculate intensive variables are based on the measured compositions of ilmenite-titanomagnetite grains that are in contact with each other. Equilibration is mediated via the kinetic process of diffusion, meaning that compositional changes occur at the boundary between the two oxide grains as a response to changes in both temperature and oxygen fugacity (fO_2), which must then propagate by diffusion gradually into crystal interiors (see details in Lasaga, 1983). Whilst compositional re-equilibration between minerals upon heating is rapid at the interface, and represents the intensive conditions immediately before the eruption, it can be possible to ascertain from the crystal cores the intensive conditions present before any re-equilibration process took place (pre-heating conditions, see details in Lasaga and Jiang, 1995), Fig. 3.1.

In Cal-160, temperatures and oxygen fugacity conditions prior to heating were calculated using ilmenite and titanomagnetite core compositions and correspond to an average temperature of 870 ºC (σ= 18 ºC); and an average oxygen fugacity of + 0.6 ΔNNO (σ= 0.18 ΔNNO; Morgado et al., 2019). The compositions of ilmenite-titanomagnetite pairs close to the interface record the late-stage equilibrium in terms of the temperature and oxygen fugacity conditions experienced during the heating of the system just prior to eruption (average temperature: 1,018 ºC, σ= 45 ºC; average oxygen fugacity: + 0.48 ΔNNO, σ= 0.16 ΔNNO; Morgado et al., 2019). The composition of the traverses measured from ilmenite to titanomagnetite represent only diffusion and are not significantly affected by measurement convolution effects or secondary fluorescence (details in next section).

In Cal-149Tb and Cal-155, the temperatures and oxygen fugacity conditions were calculated using ilmenite and titanomagnetite core compositions and correspond to an average

temperature of 933 ºC (σ= 35 ºC); and an average oxygen fugacity of 0.3 ΔNNO (σ= 0.14 ΔNNO) (Morgado et al., 2019). The compositions of ilmenite-titanomagnetite pairs close to the interface yielded no significantly different magmatic intensive conditions.

The core compositions of ilmenite-titanomagnetite pairs show fairly constant compositional profiles, the crystal pairs passed the Mg-Mn equilibrium chemical test (Fig. 3.2; Bacon and Hirschmann, 1988), and there are not resorption textures. These features suggest that all the Fe-Ti oxides in contact were in equilibrium before heating. For this study, we use all the in contact ilmenite-titanomagnetite grains within the compositional and temperature range in which the thermoxybarometers were calibrated (Ghiorso and Evans, 2008; Sauerzapf et al., 2008).

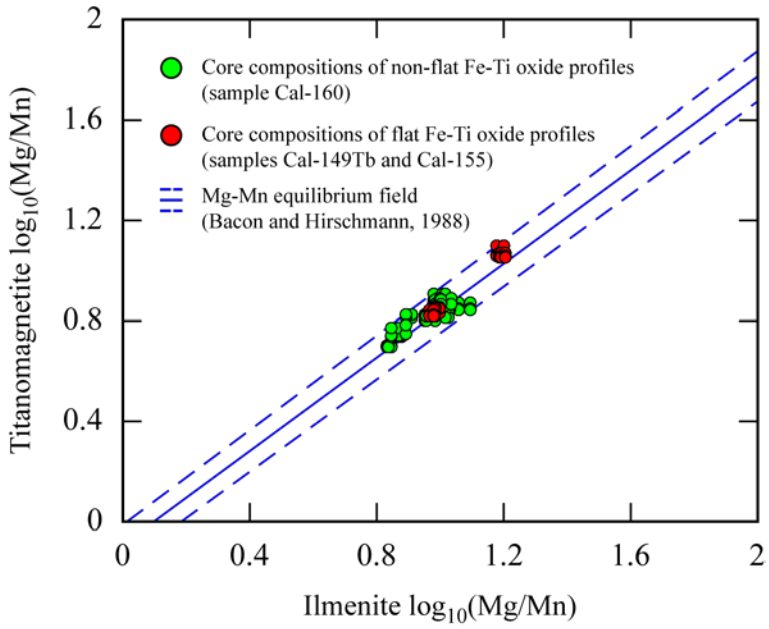

Figure 3.2. *Ilmenite-titanomagnetite Mg-Mn chemical equilibrium test (Bacon and Hirschmann, 1988) of cores of the studied Fe-Ti oxide pairs. Red circles correspond to pairs from samples Cal-149Tb and Cal-155, green circles correspond to pairs from sample Cal-160 (details in Supplementary Material 1).*

3.4. Diffusion modelling: a tool to obtain magmatic timescales

3.4.1. Modelling approach

The profile shapes observed in Figure 3.1 of ilmenite-titanomagnetites from the sample Cal-160, suggest that the minerals are responding to the heating event, governed by equations 1, 2, and 3. In practice, this leads to Ti enrichment in the titanomagnetite bordering ilmenite (Loomis, 1983). Fe-Ti interdiffusion within titanomagnetite can be described and modelled using Fick's second law and the composition-dependent form of the diffusion equation:

$$\frac{\partial C(x,t)}{\partial t} = \frac{\partial}{\partial x}\left(D_{Ti}^{*}\frac{\partial C(x,t)}{\partial x}\right) \qquad (4)$$

where C is composition, t is time, x is distance, and D_{Ti}^{*} is the diffusivity ($m^2 s^{-1}$). This diffusivity is calculated via Eq. 5 (Aragon et al., 1984):

$$D_{Ti}^{*} = D_0^0 \exp\left(-\frac{\mathrm{E_0}}{\mathrm{RT}}\right) + (1-X) \times \left(\mathrm{D_V^0}\ \exp\left(-\frac{\mathrm{E_V}}{\mathrm{RT}}\right)\left[\frac{1+X}{1-X}\right]^{8/3} {fO_2}^{2/3} - \mathrm{D_I^0}\ \exp\left(-\frac{\mathrm{E_I}}{\mathrm{RT}}\right)\left[\frac{1-X}{1+X}\right]^{8/3} {fO_2}^{-2/3}\right) \qquad (5)$$

where D_0^0, D_V^0, and D_I^0 are internal diffusion coefficients (details in Supplementary Material 2); E_0, E_V, and E_I are internal activation energies ($cal\ mol^{-1}$; details in Supplementary Material 2); T is temperature (K); R is the universal gas constant ($cal\ mol^{-1}\ K^{-1}$), fO_2 is oxygen fugacity (atm), X is the factor (from 0 to 1) representing the composition of the titanomagnetite solid solution ($(Fe_3O_4)_{1-X}(Fe_2TiO_4)_X$). An example of diffusion modelling in ilmenite-titanomagnetite pairs from the sample Cal-160 is shown in Figure 3.3a.

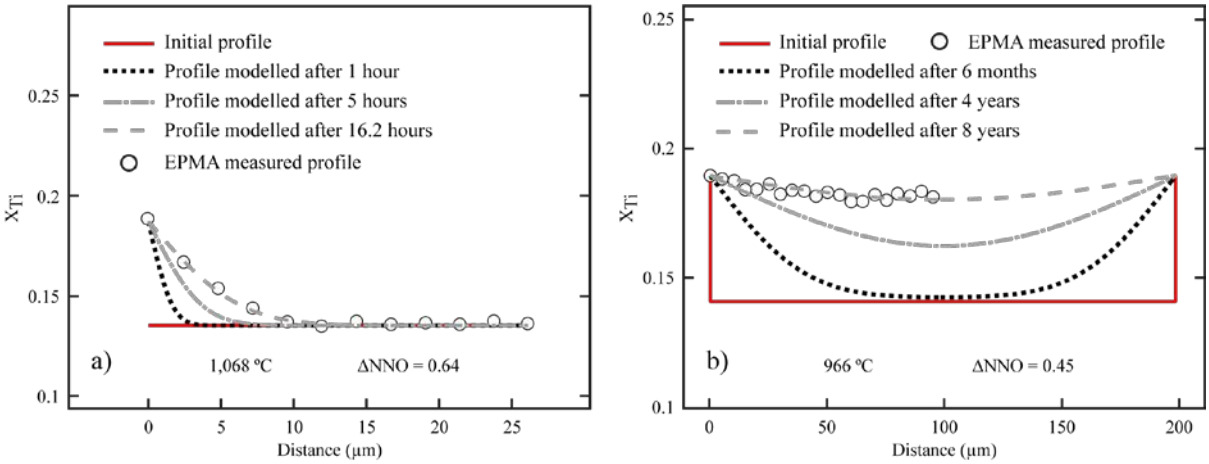

Figure 3.3. *Examples of Fe-Ti interdiffusion, showing the evolution of molar composition (X_{Ti} = Ti/(Ti+Fe_{tot})): a) profile of titanomagnetite over time from the sample Cal-160, representing the bottom of the magma reservoir (Table 3.1 and Supplementary Material 1) and b) re-equilibration profile of titanomagnetite over time from the sample Cal-149Tb, representing the middle of the magma reservoir (Table 3.2 and Supplementary Material 1).*

The ilmenite-titanomagnetite pairs in samples Cal-149Tb and Cal-155 display compositional profiles with only weak zonation, and they are considered as largely-equilibrated pairs that retain only weak disequilibrium. Although paired cores do consistently return temperatures lower than paired rims, the values are well within the uncertainty of the thermometry technique (see Supplementary Material 1). If we consider that previous heating has occurred, and that these crystals have been largely re-equilibrated, then minimum timescales of re-equilibration can be estimated in equilibrated pairs. Equally, the lack of any significant deviations between interface and cores can be taken to signify that conditions have been stable for a considerable length of time. We can use Fe-Ti interdiffusion chronometry to constrain re-equilibration timescales in titanomagnetite grains following equations 4 and 5. In performing these calculations the initial core composition has to be assumed, as no part of the profile has escaped modification. Using a low value of X_{Ti}, comparable to the lowest value found in the system would in theory yield the longest answer; using the highest value of X_{Ti} for the core would theoretically yield the shortest answer as it would require less modification. We have used the latter parameter, based upon the value X_{Ti}=0.14, from the

Cal-160 crystals, to place a minimal constraint for the long re-equilibration time of crystals in Cal-155 and Cal-149Tb. We would note that the curvature of the profile is such that it is actually relatively insensitive to the choice of initial condition.

3.4.2. Compositional equilibrium in grain boundaries

The propagation of a re-equilibrating boundary composition during ionic exchange between ilmenite and titanomagnetite can be considered as similar to the Arrhenian kinetic formula for thermally activated processes (cf. Lasaga, 1979; Loomis, 1983). Thus, we use Fick's second law for non-steady state diffusion (Eq. 4) and diffusivity following the Aragon et al. (1984) equation (Eq. 5) to determine the timescale in which the composition in equilibrium with the new intensive physical condition is reached in the grain interface. Even ignoring the significant diffusion enhancement in the grain interface inferred by Hammond and Taylor (1982), we can calculate that compositions within 10 nm of the interface will attain a new equilibrium in less than one second for all the ilmenite-titanomagnetite pairs. The results are shown in Table 3.1 and form a basis for assuming instantaneous compositional equilibrium on the interface in subsequent modelling. Such models, where equilibrium is reached instantaneously at the boundary have been used successfully in previous studies (cf. Lasaga, 1979; Venezky and Rutherford, 1999). In addition, the asymmetric shape of the composition profiles suggests that ionic exchange at the crystal boundary is the dominant process. We, therefore, interpret that a buffered exchange between the two minerals dominates the profile shapes, rather than infiltration of a third component (e.g., melt) along the grain boundary. Videos representing the evolution of compositional re-equilibration in grain boundaries are available in Supplementary Material 4.

Table 3.1. Time necessary to reach equilibrium conditions in crystal boundaries of sample Cal-160.

Pair name	Boundary eq. time (s)	Resolution (µm)
f1_p1	0.3	0.01
f1_p2	0.2	0.01
f1_p3	0.5	0.01
f13_p2	0.2	0.01
f17_p1	0.1	0.01
f17_p2	0.1	0.01
f17_p4	0.4	0.01
fb_p1	0.5	0.01
fe_p1	0.3	0.01
ff_p1	0.3	0.01
ff_p2	0.6	0.01
fh_p1	0.1	0.01

Table 3.2. Fe-Ti oxide rim intensive conditions (during heating) and associated timescales of ilmenite-titanomagnetite pairs from sample Cal-160.

Pair	T (ºC)	Error	fO_2 (ΔNNO)	Error	X_{usp}	Error	D^*_{Ti}	Min t (h)	Time (h)	Max t (h)
ff_p1	1073	23	0.21	0.09	0.55	0.011	2.29×10^{-16}	2	3.8	7
f17_p1	1029	19	0.4	0.07	0.47	0.009	1.09×10^{-16}	6.9	12.2	21.7
fe_p1	1015	18	0.43	0.06	0.46	0.009	8.51×10^{-17}	5.3	8.7	14.9
f13_p1	1013	16	0.61	0.05	0.42	0.009	8.54×10^{-17}	6.5	10.9	18.4
f17_p2	1048	14	0.75	0.03	0.42	0.009	1.66×10^{-16}	2.4	3.8	6.1
fh_p1	1068	15	0.64	0.03	0.45	0.009	2.25×10^{-16}	10.1	16.2	26.2
ff_p2	947	19	0.27	0.09	0.42	0.009	2.2×10^{-17}	10.5	19.7	36.2
fb_p1	952	18	0.32	0.09	0.42	0.009	2.44×10^{-17}	14.8	26.7	45.8
f1_p1	1067	17	0.5	0.05	0.47	0.009	2.12×10^{-16}	20.2	33.8	56.7
f1_p3	1005	15	0.56	0.05	0.42	0.009	7.3×10^{-17}	45.6	75.8	126.2
f1_p2	1041	14	0.55	0.04	0.45	0.008	1.4×10^{-16}	41.1	65.9	105.5
f17_p4	963	17	0.47	0.08	0.40	0.008	3.17×10^{-17}	31.7	58.3	91.2

3.4.3. Uncertainties

We obtain the uncertainties of diffusivity from the error propagation of temperature (T), oxygen fugacity (fO_2), and composition of titanomagnetite (X) following equation 6 (details are available as Supplementary Material 1). Finally, we consider the intrinsic experimental uncertainty in the calculation of D_{Ti}^{*} (0.1 log units, reported by Aragon et al., 1984).

$$\varepsilon\big(f(T, fO_2, X)\big)$$

$$\approx \sqrt{\left(\frac{\partial f}{\partial T}\varepsilon(T)\right)^2 + \left(\frac{\partial f}{\partial fO_2}\varepsilon(fO_2)\right)^2 + 2\left(\frac{\partial f}{\partial T}\right)\cdot\left(\frac{\partial f}{\partial fO_2}\right)\cdot\, cov\big(\varepsilon(T, fO_2)\big) + \left(\frac{\partial f}{\partial X}\varepsilon(X)\right)^2} \qquad (6)$$

We use the sum of the squares of the differences (SSD) to assess the best-fitting curve. We consider the uncertainty of the curve-fitting on the diffusive length-scale (cf. Gualda et al., 2012) as negligible because the measured profiles show high precision and low noise (details in Supplementary Material 5).

3.4.4. Do the measured profiles represent diffusion?

We can be confident that the profiles measured from ilmenite to titanomagnetite from the sample Cal-160 represent only diffusion and are not significantly affected by measurement convolution effect for the following reasons:

(i) Modelling of electron-sample interactions with the software CASINO (Hovington et al., 1997; Drouin et al., 2007) suggests that, at the analytical conditions of 15 keV accelerating potential and a 30 nA focused beam, the interaction volume in the samples is ~2 micrometres width, which we use as the analytical point spacing. In addition, the vertical interaction is < 1.5 µm length (details in Supplementary Material 6).

(ii) We can rule out secondary fluorescence effects from analysis of ilmenite-titanomagnetite pairs from the sample Cal-160, because in Cal-149Tb and Cal-155, where equilibrium appears to be reached, compositional profiles do not show the characteristic enrichment/depletion effects that we see close to the interfaces of those compositional profiles from Cal-160, which suggests that these data represent true disequilibrium profiles.

3.5. Timescales from heating to eruption

The calculated timescales obtained from the sample Cal-160 are associated with the recording of a heating event up to 4 days before the eruption (Table 3.2, Fig. 3.4). On the other hand, the results of minimum re-equilibration diffusion modelling in the crystal pairs from the samples Cal-149Tb and Cal-155 yield timescales of the order of years. All the timescales are consistent with those calculated using Aggarwal and Dieckmann (2002a, 2002b) equations for Fe-Ti (inter)diffusivity in titanomagnetite.

Cal-160. Our modelled timescales between the heating event and the eruption (at the bottom of the magma reservoir, represented by the sample Cal-160) are consistent with the seismic signals detected just before this rapid-onset eruption (SERNAGEOMIN, 2015c; Valderrama et al., 2015; Fig. 3.4). The absence of deformation until at most 1.5 days before the first eruptive pulse (Valderrama et al., 2015; Delgado et al., 2017) suggests that there were no major volumetric changes related to an ascent of volatiles or increased magma supply into the reservoir prior to the eruption. In addition, 67% of the calculated timescales lie within a 36-hour window prior to the eruption, suggesting that most of the heating of sample Cal-160 is recorded during that period. Furthermore, the peak density of the modelled timescales representing the heating of the reservoir coincides with the occurrence of the seismic swarm, starting around three hours before the first eruptive event (Fig. 3.4).

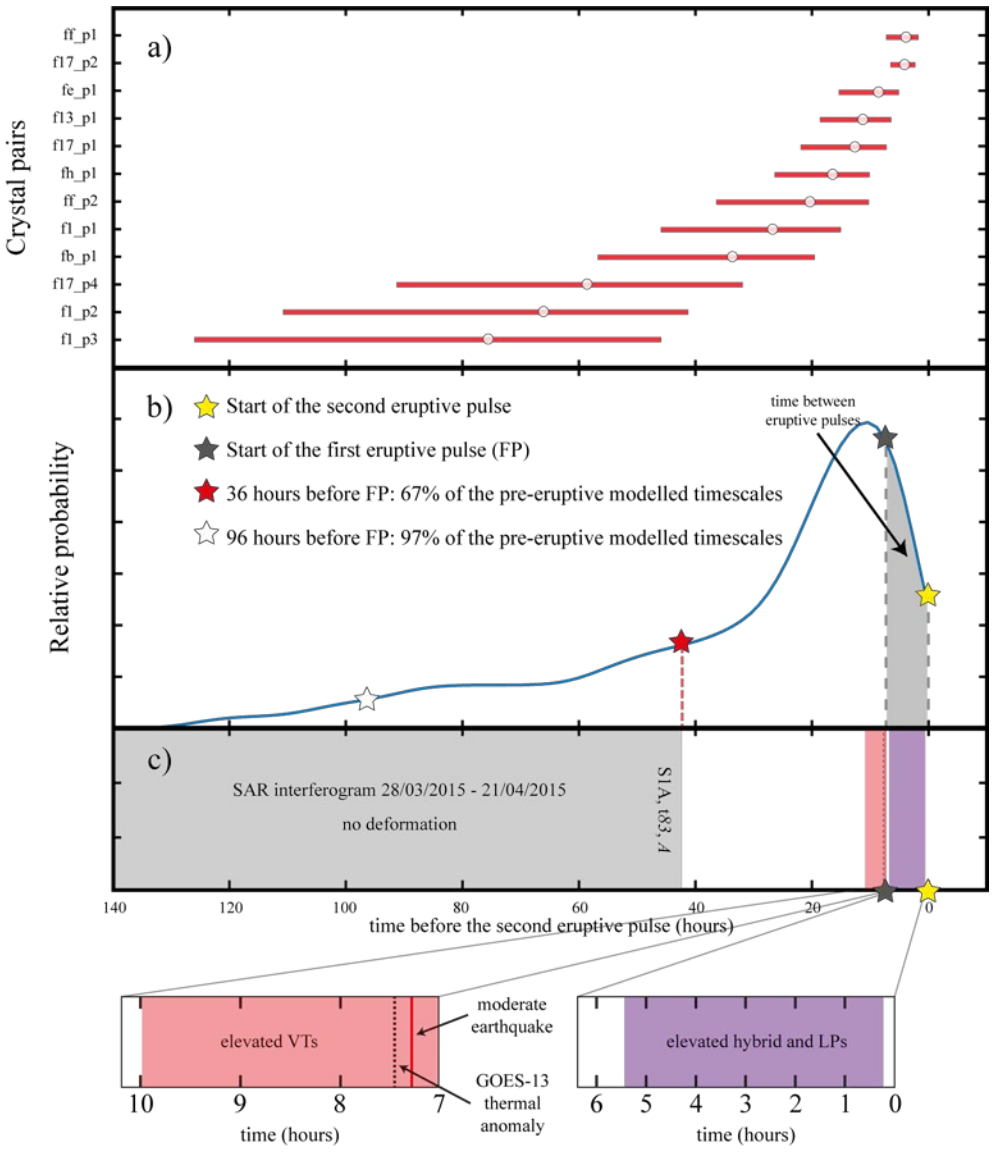

Figure 3.4. *a) Plots of modelled timescales from heating to eruption of 12 in-contact ilmenite-titanomagnetite pairs with associated errors based on temperature, oxygen fugacity and intrinsic diffusivity uncertainties; b) Kernel density estimation of probability distributions of all data, probabilities of several ranges of time are shown (details in Supplementary Material 5); c) Summary of geophysical signals at Calbuco in the 140 hours preceding the second phase of the eruption at 4:00 (UTC) on 23 April. Sentinel-1a interferograms shown no deformation in the months before and at least up until 36 hours before eruption onset (descending, track 83, 21/04/2015, 09:57 UTC). VT swarms began 3 hours before the first eruptive pulse (18:11 UTC; SERNAGEOMIN, 2015c; Valderrama et al., 2015). A thermal anomaly was detected by NOAA's Geostationary Operational Environmental Satellite (GOES-13) 20 minutes prior to the first eruptive pulse (20:45 UTC; Global Volcanism Program, 2015).*

Neither tilt nor interferograms that span the 36 hours prior to the eruption, nor the co-eruptive period, show any evidence of major volume increases during the heating event (Valderrama et al., 2015; Delgado et al., 2017). Our results are consistent with the triggering mechanism of a small mafic injection proposed by Castruccio et al. (2016), and similar to short-timescale processes suggested for large magmatic systems by Burgisser and Bergantz (2011), during which magma recharge adds heat and volatiles with the latter stalling below the mush reservoir causing crystal mush disaggregation, magma remobilisation (rheological unlock-up point of crystal mushes, cf. Vigneresse et al., 1996; Petford, 2003; Huber et al., 2011; Parmigiani et al., 2014) and eruption. Although bubbles can ascend via infiltration or volatile-rich plumes with minor (or null) contents of attached new (presumably mafic) underlying magma (Phillips and Woods, 2002; Bachmann and Bergantz, 2006), there is no direct evidence of syn-eruptive magma mixing, liquid mingling or resorption features from the new, hotter magma. This is consistent with the models that indicate crystal mush and volatiles systems would act as a rheological barrier to the inputs of new, presumably more mafic magma (Girard and Stix 2009; Huber et al 2009; 2010). In absolute terms, the rims of the Fe-Ti oxide pairs from Cal-160 are much more oxidised, two to three orders of magnitude in absolute fO_2 values, than the cores of the same sample. The bulk of this change in fO_2 is close to the NNO buffer trend and represents the effect of heating that the crystals record. These variations could be real, and could represent a degree of heterogeneity in the magma system, potentially related to volatile distributions, or could be an artefact of the difficulty of obtaining reliable measurements of fO_2. The obtained values of fO_2 buffer from the Cal-160 Fe-Ti oxide pairs correspond to + 0.48 ΔNNO (σ= 0.16 ΔNNO) and are comparable to uncertainties published in other articles (e.g. Borisov and Shapkin, 1990; Ghiorso and Evans, 2008). Regarding volatile phases during the eruption, Pardini et al. (2018) proposed the existence of exsolved volatiles (H_2O, CO_2, Cl, and SO_2) before the onset of the first eruptive

event, thus the recognised triggering heating event could be associated with a terminal input of volatiles. This could, in turn, be regarded as consistent with an increase of seismic activity (Linde et al., 1994).

Cal-149Tb and Cal-155. The absence of significant variations in both temperature and oxygen fugacity recorded in the ilmenite-titanomagnetite pairs of the lower crystallinity samples (~ 40% crystallinity, i.e., all except Cal-160), suggest that the heating effect was at a local scale, only occurring in a relatively small volume of the magma reservoir at the base of the reservoir and not thermally affecting the rest of the reservoir (Morgado et al., 2019). Our modelled re-equilibration timescales of > 1 year (Table 3.3) represents the minimum duration over which temperature and fO_2 conditions for the bulk of the erupted magma reservoir beneath Calbuco volcano were stable, prior to the 2015 eruption.

Our calculated timescales, considering all the samples, suggest that the heating event, which triggered the April 2015 Calbuco eruption only affected significantly the bottom of the system over a maximum period of 4 days, but did not affect the upper levels of the reservoir. The middle of the reservoir was not affected by that heating or by any other event, and had already been established for over a year prior to the eruption. All the compositional profiles and videos of examples of diffusion are available as Supplementary Materials 1 and 7, respectively.

Table 3.3. Fe-Ti oxide rim intensive conditions and associated timescales of re-equilibration of ilmenite-titanomagnetite pairs from samples Cal-149Tb and Cal-155.

Pair	T (ºC)	Error	fO_2 (ΔNNO)	Error	X_{usp}	Error	D^*_{Ti}	Time (y)	Min t (y)	Max t (y)
Cal-149Tb_fig14b_p1	966	22	0.45	0.09	0.44	0.01	3.6×10^{-17}	8	5	13
Cal-149Tb_fig14_p2	961	22	0.36	0.1	0.46	0.01	3.2×10^{-17}	1	0.5	1.5
Cal-155_fig3_p1	903	20	0.21	0.11	0.40	0.01	8.6×10^{-18}	6	3.5	8.5
Cal-155_fig24_p1	902	21	0.17	0.1	0.39	0.01	8.2×10^{-18}	4	2.5	7

3.6. Concluding remarks

As a consequence of the rapid rate of Fe-Ti interdiffusion in Fe-Ti oxides, these minerals can be used for the determination of short-timescale magmatic processes. In this study, magmatic timescales ranging from 2 hours up to 4 days are calculated via Fe-Ti interdiffusion profiles observed between ilmenite-titanomagnetite crystal pairs of the sample Cal-160 (the sample that represents the bottom of the reservoir), under known temperature and fO_2 conditions. These timescales represent the time elapsed between local-scale heating at the base of the magma reservoir and the beginning of the rapid-onset 2015 Calbuco eruption (Fig. 3.5). We interpret these to represent the underplating of a high-temperature, mafic melt, considerably hotter than the overlying magma body that would form the bulk of the erupted material during the eruption. There is seemingly no evidence for the mafic magma input to have directly erupted, and thus it would suggest that the eruption could have been triggered by a critical, physical failure related to overpressure following intrusion, rather than magma mixing or chemical interactions. Our results suggest that the peak of pre-eruptive activity occurred just ~3 hours prior to the eruption, coincident with the timing of a seismic swarm before the eruption onset.

By contrast, examination of Fe-Ti interdiffusion in the Fe-Ti oxides of the carrier magmas suggest minimum re-equilibration timescales of > 1 year in the samples Cal-149Tb and Cal-155, interpreted to represent the middle of the reservoir (Morgado et al., 2019). This minimum timescale suggests that the bulk of the erupted magma has resided in a stable thermal and oxidation state for at least the year prior to the April 2015 Calbuco eruption and that the bulk of the magma residing into the reservoir was not thermally affected by the intrusion.

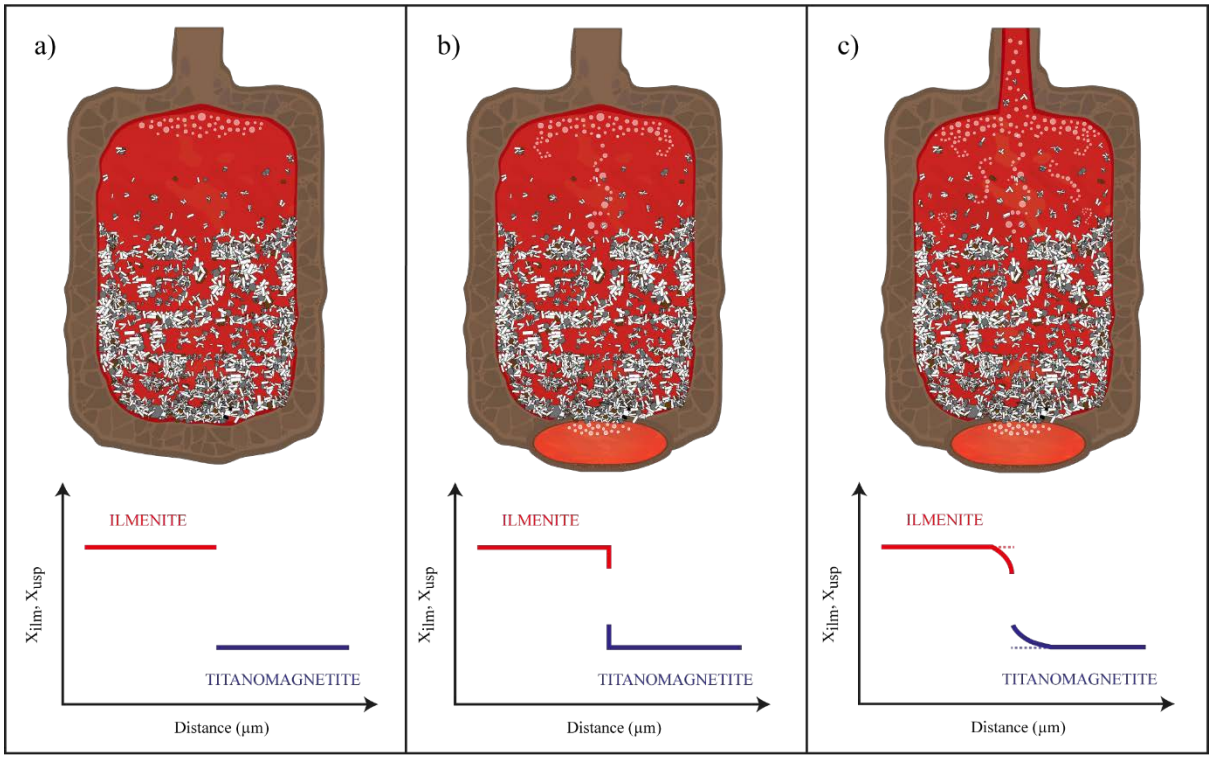

Figure 3.5. *a) Before the hotter magma arrival (before the heating transfer event), the ilmenite-titanomagnetite profiles from the bottom of the crystal much are flat, they record temperature and oxygen fugacity; b) at the moment of the heat transfer, Fe and Ti exchange between ilmenite and titanomagnetite instantaneously modifies compositions in the boundary between the two crystals from the base of the crystal mush. The internal diffusion within crystals starts at the same moment of the elemental exchange; c) due to the heating, remobilisation and stirring of the system starts, overpressure increases and the eruption is triggered. At the moment of the eruption temperature decreases and net diffusion ceases to be significant, so that the crystals from the bottom of the crystal mush recorded timescales from heating to eruption. Modified from Morgado et al. (2019).*

In summary, the 2015 Calbuco eruption involved an established magma body persisting under relatively stable conditions over the years-to-decades timescale, surrounded by a crystal mush envelope of similar origins. That system was disrupted and invaded by a pulse of mafic magma which did not produce any measurable surface deformation. This provided additional heat to the base of the magma system, disrupting a mush horizon, fragments of which would be incorporated into subsequent PDC deposits as materials like the sample Cal-160. Within hours to days of the intrusion event, VT earthquakes and subsequent LP seismicity were the heralds of the eruption commencing as the resident magmas ascended to the surface. The existence of a robust monitoring system at Calbuco strongly shows us that the run-up time to eruption at Calbuco was very short, giving us greater confidence in the relative lack of precursory activity compared to other, historical eruptions of the region. We hope that these results provide valuable insight into understanding the mechanism of rapid-onset explosive eruptions and potential methods by which to explore other, similar events for the purposes of eruption prediction and hazard mitigation.

3.7. Acknowledgements

We acknowledge the help in the field of Marcela Vollmer. The financial support through FONDAP project 15090013 (Centro de Excelencia en Geotermia de los Andes, CEGA), CONICYT PhD fellowship (72160268, EM), hosted at Leeds by DJM, and PhD fellowship Master Standard Grant to G.F. Zellmer (MAU1704, RB) are acknowledged. SKE is supported by a Leverhulme Early Career Fellowship and a Living Planet Fellowship from the European Space Agency. Fruitful discussions with the personnel from SERNAGEOMIN-OVDAS (Chile) are greatly appreciated. We would like especially thank to Claire Harnett for comments and suggestions on reading an earlier version of this manuscript. We thank two anonymous reviewers for their detailed and constructive reviews. Editorial handling of M. Ghiorso is greatly appreciated.

3.8. References

Aggarwal, S, Dieckmann, R (2002a) Point defects and cation tracer diffusion in $(Ti_xFe_{1-x})_{3-\delta}O_4$ 1. Non-stoichiometry and point defects. Phys Chem Miner 29(10): 695-706. https://doi.org/10.1007/s00269-002-0282-2

Aggarwal, S, Dieckmann, R (2002b) Point defects and cation tracer diffusion in $(Ti_xFe_{1-x})_{3-\delta}O_4$. II. Cation tracer diffusion. Phys Chem Miner 29(10): 707-718. https://doi.org/10.1007/s00269-002-0284-0

Aragon, R, McCallister, RH, Harrison, HR (1984) Cation diffusion in titanomagnetites. Contrib Mineral Petrol 85(2): 174-185. https://doi.org/10.1007/BF00371707

Bacon, CR, Hirschmann, MM (1988) Mg/Mn partitioning as a test for equilibrium between coexisting Fe-Ti oxides. Am Min 73(1-2): 57-61.

Bachmann, O, Bergantz, GW (2006) Gas percolation in upper-crustal silicic crystal mushes as a mechanism for upward heat advection and rejuvenation of near-solidus magma bodies. J Volcanol Geoth Res 149(1-2): 85-102. https://doi.org/10.1016/j.jvolgeores.2005.06.002

Borisov, AA, Shapkin, AI (1990). A new empirical equation rating Fe^{3+}/Fe^{2+} in magmas to their composition, oxygen fugacity, and temperature. Geochem. Int, 27(1): 111-116.

Brenguier, F, Shapiro, NM, Campillo, M, Ferrazzini, V, Duputel, Z, Coutant, O, Nercessian, A (2008) Towards forecasting volcanic eruptions using seismic noise. Nat Geosci 1(2): 126. https://doi.org/10.1038/ngeo104

Burgisser, A, Bergantz, GW (2011) A rapid mechanism to remobilize and homogenize highly crystalline magma bodies: Nature 471(7337): 212-215. https://doi.org/10.1038/nature09799

Carapezza, ML, Federico, C (2000) The contribution of fluid geochemistry to the volcano monitoring of Stromboli. J Volcanol Geoth Res 95(1-4): 227-245. https://doi.org/10.1016/S0377-0273(99)00128-6

Castro, JM, Dingwell, DB (2009) Rapid ascent of rhyolitic magma at Chaitén volcano, Chile. Nature 461(7265): 780. https://doi.org/10.1038/nature08458

Castruccio, A, Clavero, J, Segura, A, Samaniego, P, Roche, O, Le Pennec, J, Droguett, B (2016) Eruptive parameters and dynamics of the April 2015 sub-Plinian eruptions of Calbuco volcano (Southern Chile). B Volcanol 327: 469-483. https://doi.org/10.1007/s00445-016-1058-8

Chertkoff, DG, Gardner, JE (2004) Nature and timing of magma interactions before, during, and after the caldera-forming eruption of Volcán Ceboruco, Mexico: Contrib Mineral Petrol 146(6): 715-735. https://doi.org/10.1007/s00410-003-0530-6

Coombs, ML, Eichelberger, JC, Rutherford, MJ (2000) Magma storage and mixing conditions for the 1953–1974 eruptions of Southwest Trident volcano, Katmai National Park, Alaska. Contrib Mineral Petrol 140(1): 99-118. https://doi.org/10.1007/s004100000166

Delgado, F, Pritchard, ME, Ebmeier, S, González, P, Lara, L (2017) Recent unrest (2002-2015) imaged by space geodesy at the highest risk Chilean volcanoes: Villarrica, Llaima, and Calbuco (Southern Andes). J Volcanol Geoth Res 344: 270-288. https://doi.org/10.1016/j.jvolgeores.2017.05.020

Delgado, F, Pritchard, M, Lohman, R, Naranjo, JA (2014) The 2011 Hudson volcano eruption (Southern Andes, Chile): Pre-eruptive inflation and hotspots observed with InSAR and thermal imagery. B Volcanol 76(5): 815. https://doi.org/10.1007/s00445-014-0815-9

Devine, JD, Rutherford, MJ, Norton, GE, Young, SR (2003) Magma storage region processes inferred from geochemistry of Fe–Ti oxides in andesitic magma, Soufriere Hills Volcano, Montserrat, WI. J Petrol 44(8): 1375-1400.https://doi.org/10.1093/petrology/44.8.1375

Drouin, D, Couture, AR, Joly, D, Tastet, X, Aimez, V, Gauvin, R (2007) CASINO V2. 42—A Fast and Easy-to-use Modeling Tool for Scanning Electron Microscopy and Microanalysis Users. Scanning 29(3): 92-101. https://doi.org/10.1002/sca.20000

Ebmeier, SK, Andrews, BJ, Araya, MC, Arnold, DWD, Biggs, J, Cooper, C, Cottrell, E, Furtney, M, Hickey, J, Jay, J, Lloyd, R, Parker, AL, Pritchard, M, Robertson, E, Venzke, E, Williamson, JL (2018) Synthesis of global satellite observations of magmatic and volcanic deformation: implications for volcano monitoring & the lateral extent of magmatic domains. J Appl Volcanol 7(1): 2. https://doi.org/10.1186/s13617-018-0071-3

Einarsson, P (2018) Short-term seismic precursors to Icelandic eruptions 1973-2014. Front Earth Sci 6: 45. https://doi.org/10.3389/feart.2018.00045

Freer, R, Hauptman, Z (1978) An experimental study of magnetite-titanomagnetite interdiffusion. Phys Earth Planet In 16(3): 223-231. https://doi.org/10.1016/0031-9201(78)90015-8

Ghiorso, MS, Evans, BW (2008) Thermodynamics of rhombohedral oxide solid solutions and a revision of the Fe-Ti two-oxide geothermometer and oxygen-barometer. Am J Sci 308: 957–1039. https://doi.org/10.2475/09.2008.01

Ghiorso, MS, Sack, O (1991) Fe-Ti oxide geothermometry: thermodynamic formulation and the estimation of intensive variables in silicic magmas. Contrib Mineral Petrol 108(4): 485-510.https://doi.org/10.1007/BF00303452

Girard, G, Stix, J (2009) Buoyant replenishment in silicic magma reservoirs: Experimental approach and implications for magma dynamics, crystal mush remobilization, and eruption. J Geophys Res: Solid Earth, 114(B8).https://doi.org/10.1029/2008JB005791

Global Volcanism Program (2015) Report on Calbuco (Chile). In: Venzke, E (ed.), Bulletin of the Global Volcanism Network, 40:6. Smithsonian Institution.

Gualda, GAR, Pamukcu, AS, Ghiorso, MS, Anderson, AT Jr, Sutton, SR, Rivers, ML (2012) Timescales of quartz crystallization and the longevity of the Bishop giant magma body. PloS one, 7(5). https://doi.org/10.1371/journal.pone.0037492

Hall, M, Ramón, P, Mothes, P, LePennec, JL, García, A, Samaniego, P, Yepes, H (2004) Volcanic eruptions with little warning: the case of Volcán Reventador's Surprise November 3, 2002 Eruption, Ecuador. Rev Geol Chile 31(2): 349-358. https://doi.org/10.1007/BF00303452

Hammond, PA, Taylor, LA (1982) The ilmenite/titano-magnetite assemblage: kinetics of re-equilibration. Earth Planet Sc Lett 61(1): 143-150.

Hartley, ME, Morgan, DJ, Maclennan, J, Edmonds, M, Thordarson, T (2016) Tracking timescales of short-term precursors to large basaltic fissure eruptions through Fe–Mg diffusion in olivine. Earth Planet Sc Lett 439: 58-70. https://doi.org/10.1016/j.epsl.2016.01.018

Hovington, P, Drouin, D, and Gauvin, R (1997) CASINO: A new Monte Carlo code in C language for electron beam interaction—Part I: Description of the program. Scanning 19(1), 1-14. https://doi.org/10.1002/sca.4950190101

Huber, C, Bachmann, O, Dufek, J (2011) Thermo-mechanical reactivation of locked crystal mushes: Melting-induced internal fracturing and assimilation processes in magmas. Earth Planet Sc Lett 304(3-4): 443-454. https://doi.org/10.1016/j.epsl.2011.02.022

Huber, C, Bachmann, O, Manga, M (2009) Homogenization processes in silicic magma chambers by stirring and mushification (latent heat buffering). Earth Planet Sc Lett 283(1-4): 38-47. https://doi.org/10.1016/j.epsl.2009.03.029

Huber, C, Bachmann, O, Manga, M (2010) Two competing effects of volatiles on heat transfer in crystal-rich magmas: thermal insulation vs defrosting. J Petrol 51(4), 847-867. https://doi.org/10.1093/petrology/egq003

Lasaga, AC (1979) Multicomponent exchange and diffusion in silicates. Geochim Cosmochim Ac 43(4): 455-469. https://doi.org/10.1016/0016-7037(79)90158-3

Lasaga, AC (1983) Geospeedometry: an extension of geothermometry. In: Saxena, SK (Ed.), Kinetics and Equilibrium in Mineral Reactions. In: Advances in Physical Geochemistry 3. Springer, New York: 81–114.

Lasaga, AC, Jiang, J (1995) Thermal history of rocks; P-T-t paths for geospeedometry, petrologic data, and inverse theory techniques. Am J Sci 295(6): 697-741. https://doi.org/10.2475/ajs.295.6.697

Linde, AT, Sacks, IS, Johnston MJS, Hill, SP, Bilham, RG (1994) Increased pressure from rising bubbles as a mechanism for remotely triggered seismicity. Nature, 371: 29. https://doi.org/10.1038/371408a0

López-Escobar, L, Parada, MÁ, Moreno, H, Frey, FA, Hickey-Vargas, RL (1992) A contribution to the petrogenesis of Osomo and Calbuco volcanoes, Southern Andes (41° 00'-41° 30'S): comparative study. Andean Geol 19(2): 211-226.

Loomis, TP (1983). Compositional zoning of crystals: a record of growth and reaction history. In: Saxena, SK (Ed.), Kinetics and Equilibrium in Mineral Reactions. In: Advances in Physical Geochemistry 3. Springer, New York: 1–60.

Madonia, P, Rizzo, AL, Diliberto, IS, Favara, R (2013) Continuous monitoring of fumarole temperatures at Mount Etna (Italy). J Volcanol Geoth Res 257: 12-20. https://doi.org/10.1016/j.jvolgeores.2013.03.001

Martin, VM, Morgan, DJ, Jerram, DA, Caddick, MJ, Prior, DJ, Davidson, JP (2008) Bang! Month-scale eruption triggering at Santorini volcano. Science 321(5893): 1178-1178. https://doi.org/10.1126/science.1159584

Morgado, E, Morgan DJ, Harvey, J, Parada, MÁ, Castruccio, A, Brahm, R, Gutiérrez, F, Georgiev, B, Hammond, SJ (Accepted) Localised heating and intensive magmatic conditions prior the 22-23 April 2015 Calbuco volcano eruption (Southern Chile). B Volcanol 81:24. https://doi.org/10.1007/s00445-019-1280-2

Nakamura, M (1995) Continuous mixing of crystal mush and replenished magma in the ongoing Unzen eruption. Geology 23(9): 807-810. https://doi.org/10.1130/0091-7613(1995)023<0807:CMOCMA>2.3.CO;2

Nikkhoo, M, Walter, TR, Lundgren, PR, Prats-Iraola, P (2016) Compound dislocation models (CDMs) for volcano deformation analyses. Geophys J Int 208:877-894. https://doi.org/10.1093/gji/ggw427

Pardini, F, Burton, M, Arzilli, F, La Spina, G, Polacci, M (2018) SO_2 emissions, plume heights and magmatic processes inferred from satellite data: The 2015 Calbuco eruptions. J Volcanol Geoth Res 361: 12-24. https://doi.org/10.1016/j.jvolgeores.2018.08.001

Parmigiani, A, Huber, C, Bachmann, O (2014) Mush microphysics and the reactivation of crystal-rich magma reservoirs. J Geophys Res: Solid Earth 119(8): 6308-6322. https://doi.org/10.1002/2014JB011124

Petford, N (2003) Rheology of granitic magmas during ascent and emplacement. Annu Rev Earth Planet Sc 31(1): 399-427. https://doi.org/10.1146/annurev.earth.31.100901.141352

Phillips, JC, Woods, AW (2002) Suppression of large-scale magma mixing by melt–volatile separation. Earth Planet Sc Lett 204(1-2): 47-60. https://doi.org/10.1016/S0012-821X(02)00978-0

Romero, JE, Morgavi, D, Arzilli, F, Daga, R, Caselli, A, Reckziegel, F, Viramonte, J (2016) Eruption dynamics of the 22 – 23 April 2015 Calbuco Volcano (Southern Chile): Analyses of tephra fall deposits. J Volcanol Geoth Res 317: 15–29. https://doi.org/10.1016/j.jvolgeores.2016.02.027

Roggensack, K, Williams, SN, Schaefer, SJ, Parnell, RA (1996) Volatiles from the 1994 eruptions of Rabaul: Understanding large caldera systems. Science 273(5274): 490-493. https://doi.org/10.1126/science.273.5274.490

Rutherford, MJ, Baker, L, Pallister, JS (1993) Petrologic constraints of timing of magmatic processes in the 1991 Pinatubo volcanic system. EOS T Am Geophys Union 74, 671.

Sauerzapf, U, Lattard, D, Burchard, M, Engelmann, R (2008) The titanomagnetite–ilmenite equilibrium: new experimental data and thermo-oxybarometric application to the crystallization of basic to intermediate rocks. J Petrol 49(6): 1161-1185.https://doi.org/10.1093/petrology/egn021

Sellés, D, Moreno, H (2011) Geología del Volcán Calbuco, Región de Los Lagos. Carta Geológica de Chile. Serie Geológica Básica, No. 130. Escala 1:50.000.

SERNAGEOMIN (2015a) Reporte especial de actividad volcánica (REAV) - Región de los Lagos, 2015, abril 22 – 15:00.

SERNAGEOMIN (2015b) Reporte especial de actividad volcánica (REAV) - Región de los Lagos, 2015, abril 22 – 20:45.

SERNAGEOMIN (2015c) Reporte especial de actividad volcánica (REAV) - Región de los Lagos, 2015, abril 22 – 17:30.

SERNAGEOMIN (2016) Ranking de los 90 volcanes activos de Chile: http://sitiohistorico.sernageomin.cl/archivos/Ranking-de-Volcanes.pdf (accessed January 2019).

SERNAGEOMIN, (2017) Volcán Calbuco: http://www.sernageomin.cl/volcan-calbuco (accessed January 2019).

Tomiya, A, Miyagi, I, Saito, G, Geshi, N (2013) Short time scales of magma-mixing processes prior to the 2011 eruption of Shinmoedake volcano, Kirishima volcanic group, Japan. B Volcanol 75(10): 750. https://doi.org/10.1007/s00445-013-0750-1

Valderrama, Ó, Franco, L, Gil-Cruz, F (2015) Erupción intempestiva del volcán Calbuco, Abril 2015. XIV Congreso Geológico Chileno III: 91-93.

Van Eaton, AR, Amigo, Á, Bertin, D, Mastin, LG, Giacosa, RE, González, J, Valderrama, Ó, Fontjin, K, Behnke, SA (2016) Volcanic lightning and plume behavior reveal evolving hazards during the April 2015 eruption of Calbuco volcano, Chile. Geophys Res Lett 43(7): 3563–3571. https://doi.org/10.1002/2016GL068076

Van Orman, JA, Crispin KL (2010) Diffusion in oxides. Rev Mineral Geochem 72(1): 757-825. https://doi.org/10.2138/rmg.2010.72.17

Venezky, DY, Rutherford, MJ (1999) Petrology and Fe–Ti oxide reequilibration of the 1991 Mount Unzen mixed magma. J Volcanol Geoth Res 89(1): 213-230. https://doi.org/10.1016/S0377-0273(98)00133-4

Vigneresse, JL, Barbey, P, Cuney, M (1996) Rheological transitions during partial melting and crystallization with application to felsic magma segregation and transfer. J Petrol, 37(6): 1579-1600. https://doi.org/10.1093/petrology/37.6.1579

Chapter 4

4. Pre-eruptive conditions of the 1835 eruption of Osorno: a combined mineralogical, geochemical, and numerical approach

Eduardo Morgado* [1,2], Daniel J. Morgan [1], Jason Harvey [1], Angelo Castruccio [2,3], Raimundo Brahm [4], Lucy E. McGee[5], Bogomil Georgiev[1], Miguel-Ángel Parada [2,3]

[1] Institute of Geophysics and Tectonics, School of Earth and Environment, University of Leeds, Leeds LS2 9JT, UK.

[2] Centro de Excelencia en Geotermia de los Andes (CEGA-FONDAP 15090013), Chile.

[3] Departamento de Geología, Facultad de Ciencias Físicas y Matemáticas, Universidad de Chile, Chile.

[4] Volcanic Risk Solutions, IAE, Massey University, Palmerston North 4442, New Zealand.

[5] Earth Sciences, School of Physical Sciences, University of Adelaide, Australia.

[*] Corresponding author at: Institute of Geophysics and Tectonics, School of Earth and Environment, University of Leeds, Leeds LS2 9JT, UK.

E-mail address: eeeem@leeds.ac.uk (E. Morgado)

4.1. Abstract

Osorno volcano is a composite stratovolcano of the Central Southern Volcanic Zone of the Chilean Andes (41º06`S, 72º20`W). It is the southernmost member of an NE alignment of volcanic edifices including La Picada volcano and Puntiagudo and Cordón Cenizos. During 1835, two eruptive events occurred; the first during January-February and the second during November-December. The erupted products of both events are lavas and tephra fall deposits of basaltic-andesite composition (52.4–52.9 SiO_2 wt%) with degrees of crystallinity ranging from 23 to 45 vol% comprising: olivine, plagioclase, clinopyroxene, and Cr-spinel. These mineral phases allow us to constrain magmatic parameters including a temperature of ~1,140ºC (calculated via olivine-augite and Ca-in-olivine thermometry); oxygen fugacity patch of ΔQFM +0.3 (calculated via Cr-spinel-olivine-melt oxybarometry and numerical modelling) and numerical modelling allow us to determine dissolved water content of the melt of up to 1.5 wt% (calculated via numerical modelling) and depths up to 4.5 km (calculated via numerical modelling). We also apply diffusion chronometry to large (> 50 µm radius) olivine-hosted melt inclusions to infer that their compositions were not significantly altered due to syn-eruptive processes. The textures and mineral relationships observed in the samples cause us to infer that a crystal mush (highly-crystalline products, crystals in clots, and others), parts of which underwent disaggregation prior both eruptive events. In addition, we compare trace elements (fluid mobile/immobile and rare earth elements) and $^{87}Sr/^{86}Sr$ and $^{143}Nd/^{144}Nd$ isotope ratios of Osorno eruptive products with those from neighbouring volcanic systems in order to determine regional variations of slab-derived fluid input and crustal contamination. These analyses display higher both slab-derived fluid input and partial melting degree in the mantle beneath stratovolcanoes (Osorno, Calbuco, and La Picada). Although the most significant signature comes from the mantle source, our results suggest also the influence of crustal assimilation. These combined data allow us to determine part of

the nature of the Osorno volcanic system prior to the last eruptive events (during 1835), with implications for hazard mitigation and behaviour of the Central Southern Volcanic Zone of the Andes in general.

4.2. Introduction

In volcanically-active areas close to population centres, it is fundamental to establish appropriate hazard mitigation policies (e.g. Small and Naumann, 2001; De la Cruz-Reyna and Tilling, 2008). Volcanic activity is generally reported by aircraft pilot reports, satellite observations, ground observers, and monitoring instruments (Miller and Casadevall, 2000). Typically, volcano observatories and other transnational institutions evaluate these reports and integrate them with the information from instrumental, volcano monitoring, which assesses volcanic activity via different techniques: seismology, ground deformation, gas chemistry, etc. Several authors (e.g. Tilling, 2008; Sparks et al., 2012) have highlighted the need for complementary techniques to be used to reduce the risk related to volcanic eruptions. In particular, volcano monitoring needs to distinguish magmatic crustal processes during destabilisation to improve forecasting (Sparks and Cashman, 2017) and to recognise magmatic reservoirs that may act as seismic source (e.g., Jolly, 2019; McNutt, 2000), cause of deformation (e.g., Delgado et al., 2017), and origin of degassing (e.g., Witter et al., 2004).

Volcano monitoring is essential to assess the current activity of volcanoes, but it can be complemented by petrological techniques, which permit to study previous eruptions. Study of previous eruptions using petrological methods allows many of the key physical intensive parameters to be determined, including temperature, pressure, oxygen fugacity, and water dissolved in melt and constraint of derived parameters, such as magma viscosity, contamination, and residence times. Understanding of these parameters is fundamental to understand both past magmatic behaviour, the nature of the volcanic eruption, and in to give

correct and quick interpretations to volcano monitoring signals (Jolly, 2019). Moreover, in those cases when the last eruption of a volcano occurred before the volcano monitoring was established, petrological and geochemical studies of volcanic material are imperative, because they give information on the modus operandi of magma of previous pre-eruptive periods, which works as a reference for the upcoming volcanic activity.

In this article, we study the last eruptions of Osorno volcano (in Central Southern Volcanic Zone, of the Southern Andes of Chile) to assess the pre-eruptive physical magmatic conditions and to assess crustal assimilation processes. Although the last eruptions occurred in 1835, the volcano monitoring project in Chile, which started in 2008, has classified this volcano as the ninth-most hazardous of Chile (SERNAGEOMIN 2017a). Despite the relatively long quiescence, recently Osorno has in recent years, shown an elevation of seismicity base level, interpreted as a sign of volcanic activity (SERNAGEOMIN 2017b; 2018a, b; 2019).

4.2.1. Southern Volcanic Zone: Geological setting

The Southern Volcanic Zone (SVZ) of the Chilean Andes is a volcanic chain produced by the subduction of the oceanic Nazca plate below the South American continental plate. The SVZ comprises over 70 Pleistocene and Holocene stratovolcanoes and several large volcanic fields (Stern et al., 2007). The whole volcanic segment is ~1400 km long (33º–46ºS) and across it there is a major structure, the Liquiñe-Ofqui Fault Zone (LOFZ), which controls the compressional tectonics (between 33º and 34º30'S) and dextral-transpressional tectonics (between 34º30' and 46ºS) tectonics of the volcanic arc (Cembrano and Lara, 2009). The SVZ has been subdivided into four segments on the basis of tectonic setting, geochemical and petrologic considerations (Tormey et al., 1991; López-Escobar et al., 1995a; Stern, 2004; Stern et al., 2007; Fig. 4.1.): Northern (NSVZ, 33.3-34.4ºS), Transitional (TSVZ, 34.4-37ºS),

Central (CSVZ, 37-42ºS), and Southern (SSVZ, 42-46ºS). The present study focuses on volcanic centres from the CSVZ, the most active region of the SVZ, in which Cembrano and Lara (2009) reported different tectonic features and proposed a model including a volcano-tectonic association:

- NE-trend volcanic alignments (e.g., La Picada-Puntiagudo-Cordón Cenizos; Moreno et al., 2010; Vander Auwera et al., 2019; Fig. 4.2) related to tension cracks, which may reach the surface and then build either a stratovolcano or an elongated cluster of minor eruptive centres, depending on the balance between strain rate and magma input (cf. Takada, 1994).
- NW-trend alignments (e.g., Puyehue-Cordón Caulle, Lara et al., 2004, 2006), in which volcanoes are built on top of west-nortwest-striking, pre-Andean, oblique-slip faults.
- Small eruptive centres built over the LOFZ master fault (e.g., Caburgua-Huelemolle small eruptive centres; Hickey-Vargas et al., 1989, 2002; Morgado et al., 2015, 2017; Mcgee et al., 2017; Cayutué-La Viguería group; López-Escobar et al., 1995b). Small eruptive centres melts can be shown to have ascended rapidly, and without extensive interaction with the crust (e.g. Morgado et al., 2017) and do not interact extensively with the crust (e.g. McGee and Smith, 2016; Hickey-Vargas et al., 2016a; Smith and Németh, 2017); this volcanism is usually related to extensional domains (e.g. Nakamura, 1977; Takada, 1994; Piochi et al., 2005).

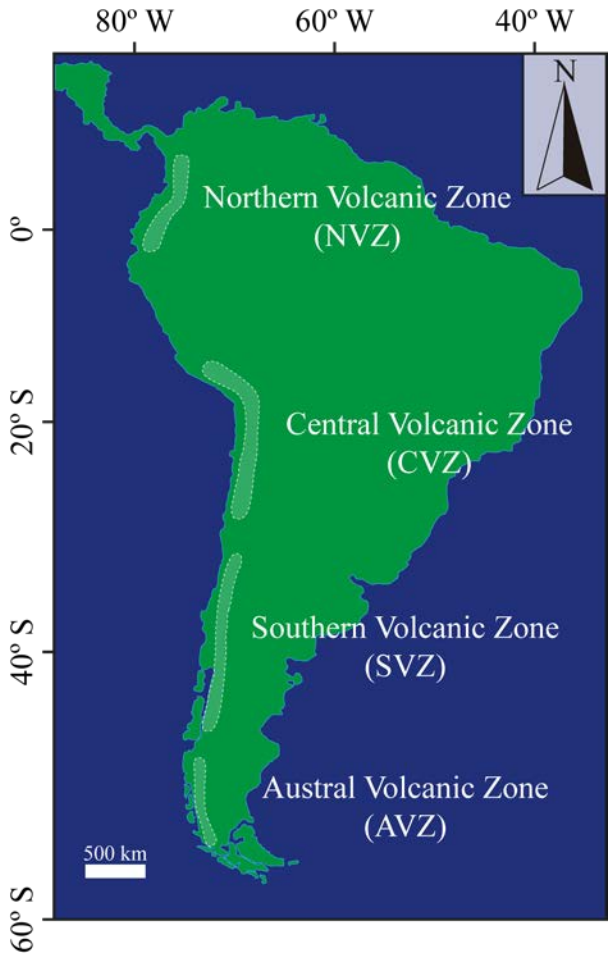

Figure 4.1. *Location of the different volcanic zones of the Andes with respect to South America.*

Volcanic products from the CSVZ exhibit a compositional range from basalts to rhyolites (e.g. Hickey-Vargas et al., 2016b) and factors such as both contamination from sediments of the trench and interaction with major regional structures (Cembrano and Lara, 2009; Hickey-Vargas et al., 2016b; López-Escobar et al., 1995b) would affect those compositions. The highest sedimentation rate of the SVZ occurs in the trench of the CSVZ (Völker et al., 2013), where ~2.2 km thick of sedimentary material covers the trench offshore (Contreras-Reyes et al., 2008). These sediments from the trench are significant contaminants of the mantle wedge and, in consequence, of the volcanic products (e.g., Hickey-Vargas et al., 1989; 2002; Kilian and Behrmann, 2003; Lucassen et al., 2004; Jacques et al., 2014). In addition, continental magmas may also receive contributions from the metamorphic Palaeozoic basement (e.g., Stern, 1991; Kilian and Behrmann, 2003; Lucassen et al., 2004; 2010; Kay et al., 2005).

4.2.2. Osorno volcano: general features

Osorno is an active stratovolcano of the Central Southern Volcanic Zone of the Chilean Andes, its maximum height is 2661 meters above sea level (m.a.s.l.) with an estimated volume of 160 km^3, covering an area of 250 km^2 (Moreno et al., 2010). It is located at 41º06`S, 72º20`W, and lies west of the LOFZ by ~13 km (Fig. 4.2). Osorno volcano is the southernmost member of an NE alignment including La Picada volcano and Puntiagudo–Cordón Cenizos volcanic chain (Fig. 4.2).

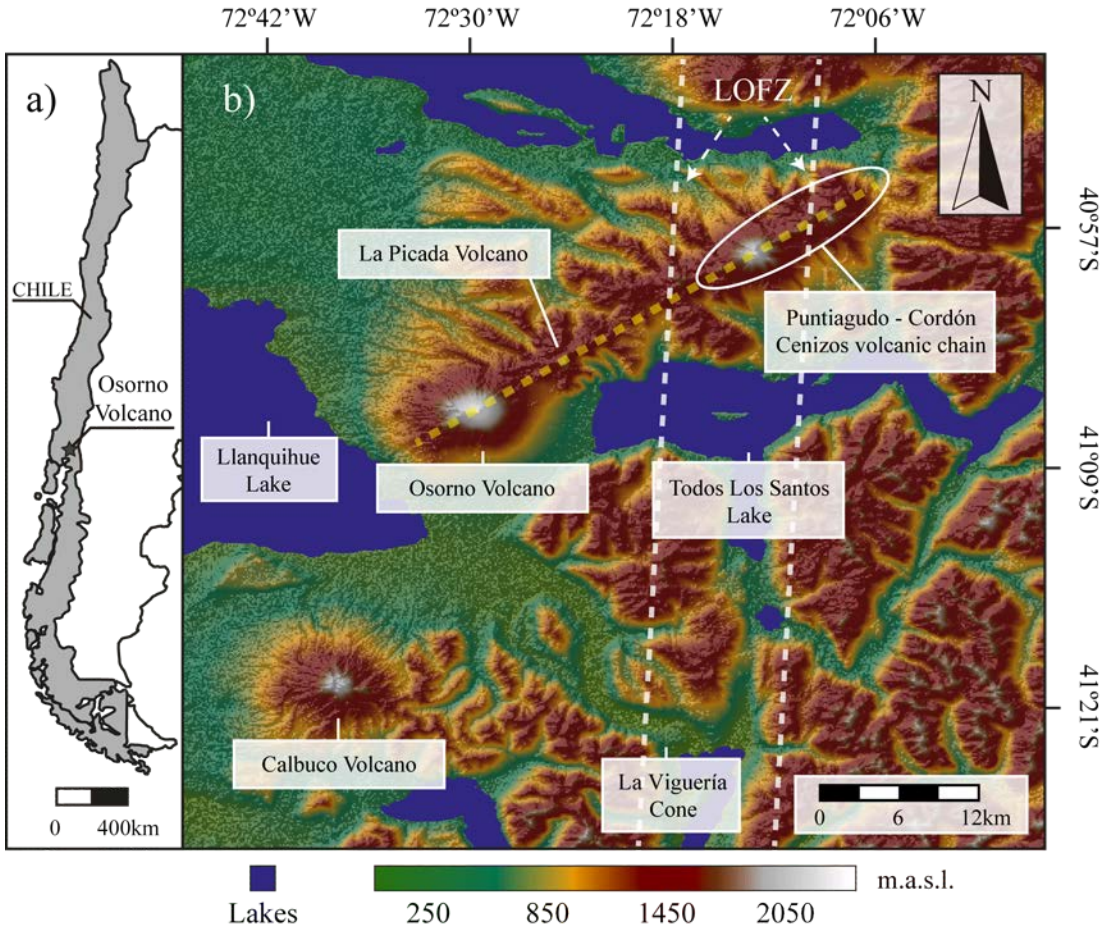

Figure 4.2. *a) Location of the Osorno volcano regarding Chile. b) Position of Osorno, La Picada, Puntiagudo, and Calbuco volcanoes and Cordón Cenizos volcanic chain, La Viguería cone, and the Liquiñe-Ofqui Fault Zone (LOFZ, white dashed line). The alignment Osorno, La Picada, Puntiagudo and Cordón Cenizos is represented by a yellow, dashed line. The advanced Spaceborne Thermal Emission and Reflection Radiometer (ASTER) Global Digital Elevation Model (GDEM) image was obtained via EarthExplorer, USGS (http://earthexplorer.usgs.gov)*

According to Moreno et al. (2010) Osorno volcano has been active since the Middle Pleistocene (ca. 200 ka). Its postglacial activity has been related mainly to main crater eruptions, but also parasitic cones and dacitic domes in the flanks (Moreno et al., 2010). The basement beneath Osorno volcano comprises Cretaceous granitoids (ca. 70 Ma; Moreno et al., 2010) and Miocene plutonic rocks from the Northern Patagonian Batholith (López-Escobar et al., 1992; Adriasola et al., 2006). Vander Auwera et al (2019) found Miocene-age (ca. 9.6 Ma) gabbroic xenolith blocks within the volcanic products of La Picada volcano, which they interpreted as basement, and Hickey-Vargas et al. (1995) described gabbroic and

granulitic xenoliths recovered from volcanic material of the 1961 eruption of Calbuco Volcano.

The products of Osorno volcano have been classified into four units depending on the age of the deposits, which are shown in Table 4.1. In the unit Osorno 4, several historical eruptions during the years 1575, 1640, 1644(?), 1719, 1737, 1765, 1778-1779, 1790, and 1834 have been recognised and briefly described, whereas activity since 1834 has been confined to fumarolic episodes in 1852, 1882-1883, 1911-1915, 1963, 1969, 1985, 1993 (details in Table 4.2).

Table 4.1. Main features of the different units of Osorno volcano

Unit	Description	Mineralogy
Osorno 1 (200-110 ka)	Unit composed of lavas from basaltic to andesite composition (49-58 wt% SiO_2) interbedded with lahars and morraine deposits, emplaced mainly during Santa María Glaciation (200–132 ky; Porter, 1981; Clapperton, 1993), conglomerates of basaltic composition (~52 wt% SiO_2) and volcanic breccias.	Plagioclase, olivine, and clinopyroxene
Osorno 2 (90-30? ka)	Unit composed mainly of lavas from basaltic to andesitic composition (50 – 58 wt% SiO_2) and scarce dacites (62 wt% SiO_2), interbedded with pyroclastic deposits and conglomerates of laharic origin emplaced during Llanquihue Glaciation (90-14 ky; Mercer, 1976; Porter, 1981; Clapperton, 1993; Denton et al., 1999).	Plagioclase, olivine, and clinopyroxene
Osorno 3 (12-4? ka)	Unit composed of lavas of basaltic and basaltic andesite composition (50-56 wt% SiO_2), also lahars have been associated to the eruptions of this unit. Over the deposits of this unit there is a 14C dated laharic deposit of ~4 ky age.	Plagioclase, olivine, and clinopyroxene
Osorno 4 (4 ka - 1835 AD)	Unit composed of lavas of composition from basalt to basaltic andesite (52 – 56 wt% SiO_2), associated lahars, and pyroclastic flows with scoriaceous bombs of basaltic composition.	Plagioclase, olivine, and clinopyroxene

Description of different units available in López-Escobar et al. (1992) and Tagiri et al. (1993).

Table 4.2. Main features of the historical eruptions of Osorno volcano*

Year of the eruption	Description
1575, 1640, 1644(?)	Eruptions are noted or suspected (?) in the referenced years (O'Compley, 1936)
1719	Eruption of Osorno volcano (Martin, 1901).
1737	Eruption of Osorno volcano (Almanaque, 1969) coinciding with an earthquake in Valdivia city (~ 150 km distance)
1765	Weak explosions are described in the main crater (Moraleda and Montero, 1888).
1778-1779	Eruptive period with eruptions in the main crater (Moraleda y Montero, 1888).
1790	Eruptive event including a parasitic cone in the east flank of the volcano. According to Moraleda y Montero (1888) the emited products are maily piroclasts, which formed eruptive columns and lava flows. It was suggested to be strombolian.
1834	The volcano had explosive activity including columns of gas and ashes (Darwin, 1939b).

* Based on Petit-Breuilh (1999) and references therein

4.2.3. The 1835 Osorno eruption: History

Charles Darwin (1839a; 1840) described two eruption stages of Osorno volcano during 1835. Although he recognised release of "smoke" in November 1834 (Darwin, 1839b), the first stage of the 1835 Osorno eruption started on 19 January with moderate to vigorous strombolian activity (VEI 2; Lara et al., 2012). The volcano was still erupting in this manner on 18 February, two days before the historically-significant, large-magnitude earthquake (M_w 8.0-8.3; Watt et al., 2009) of Concepción, Southern Chile (Darwin, 1840). During the shock period, Darwin (1839a) described the emission of a dark blue "smoke" column from the summit, following the eruption cessation, ending the first period of eruption. Basaltic lavas are associated with this first period (Moreno et al., 2010), produced from an array of eruptive fissures and small pyroclastic cones (see Fig. 4.3). According to Darwin (1840), the second eruptive stage resumed activity from the vents of the first stage (Lara et al., 2012). The second eruptive period started on 11 November, when the emission of products reached a considerable height (Darwin, 1840). During 5 December, a fissure eruption occurred and for the period of the succeeding fortnight steam and ashes were released. The 5 January 1836, the volcano was still erupting (Gillis, 1855).

4.3. Descriptions and compositions of the samples

The collected samples (Fig. 4.3) correspond to lava flows (reaching lengths from 10 to 14 km long) and lapilli fall deposits from the main crater and parasitic cones. The lava flow samples have a vesicularity of 4 to 17 vol% and the lapilli samples have a higher vesicularity of 31 to 61 vol% (Table 4.3). We obtain the quantification of the main petrographic features from the collected samples of Osorno volcano by image processing techniques of pseudo-coloured images via the freeware JMicrovision. The main phenocryst phases are plagioclase, olivine, and clinopyroxene, as described for other Osorno materials in previous studies (Tagiri et al.,

1993). The nature of the groundmass depends on the sample; those collected from lava flows (Table 4.3) possess a glass-free microcrystalline groundmass, and those corresponding to lapilli samples contain microlites and interstitial glass. The microlite phases correspond to plagioclase, olivine, clinopyroxene, and titanomagnetite and are recognised via Scanning Electron Microscope.

We recognise several cognate xenoliths in the lapilli deposits at location Os-164 and their mineralogy comprises plagioclase, orthopyroxene, olivine, ilmenite, titanomagnetite, as phenocrysts and plagioclase, clinopyroxene and titanomagnetite as microlites. Also we recognise healed microfractures (cf. Dungan and Davidson, 2004) in olivine and orthopyroxene phenocrysts from the cognate xenoliths. Olivine phenocrysts also exhibit surrounding iddingsite, which suggests weathering in oxidising conditions (Smith et al., 1987). Pyroxene microphenocrysts and phenocrysts show exsolution textures as result of slow cooling in a crystal-rich zone or assimilation beneath the Osorno reservoir (details in Supplementary Material).

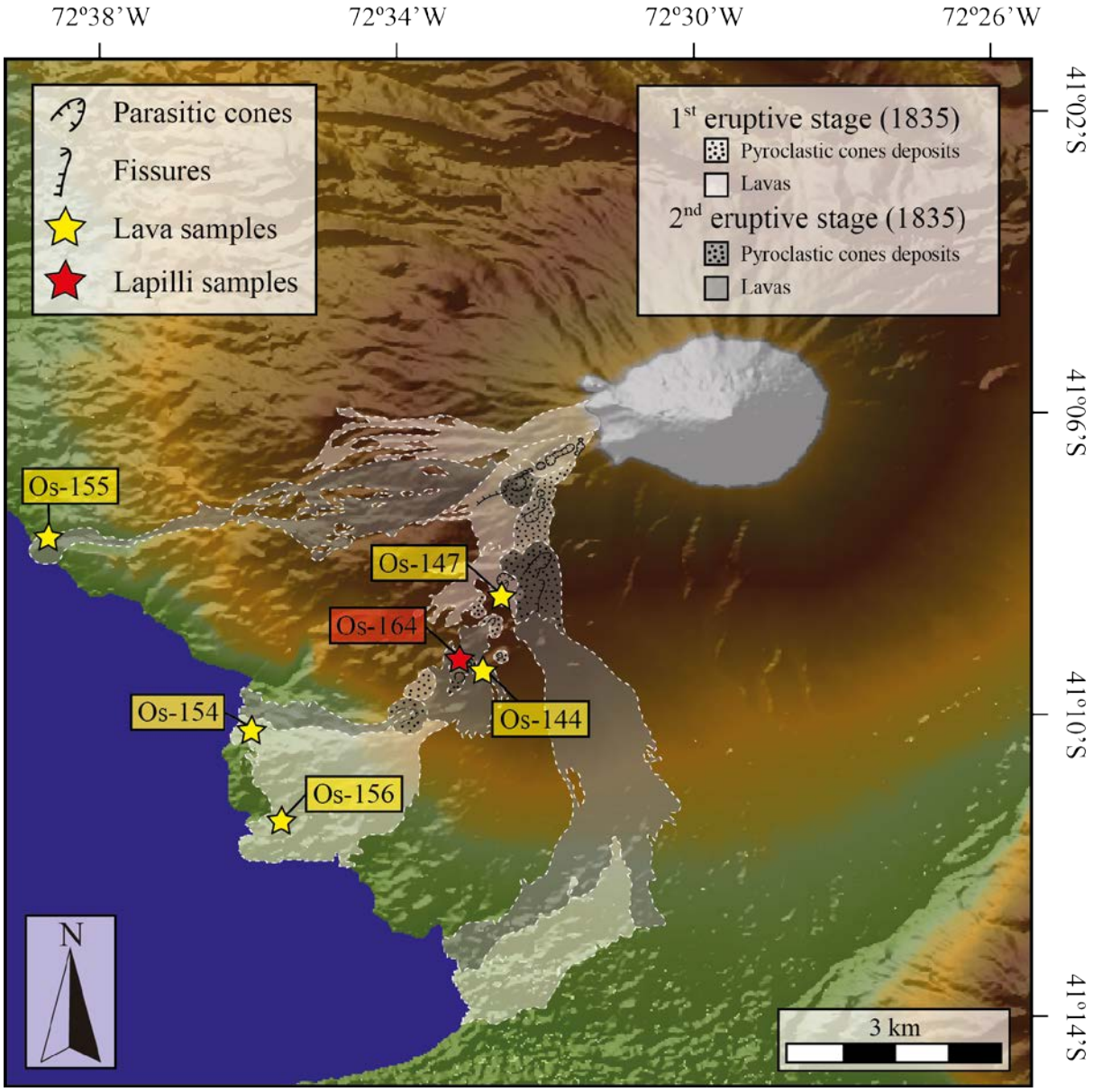

Figure 4.3. *Osorno volcano and the deposits of the 1835 first and second eruptive stages. Yellow stars represent locations where samples are collected from a lava flow, whereas lapilli sample locations are presented by red stars. Locations and dates of the lava flows and fall deposits are based on Moreno et al. (2010) and Lara et al. (2012). The ASTER–GDEM image was obtained via EarthExplorer, USGS (http://earthexplorer.usgs.gov)*

Table 4.3. Main features of the collected samples from the 1835 eruption of Osorno Volcano.

Section name (Os-)	Os-144a	Os-144b	Os-147a	Os-147b	Os-154a	Os-154b	Os-155a	Os-155b	Os-156a	Os-156b	Os-164a	Os-164b
Description	LF	LF	LF	LF	LF	LF	LF	LF	LF	LF	FD	FD
Vesicles (total %)	15.29	15.73	14.66	16.91	7.7	7.76	4.35	7.38	13.23	9.74	31.17	61.22
Groundmass (total %)	49.12	47.33	65.26	60.83	60.5	58.34	69.46	64.75	52.27	55.37	43.83	28.93
Plagioclases (total %)	33.11	34.69	19.75	21.72	30.9	32.6	25.91	27.51	33.05	32.79	23.38	9.26
Olivine (total %)	2.48	2.25	0.33	0.54	0.9	1.3	0.28	0.36	1.45	2.1	1.62	0.59
Pyroxenes (total %)	0.62	0.83	0.08	0.01	0.03	0.17	0.01	0.01	0.35	0.07	0	0
Crystallinity (%)*	42.44	44.38	23.60	26.80	34.47	36.87	27.39	30.10	40.00	38.70	36.32	25.40
Eruptive stage	2	2	1	1	1	1	2	2	1	1	2	2

LF: Sample collected from a lava flow; FD: Fall deposit (lapilli)

* Percentage not considering vesicles

4.4. Analytical procedures

4.4.1. Major elements

Whole-rock compositions of lapilli deposits of one location (Os-164), 3 lava samples from three locations from the 1835 Osorno eruption (Os-147, Os-154, and Os-164), and two samples (one lava and one bomb) from La Viguería cone were analysed via XRF (major elements) at ACME labs using OREAS-184 and SY-4 standards for all the major elements, and CCU-1D, and OREAS-700 standards for FeO. Accuracy for major elements in all standards is better than 3% (relative) except for TiO_2 in SY-4 which is 4.5% (relative) and P_2O_5 in OREAS-184 and SY-4 which were 14% and 17% (relative), respectively. The uncertainties (2σ) of measurements are reported in Table 4.4.

4.4.2. Trace element abundances

All trace element measurements were performed on an Agilent 7500a at The Open University (Milton Keynes, UK). Samples from this study were dissolved for trace element analysis by ICP MS. 0.1 g of finely powdered sample was weighed out and 1 mL of Romil UpA HNO_3 and 3 mL of Romil UpA HF were added. The samples were heated in sealed vials to 130 ºC and agitated in an ultrasonic bath for 20 minutes every 12 hours until they had completely dissolved. The samples were then dried down to incipient dryness and the resulting gel brought up in 4 mL of 18 MΩ cm^{-1} H_2O and 2 mL of Romil UpA HNO_3 and agitated in an ultrasonic bath for 20 minutes then returned to the hotplate for at least 4 hours. After drying down for a second time a further 4 mL of 18 MΩ cm^{-1} H_2O and 3 mL of Romil UpA HNO_3 were added to produce a final solution containing c 2 % HNO_3. After a further 4 hours of heating the samples were made up to a mass of 100g with 18 MΩ cm^{-1} H_2O to give a final solution with a 1000:1 dilution ratio ready for mass spectrometry. Spike was not added during the dissolution as Be, In, Rh, Tm, Re and Bi were all added online during analysis.

Samples were stored in polypropylene beakers in an Agilent integrated auto sampler and an Agilent microflow PTFE nebuliser with an uptake rate of 100–150 μL min^{-1} was used for the analysis. Integration times for each mass ranged between 0.3 and 0.9 seconds according to the expected concentration within the sample. A total of 66 masses were analysed on each run but 31 were used for the purposes of this study, the others being masses of added spikes, multiple isotopes of individual elements and elements that were subsequently discarded. After each sample had been analysed a washout period of not less than 100 seconds was allowed, using a 2% solution of Romil UpA HNO_3, to minimise cross contamination between samples. All samples were corrected for blank effects and subsequently corrected offline for instrumental drift. Where more than one analysis of a sample was undertaken during the same run the mean value was taken prior to offline corrections were performed. All data points with concentrations lower than the detection limits were discarded. The precision was better than 8% (relative, 2σ) and accuracy in the trace elements in JB-2 (n = 5), BHVO-2 (n = 2) and AGV-1 (n = 2) is better than 10% relative except in Ni (21% relative, in AGV-1) and Pb (13% relative, in BHVO-2). The uncertainties (2σ) of measurements are reported in Table 4.4.

4.4.3. Strontium and neodymium isotope measurements

All $^{87}Sr/^{86}Sr$ and $^{143}Nd/^{144}Nd$ analyses in this study were conducted on a Thermo/Finnigan Triton Thermal Ionization Mass Spectrometer (TIMS) fitted with 1011 Ohm amplifiers at the University of Leeds. Analyses were performed on ca. 100 mg of bulk rock powders digested using a combination of Romil-UpA HF, HNO_3 and HCl, using the same method as described for the trace element deteminations. Once in solution, samples were centrifuged prior to loading onto Eichrom Sr Spec™ columns with a bed volume of approximately 100 μL. The REE fraction was collected before elution of the Sr fractions into different vials. Prior to loading onto W filaments with a $TaCl_5$ activator, the Sr fraction was passed through the Sr

spec column a second time and dried with two drops of dilute $HClO_4$ to remove any organic contaminants derived from the resin. The REE fraction was passed first through a TRU Spec^{TM} column (ca. 100 µL bed volume) and finally a LN Spec^{TM} column (bed volume ca. 2 mL) before loading onto Re filaments. The USGS reference material BHVO-2 were processed alongside the samples, together with two total procedural blanks spiked with highly enriched ^{84}Sr, and ^{150}Nd solutions. Mean total procedural blanks for Sr and Nd were 326 pg and 153 pg, respectively. Accuracy of the radiogenic isotope analyses was assessed by analysing standard solutions of known composition alongside the unknowns – NBS987 for Sr, and La Jolla for Nd, which yielded $^{87}Sr/^{86}Sr$ = 0.710241±0.000006 for NBS987, $^{143}Nd/^{144}Nd$ = 0.511842±0.000002 for La Jolla, all in a good agreement with published results (e.g., GeoReM and GEOROC databases).

A static multicollection routine with standard cup configurations was used for all of the isotopic analyses. All measured $^{87}Sr/^{86}Sr$ ratios were corrected for mass bias relative to $^{88}Sr/^{86}Sr$ of 8.375209, using an exponential law. Data acquisition comprised the integration of two hundred 8 second measurements of masses 84, 85, 86, 87 and 88 for Sr isotope analyses. Mass 85 was measured to correct for any Rb interference on mass 87 assuming a natural 87Rb/85Rb of 0.386. For Nd isotope measurements, masses 143, 144, 146, 147, 148 and 150 were acquired in the same way as Sr isotopes. Mass 147 was measured to correct for Sm interferences on mass 144, 148 and 150. Natural $^{144}Sm/^{147}Sm$, $^{144}Sm/^{148}Sm$, and $^{144}Sm/^{150}Sm$ of 0.2048, 0.7498 and 0.4923, respectively were assumed for this correction.

4.4.4. Crystallographic orientation

Crystallographic orientations were determined using electron back-scatter diffraction in olivine crystals (EBSD; Prior et al. 1999) on an FEI Quanta 650 FEGSEM equipped with a Nordlys EBSD camera at the School of Earth and Environment, University of Leeds (Leeds, UK).

Table 4.4. Whole-rock analyses of samples from the 1835 Osorno eruption and La Viguería cone.

	Detection limit	Os-144a Lava	Os-147a Lava	Os-154a Lava	Os-164a Lapilli	LV-152a Lava	LV-153a Bomb
SiO2	0.01 (%)	52.4	52.9	52.7	52.9	51.3	52.3
Al2O3	0.01 (%)	20.1	19.7	20.7	19.6	17.8	17.9
TiO2	0.01 (%)	0.89	0.93	0.86	0.91	0.86	0.86
FeO	0.2 (%)	6.29	5.46	5.59	5.64	5.49	5.94
Fe2O3	0.01 (%)	1.47	2.66	2.04	2.62	3.17	2.29
MnO	0.01 (%)	0.14	0.14	0.15	0.16	0.16	0.16
MgO	0.01 (%)	4.47	4.21	4.09	4.55	7.97	7.05
CaO	0.01 (%)	10.6	10.2	10.9	10.2	9.81	10.1
Na2O	0.01 (%)	3.01	3.14	3.06	3.05	2.75	2.91
K2O	0.01 (%)	0.49	0.51	0.48	0.48	0.63	0.69
P2O5	0.01 (%)	0.13	0.13	0.13	0.13	0.2	0.2
LOI		-0.5	-0.4	-0.4	-0.4	-0.1	-0.3
TOTAL		99.99	99.98	100.7	100.24	100.14	100.4
Li	0.2 (ppm)	9.9	10.5	10.6	9.7	7.2	6.4
Sc	0.3 (ppm)	31	30	30	31	32	32
V	0.7 (ppm)	256	252	249	248	237	242
Co	0.1 (ppm)	39.8	38	36.3	49.9	55.6	43.4
Ni	0.3 (ppm)	34	26	28	24	101	65
Cu	0.7 (ppm)	93.5	87.9	92.7	74.3	84.5	80.4
Cr	0.1 (ppm)	79.7	60.1	77.7	67.6	218	167
Zn	2 (ppm)	77	81	73	75	72	71
Tl	0.04 (ppm)	0.07	0.06	0.05	0.06	0.07	0.07
Rb	0.1 (ppm)	13.8	13.8	12.9	12.5	8.8	10.2
Ba	0.5 (ppm)	141	141	135	129	162	181
Th	0.1 (ppm)	1	1	0.9	0.9	1.3	1.4
U	0.01 (ppm)	0.3	0.3	0.3	0.3	0.4	0.4
Nb	0.3 (ppm)	2	1.9	1.9	3	7.9	2.9
La	0.1 (ppm)	5.7	5.5	5.4	5.3	9.7	9.7
Ce	0.2 (ppm)	14.6	14	13.7	13.7	23.6	23.9
Pb	0.1 (ppm)	5.6	5.5	5.2	5.9	6.3	5.8
Pr	0.1 (ppm)	2	2	1.9	1.9	3.1	3.1
Sr	0.1 (ppm)	412	386	410	376	575	614
Nd	0.1 (ppm)	9.9	9.6	9.4	9.3	14.5	14.4
Zr	0.1 (ppm)	65.3	64.4	61.7	59.5	81.9	82.6
Sm	0.1 (ppm)	2.7	2.7	2.6	2.6	3.5	3.5
Eu	0.1 (ppm)	0.9	0.9	0.9	0.9	1.1	1.1
Gd	0.1 (ppm)	3	2.9	2.8	2.8	3.4	3.4
Tb	0.1 (ppm)	0.5	0.5	0.5	0.5	0.5	0.5
Dy	0.1 (ppm)	3.1	3	2.9	2.9	3.2	3.2
Ho	0.1 (ppm)	0.7	0.7	0.6	0.6	0.7	0.7
Er	0.1 (ppm)	1.9	1.9	1.8	1.8	1.9	1.9
Y	0.1 (ppm)	19.3	19.2	18.5	18.5	19.4	20.3
Yb	0.1 (ppm)	1.9	1.8	1.8	1.9	1.8	1.9
Lu	0.1 (ppm)	0.3	0.3	0.3	0.3	0.3	0.3

Table 4.5. Isotopic data of the 1835 Osorno and 2015 Calbuco volcanic material.

Sample	$^{87}Sr/^{86}Sr$	error (±)	$^{143}Nd/^{144}Nd$	error (±)
1835 Osorno products (this study)				
Os-144	0.704333	5	0.512741	12
Os-147	0.704309	4	0.512784	4
Os-154	0.704324	6	0.512766	7
Os-164	0.704310	5	0.512774	4
Other Osorno products (Jacques et al., 2014)				
CL-098	0.704300	2	0.512806	3
CL-102	0.704335	3	0.512796	3
Other Osorno products (Tagiri et al., 1993)				
OS-04	0.704410	50	-	-
OS-18	0.704470	50	-	-
OS-17	0.704450	50	-	-
OS-14	0.704460	50	-	-
OS-15	0.704330	50	-	-
OS-16	0.704340	50	-	-
OS-02	0.704350	50	-	-
OS-01	0.704410	50	-	-
OS-07	0.704370	50	-	-
OS-03	0.704330	50	-	-
OS-06	0.704440	50	-	-
OS-05	0.704450	50	-	-
OS-09	0.704510	50	-	-
2015 Calbuco products (this study)				
Cal-149a	0.704413	4	0.512685	5
Cal-149b	0.704406	8	0.512680	5
Cal-157	0.704398	5	0.512803	15
Cal-158	0.704384	8	0.512835	25
Cal-159	0.704413	5	0.512770	5
Cal-160	0.704438	8	0.512796	4
Other Calbuco products (López-Escobar et al., 1995)				
3282-2 (Unit 3)	0.704369	30	0.512774	18
3282-4 (Unit 3)	0.704644	30	0.512727	18
3282-5 (Unit 4)	0.704551	30	0.512744	18
La Viguería products (this study)				
LV-152	0.703705	6	0.512829	3
LV-153	0.703753	6	0.512763	6

Table 4.5. (continued)

Sample	$^{87}Sr/^{86}Sr$	error (±)	$^{143}Nd/^{144}Nd$	error (±)
Cayutué-LaViguería volcanic field products (López-Escobar et al., 1995)				
21282-1 (Cayutué)	0.703720	30	0.512840	18
PC-132 (Cayutué)	0.703686	30	0.512828	18
4476- lb (La Viguería)	0.703700	30	0.512852	18
AC-86-2 (La Viguería)	0.703689	30	0.512747	18
VC-42-2 (Pocoihuen)	0.703912	30	0.512796	18
PC-127-2 (Cabeza de Vaca)	0.703763	30	0.512788	18
North Patagonian Batholith, gabbro (Aragón et al., 2011)				
ANG2010-3	0.703550	-	0.512920	-
North Patagonian Batholith, granodiorite (Aragón et al., 2011)				
ANG2010-4	0.703770	-	0.512870	-
Granulite xenoliths (Hickey-Vargas et al., 1995)				
3282-2f	0.704010	30	0.513170	18
21-4	0.704210	30	0.513149	18
Gabbro xenolith (Hickey-Vargas et al., 1995)				
19-18	0.704580	30	0.512707	18
Altered oceanic crust (Jacques et al., 2014)				
AOC	0.704769	-	0.513153	-
Trench sediments from CSVZ (Kilian and Behrmann, 2003)				
859	0.708170	15	0.512450	6
860B	0.711950	15	0.512320	6
861C	0.706050	15	0.512610	6
863A	0.706140	15	0.512630	6
863B	0.706190	15	0.512640	6
Chapo Granitoids (Munizaga et al., 1988)				
CHAPO-2A	0.705010	70	-	-
CHAPO-3A	0.705580	70	-	-
CHAPO-3B	0.708890	70	-	-
CHAPO-3C	0.706800	70	-	-
CHAPO-3D	0.706210	70	-	-
CHAPO-4A	0.704830	70	-	-
CHAPO-4B	0.704770	70	-	-
CHAPO-4C	0.705040	70	-	-

4.4.5. Mineral chemistry

The mineral chemical analyses of olivine, pyroxene, plagioclase, spinel, ilmenite, titanomagnetite, and glass are measured using an electron microprobe (JEOL JXA8230) at Leeds Electron Microscopy and Spectroscopy Centre at the University of Leeds (Leeds, UK). Counting time is distributed equally between on-peak and background measurements, using the following conditions:

Olivine. Compositional profiles (spacing ~2 µm) and single-point concentrations measurements of major (Si, Mg, and Fe), minor and trace (Ni, Ca, Cr, Mn, Ti, and Al) elements are obtained in olivine phenocrysts. The analytical conditions consisted of an accelerating potential of 15 keV and electron beam current of 30 nA for major elements and 100 nA for minor and trace elements with a focused beam. Counting times for all the elements were 40 s.

Pyroxenes. Concentrations of major (Si, Mg, Fe, and Ca), minor and trace (Ni, Cr, Mn, Ti, Al, and Na) elements are obtained in clinopyroxene and orthopyroxene phenocrysts. The analytical conditions consisted of an accelerating potential of 20 keV and electron beam of 30 nA for Si, Mg, and Ca and 80 nA for Fe, Ni, Cr, Mn, Ti, Al, and Na with a focused beam. Counting times for all the elements were 40 s. For all pyroxenes the values of Fe^{3+} are obtained following the formulations of Putirka (2008).

Plagioclase. Concentrations of major (Si, Al, Ca, Na, and K) and minor (Ti, Fe, Mg, Sr, and Ba) elements are obtained in plagioclase phenocrysts. The analytical conditions consisted of an accelerating potential of 20 keV and electron beam current of 10 nA for major elements and 40 nA for minor elements with a defocused beam (2 to 5 µm) in order to avoid alkali loss. Counting times for major elements are 32 s, 240 s for Ti, Fe, and Ba, and 480 s for Mg and Sr.

Cr-Spinel. Concentrations of major (Al, Fe, Mg, Cr, and O), minor, and trace (Ti, Mn, Ca, Ni, Co, V, Zn, and Si) elements are obtained in spinels found as inclusions in olivine phenocrysts. The analytical conditions consist of an accelerating potential of 15 keV and electron current beam of 50 nA for all the elements with a focused beam. Counting times for Al, Fe, Mg, Cr, Ti, and O are 240 s and counting times for except for Ca, Ni, Co, Mn, Si, and V are 120 s. For all spinels the values of Fe^{3+} are obtained following the formulations of Droop (1987).

Fe-Ti oxides. Compositional profiles (spacing ~2 µm) measurements of major (Ti, Fe, and O), minor and trace (Mg, Al, Mn, Ca, V, Cr, Zn, Ni, Co, and Si) elements are obtained in in-contact ilmenite and titanomagnetite grains. The analytical conditions consist of an accelerating potential of 15 keV and electron beam current of 30 nA for all elements with a focused beam. Counting times for all the elements are 60 s except for O, in which counting times are 260 s. For all the ilmenites and titanomagnetites the values of Fe^{3+} are obtained following the formulations of Droop (1987) and Stormer (1983) respectively.

Glass. Concentrations of major (Si, Al, Ti, Fe, Mn, Mg, Na, K, Ca, and P) and minor (S and Cr) elements are obtained in glasses from the groundmass, interstitial glass between crystals of clots, and olivine-hosted and plagioclase-hosted melt inclusions. The analytical conditions consisted of an accelerating potential of 15 keV and electron beam current of 10 nA for all elements with a defocused beam (5 to 10 µm) to avoid alkali loss. Counting times are 20 s for K, 30 s for Si, Al and Na, 40 s for Fe and Ca, 60 s for Cr, 80 s for Ti, Mn, Mg and P, and 120 s for S.

4.5. Results

4.5.1. Geochemistry

The Osorno products are chemically similar in major elements, all of them are basaltic-andesites (52.4–52.9 SiO_2 wt%; Fig. 4.4a) with high Al_2O_3 contents (19.6–20.7 wt%) and Mg# (Mg#= molar $Mg/(Mg+Fe^{2+})$) between 0.56 and 0.59. Also similar in trace elements: rare earth elements (REE) patterns, with a narrow range of La_N/Yb_N (2.1–2.2; Fig. 4.5). The normalised values of Osorno products show similar compositions and patterns as the erupted materials from the nearby Calbuco and La Picada volcanoes and La Viguería cone (Fig. 4.5). In addition, the spider diagram of Osorno products shows similar trends in all samples and exhibit positive Rb, Pb and Sr anomalies and negative Nb, P, and Ti anomalies, which are typical of magmas from arc settings (Fig 4.4b).

4.5.2. Isotopic data

Osorno (samples Os-144a, Os-147a, Os-154a, and Os-164a; see locations in Fig. 4.3) and Calbuco (samples Cal-149Ta, Cal-149Tb, Cal-157a, Cal-158a, Cal-159a, and Cal-160; see location in Fig. 2.2) volcanic products show a narrow ranges of $^{87}Sr/^{86}Sr$ (0.704309–0.704333, Osorno; 0.704384–0.704438, Calbuco). $^{143}Nd/^{144}Nd$ Osorno and Calbuco volcanic products show ranges of 0.512741–0.512784 (Osorno) and 0.512680–0.512835 (Calbuco). Products (samples LV-152a and LV-153a) from La Viguería cone (built over the LOFZ) exhibit contents of $^{87}Sr/^{86}Sr$ lower (0.703705–0.703753), but $^{143}Nd/^{144}Nd$ contents (0.512763–0.512829) in the range of those obtained in Osorno and Calbuco samples. Non-volcanic crustal rocks of the region are potential contaminants of Osorno and Calbuco products (granulites, gabbros, and granitoids, Hickey-Vargas et al., 1995; Aragón et al., 2011) and most of their isotopic values are not within the ranges of isotopic data of Osorno and Calbuco products (see Table 4.3).

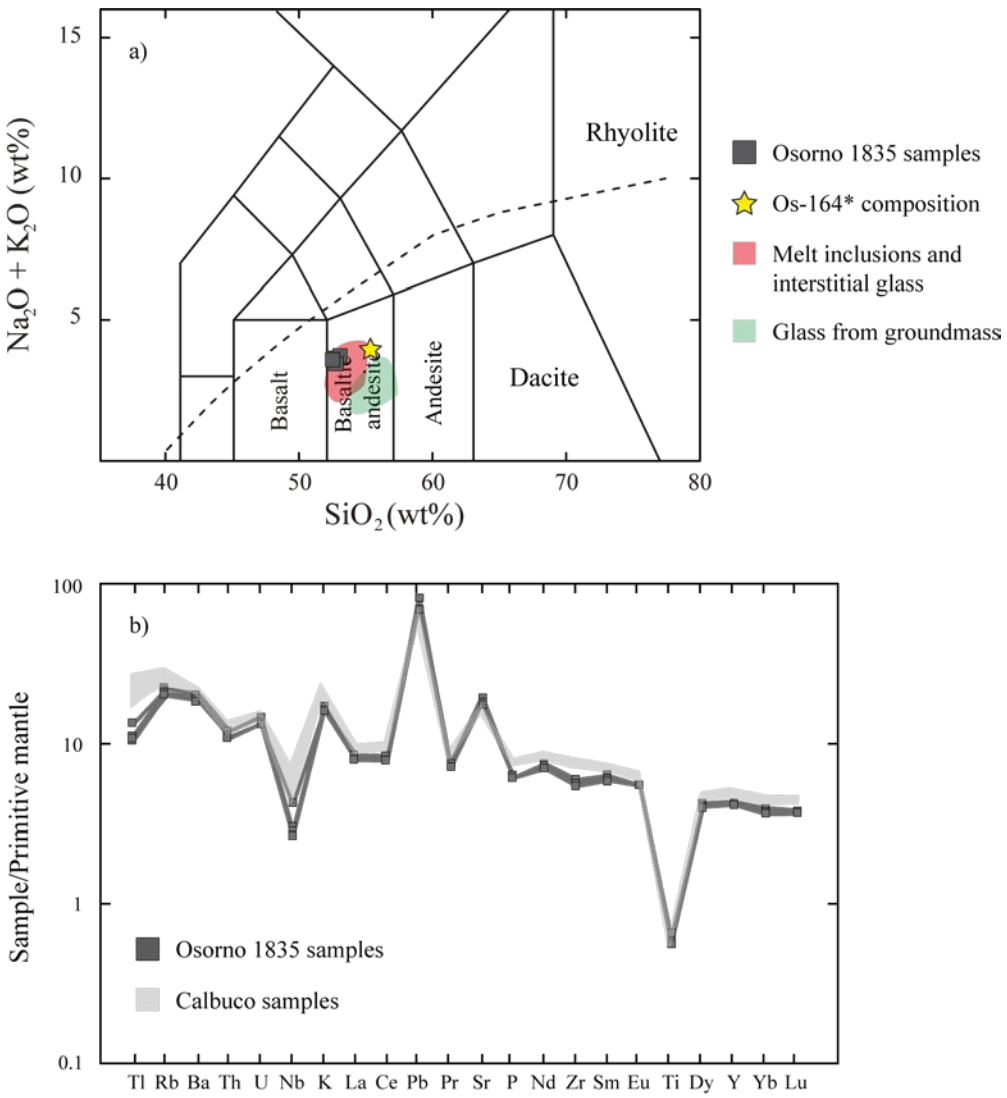

Figure 4.4. *a) Total alkali versus silica (Le Bas et al., 1986) plots of the Osorno 1835 volcanic products (grey squares), the modified composition of Os-144 (Os-144*, yellow star), melt inclusions (Group 1 of glass, red field), and glass from groundmass (Group 2 glass, green field). b) Primitive mantle-normalised (Sun and McDonough, 1989) spider diagram, the trace element contents from Calbuco products are taken from López-Escobar et al. (1995b) Morgado et al. (2019). Details of major and trace element concentrations of Osorno are available in Table 4.4.*

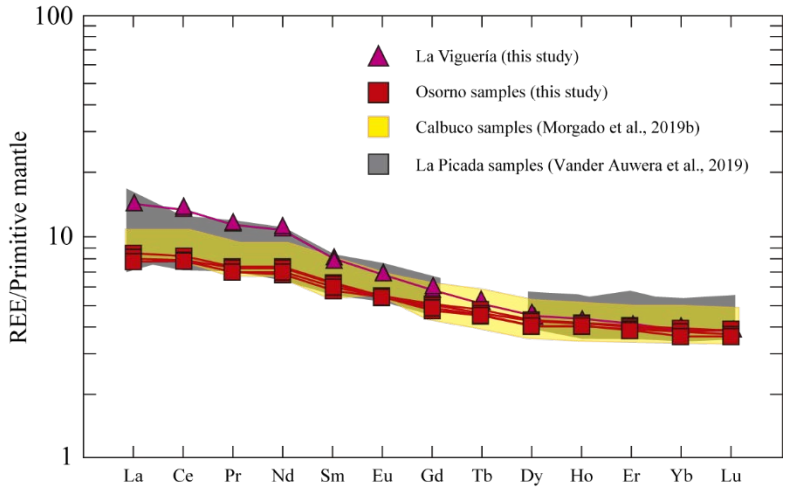

Figure 4.5. *REE patterns of samples from volcanic systems of the region (La Viguería, Osorno, Calbuco, and La Picada volcanoes).*

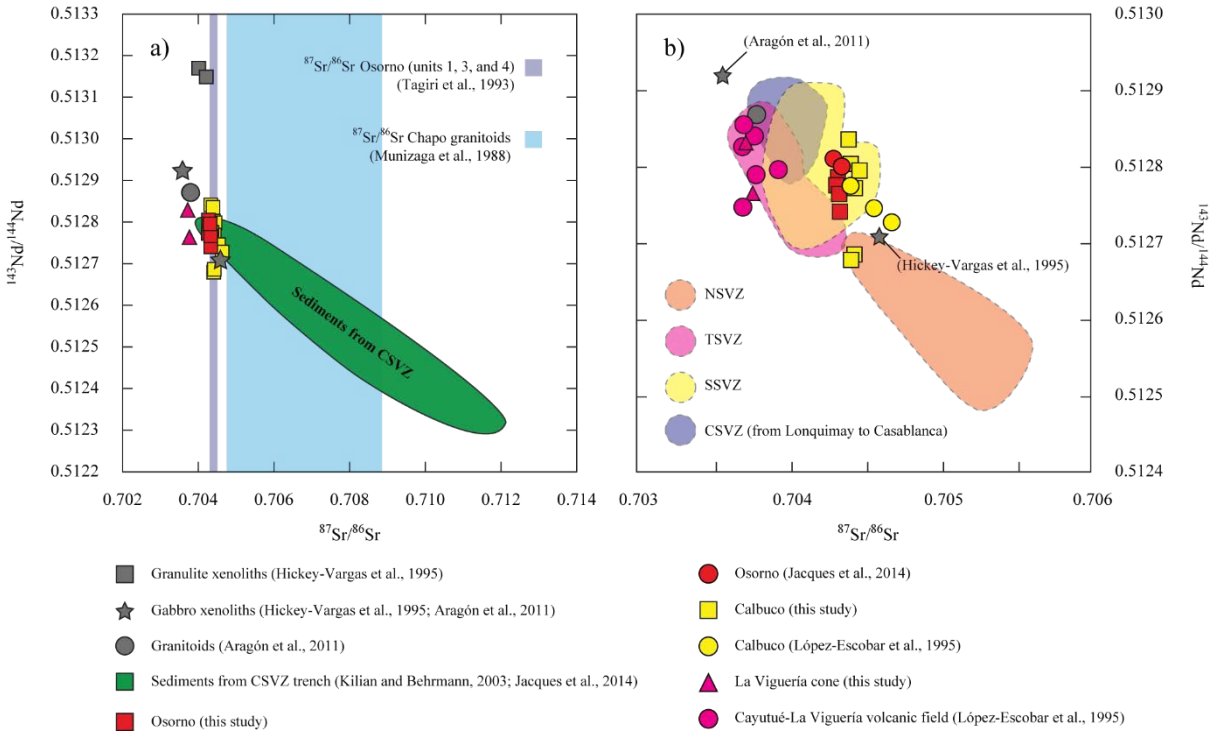

Figure 4.6. *$^{144}Nd/^{143}Nd$ versus $^{87}Sr/^{86}Sr$ of products of Osorno, Calbuco, sediments from the CSVZ trench, granulite xenoliths, gabbro xenoliths and from the basement, and granitoids from basement. a) $^{144}Nd/^{143}Nd$ versus $^{87}Sr/^{86}Sr$ plot of the samples from the studied region b) $^{144}Nd/^{143}Nd$ versus $^{87}Sr/^{86}Sr$ compared to other volcanic zones from the SVZ (from Hickey-Vargas et al., 2016 and references therein).*

4.5.2. Mineral chemistry

Plagioclase. Plagioclase phenocrysts are 0.2–2.0 mm in size, some of them exhibit euhedral textures and others show disequilibrium features: sieve, patchy zoning and partial resorption textures (Fig. 4.7). Plagioclase crystals are found as isolated crystals and also as inclusions in olivine and clinopyroxene and crystal clots, together with olivine and clinopyroxene. Regardless the crystal features, three different compositional zones are recognised in all plagioclase phenocrysts: Zone 1 corresponds to cores of phenocrysts and its composition is An_{80-89}, Zone 2 corresponds to plagioclase surrounding Zone 1 and core composition (the latter when Zone 1 is absent) in the compositional range of An_{70-79}, and Zone 3 corresponds to plagioclase rims, mainly observed in plagioclase phenocrysts from lava samples and its composition is An_{60-66} (Fig. 4.7). Plagioclase microphenocrysts (up to 200 µm in size) exhibit a composition equivalent to Zone 3 of plagioclase phenocrysts and display no zoning patterns. The plagioclase microlites (< 90 µm in size) show trachytic (flow) texture and their compositions correspond to An_{52-59}.

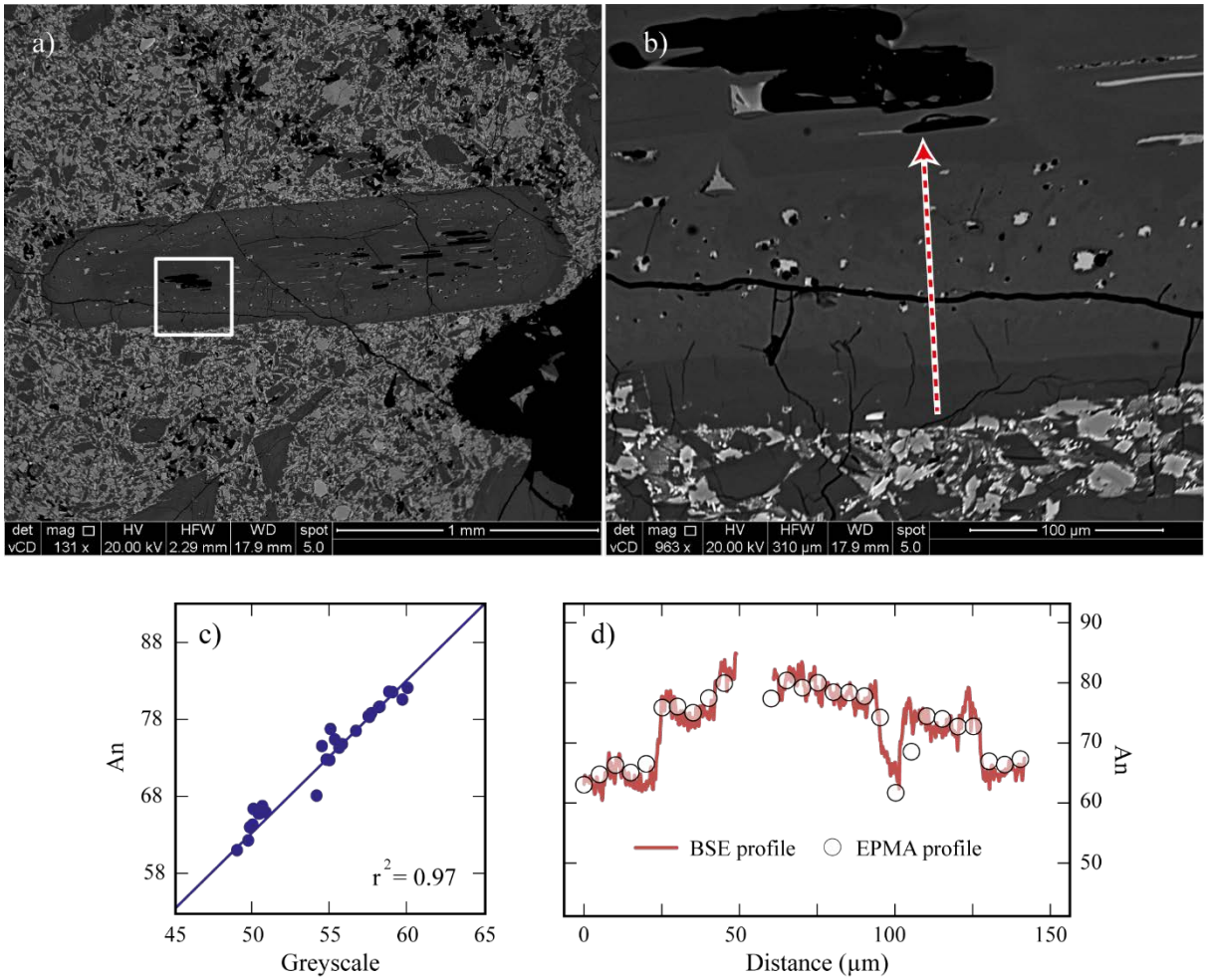

Figure 4.7. *a) Backscatter electron (BSE) images of an isolated plagioclase phenocryst where different compositional zones are found. Brighter greyscale colours are correlated to higher density. b) The arrow represents the profile measured by electron microprobe (EPMA) and its direction. c) Relation and coefficient of determination (r^2) between BSE profile and the measured anorthite content (An). "An"* is representing the composition of plagioclase because in all crystals the K content is fairly constant (details in Supplementary Material). *d) Anorthite profile composition (An = 100×Ca/(Ca+Na+K); elements in mols) by EPMA of the measured profile (circles) coupled with the backscattered electron (BSE) profile based on greyscale values calibrated with the composition measured by electron microprobe (solid line).*

Several plagioclase phenocrysts exhibit resorption textures in both the core and intermediate zones of plagioclase phenocrysts, where the compositions are equivalent to Zone 1 and Zone 2. Additionally, the composition observed in plagioclase phenocryst rims and that filling the spaces created because of resorption are the same and correspond to Zone 3 (Fig. 4.7).

Olivine. Olivine phenocrysts are 0.2–0.7 mm in size and are present as both isolated crystals and clots of crystals (together with plagioclase, and clinopyroxene). Some clots of olivine crystals possess interstitial glass of different composition from that surrounding olivine crystal clots (Fig. 4.8). Most crystals are euhedral to subhedral, but we observe embayments in some crystals. There are two groups of olivine phenocrysts regarding core compositions: Group 1 corresponds to crystals in the compositional range of Fo_{76-79}, Group 2 are crystals in the compositional range of $Fo_{69–72}$. All the olivine phenocrysts have normal zoning consisting of thin rims (< 15 µm) of composition Fo_{67-75}. EBSD maps (cf. Prior et al., 1999) show no deformation in olivine phenocrysts (Fig. 4.9). Olivine microphenocrysts (up to 70 µm in size) exhibit the same compositions as Group 1 and Group 2 of olivine phenocrysts (including ~3 µm length normal zonation rims). The olivine microlites (~10 µm in size) have a composition of $Fo_{52–60}$. Plagioclase and Cr-spinel inclusions are present in several olivine phenocrysts.

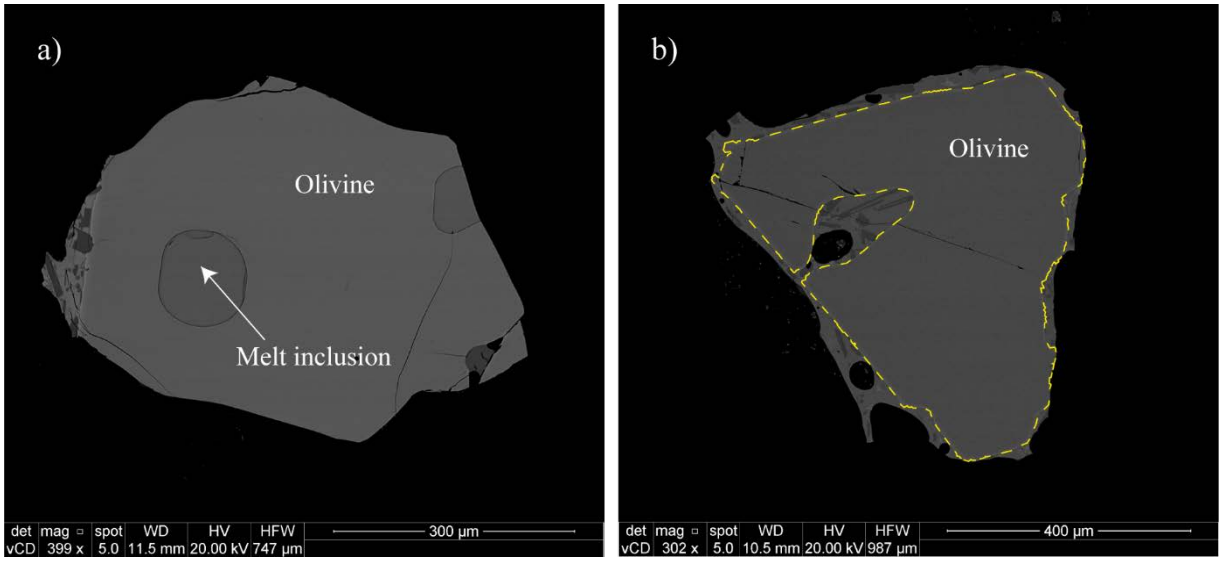

Figure 4.8. *a) Olivine-hosted melt inclusion of ~110 µm diameter, b) resorption feature (embayment) in olivine phenocryst.*

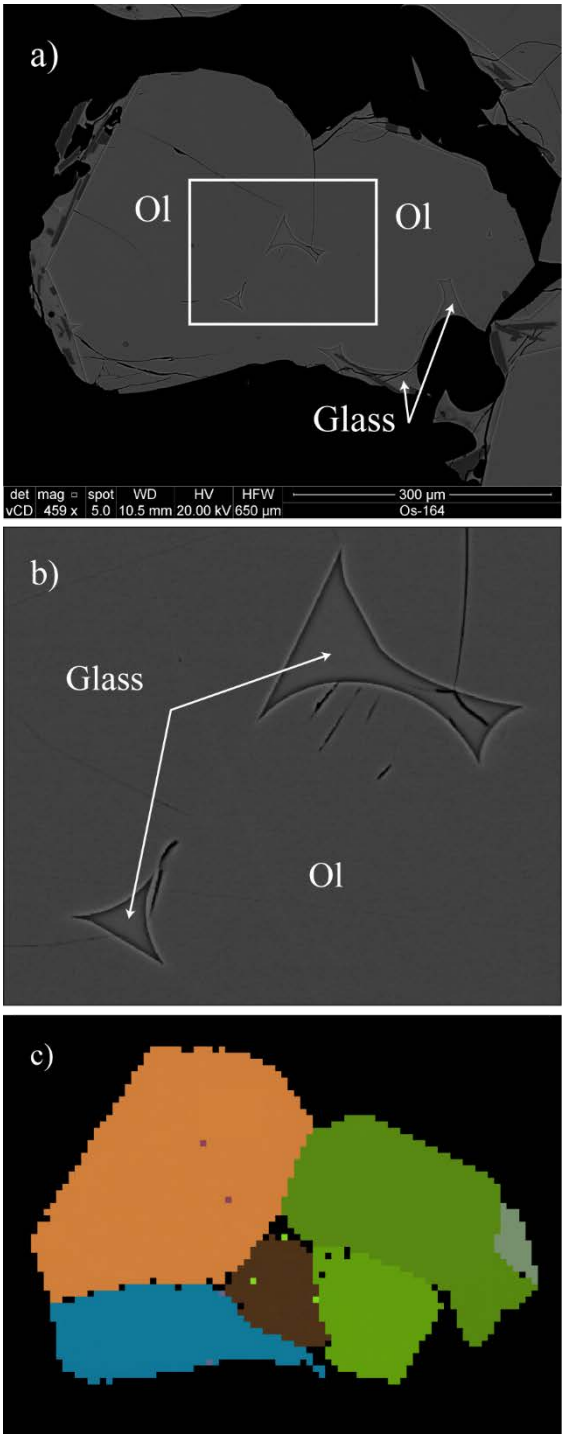

Figure 4.9. *a) Backscatter electron (BSE) image of a crystal clot of olivines. b) Zoom of the BSE image, which shows interstitial glass between the crystals constituting the clot. c) Electron backscatter diffraction (EBSD) map represents the diversity of olivine crystal orientations, which reinforces that the glasses are interstitial and are not melt inclusions.*

Pyroxene. Clinopyroxene phenocrysts correspond to isolated crystals (150–400 µm in size), inclusions (30–150 µm in size) in olivine and members of crystal clots (150–200 µm in size; together with olivine and plagioclase). The clinopyroxene compositional range corresponds to augite: $En_{43-51}Wo_{33-43}Fs_{10-18}$.

Cr-Spinel. Spinel crystals are found as octahedral crystals typically preserved as inclusions in olivine phenocrysts (12–44 µm length) and rarely (< 5% of the Cr-spinel crystals) as isolated crystals (10–35 µm length). The Mg# (Mg#= $Mg/(Fe^{2+}+Mg)$, in mols) and Cr# ($Cr\#=Cr/(Fe^{3+}+Al+Cr)$) values yield a narrow ranges: from 32 to 36 and from 36 to 44, respectively. Low measured contents of SiO_2 (< 0.2 wt%) reflects that secondary fluorescence of the silicate host phases is not a significant problem and that all the measured spinel contents are reliable.

Glass. Glasses are found in groundmass, interstitial between crystals of crystal clots, and as olivine- and plagioclase-hosted melt inclusions. Olivine-hosted melt inclusions are generally circular-shape with radii from 15 to 150 µm, whereas plagioclase-hosted melt inclusions have elliptical outlines with lengths from 40 to 160 µm and widths from 20 to 50 µm. Two different groups are recognised in glasses: Group 1 corresponds to glass from groundmass, with SiO_2 contents of 53.9–57.1 wt%. Group 2 corresponds to glass from interstitial glasses, and plagioclase- and olivine-hosted melt inclusions, which exhibit SiO_2 contents of 51.9–54.7 wt% (see Table 4.6, details in Supplementary Material).

Table 4.6. Representative values (wt%) of the interstitial melt, glass, and olivine- and plagioclase-hosted melt inclusions, measured by EPMA.

Sample Os-164	f_F4_1a	f_F4_1b	F1_1b	F1_1c	F17_1b	F17_1a	F12_2_1	F20_1_6	F10_g1	F1_g2	F13_g1a
Melt	Interstitial clots MI	Interstitial clots MI	Interstitial clots MI	Interstitial olivine MI	Plagioclase-hosted	Plagioclase-hosted	Olivine-hosted	Olivine-hosted	Glass	Glass	Glass
SiO_2	52.3	52.4	53.9	54.3	53.3	54.1	53.2	53.1	54.5	55.7	56.3
TiO_2	1.0	1.0	1.2	1.2	1.1	1.0	1.0	1.1	1.1	1.3	1.5
Al_2O_3	16.6	16.5	16.0	15.8	14.9	15.3	16.7	16.9	15.8	15.8	13.8
Cr_2O_3	0.0	0.0	0.0	0.0	0.0	0.0	0.0	0.0	0.0	0.0	0.0
FeOtot	9.5	9.4	10.4	10.6	9.8	10.0	9.2	9.7	9.3	10.2	11.1
MnO	0.2	0.1	0.2	0.2	0.2	0.1	0.2	0.2	0.2	0.2	0.2
MgO	5.0	5.0	4.2	4.1	5.7	5.9	4.8	4.5	5.6	4.2	4.0
CaO	8.9	8.7	9.0	8.8	8.2	8.3	8.5	9.2	8.2	8.7	7.9
Na_2O	2.9	2.8	3.5	3.3	3.6	3.9	3.6	3.2	3.2	3.2	3.4
K_2O	0.5	0.5	0.7	0.7	0.6	0.5	0.6	0.7	0.6	0.6	0.9
P_2O_5	0.1	0.1	0.2	0.2	0.1	0.2	0.2	0.2	0.2	0.2	0.2
SO_3	0.1	0.2	0.1	0.1	0.2	0.2	0.2	0.1	0.2	0.0	0.2
TOTAL	97.2	96.8	99.4	99.3	97.7	99.5	98.1	99.3	98.7	100.3	99.4

MI: melt inclusions

4.6. Magmatic intensive conditions

To perform numerical modelling based on melt composition, we choose the anhydrous groundmass composition of sample Os-144 (Table 4.6) because it is collected from the lower level of the second (it appears to be any difference whatsoever between first and second phases) eruptive phase lava flow (see Fig 4.3), which has had minor interaction with the atmosphere and would show oxygen fugacity conditions similar to those pre-eruptive (cf. Mollo et al., 2013). In addition, this sample possesses representative whole-rock chemistry, typical mineral assemblages and displays textural features observed in all products (see Table 4.3). The fall deposits corresponding to the second eruptive phase (Os-164) are ruled out because they are more prone to be rapid oxidation during the eruption than those from lava flows (cf. Mollo et al., 2013). The melt composition is calculated considering the Os-144 sample whole-rock composition (Table 4.4) via extraction of the modal composition of representative mineral phases (Table 4.3). From now on that composition is named as Os-144*, which is similar to several Osorno aphyric products from Unit 3 reported by Tagiri et al. (1993) and Group 2 of measured glasses. In addition, oxygen fugacity modelling is performed in olivine hosted melt inclusions from Group 2 of measured glasses (see section *Cr-spinel-melt oxybarometry).*

4.6.1. Thermodynamic equilibrium

The equilibrium conditions between olivine, clinopyroxene, and orthopyroxene are tested using Grove et al. (1997) equations to determine mineral-melt equilibrium. If the considered phases are in equilibrium with the same hypothetical melt composition in terms of K_D^{Fe-Mg} ($K_D^{Fe-Mg} = \left[X_{Fe}^{Mineral\ phase} \times X_{Mg}^{Melt}\right] / \left[X_{Mg}^{Mineral\ phase} \times X_{Fe}^{Melt}\right]$), then the system as a whole which is composed of those phases, can be considered in equilibrium too (details in Supplementary Material).

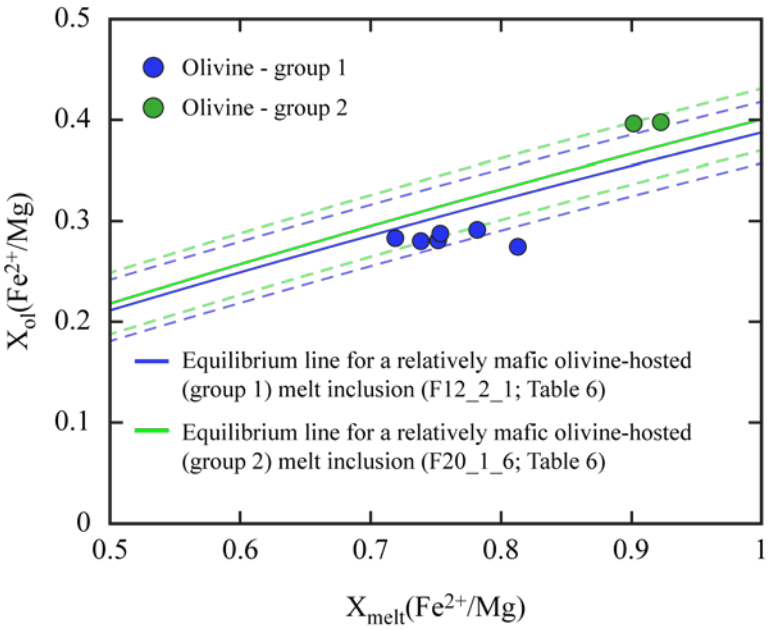

Figure 4.10. *Olivine core compositions ($X_{ol}(Fe^{2+}/Mg)$ vs $X_{melt}(Fe^{2+}/Mg)$) for products of the 1835 Osorno eruption. Most of the olivine compositions from group 1 (Fo_{76-79}) are in equilibrium with the related melt inclusions, whereas the two compositions from group 2 (Fo_{69-72}) are in equilibrium with the related melt inclusions. The Fe^{2+} in the melt is calculated using the olivine-hosted spinel inclusions Fe^{2+}/Fe^{3+}. We calculate the equilibrium lines as $X_{ol}(Fe^{2+}/Mg) = K_D \times X_{melt}(Fe^{2+}/Mg)$, where K_D is calculated via the Toplis (2005) procedure.*

4.6.2. Olivine-melt equilibrium.

The equilibrium conditions between melt inclusions and the olivine-host (Fig. 4.10) are tested using the Toplis (2005) equation for K_D^{Fe-Mg}, considering Fe^{2+} and Fe^{3+} values in melt following the methods of Maurel and Maurel (1982). We only consider glassy melt inclusions in olivine to ensure their compositions lie on the liquid line of descent (Kent, 2008). Although inclusions with visible daughter and/or co-trapped minerals exist, they are discarded from our analysis to get reliable host melt contents (Sinton et al., 1993; Danyushevsky et al., 2002a; Kent, 2008). We also discarded melt inclusions linked to the exterior of the host mineral. All the melt inclusions exhibit very thin (< 1 µm) crystallisation rims of the host mineral. The host mineral (in this case, olivine) crystallises in melt inclusions from the mineral boundary, which has lower nucleation energy (cf. Roedder, 1979).

According to Kent (2008), this growth on the inclusion wall may be apparent in compositional profiles and also backscatter images. Following that method we recognise a very thin (< 1 μm) growth. This growth is related to changes of element contents of the melt inclusion, forcing diffusive re-equilibration within it (Danyushevksy et al., 2000; 2002a). Danyushevsky et al. (2000) reported different degrees of melt inclusion re-equilibration in a single sample with the same Fo content. Larger melt inclusion diameters are associated with longer re-equilibration timescales (Danyushevsky et al. 2000; 2002b). To study pre-eruptive conditions via melt inclusions, we examine the core compositions of the largest melt inclusions (diameter > 50 μm), which we interpret would represent pre-eruptive composition before re-equilibration (cf. Danyushevsky et al., 2002b).

We can be confident that the compositional profiles of olivine-hosted melt inclusions represent diffusion and are not affected by convolution effects because the host olivine phenocrysts have higher MgO wt% contents than the melt inclusions, thus if secondary fluorescence is affecting the measurements, then the compositional profiles within melt inclusions would show an apparent increase in MgO wt% towards the rims, however we recognise a decrease in MgO content. In small melt inclusions (diameter < 50 μm) the compositional profiles do not show MgO wt% depletion rimwards we observe in big melt inclusions (diameter > 50 μm). This suggest the profiles measured represents diffusion effects, then they can be used to calculate timescales of re-equilibration (Fig. 4.11).

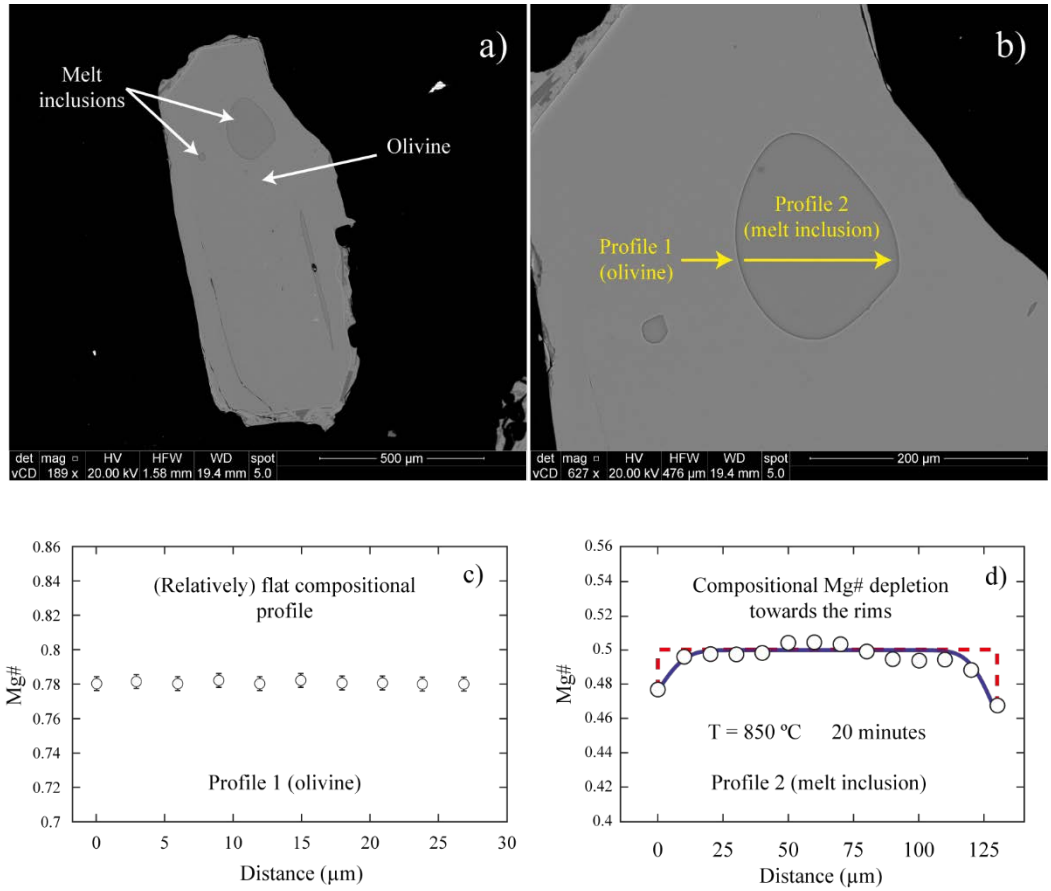

Figure 4.11. *a) BSE image of an olivine phenocryst and melt inclusions. b) Zoom of the BSE image, which shows the EPMA profiles in olivine and large melt inclusion. c) Mg# (Mg#= molar Mg/(Mg+Fe^{2+})) composition of olivine phenocryst, which are flat (not showing disequilibrium), d) Mg# composition profiles of the melt inclusion, which show depletion towards the rim. That depletion represents diffusion and the related timescales are few minutes.*

4.6.3. Physical intensive variables

The error propagation of the calculation of all the intensive conditions (temperature, pressure, oxygen fugacity, and water dissolved) are carried out considering both internal (uncertainties associated with the experimental method) and external (uncertainties associated with precision and accuracy of electron microprobe analyses) errors.

Olivine-augite thermometry. We use the olivine-augite Fe-Mg exchange geothermometer of Loucks (1996) in the cores of olivine-augite largely-equilibrated pairs, which give temperatures from 1,121 to 1,168 ± 15 ºC, with an average of 1,139 ºC (σ = 15 ºC). We

determine the thermodynamic equilibrium state between olivine and augite via the method above (see section *Thermodynamic equilibrium*).

Ca-in olivine thermometry. We use the Ca-in-olivine thermometer of Shejwalkar and Coogan (2013) in olivine cores (Fo_{70-76}), which give temperatures from 1,121 to 1,173 ± 22 ºC, with an average of 1,144 ºC (σ = 23 ºC). We assume contemporary growth in clots of olivine together with (ortho- or clino-) pyroxene and plagioclase.

Pressure and water content modelling. We calculate the solubility of water in silicate melt and pressure conditions considering a melt composition and assuming water saturation (based on high temperature and low pressure magma conditions) via the iterative combination of the expressions of Moore et al. (1998, equation 4.1) and Putirka (2005, 2008; equation 4.2):

$$2ln^{melt}X_{H_2O} = \frac{a'}{T} + \sum b'_i X_i \cdot \left(\frac{P}{T}\right) + c' \cdot log^{fluid}\left(f_{H_2O}\right) + d' \qquad equation\ 4.1$$

$$H_2O(wt\%) = 24.757 - 2.26 \cdot 10^{-3} \cdot T \cdot \log\left(\frac{An^{pl}}{Ca^{liq}(Al^{liq})^2(Si^{liq})^2}\right) - 3.847 \cdot (An^{pl}) + 1.927\left(\frac{An^{pl}\left(Ca^{liq} + Na^{liq}\right)}{Ca^{liq}}\right) \qquad equation\ 4.2$$

where $^{melt}X_{H_2O}$ is the mole fraction of water dissolved in the melt, T is temperature (Kelvin), P is pressure (bar), X_i is the anhydrous mole fraction of melt components, x is a variable state dependent on several factors (enthalpy, entropy, volume, pressure, temperature, melt, and crystallising plagioclase), cation fractions (An^{pl}, Ca^{liq}, Al^{liq}, Si^{liq}, and Na^{liq}) and a', b', c', and d' are regression coefficients.

We consider a melt composition equivalent to Oso-144*. In addition, the values of temperature (1,120 ºC = 1,393 K) and anorthite (An_{66}) are chosen to maximise the ranges of pressure and water content. The obtained results are pressure up to 1.2 kbar and water content

in magmatic melt up to 1.5 wt% (Fig. 4.12a). These results are similar to those obtained via the plagioclase-hygrometer of Lange et al. (2009) (up to 2.2 wt%) and the method of Kelley and Cottrell (2009) (~1 wt%).

Oxygen fugacity modelling. We also calculate pre-eruptive oxygen fugacity and pressure conditions of Osorno samples using iteratively the expression of Kress and Carmichael (1991) following the equation:

$$log\left(\frac{XFe_2O_3}{XFeO}\right) = a \cdot log(f_{O_2}) + \frac{b}{T} + c + \sum d_i \cdot X_i + e\left[1 - \left(\frac{T_0}{T}\right) - log\left(\frac{T}{T_0}\right)\right] + f\left(\frac{P}{T}\right) + g\frac{(T-T_0)P}{T} + h\left(\frac{P^2}{T}\right) \qquad equation\ 4.3$$

where XFe_2O_3 and XFeO are the molar fraction of Fe_2O_3 and FeO, T is temperature (1,393 K), T_0 is a fixed temperature value (1673 K), P is pressure (pascals), X_i is the anhydrous mole fraction of melt components, and a, b, c, d_i, e, *f*, g, and h are regression coefficients (details in Supplementary Material).

We use the temperature as 1,393 K and a range of pressure from 1 bar to 1.2 kbar (equivalent to 10^5 and 1.2×10^8 Pa, respectively). The calculations give an oxygen fugacity patch from -0.1 to 0 ΔNNO (ΔQFM +0.6 to +0.7) (Fig. 4.12b). The oxygen fugacity buffer results we obtain considering Os-144* composition are the lowest compared to those obtained considering other compositions of groundmass. Similar values of oxygen fugacity patch are calculated with temperature up to 1,433 K (equivalent to 1,160 ºC).

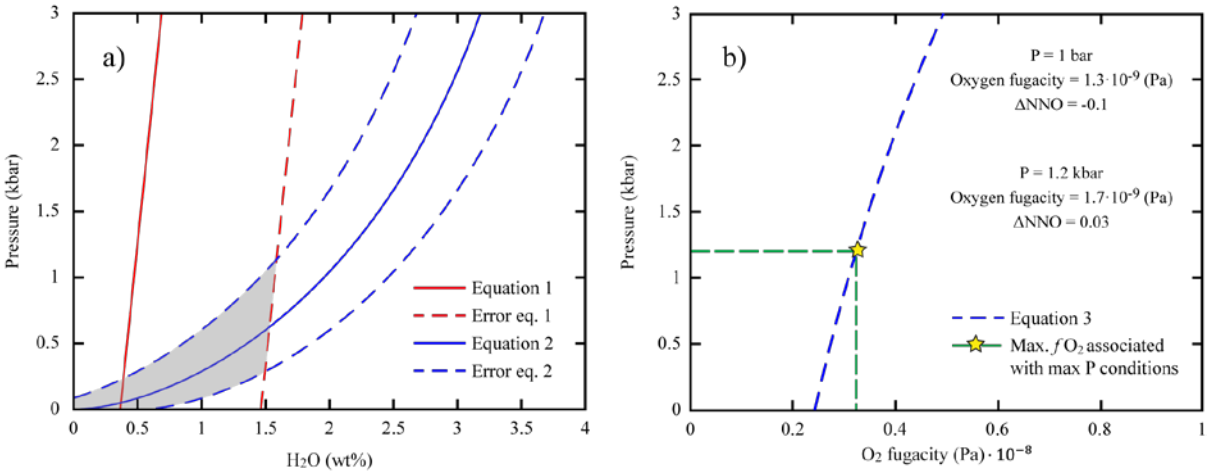

Figure 4.12. *Iterative numerical solution of: a) equations 4.1 (Putirka et al., 2005) and 4.2 (Moore et al., 1998), which gives a maximum pressure of 1.2 kbar and up to 1.6 wt.% of dissolved H_2O (the grey field corresponds to the intersection of equations 4.1 and 4.2, which represents pressure and dissolved water wt.% content); and b) equation 4.3 (Kress and Carmichael, 1991) calculations considering the whole pressure ranges calculated in a) (from 0 to 1.2 kbar).*

Cr-spinel-melt oxybarometry. The olivine-Cr-spinel coexistence in equilibrium is determined following the procedure of Kamenetsky et al. (2001) (details in Supplementary Material) and the melt inclusion-olivine host equilibrium is determined as explained in section 4.6.1. When the olivine host phenocryst is in equilibrium with both the hosted melt inclusion (details in section 4.6.1) and the hosted Cr-spinel inclusion, we use the Maurel and Maurel (1982) method to determine Fe^{2+}/Fe^{3+} ratio of olivine-hosted melt inclusions considering the Fe^{2+}/Fe^{3+} of olivine-hosted Cr-spinel composition (see section 4.4.2), which we assume equilibrated by transitivity. Finally, we apply the Borisov and Shapkin (1990) method to calculate oxygen fugacity values recorded in olivine-hosted melt inclusions. The calculations yield an oxygen fugacity patch range of ΔQFM +0.3 (± 0.55), considering temperature of 1,140 ºC (± 20 ºC), the Fe^{2+}/Fe^{3+} ratio of olivine-hosted Cr-spinel inclusions, and uncertainties in both EPMA measurements and the method of Borisov and Shapkin (1990).

4.6.4. MELTS modelling

The initial melt composition used in MELTS (Ghiorso and Sack, 1995) modelling corresponds to Os-144* (see *Intensive conditions* section). Our objective is to reproduce compositions of phenocryst phases which would represent the final stage of evolution of the system before the eruption, represented by rims of phenocrysts as well as microphenocrysts: olivine (Fo_{71-78}), clinopyroxene ($En_{43-52}Fs_{10-18}Wo_{33-43}$), and plagioclase ($An_{60-66}$). We perform modellings following magmatic intensive physical conditions in ranges consistent with the temperature (1,000–1,200 ºC), pressure (0.1–5.0 kbar), oxygen fugacity (ΔNNO buffer patch) and dissolved water content (0–3 wt% H_2O) obtained previously. We consider only the modelling results related to ≤ 20 wt% of solid phases, which would represent crystallisation in equilibrium with a melt of similar composition to the groundmass (which, in turn, represents the melt composition before the microlites crystallisation).

We reproduce in MELTS the assemblage of olivine, clinopyroxene and plagioclase phenocryst and microphenocryst compositions at a temperature range of 1,060–1,130 ºC, pressure range of 0.5–2.5 kbar, oxygen fugacity range of ΔQFM ± 1, and dissolved water content of 0.5–3 wt% (Fig. 4.13). Similar results are modelled with whole-rock compositions (Os-144, Os-147, Os-154, and Os-164), melt inclusions, and interstitial glass. Details of the MELTS modelling results are available as Supplementary Material.

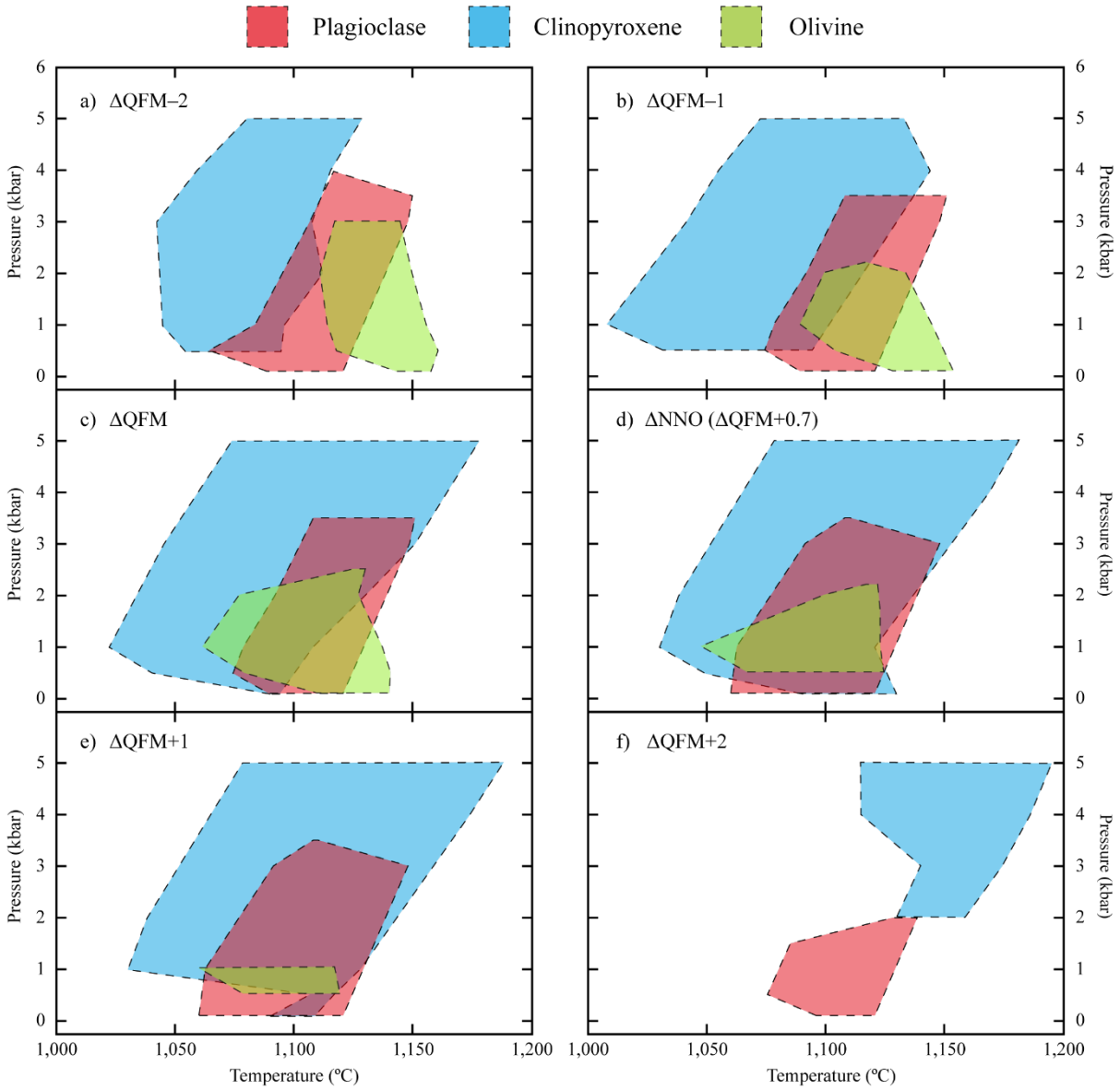

Figure 4.13. *Stability fields (obtained via MELTS modelling) of the three most abundant magmatic phases in Osorno samples: plagioclase (An_{61-66}; red), clinopyroxene (EnWoFs; blue), and olivine (Fo_{70-72} and Fo_{76-78}; green) at different oxygen fugacities patches: ΔQFM-2 (a), ΔQFM-1 (b), ΔQFM (c), ΔNNO (d), ΔQFM+1 (e), ΔQFM+2 (f). The water content dissolved in the melt varies from 0.5 to 3 wt%.*

4.7. Discussion

4.7.1. Shallow reservoir

The pressure conditions calculated iteratively (Eqs. 1 and 2) indicate a maximum pressure of 1.2 kbar (equivalent to a 4.5 km depth), which corresponds to the presence of a magmatic shallow reservoir, where the magma stalled just before the 1835 Osorno eruption. These results are consistent with the reproduced overlapped PT diagram (the intersection of the crystallisation conditions of plagioclase, clinopyroxene, and olivine) obtained via MELTS modelling (see Figure 4.14). According to that diagrams, the range of pressure conditions is 0.5–2.5 kbar (equivalent to 1.8-9.1 km depth). In addition, SERNAGEOMIN–OVDAS (2017; 2018a, b; 2019) reported recent volcano-tectonic seismic activity, in which the associated sources correspond to 2.6–3.9 km depth. In conclusion, all approaches to estimate magmatic pressure conditions point out the existence of a magmatic reservoir in the upper crust, which seems a common feature in the plumbing systems of the SVZ of the Chilean Andes (e.g., Calbuco volcano, Delgado et al., 2017; Nikkhoo et al., 2017; Morgado et al., 2019b; Llaima volcano, Bouvet de Maisonneuve et al., 2012; Villarrica volcano, Lohmar et al., 2012, Morgado et al., 2015; Quetrupillán, Brahm et al., 2018).

4.7.2. Crystal-mush within the magma reservoir and crystallisation events

We infer the existence of a crystal mush in the magmatic reservoir based on the textural features considered as evidences of crystal mushes: glomerocrysts, interstitial glass between grains of crystal clots with different composition from the outer glass (Fig. 4.9, Table 4.6), disequilibrium (zoning and resorption) textures in isolated crystals as well as crystals from clots, and high crystallinity (25–45 vol%, Table 4.3). The zoning patterns of plagioclase suggest a complex crystallisation history. According to MELTS modelling, we cannot reproduce Zone 1 (An_{80-89}) and Zone 2 (An_{70-79}) plagioclase compositions, in consequence,

we infer the first crystallisation events (when plagioclase core and intermediate zones grew), are either related to a melt composition different from Os-144*, likely during the upper-crustal crystal-mush formation process, or associated with a deep-crustal crystallisation. The resorption observed in several plagioclase phenocrysts, affecting plagioclase Zone 1 and Zone 2 compositions, suggests the occurrence of plagioclase destabilisation after the first crystallisation events. We interpret this destabilisation is related to the process which causes mush disaggregation. Several authors have given different interpretations to disequilibrium (resorption and sieve) textures in plagioclase such as fluid-absent rapid decompression (Nelson and Montana, 1992; Annen et al., 2006) or magma mixing usually related to heating (Johannes et al., 1994; Ginibre and Wörner, 2007; Pietranik et al., 2006). Additionally, the existence of patchy zoning with the same composition as plagioclase phenocryst rims and microphenocrysts, equivalent to Zone 3 composition, suggest a late pre-eruptive crystallisation episode, after mush disaggregation (Fig. 4.14). In addition, Tagiri et al. (1993) inferred that the porphyritic materials from Osorno volcano (similar to the volcanic products studied in the present article) resulted from the addition of calcic plagioclase (likely due to melting of ~ 20 wt% of XAn_{70-80}, similar to Zone 2 plagioclase compositions) to the aphyric materials (similar in composition to Os-144*). Embayments in some olivine phenocrysts and suggest a disequilibrium event (volatile input or heating event), which could be a consequence of the same process that caused resorption in plagioclase phenocrysts.

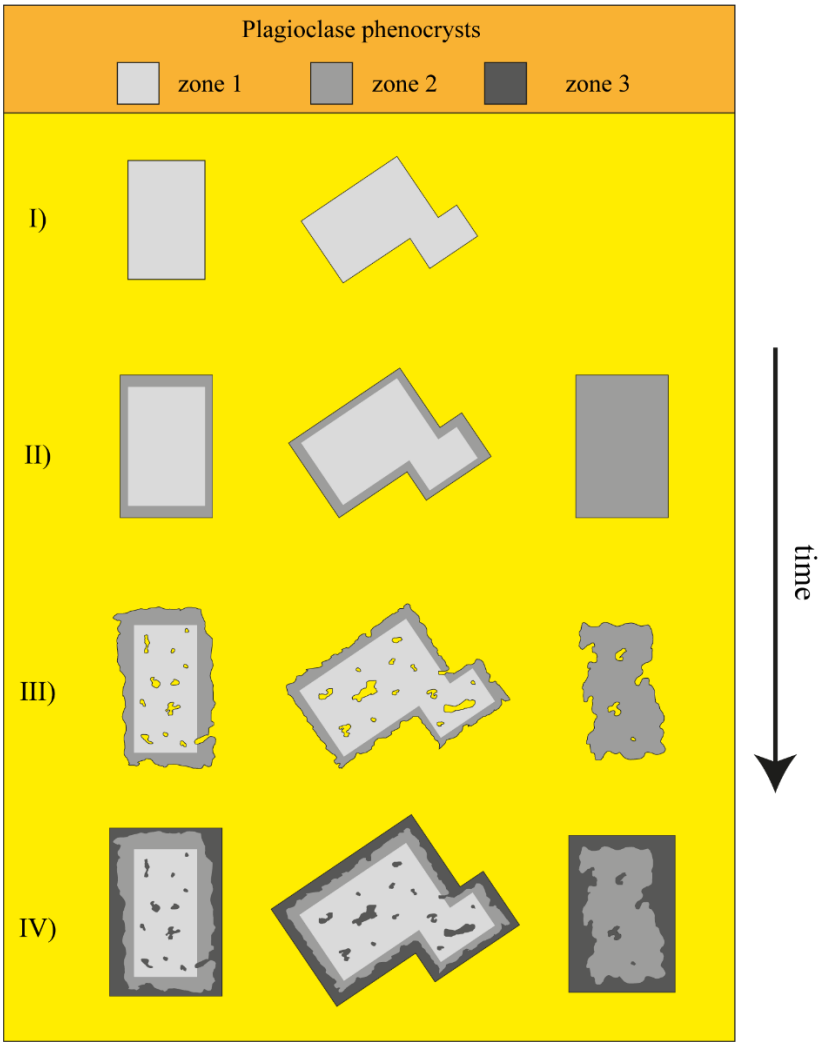

Figure 4.14. *Evolution of plagioclase zonings phenocrysts over time: first event (I) is nucleation and growth of plagioclase phenocryst cores (zone 1 composition); after that (II), growth plagioclase phenocryst rims and nucleation and growth of new plagioclase phenocrysts occurred (zone 2 composition). These two first crystallization events occurred during the crystal mush formation. After the crystal mush building, another process generating plagioclase-melt disequilibrium and resorption (we suggest volatile additions or heating) occurred (III), and finally (IV), a last growth event occurred. We infer that last growing event occurred before or during the eruption triggering.*

4.7.3. Crustal assimilation

Calbuco and Osorno, and La Picada products show higher fluid mobile/immobile (e.g. Ba/La vs Rb/Nd, Fig. 4.15) ratios than La Viguería (small eruptive centre) products. These higher fluid mobile/immobile ratios are associated with a higher slab-derived fluid component in Calbuco, Osorno and La Picada volcanic material than La Viguería products. Calbuco, Osorno, and La Viguería products also exhibit lower La/Yb ratios than La Viguería volcanic material, those lower La/Yb ratios are associated with the higher partial melting degree. The REE diagram comparing the Calbuco, Osorno, La Picada, and La Viguería sample compositions (Fig. 4.5), suggests all the volcanic systems have similar source processes (e.g. ruling out garnet as a residual phase in the mantle source).

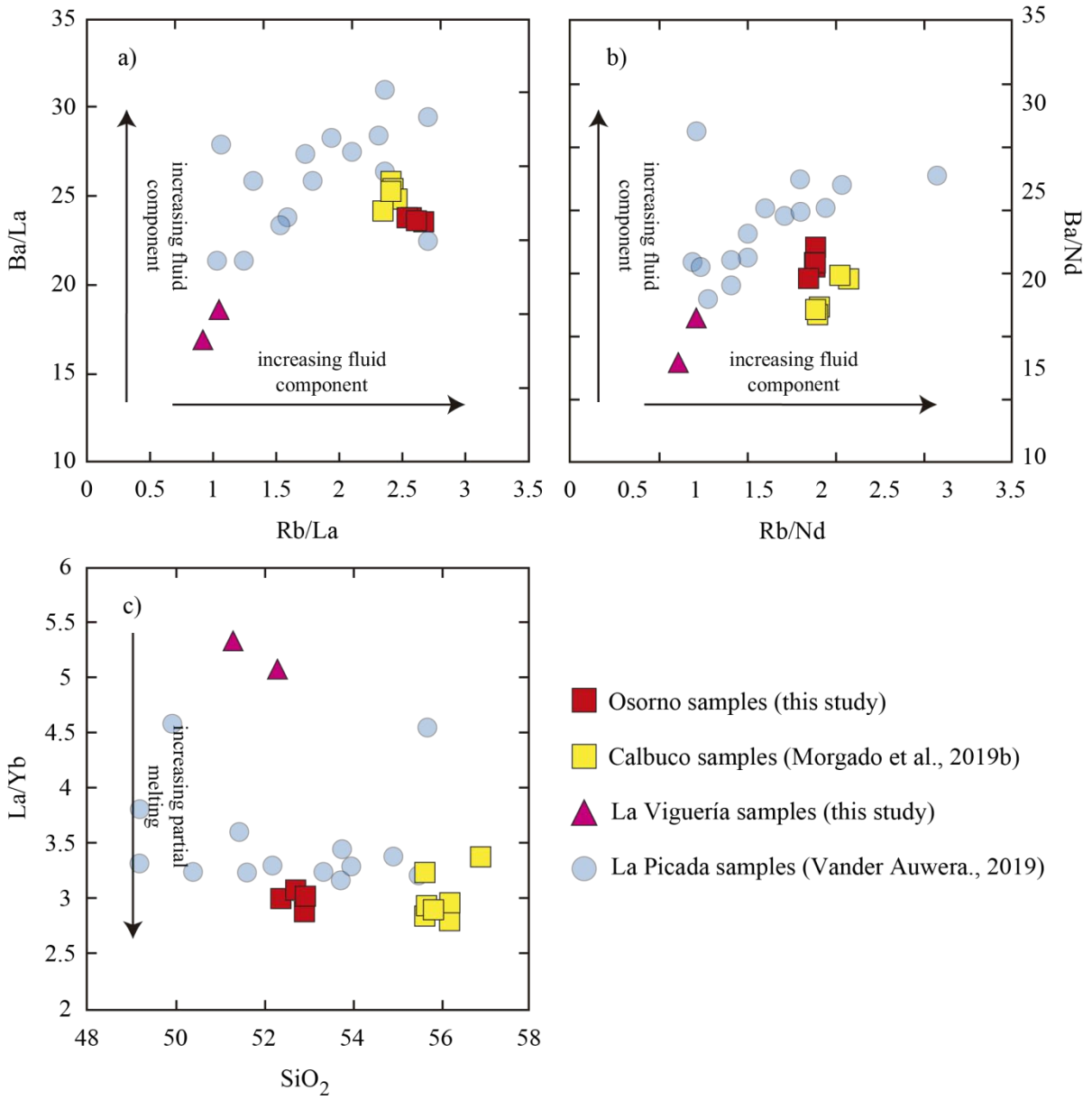

Figure 4.15. *a) Plots of fluid mobile/immobile elements of volcanic samples of the region: Ba/La vs. Rb/La,; b) plots of Ba/Nd vs. Rb/Nd. In a) and b) the arrows represent the direction in which the fluid component in the source is increasing c) La/Yb vs. SiO_2 (wt%) of volcanic samples of the region, the arrow represents the direction in which partial melting degree of the source is increasing.*

To model the Sr and Nd ratios from Calbuco and Osorno products, we use the compositions of several end-members representing rocks, which chemistry could influence the Calbuco and Osorno whole-rock chemistry: La Viguería small eruptive centres (LV, representing relatively low crustal interaction compared to Calbuco and Osorno stratovolcanoes), the highest $^{87}Sr/^{86}Sr$ sediments from the CSVZ trench (representing fluid input; Kilian and

Behrmann, 2003), altered oceanic crust (AOC, representing fluid input; Jacques et al., 2014), granulite (representing lower crust assimilation; Hickey-Vargas et al., 1995), granodiorite (representing upper crust assimilation; Aragón et al., 2011), and gabbro (Hickey-Vargas et al., 1995). Although Sr is a fluid-mobile element and their isotopic variations are related to fluid inputs from AOC and sediments, the Chapo Lake granitoid in the upper crust of the zone would also represent sedimentary contribution, due to their source containing pelitic rocks (Parada et al., 1987).

Fluid input: according to our modelling the only way to reproduce the fluid input is considering the coupled supply of the AOC and the sediments. Sediments solely representing the fluid supply would need unrealistic (over 50%) assimilation of crustal rocks (Fig. 4.16). Using LV composition as an end-member to reach the composition of Calbuco and Osorno products, the concentrations giving the best results are from 20% to 40% of sediments vs. from 60% to 80% of AOC supply. The best-fitting is around 70% of AOC and 30% of sediments, consistent with the modelling of Jacques et al. (2014) for the CSVZ. This modelling suggests the most important factors controlling the Sr-Nd isotopic ratios are mantle composition and fluid input. The results are consistent with the suggestion of minor crustal assimilation in volcanic systems of CSVZ (e.g., Gerlach et al. 1988; Hickey-Vargas et al., 1989; Jacques et al., 2014).

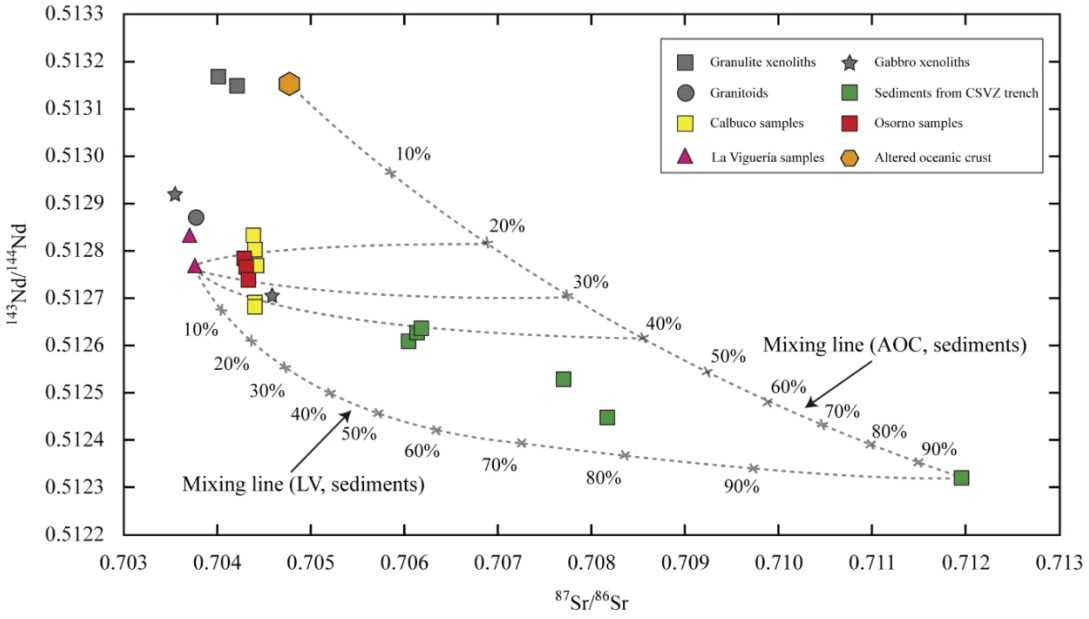

Figure 4.16. *a) $^{143}Nd/^{144}Nd$ versus $^{87}Sr/^{86}Sr$ of whole-rock compositions of the samples from the regional crustal rocks (granulite, gabbro, and granitoids; Hickey-Vargas et al., 1995; Aragón et al., 2011), Calbuco and Osorno stratovolcanoes, and La Viguería small eruptive centre and mixing lines showing possible fluid supplies. The mixing lines are built according to the isotopic values presented in the Table 4.5.*

Crustal assimilation: the presence of both granulite and gabbro xenoliths (Hickey-Vargas et al., 1995) in 1961 Calbuco products, indicate an interaction between those crustal rocks and the ascending magma. Following the mixing line described for fluid input (70% AOC, 30% sediments, LV as end-member), we simulate granodiorite, granulite, and gabbro assimilation to assess the $^{143}Nd/^{144}Nd$ trends observed in the Calbuco and Osorno products. According to granodiorite assimilation modelling, a ~25% of assimilation is necessary to simulate the trend of Calbuco products and ~10% to simulate the trend of Osorno products (Fig. 17a). The Nd isotope values of Calbuco samples only could be reached at ~30% of granulite assimilation and the Nd isotopes of Osorno products, at ~20% (Fig. 4.17b). By contrast, gabbroes (reported by Aragón et al., 2011 and Hickey-Vargas et al., 1995) assimilation solely could not explain Osorno nor Calbuco Nd isotopic ratio (Fig. 4.17c). The evolution of La Viguería products could be modelled at 40% of gabbro assimilation, which is very high, in consequence, is ruled out as explanation (Fig. 4.17c). Considering all the potential crustal

contamination sources, for Calbuco products the best-fit mixture is ~25% of granulite and ~5% of granodiorite and for Osorno products, the most plausible mixture is ~10% of granulite and ~5% of granodiorite assimilation.

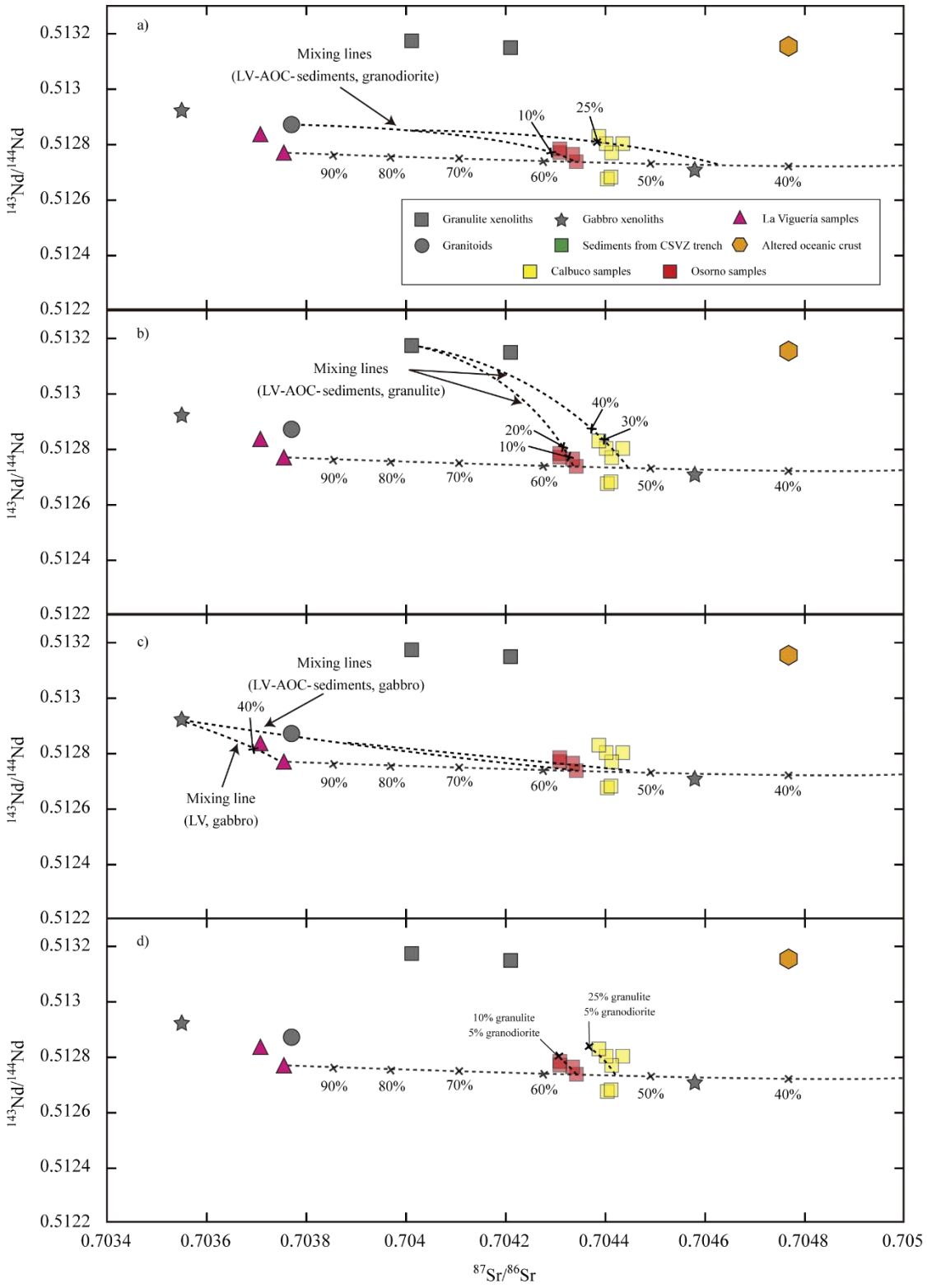
a)
Mixing lines
(LV-AOC-sediments, granodiorite)
10%
25%
90%
80%
70%
60%
50%
40%
Granulite xenoliths
Gabbro xenoliths
La Viguería samples
Granitoids
Sediments from CSVZ trench
Altered oceanic crust
Calbuco samples
Osorno samples
b)
Mixing lines
(LV-AOC-sediments, granulite)
40%
30%
20%
10%
c)
Mixing lines
(LV-AOC-sediments, gabbro)
40%
Mixing line
(LV, gabbro)
d)
10% granulite
5% granodiorite
25% granulite
5% granodiorite
0.5132
0.513
0.5128
0.5126
0.5124
0.5122
143Nd/144Nd
0.7034
0.7036
0.7038
0.704
0.7042
0.7044
0.7046
0.7048
0.705
87Sr/86Sr

Figure 4.17. *a) $^{143}Nd/^{144}Nd$ versus $^{87}Sr/^{86}Sr$ of whole-rock compositions of the samples from the regional crustal rocks (granulite, gabbro, and granitoids; Hickey-Vargas et al., 1995; Aragón et al., 2011), Calbuco and Osorno stratovolcanoes, and La Viguería small eruptive centre and mixing lines showing possible fluid supplies of several mixing lines showing possible crustal source of Nd isotopic ratio supplies (granodiorite, granulite and gabbro) according to the isotopic values presented in the Table 4.5; b) shows mixing lines for granodiorite assimilation; c) shows mixing lines for granulite assimilation; d) shows best mixing line fits considering all the potential assimilation sources.*

Partial melting and assimilation can be caused by decompression (Zeitler and Chamberlain, 1991; López-Escobar et al., 1995b), which was recognised by Barrientos et al. (1992) at the latitude of the studied volcanoes as a minimum post-seismic uplift of 75 cm. In addition, the calculated pre-eruptive temperatures for Osorno (~1,140 ºC) and Calbuco (~980 ºC; Morgado et al., 2019b; Arzilli et al., 2019) magmas are consistent with granitoid and granulite partial melting (e.g., Vielzeuf et al., 1990; Knesel and Davidson, 1996; Palin et al., 2016; Masotta et al., 2018). Moreover, the minimum residence times calculated for Calbuco magmas in the order of years (Morgado et al., 2019a) in the upper crust at relatively high temperature, would favour granodiorite assimilation during the ascent through continental crustal thickness at the CSVZ latitudes of 40-45 km thick (Tašárová, 2007; Dzierma et al., 2012). Finally, the volcanic material interpreted as xenoliths in 1835 Osorno products would not modify considerably the isotopic ratios of Sr even if they are assimilated because the volcanic units 1, 3 and 4 of Osorno exhibit the values similar to those we present in this study (Tagiri et al., 1993; Fig. 4.6).

Considering regional granulite, granodiorite, and gabbro compositions as potential assimilation sources, the isotopic trends of the 2015 Calbuco products and the 1835 Osorno products can be explained by granulite and granodiorite assimilation. Differences of $^{87}Sr/^{86}Sr$ between Calbuco and Osorno products might be related to mantle heterogeneity (as shown between products of volcanoes from the Caburgua-Huelemolle volcanic field in the CSVZ; Morgado et al., 2015; McGee et al., 2017) and variations of slab-derived fluid input (as suggested for the CSVZ, at ~39º30'S latitude by Hickey-Vargas et al., 1989). This approach could be useful to understand other Andean volcanic systems with fairly constant $^{87}Sr/^{86}Sr$ and relatively large ranges of $^{143}Nd/^{144}Nd$ (e.g., Quetrupillán volcano, Brahm et al., 2018).

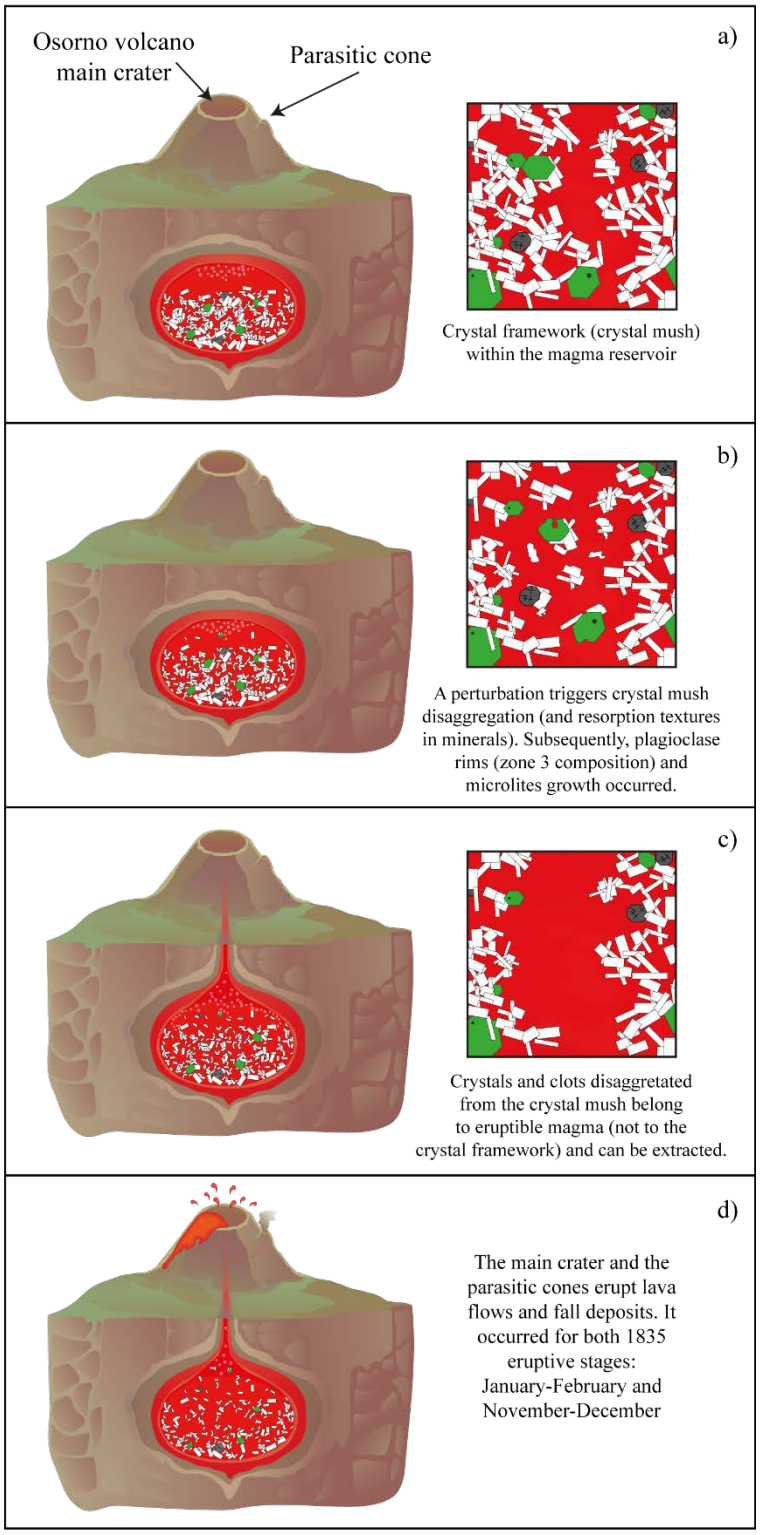

Figure 4.18. *Schematic representation of the evolution of the reservoir beneath Osorno volcano before the 1835 eruption. Figure a) shows the initial crystal mush, which is perturbed (by heating, or volatile addition), as represented in Figure b) and, as a consequence, disaggregated. Figure c) shows that the crystals are released from the crystal mush and incorporated to the eruptible magma. Finally, Figure d) shows when the eruption is triggered and it occurs in the main crater as well as the parasitic cones (image not at scale).*

4.8. Conclusions

The 1835 Osorno is an example of a monitored stratovolcano, which has not erupted during a relatively long period (including the time when the monitoring started). Beneath Osorno volcano we recognise at least one shallow magmatic reservoir at depths up to ~4.5 km, which is consistent with the recently obtained seismic source (SERNAGEOMIN, 2017; 2018a, b; 2019) of 2.6-3.9 km depth. The calculated pre-eruptive temperatures are ~1,140 ± 20 ºC, the oxygen fugacity conditions correspond to a buffer patch of ΔQFM +0.3 ± 0.55, and water contents dissolved in melt of up to 1.5 wt%. In the CSVZ, that water content is considered as low (by contrast, sub-Plinian eruptions in Calbuco 2015 and Cordón Caulle in 2011-2012 were associated with dissolved water contents up to 6% in Calbuco and 4.5% in Cordón Caulle; Arzilli et al., 2019; Jay et al., 2014), which is usually associated with both strombolian events and low risk, but the lahars generated historically during Osorno eruptions, remind us that even effusive eruptions can be devastating. For example, the strombolian 1971 Villarrica eruption (dissolved water content up to 2 wt%; Morgado et al., 2015) caused damages of infrastructure and at least a 17 death toll (Moreno and Clavero, 2006). The eruptive materials exhibit several features to infer the shallow reservoir includes a crystal mush, which underwent disaggregation (due to an increase of volatile contents in the system or a heating event) before the eruption.

The eruptive materials exhibit several features to infer the shallow reservoir includes a crystal mush, which underwent disaggregation (due to an increase of volatile contents in the system or a heating event) before the eruption. During the whole magma history, from mantle melting to the eruptions, the products of Calbuco and Osorno were likely contaminated by slab-derived fluids from sediments and altered oceanic crust and possibly by granulite and minor granodiorite contents at different depths during the ascent path. Trace elements of the

volcanic products of the at Osorno volcano latitude suggest that the mantle source beneath the stratovolcanoes (Calbuco, Osorno, and La Picada) had higher both slab-derived fluid supply and partial melting degree than the mantle beneath small eruptive centres built over the LOFZ at the same latitude (represented by La Viguería cone). Our results highlight the importance of the study of active volcanoes, of which the historical eruptive behaviour is poorly known. This behaviour is particularly significant in those volcanoes which have not erupted since they are monitored and allows us to consider it to mitigate future hazards and understand processes of neighbouring volcanic systems.

4.9. References

Adriasola, AC, Thomson, SN, Brix, MR, Hervé, F, Stöckhert, B (2006) Postmagmatic cooling and late Cenozoic denudation of the North Patagonian Batholith in the Los Lagos region of Chile, 41− 42 15′ S. Int J Earth Sci 95(3), 504-528. http://doi.org/10.1007/s00531-005-0027-9

Almanaque (1969). Historia sísmica de Chile. Revista del Domingo, Libro del Año, p. 96-98. Santiago.

Annen, C, Blundy, JD, Sparks, RSJ (2006) The genesis of intermediate and silicic magmas in deep crustal hot zones. Journal of Petrology, 47(3), 505-539.

Aragón, E, Castro, A, Díaz-Alvarado, J, Liu, D-Y (2011) The North Patagonian batholith at Paso Puyehue (Argentina-Chile). SHRIMP ages and compositional features. Journal of South American Earth Sciences 32, 547-554.

Arzilli, F, Morgavi, D, Petrelli, M, Polacci, M, Burton, M, Di Genova, D, Spina, L, La Spina, G, Hartley, ME, Romero, JE, Fellowes, J (2019) The unexpected explosive sub-Plinian eruption of Calbuco volcano (22–23 April 2015; southern Chile): Triggering mechanism implications. Journal of Volcanology and Geothermal Research, 378, 35-50.

Barrientos, SE, Plafker, G, Lorca, E (1992) Postseismic coastal uplift in southern Chile. Geophys Res Lett 19(7): 701-704.

Borisov, AA, Shapkin, AI (1990). A new empirical equation rating Fe^{3+}/Fe^{2+} in magmas to their composition, oxygen fugacity, and temperature. Geochem. Int, 27(1), 111-116.

Bouvet de Maisonneuve, C, Dungan, MA, Bachmann, O, Burgisser, A (2012). Insights into shallow magma storage and crystallization at Volcán Llaima (Andean Southern Volcanic Zone, Chile). Journal of Volcanology and Geothermal Research, 211, 76-91.

Brahm, R, Parada, MÁ, Morgado, E, Contreras, C, McGee, LE (2018) Origin of Holocene trachyte lavas of the Quetrupillán Volcanic Complex, Chile (39º30'S): Examples of residual melts in a rejuvenated crystalline mush reservoir. Journal of Volcanology and Geothermal Research 357, 163-176.

Cembrano, J, Lara, L (2009) The link between volcanism and tectonics in the southern volcanic zone of the Chilean Andes: A review. Tectonophysics 471: 96-113. doi: http://dx.doi.org/10.1016/j.tecto.2009.02.038

Clapperton, C (1993) Quaternary geology and geomorphology of South America. Elsevier Science Publishers, Amsterdam.

Contreras-Reyes, E, Grevemeyer, I, Flueh, ER, Reichert, C (2008) Upper lithospheric structure of the subduction zone offshore of southern Arauco peninsula, Chile, at ~38ºS. Journal of Geophysical Research: Solid Earth, 113(B7).

Danyushevsky, LV, Sobolev, AV (1996) Ferric-ferrous ratio and oxygen fugacity calculations for primitive mantle-derived melts: calibration of an empirical technique. Mineralogy and Petrology 57(3-4): 229-241.

Darwin, CR (1839a) Journal of Researches into the Geology and Natural History of the various countries visited by H.H.S. Beagle. London: Henry Colburn, 629 p.

Darwin, CR (1839b) Narrative of the surveying voyages of His Majesty's Ships Adventure and Beagle between the years 1826 and 1836, describing their examination of the southern shores of South America, and the Beagle's circumnavigation of the globe. Journal and remarks. 1832-1836. London: Henry Colburn.

Darwin, CR (1840) On the connexion of certain volcanic phenomena in South America; and on the formation of mountain chains and volcanos, as the effect of the same powers by which continents are elevated. Transactions of the Geological Society of London 5 (3), 601-631.

De la Cruz-Reyna, S, Tilling, RI (2008) Scientific and public responses to the ongoing volcanic crisis at Popocatépetl Volcano, Mexico: importance of an effective hazards-warning system. J Volcanol Geoth Res 170(1-2): 121-134.

Delgado, F, Pritchard, ME, Ebmeier, S, González, P, Lara, L (2017) Recent unrest (2002-2015) imaged by space geodesy at the highest risk Chilean volcanoes: Villarrica, Llaima, and Calbuco (Southern Andes). J Volcanol Geoth Res 344: 270-288. https://doi.org/10.1016/j.jvolgeores.2017.05.020

Davidson, JP, Hora, JM, Garrison, JM, Dungan, MA (2005). Crustal forensics in arc magmas. Journal of Volcanology and Geothermal Research 140(1-3): 157-170.

Denton, GH, Lowell, TV, Heusser, CJ, Andersen, BG, Heusser, LE, Moreno, PI, Marchant, DR (1999) Geomorphology, stratigraphy, and radiocarbon chronology of Llanquihue drift in the area of the Southern Lake District, Seno Reloncaví, and Isla Grande de Chiloé, Chile. Geografiska Annalaer: Series A, Physical Geography 81 (2): 167-229.

Droop, GTR (1987) A general equation for estimating Fe^{3+} concentrations in ferromagnesian silicates and oxides from microprobe analyses, using stoichiometric criteria. Mineralogical magazine 51(361): 431-435.

Dungan, MA, Davidson, J (2004) Partial assimilative recycling of the mafic plutonic roots of arc volcanoes: An example from the Chilean Andes. Geology 32(9): 773-776.

Dzierma, Y, Thorwart, M, Rabbel, W, Siegmund, C, Comte, D, Bataille, K, Iglesia, P, Prezzi, C (2012b) Seismicity near the slip maximum of the 1960 Mw 9.5 Valdivia earthquake (Chile): Plate interface lock and reactivation of the subducted Valdivia Fracture Zone. J Geophys Res 117:B06312. doi: http://dx.doi.org/10.1029/2011JB008914

Gerlach, DC, Frey, FA, Moreno-Roa, H, López-Escobar, L (1988) Recent volcanism in the Puyehue—Cordon Caulle region, Southern Andes, Chile (40· 5° S): petrogenesis of evolved lavas. J Petrol 29(2): 333-382.

Ghiorso, MS, Sack, RO (1995) Chemical mass transfer in magmatic processes IV. A revised and internally consistent thermodynamic model for the interpolation and extrapolation of liquid-solid equilibria in magmatic systems at elevated temperatures and pressures. Contrib to Mineral Petrol 119(2-3): 197-212.

Gillis, JM (1855) The US Naval Astronomical Expedition to the Southern Hemisphere during the Years 1849-'50-'51-'52: Chile: its geography, climate, earthquakes, government, social condition, mineral and agricultural resources, commerce 79. Nicholson.

Ginibre, C, Wörner, G (2007) Variable parent magmas and recharge regimes of the Parinacota magma system (N. Chile) revealed by Fe, Mg and Sr zoning in plagioclase. Lithos 98(1-4): 118-140.

Grove, TL, Donnelly-Nolan, JM, Housh, T (1997) Magmatic processes that generated the rhyolite of Glass Mountain, Medicine Lake volcano, N. California. Contrib Mineral Petrol 127(3): 205-223.

Hickey-Vargas, R, Abdollahi, MJ, Parada, MA, López-Escobar, L, Frey, FA (1995) Crustal xenoliths from Calbuco Volcano, Andean Southern Volcanic Zone: implications for crustal composition and magma-crust interaction. Contrib Mineral Petr 119(4), 331–344. http://dx.doi.org/10.1007/BF00286933

Hickey-Vargas, R, Holbik, S, Tormey, D, Frey, FA, Roa, HM (2016a) Basaltic rocks from the Andean Southern Volcanic Zone: Insights from the comparison of along-strike and small-scale geochemical variations and their sources. Lithos 258: 115-132.

Hickey-Vargas, R, Moreno-Roa, H, López-Escobar, L, Frey, FA (1989) Geochemical variations in Andean basaltic and silicic lavas from the Villarrica-Lanin volcanic chain (39.5 S): an evaluation of source heterogeneity, fractional crystallization and crustal assimilation. Contrib Mineral Petr 103(3): 361-386.

Hickey-Vargas, R, Sun, M, López-Escobar, L, Moreno-Roa, H, Reagan, MK, Morris, JD, Ryan, JG (2002) Multiple subduction components in the mantle wedge: evidence from eruptive centers in the Central Southern volcanic zone, Chile. Geology 30(3): 199-202.

Hickey-Vargas, R, Sun, M, Holbik, S (2016b) Geochemistry of basalts from small eruptive centers near Villarrica stratovolcano, Chile: evidence for lithospheric mantle components in continental arc magmas. Geochim Cosmochim Acta 185: 358-382.

Jacques, G, Hoernle, K, Gill, J, Wehrmann, H, Bindeman, I, Lara, LE (2014) Geochemical variations in the Central Southern Volcanic Zone, Chile (38–43 S): the role of fluids in generating arc magmas. Chem Geol 371: 27-45.

Johannes, W, Koepke, J, Behrens, H (1994) Partial melting reactions of plagioclases and plagioclase-bearing systems. In Feldspars and their Reactions (pp. 161-194). Springer, Dordrecht.

Jolly, AD (2019) On the shallow volcanic response to remote seismicity.Geology 47(1): 95-96.

Kamenetsky, VS, Crawford, AJ, Meffre, S (2001) Factors controlling chemistry of magmatic spinel: an empirical study of associated olivine, Cr-spinel and melt inclusions from primitive rocks. J Petrol 42(4): 655-671.

Kay, SM, Godoy, E, Kurtz, A (2005) Episodic arc migration, crustal thickening, subduction erosion, and magmatism in the south-central Andes. Geological Society of America Bulletin 117(1-2): 67-88.

Kelley, KA, Cottrell, E (2009) Water and the oxidation state of subduction zone magmas. Science 325(5940): 605-607.

Kent, AJ (2008) Melt inclusions in basaltic and related volcanic rocks. Rev Mineral Geochem 69(1): 273-331.

Kilian, R, Behrmann, JH (2003) Geochemical constraints on the sources of Southern Chile Trench sediments and their recycling in arc magmas of the Southern Andes. Journal of the Geological Society 160(1): 57-70.

Knesel, KM, Davidson, JP (1996) Isotopic disequilibrium during melting of granite and implications for crustal contamination of magmas. Geology 24(3): 243-246.

Kress, VC, Carmichael, IS (1991) The compressibility of silicate liquids containing Fe_2O_3 and the effect of composition, temperature, oxygen fugacity and pressure on their redox states. Contrib Mineral Petr 108(1-2): 82-92.

Lange, RA, Frey, HM, Hector, J (2009) A thermodynamic model for the plagioclase-liquid hygrometer/thermometer. Am Mineral 94(4): 494-506.

Lara, LE, Lavenu, A, Cembrano, J, Rodríguez, C (2006) Structural controls of volcanism in transversal chains: resheared faults and neotectonics in the Cordón Caulle–Puyehue area (40.5 S), Southern Andes. J Volcanol Geoth Res 158(1-2), 70-86.

Lara, LE, Naranjo, JA, Moreno, H (2004) Rhyodacitic fissure eruption in Southern Andes (Cordón Caulle; 40.5 S) after the 1960 (Mw: 9.5) Chilean earthquake: a structural interpretation. J Volcanol Geoth Res 138(1-2): 127-138.

Lara, LE, Orozco, G, Piña-Gauthier, M (2012) The 1835 AD fissure eruption at Osorno volcano, Southern Andes: Tectonic control by the intraarc stress field instead of remote megathrust-related dynamic strain. Tectonophysics 530: 102-110.

Le Bas, ML, Maitre, RL, Streckeisen, A, Zanettin, B, IUGS Subcommission on the Systematics of Igneous Rocks (1986) A chemical classification of volcanic rocks based on the total alkali-silica diagram. J Petrol. 27(3): 745-750. https://doi.org/10.1093/petrology/27.3.745

Lohmar, S, Parada, M, Gutiérrez, F, Robin, C, Gerbe, MC (2012) Mineralogical and numerical approaches to establish the pre-eruptive conditions of the mafic Lican Ignimbrite, Villarrica Volcano (Chilean Southern Andes). J Volcanol Geoth Res 235: 55-69.

López-Escobar, L, Cembrano, J, Moreno, H (1995a) Geochemistry and tectonics of the Chilean Southern Andes basaltic Quaternary volcanism (37-46 S). Andean geology 22(2): 219-234.

López-Escobar, L, Parada, MA, Hickey-Vargas, R, Frey, FA, Kempton, PD, Moreno, H (1995b) Calbuco Volcano and minor eruptive centers distributed along the Liquiñe-Ofqui Fault Zone, Chile (41–42 S): contrasting origin of andesitic and basaltic magma in the Southern Volcanic Zone of the Andes. Contrib Mineral Petr 119(4): 345-361.

López-Escobar, L, Parada, MÁ, Moreno, H, Frey, FA, Hickey-Vargas, R (1992) A contribution to the petrogenesis of Osorno and Calbuco volcanoes, Southern Andes (41º00' – 41º30'S): comparative study. Revista Geológica de Chile 19 (2): 211-226.

Loucks, RR (1996) A precise olivine-augite Mg-Fe-exchange geothermometer. Contrib Mineral Petr 125(2-3): 140-150.

Lucassen, F, Trumbull, R, Franz, G, Creixell, C, Vásquez, P, Romer, RL, Figueroa, O (2004) Distinguishing crustal recycling and juvenile additions at active continental margins: the Paleozoic to recent compositional evolution of the Chilean Pacific margin (36–41 S). Journal of South American Earth Sciences 17(2): 103-119.

Lucassen, F, Wiedicke, M, Franz, G (2010) Complete recycling of a magmatic arc: evidence from chemical and isotopic composition of Quaternary trench sediments in Chile (36–40 S). International Journal of Earth Sciences 99(3): 687-701.

Martin, C (1901) Los volcanes activos de Chile. Revista Chilena de Historia Natural. Año V, p. 242-250. Imprenta Gillet. Valparaíso.

Masotta, M, Laumonier, M, McCammon, C (2018) Transport of melt and volatiles in magmas inferred from kinetic experiments on the partial melting of granitic rocks. Lithos 318: 434-447.

Maurel, C, Maurel, P (1982) Etude expérimentale de l'equilibre Fe^{2+}-Fe^{3+} dans les spinelles chromifères et les liquides silicatés basiques coexistants a 1 atm. CR Acad. Sci. Paris, 285, 209-215.

Maurel, C, Maurel, P (1984) Etude expérimentale de la distribution de fer ferrique entre spinelle chromifère et bain silicaté basique. Bulletin de minéralogie 107(1): 25-33.

McGee, LE, Brahm, R, Rowe, MC, Handley, HK, Morgado, E, Lara, LE, Turner, MB, Vinet, N, Parada, MÁ, Valdivia, P (2017) A geochemical approach to distinguishing competing tectono-magmatic processes preserved in small eruptive centres. Contrib Mineral Petr 172(6): 44.

McGee, LE, Smith, IE (2016) Interpreting chemical compositions of small scale basaltic systems: a review. J Volcanol Geoth Res 325: 45-60.

McMillan, NJ, Harmon, RS, Moorbath, S, Lopez-Escobar, L, Strong, DF (1989) Crustal sources involved in continental arc magmatism: A case study of volcan Mocho-Choshuenco, southern Chile. Geology 17(12): 1152-1156.

McNurr, SR (2000) Seismic monitoring. In: Encyclopedia of Volcanoes. Sigurdsson, H, Houghton, B, McNutt, SR, Rymer, H, Stix, J. Academic Press, San Diego

Mercer, JH (1976) Glacial history of southermost South America. Quaternary Research 6, 125-166.

Miller, TP, Casadevall, TJ (2000) Volcanic ash hazards to aviation. In: Encyclopedia of Volcanoes. Sigurdsson, H, Houghton, B, McNutt, SR, Rymer, H, Stix, J. Academic Press, San Diego

Mollo, S, Scarlato, P, Lanzafame, G, Ferlito, C (2013) Deciphering lava flow post-eruption differentiation processes by means of geochemical and isotopic variations: A case study from Mt. Etna volcano. Lithos 162: 115-127.

Moore, G, Vennemann, T, Carmichael, ISE (1998) An empirical model for the solubility of H_2O in magmas to 3 kilobars. Am Mineral 83(1-2): 36-42.

Moraleda y Montero, J (1888) Exploraciones geográficas e Hidrográficas, 1789-1793. Introducción de Diego Barros Arana. Imprenta Nacional, p. 533. Santiago, Chile.

Moreno, H, Clavero, J (2006) Geología del volcán Villarrica, Regiones de la Araucanía y de los Lagos. Servicio Nacional de Geología y Minería. Carta Geológica de Chile, Serie Geología Básica 98(1).

Moreno, H, Lara, L, Orozco, G (2010) Geología del volcán Osorno. Servicio Nacional de Geología y Minería, Carta Geológica de Chile, Serie Geológica Básica, No. 126, Mapa escala 1:50000.

Morgado, E, Parada, MÁ, Contreras, C, Castruccio, A, Gutiérrez, F, McGee, LE (2015) Contrasting records from mantle to surface of Holocene lavas of two nearby arc volcanic complexes: Caburgua-Huelemolle Small Eruptive Centers and Villarrica Volcano, Southern Chile. J Volcanol Geoth Res 306: 1-16.

Morgado, E, Parada, MÁ, Morgan, DJ, Gutiérrez, F, Castruccio, A, Contreras, C (2017) Transient shallow reservoirs beneath small eruptive centres: Constraints from Mg-Fe interdiffusion in olivine. J Volcanol Geoth Res 347: 327-336.

Morgado, E, Morgan, DJ, Castruccio, A, Ebmeier, SK, Parada, MÁ, Brahm, R, Harvey, J, Gutiérrez, F, Walshaw, R (2019a) Old magma and a new, intrusive trigger: using diffusion

chronometry to understand the rapid-onset Calbuco eruption, April 2015 (Southern Chile): Contrib Mineral Petr 174(61).

Morgado, E, Morgan DJ, Harvey, J, Parada, MÁ, Castruccio, A, Brahm, R, Gutiérrez, F, Georgiev, B, Hammond, SJ (2019b) Localised heating and intensive magmatic conditions prior the 22-23 April 2015 Calbuco volcano eruption (Southern Chile): B Volcanol 81(4).

Munizaga, F, Hervé, F, Drake, R, Pankhurst, RJ, Brook, M Snelling, N (1988) Geochronology of the Lake Region of south-central Chile (39–42 S): Preliminary results. Journal of South American Earth Sciences 1(3): 309-316.

Nakamura, K. (1977). Volcanoes as possible indicators of tectonic stress orientation—principle and proposal. J Volcanol Geoth Res 2(1): 1-16.

Nakamura, M (1995) Residence time and crystallization history of nickeliferous olivine phenocrysts from the northern Yatsugatake volcanoes, Central Japan: Application of a growth and diffusion model in the system Mg-Fe-Ni. J Volcanol Geoth Res 66(1-4): 81-100.

Nelson, ST, Montana, A (1992) Sieve-textured plagioclase in volcanic rocks produced by rapid decompression. Am Mineral 77(11-12): 1242-1249.

Nikkhoo, M, Walter, TR, Lundgren, PR, Prats-Iraola, P (2016) Compound dislocation models (CDMs) for volcano deformation analyses. Geophys J Int 208:877-894. https://doi.org/10.1093/gji/ggw427

O'Compley, C (1936) Historia geográfica y topográfica descriptiva de los volcanes y cerros en los alrededores del 'Refugio Volcán Osorno', 13-16.

Palin, RM, White, RW, Green, EC (2016) Partial melting of metabasic rocks and the generation of tonalitic–trondhjemitic–granodioritic (TTG) crust in the Archaean: Constraints from phase equilibrium modelling. Precambrian Research 287: 73-90.

Parada, MÁ, Godoy, E, Hervé, F, Thiele, R (1987) Miocene calc-alkaline plutonism in the Chilean Southern Andes. Revista Brasileira de Geociencias 17(4): 450-455.

Petit-Breuilh, ME (1999) Cronología eruptiva histórica de los volcanes Osorno y Calbuco, Andes del Sur (41º-41º30´S). Servicio Nacional de Geología y Minería (SERNAGEOMIN), Chile. Boletín (n.53): 46 p.

Pietranik, A, Koepke, J, Puziewicz, J (2006) Crystallization and resorption in plutonic plagioclase: implications on the evolution of granodiorite magma (Gęsiniec granodiorite, Strzelin Crystalline Massif, SW Poland). Lithos 86(3-4): 260-280.

Piochi, M., Bruno, P. P., & De Astis, G. (2005). Relative roles of rifting tectonics and magma ascent processes: Inferences from geophysical, structural, volcanological, and geochemical data for the Neapolitan volcanic region (southern Italy). Geochem Geophys Geosy 6(7).

Porter, SC (1981) Pleistocene glaciation in the Southern Lake District of Chile. Quaternary Research 16: 263-292.

Prior, DJ, Boyle, AP, Brenker, F, Cheadle, MC, Day, A, Lopez, G, Peruzzo, L, Potts, GJ, Reddy, S, Spiess, R, Timms, NE, Trimby P, Wheeler, J, Zetterström, L (1999) The application of electron backscatter diffraction and orientation contrast imaging in the SEM to textural problems in rocks. Am Mineral 84(11-12), 1741-1759.

Putirka, KD (2005) Igneous thermometers and barometers based on plagioclase+ liquid equilibria: Tests of some existing models and new calibrations. Am Mineral 90(2-3): 336-346.

Putirka, KD (2008) Thermometers and barometers for volcanic systems. Reviews in mineralogy and geochemistry 69(1): 61-120.

Reubi, O, Bourdon, B, Dungan, MA, Koornneef, JM, Selles, D, Langmuir, CH, Aciego, S (2011) Assimilation of the plutonic roots of the Andean arc controls variations in U-series disequilibria at Volcan Llaima, Chile. Earth and Planetary Science Letters 303(1-2): 37-47.

SERNAGEOMIN (2017a) Red Nacional de Vigilancia Volcánica, Volcán Calbuco. http://www.sernageomin.cl/volcan-calbuco. Accessed 3 March 2019

SERNAGEOMIN (2017b) Reporte especial de actividad volcánica (REAV) — Región de los Lagos, volcán Osorno 2017, Diciembre 19 —18:30 (local time).

SERNAGEOMIN (2018a) Reporte especial de actividad volcánica (REAV) — Región de los Lagos, volcán Osorno 2018, Abril 14 —14:30 (local time).

SERNAGEOMIN (2018b) Reporte especial de actividad volcánica (REAV) — Región de los Lagos, volcán Osorno 2018, Junio 23 —11:00 (local time).

SERNAGEOMIN (2019) Reporte de actividad volcánica (RAV) — Región de los Lagos, volcán Osorno, Febrero 2019.

Shejwalkar, A, Coogan, LA (2013) Experimental calibration of the roles of temperature and composition in the Ca-in-olivine geothermometer at 0.1 MPa. Lithos 177: 54-60.

Small, C, Naumann, T (2001) The global distribution of human population and recent volcanism. Global Environmental Change Part B: Environmental Hazards 3(3): 93-109.

Smith, KL, Milnes, AR, Eggleton, RA (1987) Weathering of basalt: formation of iddingsite. Clays and Clay Minerals 35(6): 418-428.

Smith, IEM, Németh, K (2017) Source to surface model of monogenetic volcanism: a critical review. Geological Society, London, Special Publications 446(1): 1-28.

Sparks, RSJ, Cashman, KV (2017) Dynamic magma systems: Implications for forecasting volcanic activity. Elements 13(1): 35-40.

Sparks, RSJ, Biggs, J, Neuberg, JW (2012) Monitoring volcanoes. Science 335(6074): 1310-1311.

Stern, CR (1991) Role of subduction erosion in the generation of Andean magmas. Geology 19(1): 78-81.

Stern, CR (2004) Active Andean volcanism: its geologic and tectonic setting. Revista geológica de Chile 31(2): 161-206.

Stern, CR, Moreno, H, López-Escobar, L, Clavero, JE, Lara, LE, Naranjo, JA, Parada, MÁ, Skewes, MA (2007) Chilean Volcanoes. In: Moreno, T., Gibbons, W. (eds) The Geology of Chile, Geological Society of London, London pp. 149-180.

Stormer JC (1983) The effects of recalculation on estimates of temperature and oxygen fugacity from analyses of multicomponent iron–titanium oxides. Am Mineral 68: 586–594.

Sun, SS, McDonough, WS (1989) Chemical and isotopic systematics of oceanic basalts: implications for mantle composition and processes. Geological Society, London, Special Publications 42(1): 313-345. https://doi.org/10.1144/GSL.SP.1989.042.01.19

Tagiri, M, Moreno, H, López-Escobar, L, Notsu, K (1993) Two magma types of the high-alumina basalt series of Osorno Volcano, Southern Andes (41º06'S) – plagioclase dilution effect. Journal of Mineralogy, Petrology, and Economic Geology 88: 359-371.

Takada, A (1994) The influence of regional stress and magmatic input on styles of monogenetic and polygenetic volcanism. J Geophys Res: Solid Earth 99(B7): 13563-13573.

Tašárová, ZA (2007) Towards understanding the lithospheric structure of the southern Chilean subduction zone (36°S-42°S) and its role in the gravity field. Geophys J Int 170(3): 995–1014. http://doi.org/10.1111/j.1365-246X.2007.03466.x

Tilling, R. I. (2008). The critical role of volcano monitoring in risk reduction. Advances in Geosciences 14: 3-11.

Tormey, DR, Hickey-Vargas, R, Frey, FA, López-Escobar, L (1991) Recent lavas from the Andean volcanic front (33 to 42 S); interpretations of along-arc compositional variations. Andean magmatism and its tectonic setting: Geological Society of America Special Paper 265: 57-77.

Vander Auwera, J, Namur, O, Dutrieux, A, Wilkinson, CM, Ganerød, M, Coumont, V, Bolle, O (2019). Mantle melting and magmatic processes under La Picada stratovolcano (CSVZ, Chile). J Petrol 60(5): 907-944.

Vielzeuf, D, Clemens, JD, Pin, C, Moinet, E (1990) Granites, granulites, and crustal differentiation. In Granulites and crustal evolution (pp. 59-85). Springer, Dordrecht.

Watt, SF, Pyle, DM, Mather, TA (2009) The influence of great earthquakes on volcanic eruption rate along the Chilean subduction zone. Earth and Planetary Science Letters 277(3-4): 399-407.

Witter, JB, Kress, VC, Delmelle, P, Stix, J (2004) Volatile degassing, petrology, and magma dynamics of the Villarrica Lava Lake, Southern Chile. J Volcanol Geoth Res 134(4): 303-337.

Zeitler, PK, Chamberlain, CP (1991) Petrogenetic and tectonic significance of young leucogranites from the northwestern Himalaya, Pakistan. Tectonics 10(4): 729

Chapter 5

5. Discussion

This section of the thesis will focus on showing the main results, and using these to propose models for the studied eruptions from Calbuco and Osorno volcanoes. For the April 2015 rapid onset Calbuco eruption, this will be compared with other similar eruptions worldwide and for the 1835 Osorno eruption, the contribution of the study of that eruption to volcano monitoring and hazard mitigation will be presented. Special emphasis will be given to the implications of this study for other works and how complementary techniques can improve our understanding of magmatic systems. By comparing Calbuco and Osorno plumbing systems and linking them to the regional setting and the implications of the study for the volcanism of the Southern Volcanic Zone of the Andes will be discussed. Finally, the role of petrology in volcano monitoring and hazard mitigation worldwide will be highlighted. In particular, I will appraise the results from chapters 2, 3 and 4 against the aims of the thesis, which were:

1. Determine the physical intensive conditions of the magmas from the last eruptions of Calbuco and Osorno volcanoes.
2. Determine if there is any crystal mush within the magma chambers beneath those volcanoes and the influence of that in the eruptive features.
3. Calculate pre-eruptive timescales of the products of those volcanoes. Relate them (if possible) to geophysical observations.
4. Determine the conditions of magma generation, fluid supply and crustal contamination of the region.

5.1. Calbuco volcano

In chapter 2 of this thesis, which studied the 2015 Calbuco volcano eruption, the deposits gave the following insights:

- A magma reservoir was recognised in the upper crust (5.1–9.1 km depth), based on amphibole barometry (Ridolfi et al., 2010; Ridolfi and Renzulli, 2012).
- Beneath Calbuco volcano there is a crystal mush within the magma reservoir, inferred from textural features of samples: highly crystalline (37–60% crystallinity) samples, clots of crystals, interstitial glass with distinct composition from the outer glass, complex zoning patterns in phenocrysts.
- Thermometry for the silicate phase thermometer systems yielded ~985 ºC (Ca-in-olivine, Shejwalkar and Coogan 2013; two-pyroxenes, Brey and Köhler 1990; Putirka 2008; amphibole-plagioclase, Holland and Blundy 1994; amphibole, Ridolfi and Renzulli 2012).
- Fe-Ti oxides thermometry of samples inferred to be from the middle of the reservoir yielded temperatures of ~930ºC, based on thermometry of core compositions of ilmenite-titanomagnetite contact pairs (Ghiorso and Evans, 2008, thermometry).
- A heating event occurred before the eruption and it was recorded by in-contact Fe-Ti oxide contact pairs of ilmenite and titanomagnetite (via Ghiorso and Evans, 2008, thermometry), inferred to be from the bottom of the magma reservoir reaching temperatures up to ~1,070 ºC.
- No evidence of magma mixing was found.

In addition, diffusion chronometry constraints applied to these samples in chapter 3 gave the following information:

- Compositional profiles across ilmenite-titanomagnetite junctions from a sample inferred to be representing the bottom of the magma reservoir, gave (via diffusion chronometry) timescales from heating to eruption < 4 days. The peak of density of the calculated timescales is 3 hours before the eruption, which coincides with the seismic swarm before the eruption.
- By contrast, there was a timescale of at least one year (via diffusion chronometry) of stable physical intensive conditions (temperature, pressure, and oxygen fugacity) at middle levels of the reservoir, where Fe-Ti oxides show relatively constant composition.

Together, these studies give sufficient insight to propose a model for Calbuco volcano, constrained by these analyses. Beneath Calbuco volcano the magma system is considered to be a prolate spheroid (Delgado et al., 2017). Within the magma reservoir, a rigid crystal mush is recognised including mineral phases such as plagioclase, orthopyroxene, clinopyroxene, olivine, ilmenite and titanomagnetite (Chapter 2). The thermometry based on silicate minerals yielded higher temperature (~985 ºC) than the Fe-Ti oxide thermometry (~930 ºC). The thermometry based on silicate minerals represent a relatively long magmatic timescale temperature condition, probably associated with the crystal mush formation, whereas the Fe-Ti oxides represent relatively shorter timescale, probably associated with an evolved and (in this case) cooler stage of the crystal mush within the magma reservoir. This difference of temperature even could be related to the calculated errors of the thermometry methods applied (details in Chapter 2): from 16 to 56 ºC for thermometers based on silicate phases and from 12 to 22 ºC for thermometers based on Fe-Ti oxides.

At least one year before the April 2015 Calbuco eruption, the middle of the reservoir was at stable temperature of ~930 ºC, which kept until the eruption. The base of the reservoir in a long-term, was at slightly lower temperature of ~870 ºC, but < 4 days before the eruption there was a heating of up to 170 ºC recorded in Fe-Ti oxides only at the base of the reservoir. That heating triggered remobilisation and stirring of the system, finally leading a rapid onset eruption. This late heating could be related to a thermal triggered mush disaggregation at the bottom of the system and mechanical disaggregation in middle levels of it.

5.2. Rapid onset eruptions

The short-term precursor activity (up to few days), is characterised by swarm of small earthquakes, indicating when a magma body migrates upwards, propagating through the crust (Einarsson et al., 2018). Magmatic reservoirs are considered as closed systems from the top of the shallow magma reservoir to the surface (Stix, 2018). Usually, mafic magma input has been identified as triggering component of many rapid onset eruptions (e.g. Popocatépetl, Armienta et al., 1998; Soufrière Hills, Devine et al., 1998; Pinatubo, Pallister et al., 1992). Therefore, identifying the input of new, mafic magma, could be a main goal in forecasting rapid onset eruptions (Stix, 2018).

Rapid onset eruptions are not just seen at Calbuco. Some examples elsewhere are shown in Table 5.1, of which the following three are presented as a comparison:

- Case 1: Cordón Caulle volcanic complex (Chile), in 2011–2012, VEI ~4.
- Case 2: El Reventador volcano (Ecuador), in 2002, VEI 4.
- Case 3: Eyjafjallajökull volcano (Iceland), in April-May 2010, VEI 4.

5.2.1. Case 1: The 2011-2012 Cordón Caulle eruption

Puyehue-Cordón Caulle (40.5º S, 72.2º W) is an active volcanic complex of the Central Southern Volcanic Zone of the Andes (CSVZ), a sub-section of the Southern Volcanic Zone (SVZ) (Lara and Moreno, 2006; Fig. 1.1; Fig. 1.2). The last eruption of this complex occurred during 2011–2012 from Cordón Caulle (Silva-Parejas et al., 2012; Fig. 5.1). The eruption of Cordón Caulle started on 4 June 2011 after two months of elevated, but distributed seismicity across the ~25 km NW Puyehue-Cordón Caulle alignment. Only two days before the eruption, shallow seismicity increased (2–6 km, SERNAGEOMIN, 2011) beneath the SE sector of Cordón Caulle (Silva-Parejas et al, 2012). The eruption was moderate-sized (VEI ~4) involving both explosive and effusive phases (Silva-Parejas et al.,

2012). The erupted products have rhyolitic composition (Castro et al., 2013; Jay et al., 2014) and are crystal poor, with < 5% crystallinity (plagioclase, clinopyroxene, orthopyroxene, magnetite, ilmenite, apatite, and pyrrhotite). The calculated pre-eruptive temperatures of 870–920 ºC were obtained via in contact Fe-Ti oxides (Castro et al, 2013; Jay et al, 2014) and pressures indicating the existence of an upper crustal reservoir, via petrological experiments (Castro et al, 2013) and deformation source modelling (Jay et al, 2014).

Table 5.1. Examples of documented rapid onset eruptions.

Volcano	Country	Year	Precursor time (from detection to eruption onset)	Reference
Krafla	Iceland	1977	135 mins	Einarsson, 2018*
Krafla	Iceland	1980	65 mins	Einarsson, 2018*
Krafla	Iceland	1980	5 hours	Einarsson, 2018*
Hekla	Iceland	1980	23 mins	Einarsson, 2018*
Krafla	Iceland	1980	82 mins	Einarsson, 2018*
Krafla	Iceland	1981	7 hours	Einarsson, 2018*
Krafla	Iceland	1981	76 mins	Einarsson, 2018*
Grimsvötn	Iceland	1983	9 hours	Einarsson, 2018*
Krafla	Iceland	1984	4 hours 24 mins	Einarsson, 2018*
Hekla	Iceland	1991	30 mins	Einarsson, 2018*
Rabaul caldera	Papua New Guinea	1994	27 hours	Blong and McKee, 1995
Gjálp	Iceland	1996	34 hours	Einarsson, 2018*
Grimsvötn	Iceland	1998	6 hours	Einarsson, 2018*
Hekla	Iceland	2000	79 mins	Einarsson, 2018*
El Reventador	Ecuador	2002	7 hours	Hall et al., 2004
Chaitén	Chile	2008	36 hours	Lara, 2008
Eyjafjallajökull	Iceland	14 April, 2010	2 hours 15 min	Einarsson, 2018*
Grimsvötn	Iceland	2011	90 mins	Einarsson, 2018*
Cordón Caulle	Chile	2011	2 days	Castro et al., 2013
Tolbachik	Russia	2012	few hours	Senyukov et al., 2015
Calbuco	Chile	2015	3 hours	This study

* And references therein

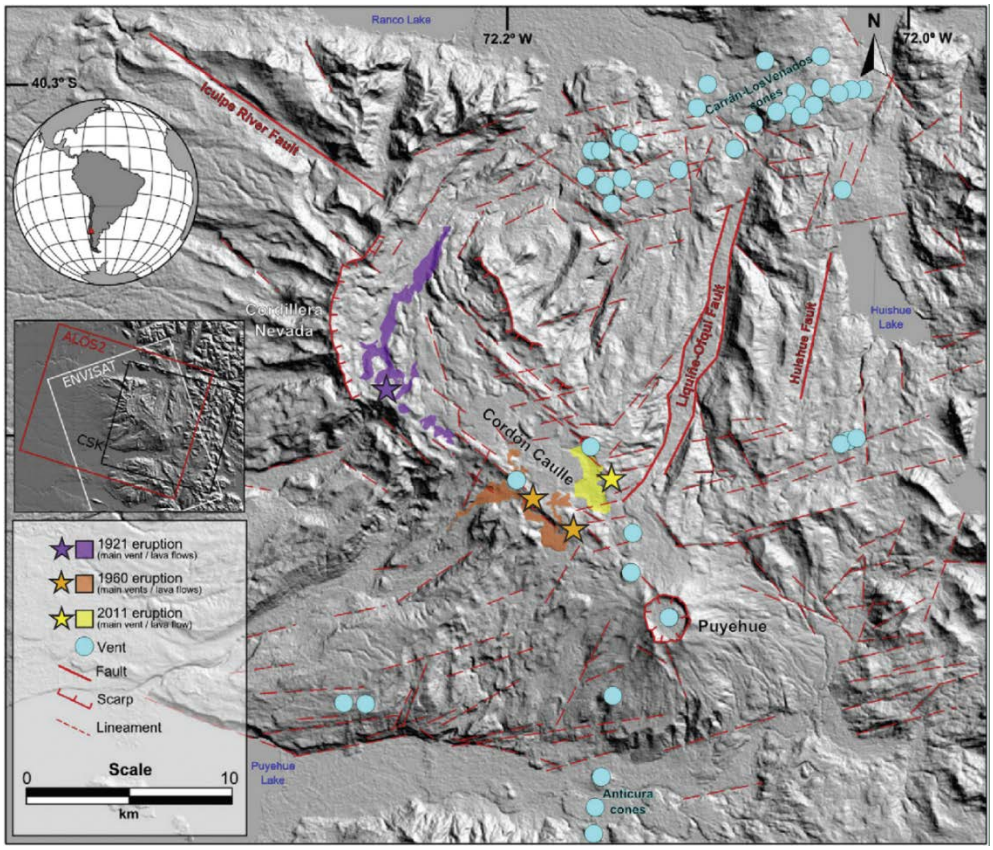

Figure 5.1. *Shaded-relief image of the Puyehue-Cordón Caulle region (with respect to South America) showing vents and lava flows of the 1921–1922, 1960, and 2011–2012 eruptions (Image taken from Jay et al., 2014).*

Based on clinopyroxene exsolution lamellae, Jay et al. (2014) suggested the magma reservoir beneath Cordón Caulle includes a crystal mush. Previous studies (e.g. Jay et al., 2014; Euillades et al., 2017) recognised ground inflations beneath Cordón Caulle and suggested that were result of new magma intrusions.

5.2.2. Case 2: The 2002 El Reventador Volcano eruption

El Reventador Volcano (0º5’ N, 77º40’ W) is a stratovolcano located at the Northern Volcanic Zone of the Andes (Aguilera et al., 1988; Fig. 1.1; Fig. 5.2). The last eruption of this volcano started in November 2002 and it is still erupting (IG-EPN Ecuador, 2019). The first precursor activity was 10 VT seismic events that occurred on October 6, interpreted as related to fault systems of the region. No other seismic activity was detected before 3 November (Hall et al., 2004). The VEI 4 eruption started on 3 November (Hall et al., 2004; Naranjo et al., 2016): between 2:00 and 3:00 local time (LT) with a seismic swarm of > 100 events. At 6:00 LT a steam column was reported (SERNAGEOMIN, 2015a, b). The NOAA (National Oceanic and Atmospheric Administration) GOES (Geostationary Operational Environmental Satellite) detected the first eruption cloud at 07:45 LT (Hall et al., 2004). According Hall et al. (2004) the chronology of the eruption (Fig. 5.3) is: 3 November sub-Plinian phase (Main eruption) and lavas erupted since 6 November (Lava 1) and 21 November (Lava 2). The pyroclastic fall and flow deposits from the Main eruption phase show dacitic composition (66.3–67.3 SiO_2 wt%; Ridolfi et al., 2008), Lava 1 phase products have andesite composition (56.4–58.8 SiO_2 wt%; Ridolfi et al., 2008), and Lava 2 products have basaltic andesite composition (53.4–54.9 SiO_2 wt%; Ridolfi et al., 2008). According to Sauerzapf et al. (2008), the mineralogy found in the products consists of plagioclase, clinopyroxene, olivine, amphibole, titanomagnetite and orthopyroxene. According to Ridolfi et al. (2008) and Samaniego et al. (2008) the seismic events of 6 October are related to a mafic intrusion, which triggered the eruption around one month later.

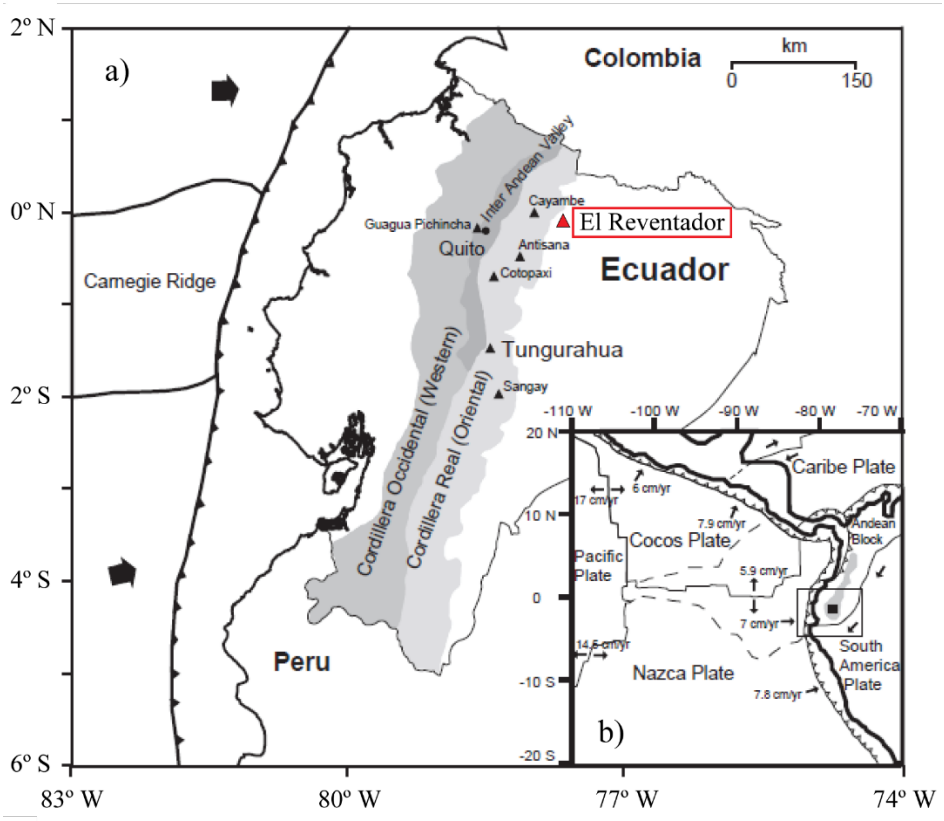

Figure 5.2. *a) Location of El Reventador Volcano (red solid triangle) with respect to Ecuador, other active volcanoes are also shown; b) Tectonic plates around Ecuador (Modified from Molina et al., 2005).*

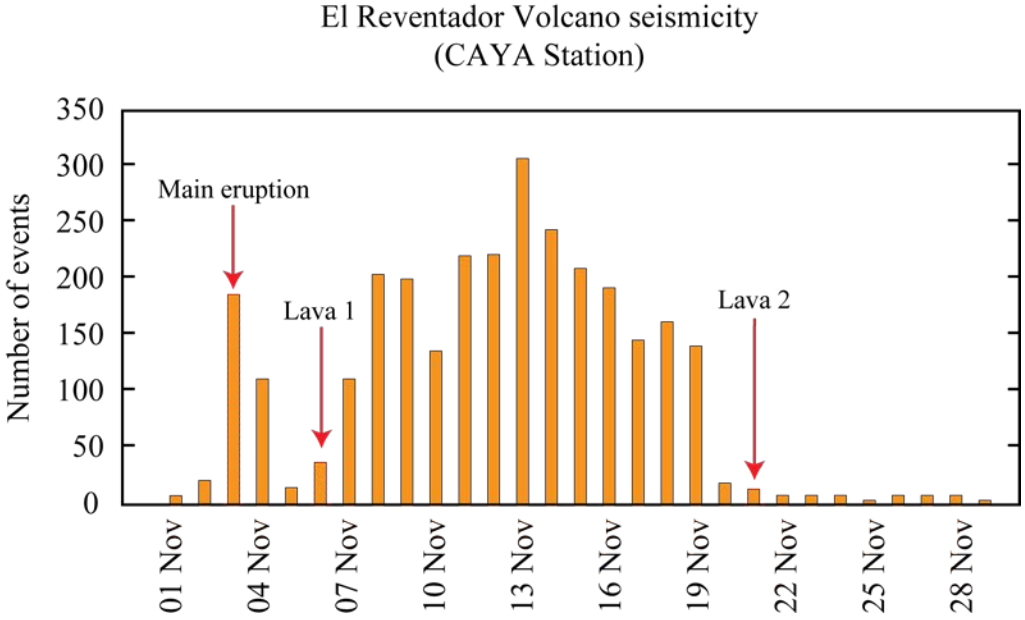

Figure 5.3. *Number of seismic events (mainly VT and hybrid) registered between 1 and 28 November, 2002 at CAYA station, 40 km NW from El Reventador Volcano (Modified from Hall et al., 2004).*

5.2.3. Case 3: The April-May 2010 Eyjafjallajökull eruption

Eyjafjallajökull volcano (63º38’ N, 19º36’W) is southern Iceland ice-covered stratovolcano. It is located at the Eastern Volcanic Zone (Viccaro et al., 2016; Fig. 5.4). The last eruption of this volcano occurred in 2010, the initial eruptive phase (Phase 1) started 20 March in Fimmvörðuháls Pass (Fig. 5.4), after 3 months of precursory activity, and it finished 12 April. The second eruptive phase (Phase 2) started two days later beneath Eyjafjallajökull summit crater (Fig. 5.4), after few hours of precursors (see Table 5.1). The eruption started as phreatomagmatic, few days later became purely magmatic and finished 22 May.

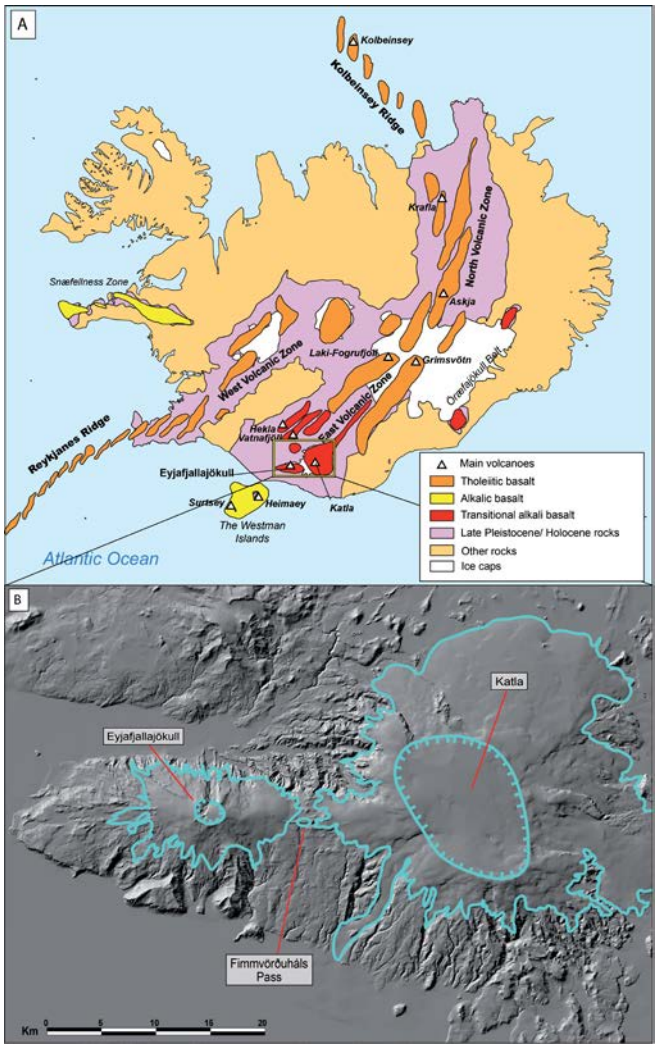

Figure 5.4. *a) Schematic map showing the location of Eyjafjallajökull volcano with respect to Iceland; b) Digital elevation model of Eyjafjallajökull and Katla volcanoes and Fimmvörðuháls Pass (Modified from Viccaro et al., 2016).*

The compositions of Phase 1 products are alkali rich basalts (Fig. 5.5), and those from Phase 2 products are from basalts to rhyolites (Sigmarsson et al., 2011; Keiding and Sigmarsson, 2012). Fall deposits from Phase 2 record rapid magma mingling of basalt and silicic melts without homogenisation (Sigmarsson et al., 2011). Geothermometry yielded temperatures of ~1,170 ºC for Phase 1 products and lower temperatures of ~1,030 ºC for Phase 2 products (Keiding and Sigmarsson, 2012). According to Keiding and Sigmarsson (2012) and Pankurst et al (2018), the Phase 1 magmas crystallised in the deeper crust (~17 km), whereas Phase 2 products crystallised at shallow levels (~4 km), which is consistent with seismic sources (Tarasewicz et al., 2011).

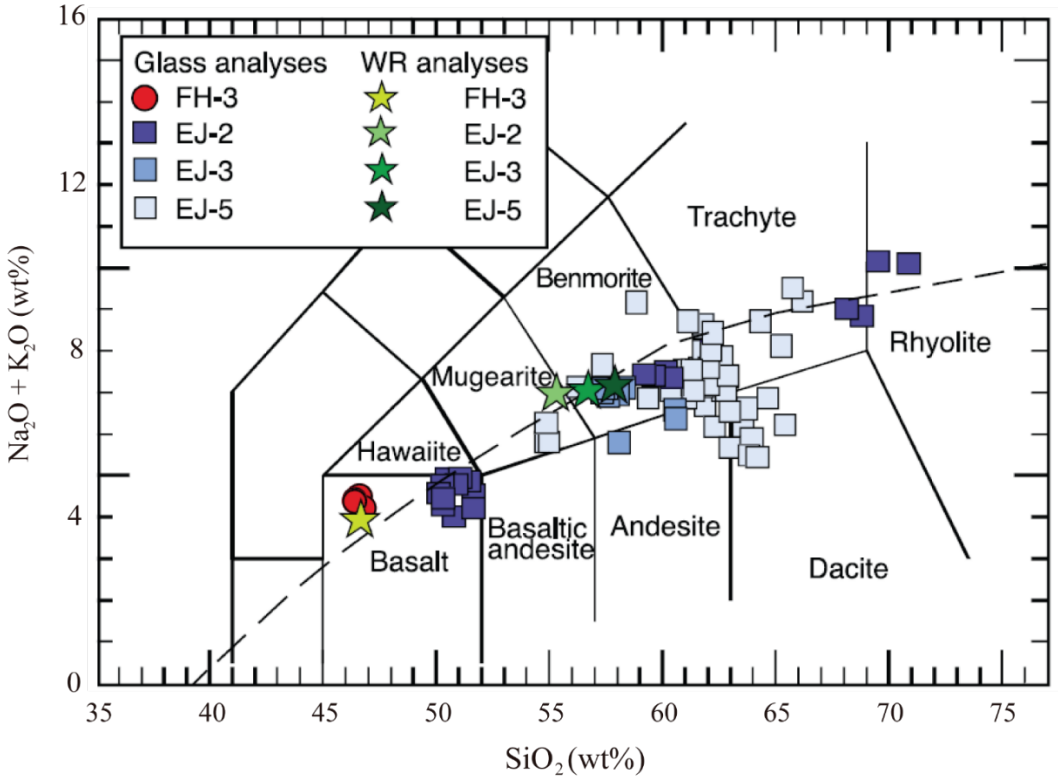

Figure 5.5. *Total alkali vs. silica (Le Maitre et al., 2005) plots of the Eyjafjallajökull 2010 volcanic products. The samples FH-3 correspond to Phase 1 (March-April), and the samples EJ-2, EJ-3, and EJ-5 correspond to Phase 2 (April-May). Image modified from Keiding and Sigmarsson (2012).*

Although diffusion chronometry (Fe-Mg in olivine) has been used integrated with seismic data to determine magma storage and migration timescales, suggesting an intrusion arrival triggering (Sigmundsson et al., 2010) ~15 days before the Phase 1 onset (Viccaro et al., 2016). Phase 2 products have olivine, plagioclase, and clinopyroxene phenocrysts and Cr-spinel, magnetite, apatite, pyrite, and orthopyroxene as minor and accessory minerals.

5.3. Comparison of rapid onset events with the April 2015 Calbuco eruption

5.3.1. Crystal mush within a magma reservoir

Cordón Caulle volcanic complex. The presence of a crystal mush in the magma reservoir at the upper crust was suggested by Jay et al. (2014) beneath Puyehue-Cordón Caulle volcanic complex based on exsolution lamellae in clinopyroxene crystals. From a petrological perspective, the 2011–2012 Cordón Caulle products have the some textural features in common with the 2015 Calbuco products: crystals in clots and complex zoning patterns. Contrary to the 2015 Calbuco products, Cordón Caulle products are crystal-poor (~5 %). Equally as crystal rich products, crystal poor products showing the rest of the mentioned textural features for the Cordón Caulle products (the same as high crystalline Calbuco products) are also associated with crystal mushes (e.g. Bachmann and Bergantz, 2004, 2008; Brahm et al., 2018). Additionally, Dufek and Bachmann (2010) and Streck (2014) presented a numerical model in which melt extraction from a crystal mush within a magma reservoir takes place most efficiently in a crystallinity window of ~50–70%. Moreover, Aravena et al. (2017) presented a time-dependent numerical modelling of late-stage interstitial, leucogranitic melt extraction by dikes from a crystalline mush (Fig. 5.6), towards the margin of the La Gloria Pluton (LGP).

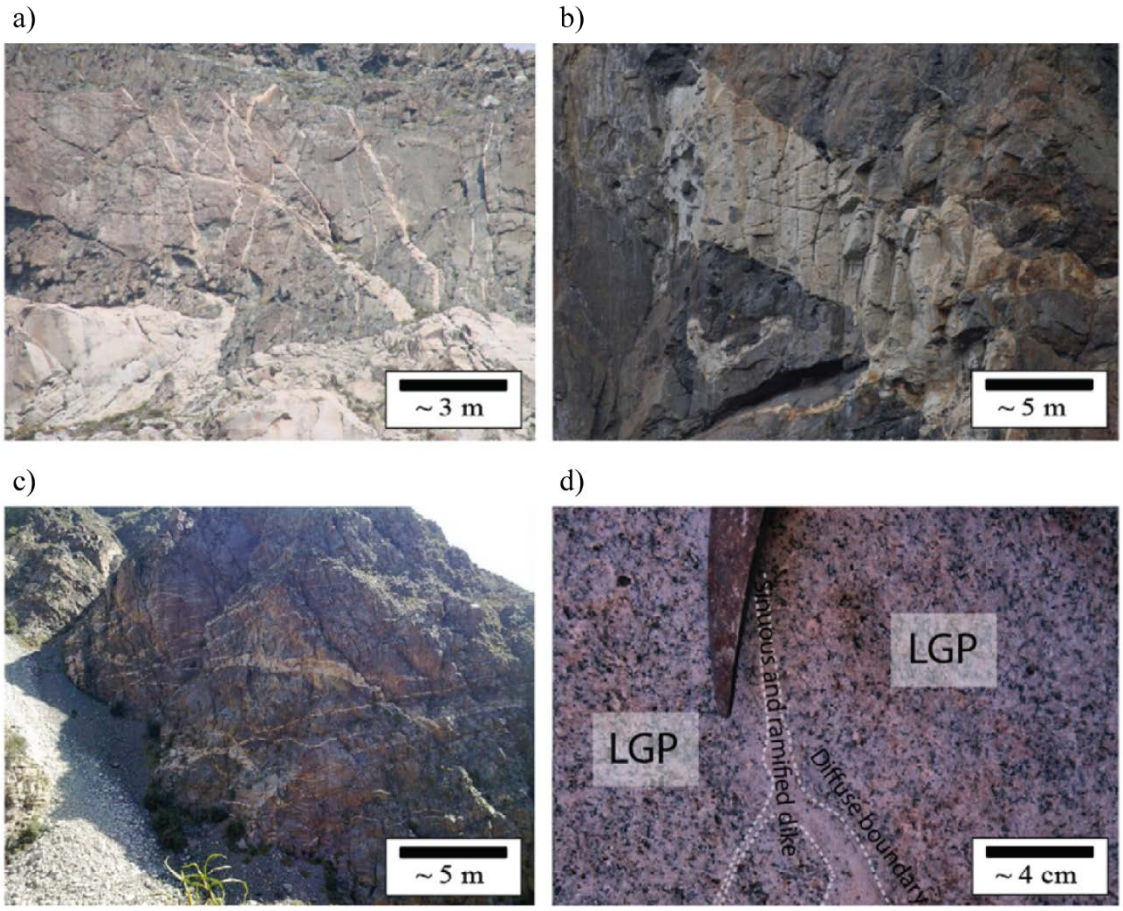

Figure 5.6. *a) Leucogranite sills and dikes at the La Gloria Pluton (LGP contact with the roof rocks); b) Leucogranite sill hosted in volcanic rocks; c) Leucogranite sills hosted in volcanic strata; d) Syn-plutonic dikes emplaced at the core of the LGP (Modified from Aravena et al., 2017).*

El Reventador Volcano. The products of the El Reventador Volcano eruption in 2002, presented some similar features (Ridolfi et al., 2008) to those shown in the 2015 Calbuco products (Chapter 2) related to a crystal mush: high crystalline products (30–38 % crystallinity), crystals in clots, and complex zoning patterns. In addition, the olivines from the erupted material from El Reventador 2002 show resorption features, the same as olivines from the 1835 Osorno products interpreted as a consequence of mush disaggregation (Chapter 4), likely related to an intrusive input. All the features indicate there is a crystal mush within the upper crustal reservoir beneath El Reventador Volcano, which has not been reported by any other article before.

Eyjafjallajökull volcano. The material of the 2010 Eyjafjallajökull eruption show some of the textural features (Keiding and Sigmarsson, 2012) also found in the 2015 Calbuco products (Chapter 2) and interpreted as evidences of crystal mushes in two sill-shaped magma reservoirs (Sigmundsson et al., 2010; Pankhurst et al., 2018). As the sill crystallises and loses heat, this promotes changes in melt and the generation of population peaks of olivine phenocrysts (Pankhurst et al., 2018; see Fig. 5.7).

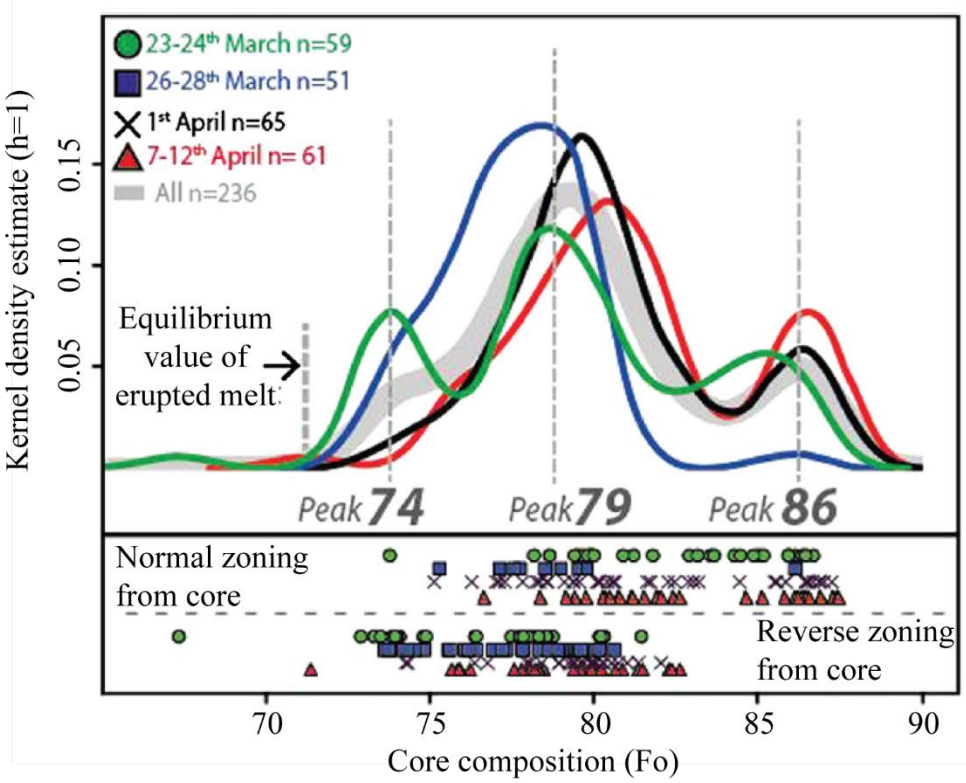

Figure 5.7. *Core compositions of olivine crystals from four samples spanning the eruption are presented using a kernel density estimation (Image modified from Pankhurst et al., 2018).*

Pankhurst et al. (2018) proposed crystal rain (crystals falling due to density higher than surrounding melt) creating crystal mushes and, at the bottom of the sills, are surrounded by a more primitive and warmer melt (creating reverse zoning; Fig. 5.8). As such, crystals formed at the bottom of the magma reservoir do not migrate and, in consequence, do not exhibit reverse zoning (Pankhurst et al., 2018). Crystal mushes within magma reservoirs have been interpreted in other Icelandic volcanoes, for example, in AD 1783–1784 Laki eruption

(Hartley et al., 2016), in which magmatic timescales reflecting the time of residence of olivine crystals in the carrier melt before the eruption.

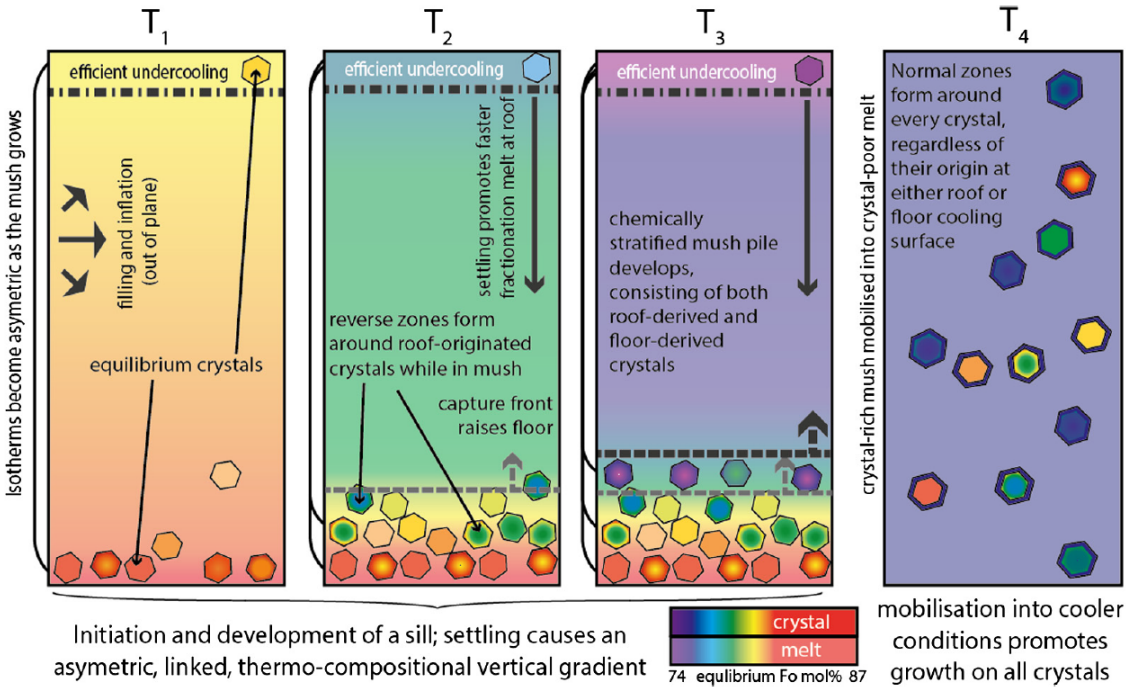

Figure 5.8. *Crystal Rain model, a shorthand description of the process by which differential nucleation and growth inside a magma body, caused by crystal settling and asymmetric thermal and compositional gradient, incorporating crystals into an insulating mush horizon and chemical stratification of crystals and melts (Image taken from Pankhurst et al., 2018).*

5.3.2. Other regional comparison

In addition, the presence of the crystal mush within the magma reservoir is important because it can work as a rheological barrier, hindering mixing and leading explosive and rapid onset eruption, as seen with the sub-Plinian 2015 Calbuco eruption (Chapter 2). For Quizapu volcano, in the Transitional Southern Volcanic Zone of the Andes (Fig. 1.2), Ruprecht and Bachmann (2010) studied a mingled dacite-andesite lava flow erupted during 1846–1847 and products of the plinian eruption of 1932. The pre-eruptive thermometry, calculated using Fe-Ti oxides in equilibrium with each other, yielded temperatures ~130 ºC higher for the 1846–1847 eruption than the 1932 eruptive event. According to the numerical model of Ruprecht and Bachmann (2010), whether the eruption is explosive or effusive depends on the magnitude of magma mixing and heat exchange: the crystal mushes hinder mixing processes, and then impede reheating of significant volumes of magma, which can lead to more explosive eruptions.

5.3.3. Heating events and diffusion chronometry

Cordón Caulle. In the products of the 2011–2012 Cordón Caulle eruption ilmenite-titanomagnetite pairs have been found (Castro et al., 2013; Jay et al., 2014). Castro et al. (2013) only performed single measurements in the cores of the grains to determine temperature and oxygen fugacity conditions, whereas Jay et al. (2014) affirm that ilmenite and titanomagnetite do not show zoning patterns. Jay et al. (2014) suggested a mafic magma input as trigger of the eruption (Fig. 5.9). Among the 2015 Calbuco products, the ilmenite-titanomagnetite grains in contact from most of the samples do not record the heating before the eruption (Chapters 2 and 3). Only those products from the bottom of the reservoir allow to determine timescales from heating to eruption (Chapter 2). Regarding long-term timescales, they can be compared with Mg profiles in plagioclase from the 2011-2012 Cordón Caulle products (Jay et al., 2014), which indicate large re-equilibration, then long residence magmatic timescales for the crystal mush within the magma reservoir.

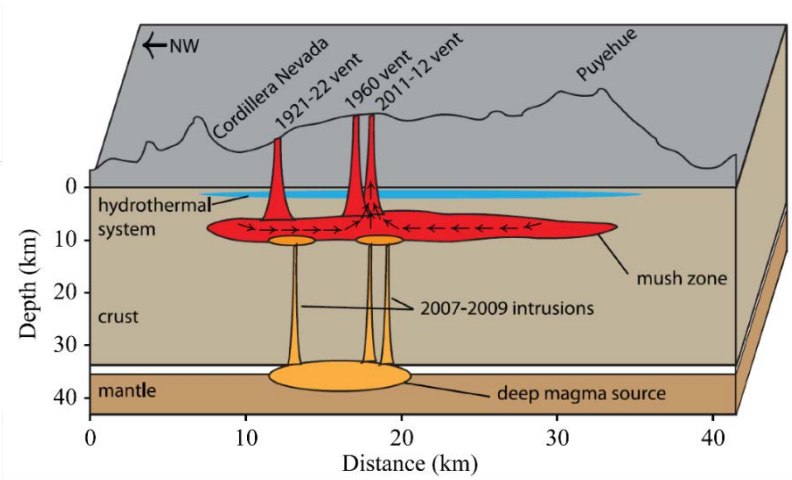

Figure 5.9. *Schematic cross-section of NW-SE Puyehue-Cordón Caulle section. The uplift before the eruption is related to magma input to the base of the crystal mush zone (image taken from Jay et al., 2014).*

El Reventador Volcano. Several studies (e.g. Ridolfi et al., 2008; Samaniego et al., 2008) suggested a mafic intrusion as the eruption triggering related to the earthquake of 6 October (Fig. 5.10). The mineral assemblage of the 2002 El Reventador Volcano products include plagioclase, clinopyroxene, olivine, amphibole, titanomagnetite and orthopyroxene (Ridolfi et al., 2008). The published studies do not include diffusion chronometry, which could be used in olivine (they show normal zoning) to determine short magmatic timescales, to understand the rapid onset El Reventador Volcano 2002 eruption as in other previous studies (e.g. Hartley et al., 2016; Morgado et al., 2017).

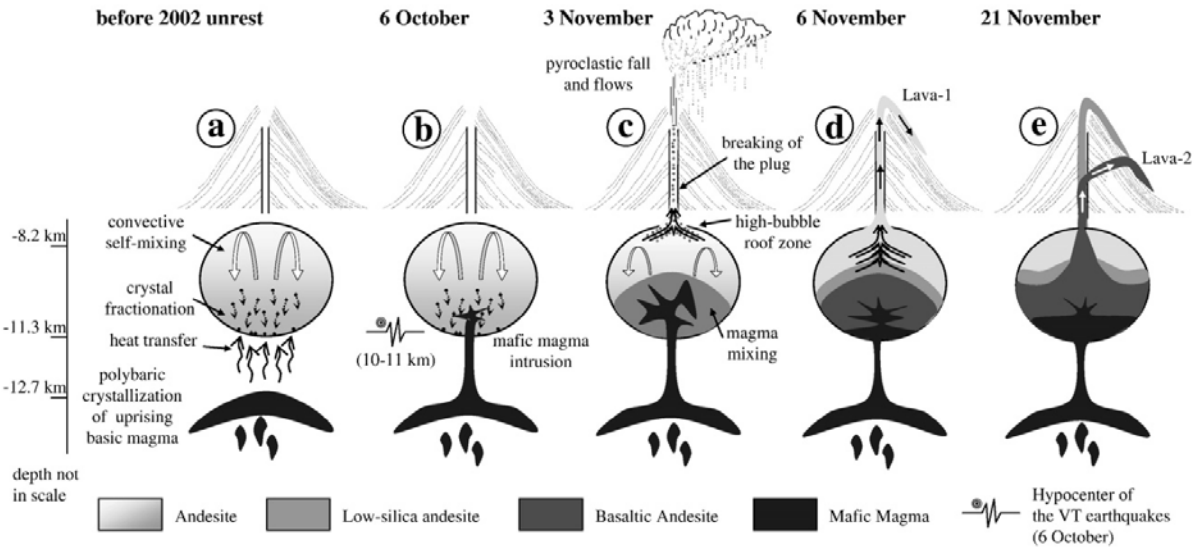

Figure 5.10. *Schematic cross-section of El Reventador Volcano plumbing system before the November 2002 eruptive event (image taken from Ridolfi et al., 2008).*

Eyjafjallajökull volcano. The first and second eruptive phases of the 2010 eruption of Eyjafjallajökull volcano have been associated with a magmatic input as the trigger (Fig. 5.11; Sigmundsson et al., 2010). Magmatic timescales were calculated via Fe-Mg interdiffusion in olivine phenocrysts from the Phase 1 (Fimmvörðuháls Pass) of the 2010 Eyjafjallajökull products (Pankhurst et al., 2018). The diffusion timescales in olivine phenocrysts of few months (Pankhurst et al., 2018), approximate to the time of sedimentation into the crystal mushes of the two sills (see Fig. 5.11), consistent with the observations of InSAR (Sigmundsson et al., 2010) before the first eruptive phase. In addition, Borisova et al. (2012) and Keiding and Sigmarsson (2012) suggested mixing and mingling processes as the eruption triggering for the second 2010 Eyjafjallajökull eruptive phase (Phase 2), which initially for rapid onset eruption would not be consistent with a crystal mush.

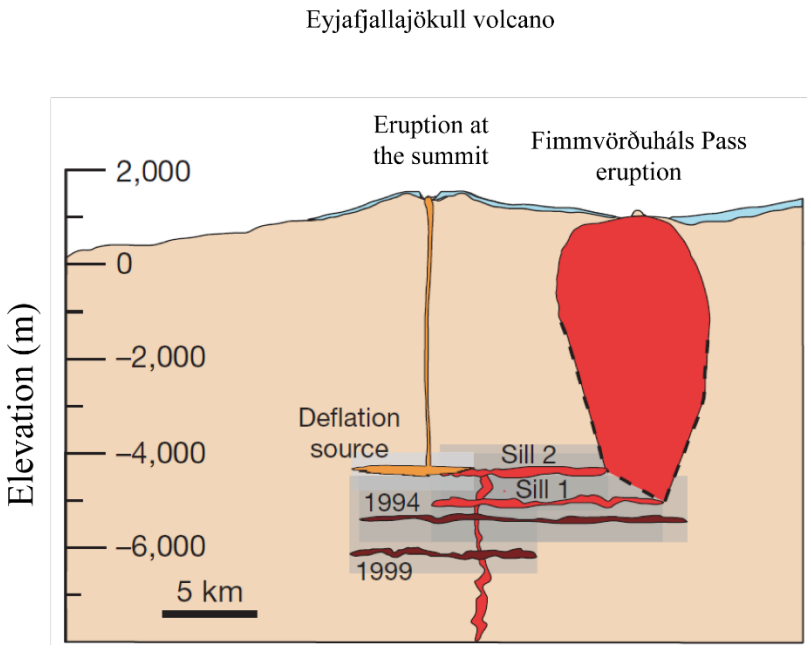

Figure 5.11. *Schematic EW cross-section across the summit area, including magmatic inputs triggering the eruption, grey zones represent uncertainties (image modified from Sigmundsson et al., 2010).*

5.4. Osorno volcano

In chapter 4 of this thesis, which studied the 1835 Osorno volcano eruption, the deposits gave the following insights:

- Pre-eruptive temperature of ~1,140 ºC (via Ca-in-olivine, Shejwalkar and Coogan 2013; olivine-augite; Loucks, 1996).
- A magma reservoir was recognised in the upper crust (up to 4.5 km depth), based on numerical modelling (Moore et al., 1998; Putirka, 2005) and the temperatures previously calculated. From the same modelling a water content dissolved of up to 1.5 wt% was calculated.
- Beneath Osorno volcano there is a crystal mush within the magma reservoir, inferred from textural features: highly crystalline (25–45% crystallinity) samples, clots of crystals, interstitial glass with distinct composition from the outer glass, complex zoning patterns in phenocrysts.
- Oxygen fugacity of ΔQFM + 0.3 was modelled from spinel-melt (Maurel and Maurel, 1982; Borisov and Shapkin, 1990).
- Mineral textures indicating mush disaggregation before the eruption.

Beneath Osorno volcano there is a magma reservoir at the upper crust (up to 4.5 km depth), where the magma stalled just before the 1835 eruption (Chapter 4). From the 1835 Osorno products, a crystal mush within the reservoir is inferred in Chapter 4, at a temperature of ~1,140 ± 20ºC and oxygen fugacity patch of ΔQFM +0.3 ±0.5. Embayments in some olivine phenocrysts and suggest a disequilibrium event (see Fig. 4.18; volatile input or heating event), which could be a consequence of the same process that caused resorption in plagioclase phenocrysts. Other similar eruptions have occurred in the CSVZ, for example, the 1971 Villarrica eruption.

5.4.1. The 1971 Villarrica volcano eruption

Villarrica volcano (39°25'S, 71°56'W; Moreno and Clavero, 2006) is an active stratovolcano located at the CSVZ (Fig. 1.2). Villarrica volcano is located at the westernmost member of an NW-alignment including also Quetrupillán and Lanín volcanoes (López-Escobar et al., 1995; Stern et al., 2007; Fig. 5.12). One of the most destructive eruptions of Villarrica volcano occurred during 1971-1972 (Moreno, 1993). The eruption started on 29 October of 1971 with strombolian explosions and lava effusions from the main crater (Moreno and Clavero, 2006). The night of 30 December, the eruption reached its paroxysmal phase, a fissure eruption occurred. At the same time, lahars from different flanks (NE, N, W and SW) descending at speeds ~60 km/h (Marangunic, 1974) causing damages of infrastructure and at least a 17 death toll (Moreno and Clavero, 2006). Two Aa-type lavas, which reached lengths of 6 km and 18 km long in less than 48 h, were erupted during that phase. Moreno (1993) classified this eruption as strombolian (VEI 2). As introduced in the section 1.1, Villarrica is the most hazardous volcano of Chile (see Table 1.1).

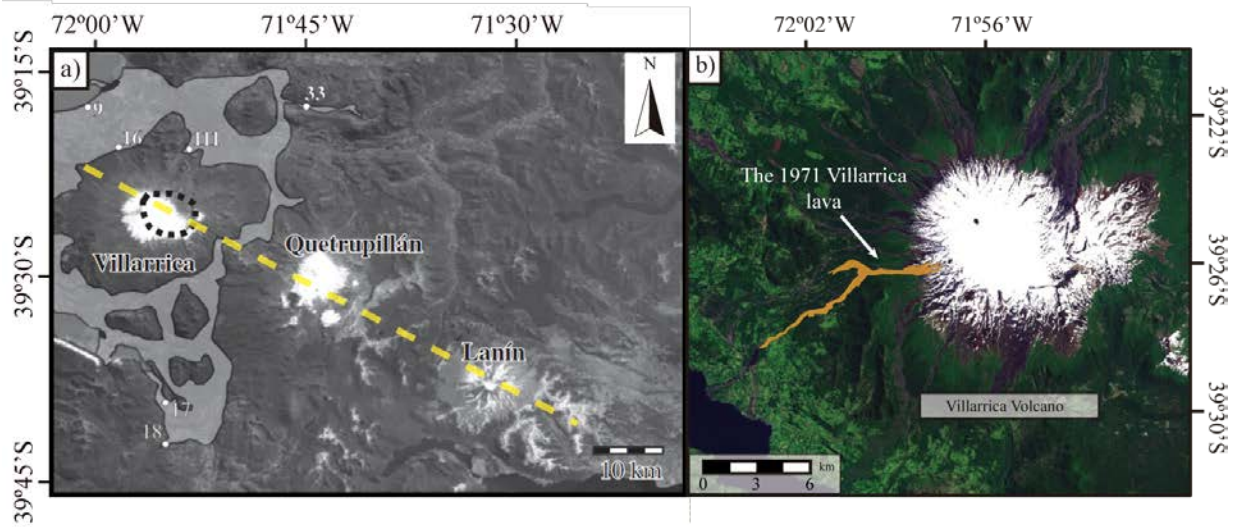

Figure 5.12. *a) Location of Villarrica volcano and surrounding areas including the location of Quetrupillán and Lanín volcanoes. Yellow dashed line indicate the NW-alignment; b) Villarrica volcano and the lava erupted during the 1971 eruption (Image modified from Lohmar et al., 2012 and Morgado et al., 2015).*

According to Morgado et al. (2015) the composition of the erupted products are basaltic andesitic (51.8–52.9 SiO_2 wt%) with mineral assemblage of plagioclase, olivine, and clinopyroxene as phenocrysts and Cr-spinel as inclusions in olivine phenocrysts. In addition, Morgado et al. (2015) presented pre-eruptive temperature of ~1,170 ± 10ºC obtained via in contact olivine-clinopyroxene phenocrysts (Loucks, 1996) and upper crustal pressure of up to 1.4 kbar (equivalent to a depth of up to ~5.3 km; Fig. 5.13) was calculated via iteration of Moore et al. (1998) and Lange et al. (2009) equations. Volatile exsolution due to a heating event was inferred as the eruption triggering (Morgado et al., 2015). Additionally, Morgado et al. (2015) reported a magma reservoir at the base of the crust (Fig. 5.13).

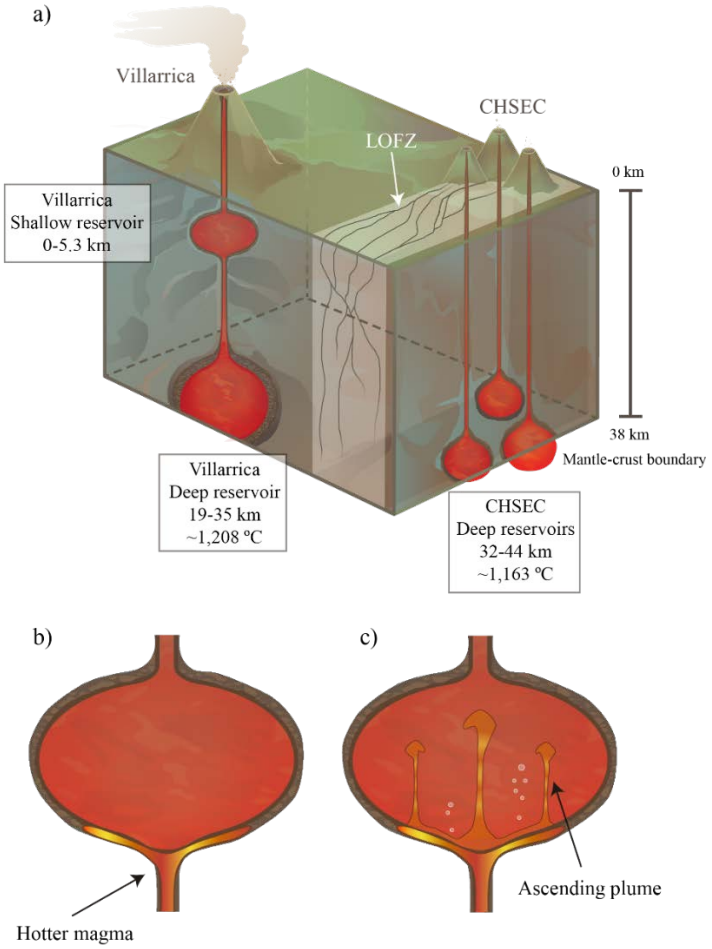

Figure 5.13. *a) Schematic representation of the main characteristics of the reservoirs beneath Villarrica and Caburgua-Huelemolle small eruptive centres (CHSEC, ~20 km from Villarrica volcano). b) The shallow reservoir beneath Villarrica volcano during the arrival of hotter magma. c) Ascending plumes heating the upper crustal magma reservoir prior to eruption of 1971 (Image modified from Morgado et al., 2015).*

5.4.2. Comparison with the 1835 Osorno eruption products

This study shows the existence of similarities between the 1835 Osorno eruption and the 1971 Villarrica eruption: both are fissure eruptions, strombolian (VEI 2), erupting large lavas (lengths of 14 km long for Osorno and 18 km long for Villarrica). Also, the erupted products are similar: basaltic andesite composition, the same mineral assemblages, and similar textural features to those observed in the Osorno products (crystals in clots and complex zoning patterns, and olivine and plagioclase phenocrysts exhibiting resorption textures); the main difference is crystallinity (~30% of Osorno products and ~20% of Villarrica products). Other products of similar eruptions of Villarrica volcano during the 20th century (e.g. 1921, 1948, and 1984) have crystallinity of up to ~35% (Pizarro et al., 2019). I interpret the textural features of the 1971 Villarrica products as representing a crystal mush within the magma reservoir at the upper crust, which has not been reported by any other article before.

5.5. Implications for further work on Calbuco and Osorno volcanoes

The results and discussions of this study can be used in other studies as an input to apply different techniques as well as to improve volcano monitoring of Calbuco and Osorno volcanoes. Some examples of these likely implications for further work are:

Seismic tomography studies. The pre-eruptive temperature and composition of magmas influence in the results of seismic tomography studies (Lees, 2007) beneath volcanoes, so then can be used as a reference to study the crust beneath Calbuco and Osorno volcanoes (e.g. Mount Etna, Patanè et al., 2006; Soufrière Hills Volcano; Paulatto et al., 2012).

Lava flow dynamics. The pre-eruptive temperatures, whole-rock composition, and crystallinity can be used as parameters to model past eruptions and assess likely scenarios during an eruption in the future (e.g. Guilbaud et al., 2005; Del Negro et al., 2008). For example, the mentioned magmatic features were used by Castruccio and Contreras (2016) to

model the 1971 Villarrica lava flow dynamics. As the 1835 Osorno eruption represents typical composition and mineralogy of the historical products (see section 4.2), the results presented in this study (Chapter 4) can be used as an input.

Interferometry synthetic-aperture radar (InSAR). For InSAR studies of surface deformation in a volcanic area, magma reservoirs can act as deformation source (e.g. Ebmeier et al., 2016; Pritchard et al., 2018). Often, distinction of signals from magmatic and hydrothermal processes is not clear (Pritchard et al., 2018), then if the location of the magma reservoir beneath a volcano is known (as in the case of Osorno volcano), magmatic and hydrothermal signals can be distinguished. For example, Delgado et al. (2017) considered the location of the upper-crustal reservoir beneath Villarrica volcano (determined using the 1971 Villarrica products by Morgado et al, 2015; section 5.4.1) as a reference to model the deformation source during the 2015 Villarrica eruption.

5.6. Implications for further monitoring of Calbuco and Osorno volcanoes

The ascent of magma through the crust is usually together with many small earthquakes, surface deformation and release of magmatic gases (e.g. Sparks, 2003; Sparks et al., 2012). All these precursors are supervised by the Chilean Volcano Observatory (Observatorio Volcanológico de los Andes del Sur, OVDAS-SERNAGEOMIN) and their reports were very useful to achieve the aims of this thesis.

Calbuco volcano. The barometry results show an upper crustal magma reservoir (5.5–9 km depth, Chapter 2) at pressures consistent with the source of VT activity reported from months to hours before the eruption (SERNAGEOMIN, 2015a, b). The diffusion chronometry modelling results suggest that a magma input triggered the eruption in less than four days (Chapter 3) after the arrival of this hotter, presumably more mafic magma. This rapid onset

behaviour has to be considered by OVDAS-SERNAGEOMIN during future seismic and other precursory activity beneath Calbuco volcano.

Osorno volcano. The locations of seismic signals related to the last seismic activity recognised beneath Osorno volcano (2.6–3.9 km depth; SERNAGEOMIN, 2017a, b; see Chapter 1) are consistent with the pre-eruptive pressure yielded by the 1835 Osorno products (Chapter 4) of up to 1.2 kbar (equivalent to up to ~4.5 km depth). In addition, it is useful as a constraint for deformation sources in interferometry studies of Andean volcanoes (e.g. the 2011–2012 Cordón Caulle eruption, Jay et al., 2014; the 2015 Villarrica volcano eruption, Delgado et al., 2017). Finally, the presence and physical intensive conditions of an upper crustal crystal mush within the reservoir beneath Osorno volcano suggest there is significantly less volume of liquid (melt) than the total volume of the magma reservoir. This has to be considered in the interpretation of seismic tomography (e.g. Artemieva et al., 2009) and magnetotelluric studies (e.g. Hill et al., 2015) beneath Osorno volcano.

5.7. Comparison of Calbuco and Osorno: similarities

As introduced in section 1.3, Calbuco and Osorno volcanoes are members of the CSVZ of the Chilean Andes and they located close to each other, in a similar latitude (~41º15'S 72º35' W), but Osorno is located ~20 km NNE from Calbuco (Fig. 1.6).

In terms of whole-rock chemistry, although the 2015 Calbuco and the 1835 Osorno and products both have basaltic andesite composition, Osorno products are slightly more primitive (55.7–56.9 SiO_2 wt% for Calbuco and 52.4–52.9 SiO_2 wt% for Osorno products). In addition, rare earth element and spider diagrams of the two eruptions exhibit overlapping, similar patterns (see Fig. 4.5), suggesting that the 2015 Calbuco and the 1835 Osorno products underwent similar processes from mantle to surface.

Beneath Calbuco and Osorno volcanoes crystal mushes were recognised within the magma reservoirs, with the same textural evidence: high crystallinity, complex textural zoning, crystals in clots, and interstitial glasses different from carrier melts. In addition, the products of both eruptions show evidence of processes usually interpreted to be mush disaggregation: resorption textural features and (re)heating (e.g. Bachmann and Bergantz, 2004; 2006; Huber et al., 2009; 2011; Spera and Bohrson, 2018).

5.8. Comparison of Calbuco with Osorno: differences

Although Calbuco and Osorno products come from an upper crustal magma reservoir including crystal mush with basaltic andesite composition, the eruption dynamics of the eruptions are different. The 2015 Calbuco eruption was described as sub-Plinian (VEI 4; Romero et al., 2016; Castruccio et al., 2016) and the 1835 Osorno eruption as strombolian (VEI 2; Lara et al., 2012). This difference in eruptive explosivity could be due to the higher content of water dissolved in the 2015 Calbuco products (up to 4 wt%, Chapter 2) than in the 1835 Osorno products (up to 1.5 wt%, Chapter 4). The higher water content dissolved of the 2015 Calbuco products is consistent with its slightly more evolved composition (55.7–56.9 SiO_2 wt% for Calbuco and 52.4–52.9 SiO_2 wt% for Osorno products), lower temperature (~970 ºC for Calbuco and ~1,140 ºC for Osorno products), and slightly higher pressure related to higher depth of the magma reservoir (from 5.5 to 11 km for Calbuco and up to 4 km for Osorno products). In addition, degassing processes before the eruption are also significant for the explosivity (e.g. Eichelberger et al., 1986; Burgisser and Gardner, 2004; Moretti et al., 2013). Finally, the 2015 Calbuco and the 1835 Osorno products have some mineral phases in common (plagioclase, olivine, clino-, and orthopyroxene; Chapters 2 and 4), but the 1835 Osorno samples do not have Fe-Ti oxides, such that the same techniques used on the Calbuco eruption cannot be deployed at Osorno.

5.9. Link to the regional setting

I compared the whole-rock chemistry of products from the studied region: Calbuco, Osorno and La Picada stratovolcanoes and La Viguería cones (representing small eruptive centres built over the LOFZ). Trace element mobile/immobile ratios of suggested higher subducting slab fluid input in the mantle wedge beneath the stratovolcanoes (Chapter 4). This is consistent with the prevalence of decompression melting of small eruptive centres built over LOFZ at the 39º15'S latitude in the CSVZ (McGee et al., 2017). Sr mixing modelling suggests there is a fluid input from altered oceanic crust (AOC) and sediments in a ratio of 7:3 (AOC:sediments).

In addition, modelling of trends of Nd isotope ratios recognised in the products of one single eruption were performed following mixing patterns considering granulite (Hickey-Vargas et al., 1995), gabbro (Aragón et al., 2011), and granodiorite (Aragón et al., 2011) from the region as potential contaminants end-members. For Calbuco products the best-fit mixture is ~25% of granulite and ~5% of granodiorite and for Osorno products, the most plausible mixture is ~10% of granulite and ~5% of granodiorite assimilation. Gabbro assimilation is ruled out to be significant (< 1% assimilation). This model was proposed for a region at latitude of ~41º15' S including a NE-striking volcano alignment (Osorno-La Picada-Puntiagudo-Cordón Cenizos). By contrast, Hickey-Vargas et al. (1989) proposed a theoretical model for the region at latitude ~39º30' S suggesting variations from west to east decreasing slab-derived fluid input and melting degree for another region of the CSVZ, including NW-striking volcano alignment (Villarrica-Quetrupillán-Lanín).

5.10. Volcanism in the CSVZ: The prevalence of crystal mush

According to Cembrano and Lara (2009), there are different tectonic settings within the Andes, which influence the crustal processing of volcanic material. South of 37ºS stratovolcanoes are built over NE-striking tension cracks (e.g. Osorno–La Picada–Cordón Cenizos), NW-striking basement structures (e.g. Villarrica–Quetrupillán–Lanín) or not related to any major structures (e.g. Calbuco) (Cembrano and Lara, 2009). In addition, small eruptive centres (monogenetic cones) lie over the LOFZ master faults (e.g. Caburgua–Huelemolle, Morgado et al., 2015, 2017; Carrán–Los Venados; Bucchi et al., 2015).

This study shows key features that the magmatic reservoirs beneath Calbuco and Osorno volcanoes have in common: they both are located in the upper crust, possess a crystal mush within (where most of the erupted crystals come from), and before the eruptions, perturbating events occurred that trigger crystal mush disaggregation and, likely, the eruptive events themselves. The presence of an upper-crustal crystal mush seems to be typical of the magmatic reservoirs beneath volcanoes of the Southern Volcanic Zone of the Andes (e.g. Llaima, Bouvet de Maisonneuve et al., 2012) and not be related to any particular regional structural configuration. Previous studies and this thesis have shown evidence of the existence of an upper-crustal crystal mush reservoirs beneath volcanoes not related to major structures (e.g. Calbuco, Chapter 2), NW-striking volcano alignments (e.g. Villarrica, Morgado et al., 2015; Quetrupillán, Brahm et al., 2018), NE-striking volcano alignments (Osorno-La Picada-Puntiagudo-Cordón Cenizos, Chapter 2; Vander Auwera et al., 2019), and small eruptive centres over the master fault of Liquiñe-Ofqui Fault Zone (e.g. Caburgua cones, Morgado et al., 2017).

5.10.1. The mush model paradigm for understanding volcanism

Textural features and geochemical evidence indicate that voluminous silicic magma reservoirs are controlled by fractional crystallisation processes leading to higher crystal contents (e.g. Hildreth, 1981; 2004; Bacon and Druitt, 1988; Marsh, 1996; Bachmann and Bergantz, 2003). According to the mush paradigm (Fig. 1.13), within the continental crust, magma reservoirs are represented by both *magma chambers*, continuous, melt-rich, lenticular regions where the magma is fluid and eruptible and within which magma crystallinity is < 45 vol.%, and *crystal mushes*, a rigid crystal framework of crystallinity >45% (Marsh 1989, 1996; Hildreth 2004; Bachmann and Bergantz 2008). Also, crystallinities of >45 vol.% are associated with rheological properties which impede convection (e.g. Bachmann and Bergantz 2004, 2008; Huber et al. 2010; Burgisser and Bergantz 2011; Parmigiani et al. 2014). Such reservoirs exist within the shallow crust (≤ 10 km depth) and may evolve over long cooling periods to become plutons (e.g. Koyaguchi and Kaneko 1999; Claiborne et al. 2010; Cooper and Kent 2014; Molina et al. 2015; Szymanowski et al. 2017; Cooper et al. 2017).

Although the existence of crystal mushes within magma reservoirs is an established paradigm for magmatic systems of felsic magmatic composition and calderas (e.g. La Picana caldera system, Chile, Lindsay et al., 2001; Fish Canyon tuff, U.S., Bachmann and Bergantz, 2003, 2004; Bishop tuff, U.S., Hildreth, 2004; Hildreth and Wilson, 2007), crystal mushes have been documented in smaller and more mafic magma reservoirs (e.g. Laki volcano, Passmore et al., 2012; Kīlauea volcano, Rae et al., 2016). Crystal mushes have also been recognised (or evidence of their existence) beneath volcanoes of distinctly different magma compositions and at a regional scale, across all of the structural settings of the SVZ of the Andes, particularly in the CSVZ. For example, in Quetrupillán volcano (trachydacite composition, Brahm et al., 2018) part of a NW-striking volcano alignment; in Caburgua-Huelemolle small eruptive field (basaltic composition, Morgado et al., 2015) over the Liquiñe-Ofqui Fault Zone; at Calbuco volcano (basaltic andesite composition, Chapter 2), which is not related to any major structure; and at Osorno volcano (basaltic andesite composition, Chapter 4) part of a NE-striking volcano alignment.

In addition, crystal mushes can act as rheological barriers, which has been proposed by (e.g. Bachmann and Bergantz, 2006; Costa et al., 2013) to inhibit compositional mixing of the magma from the chamber and new magma inputs (Bachmann and Bergantz, 2006) and which according to Ruprecht and Bergantz, (2010) has the potential to influence volcano explosivity. If the conclusions of Ruprecht and Bergantz, (2010) are correct, therefore the presence of a crystal mush within magma reservoirs enhance both explosive potential and rapid onset of eruptions.

5.11. Implications for Andean volcanism

Upper crustal crystal mush within magma reservoir. This study shows key features that the magmatic reservoirs beneath Calbuco and Osorno volcanoes have in common: they both are located in the upper crust, possess a crystal mush within (where most of the erupted crystals come from), and before the eruptions, perturbating events occurred that trigger crystal mush disaggregation and, likely, the eruptive events. As the number of studies increases, the presence of an upper-crustal crystal mush seems to be typical of the magmatic reservoirs beneath volcanoes of the Southern Volcanic Zone of the Andes (e.g. Llaima, Bouvet de Maisonneuve et al., 2012) and not be related to any particular regional structural configuration (see section 5.11). The presence of ubiquitous upper-crustal mush has the following consequences for our study of Andean volcanism and hazard prediction:

- In the shallow crust, long-period earthquakes, associated with rapid decompression, can be large enough to deform the crust (Sparks and Cashman, 2017). This presence allows to relate earthquakes to a likely location of a magma reservoir and to use InSAR methods reliably considering an upper-crustal magma reservoir.
- Products of Andean volcanoes coming from a crystal mush record multiple processes: mush formation (e.g. Bachmann et al., 2002), disaggregation (e.g. Chapter 4), eruptive triggering (e.g. Chapter 3) and syn-eruptive (e.g. Blundy et al., 2006). The textural features have to be considered in the context of a crystal mush to interpret them properly.

Diffusion chronometry. Results from this study confirm the utility of oxide diffusion chronometry and demonstrate that such petrologic methods are consistent with volcanic and geophysical observations. This thesis also demonstrates that relatively short- and long-term timescales can be yielded from the same mineral phases recording different pre-eruptive processes. Therefore, the methodology presented in this thesis could be reproduced in other systems to recognise eruption triggering and the timescales of those pre-eruptive processes in the Southern Volcanic Zone of the Andes and worldwide, in which erupted products have Fe-Ti oxide grains (e.g. Quizapú, Ruprecht and Bachmann, 2010; Quetrupillán, Brahm et al., 2018; Chaitén, Castro and Dingwell, 2009) as well as other mineral phases presenting zoning patterns. This study has implications for diffusion chronometry in the context of crystals and melts derived from an upper-crustal crystal mush:

- After the arrival of a new, hotter mafic, the eruption could start before the thermal homogenisation of the magma reservoir is reached, then a portion of the erupted products do not record the triggering event (e.g. Chapter 3). In consequence, a complete sampling, representing different locations of the magma reservoir is strongly recommended for studies of rapid-onset eruptions, which are relatively common in the SVZ (e.g. Chaitén in 2008, Lara, 2008; Cordón Caulle in 2011-2012, Castro et al., 2013; Calbuco in 2015, Castruccio et al., 2016).

Geochemical variations of CSVZ volcanoes. Jacques et al. (2014) proposed the crustal contamination was negligible in CSVZ volcanoes, but they did not study any volcanic centres in detail. This thesis shows a difference in the mantle source between stratovolcanoes and small eruptive centres built over the LOFZ. In comparison to stratovolcanoes, small eruptive centre products have lower both slab-derived fluid supply and partial melting degree of the mantle wedge. According to the results of this thesis, the variations of composition of the products is controlled by fluid input from the subducting slab (Chapter 4) and presumably mantle heterogeneity (e.g. Morgado et al., 2015; McGee et al., 2017) rather than crustal assimilation. These variations in a particular region should be considered in future studies of Andean volcanoes located in alignments and located close from volcanic fields (with several cinder cones such as Cayutué-La Viguería small eruptive centres).

5.12. The role of petrology in volcano monitoring and hazard mitigation

There are several methods used in volcano monitoring giving real-time information on perturbations of the volcanic base activity. The most common are:

- Seismology: Seismic signals are a key aspect and a robust network of seismometers near the volcanic edifice because the signals are typically weak (Sparks et al., 2012). Seismology allows to recognise and quantify fluid or magma movements, stress changes in the volcanic edifice, and failure of host rocks.
- Ground deformation: Most volcanic eruptions are preceded by ground deformation. The methods to assess these surface movements include ground tiltmeters and electronic distance measurement with lasers, among others (Gambino et al., 2014).
- Satellite-based methods: give the opportunity to detect unrest even in unmonitored volcanoes. Interferometric synthetic aperture radar (InSAR) uses images from different radars to generate digital elevation maps. It allows measuring deformation: inflation or deflation (Hu et al., 2014).

Although these methods are essential in volcano monitoring, the only discipline that allows the study of magmatic processes directly is igneous petrology. Nevertheless, it only can describe magmatic features of volcanic products after an eruption occurs. Considering that, combining continuous volcano monitoring and petrological constraints of previous eruptions is a strong tool for volcano observatories to understand pre-eruptive processes and to plan hazard mitigation policies. First, petrology allows us to obtain different intensive physical conditions, which can be compared and used coupled with geophysical studies (see section 5.7). It allows us to place timescale constraints on magmatic processes; these can then be compared against geophysics if we think the controlling processes are the same, which can be coupled with surficial-measured geophysical signals (seismology, InSAR, tiltmeters, etc.) and can be considered as a reference. This thesis, studying the last eruptions of Calbuco and

Osorno volcanoes, shows how these different approaches can work together to generate a complete eruptive model (in the case of April 2015 Calbuco eruption) and give new perspectives for future eruptions (determining magmatic features via the 1835 Osorno erupted products). In consequence, multidisciplinary studies are strongly suggested to have a deeper understanding of volcanic processes, which are not common in the studies of volcanoes from CSVZ.

By comparison, the products of the 1835 Osorno eruption are typical of recent eruptions from this volcano, showing very similar whole-rock chemistry, mineral assemblage, and textural features observed in other Osorno products (López-Escobar et al., 1992; Tagiri et al., 1993; Moreno et al., 2010; see Table 4.1.), suggesting the features expected for next eruptions. In addition, the upper crustal location of the reservoir constrained by petrology (Chapter 4) is consistent with the seismic source recorded since 2016 and in 2018 was related to the announced yellow alert. This seismic activity together with the relatively long time gap since the last eruption (> 180 years), and the length of up to 14 km long imply Osorno volcano should be priority for OVDAS-SERNAGEOMIN, the institution in charge volcano monitoring and hazard mitigation policies in Chile.

5.13. Future work

The results of this thesis show how a multidisciplinary study gives different approaches, which allow a better understanding of volcano-magmatic processes. The suggestions of future work are divided into the local scale (Calbuco and Osorno volcanoes separately) and regional scale (studies along the volcanic zone at Osorno and Calbuco volcanoes latitude).

5.13.1. Calbuco volcano

Numerical modelling of magma chamber dynamics. Several authors have performed numerical modelling of magma chambers to understand the long-term evolution of an upper crustal magmatic reservoir (e.g. Gutiérrez and Parada, 2010; Huber et al., 2011; Lohmar et al., 2012). I suggest similar models could be performed in the timescales calculated in Chapter 3 for the April 2015 products. Also, other features should be considered to have a better understanding the rapid magma disaggregation such as: magma chamber shape (e.g. Pietruszka and García, 1999; Delgado et al., 2017), magmatic textural features in crystals from clots (including zoning patterns, e.g. Chapter 2, Allan et al., 2013; Chamberlain et al., 2014), and the location of the magma reservoir (e.g. Chapter 2; Tait et al., 1989; Cooper et al., 2017).

Timescales of crystal mush formation. In the products of April 2015 Calbuco eruption, some clino- orthopyroxene phenocrysts from crystal clots show internally-buffered diffusion profiles (see Fig. 2.9e). Those profiles could be used to determine timescales from the development of crystal-mush within the magma reservoir to the eruption. In such an investigation, the samples from the middle levels of the reservoir would be adequate targets, in which the timescales show established conditions in timescales of > one year. To perform those modelling, the temperature conditions were reliably calculated via several methods (two-pyroxenes, Ca-in-olivine, and amphibole-plagioclase, see Chapter 2).

5.13.2. Osorno volcano

Direct measurement of volatiles. Measurement of volatiles in glass is strongly suggested using techniques such as Raman spectroscopy and Ion Microprobe in glass (melt inclusions, interstitial glass between crystals from clots, and glass from groundmass). Accurately determining this volatile content is relevant to hazard mitigation because volatile exsolution is a main factor controlling the eruptive style (Roggensack et al., 1996; 1997; Del Carlo and Pompilio, 2004; Cassidy et al., 2018) and also can give new perspectives on crystallisation, and eruptive triggering processes providing complementary information to the presented in this study (Chapter 4).

Determining deformation source. I suggest to study surface deformation of Osorno volcano before and after the increase of seismic activity in 2016 (see Fig. 1.12). If deformation is recognised via interferometric synthetic-aperture radar, it could give deformation source and geometry of that source (e.g. Delgado et al., 2017; Ebmeier et al., 2016), which could be related to magmatic reservoir if the depth of the deformation source and the reservoir (up to 4.5 km, see Chapter 4) are consistent.

Magma ascent rates. Ferguson et al (2016) studied magma decompression rates recorded by melt embayments during explosive eruptions of Kīlauea volcano. It may be possible to use the olivine phenocrysts from the fall deposits from the Osorno 1835 eruption, which exhibit similar embayments in the groundmass.

5.13.3. CSVZ

Time-dependent seismic tomography. Koulakov et al (2013), via time-dependent local earthquake tomography, reported the existence of intermediate crustal magmatic reservoirs beneath Kluchevskoy and Bezymianny volcanoes (Fig. 5.14), which were feeding them before the eruptions of 2005. I suggest, therefore, the same procedure could be applied beneath the latitude of Calbuco and Osorno volcanoes to assess the evolution of the magmatic reservoirs in time, including the crystal-mush vs. eruptible magma relation.

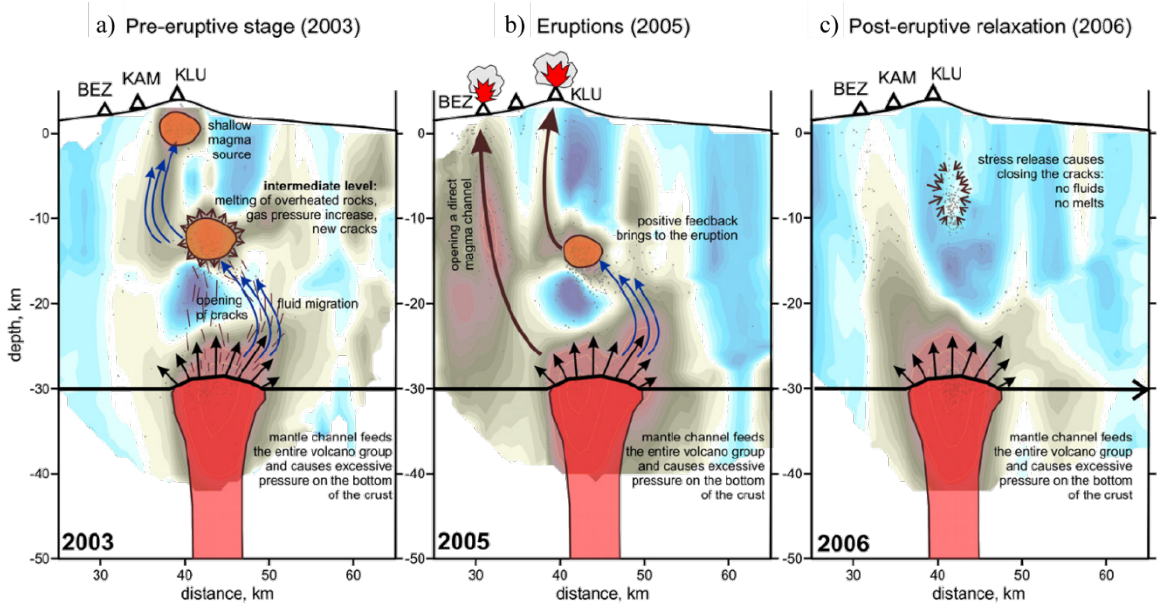

Figure 5.14. *Eruption cycle in the Kluchevskoy group of volcanoes based on 4D tomography. a) During the pre-eruptive stage, the mantle channel causes stresses and crack formation in the crust. b) Positive feedback between fluid migration, melting and crack formation result in the eruption of at the beginning of 2005. At this stage a short-lived opening of a channel feeding Bezymianny eruption. c) After the eruptions, the stresses are released and the cracks are closed. A decrease in fluid content triggers solidification of magma (Modified from Koulakov et al., 2013)*

Magnetotelluric studies. Perform the method of three-dimensional electrical resistivity at the Calbuco volcano and Osorno–La Picada–Puntiagudo–Cordón Cenizos volcano alignment and La Viguería-Cayutué volcanic field (~41º20'S latitude). The magnetotelluric method can be applied together with petrology (e.g. Harangi et al., 2015) to obtain the magma distribution, the shape of the magma reservoirs and to find out if there are other magma chambers, different from the reported in this thesis, presumably in the lower crust. A similar study was published by Kapinos et al. (2016) along the Chilean subduction zone at the latitudes of Llaima volcano (~38º42'S) and Villarrica–Quetrupillán–Lanín volcanoes alignment (~39º25'S; Fig. 5.15).

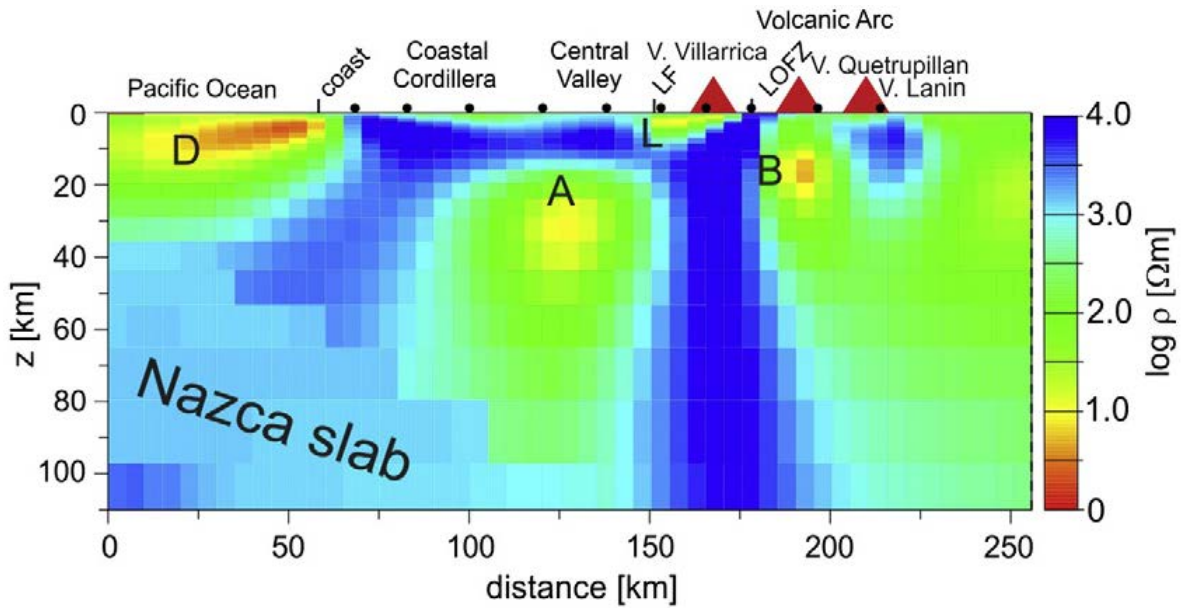

Figure 5.15. *Vertical cross sections of the 3D model along profiles. LOFZ and LF correspond to Liquiñe-Ofqui and Lanalhue faults, respectively. The anomalies are: A: below the central Valley, B: beneath volcanic front, D: beneath continental shelf, L: related to Lanalhue fault (Figure modified from Kapinos et al., 2016).*

Increase the density of the monitoring network. Currently, the monitoring instruments tracking Calbuco and Osorno volcanoes are relatively low (3 seismometers in Calbuco, 4 seismometers and 1 accelerometer in Osorno), considering these are two of the most hazardous volcanoes of the Chilean Andes (SERNAGEOMIN, 2017a, b). To improve the monitoring network I suggest the installation of: seismometers (give more details into measuring seismic signals and locating seismic sources with higher accuracy), more tiltmeters in different locations (to determine pre-, syn-, and post-eruptive deformation processes), and infrasound sensors (to improve the assessment of eruption dynamics and determine when the vents are open or closed).

5.14. References

Adriasola, AC, Thomson, SN, Brix, MR, Hervé, F, Stöckhert, B (2006) Postmagmatic cooling and late Cenozoic denudation of the North Patagonian Batholith in the Los Lagos region of Chile, 41− 42 15′ S. Inter J Earth Sci 95(3): 504-528.

Aguilera, E, Almeida, E, Balseca, W (1988) El Reventador: an active volcano in the sub-Andean zone of Ecuador. Rendiconti della Società Italiana di Mineralogia e Petrologia 43: 853-875.

Allan, AS, Morgan, DJ, Wilson, CJ, Millet, MA (2013) From mush to eruption in centuries: assembly of the super-sized Oruanui magma body. Contrib Mineral Petrol 166(1): 143-164.

Aragón, E., Castro, A., Díaz-Alvarado, J., Liu, D.-Y. (2011) The North Patagonian batholith at Paso Puyehue (Argentina-Chile). SHRIMP ages and compositional features. Journal of South American Earth Sciences 32, 547-554.

Aravena, A, Gutiérrez, FJ, Parada, MA, Payacán, Í, Bachmann, O, Poblete, F (2017) Compositional zonation of the shallow La Gloria pluton (Central Chile) by late-stage extraction/redistribution of residual melts by channelization: Numerical modeling. Lithos 284: 578-587.

Armienta, MA, Martin-Del-Pozzo, AL, Espinasa, R, Cruz, O, Ceniceros, N, Aguayo, A, Butron, MA (1998) Geochemistry of ash leachates during the 1994–1996 activity of Popocatepetl volcano. Appl Geochemi 13(7): 841-850.

Artemieva, IM (2009) The continental lithosphere: reconciling thermal, seismic, and petrologic data. Lithos 109(1-2): 23-46.

Bachmann, O, Bergantz, GW (2003) Rejuvenation of the Fish Canyon magma body: A window into the evolution of large-volume silicic magma systems. Geology 31(9): 789-792.

Bachmann, O, Bergantz, GW (2004) On the Origin of Crystal-poor Rhyolites: Extracted from a Batholithic Crystal Mushes. J Petrol 45(8), 1565-1582. http://doi.org/10.1093/petrology/egh019

Bachmann, O, Bergantz, GW (2006) Gas percolation in upper-crustal silicic crystal mushes as a mechanism for upward heat advection and rejuvenation of near-solidus magma bodies. J Volcanol Geotherm Res 149(1), 85-102. https://doi.org/10.1016/j.jvolgeores.2005.06.002

Bachmann, O, Bergantz, G (2008). The magma reservoirs that feed supereruptions. Elements, 4(1), 17-21.

Bachmann, O, Dungan, MA, Lipman, PW (2002) The Fish Canyon magma body, San Juan volcanic field, Colorado: rejuvenation and eruption of an upper-crustal batholith. J Petrology 43(8): 1469-1503.

Bacon, CR, Druitt, TH (1988) Compositional evolution of the zoned calcalkaline magma chamber of Mount Mazama, Crater Lake, Oregon. Contrib Mineral Petrol 98(2): 224-256.

Blong, R, McKee, C (1995) The Rabaul eruption 1994: destruction of a town. Natural Hazards Research Centre.

Blundy, J, Cashman, K, Humphreys, M (2006) Magma heating by decompression-driven crystallization beneath andesite volcanoes. Nature 443(7107): 76.

Borisov, AA, Shapkin, AI (1990) A new empirical equation rating Fe^{3+}/Fe^{2+} in magmas to their composition, oxygen fugacity, and temperature. Geochem. Int 27(1): 111-116.

Borisova, AY, Toutain, JP, Stefansson, A, Gouy, S, de Parseval, P (2012) Processes controlling the 2010 Eyjafjallajökull explosive eruption. J Geophys Res: Solid Earth 117(B5).

Bouvet de Maisonneuve, C, Dungan, MA, Bachmann, O, Burgisser, A (2012). Insights into shallow magma storage and crystallization at Volcán Llaima (Andean Southern Volcanic Zone, Chile). J Volcanol Geoth Res 211, 76-91.

Brahm, R, Parada, MA, Morgado, E, Contreras, C, McGee, L (2018) Origin of trachyte lavas of the Quetrupillán Volcanic Complex, Chile (39º30'S): Examples of residual melts in rejuvenated crystalline mush reservoir. J Volcanol Geotherm Res 357, 163-176. http://doi.org/10.1016/j.jvolgeores.2018.04.020

Brey, GP, Köhler, T (1990) Geothermobarometry in four-phase lherzolites II. New thermobarometers, and practical assessment of existing thermobarometers. J Petrol 31(6): 1353-1378.

Bucchi, F, Lara, LE, Gutiérrez, F (2015) The Carrán–Los Venados volcanic field and its relationship with coeval and nearby polygenetic volcanism in an intra-arc setting. J Volcanol Geotherm Res 308: 70-81.

Burgisser, A, Bergantz, GW (2011) A rapid mechanism to remobilize and homogenize highly crystalline magma bodies. Nature, 471, 212-216. http://dx.doi.org/10.1038/nature09799

Burgisser, A, Gardner, JE (2004) Experimental constraints on degassing and permeability in volcanic conduit flow. Bull Volcanol 67(1): 42-56.

Cassidy, M, Manga, M, Cashman, K, Bachmann, O (2018) Controls on explosive-effusive volcanic eruption styles. Nature communications 9(1): 2839.

Castro, JM, Dingwell, DB (2009) Rapid ascent of rhyolitic magma at Chaitén volcano, Chile. Nature 461(7265): 780. https://doi.org/10.1038/nature08458

Castro, JM, Schipper, CI, Mueller, SP, Militzer, AS, Amigo, A, Parejas, CS, Jacob, D (2013) Storage and eruption of near-liquidus rhyolite magma at Cordón Caulle, Chile. Bull Volcanol 75(4): 702.

Castruccio, A, Clavero, J, Segura, A, Samaniego, P, Roche, O, Le Pennec, J, Droguett, B (2016). Eruptive parameters and dynamics of the April 2015 sub-Plinian eruptions of Calbuco volcano (Southern Chile). Bull Volcanol 327: 469-483. http://dx.doi.org/10.1007/s00445-016-1058-8

Castruccio, A, Contreras, MA (2016) The influence of effusion rate and rheology on lava flow dynamics and morphology: A case study from the 1971 and 1988–1990 eruptions at Villarrica and Lonquimay volcanoes, Southern Andes of Chile. J Volcanol Geoth Res 327: 469-483.

Cembrano, J, Hervé, F, Lavenu, A (1996) The Liquiñe Ofqui fault zone: a long-lived intra-arc fault system in southern Chile. Tectonophysics 259(1-3): 55-66.

Cembrano, J, Lara, L (2009) The link between volcanism and tectonics in the southern volcanic zone of the Chilean Andes: a review. Tectonophysics 471(1-2), 96-113. http://doi.org/10.1016/j.tecto.2009.02.038

Chamberlain, KJ, Wilson, CJ, Wooden, JL, Charlier, BL, Ireland, TR (2013) New perspectives on the Bishop Tuff from zircon textures, ages and trace elements. J Petrol 55(2): 395-426.

Claiborne, LL, Miller, CF, Flanagan, DM, Clynne, MA, Wooden, JL (2010) Zircon reveals protracted magma storage and recycling beneath Mount St. Helens. Geology 38(11), 1011-1014. https://doi.org/10.1130/G31285.1

Costa, F, Andreastuti, S, de Maisonneuve, CB, Pallister, JS (2013) Petrological insights into the storage conditions, and magmatic processes that yielded the centennial 2010 Merapi explosive eruption. J of Volcanol Geoth Res 261: 209-235.

Cooper, KM, Kent, AJ (2014). Rapid remobilization of magmatic crystals kept in cold storage. Nature, 506(7489), 480.

Cooper, GF, Morgan, DJ, Wilson, CJ (2017) Rapid assembly and rejuvenation of a large silicic magmatic system: Insights from mineral diffusive profiles in the Kidnappers and Rocky Hill deposits, New Zealand. Earth Planet Sci Lett 473: 1-13.

Del Carlo, P, Pompilio, M (2004) The relationship between volatile content and the eruptive style of basaltic magma: the Etna case. Annals Geophys 47(4).

Del Negro, C, Fortuna, L, Herault, A, Vicari, A (2008) Simulations of the 2004 lava flow at Etna volcano using the magflow cellular automata model. Bull Volcanol 70(7): 805-812.

Delgado, F, Pritchard, ME, Ebmeier, S, González, P, Lara, L (2017) Recent unrest (2002-2015) imaged by space geodesy at the highest risk Chilean volcanoes: Villarrica, Llaima, and Calbuco (Southern Andes). J Volcanol Geoth Res 344: 270-288. https://doi.org/10.1016/j.jvolgeores.2017.05.020

Devine, JD, Murphy, MD, Rutherford, MJ, Barclay, J, Sparks, RSJ, Carroll, MR, Young, SR, Gardner, JE (1998) Petrologic evidence for pre-eruptive pressure-temperature conditions, and recent reheating, of andesitic magma erupting at the Soufriere Hills Volcano, Montserrat, WI. Geophys Res Lett 25(19): 3669-3672.

Dufek, J, Bachmann, O (2010) Quantum magmatism: Magmatic compositional gaps generated by melt-crystal dynamics. Geology 38(8): 687-690.

Ebmeier, SK, Elliott, JR, Nocquet, JM, Biggs, J, Mothes, P, Jarrín, P, Yépez, M, Aguaiza, S, Lundgren, P, Samsonov, SV (2016) Shallow earthquake inhibits unrest near Chiles–Cerro Negro volcanoes, Ecuador–Colombian border. Earth Planet Sci Lett 450: 283-291.

Eichelberger, JC, Carrigan, CR, Westrich, HR, Price, RH (1986) Non-explosive silicic volcanism. Nature 323(6089): 598.

Einarsson, P (2018) Short-term seismic precursors to Icelandic eruptions 1973–2014.Frontiers Earth Sci 6, 45.

Euillades, PA, Euillades, LD, Blanco, MH, Velez, ML, Grosse, P, Sosa, GJ (2017) Co-eruptive subsidence and post-eruptive uplift associated with the 2011–2012 eruption of Puyehue-Cordón Caulle, Chile, revealed by DInSAR. J Volcanol Geoth Res 344: 257-269.

Ferguson, DJ, Gonnermann, HM, Ruprecht, P, Plank, T, Hauri, EH, Houghton, BF, Swanson, DA (2016) Magma decompression rates during explosive eruptions of Kīlauea volcano, Hawaii, recorded by melt embayments. Bull of Volcanol 78(10): 71.

Ebmeier, SK, Elliott, JR, Nocquet, JM, Biggs, J, Mothes, P, Jarrín, P, Yépez, M, Aguaiza, S, Lundgren, P, Samsonov, SV (2016) Shallow earthquake inhibits unrest near Chiles–Cerro Negro volcanoes, Ecuador–Colombian border. Earth Planet Sci Lett 450: 283-291.

Ghiorso, MS, Evans, BW (2008) Thermodynamics of rhombohedral oxide solid solutions and a revision of the Fe-Ti two-oxide geothermometer and oxygen-barometer. Am J Sci 308: 957–1039. https://doi.org/10.2475/09.2008.01

Gambino, S, Falzone, G, Ferro, A, Laudani, G (2014) Volcanic processes detected by tiltmeters: A review of experience on Sicilian volcanoes. J Volcanol Geoth Res 271: 43-54.

Guilbaud, M.-N., Self, S., Thordarson, T., Blake, S., 2005. Morphology, surface structures, and emplacement of lavas produced by Laki, A.D. 1783–1784. In: Manga, M, Ventura, G (Eds.), Kinematics and Dynamics of Lava Flows: Geological Society of America Special Paper 396: 81–102.

Gutiérrez, F, Parada, MÁ (2010) Numerical 232hermos232g of time-dependent fluid dynamics and differentiation of a shallow basaltic magma chamber. J Petrol 51(3), 731-762. http://doi.org/10.1093/petrology/egp101

Hall, M, Ramón, P, Mothes, P, LePennec, JL, García, A, Samaniego, P, Yepes, H (2004) Volcanic eruptions with little warning: the case of Volcán Reventador's Surprise November 3, 2002 Eruption, Ecuador. Rev Geol Chile 31(2): 349-358. https://doi.org/10.1007/BF00303452

Harangi, S, Novák, A, Kiss, B, Seghedi, I, Lukács, R, Szarka, L, Weszyrtgom, V, Metwaly, M, Gribovszki, K. (2015). Combined magnetotelluric and petrologic constrains for the nature of the magma storage system beneath the Late Pleistocene Ciomadul volcano (SE Carpathians). J Volcanol Geoth Res 290: 82-96.

Hartley, ME, Morgan, DJ, Maclennan, J, Edmonds, M, Thordarson, T (2016) Tracking timescales of short-term precursors to large basaltic fissure eruptions through Fe–Mg diffusion in olivine. Earth Planet Sci Lett 439: 58-70.

Hickey-Vargas, R, Abdollahi, MJ, Parada, MA, López-Escobar, L, Frey, FA (1995) Crustal xenoliths from Calbuco Volcano, Andean Southern Volcanic Zone: implications for crustal composition and magma-crust interaction. Contrib Mineral Petr 119(4), 331–344. http://dx.doi.org/10.1007/BF00286933

Hickey-Vargas, R, Moreno-Roa, H, López-Escobar, L, Frey, FA (1989) Geochemical variations in Andean basaltic and silicic lavas from the Villarrica-Lanin volcanic chain (39.5 S): an evaluation of source heterogeneity, fractional crystallization and crustal assimilation. Contributions to Mineralogy and Petrology 103(3), 361-386.

Hildreth, W (1981) Gradients in silicic magma chambers: implications for lithospheric magmatism. J Geophys Res: Solid Earth 86(B11): 10153-10192.

Hildreth, W (2004) Volcanological perspectives on Long Valley, Mammoth Mountain, and Mono Craters: several contiguous but discrete systems. J Volcanol Geotherm Res *136*(3), 169-198. https://doi.org/10.1016/j.jvolgeores.2004.05.019

Hill, GJ, Bibby, HM, Ogawa, Y, Wallin, EL, Bennie, SL, Caldwell, TG, Keys, H, Bertrand, EA, Heise, W (2015) Structure of the Tongariro Volcanic system: Insights from magnetotelluric imaging. Earth Planet Scie Lett 432, 115-125.

Holland, T, Blundy, J (1994) Non-ideal interactions in calcic amphiboles and their bearing on amphibole-plagioclase thermometry. Contrib Mineral Petrol 116(4), 433–447. http://dx.doi.org/10.1007/BF00310910

Hu, J., Li, Z. W., Ding, X. L., Zhu, J. J., Zhang, L., Sun, Q. (2014). Resolving three-dimensional surface displacements from InSAR measurements: A review. Earth-Sc Rev 133: 1-17.

Huber, C, Bachmann, O, Dufek, J (2010) The limitations of melting on the reactivation of silicic mushes. J Volcanol Geoth Res 195(2-4), 97-105.

Huber, C, Bachmann, O, Dufek, J (2011) Thermo-mechanical reactivation of locked crystal mushes: Melting-induced internal fracturing and assimilation processes in magmas. Earth Planet Sci Lett 304(3-4): 443-454.

Huber, C, Bachmann, O, Manga, M (2009) Homogenization processes in silicic magma chambers by stirring and mushification (latent heat buffering). Earth Planet Sci Letters 283(1-4): 38-47.

IG-EPN Ecuador (2019) Monitoreo Volcán Reventador https://www.igepn.edu.ec/reventador/content/16-reventador. Accessed Aug 2019

Jacques, G, Hoernle, K, Gill, J, Wehrmann, H, Bindeman, I, Lara, LE (2014) Geochemical variations in the Central Southern Volcanic Zone, Chile (38–43 S): the role of fluids in generating arc magmas. Chem Geology 371: 27-45.

Jay, J, Costa, F, Pritchard, M, Lara, L, Singer, B, Herrin, J (2014) Locating magma reservoirs using InSAR and petrology before and during the 2011–2012 Cordón Caulle silicic eruption. Earth Planet Sci Lett 395: 254-266.

Kapinos, G, Montahaei, M, Meqbel, N, Brasse, H (2016) Three-dimensional electrical resistivity image of the South-Central Chilean subduction zone. Tectonophysics 666: 76-89.

Keiding, JK, Sigmarsson, O (2012) Geothermobarometry of the 2010 Eyjafjallajökull eruption: New constraints on Icelandic magma plumbing systems J Geophys Res: Solid Earth 117(B9).

Knesel, KM, Davidson, JP (1996) Isotopic disequilibrium during melting of granite and implications for crustal contamination of magmas. Geology 24(3): 243-246.

Koulakov, I, Gordeev, EI, Dobretsov, NL, Vernikovsky, VA, Senyukov, S, Jakovlev, A, Jaxybulatov, K (2013) Rapid changes in magma storage beneath the Klyuchevskoy group of volcanoes inferred from time-dependent seismic tomography. J Volcanol Geoth Res 263: 75-91.

Koyaguchi, T, Kaneko, K (1999) A two-stage thermal evolution model of magmas in continental crust. J Petrol 40(2), 241-254. https://doi.org/10.1093/petroj/40.2.241

Lange, RA, Frey, HM, Hector, J (2009) A thermodynamic model for the plagioclase-liquid hygrometer/thermometer. Am Mineral 94(4): 494-506.

Lara, LE (2009) The 2008 eruption of the Chaitén Volcano, Chile: a preliminary report. Andean Geol 36(1): 125-129.

Lara, L, Moreno, H (2006). Geología del Complejo Volcánico Puyehue-Cordón Caulle. Región de los Lagos. Carta Geológica de Chile, Serie Geología Básica, No 99. Escala 1:50000.

Lara, LE, Orozco, G, Piña-Gauthier, M (2012) The 1835 AD fissure eruption at Osorno volcano, Southern Andes: Tectonic control by the intraarc stress field instead of remote megathrust-related dynamic strain. Tectonophysics 530, 102-110.

Le Maitre, RW, Streckeisen, A, Zanettin, B, Le Bas, MJ, Bonin, B, Bateman, P (2005) Igneous rocks: a classification and glossary of terms: recommendations of the International Union of Geological Sciences Subcommission on the Systematics of Igneous Rocks. Cambridge University Press.

Lees, JM (2007) Seismic tomography of magmatic systems. J Volcanol Geoth Res 167(1-4): 37-56.

Lohmar, S, Parada, M, Gutiérrez, F, Robin, C, Gerbe, MC (2012) Mineralogical and numerical approaches to establish the pre-eruptive conditions of the mafic Lican Ignimbrite, Villarrica Volcano (Chilean Southern Andes). J Volcanol Geotherm Res *235*, 55-69. Doi: http://doi.org/10.1016/j.jvolgeores.2012.05.006

López-Escobar, L, Cembrano, J, Moreno, H (1995) Geochemistry and tectonics of the Chilean Southern Andes basaltic Quaternary volcanism (37-46 S). Andean Geol 22(2): 219-234.

Loucks, RR (1996) A precise olivine-augite Mg-Fe-exchange geothermometer. Contrib Mineral Petrol 125(2-3): 140-150.

Marangunic, C (1974) The lahar provoked by the eruption of the Villarrica Volcano on December of 1971. In International Symposium on Volcanology, International Association of Volcanology and Chemistry of the Earth's Interior, Santiago.

Marsh, BD (1989) Magma chambers. Annu Rev Earth Pl Sc 17(1), 439-472. http://dx.doi.org/10.1146/annurev.ea.17.050189.002255

Marsh, BD (1996) Solidification fronts and magmatic evolution. Mineral Mag 60(1), 5-40. http://doi.org/10.1180/minmag.1996.060.398.03

Maurel, C, Maurel, P (1982) Étude expérimentale de la distribution de l'aluminium entre bain silicaté basique et spinelle chromifère. Implications pétrogénétiques: teneur en chrome des spinelles. Bull. Minéral 105: 197-202.

McGee, LE, Brahm, R, Rowe, MC, Handley, HK, Morgado, E, Lara, LE, Turner, MB, Vinet, N, Parada, MA. Valdivia, P (2017) A geochemical approach to distinguishing competing tectono-magmatic processes preserved in small eruptive centres. Contrib Mineral Petrol 172(6): 44.

Molina, I, Kumagai, H, Le Pennec, JL, Hall, M (2005) Three-dimensional P-wave velocity structure of Tungurahua Volcano, Ecuador. J Volcanol Geoth Res 147(1-2): 144-156.

Molina, PG, Parada, MÁ, Gutiérrez, FJ, Ma, C, Li, J, Yuanyuan, L, Reich, M, Aravena, Á (2015) Protracted late magmatic stage of the Caleu pluton (central Chile) as a consequence of heat redistribution by diking: Insights from zircon data and thermal 235hermos235g. Lithos *227*, 255-268.

Moore, G, Vennemann, T, Carmichael, ISE (1998) An empirical model for the solubility of H_2O in magmas to 3 kilobars. Am Mineral 83(1-2): 36-42.

Moreno, H (1993) Volcán Villarrica. Geología y evaluación del riesgo volcánico, Regiones IX y X, 39º25'S. Mapa geológico escala 1:50000.

Moreno, H, Clavero, J (2006) Carta Geológica de Chile. Serie Geológica Básica 98. Escala 1:50000.

Moreno, H, Lara, L, Orozco, G (2010) Geología del volcán Osorno. Servicio Nacional de Geología y Minería, Carta Geológica de Chile, Serie Geológica Básica, No. 126, Mapa escala 1:50000.

Moretti, R, Arienzo, I, Civetta, L, Orsi, G, Papale, P (2013) Multiple magma degassing sources at an explosive volcano. Earth Planet Sci Lett 367: 95-104.

Morgado, E, Parada, MÁ, Contreras, C, Castruccio, A, Gutiérrez, F, McGee, L (2015) Contrasting records from mantle to 236hermos of two nearby arc volcanic complexes: Caburgua-Huelemolle Small Eruptive Centers and Villarrica Volcano**.** J Volcanol. Geotherm Res 306:1-16. http://dx.doi.org/10.1016/j.jvolgeores.2015.09.023

Morgado, E, Parada, MÁ, Morgan, DJ, Gutiérrez, F, Castruccio, A, Contreras, C (2017) Transient shallow reservoirs beneath small eruptive centres: Constraints from Mg-Fe interdiffusion in olivine. J Volcanol Geotherm Res 347, 327-336. http://doi.org/10.1016/j.jvolgeores.2017.10.002

Munizaga, F, Hervé, F, Drake, R, Pankhurst, RJ, Brook, M, Snelling, N (1988) Geochronology of the Lake Region of south-central Chile (39–42 S): Preliminary results. J South Am Earth Sci 1(3): 309-316.

Naranjo, MF, Ebmeier, SK, Vallejo, S, Ramón, P, Mothes, P, Biggs, J, Herrera, F (2016) Mapping and measuring lava volumes from 2002 to 2009 at El Reventador Volcano, Ecuador, from field measurements and satellite remote sensing. J Appl Volcanol 5(1): 8.

Nikkhoo, M, Walter, TR, Lundgren, PR, Prats-Iraola, P (2016) Compound dislocation models (CDMs) for volcano deformation analyses. Geophys J Int 208:877-894. https://doi.org/10.1093/gji/ggw427

Pallister, JS, Hoblitt, RP, Reyes, AG (1992) A basalt trigger for the 1991 eruptions of Pinatubo volcano? Nature 356(6368): 426.

Pankhurst, MJ, Morgan, DJ, Thordarson, T, Loughlin, SC (2018) Magmatic crystal records in time, space, and process, causatively linked with volcanic unrest. Earth Planet Sci Lett 493: 231-241.

Parmigiani, A, Huber, C, Bachmann, O (2014) Mush microphysics and the reactivation of crystal-rich magma reservoirs. J. of Geophys. Res Solid Earth 119(8), 6308-6322. http://doi.org/10.1002/2014JB011124

Patanè, D, Barberi, G, Cocina, O, De Gori, P, Chiarabba, C (2006) Time-resolved seismic tomography detects magma intrusions at Mount Etna. Science 313(5788): 821-823.

Paulatto, M., Annen, C., Henstock, T. J., Kiddle, E., Minshull, T. A., Sparks, R. S. J., & Voight, B. (2012). Magma chamber properties from integrated seismic tomography and thermal modeling at Montserrat. Geochem Geophys 13(1).

Pietruszka, AJ, Garcia, MO (1999) The size and shape of Kilauea Volcano's summit magma storage reservoir: a geochemical probe. Earth Planet Sci Lett 167(3-4): 311-320.

Pizarro, C, Parada, MÁ, Contreras, C, Morgado, E (2019) Cryptic magma recharge associated with the most voluminous 20th century eruptions (1921, 1948 and 1971) at Villarrica Volcano. J Volcanol Geoth Res 384: 48-63.

Pritchard, ME, Biggs, J, Wauthier, C, Sansosti, E, Arnold, DW, Delgado, F, Ebmeier, SK, Henderson, ST, Stephens, K, Cooper, C, Wnuk, K, Amelung, F, Aguilar, V, Mothes, P, Macedo, O, Lara, LE, Poland, MP, Zoffoli, S (2018) Towards coordinated regional multi-satellite InSAR volcano observations: results from the Latin America pilot project. J Appl Volcanol 7(1): 1-28.

Putirka, KD (2005). Igneous thermometers and barometers based on plagioclase liquid equilibria: Tests of some existing models and new calibrations. Am Mineral 90(2-3): 336-346.

Putirka, KD (2008). Thermometers and barometers for volcanic systems. Rev Mineral Geochem 69(1): 61-120.

Ridolfi, F, Puerini, M, Renzulli, A, Menna, M, Toulkeridis, T (2008) The magmatic feeding system of El Reventador volcano (Sub-Andean zone, Ecuador) constrained by texture, mineralogy and thermobarometry of the 2002 erupted products. J Volcanol Geoth Res 176(1): 94-106.

Ridolfi, F, Renzulli, A (2012) Calcic amphiboles in calc-alkaline and alkaline magmas : thermobarometric and chemometric empirical equations valid up to 1,130 ° C and 2.2 Gpa, Contrib Mineral Petrol 163: 877–895. http://dx.doi.org/10.1007/s00410-011-0704-6

Ridolfi, F, Renzulli, A, Puerini, M (2010) Stability and chemical equilibrium of amphibole in calc-alkaline magmas: an overview, new thermobarometric formulations and application to subduction-related volcanoes. Contrib Mineral Petrol 160(1), 45–66. http://dx.doi.org/10.1007/s00410-009-0465-7

Roggensack, K, Hervig, RL, McKnight, SB, Williams, SN (1997) Explosive basaltic volcanism from Cerro Negro volcano: influence of volatiles on eruptive style. Science 277(5332): 1639-1642.

Roggensack, K, Williams, SN, Schaefer, SJ, Parnell, RA (1996) Volatiles from the 1994 eruptions of Rabaul: Understanding large caldera systems. Science 273(5274): 490-493. https://doi.org/10.1126/science.273.5274.490

Romero, JE, Morgavi, D, Arzilli, F, Daga, R, Caselli, A, Reckziegel, F, Viramonte, J (2016) Eruption dynamics of the 22 – 23 April 2015 Calbuco Volcano (Southern Chile): Analyses of tephra fall deposits. J Volcanol Geoth Res 317: 15–29. https://doi.org/10.1016/j.jvolgeores.2016.02.027

Ruprecht, P, Bachmann, O (2010) Pre-eruptive reheating during magma mixing at Quizapu volcano and the implications for the explosiveness of silicic arc volcanoes. Geology 38(10), 919-922. http://doi.org/10.1130/G31110.1

Samaniego, P, Eissen, JP, Le Pennec, JL, Robin, C, Hall, ML, Mothes, P, Chavrit, D, I, J (2008) Pre-eruptive physical conditions of El Reventador volcano (Ecuador) inferred from the petrology of the 2002 and 2004–05 eruptions. J Volcanol Geoth Res 176(1), 82-93.

Sauerzapf, U, Lattard, D, Burchard, M, Engelmann, R (2008) The titanomagnetite–ilmenite equilibrium: new experimental data and 238hermos-oxybarometric application to the crystallization of basic to intermediate rocks. J Petrol 49(6): 1161-1185. https://doi.org/10.1093/petrology/egn021

Senyukov, SL, Nuzhdina, IN, Droznina, SY, Garbuzova, VT, Kozhevnikova, TY, Sobolevskaya, OV, Nazarova, ZA, Bliznetsov, VE (2015) Reprint of" Seismic monitoring of the Plosky Tolbachik eruption in 2012–2013 (Kamchatka Peninsula Russia)". J Volcanol Geoth Res 307: 47-59.

SERNAGEOMIN (2011) Reporte especial de actividad volcánica (REAV) – Región de los Ríos, 2015. Boletín 26.

SERNAGEOMIN (2015a) Reporte especial de actividad volcánica (REAV)—Región de los Lagos, 2015, Abril 22

SERNAGEOMIN (2015b) Reporte especial de actividad volcánica (REAV)—Región de los Lagos, 2015, Abril—Volumen 4ª

SERNAGEOMIN (2017a) Red Nacional de Vigilancia Volcánica, Volcán Calbuco. http://www.sernageomin.cl/volcan-calbuco/. Accesed 27 June 2018.

SERNAGEOMIN (2017b) Red Nacional de Vigilancia Volcánica, Volcán Osorno. https://www.sernageomin.cl/volcan-osorno/. Accesed 27 June 2018.

Shejwalkar, A, Coogan, LA (2013). Experimental calibration of the roles of temperature and composition in the Ca-in-olivine geothermometer at 0.1 Mpa. Lithos, 177, 54-60.

Sigmarsson, O, Vlastelic, I, Andreasen, R, Bindeman, I, Devidal, JL, Moune, S, Keiding, JK, Larsen, G, Höskuldsson, A, Thordarson, T. (2011). Remobilization of silicic intrusion by mafic magmas during the 2010 Eyjafjallajökull eruption. Solid Earth 2(2): 271-281.

Sigmundsson, F, Hreinsdóttir, S, Hooper, A, Árnadóttir, T, Pedersen, R, Roberts, MJ, Óskarsson N, Auriac, A, Decriem, J, Einarsson, P, Geirsson, H, Hensch, M, Ófeigsson BG,

Sturkell E, Sveinbjörnsson H, Feigl, KL (2010). Intrusion triggering of the 2010 Eyjafjallajökull explosive eruption. Nature 468(7322): 426.

Silva-Parejas, C, Lara, LE, Bertin, D, Amigo, Á, Orozco, G (2012) The 2011-2012 eruption of Cordón Caulle volcano (Southern Andes): Evolution, crisis management and current hazards. EGU General Assembly Vienna.

Sparks, RSJ (2003) Forecasting volcanic eruptions. Earth Planet Sci Lett 210(1-2): 1-15.

Sparks, RSJ, Biggs, J, Neuberg, JW (2012) Monitoring volcanoes. Science 335(6074): 1310-1311.

Sparks, RSJ, Cashman, KV (2017) Dynamic magma systems: Implications for forecasting volcanic activity. Elements 13(1): 35-40.

Spera, FJ, Bohrson, WA (2018) Rejuvenation of crustal magma mush: A tale of multiply nested processes and timescales. Am J Sci 318, 90-140. http://doi.org/10.2475/01.2018.05

Stern, CR, Moreno, H, López-Escobar, L, Clavero, JE, Lara, LE, Naranjo, JA, Parada, MÁ, Skewes, MA (2007) Chilean Volcanoes. In: Moreno, T., Gibbons, W. (eds) The Geology of Chile, Geological Society of London, London pp. 149-180.

Stix, J (2018) Understanding Fast and Slow Unrest at Volcanoes and Implications for Eruption Forecasting. Frontiers Earth Sci 6.

Streck, M. J. (2014). Evaluation of crystal mush extraction models to explain crystal-poor rhyolites. J Volcanol Geoth Res 284: 79-94.

Sun, SS, McDonough, WS (1989) Chemical and isotopic systematics of oceanic basalts: implications for mantle composition and processes. Geological Society, London, Special Publications, 42(1), 313-345. https://doi.org/10.1144/GSL.SP.1989.042.01.19

Szymanowski, D, Wotzlaw, JF, Ellis, BS, Bachmann, O, Guillong, M, von Quadt, A (2017) Protracted near-solidus storage and pre-eruptive rejuvenation of large magma reservoirs. Nat Geosci.

Tait, S, Jaupart, C, Vergniolle, S (1989) Pressure, gas content and eruption periodicity of a shallow, crystallising magma chamber. Earth Planet Sci Lett 92(1): 107-123.

Tarasewicz, J, White, RS, Brandsdóttir, B, Thorbjarnardóttir, B (2011) Location accuracy of earthquake hypocentres beneath Eyjafjallajökull, Iceland, prior to the 2010 eruptions. Jökull 61: 33-50.

Vander Auwera, J, Namur, O, Dutrieux, A, Wilkinson, CM, Ganerød, M, Coumont, V, Bolle, O (2019) Mantle melting and magmatic processes under La Picada stratovolcano (CSVZ, Chile). J Petrol 60(5): 907-944.

Viccaro, M, Giuffrida, M, Nicotra, E, Cristofolini, R (2016) Timescales of magma storage and migration recorded by olivine crystals in basalts of the March–April 2010 eruption at Eyjafjallajökull volcano, Iceland. Am Mineral 101(1): 222-230.

Chapter 6

6. Conclusions

In this thesis, I have investigated the last eruptions of two active stratovolcanoes from the Central Southern Volcanic Zone of the Andes: the April 2015 Calbuco and the 1835 Osorno eruptions. These are the main conclusions for the studied volcanoes and the region:

- Magma reservoirs were recognised beneath Calbuco and Osorno in the upper crust, based on amphibole barometry (Calbuco, Chapter 2) and numerical modelling (Osorno, Chapter 4). Those magma reservoirs have crystal mushes within, inferred from textural features, this feature could work as rheological barrier to new magma inputs, preventing magma mixing and enhancing explosive eruptions (Chapter 5).
- Thermometry of silicate mineral phases yielded temperatures of ~985 ºC for Calbuco products (Chapter 2) and ~1,140 ºC for Osorno products (Chapter 4).
- Fe-Ti oxides thermometry in Calbuco samples inferred to be from the middle of the reservoir yielded temperatures of ~930ºC (Chapter 2). Whereas Fe-Ti oxides thermometry in Calbuco one sample inferred to be from the bottom of the magma reservoir recorded a heating event of temperatures up to ~1,070 ºC. No evidence of magma mixing was found (Chapter 2).
- In those samples from Calbuco, which are inferred to be from the middle of the reservoir, compositional profiles across ilmenite-titanomagnetite junctions gave, via diffusion chronometry, a timescale of stable temperature and oxygen fugacity conditions at > one year (Chapter 3). By contrast, in the sample recording the heating, compositional profiles across ilmenite-titanomagnetite junctions, which gave (via diffusion chronometry) timescales from heating to eruption < 4 days. The peak of

density of the calculated timescales coincides with the seismic swarm before the eruption (Chapter 3).

- In Osorno samples, mineral textures indicate mush disaggregation before the eruption (presumably due to heating or volatile addition; Chapter 4).
- In the region (including Calbuco, Osorno, and La Picada stratovolcanoes and La Viguería small eruptive centre), stratovolcano products exhibit both higher fluid input from slab to the mantle wedge (represented as a mixture between sediments from the trench and the altered oceanic crust) and partial melting degree (Chapter 4). Sr and Nd isotopic ratios suggest the fluid input comes from altered oceanic crust (AOC) and sediments in a ratio of 7:3 (AOC:sediments). The variations of composition of the products of the region are controlled by fluid input from the subducting slab (Chapter 4) and presumably mantle heterogeneity rather than crustal assimilation.
- Considering that fluid input, the potential of crustal contamination was investigated: for Calbuco products the most plausible mixture is ~25% of granulite and ~5% of granodiorite and for Osorno products the most plausible mixture is ~10% of granulite and ~5% of granodiorite assimilation. The pre-eruptive temperatures calculated for Calbuco and Osorno magmas (Chapters 2 and 4, respectively) are consistent with the assimilation of granulite at the lower crust (> 15 km; Vielzeuf et al., 1990) and granodiorite at upper crust (< 10 km; Munizaga et al., 1988; Knesel and Davidson, 1996; Adriasola et al., 2006; Aragón et al., 2011).

6.1. References

Adriasola, AC, Thomson, SN, Brix, MR, Hervé, F, Stöckhert, B (2006) Postmagmatic cooling and late Cenozoic denudation of the North Patagonian Batholith in the Los Lagos region of Chile, 41− 42 15′ S. Inter J Earth Sci 95(3): 504-528.

Aragón, E., Castro, A., Díaz-Alvarado, J., Liu, D.-Y. (2011) The North Patagonian batholith at Paso Puyehue (Argentina-Chile). SHRIMP ages and compositional features. Journal of South American Earth Sciences 32, 547-554.

Knesel, KM, Davidson, JP (1996) Isotopic disequilibrium during melting of granite and implications for crustal contamination of magmas. Geology 24(3): 243-246.

Munizaga, F, Hervé, F, Drake, R, Pankhurst, RJ, Brook, M, Snelling, N (1988) Geochronology of the Lake Region of south-central Chile (39–42 S): Preliminary results. J South Am Earth Sci 1(3): 309-316.

Vielzeuf, D, Clemens, JD, Pin, C, Moinet, E (1990) Granites, granulites, and crustal differentiation. In Granulites and crustal evolution (pp. 59-85). Springer, Dordrecht

Appendix A

Supplementary Material for Chapter 2

The material presented in the Appendix A was included as online Supplementary Material in the following article:

Morgado, E., Morgan, D.J., Harvey, J., Parada, M.Á., Castruccio, A., Brahm, R., Gutiérrez, F., Georgiev, B., Hammond, S.J., 2019. Localised heating and intensive magmatic conditions prior to the 22–23 April 2015 Calbuco volcano eruption (Southern Chile). Bulletin of Volcanology, v. 81:24. DOI: 10.1007/s00445-019-1280-2

A.1. Rare earth elements

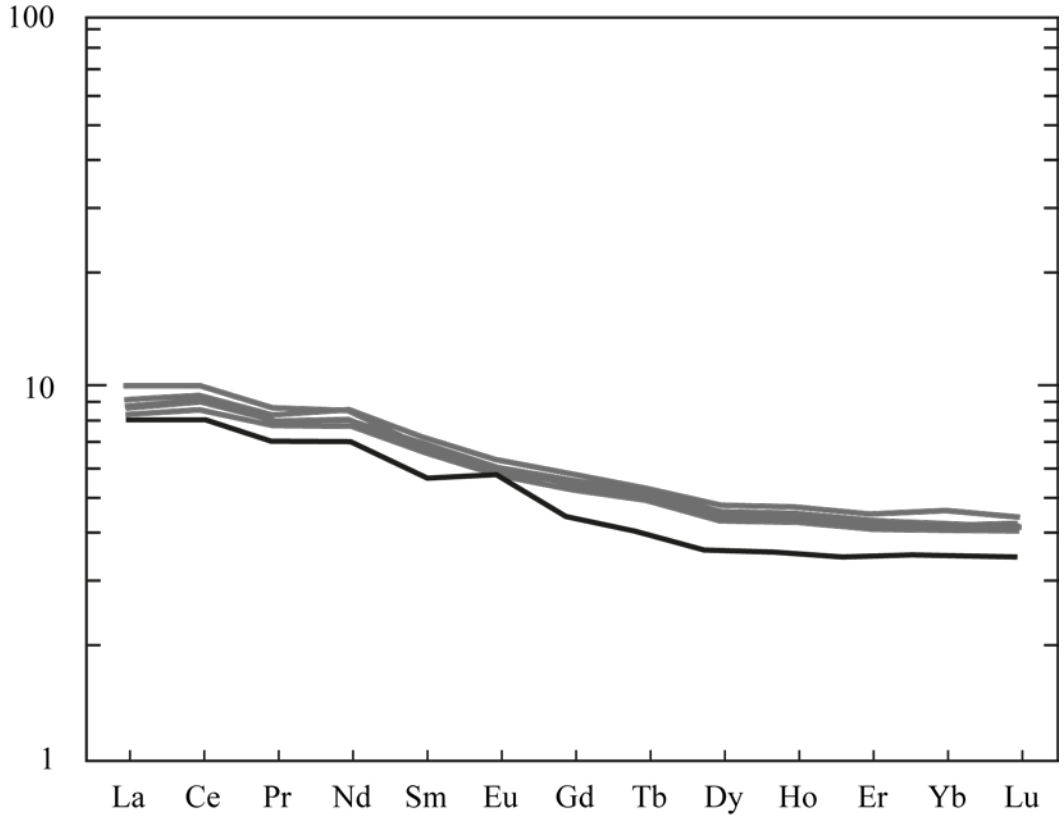

Figure A1. Rare earth elements (REE) diagram showing a narrow range of La_N/Yb_N from 2 to 2.4. Only the sample Cal-155 (black solid line) shows a slight Eu positive anomaly. Values normalised to chondrite composition (Sun and McDonough, 1989).

A.2. Mineral chemistry

Table A1. Compositions of amphibole from the April 2015 Calbuco eruption (wt%).

SAMPLE	SiO_2	TiO_2	Al_2O_3	FeO	MnO	MgO	CaO	Na_2O	K_2O	Cr_2O_3	F	Cl	TOTAL
149TA_amph_Fig42a_cx1_1	42.603	3.089	9.869	14.186	0.011	12.573	10.824	2.609	0.217	0.000	0.056	0.072	96.109
149TA_amph_Fig42a_cx1_2	42.669	3.086	9.769	14.031	0.000	12.659	10.942	2.533	0.218	0.000	0.066	0.108	96.081
149TA_amph_Fig41a_cx1_1	42.666	3.188	10.297	13.983	0.000	12.378	10.963	2.680	0.219	0.002	0.054	0.115	96.545
149TA_amph_Fig41a_cx3	42.992	3.019	9.923	14.549	0.000	12.634	10.928	2.608	0.231	0.006	0.057	0.089	97.037
149TA_amph_Fig40a_cx1	42.440	3.105	9.951	14.433	0.000	12.487	10.926	2.592	0.215	0.004	0.061	0.072	96.285
149TA_amph_Fig40a_cx2	42.910	2.999	10.077	14.457	0.007	12.495	10.881	2.611	0.238	0.017	0.063	0.087	96.840
149TA_amph_Fig39a_cx1	42.807	2.998	9.865	14.110	0.000	12.653	11.048	2.494	0.222	0.026	0.059	0.067	96.351
149TA_amph_Fig38a_cx2_1	42.955	3.041	10.016	14.275	0.011	12.440	11.059	2.626	0.234	0.000	0.055	0.096	96.807
149TA_amph_Fig38a_cx2_2	42.890	3.042	10.080	14.471	0.021	12.522	10.950	2.670	0.226	0.009	0.058	0.102	97.041
149TA_amph_Fig38a_cx1	43.086	3.067	9.870	14.159	0.000	12.940	10.866	2.589	0.236	0.000	0.062	0.079	96.954
149TA_amph_Fig37a_cx1_1	43.187	2.897	9.723	14.014	0.000	12.764	10.830	2.632	0.245	0.004	0.054	0.157	96.507
149TA_amph_Fig37a_cx1_2	42.851	2.964	9.899	14.222	0.000	12.374	10.783	2.635	0.242	0.032	0.055	0.148	96.204
149TA_amph_Fig36a_cx2	42.757	3.037	9.976	14.161	0.007	12.597	10.768	2.618	0.226	0.000	0.023	0.172	96.341
149TA_amph_Fig36a_cx1	43.022	3.064	9.601	13.882	0.006	12.544	10.844	2.664	0.242	0.000	0.021	0.146	96.035
149TA_amph_Fig34a_cx1_1	42.201	3.132	10.127	13.944	0.000	12.598	10.861	2.703	0.227	0.014	0.055	0.123	95.986
149TA_amph_Fig34a_cx1_2	43.028	3.047	10.083	14.257	0.026	12.591	10.735	2.638	0.230	0.002	0.054	0.100	96.791
149TA_amph_Fig33a_cx1	43.121	3.096	9.871	13.948	0.000	12.839	10.878	2.569	0.235	0.009	0.056	0.110	96.731
149TA_amph_Fig33a_cx3	43.061	3.069	10.040	14.350	0.000	12.457	11.051	2.579	0.229	0.000	0.054	0.126	97.015
149TA_amph_Fig33a_cx2	42.930	3.113	10.054	14.018	0.010	12.604	10.837	2.598	0.238	0.002	0.055	0.041	96.499
149TA_amph_Fig32a_cx1	43.098	2.997	9.966	14.252	0.006	12.577	10.779	2.552	0.218	0.000	0.063	0.086	96.593

Table A1. (Continued)

SAMPLE	SiO_2	TiO_2	Al_2O_3	FeO	MnO	MgO	CaO	Na_2O	K_2O	Cr_2O_3	F	Cl	TOTAL
149TA_am_Fig32a_cx2_1	42.715	3.061	9.950	14.150	0.000	12.601	10.883	2.734	0.227	0.000	0.055	0.117	96.492
149TA_am_Fig32a_cx2_2	42.974	2.958	9.816	14.058	0.000	12.524	10.930	2.543	0.230	0.005	0.057	0.118	96.214
149TA_am_Fig31a_cx2	42.603	3.124	9.931	14.145	0.021	12.594	10.912	2.591	0.233	0.000	0.054	0.055	96.263
149TA_am_Fig31a_cx1_1	42.669	3.068	9.909	14.133	0.000	12.496	10.937	2.611	0.241	0.000	0.059	0.076	96.201
149TA_am_Fig31a_cx1_2	42.789	2.958	9.954	14.294	0.000	12.462	10.902	2.533	0.237	0.000	0.055	0.070	96.254
149TA_am_Fig31a_cx3	42.732	3.078	10.193	14.033	0.000	12.595	10.825	2.671	0.225	0.014	0.059	0.071	96.497
149TA_am_Fig31a_cx5	43.152	2.943	10.047	14.363	0.011	12.478	10.930	2.567	0.228	0.001	0.025	0.157	96.903
149TA_am_Fig30a_2	43.147	3.010	9.864	14.253	0.000	12.585	10.908	2.623	0.240	0.011	0.053	0.146	96.840
149TA_am_Fig29a_cx2	42.809	3.129	10.132	14.195	0.003	12.420	10.864	2.642	0.236	0.001	0.061	0.033	96.526
149TA_am_Fig29a_cx3	42.893	3.112	9.927	14.114	0.000	12.529	10.856	2.655	0.248	0.020	0.000	-0.098	96.256
149TA_am_Fig29a_cx1	42.813	2.968	9.702	14.347	0.000	12.455	10.827	2.569	0.220	0.000	0.058	0.122	96.082
149TA_am_Fig28a_cx7_1	42.661	3.146	10.048	13.954	0.000	12.814	10.884	2.652	0.241	0.000	0.095	0.277	96.771
149TA_am_Fig28a_cx7_2	42.755	3.097	10.002	13.906	0.000	12.715	10.953	2.699	0.220	0.008	0.131	0.039	96.525
149TA_am_Fig28a_cx3_1	42.911	3.045	10.047	14.195	0.000	12.626	10.767	2.519	0.246	0.000	0.000	0.041	96.396
149TA_am_Fig28a_cx3_2	43.256	2.984	10.017	13.911	0.000	12.780	10.903	2.606	0.215	0.015	0.041	0.054	96.781
149TA_am_Fig27a_cx3_1	43.453	2.849	9.647	14.109	0.000	12.750	10.838	2.493	0.247	0.020	0.143	0.046	96.595
149TA_am_Fig27a_cx3_2	42.629	3.126	10.144	13.896	0.035	12.531	10.802	2.598	0.244	0.008	0.000	0.047	96.058
149TA_am_Fig27a_cx3_3	42.819	3.065	9.930	13.980	0.000	12.852	10.768	2.630	0.224	0.000	0.082	0.047	96.398
149TA_am_Fig26a_cx4_1	42.970	3.061	10.002	13.835	0.001	12.792	10.807	2.615	0.225	0.025	0.000	0.041	96.375
149TA_am_Fig26a_cx4_2	42.911	3.017	9.695	14.056	0.000	12.747	10.717	2.611	0.244	0.000	0.000	0.046	96.045

Table A1. (Continued)

SAMPLE	SiO_2	TiO_2	Al_2O_3	FeO	MnO	MgO	CaO	Na_2O	K_2O	Cr_2O_3	F	Cl	TOTAL
149TA_amph_Fig25a_cx3_1	42.958	3.091	9.838	13.831	0.022	12.878	10.856	2.515	0.220	0.016	0.000	0.043	96.267
149TA_amph_Fig25a_cx3_2	42.983	3.064	9.919	13.973	0.009	12.993	10.976	2.698	0.243	0.025	0.318	0.058	97.258
149TA_amph_Fig24a_cx2_1	42.729	2.954	10.024	13.942	0.000	12.598	10.816	2.601	0.226	0.026	0.000	0.062	95.978
149TA_amph_Fig24a_cx2_2	42.758	2.998	10.020	14.280	0.005	12.568	10.861	2.574	0.220	0.003	0.108	0.043	96.437
149TA_amph_Fig24a_cx3	42.782	3.049	10.062	14.298	0.000	12.679	10.784	2.673	0.241	0.000	0.000	0.063	96.630
149TA_amph_Fig23a_cx2	42.749	3.136	10.002	14.152	0.149	12.789	10.880	2.551	0.245	0.005	0.208	0.052	96.918
149TA_amph_Fig23a_cx3	42.696	2.992	9.834	14.298	0.012	12.661	11.041	2.635	0.238	0.006	0.033	0.057	96.502
149TA_amph_Fig22a_cx2_1	43.082	3.089	9.982	14.197	0.001	12.718	10.813	2.651	0.221	0.002	0.000	0.056	96.813
149TA_amph_Fig22a_cx2_2	42.943	3.109	9.964	13.960	0.000	12.773	10.900	2.600	0.255	0.000	0.004	0.045	96.553
149TA_amph_Fig21a_cx2_1	42.670	3.018	10.017	13.742	0.000	12.859	10.850	2.587	0.236	0.032	0.000	0.035	96.047
149TA_amph_Fig21a_cx2_2	43.158	2.905	9.546	13.634	0.000	12.913	10.827	2.608	0.225	0.011	0.243	0.048	96.117
149TA_amph_Fig21a_cx2_3	42.815	3.042	9.985	13.962	0.005	12.571	10.907	2.616	0.222	0.002	0.000	0.042	96.170
149TA_amph_Fig20a_cx2_1	42.946	3.117	10.098	14.283	0.006	12.643	10.933	2.628	0.246	0.009	0.000	0.039	96.947
149TA_amph_Fig20a_cx2_2	42.535	3.158	10.105	14.315	0.000	12.671	10.917	2.675	0.243	0.007	0.000	0.047	96.672
149TA_amph_Fig19a_cx2_1	43.072	2.945	9.789	13.854	0.028	12.858	10.852	2.606	0.218	0.020	0.000	0.039	96.283
149TA_amph_Fig19a_cx2_2	42.750	3.017	10.033	14.247	0.003	12.369	10.928	2.650	0.234	0.011	0.072	0.050	96.362
149TA_amph_Fig19a_cx2_3	42.931	2.960	9.663	13.765	0.032	12.858	10.801	2.559	0.227	0.000	0.071	0.045	95.909
149TA_amph_Fig19a_cx3	42.738	3.171	9.976	14.030	0.000	12.699	10.942	2.638	0.233	0.010	0.010	0.053	96.498
149TA_amph_Fig18a_cx2_1	43.108	2.956	9.917	14.332	0.000	12.779	10.808	2.558	0.240	0.080	0.142	0.059	96.977
149TA_amph_Fig18a_cx2_2	42.932	2.990	10.106	14.109	0.003	12.667	10.932	2.614	0.234	0.000	0.203	0.028	96.817

Table A1. (Continued)

SAMPLE	SiO_2	TiO_2	Al_2O_3	FeO	MnO	MgO	CaO	Na_2O	K_2O	Cr_2O_3	F	Cl	TOTAL
149TA_amph_Fig18a_cx3	43.046	3.152	9.990	13.878	0.000	12.836	10.780	2.590	0.213	0.000	0.156	0.031	96.672
149TA_amph_Fig17_cx3_1	42.570	3.018	10.067	14.337	0.011	12.616	10.956	2.631	0.242	0.000	0.023	0.052	96.524
149TA_amph_Fig17_cx3_2	43.311	2.676	9.580	13.864	0.000	12.651	11.812	2.501	0.221	0.003	0.071	0.042	96.732
149TA_amph_Fig16a_1	43.127	2.966	9.935	14.099	0.001	12.813	10.805	2.543	0.226	0.000	0.000	0.040	96.554
149TA_amph_Fig16a_2	42.698	3.039	9.948	14.029	0.000	12.850	10.986	2.558	0.242	0.008	0.034	0.052	96.443
149TA_amph_Fig15a_cx2_1	42.786	3.027	9.845	13.900	0.000	12.709	10.871	2.534	0.236	0.000	0.000	0.054	95.960
149TA_amph_Fig15a_cx2_2	42.781	3.122	10.021	13.967	0.000	12.833	10.848	2.593	0.238	0.010	0.035	0.052	96.499
149TA_amph_Fig15a_cx2_3	42.738	3.092	9.811	14.199	0.000	12.588	10.889	2.563	0.227	0.013	0.116	0.048	96.285
149TA_amph_Fig14a_cx2	42.717	3.127	10.006	13.930	0.009	12.696	10.901	2.535	0.213	0.012	0.282	0.047	96.476
149TA_amph_Fig14a_cx3_1	42.571	3.258	9.919	14.055	0.007	12.599	10.895	2.528	0.235	0.017	0.000	0.049	96.133
149TA_amph_Fig14a_cx4_1	42.262	3.353	10.224	14.041	0.006	12.425	10.969	2.549	0.239	0.000	0.169	0.053	96.289
149TA_amph_Fig14a_cx4_2	42.734	3.143	9.761	14.258	0.021	12.587	10.842	2.564	0.245	0.018	0.057	0.054	96.284
149TA_amph_Fig11a_cx1	42.672	3.232	10.022	14.100	0.027	12.667	10.888	2.548	0.225	0.001	0.000	0.042	96.423
149TA_amph_Fig11a_cx2	42.713	3.150	10.171	14.460	0.028	12.614	10.858	2.567	0.241	0.020	0.046	0.053	96.922
149TA_amph_Fig10a_cx2_1	42.789	3.083	10.093	14.339	0.000	12.653	10.790	2.620	0.219	0.027	0.119	0.042	96.774
149TA_amph_Fig10a_cx2_2	42.627	3.206	10.341	14.100	0.000	12.458	10.741	2.661	0.239	0.002	0.168	0.057	96.601
149TA_amph_Fig10a_cx4	42.408	3.163	10.013	14.242	0.009	12.337	10.847	2.595	0.250	0.000	0.000	0.061	95.924
149TA_amph_Fig9a_cx1	43.345	3.102	9.614	14.356	0.000	12.557	10.752	2.625	0.240	0.000	0.167	0.058	96.817
149TA_amph_Fig9a_cx3_1	42.808	3.215	10.001	13.778	0.000	12.636	10.813	2.637	0.234	0.000	0.209	0.041	96.371
149TA_amph_Fig9a_cx3_2	42.652	3.208	9.891	13.992	0.030	12.404	10.757	2.491	0.223	0.000	0.035	0.043	95.727

Table A1. Continued.

SAMPLE	SiO_2	TiO_2	Al_2O_3	FeO	MnO	MgO	CaO	Na_2O	K_2O	Cr_2O_3	F	Cl	TOTAL
149TA_amph_Fig8a_cx2	42.972	3.011	9.795	14.063	0.000	12.614	10.782	2.570	0.223	0.011	0.020	0.049	96.108
149TA_amph_Fig8a_cx3	43.064	3.111	9.853	14.157	0.003	12.518	10.857	2.580	0.251	0.009	0.246	0.060	96.711
149TA_amph_Fig7a_cx1_1	43.336	3.036	9.447	13.811	0.002	13.115	10.786	2.589	0.220	0.006	0.047	0.044	96.438
149TA_amph_Fig7a_cx1_2	42.650	3.071	9.680	13.903	0.025	12.836	10.897	2.501	0.226	0.000	0.144	0.059	95.993
149TA_amph_Fig6a_cx1_1	42.719	3.267	9.917	13.894	0.000	12.620	10.838	2.569	0.225	0.000	0.000	0.056	96.106
149TA_amph_Fig6a_cx1_2	42.779	3.263	10.033	14.192	0.014	12.604	10.785	2.603	0.232	0.000	0.132	0.043	96.681
149TA_amph_Fig5a_cx1_1	42.884	3.158	9.942	14.205	0.000	12.494	10.814	2.548	0.236	0.005	0.000	0.055	96.342
149TA_amph_Fig5a_cx1_2	42.980	3.146	9.859	14.005	0.000	12.730	10.873	2.597	0.218	0.000	0.000	0.047	96.456
149TA_amph_Fig4a_cx1_1	42.847	3.119	9.969	14.128	0.000	12.666	10.816	2.596	0.244	0.022	0.107	0.062	96.576
149TA_amph_Fig4a_cx2_1	42.492	3.204	9.877	14.152	0.016	12.534	10.950	-0.301	0.231	0.018	0.020	0.050	93.242
149TA_amph_Fig3a_cx4_1	42.833	3.150	10.061	14.229	0.008	12.737	10.727	2.538	0.245	0.004	0.208	0.047	96.786
149TA_amph_Fig3a_cx3_1	43.165	3.133	9.904	13.837	0.010	12.801	10.781	2.555	0.246	0.000	0.000	0.052	96.485
149TA_amph_Fig3a_cx2_1	42.881	3.192	9.856	14.289	0.000	12.590	10.847	2.611	0.236	0.000	0.057	0.048	96.607
149TA_amph_Fig2a_cx1_1	42.738	3.007	9.883	14.092	0.000	12.600	10.847	2.587	0.244	0.007	0.317	0.047	96.370
149TA_amph_Fig2a_cx1_2	42.665	3.138	10.068	14.065	0.000	12.747	10.863	2.551	0.233	0.000	0.097	0.054	96.482
149TA_amph_Fig1a_cx1_1	42.900	3.065	9.872	14.273	0.000	12.535	10.953	2.602	0.217	0.000	0.195	0.056	96.668
149TA_amph_Fig1a_cx1_2	42.907	3.105	9.824	14.100	0.004	12.760	10.853	2.652	0.230	0.029	0.315	0.051	96.832
160_amph_Fig1a_cx1	43.700	2.608	9.289	14.135	0.000	12.910	10.849	2.285	0.295	0.013	0.099	0.254	96.438
160_amph_Fig1a_cx2	44.002	2.526	9.147	14.423	0.000	13.022	10.728	2.273	0.294	0.003	0.091	0.238	96.747
160_amph_Fig1a_cx3	43.573	2.644	9.226	14.718	0.009	12.512	10.873	2.364	0.283	0.014	0.100	0.257	96.574

Table A1. (Continued)

SAMPLE	SiO_2	TiO_2	Al_2O_3	FeO	MnO	MgO	CaO	Na_2O	K_2O	Cr_2O_3	F	Cl	TOTAL
160_amph_Fig2a_cx1_1	43.664	2.626	9.030	14.427	0.000	12.605	10.773	2.238	0.313	0.018	0.117	0.287	96.098
160_amph_Fig2a_cx1_2	43.817	2.656	9.020	14.301	0.000	12.835	10.782	2.341	0.334	0.003	0.118	0.219	96.426
160_amph_Fig3a_cx1_1	43.445	2.660	9.035	14.532	0.005	12.446	10.987	2.420	0.321	0.000	0.108	0.326	96.285
160_amph_Fig4a_cx2_1	43.608	2.596	9.247	14.490	0.000	12.776	11.091	2.324	0.321	0.008	0.106	0.286	96.854
160_amph_Fig5a_cx4_1	44.111	2.443	8.766	14.141	0.007	13.066	11.087	2.170	0.295	0.019	0.094	0.304	96.503
160_amph_Fig5a_cx4_2	44.031	2.535	8.919	14.155	0.005	13.071	11.006	2.175	0.304	0.012	0.027	0.161	96.400
160_amph_Fig6a_cx1_1	44.147	2.462	8.878	14.151	0.000	12.857	10.827	2.129	0.323	0.009	0.024	0.139	95.947
160_amph_Fig6a_cx1_2	44.116	2.431	9.022	14.524	0.006	12.777	10.927	2.224	0.298	0.034	0.008	0.093	96.461
160_amph_Fig7a_cx1_1	44.061	2.471	8.866	14.308	0.000	12.975	10.819	2.224	0.326	0.000	0.106	0.094	96.251
160_amph_Fig7a_cx1_3	43.875	2.511	8.820	14.182	0.000	12.797	10.957	2.275	0.337	0.000	0.156	0.096	96.006
160_amph_Fig8a_cx1	44.442	2.338	8.590	13.806	0.023	13.253	11.062	2.161	0.323	0.027	0.180	0.106	96.311
160_amph_Fig9a_cx1_1	44.485	2.252	8.493	14.511	0.000	13.182	11.070	2.215	0.334	0.018	0.172	0.102	96.835
160_amph_Fig3a_cx1_2	43.660	2.655	9.168	14.337	0.000	13.045	11.095	2.231	0.326	0.036	0.628	0.103	97.283
160_amph_Fig4a_cx1_1	43.616	2.619	9.239	14.239	0.022	12.937	11.056	2.324	0.340	0.015	0.500	0.099	97.008
160_amph_Fig5a_cx1	41.990	2.664	10.994	13.638	0.000	12.833	11.269	2.654	0.356	0.000	0.316	0.083	96.798
160_amph_Fig7a_cx1_2	44.011	2.544	8.848	13.904	0.003	12.964	11.051	2.243	0.326	0.000	0.479	0.106	96.479
160_amph_Fig8a_cx3	43.963	2.416	8.764	14.416	0.000	12.972	11.002	2.136	0.322	0.004	0.000	0.108	96.102

Table A2. Compositions of ortho- and clino- pyroxenes from the April 2015 Calbuco eruption (wt%).

SAMPLE	SiO_2	TiO_2	Al_2O_3	FeO	MnO	MgO	CaO	Cr_2O_3	K_2O	Na_2O	NiO	TOTAL
Cal-149TA_Fig2_cx13	52.835	0.198	0.836	19.238	0.562	24.357	1.394	0.000	0.002	0.000	0.000	99.421
Cal-149TA_Fig2_cx12_2	51.888	0.562	2.386	9.720	0.339	14.459	21.167	0.000	0.000	0.358	0.000	100.879
Cal-149TA_Fig2_cx14	53.435	0.124	0.668	19.682	0.541	23.842	1.370	0.016	0.000	0.027	0.005	99.710
Cal-149TA_Fig2_cx12_1	51.777	0.466	2.036	9.619	0.375	14.526	21.192	0.003	0.000	0.321	0.000	100.313
Cal-149TA_Fig2_cx16_1	51.593	0.467	1.860	9.345	0.334	15.161	20.965	0.008	0.003	0.308	0.001	100.045
Cal-149TA_Fig2_cx16_2	51.376	0.493	2.003	9.595	0.335	14.824	20.928	0.000	0.002	0.332	0.000	99.887
Cal-149TA_Fig2_cx15	52.502	0.473	1.892	9.358	0.327	15.006	21.168	0.010	0.000	0.323	0.005	101.063
Cal-149TA_Fig10_cx2	53.535	0.150	0.594	19.267	0.601	24.472	1.358	0.011	0.000	0.007	0.001	99.996
Cal-149TA_Fig10_cx3	52.326	0.261	1.585	20.148	0.627	23.328	1.406	0.004	0.002	0.015	0.000	99.703
Cal-149TA_Fig10_cx5	52.893	0.163	0.691	19.718	0.634	24.136	1.428	0.000	0.000	0.003	0.000	99.665
Cal-149TA_Fig10_cx6	52.906	0.167	0.724	19.688	0.649	23.843	1.412	0.007	0.001	0.010	0.000	99.407
Cal-149TA_Fig14_cx17	52.686	0.254	0.872	19.490	0.598	23.774	1.424	0.000	0.003	0.007	0.000	99.109
Cal-149TA_Fig14_cx10	52.303	0.357	1.622	19.939	0.529	23.194	1.583	0.010	0.001	0.021	0.000	99.558
Cal-149TA_Fig14_cx18	51.840	0.447	1.614	10.038	0.385	14.482	21.153	0.004	0.007	0.302	0.003	100.275
Cal-149TA_Fig14_cx11	50.394	0.647	2.268	9.628	0.321	14.770	20.702	0.008	0.000	0.357	0.000	99.095
Cal-149TA_Fig14_cx11a	51.583	0.431	1.442	9.951	0.375	14.487	21.267	0.000	0.002	0.307	0.000	99.845
Cal-149TA_Fig14_cx20	51.557	0.321	1.444	19.062	0.478	23.982	1.622	0.000	0.003	0.017	0.001	98.486
Cal-149TA_Fig14_cx19	49.525	0.820	3.034	10.321	0.345	13.800	20.821	0.009	0.001	0.339	0.000	99.015
Cal-149TA_Fig14_cx1_1	50.790	0.596	2.129	9.594	0.310	14.806	20.935	0.004	0.000	0.348	0.000	99.512
Cal-149TA_Fig14_cx2	52.358	0.315	1.269	18.422	0.510	24.715	1.536	0.000	0.000	0.019	0.003	99.147
Cal-149TA_Fig23_c12_1	51.081	0.422	1.447	10.510	0.457	14.245	21.103	0.003	0.003	0.307	0.000	99.578
Cal-149TA_Fig23_cx1_1	51.291	0.336	1.383	19.773	0.515	23.405	1.816	0.000	0.000	0.022	0.000	98.543
Cal-149TA_Fig23_cx12	50.538	0.563	1.995	9.756	0.322	14.742	20.911	0.000	0.000	0.313	0.003	99.142

Table A2. (Continued)

SAMPLE	SiO_2	TiO_2	Al_2O_3	FeO	MnO	MgO	CaO	Cr_2O_3	K_2O	Na_2O	NiO	TOTAL
Cal-149TA_Fig23_cx1_2	51.416	0.320	1.327	19.533	0.504	23.677	1.805	0.002	0.002	0.025	0.013	98.624
Cal-149TA_F31_cx12_1	52.187	0.228	0.713	21.433	0.585	22.690	1.575	0.008	0.000	0.020	0.000	99.438
Cal-149TA_F31_cx8	50.910	0.513	1.722	9.589	0.329	15.105	20.806	0.000	0.000	0.309	0.000	99.284
Cal-149TA_F31_cx12_2	51.733	0.264	0.859	21.548	0.590	22.507	1.650	0.000	0.001	0.015	0.001	99.167
Cal-149TA_Fig31_cx9_1	52.213	0.345	1.263	21.147	0.580	22.633	1.520	0.000	0.004	0.008	0.006	99.718
Cal-149TA_Fig31_cx8_1	51.151	0.501	1.523	10.826	0.390	14.272	21.036	0.002	0.000	0.307	0.002	100.011
Cal-149TA_Fig31_cx4	51.237	0.383	1.399	10.436	0.414	14.293	21.094	0.000	0.000	0.307	0.002	99.564
Cal-149TA_Fig31_cx5	49.590	0.649	2.311	9.549	0.307	14.810	20.557	0.001	0.001	0.353	0.000	98.129
Cal-149TB_Fig3_cx10	50.531	0.642	2.322	8.983	0.285	15.135	21.047	0.000	0.000	0.310	0.005	99.258
Cal-149TB_Fig3_cx9	52.258	0.196	0.853	19.100	0.605	24.325	1.472	0.000	0.000	0.007	0.000	98.816
Cal-149TB_Fig3_cx2	51.594	0.248	1.088	19.005	0.582	24.336	1.406	0.000	0.000	0.015	0.000	98.275
Cal-149TB_Fig3_cx3	50.390	0.403	1.720	9.528	0.356	14.641	21.238	0.004	0.000	0.308	0.000	98.587
Cal-149TB_Fig3_cx8	52.880	0.269	1.306	19.724	0.607	23.580	1.530	0.000	0.001	0.012	0.000	99.910
Cal-149TB_Fig3_cx7	52.976	0.295	1.050	18.071	0.547	25.048	1.492	0.000	0.000	0.020	0.000	99.498
Cal-149TB_Fig4_cx6	51.791	0.299	1.188	18.843	0.576	24.265	1.568	0.000	0.000	0.023	0.000	98.553
Cal-149TB_Fig4_cx9	51.221	0.566	1.888	9.034	0.300	15.159	20.853	0.002	0.000	0.312	0.000	99.335
Cal-149TB_Fig4_cx3	51.237	0.471	1.624	9.219	0.318	15.937	19.977	0.000	0.000	0.226	0.005	99.015
Cal-149TB_Fig4_cx2	52.451	0.237	0.940	17.704	0.523	25.007	1.505	0.000	0.000	0.014	0.000	98.382
Cal-149TB_Fig6_cx8	52.802	0.261	0.905	17.940	0.508	24.892	1.554	0.003	0.000	0.010	0.018	98.893
Cal-149TB_Fig6_cx7	50.473	0.670	2.404	9.440	0.312	14.868	20.651	0.001	0.003	0.329	0.003	99.154
Cal-149TB_Fig5_cx6	52.753	0.282	1.118	17.730	0.505	24.987	1.515	0.000	0.001	0.006	0.001	98.898
Cal-149TB_Fig5_cx3	52.428	0.289	1.035	18.351	0.537	24.775	1.428	0.000	0.000	0.016	0.000	98.859
Cal-149TB_Fig6_cx7	49.695	0.675	2.497	10.022	0.315	14.753	20.167	0.000	0.000	0.371	0.001	98.496

Table A2. (Continued)

SAMPLE	SiO_2	TiO_2	Al_2O_3	FeO	MnO	MgO	CaO	Cr_2O_3	K_2O	Na_2O	NiO	TOTAL
Cal-149TB_Fig6_cx9	52.311	0.206	0.716	17.706	0.521	25.269	1.513	0.002	0.002	0.008	0.000	98.252
Cal-149TB_Fig8_cx1	52.530	0.258	1.005	17.888	0.538	24.814	1.842	0.000	0.001	0.025	0.000	98.901
Cal-149TB_Fig8_cx3	50.728	0.628	2.241	9.229	0.323	14.818	20.944	0.002	0.000	0.345	0.002	99.261
Cal-149TB_Fig8_cx13	50.370	0.723	2.664	9.702	0.317	14.555	20.554	0.002	0.000	0.349	0.007	99.241
Cal-149TB_Fig8_cx4	51.941	0.282	1.148	17.716	0.550	24.907	1.550	0.004	0.001	0.022	0.000	98.123
Cal-149TB_Fig8_cx4	52.559	0.229	0.861	17.774	0.552	24.839	1.720	0.000	0.001	0.031	0.015	98.580
Cal-149TB_Fig8_cx6	51.098	0.618	2.228	9.571	0.339	15.432	19.883	0.000	0.001	0.272	0.000	99.441
Cal-149TB_Fig8_cx7_8	51.864	0.387	1.567	17.468	0.539	24.668	2.187	0.000	0.002	0.019	0.000	98.700
Cal-149TB_Fig8_cx14	51.327	0.545	1.987	9.293	0.307	14.969	20.797	0.005	0.000	0.342	0.000	99.572
Cal-149TB_Fig9_med1a	52.873	0.233	0.562	17.907	0.541	25.030	1.525	0.000	0.000	0.007	0.000	98.676
Cal-149TB_Fig9_med1b	50.100	0.888	2.648	10.000	0.346	14.320	20.662	0.006	0.000	0.347	0.002	99.321
Cal-149TB_Fig9_med2a	49.740	0.818	2.449	9.707	0.328	14.529	21.023	0.000	0.000	0.342	0.000	98.937
Cal-149TB_Fig9_med2b	51.070	0.513	1.747	9.283	0.294	15.139	21.008	0.000	0.000	0.320	0.000	99.375
Cal-149TB_Fig9_med3a	51.280	0.239	1.007	9.850	0.368	14.309	21.478	0.000	0.000	0.286	0.000	98.818
Cal-149TB_Fig9_med3b	51.579	0.221	0.956	9.885	0.353	14.294	21.508	0.000	0.000	0.281	0.012	99.088
Cal-149TB_Fig9_med4a	51.915	0.371	1.401	18.385	0.537	24.465	1.500	0.000	0.000	0.015	0.000	98.588
Cal-149TB_Fig9_med4b	51.650	0.380	1.452	18.364	0.542	24.499	1.454	0.003	0.000	0.000	0.002	98.347
Cal-149TB_Fig9_med5a	52.012	0.614	2.142	9.404	0.301	14.965	20.867	0.000	0.001	0.345	0.001	100.651
Cal-149TB_Fig9_med5b	52.099	0.559	1.945	9.162	0.307	15.056	20.926	0.012	0.000	0.308	0.000	100.374
Cal-149TB_Fig9_med6a	51.382	0.638	2.297	9.288	0.287	14.843	20.910	0.001	0.000	0.330	0.009	99.985
Cal-149TB_Fig9_med6b	50.633	0.687	2.451	9.352	0.281	14.780	20.906	0.005	0.000	0.342	0.009	99.445
Cal-149TB_Fig9_med7a	53.048	0.318	1.160	18.366	0.552	24.780	1.486	0.007	0.000	0.028	0.001	99.744
Cal-149TB_Fig9_med7b	52.797	0.341	1.258	18.388	0.593	24.535	1.549	0.013	0.000	0.019	0.000	99.493

Table A2. (Continued)

SAMPLE	SiO_2	TiO_2	Al_2O_3	FeO	MnO	MgO	CaO	Cr_2O_3	K_2O	Na_2O	NiO	TOTAL
Cal-149TB_Fig9_med8a	53.213	0.302	1.131	18.306	0.546	24.899	1.469	0.004	0.000	0.015	0.005	99.888
Cal-149TB_Fig9_med8b	53.117	0.269	0.997	18.395	0.538	24.838	1.456	0.000	0.003	0.007	0.010	99.630
Cal-149TB_Fig9_med9a	52.378	0.303	1.200	18.482	0.551	24.682	1.450	0.009	0.000	0.007	0.016	99.079
Cal-149TB_Fig9_med9b	51.799	0.334	1.168	18.253	0.542	24.640	1.699	0.000	0.003	0.015	0.000	98.455
Cal-149TB_Fig9_med10a	50.794	0.702	2.466	9.355	0.328	14.833	21.042	0.000	0.000	0.322	0.003	99.846
Cal-149TB_Fig9_med10b	51.084	0.627	2.223	9.176	0.299	15.050	20.833	0.000	0.002	0.324	0.001	99.620
Cal-149TB_Fig10_opx1	51.153	0.492	1.728	9.150	0.319	15.246	20.845	0.008	0.003	0.314	0.003	99.261
Cal-149TB_Fig10_cpx2	50.352	0.640	2.395	9.279	0.291	14.801	20.777	0.004	0.004	0.314	0.004	98.861
Cal-149TB_Fig10_cx3	53.293	0.223	0.657	17.101	0.500	25.578	1.667	0.000	0.000	0.020	0.000	99.040
Cal-149TB_Fig10_cx5	52.613	0.240	0.882	17.781	0.502	25.146	1.485	0.004	0.000	0.000	0.007	98.660
149TB_Fig11_cx2	53.045	0.262	1.231	17.227	0.499	25.787	1.249	0.000	0.000	0.011	0.000	99.312
Cal-149TB_Fig11_cx4	51.957	0.359	2.198	18.145	0.512	24.587	1.559	0.000	0.000	0.014	0.005	99.335
Cal-149TB_Fig11_cx3	51.833	0.325	1.655	18.021	0.515	25.108	1.360	0.012	0.000	0.017	0.000	98.846
Cal-149TB_Fig11_cx5	52.877	0.377	2.225	17.762	0.482	24.720	1.653	0.000	0.004	0.021	0.000	100.119
Cal-149TB_Fig13_cx12	50.072	0.726	2.536	10.394	0.373	14.583	19.587	0.000	0.003	0.349	0.000	98.623
Cal-149TB_Fig13_cx5	53.652	0.323	1.228	18.063	0.506	24.856	1.560	0.005	0.003	0.021	0.000	100.216
Cal-149TB_Fig14_cx2	52.858	0.201	0.712	18.112	0.544	24.881	1.618	0.000	0.001	0.016	0.000	98.944
Cal-149TB_Fig14_cx1	50.126	0.771	2.683	9.292	0.295	15.201	20.422	0.000	0.000	0.324	0.000	99.114
Cal-149TB_Fig14_cx6	52.719	0.091	0.562	20.825	0.746	23.458	0.902	0.002	0.003	0.001	0.005	99.313
Cal-149TB_Fig14_cx12	51.729	0.316	1.174	20.570	0.562	22.930	1.581	0.012	0.000	0.018	0.000	98.892
Cal-149TB_Fig14_cx7	52.532	0.264	1.018	20.305	0.540	23.434	1.410	0.000	0.004	0.010	0.000	99.517
Cal-149TB_Fig17_cx2-3	52.316	0.328	1.350	18.277	0.504	24.381	1.693	0.005	0.002	0.010	0.000	98.867
Cal-149TB_Fig17_cx7	51.139	0.606	2.115	9.330	0.292	14.893	20.821	0.005	0.006	0.342	0.010	99.560

Table A2. (Continued)

SAMPLE	SiO_2	TiO_2	Al_2O_3	FeO	MnO	MgO	CaO	Cr_2O_3	K_2O	Na_2O	NiO	TOTAL
Cal-149TB_Fig19_cx7	49.551	0.768	3.002	9.780	0.326	15.154	19.865	0.001	0.000	0.310	0.000	98.758
Cal-149TB_Fig19_cx5	52.013	0.236	1.059	19.706	0.628	23.774	1.360	0.007	0.000	0.010	0.007	98.799
Cal-149TB_Fig23_med1a	36.517	0.005	0.012	26.817	0.478	35.506	0.111	0.000	0.000	0.094	0.017	99.533
Cal-149TB_Fig23_med1b	36.507	0.009	0.017	26.962	0.481	35.280	0.113	0.000	0.000	0.000	0.035	99.369
Cal-149TB_Fig23_med2a	53.137	0.330	1.508	17.762	0.498	25.048	1.590	0.000	0.000	0.022	0.000	99.894
Cal-149TB_Fig23_med2b	50.428	0.684	2.340	9.211	0.315	15.218	20.491	0.012	0.004	0.315	0.000	99.019
Cal-149TB_Fig23_med3a	52.517	0.235	0.847	17.992	0.504	24.952	1.566	0.000	0.005	0.024	0.005	98.647
Cal-149TB_Fig23_med3b	50.716	0.582	2.065	9.244	0.298	15.057	20.718	0.000	0.000	0.333	0.000	99.013
Cal-149TB_Fig23_med4a	51.993	0.292	1.188	18.213	0.494	24.966	1.467	0.005	0.000	0.027	0.000	98.645
Cal-149TB_Fig23_med4b	52.077	0.325	1.380	17.881	0.516	24.860	1.703	0.012	0.000	0.025	0.000	98.779
Cal-149TB_Fig23_med5a	53.065	0.277	1.143	18.115	0.502	25.169	1.435	0.000	0.001	0.018	0.012	99.739
Cal-149TB_Fig23_med5b	53.653	0.262	0.904	17.861	0.527	25.058	1.690	0.016	0.002	0.022	0.001	99.996
Cal-149TB_Fig23_med6a	52.675	0.271	1.061	18.362	0.530	24.844	1.445	0.000	0.000	0.015	0.002	99.205
Cal-149TB_Fig23_med6b	53.084	0.206	0.766	18.162	0.517	25.007	1.505	0.001	0.000	0.016	0.000	99.265
Cal-149TB_Fig26_cx9	53.325	0.249	0.966	18.148	0.509	24.883	1.492	0.000	0.003	0.015	0.000	99.590
Cal-149TB_Fig26_cx6	50.416	0.638	2.315	9.344	0.318	14.984	21.013	0.000	0.000	0.338	0.000	99.366
Cal-149TB_Fig26_cx11	53.845	0.252	0.961	18.320	0.548	24.735	1.440	0.000	0.001	0.027	0.003	100.132
Cal-149TB_Fig26_cx10	52.677	0.245	0.963	18.412	0.555	24.538	1.487	0.002	0.003	0.013	0.000	98.895
Cal-149TB_Fig27_cx4	53.437	0.238	0.744	16.914	0.480	25.826	1.649	0.007	0.000	0.025	0.000	99.321
Cal-149TB_Fig27_cx3	52.113	0.331	1.671	17.678	0.489	25.090	1.541	0.000	0.000	0.018	0.000	98.930
Cal-149TB_Fig27_cx8	53.660	0.283	1.311	18.004	0.518	25.113	1.331	0.014	0.000	0.007	0.011	100.252
Cal-149TB_Fig28_cx3	53.822	0.225	0.796	17.510	0.499	25.566	1.597	0.007	0.000	0.012	0.002	100.036
Cal-149TB_Fig28_cx2	50.675	0.835	2.953	9.359	0.304	14.641	20.801	0.005	0.000	0.347	0.000	99.920

Table A2. (Continued)

SAMPLE	SiO_2	TiO_2	Al_2O_3	FeO	MnO	MgO	CaO	Cr_2O_3	K_2O	Na_2O	NiO	TOTAL
Cal-149TB_Fig28_cx5	53.506	0.278	1.279	18.489	0.536	24.677	1.487	0.000	0.000	0.026	0.000	100.277
Cal-149TB_Fig29_cx4	52.245	0.327	1.804	17.619	0.508	24.989	1.658	0.000	0.000	0.023	0.000	99.173
Cal-149TB_Fig29_cx6	53.942	0.214	0.785	17.665	0.489	25.245	1.532	0.005	0.004	0.015	0.000	99.894
Cal-149TB_Fig29_cx3	52.826	0.242	0.948	17.676	0.508	25.130	1.637	0.003	0.002	0.009	0.000	98.984
Cal-149TB_Fig30_(1)	53.304	0.240	1.170	17.927	0.509	25.270	1.272	0.000	0.002	0.002	0.000	99.695
Cal-149TB_Fig30_2a	52.922	0.282	1.068	18.487	0.545	24.734	1.481	0.000	0.001	0.017	0.003	99.541
Cal-149TB_Fig30_2b	53.151	0.246	0.946	18.416	0.536	24.623	1.452	0.003	0.005	0.013	0.006	99.397
Cal-149TB_Fig30_3a	52.861	0.248	1.095	18.506	0.547	24.690	1.319	0.007	0.004	0.020	0.000	99.296
Cal-149TB_Fig30_3b	54.300	0.242	0.989	18.469	0.567	24.748	1.393	0.000	0.005	0.027	0.005	100.747
Cal-149TB_Fig30_4a	53.418	0.248	0.966	18.353	0.550	24.756	1.477	0.000	0.003	0.020	0.000	99.792
Cal-149TB_Fig30_4b	52.979	0.288	1.181	18.506	0.545	24.553	1.483	0.000	0.005	0.014	0.003	99.556
Cal-149TB_Fig30_5a	53.079	0.276	1.053	18.473	0.545	24.706	1.451	0.012	0.001	0.005	0.000	99.601
Cal-149TB_Fig30_5b	53.807	0.256	1.023	18.587	0.544	24.828	1.433	0.006	0.002	0.004	0.000	100.491
Cal-149TB_Fig32_cx10	52.612	0.305	1.384	18.488	0.525	24.591	1.483	0.005	0.001	0.027	0.000	99.420
Cal-149TB_Fig32_cx8	52.511	0.313	1.222	17.854	0.513	24.873	1.534	0.002	0.002	0.022	0.000	98.845
Cal-149TB_Fig33_c3_1	53.250	0.243	0.920	17.129	0.486	25.567	1.587	0.005	0.002	0.022	0.004	99.215
Cal-149TB_Fig33_c5_1	53.361	0.239	0.944	16.941	0.474	25.845	1.504	0.003	0.000	0.022	0.001	99.333
Cal-149TB_Fig33_c5_2	53.453	0.212	0.700	17.084	0.488	25.780	1.572	0.000	0.001	0.013	0.004	99.305
Cal-149TB_Fig33_c3_2	53.007	0.213	0.681	17.098	0.495	25.750	1.577	0.000	0.002	0.015	0.000	98.838
Cal-156_fig1_cx13_1	52.979	0.302	1.238	17.642	0.494	24.516	1.825	0.000	0.000	0.000	0.000	98.996
Cal-156_fig1_cx14_1	50.348	0.736	2.710	9.511	0.310	14.696	20.458	0.000	0.000	0.000	0.000	98.768
Cal-156_fig1_cx16_1	49.953	0.873	3.141	9.633	0.283	14.658	19.843	0.000	0.000	0.000	0.000	98.384
Cal-156_fig1_cx17_1	52.319	0.399	1.610	17.857	0.521	24.324	1.870	0.000	0.000	0.000	0.000	98.898

Table A2. (Continued)

SAMPLE	SiO_2	TiO_2	Al_2O_3	FeO	MnO	MgO	CaO	Cr_2O_3	K_2O	Na_2O	NiO	TOTAL
Cal-156_fig1_cx16_2	53.259	0.326	1.259	17.189	0.477	24.002	3.256	0.000	0.000	0.000	0.000	99.768
Cal-156_fig1_cx18_2	52.066	0.405	1.840	18.030	0.506	24.117	1.881	0.000	0.000	0.000	0.000	98.845
Cal-156_fig2_cx8_1	53.297	0.250	0.693	17.046	0.486	25.187	1.599	0.000	0.000	0.000	0.000	98.558
Cal-156_fig2_cx1_1	52.372	0.364	1.436	16.996	0.482	23.557	3.760	0.000	0.000	0.000	0.003	98.966
Cal-156_fig2_cx1_1a	50.688	0.742	2.744	9.072	0.276	14.808	20.422	0.000	0.000	0.000	0.000	98.751
Cal-156_fig2_cx2_11	49.931	0.939	3.590	8.778	0.256	14.507	20.756	0.000	0.000	0.000	0.000	98.756
Cal-156_fig2_cx2_12	51.072	0.658	2.549	9.214	0.300	15.066	19.902	0.000	0.000	0.000	0.000	98.761
Cal-156_fig2_cx2_13	50.881	0.810	2.714	9.546	0.297	14.812	20.039	0.000	0.000	0.000	0.000	99.098
Cal-156_fig2_cx2_13a	51.367	0.694	2.432	9.191	0.292	14.941	20.218	0.000	0.000	0.000	0.000	99.135
Cal-156_fig2_cx2_14	50.531	0.750	2.723	9.289	0.289	14.872	20.031	0.000	0.000	0.000	0.000	98.485
Cal-156_fig2_cx4_15	50.563	0.634	2.465	9.069	0.302	14.925	20.364	0.000	0.000	0.000	0.002	98.321
Cal-156_fig2_cx4_16	50.625	0.700	2.559	9.020	0.280	14.806	20.411	0.000	0.000	0.000	0.000	98.401
Cal-156_fig23_cx6_8a	52.071	0.488	1.552	15.295	0.417	21.884	7.881	0.000	0.000	0.000	0.000	99.588
Cal-156_fig23_cx6_8b	53.353	0.204	0.766	17.405	0.479	24.780	1.527	0.000	0.000	0.000	0.004	98.512
Cal-157A_fig1_cx3_1	51.249	0.644	2.581	9.422	0.312	15.171	20.166	0.006	0.000	0.000	0.008	99.560
Cal-157A_fig1_cx2_1	53.902	0.217	0.775	17.328	0.511	25.838	1.578	0.001	0.000	0.000	0.006	100.156
Cal-157A_fig1_cx2_2	51.930	0.404	2.617	17.934	0.479	24.752	1.660	0.000	0.000	0.000	0.000	99.764
Cal-157A_fig3_cx10_1	51.430	0.603	2.255	9.296	0.297	15.216	20.456	0.008	0.000	0.000	0.006	99.567
Cal-157A_fig3_cx10_2	51.686	0.651	2.518	9.235	0.269	15.050	20.881	0.011	0.000	0.000	0.000	100.298
Cal-157A_fig3_cx11_1	52.958	0.307	1.352	18.033	0.505	25.219	1.500	0.007	0.000	0.000	0.000	99.877
Cal-157A_fig3_cx11_2	53.071	0.292	1.315	18.012	0.501	25.021	1.531	0.003	0.000	0.000	0.003	99.748
Cal-157A_fig3_cx5_1	52.067	0.410	1.538	9.028	0.309	15.255	20.936	0.000	0.000	0.000	0.000	99.532
Cal-157A_fig3_cx4_1	53.144	0.219	0.971	19.131	0.617	24.420	1.317	0.000	0.000	0.000	0.000	99.811

Table A2. (Continued)

SAMPLE	SiO_2	TiO_2	Al_2O_3	FeO	MnO	MgO	CaO	Cr_2O_3	K_2O	Na_2O	NiO	TOTAL
Cal-157A_fig20_cx9_1	52.802	0.287	1.074	19.079	0.574	24.360	1.435	0.000	0.000	0.000	0.048	99.657
Cal-157A_fig20_cx8_1	52.806	0.292	1.072	19.090	0.585	24.339	1.427	0.003	0.000	0.000	0.057	99.670
Cal-157A_fig20_cx8_2	48.648	0.454	1.810	8.795	0.293	14.973	19.039	0.004	0.000	0.000	0.044	94.060
Cal-157A_fig21_cx7_1	49.787	0.529	2.000	8.851	0.288	15.482	20.138	0.000	0.000	0.000	0.000	97.063
Cal-157A_fig21_cx8_1	52.367	0.221	0.788	17.230	0.502	25.829	1.598	0.004	0.000	0.000	0.000	98.531
Cal-157A_fig21_cx8_2	51.606	0.367	1.697	17.483	0.485	25.210	1.701	0.004	0.000	0.000	0.010	98.560
Cal-157A_fig21_cx9_1	50.244	0.608	2.214	9.423	0.336	14.819	20.362	0.005	0.000	0.000	0.000	98.004
Cal-157A_fig21_cx2_1	50.355	0.526	1.907	9.345	0.313	15.585	19.918	0.009	0.000	0.000	0.009	97.966
Cal-157A_fig21_cx19_1	52.281	0.214	0.826	17.715	0.515	25.540	1.475	0.003	0.000	0.000	0.000	98.569
Cal-157A_fig21_cx23_1	50.440	0.534	1.958	9.036	0.312	15.726	19.646	0.000	0.000	0.000	0.000	97.639
Cal-157A_fig21_cx22_1	51.946	0.307	1.369	17.822	0.492	25.178	1.497	0.000	0.000	0.000	0.000	98.602
Cal-157A_fig30_cx9_1	50.671	0.565	2.076	9.241	0.291	15.106	20.253	0.012	0.000	0.000	0.000	98.208
Cal-157A_fig30_cx9_2	50.390	0.588	2.305	9.414	0.300	14.748	20.379	0.001	0.000	0.000	0.000	98.125
Cal-157A_fig30_cx10_1	51.335	0.251	1.597	20.318	0.678	23.391	1.256	0.000	0.000	0.000	0.000	98.820
Cal-157A_fig30_cx10_2	51.717	0.248	1.585	20.105	0.680	23.690	1.245	0.002	0.000	0.000	0.000	99.264
Cal-157A_fig8_cx1_1	52.074	0.285	1.443	17.908	0.518	25.174	1.460	0.000	0.000	0.000	0.000	98.852
Cal-157A_fig8_cx1_2	52.092	0.305	1.523	17.456	0.480	25.403	1.471	0.007	0.000	0.000	0.000	98.724
Cal-157A_fig8_cx2_1	51.130	0.332	1.996	19.374	0.574	23.747	1.553	0.014	0.000	0.000	0.000	98.713
Cal-157A_fig8_cx3_1	52.682	0.281	1.176	17.076	0.466	25.866	1.469	0.004	0.000	0.000	0.004	99.024
Cal-157A_fig11_cx1_1	51.725	0.422	1.441	9.476	0.342	15.371	20.206	0.001	0.000	0.000	0.001	98.986
Cal-157A_fig11_cx1_2	50.834	0.560	2.076	9.662	0.330	15.095	19.898	0.000	0.000	0.000	0.000	98.438
Cal-157A_fig11_cx2_1	52.616	0.259	1.131	18.029	0.523	25.028	1.463	0.005	0.000	0.000	0.000	99.039
Cal-157A_fig11_cx2_2	51.972	0.336	1.545	18.023	0.493	24.510	1.908	0.000	0.000	0.000	0.006	98.793

Table A2. (Continued)

SAMPLE	SiO_2	TiO_2	Al_2O_3	FeO	MnO	MgO	CaO	Cr_2O_3	K_2O	Na_2O	NiO	TOTAL
Cal-157B_fig3_cx11_2	50.858	0.560	2.184	9.580	0.309	15.055	20.107	0.008	0.000	0.000	0.000	98.650
Cal-157B_fig3_cx11_1	51.196	0.557	2.223	9.433	0.297	14.990	20.389	0.000	0.000	0.000	0.001	99.082
Cal-157B_fig3_cx7_1	52.502	0.292	1.227	18.556	0.515	24.575	1.546	0.001	0.000	0.000	0.000	99.212
Cal-157B_fig3_cx7_2	52.161	0.340	1.468	18.511	0.505	24.414	1.604	0.004	0.000	0.000	0.000	99.005
Cal-157B_fig3_cx9_1	51.549	0.472	1.739	9.506	0.335	15.275	20.172	0.000	0.000	0.000	0.000	99.042
Cal-157B_fig3_cx9_2	51.447	0.496	1.804	9.738	0.353	15.253	19.986	0.000	0.000	0.000	0.000	99.074
Cal-157B_fig3_cx17_1	52.283	0.292	1.354	18.335	0.500	24.504	1.448	0.005	0.000	0.000	0.000	98.707
Cal-157B_fig3_cx10_1	52.873	0.259	1.246	18.495	0.529	24.734	1.529	0.006	0.000	0.000	0.004	99.674
Cal-157B_fig3_cx10_2	50.796	0.650	2.511	9.522	0.313	14.785	20.302	0.000	0.000	0.000	0.000	98.864
Cal-157B_fig7_cx1_1	50.687	0.675	2.479	9.303	0.287	14.889	20.079	0.004	0.000	0.000	0.000	98.395
Cal-157B_fig7_cx1_2	50.529	0.754	2.702	9.420	0.293	14.735	20.101	0.000	0.000	0.000	0.000	98.530
Cal-157B_fig7_cx2_1	51.027	0.558	2.137	9.114	0.301	15.003	20.312	0.001	0.000	0.000	0.000	98.441
Cal-157B_fig7_cx2_2	50.940	0.610	2.422	9.397	0.284	15.120	20.247	0.005	0.000	0.000	0.008	99.034
Cal-157B_fig16_cx4_2	51.817	0.527	1.980	9.045	0.307	15.263	20.498	0.003	0.000	0.000	0.000	99.429
Cal-157B_fig7_cx7_1	53.538	0.241	0.897	17.708	0.512	25.298	1.589	0.001	0.000	0.000	0.000	99.781
Cal-157B_fig7_cx1_1	52.969	0.255	1.067	17.968	0.505	25.297	1.397	0.002	0.000	0.000	0.002	99.462
Cal-157B_fig7_cx4_2	52.292	0.477	1.691	9.261	0.311	15.778	20.133	0.000	0.000	0.000	0.003	99.943
Cal-157B_fig20_cx1_1	50.011	0.833	3.213	9.739	0.313	14.866	19.673	0.009	0.000	0.000	0.000	98.648
Cal-157B_fig20_cx8_1	52.187	0.347	1.863	18.744	0.531	24.087	1.655	0.001	0.000	0.000	0.002	99.417
Cal-157B_fig20_cx8_2	53.027	0.222	0.894	18.258	0.536	24.593	1.531	0.006	0.000	0.000	0.000	99.066
Cal-157B_fig20_cx4_1	52.258	0.340	1.709	18.699	0.531	24.165	1.515	0.007	0.000	0.000	0.000	99.224
Cal-158_fig1_cx7_2	52.487	0.275	1.022	17.741	0.508	24.782	1.499	0.000	0.000	0.000	0.000	98.315
Cal-158_fig1_cx8_1	50.129	0.752	3.267	9.456	0.304	14.384	20.524	0.000	0.000	0.000	0.000	98.817

Table A2. (Continued)

SAMPLE	SiO_2	TiO_2	Al_2O_3	FeO	MnO	MgO	CaO	Cr_2O_3	K_2O	Na_2O	NiO	TOTAL
Cal-158_fig3_cx5_1	51.907	0.462	1.428	9.395	0.335	15.472	19.762	0.000	0.000	0.000	0.013	98.762
Cal-158_fig3_cx4_1	51.105	0.646	2.560	9.360	0.306	14.716	20.346	0.000	0.000	0.000	0.000	99.038
Cal-158_fig3_cx1_1	52.817	0.346	1.344	17.802	0.505	24.108	2.559	0.000	0.000	0.000	0.000	99.480
Cal-158_fig3_cx2_1	53.710	0.232	0.720	17.971	0.541	24.630	1.543	0.000	0.000	0.000	0.002	99.346
Cal-158_fig6_cx6_2	53.125	0.408	1.725	15.467	0.446	19.960	7.606	0.000	0.000	0.000	0.000	98.735
Cal-158_fig6_cx5_2	53.274	0.239	0.833	17.083	0.487	25.205	1.555	0.000	0.000	0.000	0.000	98.676
Cal-158_fig6_cx6_1	51.271	0.600	2.203	9.399	0.308	14.687	19.885	0.000	0.000	0.000	0.000	98.353
Cal-158_fig6_cx7_1	53.683	0.236	0.929	16.891	0.465	25.427	1.436	0.000	0.000	0.000	0.000	99.065
Cal-158_fig6_cx12_1	50.684	0.737	2.790	8.986	0.272	14.666	20.406	0.000	0.000	0.000	0.000	98.540
Cal-158_fig6_cx11_1	52.900	0.275	1.043	17.317	0.501	24.910	1.784	0.000	0.000	0.000	0.004	98.729
Cal-158_fig12_cx1_1	51.905	0.306	1.562	18.256	0.528	24.108	1.536	0.000	0.000	0.000	0.000	98.203
Cal-158_fig13_cx4_1	51.290	0.556	2.024	9.417	0.315	14.804	20.143	0.000	0.000	0.000	0.000	98.550
Cal-158_fig13_cx1_1	52.561	0.332	1.318	18.247	0.527	24.129	1.712	0.000	0.000	0.000	0.000	98.826
Cal-158_fig13_cx1_2	52.868	0.323	1.176	17.945	0.501	24.553	1.442	0.000	0.000	0.000	0.008	98.809
Cal-158_fig13_cx2_2	51.546	0.590	2.085	9.391	0.307	14.824	20.067	0.000	0.000	0.000	0.000	98.810
Cal-158_fig15_cx10_1	53.310	0.221	0.823	17.788	0.537	24.710	1.559	0.000	0.000	0.000	0.003	98.947
Cal-158_fig15_cx11_2	52.381	0.331	1.643	18.527	0.524	23.808	1.579	0.000	0.000	0.000	0.001	98.792
Cal-158_fig23_cx4_2	53.021	0.277	1.092	18.041	0.511	24.457	1.473	0.000	0.000	0.000	0.000	98.872
Cal-158_fig23_cx3_2	51.443	0.583	2.091	9.320	0.299	14.927	20.119	0.000	0.000	0.000	0.004	98.782
Cal-158_fig23_cx4_1	53.187	0.256	1.116	17.685	0.490	24.593	1.632	0.000	0.000	0.000	0.010	98.957
Cal-158_fig23_cx3_1	50.618	0.735	2.616	9.616	0.297	14.493	20.015	0.000	0.000	0.000	0.008	98.391
Cal-158_fig24_cx4_1	52.389	0.357	1.635	18.002	0.509	24.140	1.563	0.000	0.000	0.000	0.000	98.596
Cal-158_fig24_cx3_1	50.975	0.655	2.484	9.485	0.293	14.644	20.284	0.000	0.000	0.000	0.000	98.820

Table A2. (Continued)

SAMPLE	SiO_2	TiO_2	Al_2O_3	FeO	MnO	MgO	CaO	Cr_2O_3	K_2O	Na_2O	NiO	TOTAL
Cal-158_fig24_cx4_2	52.565	0.379	1.522	18.233	0.492	24.338	1.611	0.000	0.000	0.000	0.005	99.140
Cal-158_fig24_cx3_2	51.131	0.622	2.228	9.379	0.308	14.887	20.043	0.000	0.000	0.000	0.003	98.598
Cal-158_fig24_cx5_3	50.873	0.648	2.374	9.252	0.288	14.637	20.575	0.000	0.000	0.000	0.000	98.647
Cal-158_fig24_cx4_3	53.220	0.294	0.955	17.835	0.492	24.677	1.586	0.000	0.000	0.000	0.000	99.060
Cal-159_Fig2_cx2_1	52.194	0.687	2.567	9.254	0.297	14.643	20.392	0.006	0.000	0.000	0.003	100.042
Cal-159_Fig2_cx2_2	51.704	0.823	3.280	9.783	0.318	14.626	19.584	0.006	0.000	0.000	0.000	100.113
Cal-159_Fig2_cx2_3	52.027	0.681	2.783	9.079	0.300	14.656	20.481	0.014	0.000	0.000	0.007	100.029
Cal-159_Fig6_cx13_c	52.617	0.621	2.482	9.459	0.300	14.742	20.122	0.004	0.000	0.000	0.003	100.335
Cal-159_Fig1_cx4	51.639	0.616	2.442	8.838	0.291	14.598	20.347	0.010	0.000	0.000	0.002	98.763
Cal-159_Fig1_cx3	54.635	0.197	0.696	17.115	0.496	24.438	1.686	0.004	0.000	0.000	0.000	99.267
Cal-159_Fig7_cx12	54.099	0.276	1.405	18.003	0.511	23.718	1.662	0.004	0.000	0.000	0.000	99.661
Cal-159_Fig7_cx6	52.493	0.558	2.197	9.495	0.306	14.622	20.271	0.005	0.000	0.000	0.004	99.942
Cal-159_Fig7_cx1	54.337	0.239	1.029	17.606	0.520	24.258	1.552	0.006	0.000	0.000	0.004	99.553
Cal-159_Fig7_cx2	52.733	0.604	2.331	9.309	0.312	14.636	20.304	0.004	0.000	0.000	0.003	100.236
Cal-159_Fig18_cx10	53.885	0.329	1.518	17.827	0.482	23.875	2.054	0.002	0.000	0.000	0.005	99.973
Cal-159_Fig18_cx11	52.709	0.520	2.105	9.350	0.325	14.674	20.315	0.008	0.000	0.000	0.005	100.011
Cal-159_Fig18_cx4	53.676	0.323	1.797	18.455	0.519	23.674	1.718	0.000	0.000	0.000	0.003	100.164
Cal-159_Fig18_cx3	52.564	0.510	2.065	9.178	0.309	14.494	20.465	0.004	0.000	0.000	0.006	99.586
Cal-160_fig12_c10_1	52.681	0.339	0.613	20.966	0.651	22.899	1.271	0.011	0.000	0.000	0.008	99.424
Cal-160_fig12_c10_2	52.574	0.308	0.646	21.156	0.669	22.796	1.253	0.004	0.000	0.000	0.000	99.389
Cal-160_fig12_cx1_1	52.009	0.279	1.153	10.829	0.385	13.830	20.818	0.001	0.000	0.000	0.000	99.303

Table A2. (Continued)

SAMPLE	SiO_2	TiO_2	Al_2O_3	FeO	MnO	MgO	CaO	Cr_2O_3	K_2O	Na_2O	NiO	TOTAL
Cal-160_fig12_cx9_1	52.797	0.279	0.575	21.177	0.703	23.085	1.073	0.000	0.000	0.000	0.000	99.682
Cal-160_fig12_cx9_2	52.777	0.291	0.524	21.174	0.689	23.115	1.139	0.000	0.000	0.000	0.004	99.710
Cal-160_fig_16_cx6_1	51.948	0.364	1.166	10.800	0.368	14.242	20.514	0.006	0.000	0.000	0.000	99.393
Cal-160_fig_16_cx5_1	52.364	0.234	0.924	21.899	0.630	22.454	1.293	0.000	0.000	0.000	0.000	99.796
Cal-160_fig_16_cx7_1	52.878	0.188	1.068	20.016	0.526	23.854	1.304	0.003	0.000	0.000	0.009	99.845
Cal-160_fig_16_cx7_2	52.678	0.185	1.316	19.887	0.525	23.802	1.321	0.009	0.000	0.000	0.004	99.727
Cal-160_fig_16_cx13_1	51.388	0.502	1.643	10.556	0.360	14.030	20.759	0.000	0.000	0.000	0.000	99.221
Cal-160_fig_16_cx11_1	52.183	0.266	0.866	21.774	0.679	22.144	1.457	0.002	0.000	0.000	0.004	99.374
Cal-160_fig_17_cx4_1	52.905	0.267	1.062	18.045	0.539	24.935	1.478	0.000	0.000	0.000	0.000	99.207
Cal-160_fig_17_cx1_1	51.449	0.567	1.979	9.890	0.350	14.456	20.563	0.008	0.000	0.000	0.002	99.263
Cal-160_fig_17_cx2_1	52.487	0.311	1.026	20.244	0.545	23.410	1.398	0.000	0.000	0.000	0.000	99.407
Cal-160_fig_17_cx1_3	51.406	0.480	1.818	9.921	0.352	14.395	20.700	0.013	0.000	0.000	0.005	99.088
Cal-160_fig_21_cx3_1	51.916	0.243	0.948	21.900	0.654	21.997	1.392	0.000	0.000	0.000	0.000	99.047
Cal-160_fig_21_cx3_2	52.253	0.182	0.744	21.755	0.670	22.263	1.336	0.004	0.000	0.000	0.000	99.196
Cal-160_fig_21_cx2_1	51.705	0.320	1.363	10.280	0.378	14.300	20.768	0.003	0.000	0.000	0.000	99.111
Cal-160_fig_21_cx2_2	51.756	0.334	1.275	10.393	0.367	14.058	21.027	0.000	0.000	0.000	0.000	99.197
Cal-160_fig_21_cx8_1	52.078	0.186	0.729	22.506	0.668	21.895	1.293	0.001	0.000	0.000	0.005	99.361
Cal-160_fig_27_cx2_1	52.473	0.297	0.837	20.974	0.555	22.847	1.655	0.000	0.000	0.000	0.000	99.624
Cal-160_fig_27_cx3_1	51.669	0.463	1.604	10.200	0.368	14.168	20.875	0.005	0.000	0.000	0.000	99.350
Cal-160_fig_27_cx1_1	51.457	0.327	1.264	21.440	0.621	21.977	1.581	0.000	0.000	0.000	0.000	98.655
Cal-160_fig_27_cx4_1	52.677	0.194	0.566	20.854	0.706	23.237	1.112	0.000	0.000	0.000	0.000	99.334
Cal-160_fig_27_cx1_3	51.837	0.370	1.500	20.039	0.491	23.209	1.580	0.000	0.000	0.000	0.000	99.016
Cal-160_fig_28_cx2_1	52.411	0.338	0.839	9.758	0.386	14.766	20.713	0.011	0.000	0.000	0.000	99.217

Table A2. (Continued)

SAMPLE	SiO_2	TiO_2	Al_2O_3	FeO	MnO	MgO	CaO	Cr_2O_3	K_2O	Na_2O	NiO	TOTAL
Cal-160_fig_28_cx3_1	52.872	0.155	0.380	20.641	0.685	23.294	1.167	0.002	0.000	0.000	0.000	99.194
Cal-160_fig_32_cx70_1	52.290	0.164	0.610	22.051	0.731	22.176	1.254	0.006	0.000	0.000	0.003	99.285
Cal-160_fig_32_cx6_1	52.129	0.257	1.069	10.390	0.380	14.133	21.162	0.006	0.000	0.000	0.000	99.520
Cal-160_fig_32_cx3_1	52.117	0.237	0.640	21.856	0.661	22.095	1.404	0.001	0.000	0.000	0.000	99.005
Cal-160_fig_32_cx5_1	51.653	0.428	1.420	10.081	0.370	14.427	20.692	0.000	0.000	0.000	0.000	99.046
Cal-160_fig_33_cx4_1	51.673	0.276	0.784	22.154	0.739	21.794	1.445	0.000	0.000	0.000	0.000	98.843
Cal-160_fig_33_cx2_1	51.408	0.428	1.309	10.443	0.403	14.157	20.478	0.000	0.000	0.000	0.000	98.613
Cal-160_fig_34_cx3_1	52.406	0.350	1.309	18.963	0.538	24.032	1.653	0.000	0.000	0.000	0.008	99.259
Cal-160_fig_34_cx4_1	51.541	0.501	1.690	9.770	0.354	14.966	20.209	0.004	0.000	0.000	0.002	99.036
Cal-160_fig_34_cx5_1	51.628	0.527	1.744	10.071	0.341	15.474	19.513	0.011	0.000	0.000	0.000	99.306
Cal-160_fig_34_cx2_1	51.703	0.333	1.301	20.725	0.591	22.773	1.391	0.006	0.000	0.000	0.001	98.825
Cal-160_fig_36_cx90_1	50.984	0.475	1.518	10.595	0.379	14.165	20.509	0.003	0.000	0.000	0.000	98.621
Cal-160_fig_36_cx4_1	51.910	0.266	0.975	10.730	0.394	13.859	20.929	0.008	0.000	0.000	0.007	99.077

Table A3. Compositions of titanomagnetite from the April 2015 Calbuco eruption (wt%).

SAMPLE	SiO_2	TiO_2	Al_2O_3	FeOt	MnO	MgO	CaO	CoO	V_2O_3	Cr_2O_3	ZnO	Nb_2O_5	TOTAL
Cal-149Tb - f14b_1_17	0.098	14.997	3.088	74.631	0.466	2.974	0.007	0.156	0.389	0.010	0.012	0.000	97.040
Cal-149Tb - f14b_1_18	0.058	14.915	3.112	74.991	0.433	2.891	0.005	0.146	0.396	0.003	0.060	0.000	97.226
Cal-149Tb - f14b_1_36	0.092	14.124	3.214	74.814	0.431	2.805	0.010	0.187	0.407	0.012	0.057	0.000	96.374
Cal-149Tb - f14b_2_16	0.076	15.176	3.095	74.507	0.423	2.839	0.010	0.183	0.364	0.023	0.097	0.009	96.998
Cal-149Tb - f14b_2_17	0.056	15.096	3.055	74.936	0.456	2.891	0.011	0.158	0.377	0.020	0.049	0.000	97.309
Cal-149Tb - f14b_2_30	0.069	14.037	3.173	74.844	0.460	2.951	0.019	0.154	0.400	0.018	0.060	0.000	96.402
Cal-155_fig3_p1_11	0.111	13.277	2.687	76.198	0.448	1.810	0.015	0.146	0.370	0.009	0.036	0.000	95.106
Cal-155_fig3_p1_12	0.128	13.245	2.702	76.955	0.450	1.820	0.015	0.173	0.386	0.025	0.028	0.000	95.926
Cal-155_fig3_p1_19	0.093	12.860	2.690	77.345	0.449	1.808	0.006	0.168	0.374	0.031	0.000	0.000	95.824
Cal-155_fig24_p1_8	0.110	12.854	2.673	77.157	0.462	1.795	0.049	0.141	0.347	0.023	0.011	0.014	95.824
Cal-155_fig24_p1_9	0.157	12.877	2.628	77.234	0.503	1.803	0.035	0.184	0.319	0.026	0.041	0.000	95.980
Cal-155_fig24_p1_17	0.109	13.166	2.609	78.133	0.473	1.782	0.007	0.140	0.367	0.008	0.058	0.022	97.074
Cal-160_fig1_p1_8	0.011	16.352	1.049	75.312	0.497	2.081	0.014	0.167	0.304	0.017	0.068	0.000	96.037
Cal-160_fig1_p1_9	0.051	14.369	1.144	77.603	0.465	2.097	0.017	0.115	0.335	0.035	0.113	0.000	96.527
Cal-160_fig1_p1_20	0.050	8.499	1.436	83.429	0.465	1.279	0.007	0.163	0.440	0.045	0.006	0.000	96.059
Cal-160_fig1_p2_9	0.035	15.994	1.108	78.182	0.532	1.509	0.044	0.177	0.298	0.025	0.070	0.000	98.137
Cal-160_fig1_p2_10	0.034	13.706	1.217	79.011	0.508	1.499	0.033	0.173	0.355	0.016	0.753	0.012	97.509
Cal-160_fig1_p2_19	0.043	8.387	1.458	83.032	0.443	1.255	0.018	0.189	0.444	0.027	0.114	0.000	95.650

Table A3. (Continued)

SAMPLE	SiO_2	TiO_2	Al_2O_3	FeOt	MnO	MgO	CaO	CoO	V_2O_3	Cr_2O_3	ZnO	Nb_2O_5	TOTAL
160_fig13_profile2_6	0.056	14.481	1.821	77.266	0.438	1.856	0.011	0.169	0.415	0.047	0.095	0.010	96.892
160_fig13_profile2_7	0.060	11.823	2.038	79.726	0.391	1.671	0.000	0.171	0.478	0.018	0.086	0.000	96.722
160_fig13_profile2_18	0.071	10.415	2.048	81.043	0.396	1.636	0.021	0.162	0.492	0.042	0.023	0.000	96.616
160_fig17_profile1_8	0.029	16.471	1.823	77.120	0.437	1.935	0.007	0.193	0.378	0.049	0.105	0.004	98.756
160_fig17_profile1_9	0.051	12.193	2.020	78.605	0.405	1.780	0.018	0.165	0.455	0.028	0.091	0.025	96.081
160_fig17_profile1_18	0.063	10.754	2.079	80.262	0.385	1.757	0.010	0.198	0.473	0.063	0.046	0.027	96.376
160_fig17_profile2_10	0.044	14.210	1.881	76.746	0.447	1.898	0.024	0.150	0.425	0.072	0.114	0.007	96.248
160_fig17_profile2_11	0.063	11.683	2.112	79.668	0.381	1.744	0.000	0.167	0.442	0.018	0.027	0.049	96.592
160_fig17_p4_19	0.058	10.965	2.090	81.024	0.401	1.663	0.015	0.162	0.499	0.050	0.071	0.000	97.266
160_figb_p1_13	0.041	14.215	1.813	77.584	0.441	1.644	0.017	0.176	0.492	0.010	0.101	0.009	96.810
160_figb_p1_14	0.043	11.893	2.007	79.788	0.398	1.580	0.012	0.190	0.474	0.040	0.125	0.000	96.808
160_figb_p1_21	0.050	10.685	1.992	79.659	0.403	1.505	0.018	0.171	0.513	0.045	0.053	0.000	95.371
160_cx_e_p1_16	0.047	15.687	1.741	76.304	0.544	1.808	0.012	0.129	0.385	0.081	0.084	0.000	97.030
160_cx_e_p1_17	0.044	11.718	2.042	79.193	0.503	1.546	0.015	0.154	0.503	0.052	0.144	0.009	96.197
160_cx_e_p1_24	0.046	10.959	2.041	80.269	0.449	1.502	0.013	0.149	0.494	0.021	0.000	0.000	96.211

Table A3. Continued.

SAMPLE	SiO_2	TiO_2	Al_2O_3	FeOt	MnO	MgO	CaO	CoO	V_2O_3	Cr_2O_3	ZnO	Nb_2O_5	TOTAL
Cal-160_ff_p1_7	0.042	18.959	1.568	73.528	0.456	1.694	0.027	0.172	0.311	0.049	0.111	0.000	97.085
Cal-160_ff_p1_8	0.057	12.919	1.993	77.866	0.435	1.526	0.023	0.135	0.490	0.057	0.109	0.000	95.878
Cal-160_ff_p1_14	0.063	10.758	2.123	79.621	0.400	1.519	0.026	0.164	0.496	0.004	0.053	0.003	95.500
Cal-160_ff_p2_3	0.070	14.226	1.732	76.887	0.474	1.529	0.050	0.150	0.388	0.059	0.069	0.063	95.908
Cal-160_ff_p2_4	0.069	11.221	2.082	79.143	0.425	1.369	0.042	0.135	0.454	0.044	0.027	0.014	95.273
Cal-160_ff_p2_8	0.050	10.824	2.111	79.655	0.413	1.420	0.041	0.174	0.464	0.035	0.046	0.000	95.493
Cal-160_fh_p1_9	0.055	15.259	1.774	75.675	0.472	1.520	0.033	0.140	0.443	0.025	0.015	0.014	95.665
Cal-160_fh_p1_10	0.039	13.157	1.933	77.587	0.460	1.620	0.029	0.153	0.542	0.045	0.103	0.000	95.963
Cal-160_fh_p1_20	0.055	10.417	2.105	79.989	0.416	1.455	0.027	0.145	0.553	0.037	0.043	0.010	95.554

Table A4. Compositions of ilmenite from the April 2015 Calbuco eruption (wt%).

SAMPLE	SiO_2	TiO_2	Al_2O_3	FeOt	MnO	MgO	CaO	CoO	V_2O_3	Cr_2O_3	ZnO	Nb_2O_5	TOTAL
Cal-149Tb - f14b_p1_1	0.003	45.679	0.390	48.034	0.468	3.983	0.024	0.093	0.140	0.014	0.000	0.000	98.905
Cal-149Tb - f14b_p1_2	0.005	45.960	0.376	47.973	0.465	3.993	0.024	0.103	0.142	0.000	0.000	0.009	99.127
Cal-149Tb - f14b_p1_3	0.000	46.256	0.388	47.855	0.447	4.019	0.017	0.123	0.110	0.000	0.000	0.030	99.305
Cal-149Tb - f14b_1_14	0.146	46.659	0.386	48.214	0.467	3.993	0.024	0.092	0.104	0.022	0.000	0.000	100.164
Cal-149Tb – f14b_1_15	0.014	47.146	0.380	48.427	0.451	4.039	0.011	0.114	0.137	0.015	0.018	0.015	100.842
Cal-149Tb - f14b_1_16	0.000	45.440	0.365	48.449	0.466	4.034	0.012	0.089	0.115	0.015	0.021	0.000	99.075
Cal-149Tb - f14b_2_01	0.000	46.311	0.382	48.334	0.453	3.974	0.019	0.120	0.133	0.000	0.000	0.020	99.817
Cal-149Tb - f14b_2_02	0.000	46.599	0.369	48.309	0.449	3.954	0.016	0.096	0.135	0.014	0.047	0.000	100.061
Cal-149Tb - f14b_2_03	0.000	46.313	0.379	48.244	0.440	4.022	0.020	0.082	0.121	0.009	0.079	0.030	99.804
Cal-149Tb - f14b_2_13	0.005	45.929	0.377	48.216	0.451	4.121	0.015	0.097	0.158	0.003	0.071	0.029	99.559
Cal-149Tb - f14b_2_14	0.007	45.927	0.372	48.342	0.448	4.061	0.022	0.130	0.138	0.005	0.000	0.031	99.559
Cal-149Tb - f14b_2_15	0.010	45.319	0.389	48.479	0.450	4.092	0.020	0.092	0.169	0.028	0.000	0.020	99.161
Cal-155_fig3_p1_1	0.033	45.842	0.268	48.288	0.539	2.904	0.006	0.105	0.154	0.003	0.033	0.000	98.174
Cal-155_fig3_p1_2	0.086	45.622	0.249	48.653	0.523	2.947	0.013	0.120	0.101	0.000	0.000	0.008	98.322
Cal-155_fig3_p1_9	0.050	45.795	0.265	48.494	0.557	2.921	0.014	0.111	0.122	0.000	0.018	0.000	98.346
Cal-155_fig3_p1_10	0.067	46.375	0.247	48.787	0.534	2.911	0.010	0.115	0.129	0.022	0.000	0.000	99.198

Table A4. (Continued)

SAMPLE	SiO_2	TiO_2	Al_2O_3	FeOt	MnO	MgO	CaO	CoO	V_2O_3	Cr_2O_3	ZnO	Nb_2O_5	TOTAL
Cal-155_fig24_p1_1	0.032	47.267	0.255	47.988	0.561	3.037	0.055	0.098	0.067	0.000	0.000	0.025	99.424
Cal-155_fig24_p1_2	0.104	46.387	0.258	47.940	0.571	3.009	0.046	0.130	0.117	0.000	0.000	0.000	98.626
Cal-155_fig24_p1_3	0.040	45.128	0.243	47.933	0.553	3.001	0.051	0.093	0.111	0.012	0.015	0.014	97.253
Cal-155_fig24_p1_7	0.064	46.492	0.256	48.386	0.530	2.941	0.107	0.091	0.049	0.007	0.000	0.003	98.952
Cal-160_fig1_p1_1	0.019	41.730	0.344	52.066	0.455	2.722	0.059	0.092	0.149	0.000	0.039	0.011	97.767
Cal-160_fig1_p1_2	0.029	43.170	0.305	52.220	0.428	2.774	0.043	0.091	0.115	0.007	0.000	0.026	99.271
Cal-160_fig1_p1_3	0.022	42.890	0.259	51.989	0.404	2.850	0.038	0.116	0.151	0.000	0.015	0.008	98.826
Cal-160_fig1_p1_7	0.041	42.934	0.176	51.740	0.432	3.245	0.025	0.114	0.149	0.000	0.000	0.053	98.988
Cal-160_fig1_p2_1	0.050	42.689	0.183	52.405	0.538	2.134	0.444	0.105	0.146	0.015	0.016	0.017	98.822
Cal-160_fig1_p2_2	0.022	41.305	0.191	52.665	0.537	2.073	0.317	0.114	0.140	0.011	0.000	0.015	97.466
Cal-160_fig1_p2_3	0.024	41.694	0.174	52.956	0.536	2.089	0.235	0.126	0.140	0.040	0.000	0.005	98.094
Cal-160_fig1_p2_8	0.012	42.045	0.179	53.009	0.507	2.137	0.069	0.109	0.126	0.000	0.000	0.019	98.286
160_fig1_p3_1	0.011	42.496	0.282	51.812	0.484	2.880	0.086	0.077	0.138	0.000	0.031	0.038	98.410
160_fig1_p3_2	0.030	42.951	0.277	52.096	0.456	2.783	0.086	0.104	0.118	0.000	0.022	0.057	99.046
160_fig1_p3_6	0.017	43.414	0.190	52.146	0.489	2.815	0.040	0.125	0.122	0.003	0.000	0.000	99.427
Cal-160_figf_p1_1	0.009	44.839	0.221	50.098	0.499	2.303	0.047	0.105	0.159	0.025	0.014	0.017	98.422
Cal-160_figf_p1_2	0.018	45.379	0.193	50.191	0.503	2.330	0.060	0.050	0.118	0.012	0.000	0.021	98.938
Cal-160_figf_p1_6	0.007	45.201	0.204	50.611	0.508	2.360	0.036	0.080	0.155	0.012	0.023	0.021	99.303

Table A4. (Continued)

SAMPLE	SiO_2	TiO_2	Al_2O_3	FeOt	MnO	MgO	CaO	CoO	V_2O_3	Cr_2O_3	ZnO	Nb_2O_5	TOTAL
Cal-160_fig13_p2_1	0.000	44.979	0.224	50.911	0.457	2.757	0.025	0.105	0.147	0.000	0.015	0.020	99.720
Cal-160_fig13_p2_2	0.019	45.595	0.215	50.970	0.503	2.764	0.014	0.125	0.189	0.005	0.002	0.000	100.503
Cal-160_fig13_p2_5	0.014	42.914	0.263	51.771	0.496	2.813	0.006	0.097	0.181	0.039	0.000	0.014	98.705
Cal-160_fig17_p1_1	0.046	43.669	0.226	50.349	0.527	2.861	0.046	0.113	0.173	0.019	0.003	0.000	98.126
Cal-160_fig17_p1_2	0.008	43.450	0.236	50.671	0.501	2.900	0.042	0.107	0.192	0.000	0.000	0.016	98.228
Cal-160_fig17_p1_7	0.009	44.279	0.230	50.245	0.524	2.919	0.016	0.094	0.132	0.008	0.023	0.006	98.555
Cal-160_fig17_p2_1	0.000	44.590	0.216	50.582	0.484	2.963	0.016	0.077	0.154	0.002	0.014	0.046	99.229
Cal-160_fig17_p2_2	0.033	47.323	0.219	50.397	0.510	2.896	0.020	0.099	0.148	0.013	0.046	0.021	101.806
Cal-160_fig17_p2_9	0.014	40.605	0.411	53.020	0.487	2.868	0.008	0.111	0.170	0.023	0.039	0.000	97.849
Cal-160_fig17_p4_1	0.020	45.476	0.213	50.912	0.503	2.749	0.044	0.099	0.187	0.006	0.026	0.031	100.368
Cal-160_fig17_p4_2	0.017	46.252	0.227	50.723	0.491	2.787	0.040	0.103	0.136	0.010	0.006	0.000	100.866
Cal-160_fig17_p4_10	0.000	44.528	0.220	50.538	0.501	2.759	0.017	0.112	0.156	0.003	0.052	0.023	98.993
Cal-160_figb_p1_1	0.000	45.864	0.226	50.520	0.509	2.584	0.017	0.090	0.139	0.003	0.000	0.016	100.044
Cal-160_figb_p1_2	0.006	45.894	0.209	50.345	0.483	2.631	0.025	0.103	0.124	0.016	0.059	0.007	99.969
Cal-160_figb_p1_12	0.001	45.580	0.197	50.326	0.513	2.574	0.003	0.099	0.182	0.020	0.000	0.015	99.610
Cal-160_cx_e_p1_1	0.050	44.014	0.254	50.353	0.581	2.503	0.079	0.084	0.137	0.026	0.000	0.016	98.170
Cal-160_cx_e_p1_2	0.044	44.721	0.231	50.696	0.589	2.480	0.046	0.065	0.160	0.000	0.018	0.012	99.149
Cal-160_cx_e_p1_15	0.012	44.457	0.233	51.392	0.588	2.554	0.013	0.100	0.168	0.026	0.048	0.012	99.691

Table A4. (Continued)

SAMPLE	SiO_2	TiO_2	Al_2O_3	FeOt	MnO	MgO	CaO	CoO	V_2O_3	Cr_2O_3	ZnO	Nb_2O_5	TOTAL
Cal-160_figf_p2_1	0.046	45.280	0.227	49.970	0.521	2.313	0.085	0.115	0.113	0.017	0.000	0.043	98.791
Cal-160_figf_p2_2	0.041	45.562	0.202	50.201	0.521	2.300	0.057	0.119	0.101	0.000	0.000	0.000	99.159
160_figh_p1_1	0.009	45.507	0.236	50.483	0.510	2.479	0.090	0.107	0.165	0.000	0.074	0.019	99.768
160_figh_p1_2	0.000	45.996	0.239	50.122	0.520	2.463	0.072	0.108	0.133	0.017	0.000	0.000	99.743
160_figh_p1_8	0.025	41.134	0.352	53.087	0.476	2.566	0.026	0.081	0.219	0.012	0.000	0.020	98.116

Table A5. Compositions of olivine from the April 2015 Calbuco eruption (wt%).

SAMPLE	SiO_2	TiO_2	Al_2O_3	FeO	MnO	MgO	CaO	Cr_2O_3	NiO	TOTAL
Cal-149Ta_fig9_1	36.306	0.014	0.000	32.967	0.744	28.979	0.100	0.003	0.011	99.126
Cal-149Ta_fig9_2	36.834	0.014	0.000	33.094	0.748	29.116	0.102	0.004	0.015	99.926
Cal-149Ta_fig9_3	36.350	0.017	0.000	33.757	0.775	28.506	0.100	0.002	0.012	99.517
Cal-149Ta_fig9_4	36.354	0.009	0.000	33.485	0.753	28.695	0.099	0.004	0.016	99.415
Cal-149Ta_fig10_1	36.947	0.014	0.000	30.606	0.647	31.382	0.133	0.000	0.018	99.747
Cal-149Ta_fig10_2	36.850	0.019	0.000	30.963	0.657	31.052	0.124	0.002	0.027	99.694
Cal-149Ta_fig10_3	36.864	0.014	0.000	31.227	0.674	30.784	0.110	0.004	0.024	99.701
Cal-149Ta_fig10_4	37.260	0.019	0.000	30.357	0.636	31.407	0.112	0.004	0.024	99.818
Cal-149Tb_fig6_ol2_1	38.424	0.009	0.000	22.350	0.372	38.165	0.129	0.000	0.022	99.470
Cal-149Tb_fig6_ol2_2	38.602	0.008	0.000	21.823	0.353	38.469	0.131	0.000	0.026	99.411
Cal-149Tb_fig6_ol2_3	38.361	0.009	0.000	22.712	0.390	37.604	0.130	0.000	0.021	99.235
Cal-149Tb_fig6_ol3_1	38.080	0.015	0.000	25.080	0.471	35.624	0.127	0.003	0.016	99.416
Cal-149Tb_fig6_ol3_2	38.179	0.009	0.000	24.236	0.443	36.556	0.128	0.003	0.020	99.574
Cal-149Tb_fig6_ol3_3	38.143	0.010	0.000	24.491	0.458	36.272	0.127	0.000	0.021	99.518
Cal-149Tb_fig6_ol3_4	38.040	0.010	0.000	24.550	0.458	35.991	0.122	0.000	0.014	99.187
Cal-149Tb_fig9_ol1_1	37.336	0.012	0.000	27.982	0.579	33.204	0.124	0.000	0.020	99.252
Cal-149Tb_fig9_ol1_2	37.659	0.015	0.000	28.492	0.592	32.914	0.127	0.000	0.013	99.806
Cal-149Tb_fig9_ol1_3	37.741	0.014	0.000	28.009	0.582	33.570	0.123	0.004	0.016	100.058
Cal-149Tb_fig9_ol1_4	37.572	0.014	0.000	28.248	0.584	33.269	0.124	0.000	0.018	99.827
Cal-149Tb_fig18_ol3_1	37.535	0.013	0.000	26.967	0.509	33.945	0.120	0.000	0.023	99.107
Cal-149Tb_fig18_ol3_3	38.003	0.017	0.000	25.336	0.468	35.421	0.116	0.000	0.023	99.384

Table A5. Continued.

SAMPLE	SiO_2	TiO_2	Al_2O_3	FeO	MnO	MgO	CaO	Cr_2O_3	NiO	TOTAL
Cal-149Tb_fig18_ol3_4	37.794	0.013	0.000	25.746	0.479	35.133	0.118	0.001	0.022	99.307
Cal-149Tb_fig18_ol3_5	37.367	0.013	0.000	27.466	0.529	33.627	0.124	0.003	0.019	99.149
Cal-149Tb_fig18_ol2_1	37.295	0.021	0.000	29.024	0.571	32.551	0.130	0.000	0.020	99.609
Cal-157a_fig6_ol1_1	37.014	0.016	0.000	28.709	0.570	33.137	0.128	0.007	0.022	99.602
Cal-157a_fig6_ol1_2	36.994	0.012	0.000	28.859	0.572	33.167	0.127	0.001	0.017	99.750
Cal-157a_fig6_ol2_1	37.155	0.015	0.000	28.651	0.570	33.316	0.127	0.003	0.025	99.861
Cal-157a_fig6_ol2_2	37.201	0.016	0.000	28.785	0.570	33.138	0.129	0.005	0.026	99.871
Cal-157a_fig11_ol1_1	36.984	0.018	0.000	28.641	0.553	33.172	0.130	0.005	0.017	99.522
Cal-157a_fig11_ol1_2	37.373	0.013	0.000	28.868	0.570	33.321	0.134	0.005	0.012	100.295
Cal-157a_fig11_ol1_2	37.027	0.010	0.000	28.680	0.557	33.080	0.136	0.004	0.013	99.507
Cal-157a_fig11_ol1_3	37.183	0.012	0.000	28.567	0.564	33.262	0.129	0.001	0.010	99.728
Cal-157a_fig20_ol1_1	37.230	0.013	0.000	28.399	0.550	33.351	0.126	0.000	0.021	99.692
Cal-157a_fig20_ol1_2	37.222	0.017	0.000	28.613	0.549	33.170	0.125	0.000	0.022	99.715
Cal-157a_fig26_ol1_1	37.317	0.016	0.000	27.166	0.520	34.130	0.121	0.000	0.006	99.276
Cal-157a_fig26_ol1_2	38.077	0.015	0.000	26.800	0.522	35.145	0.116	0.000	0.015	100.608
Cal-158_Fig18_ol2_1	38.417	0.004	0.000	26.772	0.449	34.943	0.132	0.004	0.015	100.736
Cal-158_Fig18_ol2_2	38.636	0.000	0.001	26.474	0.473	34.668	0.131	0.002	0.022	100.407
Cal-158_Fig1_ol2_3	38.513	0.000	0.002	26.857	0.498	34.281	0.131	0.008	0.009	100.398
Cal-159_fig14_ol_1	38.050	0.003	0.010	28.207	0.522	33.049	0.122	0.006	0.011	99.981
Cal-159_fig14_ol_2	38.308	0.009	0.003	28.924	0.530	32.705	0.142	0.006	0.022	100.649
Cal-159_fig14_ol_5	38.267	0.000	0.011	27.023	0.502	33.933	0.119	0.000	0.000	99.854

Table A6. Compositions of plagioclase from the April 2015 Calbuco eruption (wt%).

SAMPLE	SiO_2	TiO_2	Al_2O_3	FeO	MgO	CaO	SrO	BaO	Na_2O	K_2O	TOTAL
Cal-149Ta_figa_p1_1	54.317	0.021	27.812	0.377	0.032	11.465	0.121	0.001	5.677	0.099	99.922
Cal-149Ta_figa_p1_2	53.362	0.026	28.136	0.393	0.035	12.158	0.103	0.000	5.206	0.086	99.502
Cal-149Ta_figa_p1_3	52.588	0.033	28.603	0.410	0.033	12.630	0.095	0.020	5.020	0.081	99.513
Cal-149Ta_figa_p1_4	48.766	0.029	30.887	0.504	0.039	15.309	0.117	0.009	3.215	0.042	98.918
Cal-149Ta_figa_p1_5	51.210	0.031	29.588	0.535	0.047	13.890	0.107	0.012	4.237	0.057	99.715
Cal-149Ta_figa_p1_6	50.359	0.032	30.021	0.512	0.041	14.402	0.139	0.010	3.860	0.054	99.431
Cal-149Ta_figa_p1_7	49.434	0.031	30.649	0.512	0.038	14.992	0.108	0.000	3.550	0.047	99.358
Cal-149Ta_figa_p1_8	46.143	0.028	28.375	0.494	0.040	14.151	0.074	0.001	3.432	0.047	92.786
Cal-149Ta_figa_p1_9	49.571	0.032	30.623	0.539	0.044	14.973	0.114	0.004	3.634	0.041	99.576
Cal-149Ta_figa_p1_10	51.594	0.034	29.476	0.488	0.046	13.662	0.102	0.004	4.467	0.061	99.934
Cal-149Ta_figa_p1_11	51.045	0.028	29.951	0.497	0.040	14.113	0.106	0.005	4.045	0.055	99.883
Cal-149Ta_figa_p1_12	49.839	0.027	30.672	0.518	0.044	15.028	0.109	0.008	3.540	0.045	99.831
Cal-149Ta_figa_p1_13	51.590	0.030	29.045	0.492	0.048	13.536	0.117	0.010	4.460	0.064	99.392
Cal-149Ta_figa_p1_14	47.992	0.023	31.336	0.505	0.037	16.174	0.097	0.008	2.666	0.033	98.873
Cal-149Ta_figa_p1_15	45.400	0.020	32.838	0.515	0.027	18.202	0.102	0.016	1.596	0.018	98.734
Cal-149Ta_figa_p1_16	45.022	0.023	33.336	0.530	0.025	18.608	0.135	0.012	1.297	0.014	99.002
Cal-149Ta_figa_p1_17	44.789	0.019	33.309	0.513	0.022	18.596	0.099	0.000	1.300	0.018	98.654
Cal-149Ta_figa_p1_18	45.031	0.024	33.505	0.500	0.025	18.715	0.111	0.000	1.321	0.010	99.237
Cal-149Ta_figa_p1_19	44.931	0.016	33.286	0.510	0.028	18.570	0.091	0.000	1.412	0.011	98.845
Cal-149Ta_figa_p1_20	44.683	0.017	33.369	0.515	0.023	18.666	0.093	0.000	1.281	0.004	98.636

Table A6. (Continued).

SAMPLE	SiO_2	TiO_2	Al_2O_3	FeO	MgO	CaO	SrO	BaO	Na_2O	K_2O	TOTAL
Cal-149Ta_fign_p1_1	52.288	0.034	28.981	0.439	0.036	12.663	0.124	0.016	5.092	0.082	99.755
Cal-149Ta_fign_p1_2	49.773	0.037	30.173	0.505	0.042	14.354	0.120	0.011	3.962	0.055	99.032
Cal-149Ta_fign_p1_3	49.388	0.028	30.286	0.512	0.028	14.588	0.142	0.006	3.810	0.046	98.833
Cal-149Ta_fign_p1_4	50.028	0.024	30.149	0.483	0.000	14.529	0.084	0.013	3.987	0.048	99.039
Cal-149Ta_fign_p1_5	49.101	0.033	30.338	0.506	0.045	14.892	0.117	0.000	3.725	0.044	98.801
Cal-149Ta_fign_p1_6	51.507	0.040	28.812	0.490	0.051	13.082	0.120	0.000	4.776	0.072	98.943
Cal-149Ta_fign_p1_7	48.766	0.028	30.677	0.496	0.045	15.137	0.131	0.000	3.438	0.048	98.763
Cal-149Ta_fign_p1_8	44.728	0.014	33.374	0.599	0.035	18.476	0.088	0.000	1.399	0.016	98.729
Cal-149Ta_fign_p1_9	44.618	0.027	32.968	0.610	0.025	18.402	0.088	0.000	1.451	0.011	98.196
Cal-149Ta_fign_p1_10	44.611	0.016	33.045	0.612	0.043	18.379	0.103	0.000	1.402	0.007	98.214
Cal-149Ta_fign_p1_11	44.790	0.023	33.245	0.603	0.047	18.344	0.117	0.003	1.461	0.016	98.648
Cal-149Ta_fign_p1_12	44.849	0.019	33.094	0.617	0.047	18.357	0.089	0.009	1.502	0.015	98.598
Cal-149Ta_fign_p1_13	44.890	0.015	33.284	0.601	0.048	18.607	0.069	0.005	1.457	0.012	98.988
Cal-149Ta_fign_p1_14	44.954	0.027	33.142	0.615	0.052	18.435	0.068	0.000	1.494	0.012	98.800
Cal-149Ta_fign_p1_15	44.797	0.012	33.306	0.593	0.055	18.466	0.093	0.012	1.425	0.012	98.770
Cal-149Ta_fign_p1_16	45.021	0.026	33.154	0.567	0.061	18.422	0.062	0.000	1.482	0.013	98.804
Cal-149Ta_fign_p1_17	44.744	0.023	33.047	0.548	0.057	18.255	0.111	0.006	1.431	0.016	98.236

Table A6. (Continued).

SAMPLE	SiO_2	TiO_2	Al_2O_3	FeO	MgO	CaO	SrO	BaO	Na_2O	K_2O	TOTAL
Cal-149Ta_figp_p1_1	52.635	0.027	30.636	0.503	0.047	11.298	0.130	0.004	4.372	0.064	99.715
Cal-149Ta_figp_p1_2	52.213	0.033	31.215	0.461	0.034	11.849	0.128	0.000	4.179	0.045	100.157
Cal-149Ta_figp_p1_3	50.848	0.031	31.675	0.504	0.042	12.628	0.130	0.010	3.564	0.043	99.476
Cal-149Ta_figp_p1_4	51.855	0.029	30.809	0.485	0.038	11.901	0.100	0.001	4.119	0.054	99.391
Cal-149Ta_figp_p1_5	50.596	0.026	32.358	0.478	0.035	12.741	0.124	0.014	3.578	0.049	99.998
Cal-149Ta_figp_p1_6	49.772	0.021	32.216	0.472	0.033	13.535	0.128	0.014	3.070	0.033	99.295
Cal-149Ta_figp_p1_7	48.910	0.025	32.658	0.476	0.039	13.869	0.135	0.007	2.856	0.036	99.011
Cal-149Ta_figp_p1_8	50.860	0.025	32.011	0.455	0.040	13.009	0.354	0.012	3.511	0.052	100.329
Cal-149Ta_figp_p1_9	49.124	0.024	33.261	0.475	0.033	14.172	0.112	0.016	2.665	0.040	99.922
Cal-149Ta_figp_p1_10	49.219	0.022	33.008	0.468	0.040	13.698	0.121	0.011	2.984	0.038	99.609
Cal-149Ta_figp_p1_11	50.786	0.021	31.779	0.461	0.042	13.058	0.069	0.007	3.409	0.039	99.672
Cal-149Ta_figp_p1_12	48.826	0.021	33.072	0.481	0.038	14.276	0.093	0.007	2.728	0.029	99.571
Cal-149Ta_figp_p1_13	49.324	0.023	32.711	0.478	0.040	13.896	0.091	0.015	2.882	0.040	99.498
Cal-149Ta_figp_p1_14	50.270	0.025	32.208	0.459	0.039	13.198	0.088	0.005	3.192	0.033	99.517
Cal-149Ta_figp_p1_15	49.799	0.026	32.366	0.476	0.038	13.512	0.105	0.003	3.110	0.034	99.469
Cal-149Ta_figp_p1_16	49.501	0.024	32.377	0.497	0.043	13.573	0.112	0.000	3.015	0.033	99.171
Cal-149Ta_figp_p1_17	49.932	0.038	31.751	0.554	0.050	13.407	0.081	0.007	2.976	0.062	98.858
Cal-149Ta_figp_p1_18	53.984	0.199	27.851	1.232	0.201	10.195	0.104	0.000	3.396	0.307	97.460
Cal-149Ta_figp_p1_19	51.825	0.108	29.512	0.786	0.109	11.551	0.102	0.002	3.355	0.193	97.543
Cal-149Ta_figp_p1_20	50.520	0.028	31.897	0.481	0.042	12.885	0.082	0.010	3.308	0.051	99.302
Cal-149Ta_figp_p1_21	49.460	0.030	32.391	0.482	0.036	13.423	0.112	0.008	3.165	0.038	99.145
Cal-149Ta_figp_p1_22	50.817	0.031	31.872	0.452	0.042	12.705	0.090	0.012	3.600	0.049	99.671
Cal-149Ta_figp_p1_23	50.313	0.027	31.886	0.450	0.041	13.053	0.107	0.002	3.395	0.042	99.317
Cal-149Ta_figp_p1_24	50.500	0.021	31.965	0.449	0.041	12.916	0.098	0.000	3.358	0.034	99.380
Cal-149Ta_figp_p1_25	50.048	0.023	32.695	0.452	0.042	13.775	0.108	0.000	3.015	0.034	100.192
Cal-149Ta_figp_p1_26	50.479	0.028	32.252	0.447	0.041	13.126	0.112	0.018	3.451	0.053	100.008

Table A6. (Continued).

SAMPLE	SiO_2	TiO_2	Al_2O_3	FeO	MgO	CaO	SrO	BaO	Na_2O	K_2O	TOTAL
Cal-149Ta_figr_p1_1	56.105	0.033	27.721	0.416	0.032	9.063	0.122	0.019	5.649	0.126	99.286
Cal-149Ta_figr_p1_2	53.661	0.027	28.746	0.395	0.032	10.307	0.109	0.010	5.005	0.084	98.376
Cal-149Ta_figr_p1_3	53.595	0.027	29.199	0.386	0.036	10.416	0.092	0.008	4.803	0.070	98.631
Cal-149Ta_figr_p1_4	53.338	0.027	28.875	0.397	0.034	10.585	0.106	0.008	4.844	0.078	98.290
Cal-149Ta_figr_p1_5	52.903	0.031	29.092	0.409	0.037	10.807	0.114	0.002	4.708	0.070	98.171
Cal-149Ta_figr_p1_6	53.116	0.031	29.639	0.425	0.044	11.121	0.109	0.000	4.598	0.070	99.148
Cal-149Ta_figr_p1_7	53.227	0.031	29.889	0.440	0.046	11.110	0.112	0.007	4.565	0.076	99.501
Cal-149Ta_figr_p1_8	52.087	0.034	29.621	0.467	0.047	11.424	0.132	0.002	4.405	0.068	98.287
Cal-149Ta_figr_p1_9	51.519	0.037	30.257	0.494	0.047	11.865	0.070	0.002	4.084	0.059	98.436
Cal-149Ta_figr_p1_10	50.305	0.039	31.287	0.533	0.052	12.973	0.116	0.013	3.460	0.038	98.815
Cal-149Ta_figr_p1_11	51.839	0.042	30.093	0.522	0.060	11.686	0.080	0.005	4.248	0.052	98.628
Cal-149Ta_figr_p1_12	51.969	0.039	29.987	0.515	0.056	11.493	0.093	0.003	4.256	0.064	98.474
Cal-149Ta_figr_p1_13	50.521	0.029	30.595	0.528	0.051	12.359	0.069	0.005	3.496	0.054	97.705
Cal-149Ta_figr_p1_14	51.016	0.038	30.166	0.510	0.057	11.976	0.098	0.000	3.953	0.056	97.867
Cal-149Ta_figr_p1_15	48.622	0.025	31.853	0.508	0.036	13.789	0.078	0.004	2.578	0.044	97.537
Cal-149Ta_figr_p1_16	45.466	0.026	34.305	0.581	0.032	16.014	0.093	0.000	1.504	0.016	98.027
Cal-149Ta_figr_p1_17	45.934	0.022	33.932	0.591	0.039	15.973	0.097	0.002	1.501	0.008	98.098
Cal-149Ta_figr_p1_18	45.964	0.017	33.694	0.575	0.037	15.688	0.115	0.008	1.539	0.014	97.651
Cal-149Ta_figr_p1_19	45.961	0.018	33.959	0.592	0.040	15.674	0.110	0.006	1.696	0.013	98.069
Cal-149Ta_figr_p1_20	45.950	0.022	33.674	0.589	0.042	15.583	0.103	0.000	1.694	0.021	97.670
Cal-149Ta_figr_p1_21	46.310	0.025	34.085	0.576	0.040	15.466	0.085	0.003	1.685	0.017	98.290
Cal-149Ta_figr_p1_22	45.966	0.012	34.559	0.587	0.043	15.740	0.061	0.007	1.554	0.009	98.538
Cal-149Ta_figr_p1_23	46.270	0.025	34.099	0.581	0.046	15.540	0.105	0.001	1.703	0.017	98.387

Table A6. (Continued).

SAMPLE	SiO_2	TiO_2	Al_2O_3	FeO	MgO	CaO	SrO	BaO	Na_2O	K_2O	TOTAL
Cal-157a_figh_p1_1	51.573	0.043	30.973	0.582	0.072	11.634	0.115	0.014	4.206	0.064	99.275
Cal-157a_figh_p1_2	51.518	0.036	30.867	0.590	0.069	11.690	0.104	0.011	4.258	0.063	99.206
Cal-157a_figh_p1_3	50.664	0.038	31.705	0.604	0.079	12.711	0.087	0.005	3.620	0.043	99.557
Cal-157a_figh_p1_4	45.322	0.018	34.716	0.624	0.046	15.781	0.090	0.010	1.562	0.018	98.186
Cal-157a_figh_p1_5	45.302	0.027	35.075	0.609	0.041	16.168	0.082	0.007	1.505	0.016	98.833
Cal-157a_figh_p1_6	44.457	0.012	35.653	0.554	0.046	16.651	0.091	0.000	1.195	0.016	98.662
Cal-157a_figh_p1_7	44.373	0.019	35.453	0.547	0.045	16.529	0.094	0.000	1.213	0.006	98.271
Cal-157a_figh_p1_8	44.602	0.017	35.547	0.517	0.045	16.769	0.121	0.000	1.233	0.004	98.854
Cal-157a_figh_p1_9	44.237	0.014	35.579	0.510	0.049	16.637	0.089	0.002	1.158	0.008	98.283
Cal-157a_figh_p1_10	44.388	0.011	35.105	0.511	0.052	16.229	0.100	0.000	1.294	0.007	97.692
Cal-157a_figh_p1_11	44.394	0.013	35.419	0.479	0.050	16.611	0.113	0.000	1.036	0.015	98.121
Cal-157a_figh_p1_12	44.478	0.014	35.461	0.461	0.049	16.861	0.090	0.000	1.007	0.005	98.423
Cal-157a_figh_p1_13	44.382	0.014	34.888	0.477	0.053	16.415	0.057	0.000	1.166	0.006	97.451
Cal-157a_figh_p1_14	44.680	0.018	35.240	0.476	0.050	16.416	0.073	0.001	1.236	0.015	98.204

Table A6. (Continued).

SAMPLE	SiO_2	TiO_2	Al_2O_3	FeO	MgO	CaO	SrO	BaO	Na_2O	K_2O	TOTAL
Cal-158_figg_p1_1	51.529	0.046	30.544	0.623	0.070	11.556	0.113	0.011	4.125	0.061	98.679
Cal-158_figg_p1_2	53.151	0.047	30.780	0.613	0.066	11.612	0.119	0.007	4.347	0.086	100.827
Cal-158_figg_p1_3	50.814	0.028	31.139	0.591	0.054	12.501	0.062	0.003	3.550	0.051	98.792
Cal-158_figg_p1_4	51.447	0.042	30.619	0.592	0.069	12.058	0.095	0.010	3.801	0.059	98.794
Cal-158_figg_p1_5	51.927	0.048	30.417	0.589	0.067	11.704	0.113	0.011	4.148	0.064	99.086
Cal-158_figg_p1_6	51.445	0.046	30.454	0.586	0.067	12.027	0.091	0.010	3.940	0.061	98.726
Cal-158_figg_p1_7	50.834	0.040	31.193	0.590	0.061	12.775	0.089	0.015	3.600	0.060	99.258
Cal-158_figg_p1_8	50.524	0.041	31.117	0.575	0.071	12.792	0.064	-0.003	3.472	0.047	98.701
Cal-158_figg_p1_9	46.944	0.019	33.429	0.583	0.040	15.791	0.093	-0.009	1.577	0.018	98.484
Cal-158_figg_p1_10	45.844	0.020	34.514	0.564	0.036	16.362	0.104	-0.002	1.259	0.008	98.710
Cal-158_figg_p1_11	45.279	0.012	35.143	0.544	0.032	16.549	0.117	0.008	1.165	0.019	98.869
Cal-158_figg_p1_12	45.218	0.019	34.704	0.524	0.032	16.552	0.087	0.004	1.094	0.009	98.244
Cal-158_figg_p1_13	45.708	0.016	35.271	0.529	0.032	16.442	0.101	0.007	1.150	0.007	99.262
Cal-158_figg_p1_14	45.398	0.019	34.498	0.520	0.037	16.331	0.095	0.012	1.304	0.011	98.225
Cal-158_figg_p1_15	45.131	0.014	34.502	0.516	0.036	16.392	0.118	0.007	1.212	0.006	97.933
Cal-158_figg_p1_16	45.091	0.015	35.061	0.507	0.033	16.682	0.102	0.004	1.117	0.018	98.629
Cal-158_figg_p1_17	45.015	0.015	34.939	0.499	0.031	16.396	0.068	0.002	1.102	0.008	98.074
Cal-158_figg_p1_18	45.583	0.016	35.202	0.511	0.037	16.476	0.138	0.000	1.289	0.021	99.273

Table A6. (Continued).

SAMPLE	SiO_2	TiO_2	Al_2O_3	FeO	MgO	CaO	SrO	BaO	Na_2O	K_2O	TOTAL
Cal-159a_figp_p1_1	52.328	0.043	30.244	0.581	0.065	11.168	0.120	0.004	4.479	0.066	99.097
Cal-159a_figp_p1_2	51.726	0.043	30.240	0.583	0.069	11.597	0.117	0.012	4.156	0.057	98.599
Cal-159a_figp_p1_3	49.019	0.026	32.585	0.598	0.057	13.524	0.120	0.000	2.933	0.040	98.898
Cal-159a_figp_p1_4	48.257	0.027	33.148	0.577	0.057	14.276	0.117	0.000	2.673	0.037	99.156
Cal-159a_figp_p1_5	45.329	0.020	34.768	0.566	0.044	15.903	0.112	0.000	1.523	0.020	98.285
Cal-159a_figp_p1_6	45.907	0.021	35.236	0.581	0.046	15.874	0.099	0.004	1.546	0.019	99.333
Cal-159a_figp_p1_7	45.698	0.020	34.648	0.580	0.047	15.991	0.084	0.010	1.531	0.015	98.623
Cal-159a_figp_p1_8	45.813	0.022	34.301	0.562	0.054	15.609	0.100	0.000	1.484	0.021	97.960
Cal-159a_figp_p1_9	45.257	0.015	34.485	0.571	0.054	15.645	0.097	0.000	1.531	0.015	97.660
Cal-159a_figp_p1_10	45.984	0.019	34.284	0.563	0.057	15.754	0.098	0.012	1.583	0.015	98.368
Cal-159a_figp_p1_11	45.854	0.018	34.211	0.559	0.057	15.502	0.086	0.009	1.729	0.021	98.045
Cal-159a_figp_p1_12	45.626	0.020	34.231	0.541	0.059	15.603	0.099	0.001	1.667	0.018	97.865
Cal-159a_figp_p1_13	44.991	0.023	34.258	0.516	0.053	16.033	0.113	0.006	1.432	0.015	97.440
Cal-159a_figp_p1_14	45.451	0.015	34.134	0.503	0.056	15.845	0.086	0.000	1.518	0.010	97.402
Cal-159a_figp_p1_15	45.410	0.015	34.182	0.499	0.053	15.904	0.075	0.000	1.463	0.009	97.607
Cal-159a_figp_p1_16	44.973	0.015	34.602	0.484	0.052	16.278	0.092	0.004	1.352	0.022	97.873
Cal-159a_figp_p1_17	45.290	0.018	34.657	0.482	0.051	15.904	0.092	0.000	1.316	0.020	97.823
Cal-159a_figp_p1_18	45.075	0.018	34.540	0.476	0.055	15.987	0.105	0.002	1.422	0.014	97.694
Cal-159a_figp_p1_19	45.314	0.017	34.845	0.469	0.051	15.967	0.082	0.000	1.511	0.011	98.265
Cal-159a_figp_p1_20	45.498	0.013	34.653	0.464	0.056	15.840	0.082	0.000	1.578	0.025	98.210
Cal-159a_figp_p1_21	45.497	0.017	34.826	0.471	0.056	15.867	0.108	0.000	1.503	0.015	98.357
Cal-159a_figp_p1_22	45.554	0.018	34.888	0.472	0.062	15.947	0.098	0.001	1.581	0.028	98.647

Table A6. (Continued).

SAMPLE	SiO_2	TiO_2	Al_2O_3	FeO	MgO	CaO	SrO	BaO	Na_2O	K_2O	TOTAL
Cal-160_figk_p1	52.072	0.087	30.409	0.949	0.066	12.380	0.108	0.000	3.215	0.152	99.561
Cal-160_figk_p2	50.116	0.039	32.017	0.634	0.060	13.615	0.102	0.017	2.968	0.050	99.617
Cal-160_figk_p3	51.385	0.034	31.012	0.628	0.066	12.678	0.124	0.000	3.679	0.052	99.656
Cal-160_figk_p4	47.803	0.025	33.767	0.640	0.048	15.302	0.113	0.001	2.031	0.027	99.756
Cal-160_figk_p5	46.853	0.021	34.152	0.654	0.046	15.804	0.105	0.009	1.620	0.016	99.281
Cal-160_figk_p6	47.395	0.019	34.043	0.637	0.049	15.537	0.101	0.000	1.835	0.014	99.630
Cal-160_figk_p7	46.984	0.024	34.280	0.609	0.047	16.075	0.100	0.005	1.630	0.011	99.763
Cal-160_figk_p8	46.619	0.014	34.359	0.608	0.049	16.112	0.112	0.002	1.556	0.011	99.443
Cal-160_figk_p9	46.574	0.018	34.670	0.603	0.049	16.059	0.119	0.006	1.508	0.015	99.622
Cal-160_figk_p10	46.339	0.017	34.570	0.588	0.047	16.020	0.088	0.000	1.615	0.012	99.295
Cal-160_figk_p11	46.493	0.018	34.816	0.573	0.048	16.232	0.130	0.000	1.553	0.017	99.873
Cal-160_figk_p12	46.187	0.014	34.578	0.578	0.053	15.975	0.102	0.004	1.578	0.013	99.083
Cal-160_figk_p13	46.409	0.012	34.457	0.567	0.050	16.064	0.118	0.002	1.565	0.024	99.267
Cal-160_figk_p14	45.721	0.015	34.735	0.558	0.047	16.216	0.095	0.000	1.397	0.018	98.799
Cal-160_figk_p15	45.796	0.014	34.324	0.542	0.049	16.093	0.083	0.000	1.478	0.021	98.394
Cal-160_figk_p16	45.789	0.016	34.444	0.531	0.055	15.956	0.088	0.000	1.569	0.002	98.445

Table A6. (Continued).

SAMPLE	SiO_2	TiO_2	Al_2O_3	FeO	MgO	CaO	SrO	BaO	Na_2O	K_2O	TOTAL
Cal-160_figu_p1_1	55.175	0.030	28.673	0.418	0.047	10.149	0.113	0.003	5.295	0.088	99.992
Cal-160_figu_p1_2	52.598	0.032	29.436	0.422	0.036	10.790	0.088	0.005	4.762	0.079	98.248
Cal-160_figu_p1_3	52.700	0.036	29.550	0.430	0.037	10.933	0.089	0.000	4.684	0.074	98.533
Cal-160_figu_p1_4	50.938	0.034	30.606	0.454	0.041	12.398	0.133	0.010	3.953	0.050	98.616
Cal-160_figu_p1_5	44.884	0.020	34.713	0.553	0.025	16.418	0.070	0.002	1.143	0.018	97.846
Cal-160_figu_p1_6	45.042	0.021	34.550	0.610	0.031	16.451	0.088	0.000	1.284	0.012	98.086
Cal-160_figu_p1_7	44.545	0.019	34.160	0.610	0.031	16.177	0.095	0.001	1.241	0.008	96.888
Cal-160_figu_p1_8	45.177	0.021	35.107	0.603	0.036	16.209	0.103	0.001	1.310	0.008	98.575
Cal-160_figu_p1_9	45.153	0.021	34.603	0.598	0.042	16.230	0.106	0.006	1.341	0.008	98.108
Cal-160_figu_p1_10	44.929	0.017	34.398	0.583	0.042	16.284	0.093	0.003	1.453	0.014	97.815
Cal-160_figu_p1_11	45.047	0.017	34.643	0.548	0.036	16.672	0.082	0.006	1.230	0.005	98.286
Cal-160_figu_p1_12	44.521	0.018	35.166	0.524	0.032	16.555	0.099	0.012	1.125	0.008	98.061
Cal-160_figu_p1_13	44.715	0.014	35.425	0.498	0.036	16.837	0.113	0.006	1.107	0.003	98.755
Cal-160_figu_p1_14	44.950	0.024	35.096	0.489	0.039	16.464	0.089	0.007	1.168	0.010	98.336
Cal-160_figu_p1_15	44.870	0.017	35.045	0.481	0.042	16.378	0.113	0.000	1.217	0.010	98.166
Cal-160_figu_p1_16	44.556	0.015	35.088	0.477	0.038	16.403	0.092	0.003	1.168	0.011	97.850
Cal-160_figu_p1_17	44.692	0.014	35.617	0.486	0.037	16.458	0.093	0.000	1.232	0.011	98.639
Cal-160_figu_p1_18	44.738	0.016	35.505	0.473	0.041	16.476	0.093	0.018	1.144	0.002	98.507

A.3. MELTS Modelling – Melt composition

The composition was adjusted via an extraction of the modal composition of representative mineral phases to the whole-rock composition of the sample (see Table 2.3) in order to determine the groundmass (pre-eruptive melt) composition. The modelling intensive conditions ranges were based on thermometers, barometers, and oxybarometers presented above (850-1,070 °C; from 1 bar to 10 kbar; ΔNNO+0.5 oxygen fugacity buffer; see values and associated errors in Tables 5, 6, and 7). All the intensive conditions were considered except when MELTS failed to converge or when ≥ 40% of the total mass of the system correspond to solid phases.

A.4. Pictures of textural features

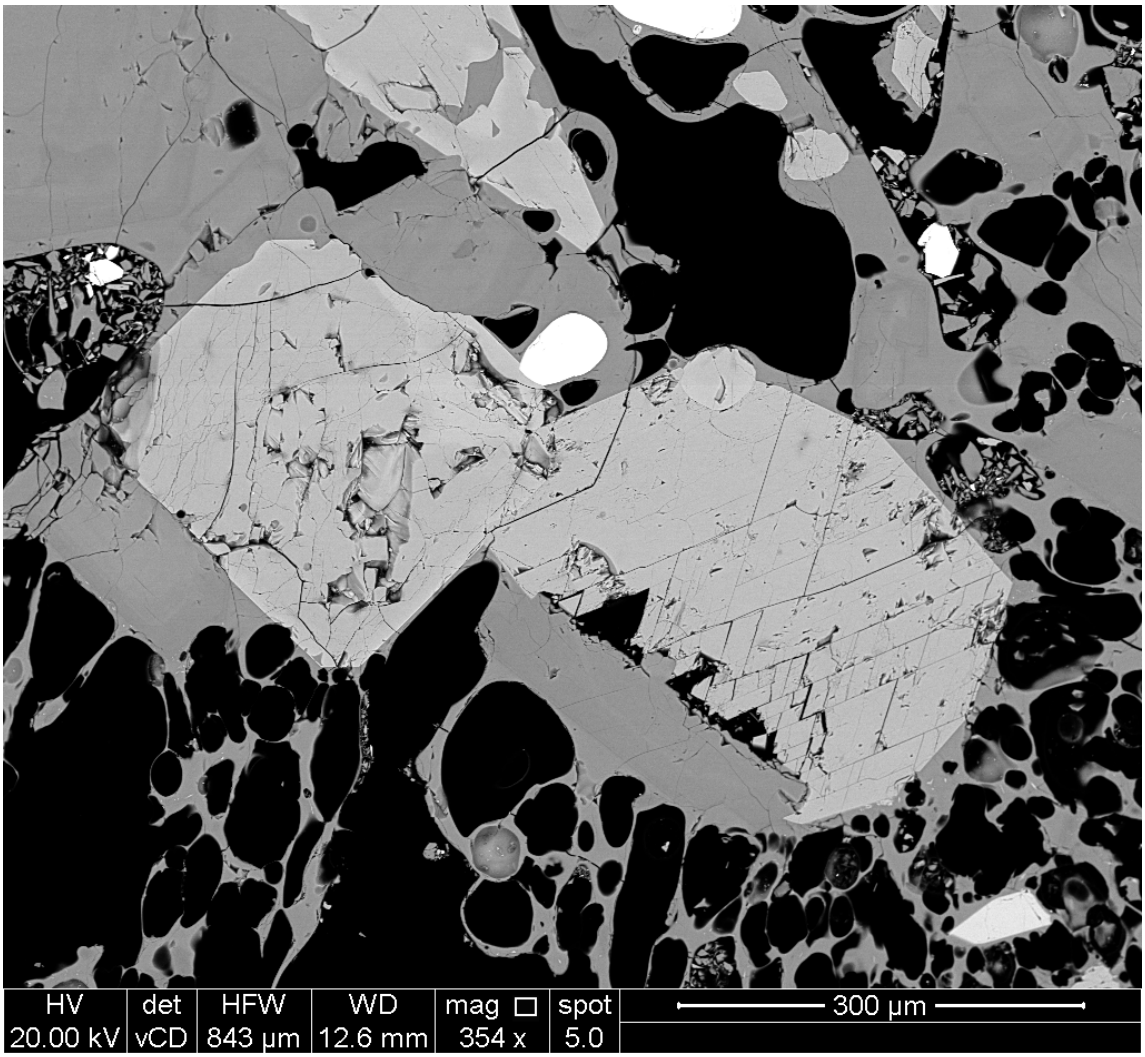

Figure A.2. *Plagioclase and amphibole in contact (Sample Cal-149Ta).*

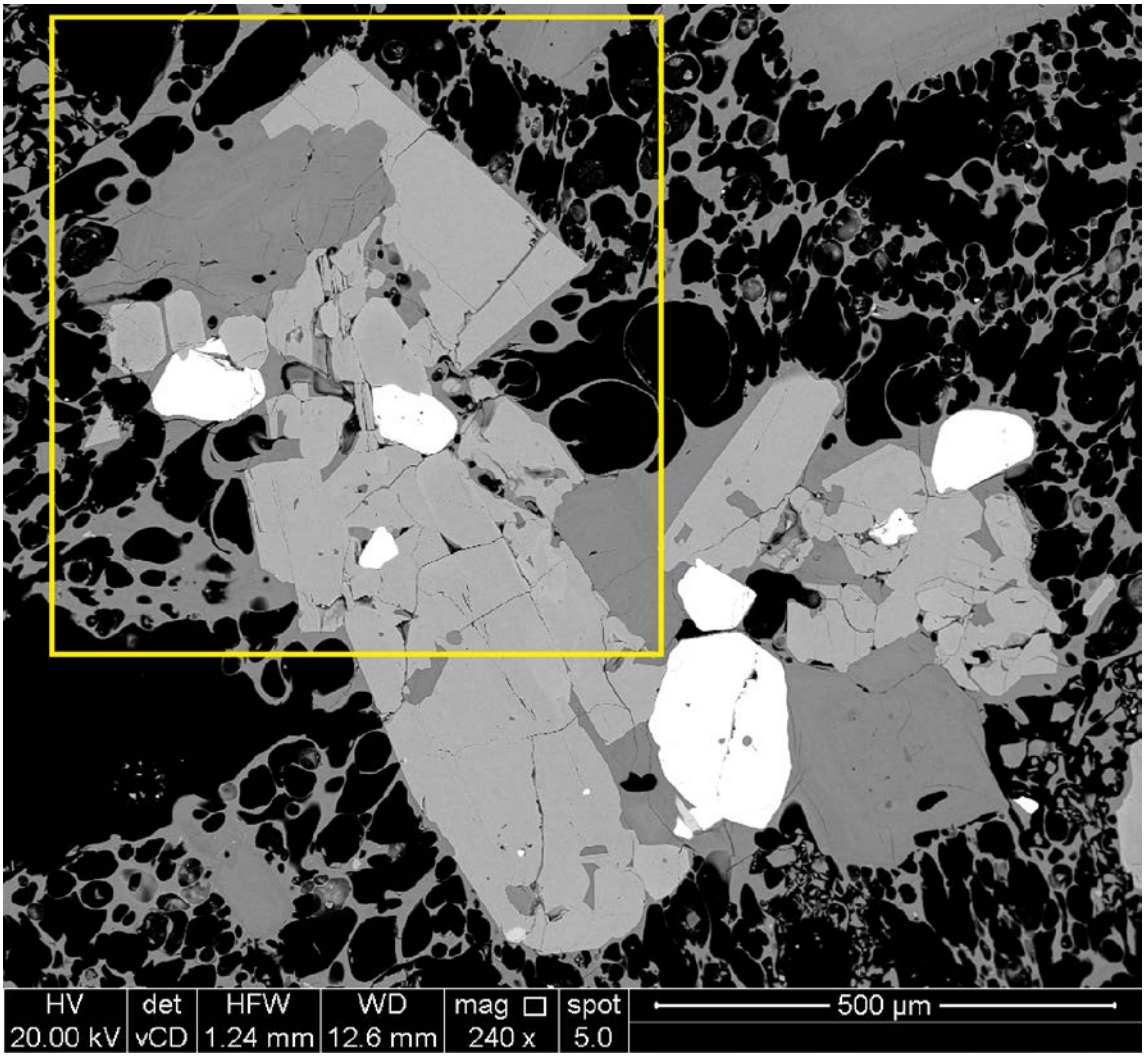

Figure A.3. *Plagioclase, amphibole, clinopyroxene, and orthopyroxene in one clot of crystals (Sample Cal-149Ta).*

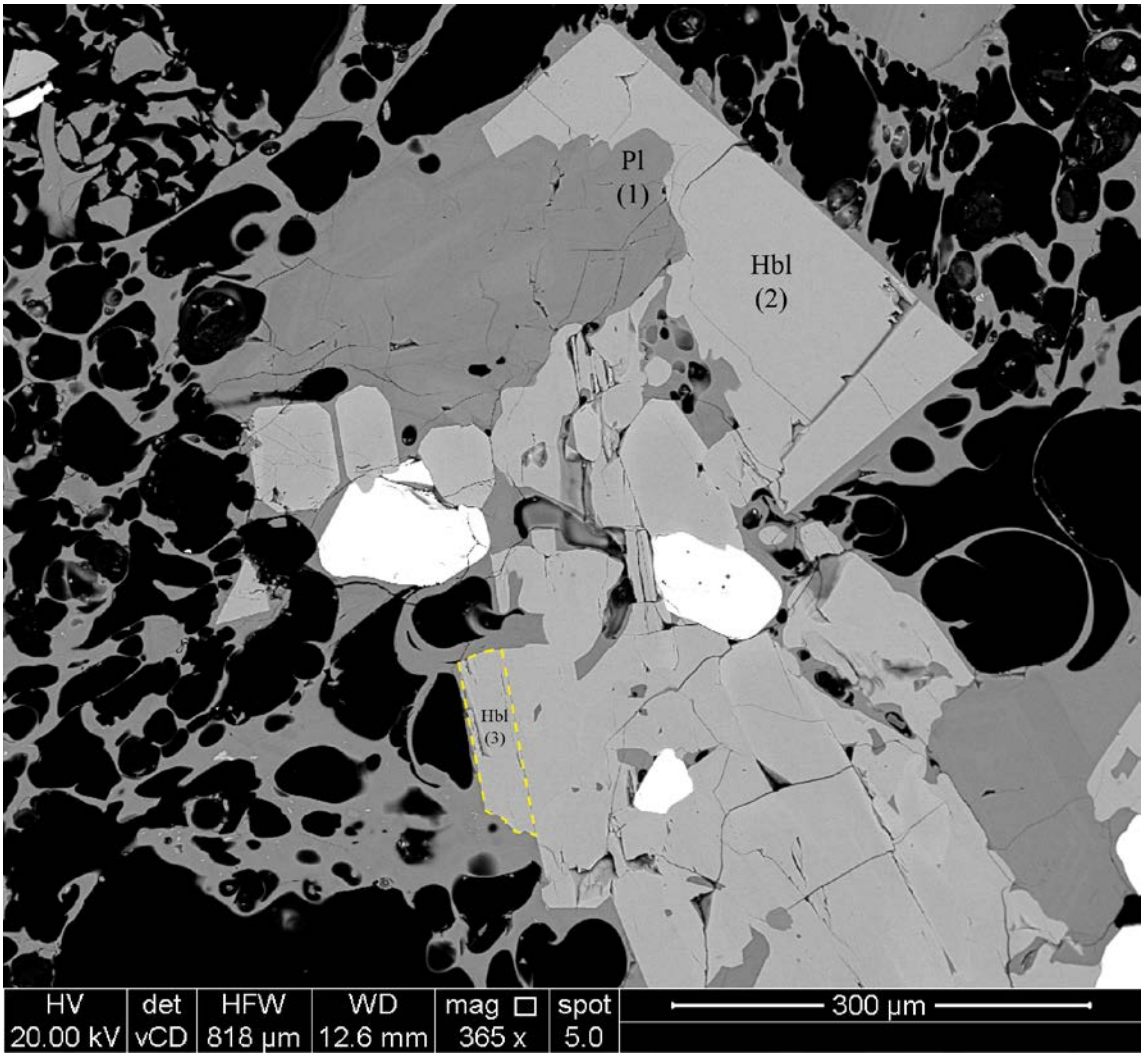

Figure A.4. *Plagioclase and amphibole in contact (Sample Cal-149Ta, zoom of Fig. S2).*

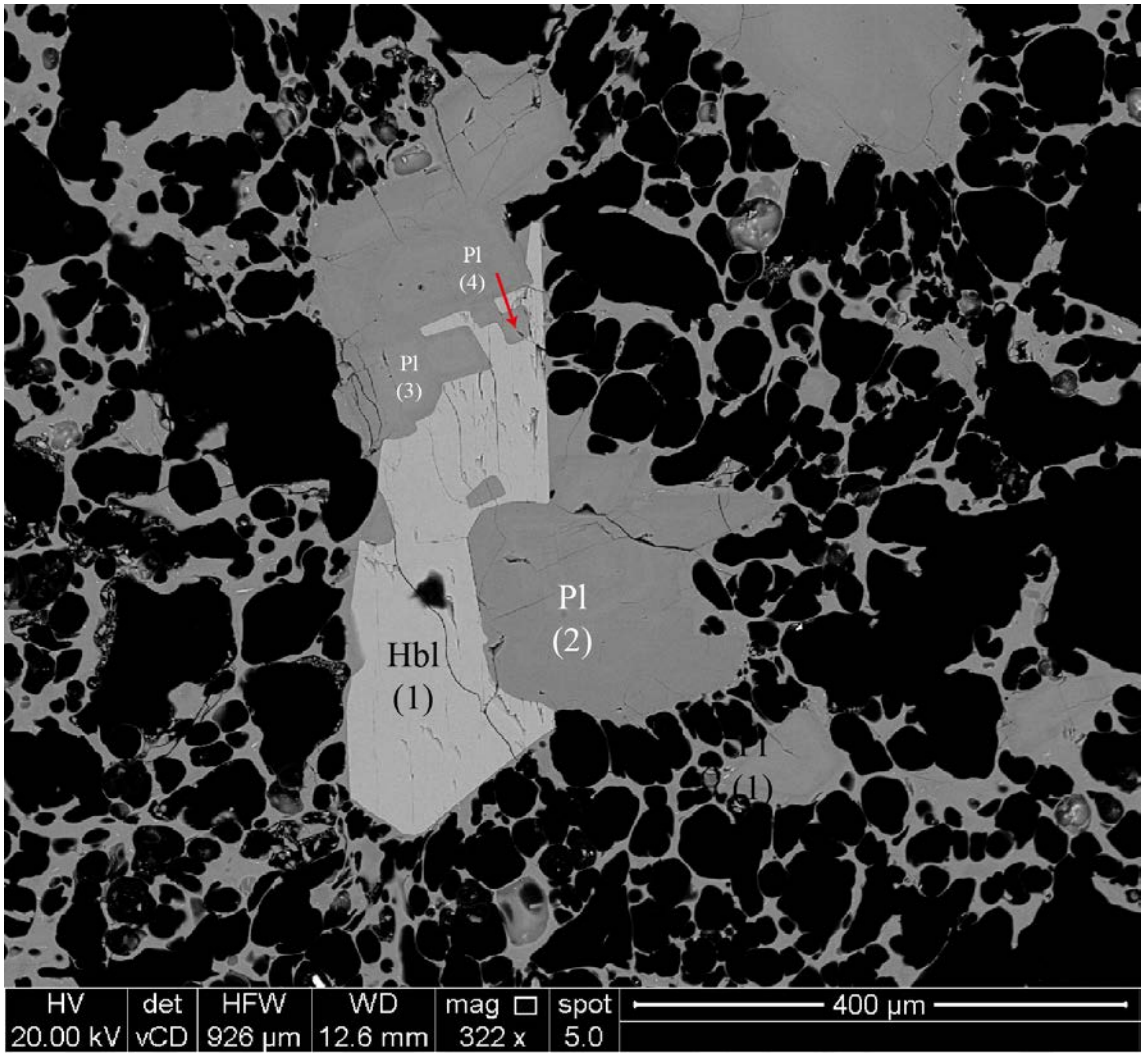

Figure A.5. *Plagioclase and amphibole in contact (Sample Cal-149Ta).*

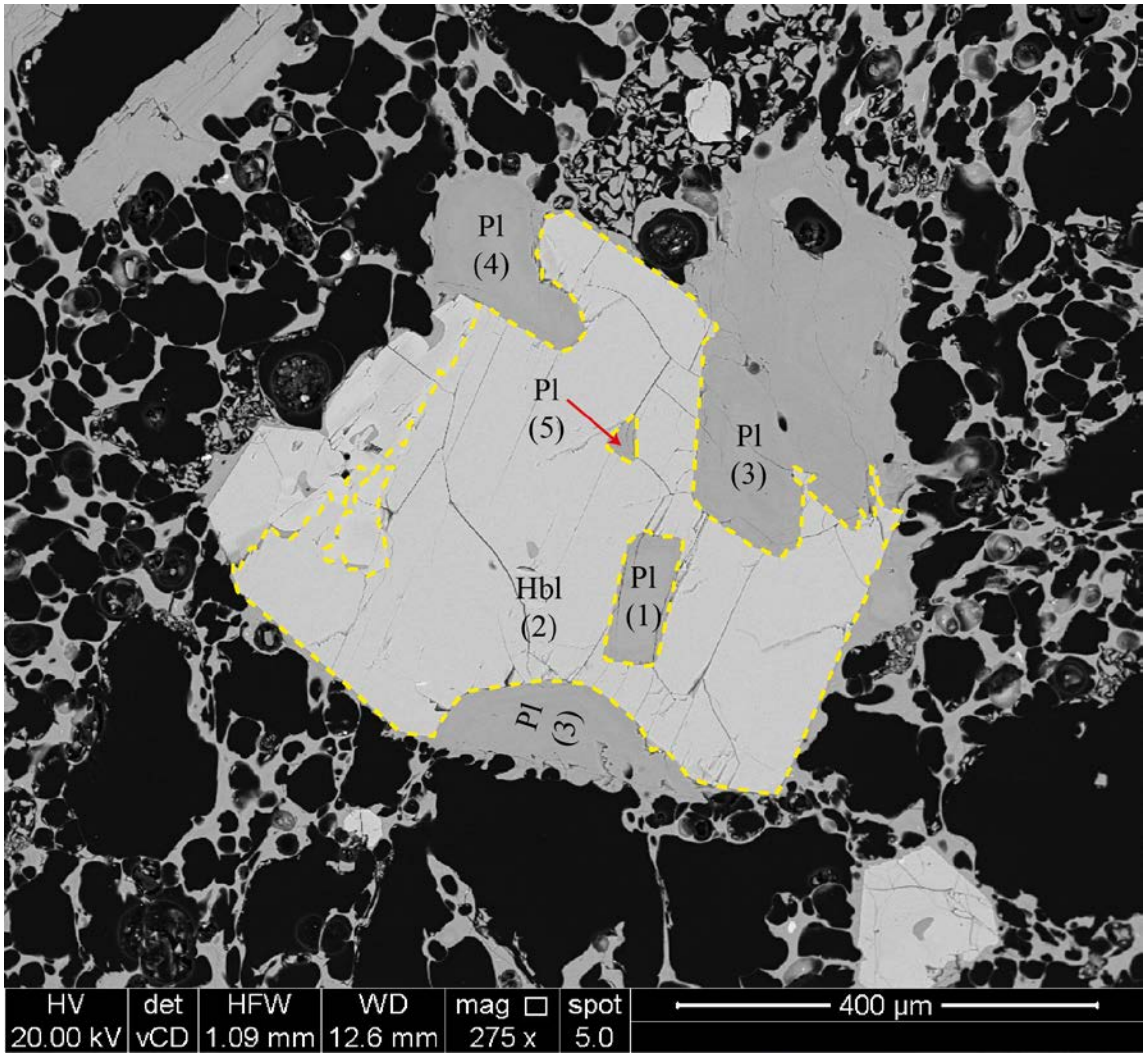

Figure A.6. *Plagioclase and amphibole in contact (Sample Cal-149Ta).*

Figure A.7. *Olivine surrounded by orthopyroxenes and Fe-Ti oxides. The crystal clot is comprised also of plagioclase (Sample Cal-157a).*

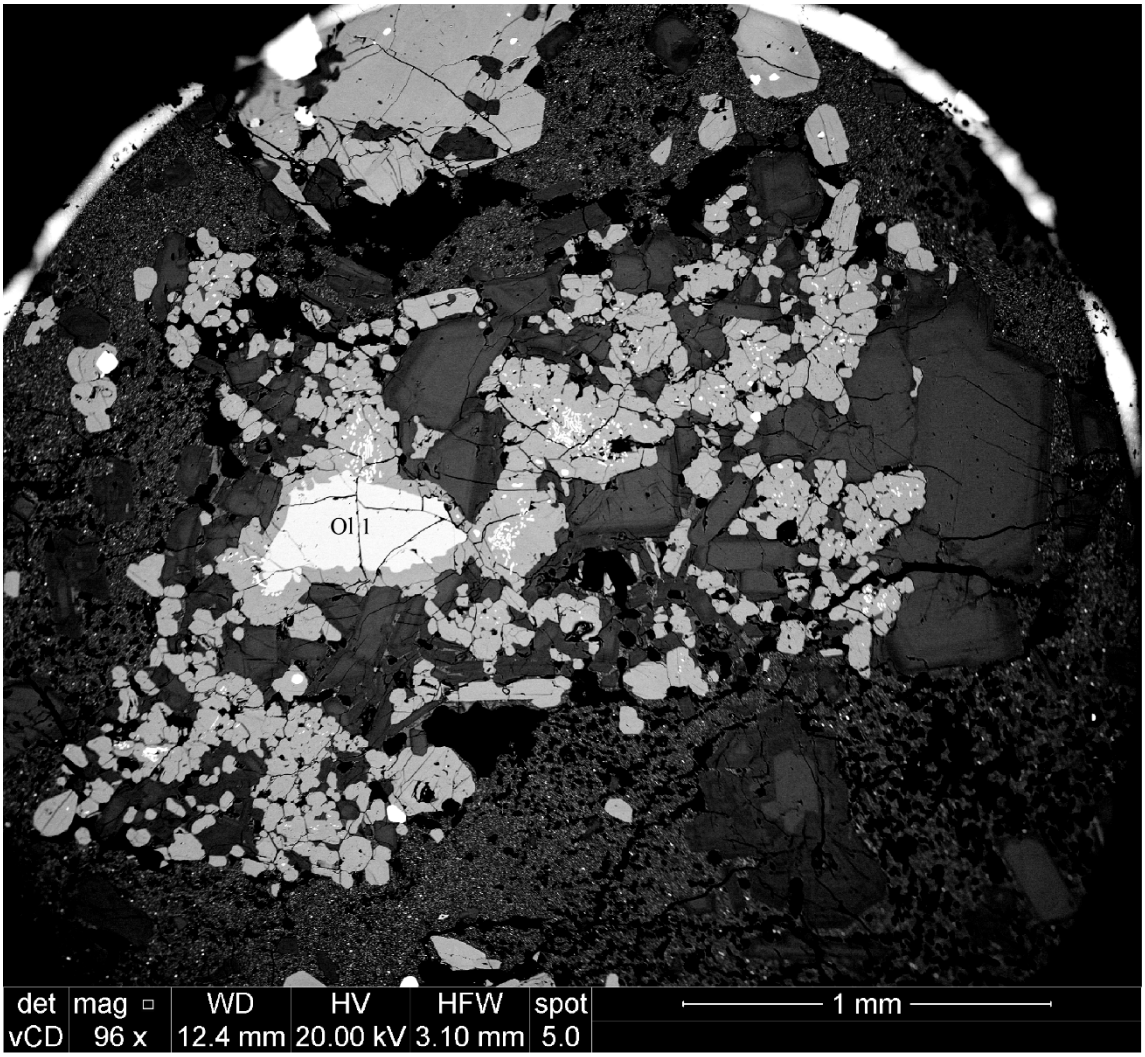

Figure A.8. *Crystal clot comprised of plagioclase, pyroxenes, Fe-Ti oxides, and olivine (Cal159).*

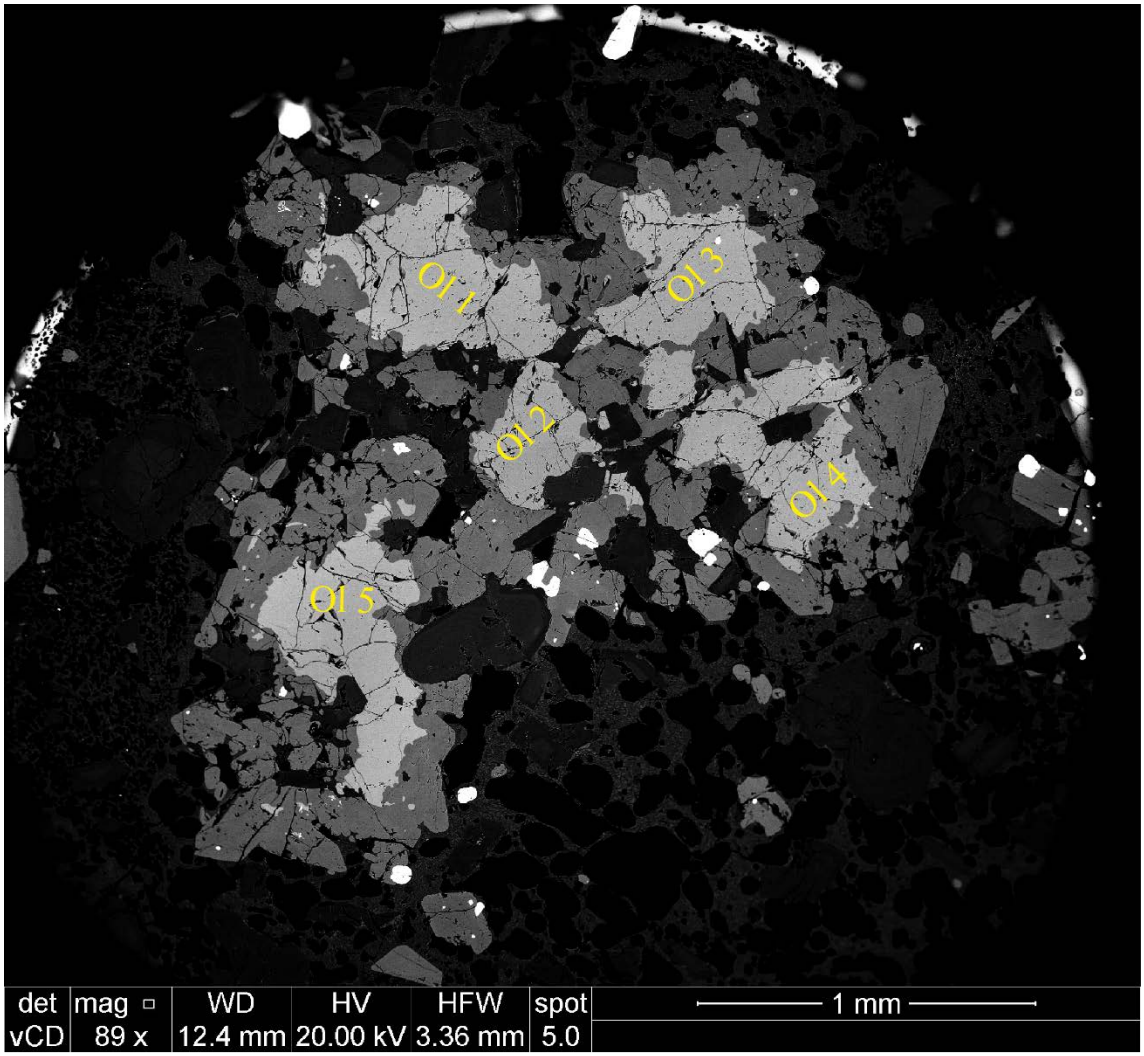

Figure A.9. *Crystal clot comprised of plagioclase, olivine, Fe-Ti oxides, and pyroxenes (Cal158).*

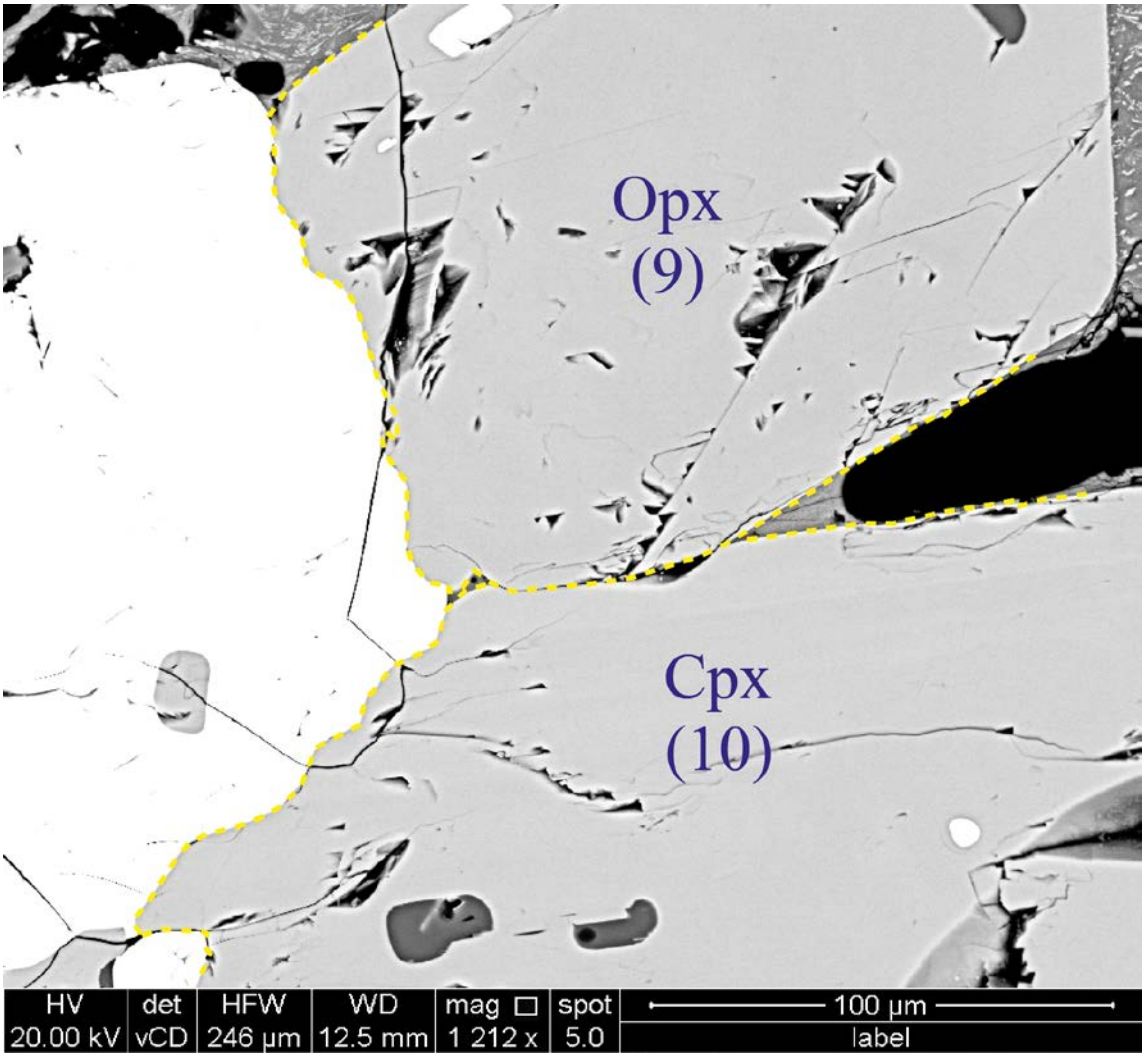

Figure A.10. *Crystal clot comprised of orthopyroxene, clinopyroxene, and Fe-Ti oxides (Cal-159).*

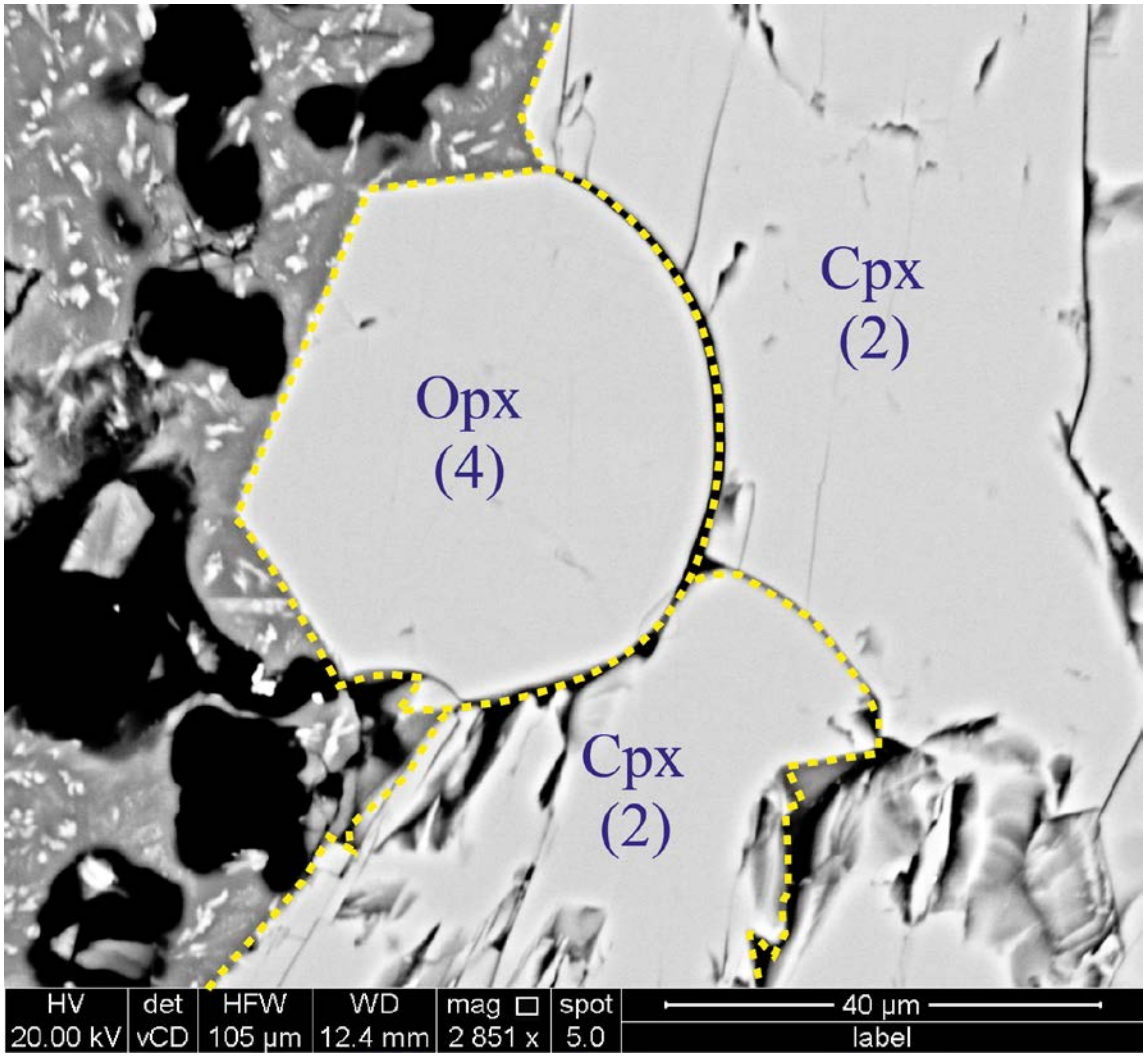

Figure A.11. *Crystal clot comprised of orthopyroxene, clinopyroxene, and Fe-Ti oxides (Cal159).*

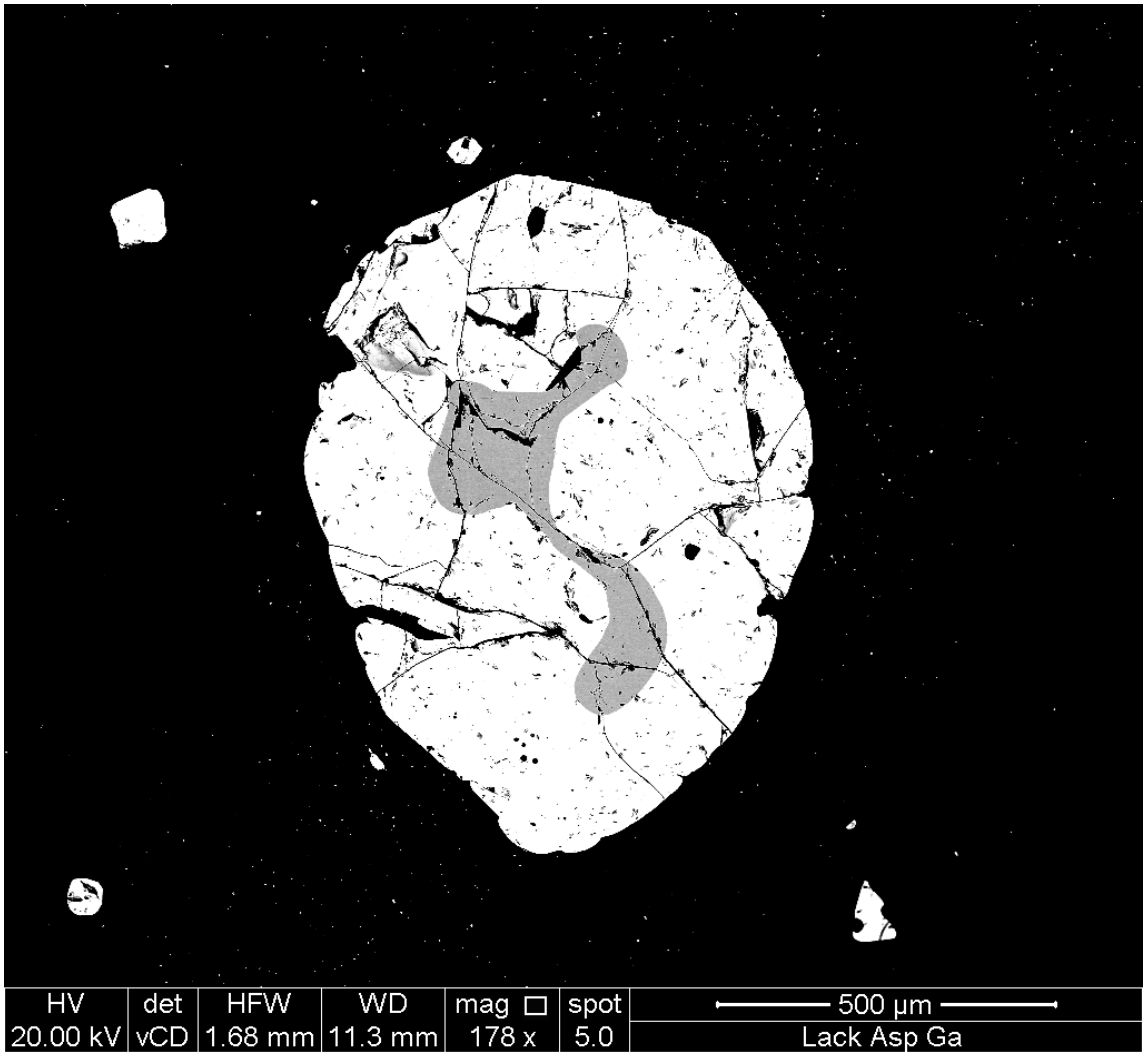

Figure A.12. *Crystal clot ilmenite and titanomagnetite (Cal-149Tb).*

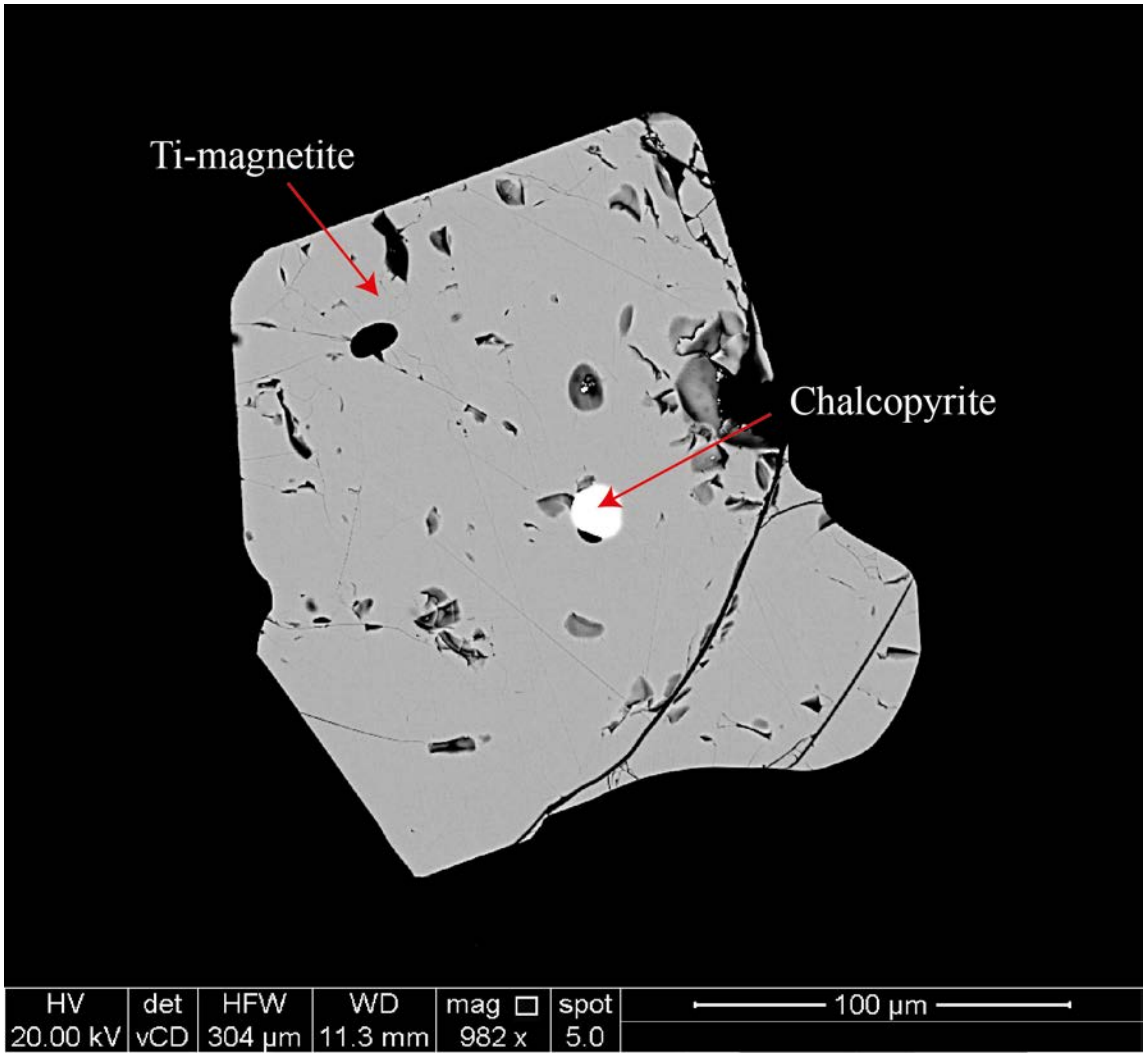

Figure A.13. *Titanomagnetite with inclusion of chalcopyrite (Cal-159).*

A.5. Stability fields-MELTS modelling

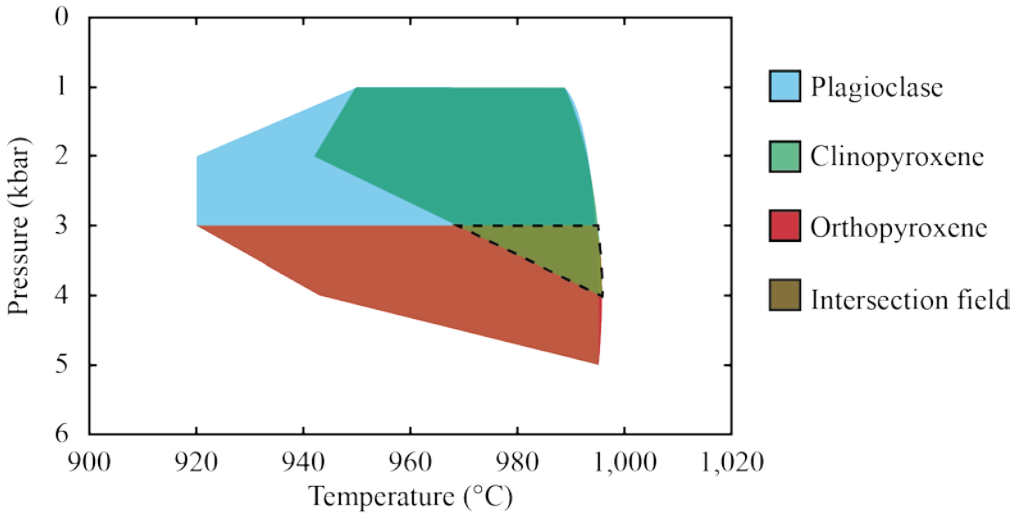

Figure A.14. *Stability fields (obtained via MELTS modelling) of the three most abundant magmatic phases in Calbuco samples: plagioclase (blue), clinopyroxene (green), and orthopyroxene (red) at ΔQFM oxygen fugacity patch. The water content dissolved in the melt varies from 0.5 to 3 wt%.*

A.6. References

Sun, SS, McDonough, WS (1989) Chemical and isotopic systematics of oceanic basalts: implications for mantle composition and processes. Geological Society, London, Special Publications, 42(1), 313-345. https://doi.org/10.1144/GSL.SP.1989.042.01.19

Appendix B

Supplementary Material for Chapter 3

The material presented in the Appendix B was included as online Supplementary Material in the following article:

Morgado, E., Morgan, D.J., Castruccio, A., Ebmeier, S.K., Parada, M.Á., Brahm, R., Harvey, J., Gutiérrez, F., Walshaw, R., 2019. Old magma and a new, intrusive trigger: using diffusion chronometry to understand the rapid-onset Calbuco eruption, April 2015 (Southern Chile). Contributions to Mineralogy and Petrology.

The videos and spreadsheet are attached as Supplementary Material online.

B.1. Comparison of re-equilibration timescales considering different XTi values

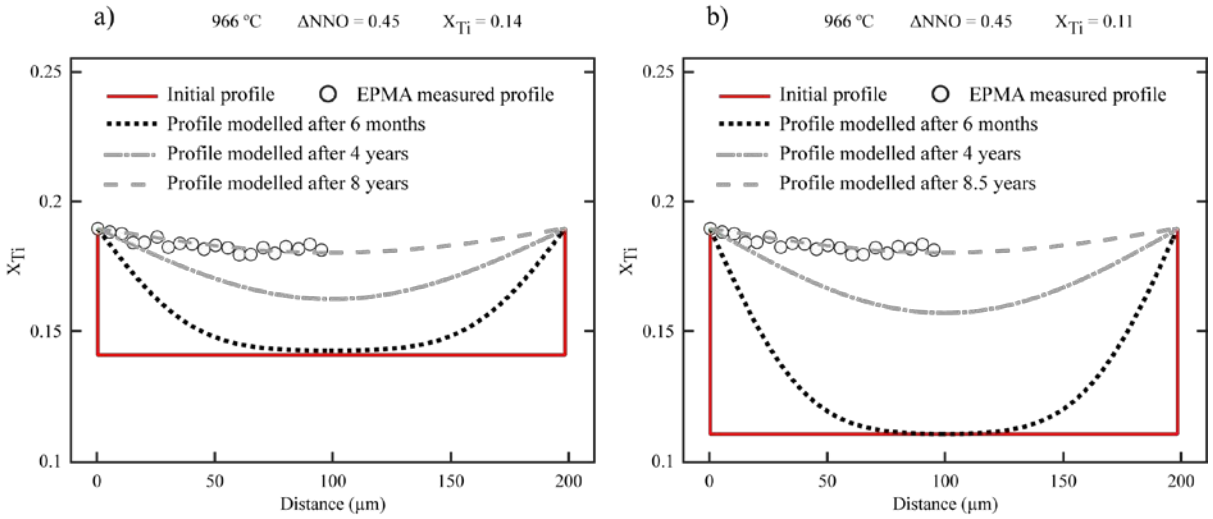

Figure B1. *Example of comparison of re-equilibration timescales for maximum (0.14) and minimum (0.11) X_{Ti} initial values. There is no significant difference in re-equilibration timescale.*

B.2. Error propagation

The error propagated (ε) of any function (f (x, y)) for x,… and z independent variables can be calculated as follows (details in Barlow, 1989):

$$\varepsilon\big(f(x,\dots,z)\big)^2 = \left(\left|\frac{\partial f}{\partial x}\right|\varepsilon(x)\right)^2 + \dots + \left(\left|\frac{\partial f}{\partial z}\right|\varepsilon(z)\right)^2 \qquad (B1)$$

The error propagated (ε) of any function (f (x, y)) for x and y dependent variables can be calculated as follows (only the maximum value of $cov(\varepsilon(x,y))$ is considered, details in the attached spreadsheet and Barlow, 1989):

$$\varepsilon\big(f(x,y)\big)^2 = \left(\left|\frac{\partial f}{\partial x}\right|\varepsilon(x)\right)^2 + \left(\left|\frac{\partial f}{\partial y}\right|\varepsilon(y)\right)^2 + 2\left(\frac{\partial f}{\partial x}\right)\cdot\left(\frac{\partial f}{\partial y}\right) cov(\varepsilon(x,y)) \qquad (B2)$$

If the errors are small and known, the error can be calculated according to the expression:

$$\frac{f(x+\varepsilon(x)) - f(x)}{\varepsilon(x)} \approx f'(x) \qquad (B3)$$

$$f(x+\varepsilon(x)) - f(x) \approx f'(x)\varepsilon(x) \qquad (B4)$$

Equations A3 and A4 are used to determine the expressions of the equations B1 and B2 (details in the attached spreadsheet).

Finally, combining equations B1 and B2, the systematic error (ε) associated with a function ($f = D_{Ti}^{*}$ (T, fO_2, X)) is calculated as follows:

$$\varepsilon\big(f(T, fO_2, X)\big)$$

$$\approx \sqrt{\left(\frac{\partial f}{\partial T}\varepsilon(T)\right)^2 + \left(\frac{\partial f}{\partial fO_2}\varepsilon(fO_2)\right)^2 + 2\left(\frac{\partial f}{\partial T}\right)\cdot\left(\frac{\partial f}{\partial fO_2}\right)\cdot cov\big(\varepsilon(T, fO_2)\big) + \left(\frac{\partial f}{\partial X}\varepsilon(X)\right)^2} \qquad (B5)$$

Where f corresponds to Eq. B5 (Eq. 21 from Aragon et al., 1984). The systematic errors of T, fO_2, and X_{usp}, are one (fO_2) or two (T, X_{usp}) orders of magnitude lower than those values

related to them, so the errors correspond to ε(T), ε(fO_2), ε(X_{usp}). These uncertainty values are variables, then the error values and error propagations are included in the attached spreadsheet. Finally, the random error of the calculation of D_{Ti}^{*} (0.1 log units) is considered (see the attached spreadsheet).

B.3. Calculation of probability in ranges of time

We approximate the equation of kernel density estimation of probability distributions of all data (Figure 2, Morgado et al., 2019) using a polynomial expression of 19 terms, which fits the data distribution (minimum SSD). That equation is integrated (using MATLAB® "polyfit" function, details in the attached script) between 0 and 140 hours to obtain the total probability. In the online script (SM4_Fitfunc.m) there are details of different probabilities of several times before the eruption.

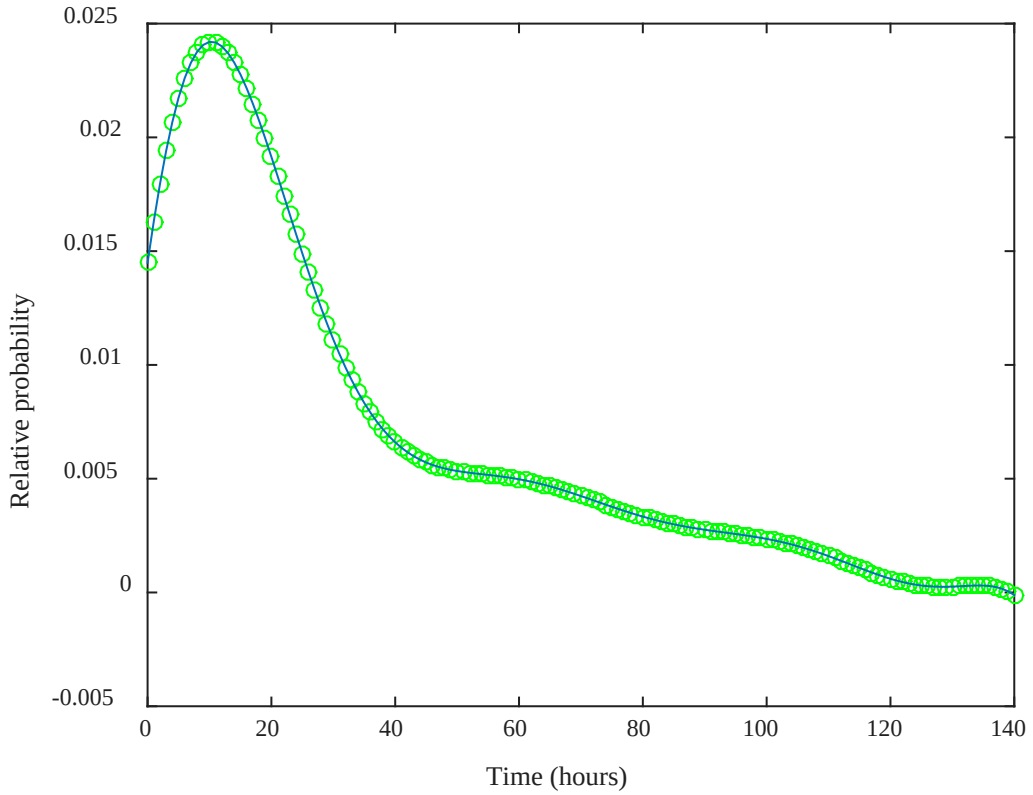

Figure B.2. *The solid line corresponds to Kernel density estimation of probability distributions of all data (pre-eruptive timescales) and the red circles represent the approximated polynomial expression, which is integrated to know the probability in several ranges of time.*

B.4. Modelling electron-sample interactions with the software CASINO

We model the electron-sample interactions with the software CASINO (monte CArlo SImulation of electroN trajectory in sOlids; Hovington et al., 1997; Drouin et al., 2007) at the analytical conditions of 15 keV accelerating potential and a 30 nA focused beam. In all the Fe-Ti oxide end-members the radius of horizontal interaction is < 1 µm and the length of vertical interaction is < 1.5 µm (see Figures).

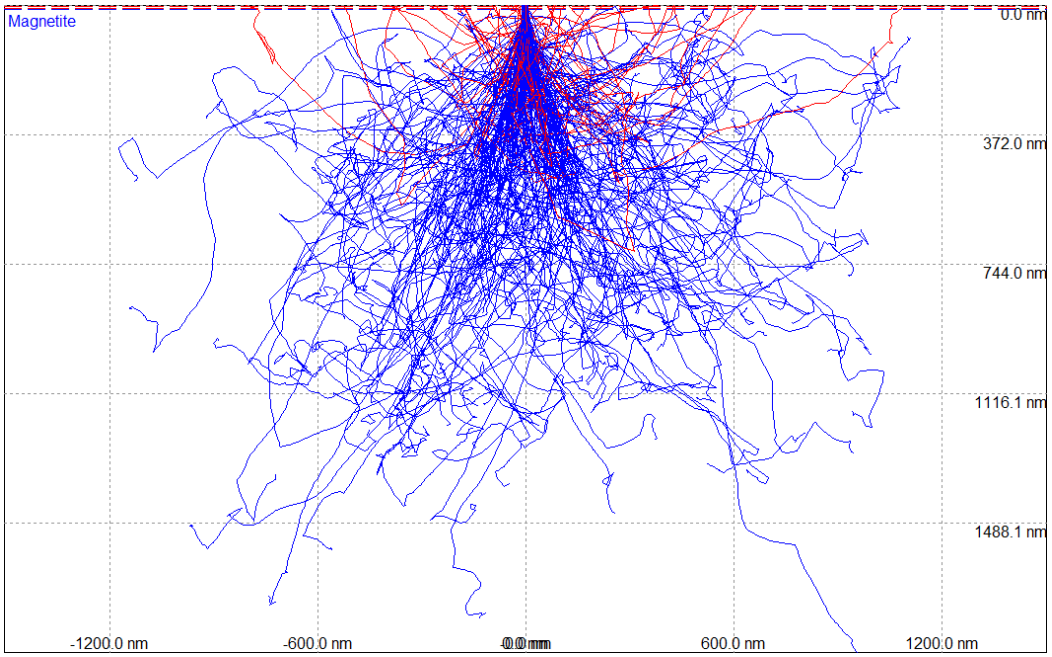

Figure B3. *Image representing the interaction volume of the electron beam and the magnetite end-member of the Fe-Ti oxides solid solution.*

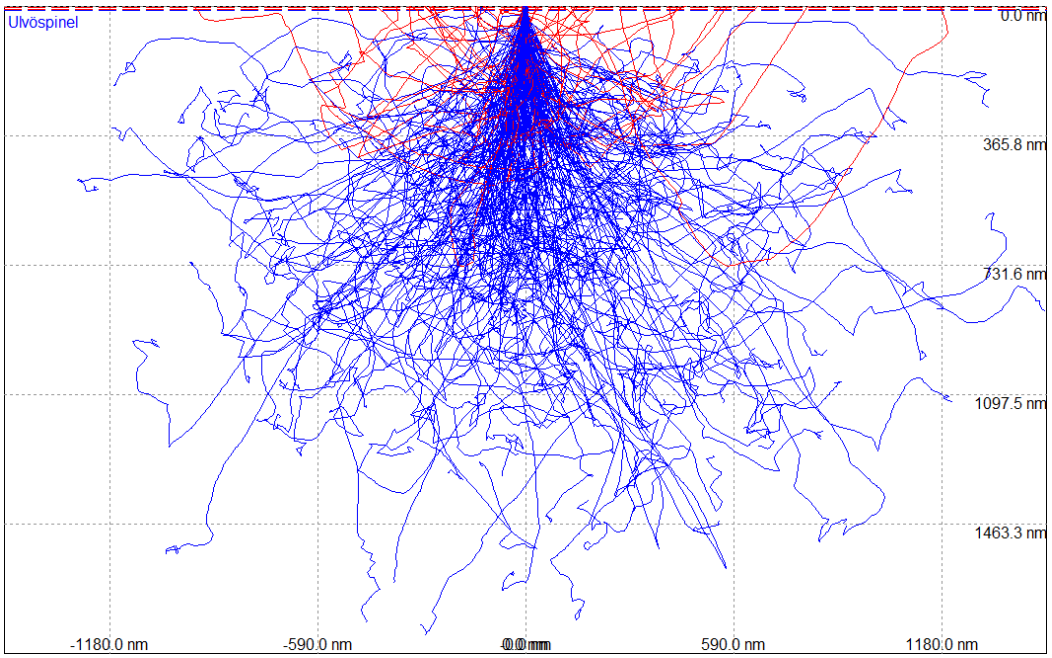

Figure B.4. *Image representing the interaction volume of the electron beam and the ulvöspinel end-member of the Fe-Ti oxides solid solution.*

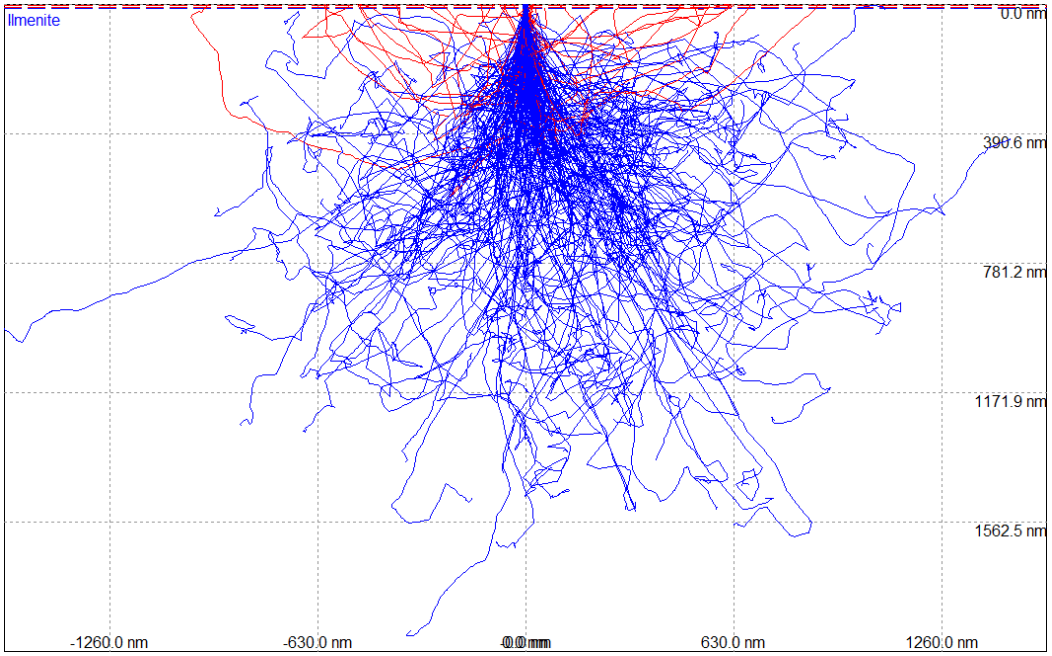

Figure B.5. *Image representing the interaction volume of the electron beam and the ilmenite end-member of the Fe-Ti oxides solid solution.*

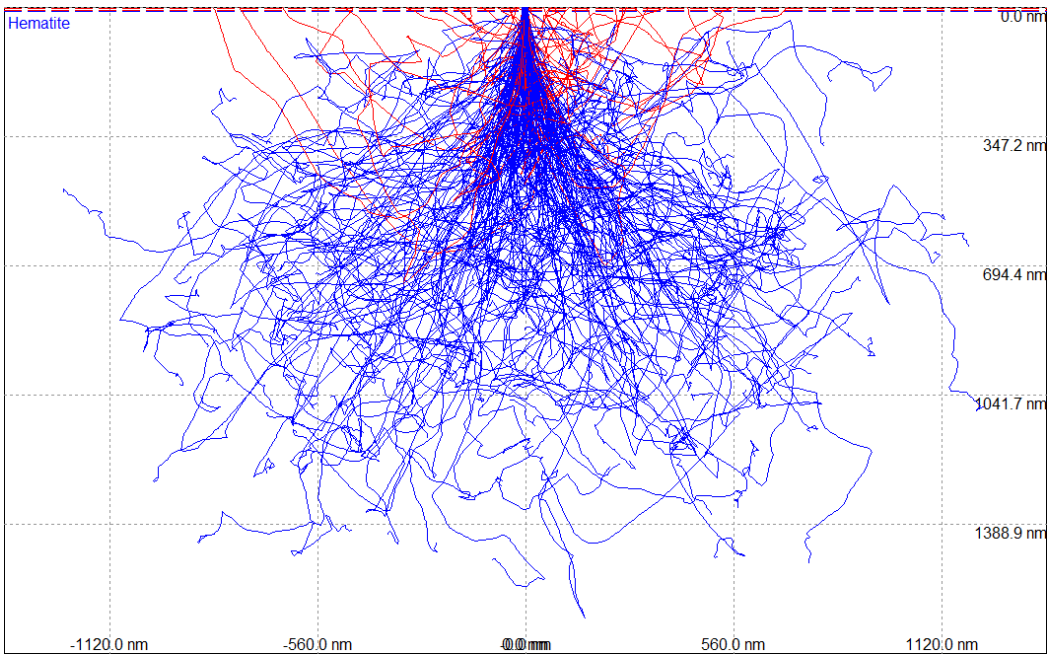

Figure B.6. *Image representing the interaction volume of the electron beam and the hematite end-member of the Fe-Ti oxides solid solution.*

B.5. Mineral chemistry

Table B1. Compositions of compositional profiles of ilmenite from the April 2015 Calbuco eruption (wt%).

SAMPLE	SiO_2	TiO_2	Al_2O_3	FeOt	MnO	MgO	CaO	CoO	V_2O_3	Cr_2O_3	ZnO	Nb_2O_5	TOTAL
Cal-149Tb - fig14b_p1_01	0.003	45.679	0.390	48.034	0.468	3.983	0.024	0.093	0.140	0.014	0.000	0.000	98.905
Cal-149Tb - fig14b_p1_02	0.005	45.960	0.376	47.973	0.465	3.993	0.024	0.103	0.142	0.000	0.000	0.009	99.127
Cal-149Tb - fig14b_p1_03	0.000	46.256	0.388	47.855	0.447	4.019	0.017	0.123	0.110	0.000	0.000	0.030	99.305
Cal-149Tb - fig14b_p1_04	0.000	46.888	0.378	47.836	0.441	4.035	0.028	0.114	0.140	0.014	0.000	0.003	99.953
Cal-149Tb - fig14b_p1_05	0.000	46.323	0.381	48.035	0.434	4.037	0.028	0.109	0.085	0.000	0.055	0.000	99.533
Cal-149Tb - fig14b_p1_06	0.000	46.810	0.385	48.301	0.465	4.047	0.030	0.121	0.104	0.011	0.000	0.022	100.353
Cal-149Tb - fig14b_p1_07	0.015	46.082	0.381	48.328	0.401	4.029	0.028	0.133	0.127	0.013	0.000	0.032	99.637
Cal-149Tb - fig14b_p1_08	0.005	45.886	0.389	48.050	0.440	4.038	0.031	0.098	0.147	0.000	0.000	0.039	99.203
Cal-149Tb - fig14b_p1_09	0.000	46.202	0.385	48.004	0.455	4.064	0.027	0.127	0.134	0.032	0.000	0.000	99.504
Cal-149Tb - fig14b_p1_10	0.007	45.874	0.367	48.039	0.436	3.990	0.023	0.095	0.143	0.016	0.000	0.008	99.075
Cal-149Tb - fig14b_p1_11	0.000	45.808	0.382	47.296	0.449	4.149	0.026	0.121	0.118	0.018	0.008	0.004	98.444
Cal-149Tb - fig14b_p1_12	0.013	45.125	0.389	47.863	0.435	4.086	0.020	0.105	0.160	0.000	0.000	0.011	98.294
Cal-149Tb - fig14b_p1_13	0.000	46.363	0.392	48.223	0.434	4.075	0.017	0.092	0.134	0.000	0.014	0.000	99.817
Cal-149Tb - fig14b_p1_14	0.146	46.659	0.386	48.214	0.467	3.993	0.024	0.092	0.104	0.022	0.000	0.000	100.164
Cal-149Tb - fig14b_p1_15	0.014	47.146	0.380	48.427	0.451	4.039	0.011	0.114	0.137	0.015	0.018	0.015	100.842
Cal-149Tb - fig14b_p1_16	0.000	45.440	0.365	48.449	0.466	4.034	0.012	0.089	0.115	0.015	0.021	0.000	99.075

Table B1. (Continued)

SAMPLE	SiO_2	TiO_2	Al_2O_3	FeOt	MnO	MgO	CaO	CoO	V_2O_3	Cr_2O_3	ZnO	Nb_2O_5	TOTAL
Cal-149Tb - fig14b_p2_01	0.000	46.311	0.382	48.334	0.453	3.974	0.019	0.120	0.133	0.000	0.000	0.020	99.817
Cal-149Tb - fig14b_p2_02	0.000	46.599	0.369	48.309	0.449	3.954	0.016	0.096	0.135	0.014	0.047	0.000	100.061
Cal-149Tb - fig14b_p2_03	0.000	46.313	0.379	48.244	0.440	4.022	0.020	0.082	0.121	0.009	0.079	0.030	99.804
Cal-149Tb - fig14b_p2_04	0.000	46.186	0.373	47.981	0.472	3.960	0.012	0.105	0.085	0.000	0.055	0.024	99.298
Cal-149Tb - fig14b_p2_05	0.000	45.574	0.371	48.427	0.436	4.028	0.012	0.085	0.145	0.015	0.083	0.013	99.268
Cal-149Tb - fig14b_p2_06	0.000	45.473	0.394	48.268	0.448	4.071	0.012	0.107	0.153	0.003	0.000	0.000	99.011
Cal-149Tb - fig14b_p2_07	0.000	46.457	0.391	48.355	0.478	4.089	0.023	0.112	0.148	0.000	0.001	0.006	100.140
Cal-149Tb - fig14b_p2_08	0.000	45.863	0.386	48.257	0.440	4.064	0.016	0.104	0.124	0.014	0.000	0.029	99.364
Cal-149Tb - fig14b_p2_09	0.000	46.139	0.406	48.166	0.457	4.024	0.018	0.115	0.125	0.000	0.021	0.014	99.553
Cal-149Tb - fig14b_p2_10	0.011	45.026	0.389	47.836	0.441	4.064	0.016	0.095	0.125	0.022	0.000	0.000	98.094
Cal-149Tb - fig14b_p2_11	0.000	45.572	0.387	48.237	0.443	4.099	0.016	0.108	0.116	0.000	0.037	0.014	99.091
Cal-149Tb - fig14b_p2_12	0.003	45.759	0.384	48.398	0.443	4.058	0.014	0.109	0.157	0.000	0.023	0.019	99.453
Cal-149Tb - fig14b_p2_13	0.005	45.929	0.377	48.216	0.451	4.121	0.015	0.097	0.158	0.003	0.071	0.029	99.559
Cal-149Tb - fig14b_p2_14	0.007	45.927	0.372	48.342	0.448	4.061	0.022	0.130	0.138	0.005	0.000	0.031	99.559
Cal-149Tb - fig14b_p2_15	0.010	45.319	0.389	48.479	0.450	4.092	0.020	0.092	0.169	0.028	0.000	0.020	99.161

Table B1. (Continued)

SAMPLE	SiO_2	TiO_2	Al_2O_3	FeOt	MnO	MgO	CaO	CoO	V_2O_3	Cr_2O_3	ZnO	Nb_2O_5	TOTAL
Cal-155_fig3_p1_1	0.033	45.842	0.268	48.288	0.539	2.904	0.006	0.105	0.154	0.003	0.033	0.000	98.174
Cal-155_fig3_p1_2	0.086	45.622	0.249	48.653	0.523	2.947	0.013	0.120	0.101	0.000	0.000	0.008	98.322
Cal-155_fig3_p1_3	0.056	47.883	0.260	48.816	0.527	2.875	0.010	0.094	0.025	0.016	0.000	0.000	100.561
Cal-155_fig3_p1_4	0.088	48.160	0.260	48.653	0.534	2.863	0.012	0.115	0.078	0.024	0.016	0.000	100.804
Cal-155_fig3_p1_5	0.073	47.163	0.264	49.108	0.528	2.882	0.010	0.080	0.103	0.000	0.001	0.025	100.239
Cal-155_fig3_p1_6	0.060	46.622	0.269	48.528	0.554	2.912	0.016	0.095	0.087	0.012	0.000	0.000	99.155
Cal-155_fig3_p1_7	0.030	45.589	0.261	49.164	0.550	2.883	0.010	0.096	0.098	0.000	0.031	0.008	98.720
Cal-155_fig3_p1_8	0.045	46.673	0.278	48.747	0.522	2.894	0.005	0.098	0.088	0.008	0.000	0.000	99.358
Cal-155_fig3_p1_9	0.050	45.795	0.265	48.494	0.557	2.921	0.014	0.111	0.122	0.000	0.018	0.000	98.346
Cal-155_fig3_p1_10	0.067	46.375	0.247	48.787	0.534	2.911	0.010	0.115	0.129	0.022	0.000	0.000	99.198

Table B1. (Continued)

SAMPLE	SiO_2	TiO_2	Al_2O_3	FeOt	MnO	MgO	CaO	CoO	V_2O_3	Cr_2O_3	ZnO	Nb_2O_5	TOTAL
Cal-155_fig24_p1_1	0.032	47.267	0.255	47.988	0.561	3.037	0.055	0.098	0.067	0.000	0.000	0.025	99.424
Cal-155_fig24_p1_2	0.104	46.387	0.258	47.940	0.571	3.009	0.046	0.130	0.117	0.000	0.000	0.000	98.626
Cal-155_fig24_p1_3	0.040	45.128	0.243	47.933	0.553	3.001	0.051	0.093	0.111	0.012	0.015	0.014	97.253
Cal-155_fig24_p1_4	0.044	45.926	0.267	48.145	0.569	3.002	0.062	0.095	0.085	0.001	0.000	0.000	98.242
Cal-155_fig24_p1_5	0.050	47.286	0.245	48.634	0.568	3.026	0.081	0.095	0.066	0.000	0.000	0.000	100.086
Cal-155_fig24_p1_6	0.040	44.917	0.279	48.129	0.581	3.017	0.097	0.096	0.083	0.021	0.000	0.000	97.304
Cal-155_fig24_p1_7	0.064	46.492	0.256	48.386	0.530	2.941	0.107	0.091	0.049	0.007	0.000	0.003	98.952
Cal-160_fig1_p1_1	0.019	41.730	0.344	52.066	0.455	2.722	0.059	0.092	0.149	0.000	0.039	0.011	97.767
Cal-160_fig1_p1_2	0.029	43.170	0.305	52.220	0.428	2.774	0.043	0.091	0.115	0.007	0.000	0.026	99.271
Cal-160_fig1_p1_3	0.022	42.890	0.259	51.989	0.404	2.850	0.038	0.116	0.151	0.000	0.015	0.008	98.826
Cal-160_fig1_p1_4	0.009	41.878	0.240	51.970	0.436	2.952	0.029	0.075	0.163	0.027	0.010	0.000	97.877
Cal-160_fig1_p1_5	0.001	43.400	0.215	52.143	0.454	2.976	0.026	0.106	0.112	0.021	0.000	0.031	99.545
Cal-160_fig1_p1_6	0.228	41.996	0.221	52.067	0.425	2.949	0.035	0.079	0.139	0.027	0.028	0.047	98.316
Cal-160_fig1_p1_7	0.041	42.934	0.176	51.740	0.432	3.245	0.025	0.114	0.149	0.000	0.000	0.053	98.988

Table B1. (Continued)

SAMPLE	SiO_2	TiO_2	Al_2O_3	FeOt	MnO	MgO	CaO	CoO	V_2O_3	Cr_2O_3	ZnO	Nb_2O_5	TOTAL
Cal-160_fig1_p2_1	0.050	42.689	0.183	52.405	0.538	2.134	0.444	0.105	0.146	0.015	0.016	0.017	98.822
Cal-160_fig1_p2_2	0.022	41.305	0.191	52.665	0.537	2.073	0.317	0.114	0.140	0.011	0.000	0.015	97.466
Cal-160_fig1_p2_3	0.024	41.694	0.174	52.956	0.536	2.089	0.235	0.126	0.140	0.040	0.000	0.005	98.094
Cal-160_fig1_p2_4	0.011	42.890	0.164	52.958	0.522	2.170	0.169	0.138	0.130	0.011	0.000	0.026	99.258
Cal-160_fig1_p2_5	0.001	42.428	0.164	52.916	0.514	2.137	0.136	0.113	0.129	0.023	0.000	0.007	98.636
Cal-160_fig1_p2_6	0.016	42.062	0.186	53.050	0.510	2.137	0.107	0.115	0.136	0.019	0.000	0.010	98.421
Cal-160_fig1_p2_7	0.006	42.075	0.183	52.945	0.527	2.137	0.088	0.118	0.148	0.008	0.000	0.009	98.325
Cal-160_fig1_p2_8	0.012	42.045	0.179	53.009	0.507	2.137	0.069	0.109	0.126	0.000	0.000	0.019	98.286
160_fig1_p3_1	0.011	42.496	0.282	51.812	0.484	2.880	0.086	0.077	0.138	0.000	0.031	0.038	98.410
160_fig1_p3_2	0.030	42.951	0.277	52.096	0.456	2.783	0.086	0.104	0.118	0.000	0.022	0.057	99.046
160_fig1_p3_3	0.023	42.366	0.246	52.176	0.462	2.779	0.062	0.105	0.129	0.000	0.000	0.024	98.442
160_fig1_p3_4	0.014	43.220	0.231	52.048	0.456	2.796	0.049	0.099	0.144	0.010	0.000	0.014	99.163
160_fig1_p3_5	0.022	43.058	0.226	52.278	0.484	2.760	0.044	0.109	0.155	0.026	0.015	0.008	99.271
160_fig1_p3_6	0.017	43.414	0.190	52.146	0.489	2.815	0.040	0.125	0.122	0.003	0.000	0.000	99.427
Cal-160_fig13_p2_1	0.000	44.979	0.224	50.911	0.457	2.757	0.025	0.105	0.147	0.000	0.015	0.020	99.720
Cal-160_fig13_p2_2	0.019	45.595	0.215	50.970	0.503	2.764	0.014	0.125	0.189	0.005	0.002	0.000	100.503
Cal-160_fig13_p2_3	0.013	44.804	0.229	51.239	0.475	2.797	0.010	0.097	0.157	0.008	0.000	0.001	99.917
Cal-160_fig13_p2_4	0.029	44.636	0.230	50.535	0.523	2.797	0.018	0.102	0.179	0.025	0.043	0.001	99.215
Cal-160_fig13_p2_5	0.014	42.914	0.263	51.771	0.496	2.813	0.006	0.097	0.181	0.039	0.000	0.014	98.705

Table B1. (Continued)

SAMPLE	SiO_2	TiO_2	Al_2O_3	FeOt	MnO	MgO	CaO	CoO	V_2O_3	Cr_2O_3	ZnO	Nb_2O_5	TOTAL
Cal-160_fig17_p1_1	0.046	43.669	0.226	50.349	0.527	2.861	0.046	0.113	0.173	0.019	0.003	0.000	98.126
Cal-160_fig17_p1_2	0.008	43.450	0.236	50.671	0.501	2.900	0.042	0.107	0.192	0.000	0.000	0.016	98.228
Cal-160_fig17_p1_3	0.006	45.909	0.222	50.648	0.494	2.912	0.029	0.101	0.147	0.006	0.000	0.003	100.558
Cal-160_fig17_p1_4	0.000	45.057	0.208	50.322	0.496	2.848	0.020	0.114	0.145	0.009	0.000	0.017	99.316
Cal-160_fig17_p1_5	0.007	45.919	0.215	50.832	0.487	2.948	0.018	0.100	0.154	0.000	0.000	0.003	100.770
Cal-160_fig17_p1_6	0.014	46.237	0.196	50.540	0.487	2.888	0.019	0.113	0.144	0.009	0.000	0.000	100.726
Cal-160_fig17_p1_7	0.009	44.279	0.230	50.245	0.524	2.919	0.016	0.094	0.132	0.008	0.023	0.006	98.555
Cal-160_fig17_p2_1	0.000	44.590	0.216	50.582	0.484	2.963	0.016	0.077	0.154	0.002	0.014	0.046	99.229
Cal-160_fig17_p2_2	0.033	47.323	0.219	50.397	0.510	2.896	0.020	0.099	0.148	0.013	0.046	0.021	101.806
Cal-160_fig17_p2_3	0.015	45.308	0.208	50.384	0.512	2.875	0.013	0.111	0.157	0.013	0.000	0.000	99.682
Cal-160_fig17_p2_4	0.000	44.715	0.226	50.867	0.457	2.885	0.016	0.074	0.109	0.000	0.020	0.000	99.428
Cal-160_fig17_p2_5	0.014	44.799	0.228	50.878	0.492	2.893	0.013	0.077	0.160	0.016	0.030	0.027	99.713
Cal-160_fig17_p2_6	0.003	45.055	0.233	50.810	0.502	2.940	0.012	0.099	0.150	0.000	0.003	0.000	99.889
Cal-160_fig17_p2_7	0.013	44.360	0.228	50.609	0.491	2.907	0.010	0.082	0.155	0.002	0.058	0.000	98.999
Cal-160_fig17_p2_8	0.000	44.333	0.217	50.942	0.491	2.932	0.016	0.093	0.180	0.025	0.007	0.023	99.358
Cal-160_fig17_p2_9	0.014	40.605	0.411	53.020	0.487	2.868	0.008	0.111	0.170	0.023	0.039	0.000	97.849

Table B1. (Continued)

SAMPLE	SiO_2	TiO_2	Al_2O_3	FeOt	MnO	MgO	CaO	CoO	V_2O_3	Cr_2O_3	ZnO	Nb_2O_5	TOTAL
Cal-160_fig17_p4_1	0.020	45.476	0.213	50.912	0.503	2.749	0.044	0.099	0.187	0.006	0.026	0.031	100.368
Cal-160_fig17_p4_2	0.017	46.252	0.227	50.723	0.491	2.787	0.040	0.103	0.136	0.010	0.006	0.000	100.866
Cal-160_fig17_p4_3	0.010	46.196	0.215	50.676	0.495	2.829	0.033	0.093	0.135	0.016	0.000	0.040	100.811
Cal-160_fig17_p4_4	0.009	46.201	0.216	50.427	0.487	2.817	0.027	0.112	0.179	0.025	0.063	0.018	100.679
Cal-160_fig17_p4_5	0.008	45.531	0.222	50.384	0.516	2.864	0.020	0.096	0.166	0.000	0.000	0.000	99.897
Cal-160_fig17_p4_6	0.034	45.093	0.232	50.684	0.493	2.870	0.023	0.084	0.177	0.005	0.032	0.024	99.847
Cal-160_fig17_p4_7	0.000	46.678	0.221	50.735	0.530	2.795	0.018	0.103	0.134	0.028	0.004	0.058	101.378
Cal-160_fig17_p4_8	0.013	45.602	0.200	50.514	0.493	2.818	0.022	0.103	0.146	0.014	0.000	0.000	100.002
Cal-160_fig17_p4_9	0.000	45.934	0.221	50.432	0.506	2.860	0.019	0.106	0.171	0.012	0.000	0.041	100.394
Cal-160_fig17_p4_10	0.000	44.528	0.220	50.538	0.501	2.759	0.017	0.112	0.156	0.003	0.052	0.023	98.993
Cal-160_figb_p1_1	0.000	45.864	0.226	50.520	0.509	2.584	0.017	0.090	0.139	0.003	0.000	0.016	100.044
Cal-160_figb_p1_2	0.006	45.894	0.209	50.345	0.483	2.631	0.025	0.103	0.124	0.016	0.059	0.007	99.969
Cal-160_figb_p1_3	0.007	45.069	0.202	49.674	0.509	2.620	0.019	0.120	0.138	0.031	0.042	0.000	98.504
Cal-160_figb_p1_4	0.011	45.593	0.214	50.003	0.495	2.612	0.014	0.120	0.170	0.000	0.005	0.016	99.346
Cal-160_figb_p1_5	0.002	45.630	0.192	50.148	0.487	2.613	0.017	0.092	0.157	0.000	0.004	0.000	99.429
Cal-160_figb_p1_6	0.002	44.925	0.190	50.061	0.502	2.630	0.018	0.089	0.163	0.000	0.000	0.023	98.690
Cal-160_figb_p1_7	0.012	44.690	0.206	50.279	0.481	2.647	0.011	0.117	0.137	0.008	0.017	0.000	98.681
Cal-160_figb_p1_8	0.000	46.018	0.202	50.385	0.512	2.584	0.019	0.124	0.118	0.000	0.000	0.019	100.043
Cal-160_figb_p1_9	0.000	46.917	0.198	50.295	0.516	2.553	0.011	0.119	0.122	0.024	0.000	0.000	100.823
Cal-160_figb_p1_10	0.009	44.626	0.201	50.629	0.506	2.636	0.021	0.114	0.166	0.010	0.000	0.000	99.025
Cal-160_figb_p1_11	0.007	44.646	0.208	50.023	0.517	2.588	0.014	0.120	0.142	0.000	0.003	0.001	98.347
Cal-160_figb_p1_12	0.001	45.580	0.197	50.326	0.513	2.574	0.003	0.099	0.182	0.020	0.000	0.015	99.610

Table B1. (Continued)

SAMPLE	SiO_2	TiO_2	Al_2O_3	FeOt	MnO	MgO	CaO	CoO	V_2O_3	Cr_2O_3	ZnO	Nb_2O_5	TOTAL
Cal-160_cx_e_p1_1	0.050	44.014	0.254	50.353	0.581	2.503	0.079	0.084	0.137	0.026	0.000	0.016	98.170
Cal-160_cx_e_p1_2	0.044	44.721	0.231	50.696	0.589	2.480	0.046	0.065	0.160	0.000	0.018	0.012	99.149
Cal-160_cx_e_p1_3	0.044	46.061	0.224	50.770	0.629	2.501	0.044	0.130	0.167	0.000	0.030	0.000	100.690
Cal-160_cx_e_p1_4	0.014	45.866	0.221	50.968	0.000	2.504	0.041	0.085	0.139	0.007	0.022	0.000	99.943
Cal-160_cx_e_p1_5	0.015	45.146	0.222	50.186	0.596	2.492	0.031	0.103	0.192	0.000	0.041	0.033	99.163
Cal-160_cx_e_p1_6	0.009	43.987	0.229	50.314	0.583	2.495	0.030	0.079	0.167	0.024	0.017	0.015	98.048
Cal-160_cx_e_p1_7	0.023	44.221	0.237	50.358	0.613	2.513	0.034	0.111	0.141	0.022	0.000	0.000	98.350
Cal-160_cx_e_p1_8	0.007	45.122	0.243	50.472	0.564	2.554	0.023	0.089	0.185	0.000	0.052	0.127	99.538
Cal-160_cx_e_p1_9	0.003	44.520	0.214	50.989	0.602	2.547	0.017	0.105	0.127	0.000	0.042	0.040	99.275
Cal-160_cx_e_p1_10	0.021	44.960	0.213	50.887	0.593	2.621	0.007	0.074	0.180	0.000	0.000	0.009	99.663
Cal-160_cx_e_p1_11	0.020	45.888	0.235	50.975	0.618	2.594	0.016	0.115	0.190	0.004	0.054	0.000	100.810
Cal-160_cx_e_p1_12	0.000	45.253	0.236	50.629	0.609	2.629	0.018	0.119	0.154	0.000	0.016	0.021	99.768
Cal-160_cx_e_p1_13	0.019	43.689	0.217	50.851	0.602	2.598	0.020	0.096	0.176	0.000	0.075	0.001	98.440
Cal-160_cx_e_p1_14	0.000	44.412	0.222	51.217	0.579	2.571	0.018	0.124	0.247	0.019	0.006	0.004	99.554
Cal-160_cx_e_p1_15	0.012	44.457	0.233	51.392	0.588	2.554	0.013	0.100	0.168	0.026	0.048	0.012	99.691
Cal-160_figf_p1_1	0.009	44.839	0.221	50.098	0.499	2.303	0.047	0.105	0.159	0.025	0.014	0.017	98.422
Cal-160_figf_p1_2	0.018	45.379	0.193	50.191	0.503	2.330	0.060	0.050	0.118	0.012	0.000	0.021	98.938
Cal-160_figf_p1_3	0.015	45.493	0.213	50.318	0.531	2.346	0.042	0.097	0.159	0.025	0.000	0.000	99.325
Cal-160_figf_p1_4	0.024	43.568	0.212	50.260	0.514	2.385	0.034	0.131	0.147	0.044	0.000	0.008	97.408
Cal-160_figf_p1_5	0.015	45.571	0.213	50.469	0.525	2.343	0.025	0.103	0.130	0.022	0.005	0.009	99.502
Cal-160_figf_p1_6	0.007	45.201	0.204	50.611	0.508	2.360	0.036	0.080	0.155	0.012	0.023	0.021	99.303

Table B1. (Continued)

SAMPLE	SiO_2	TiO_2	Al_2O_3	FeOt	MnO	MgO	CaO	CoO	V_2O_3	Cr_2O_3	ZnO	Nb_2O_5	TOTAL
Cal-160_figf_p2_1	0.046	45.280	0.227	49.970	0.521	2.313	0.085	0.115	0.113	0.017	0.000	0.043	98.791
Cal-160_figf_p2_2	0.041	45.562	0.202	50.201	0.521	2.300	0.057	0.119	0.101	0.000	0.000	0.000	99.159
160_figh_p1_1	0.009	45.507	0.236	50.483	0.510	2.479	0.090	0.107	0.165	0.000	0.074	0.019	99.768
160_figh_p1_2	0.000	45.996	0.239	50.122	0.520	2.463	0.072	0.108	0.133	0.017	0.000	0.000	99.743
160_figh_p1_3	0.000	45.069	0.220	50.640	0.525	2.499	0.052	0.114	0.192	0.013	0.003	0.009	99.441
160_figh_p1_4	0.008	44.113	0.225	50.805	0.519	2.509	0.052	0.123	0.193	0.025	0.000	0.027	98.706
160_figh_p1_5	0.004	45.245	0.226	50.359	0.497	2.492	0.039	0.076	0.187	0.017	0.009	0.015	99.267
160_figh_p1_6	0.012	44.985	0.236	50.769	0.508	2.503	0.039	0.126	0.185	0.024	0.031	0.000	99.517
160_figh_p1_7	0.018	44.125	0.219	51.253	0.470	2.542	0.027	0.107	0.187	0.000	0.000	0.003	99.052
160_figh_p1_8	0.025	41.134	0.352	53.087	0.476	2.566	0.026	0.081	0.219	0.012	0.000	0.020	98.116

Table B2. Compositions of compositional profiles of titanomagnetite from the April 2015 Calbuco eruption (wt%).

SAMPLE	SiO_2	TiO_2	Al_2O_3	FeOt	MnO	MgO	CaO	CoO	V_2O_3	Cr_2O_3	ZnO	Nb_2O_5	TOTAL
Cal-149Tb - fig14b_p1_17	0.098	14.997	3.088	74.631	0.466	2.974	0.007	0.156	0.389	0.010	0.012	0.000	97.040
Cal-149Tb - fig14b_p1_18	0.058	14.915	3.112	74.991	0.433	2.891	0.005	0.146	0.396	0.003	0.060	0.000	97.226
Cal-149Tb - fig14b_p1_19	0.100	14.889	3.093	75.308	0.442	2.885	0.009	0.172	0.394	0.000	0.013	0.000	97.519
Cal-149Tb - fig14b_p1_20	0.071	14.438	3.136	74.873	0.443	2.907	0.031	0.154	0.374	0.029	0.083	0.014	96.758
Cal-149Tb - fig14b_p1_21	0.107	14.431	3.099	74.678	0.459	2.853	0.025	0.151	0.431	0.024	0.030	0.000	96.521
Cal-149Tb - fig14b_p1_22	0.075	14.595	3.130	74.380	0.460	2.799	0.020	0.157	0.383	0.025	0.025	0.000	96.257
Cal-149Tb - fig14b_p1_23	0.052	14.064		75.043	0.453	2.952	0.017	0.150	0.410	0.013	0.008	0.000	93.385
Cal-149Tb - fig14b_p1_24	0.082	14.515	3.139	75.502	0.446	2.915	0.023	0.152	0.383	0.008	0.043	0.001	97.419
Cal-149Tb - fig14b_p1_25	0.054	14.376	3.116	75.024	0.414	2.916	0.023	0.155	0.390	0.040	0.011	0.000	96.731
Cal-149Tb - fig14b_p1_26	0.054	14.162	3.121	74.904	0.424	2.930	0.009	0.143	0.422	0.020	0.060	0.000	96.477
Cal-149Tb - fig14b_p1_27	0.070	14.277	3.192	74.776	0.449	2.920	0.011	0.161	0.382	0.020	0.053	0.000	96.519
Cal-149Tb - fig14b_p1_28	0.068	14.212	3.171	74.789	0.437	2.873	0.009	0.160	0.391	0.027	0.064	0.012	96.426
Cal-149Tb - fig14b_p1_29	0.083	13.983	3.148	75.119	0.438	2.943	0.011	0.151	0.426	0.003	0.041	0.000	96.576
Cal-149Tb - fig14b_p1_30	0.082	13.922	3.212	74.771	0.415	2.877	0.002	0.139	0.399	0.009	0.012	0.000	96.055
Cal-149Tb - fig14b_p1_31	0.092	14.242	3.176	75.090	0.454	2.896	0.010	0.188	0.411	0.002	0.000	0.000	96.784
Cal-149Tb - fig14b_p1_32	0.088	14.050	3.225	75.249	0.438	2.916	0.011	0.150	0.390	0.000	0.044	0.013	96.788
Cal-149Tb - fig14b_p1_33	0.086	14.321	3.190	75.065	0.458	2.917	0.010	0.151	0.403	0.000	0.007	0.000	96.826
Cal-149Tb - fig14b_p1_34	0.073	14.210	3.200	75.060	0.438	2.892	0.006	0.146	0.433	0.024	0.021	0.000	96.739
Cal-149Tb - fig14b_p1_35	0.087	14.349	3.245	74.883	0.409	2.929	0.010	0.131	0.437	0.012	0.007	0.005	96.742
Cal-149Tb - fig14b_p1_36	0.092	14.124	3.214	74.814	0.431	2.805	0.010	0.187	0.407	0.012	0.057	0.000	96.374

Table B2. (Continued)

SAMPLE	SiO_2	TiO_2	Al_2O_3	FeOt	MnO	MgO	CaO	CoO	V_2O_3	Cr_2O_3	ZnO	Nb_2O_5	TOTAL
Cal-149Tb - fig14b_p2_16	0.076	15.176	3.095	74.507	0.423	2.839	0.010	0.183	0.364	0.023	0.097	0.009	96.998
Cal-149Tb - fig14b_p2_17	0.056	15.096	3.055	74.936	0.456	2.891	0.011	0.158	0.377	0.020	0.049	0.000	97.309
Cal-149Tb - fig14b_p2_18	0.069	15.049	3.061	75.063	0.499	2.927	0.007	0.152	0.416	0.000	0.084	0.007	97.559
Cal-149Tb - fig14b_p2_19	0.083	14.830	3.111	74.972	0.439	2.900	0.004	0.173	0.401	0.000	0.000	0.005	97.136
Cal-149Tb - fig14b_p2_20	0.081	14.546	3.137	74.708	0.437	2.927	0.022	0.155	0.470	0.018	0.059	0.000	96.813
Cal-149Tb - fig14b_p2_21	0.069	14.616	3.113	75.058	0.463	2.921	0.005	0.151	0.363	0.000	0.039	0.000	96.996
Cal-149Tb - fig14b_p2_22	0.083	14.356	3.074	74.525	0.423	2.966	0.009	0.175	0.393	0.005	0.097	0.001	96.320
Cal-149Tb - fig14b_p2_23	0.077	14.189	3.115	74.861	0.440	2.965	0.008	0.168	0.384	0.016	0.083	0.027	96.541
Cal-149Tb - fig14b_p2_24	0.065	14.468	3.110	74.689	0.434	2.909	0.012	0.137	0.398	0.018	0.078	0.000	96.534
Cal-149Tb - fig14b_p2_25	0.071	14.522	3.148	75.246	0.441	2.936	0.006	0.182	0.383	0.000	0.037	0.000	97.180
Cal-149Tb - fig14b_p2_26	0.073	14.621	3.110	75.234	0.466	2.881	0.004	0.166	0.421	0.003	0.040	0.000	97.246
Cal-149Tb - fig14b_p2_27	0.082	14.259	3.088	75.037	0.459	2.889	0.007	0.162	0.404	0.002	0.052	0.008	96.669
Cal-149Tb - fig14b_p2_28	0.083	14.687	3.131	75.403	0.436	2.905	0.008	0.187	0.422	0.002	0.046	0.000	97.539
Cal-149Tb - fig14b_p2_29	0.067	14.369	3.125	75.038	0.448	2.901	0.006	0.162	0.394	0.030	0.017	0.000	96.770
Cal-149Tb - fig14b_p2_30	0.069	14.037	3.173	74.844	0.460	2.951	0.019	0.154	0.400	0.018	0.060	0.000	96.402
Cal-155_fig3_p1_11	0.111	13.277	2.687	76.198	0.448	1.810	0.015	0.146	0.370	0.009	0.036	0.000	95.106
Cal-155_fig3_p1_12	0.128	13.245	2.702	76.955	0.450	1.820	0.015	0.173	0.386	0.025	0.028	0.000	95.926
Cal-155_fig3_p1_13	0.120	12.297	2.906	71.360	0.395	1.989	0.000	0.143	0.336	0.009	0.019	0.000	89.574
Cal-155_fig3_p1_14	0.128	13.142	2.712	77.047	0.451	1.826	0.014	0.180	0.348	0.009	0.123	0.007	95.985
Cal-155_fig3_p1_15	0.114	12.677	2.684	77.337	0.462	1.806	0.009	0.179	0.374	0.000	0.016	0.027	95.685
Cal-155_fig3_p1_16	0.114	12.673	2.733	77.030	0.421	1.794	0.012	0.170	0.370	0.019	0.043	0.000	95.378
Cal-155_fig3_p1_17	0.108	12.826	2.762	77.117	0.472	1.815	0.000	0.171	0.382	0.002	0.107	0.000	95.761
Cal-155_fig3_p1_18	0.097	12.755	2.670	77.079	0.445	1.805	0.011	0.167	0.373	0.023	0.106	0.000	95.530
Cal-155_fig3_p1_19	0.093	12.860	2.690	77.345	0.449	1.808	0.006	0.168	0.374	0.031	0.000	0.000	95.824

Table B2. (Continued)

SAMPLE	SiO_2	TiO_2	Al_2O_3	FeOt	MnO	MgO	CaO	CoO	V_2O_3	Cr_2O_3	ZnO	Nb_2O_5	TOTAL
Cal-155_fig24_p1_8	0.110	12.854	2.673	77.157	0.462	1.795	0.049	0.141	0.347	0.023	0.011	0.014	95.824
Cal-155_fig24_p1_9	0.157	12.877	2.628	77.234	0.503	1.803	0.035	0.184	0.319	0.026	0.041	0.000	95.980
Cal-155_fig24_p1_10	0.111	12.965	2.647	77.234	0.454	1.819	0.016	0.147	0.325	0.016	0.000	0.034	95.944
Cal-155_fig24_p1_11	0.101	13.244	2.648	78.076	0.490	1.776	0.021	0.150	0.358	0.013	0.031	0.000	97.102
Cal-155_fig24_p1_12	0.105	12.628	2.633	77.285	0.461	1.787	0.016	0.162	0.357	0.033	0.048	0.000	95.709
Cal-155_fig24_p1_13	0.117	12.809	2.690	77.032	0.452	1.814	0.005	0.140	0.374	0.010	0.070	0.000	95.716
Cal-155_fig24_p1_14	0.111	12.727	2.634	77.467	0.486	1.821	0.018	0.175	0.353	0.000	0.052	0.000	96.036
Cal-155_fig24_p1_15	0.113	13.009	2.642	77.666	0.465	1.830	0.010	0.147	0.361	0.014	0.050	0.011	96.514
Cal-155_fig24_p1_16	0.106	13.231	2.615	77.701	0.474	1.808	0.004	0.152	0.369	0.023	0.042	0.000	96.724
Cal-155_fig24_p1_17	0.109	13.166	2.609	78.133	0.473	1.782	0.007	0.140	0.367	0.008	0.058	0.022	97.074
Cal-160_fig1_p1_8	0.011	16.352	1.049	75.312	0.497	2.081	0.014	0.167	0.304	0.017	0.068	0.000	96.037
Cal-160_fig1_p1_9	0.051	14.369	1.144	77.603	0.465	2.097	0.017	0.115	0.335	0.035	0.113	0.000	96.527
Cal-160_fig1_p1_10	0.039	12.602	1.245	78.571	0.443	2.000	0.008	0.164	0.399	0.025	0.114	0.012	95.838
Cal-160_fig1_p1_11	0.048	11.017	1.327	79.698	0.427	1.862	0.004	0.157	0.416	0.021	0.110	0.000	95.311
Cal-160_fig1_p1_12	0.034	10.033	1.408	81.127	0.430	1.705	0.015	0.188	0.430	0.022	0.084	0.000	95.722
Cal-160_fig1_p1_13	0.044	9.033	1.457	81.873	0.389	1.571	0.005	0.148	0.454	0.036	0.056	0.000	95.313
Cal-160_fig1_p1_14	0.042	8.481	1.463	82.059	0.424	1.457	0.012	0.195	0.435	0.021	0.113	0.022	94.961
Cal-160_fig1_p1_15	0.076	7.549	1.290	75.600	0.377	1.272	0.014	0.163	0.387	0.044	0.035	0.031	87.055
Cal-160_fig1_p1_16	0.051	8.029	1.462	82.901	0.429	1.375	0.008	0.163	0.415	0.046	0.083	0.000	95.188
Cal-160_fig1_p1_17	0.040	7.955	1.461	82.808	0.426	1.328	0.021	0.175	0.409	0.018	0.065	0.000	94.926
Cal-160_fig1_p1_18	0.038	8.095	1.455	83.379	0.440	1.355	0.010	0.196	0.401	0.014	0.124	0.000	95.723
Cal-160_fig1_p1_19	0.058	8.333	1.456	83.723	0.454	1.294	0.004	0.171	0.395	0.039	0.030	0.011	96.181
Cal-160_fig1_p1_20	0.050	8.499	1.436	83.429	0.465	1.279	0.007	0.163	0.440	0.045	0.006	0.000	96.059

Table B2. (Continued)

SAMPLE	SiO_2	TiO_2	Al_2O_3	FeOt	MnO	MgO	CaO	CoO	V_2O_3	Cr_2O_3	ZnO	Nb_2O_5	TOTAL
Cal-160_fig1_p2_9	0.035	15.994	1.108	78.182	0.532	1.509	0.044	0.177	0.298	0.025	0.070	0.000	98.137
Cal-160_fig1_p2_10	0.034	13.706	1.217	79.011	0.508	1.499	0.033	0.173	0.355	0.016	0.753	0.012	97.509
Cal-160_fig1_p2_11	0.051	12.631	1.302	79.577	0.513	1.479	0.034	0.146	0.370	0.023	0.076	0.034	96.435
Cal-160_fig1_p2_12	0.043	11.195	1.410	81.099	0.470	1.425	0.029	0.151	0.424	0.041	0.102	0.013	96.631
Cal-160_fig1_p2_13	0.050	9.858	1.449	81.430	0.453	1.393	0.032	0.144	0.407	0.028	0.080	0.000	95.544
Cal-160_fig1_p2_14	0.046	9.268	1.491	82.780	0.416	1.349	0.027	0.173	0.412	0.047	0.162	0.002	96.398
Cal-160_fig1_p2_15	0.042	8.662	1.547	83.466	0.471	1.310	0.022	0.171	0.455	0.017	0.048	0.000	96.458
Cal-160_fig1_p2_16	0.046	8.322	1.476	83.322	0.469	1.293	0.014	0.154	0.447	0.024	0.092	0.013	95.915
Cal-160_fig1_p2_17	0.048	8.541	1.454	83.536	0.438	1.249	0.022	0.171	0.429	0.032	0.094	0.025	96.273
Cal-160_fig1_p2_18	0.036	8.270	1.489	83.057	0.455	1.290	0.021	0.165	0.441	0.040	0.029	0.000	95.532
Cal-160_fig1_p2_19	0.043	8.387	1.458	83.032	0.443	1.255	0.018	0.189	0.444	0.027	0.114	0.000	95.650
Cal-160_fig1_p3_7	0.035	14.575	1.132	76.631	0.492	1.925	0.031	0.182	0.344	0.019	0.000	0.000	95.557
Cal-160_fig1_p3_8	0.035	13.353	1.209	77.706	0.454	1.820	0.034	0.182	0.359	0.025	0.121	0.026	95.518
Cal-160_fig1_p3_9	0.052	11.987	1.333	79.448	0.472	1.709	0.025	0.143	0.414	0.025	0.072	0.000	95.905
Cal-160_fig1_p3_10	0.061	10.829	1.384	81.118	0.497	1.610	0.015	0.160	0.439	0.035	0.111	0.010	96.508
Cal-160_fig1_p3_11	0.046	9.385	1.427	81.901	0.429	1.511	0.016	0.147	0.438	0.030	0.124	0.000	95.691
Cal-160_fig1_p3_12	0.056	8.637	1.446	82.030	0.428	1.370	0.028	0.169	0.433	0.033	0.096	0.008	94.968
Cal-160_fig1_p3_13	0.073	8.492	1.452	83.197	0.420	1.328	0.016	0.121	0.447	0.031	0.039	0.000	95.858
Cal-160_fig1_p3_14	0.039	8.484	1.441	83.433	0.421	1.268	0.010	0.177	0.418	0.045	0.082	0.018	96.063
Cal-160_fig1_p3_15	0.030	8.352	1.419	83.393	0.425	1.327	0.016	0.191	0.449	0.020	0.049	0.000	95.915

Table B2. (Continued)

SAMPLE	SiO_2	TiO_2	Al_2O_3	FeOt	MnO	MgO	CaO	CoO	V_2O_3	Cr_2O_3	ZnO	Nb_2O_5	TOTAL
160_fig13_profile2_6	0.056	14.481	1.821	77.266	0.438	1.856	0.011	0.169	0.415	0.047	0.095	0.010	96.892
160_fig13_profile2_7	0.060	11.823	2.038	79.726	0.391	1.671	0.000	0.171	0.478	0.018	0.086	0.000	96.722
160_fig13_profile2_8	0.074	10.745	2.084	79.831	0.414	1.673	0.009	0.216	0.495	0.028	0.027	0.030	95.895
160_fig13_profile2_9	0.074	10.552	2.021	80.530	0.388	1.677	0.011	0.156	0.488	0.033	0.056	0.000	96.251
160_fig13_profile2_10	0.071	10.521	2.080	80.431	0.404	1.706	0.012	0.162	0.516	0.043	0.065	0.000	96.290
160_fig13_profile2_11	0.065	10.826	2.090	80.356	0.403	1.686	0.014	0.162	0.494	0.063	0.120	0.000	96.546
160_fig13_profile2_12	0.061	10.598	2.097	80.446	0.406	1.698	0.013	0.164	0.510	0.034	0.085	0.011	96.399
160_fig13_profile2_13	0.046	10.708	2.036	80.766	0.396	1.640	0.013	0.163	0.481	0.056	0.057	0.000	96.634
160_fig13_profile2_14	0.074	10.643	2.069	80.791	0.400	1.661	0.011	0.167	0.468	0.023	0.054	0.016	96.910
160_fig13_profile2_15	0.068	10.274	2.045	80.880	0.384	1.658	0.023	0.169	0.528	0.039	0.032	0.000	96.385
160_fig13_profile2_16	0.062	10.695	2.088	80.352	0.415	1.636	0.015	0.183	0.530	0.040	0.145	0.006	96.454
160_fig13_profile2_17	0.054	10.373	2.071	79.944	0.445	1.643	0.020	0.145	0.495	0.019	0.047	0.000	95.526
160_fig13_profile2_18	0.071	10.415	2.048	81.043	0.396	1.636	0.021	0.162	0.492	0.042	0.023	0.000	96.616
160_fig17_profile1_8	0.029	16.471	1.823	77.120	0.437	1.935	0.007	0.193	0.378	0.049	0.105	0.004	98.756
160_fig17_profile1_9	0.051	12.193	2.020	78.605	0.405	1.780	0.018	0.165	0.455	0.028	0.091	0.025	96.081
160_fig17_profile1_10	0.031	11.798	2.071	79.897	0.402	1.726	0.002	0.159	0.450	0.020	0.107	0.000	96.909
160_fig17_profile1_11	0.060	11.510	2.069	80.411	0.414	1.734	0.012	0.158	0.467	0.039	0.049	0.000	97.178
160_fig17_profile1_12	0.052	11.212	2.111	79.712	0.372	1.753	0.000	0.164	0.468	0.025	0.092	0.006	96.220
160_fig17_profile1_13	0.057	10.876	2.065	80.069	0.417	1.759	0.005	0.169	0.464	0.000	0.069	0.001	96.203
160_fig17_profile1_14	0.033	10.900	2.049	80.412	0.425	1.718	0.007	0.186	0.445	0.014	0.000	0.003	96.434
160_fig17_profile1_15	0.045	10.878	2.086	80.272	0.396	1.739	0.007	0.185	0.452	0.033	0.000	0.000	96.339
160_fig17_profile1_16	0.046	11.030	2.101	80.684	0.416	1.761	0.008	0.192	0.418	0.018	0.092	0.012	97.004
160_fig17_profile1_17	0.030	10.778	2.122	80.784	0.404	1.760	0.005	0.130	0.457	0.047	0.000	0.000	96.766
160_fig17_profile1_18	0.063	10.754	2.079	80.262	0.385	1.757	0.010	0.198	0.473	0.063	0.046	0.027	96.376

Table B2. (Continued)

SAMPLE	SiO_2	TiO_2	Al_2O_3	FeOt	MnO	MgO	CaO	CoO	V_2O_3	Cr_2O_3	ZnO	Nb_2O_5	TOTAL
160_fig17_profile2_10	0.044	14.210	1.881	76.746	0.447	1.898	0.024	0.150	0.425	0.072	0.114	0.007	96.248
160_fig17_profile2_11	0.063	11.683	2.112	79.668	0.381	1.744	0.000	0.167	0.442	0.018	0.027	0.049	96.592
160_fig17_profile2_12	0.052	11.083	2.100	80.260	0.400	1.757	0.001	0.193	0.448	0.035	0.050	0.000	96.620
160_fig17_profile2_13	0.060	11.007	2.109	80.678	0.423	1.749	0.006	0.182	0.475	0.017	0.049	0.014	97.027
160_fig17_profile2_14	0.034	10.781	2.084	79.917	0.396	1.751	0.004	0.167	0.496	0.027	0.118	0.010	96.055
160_fig17_profile2_15	0.058	10.854	2.112	80.587	0.414	1.776	0.014	0.195	0.500	0.059	0.061	0.013	96.914
160_fig17_profile2_16	0.051	11.062	2.101	81.081	0.412	1.789	0.009	0.156	0.482	0.049	0.000	0.000	97.453
160_fig17_profile2_17	0.050	11.075	2.107	81.056	0.405	1.777	0.000	0.193	0.449	0.030	0.121	0.025	97.533
160_fig17_profile2_18	0.040	11.085	2.117	80.599	0.426	1.767	0.001	0.146	0.435	0.014	0.113	0.005	96.982
160_fig17_p4_11	0.058	13.830	1.952	78.447	0.419	1.782	0.016	0.178	0.459	0.050	0.031	0.000	97.472
160_fig17_p4_12	0.064	11.960	2.090	79.987	0.402	1.632	0.018	0.154	0.472	0.034	0.100	0.010	97.179
160_fig17_p4_13	0.034	11.319	2.104	80.154	0.419	1.634	0.014	0.166	0.472	0.043	0.101	0.000	96.717
160_fig17_p4_14	0.062	10.895	2.085	80.948	0.404	1.634	0.014	0.157	0.480	0.014	0.083	0.000	97.036
160_fig17_p4_15	0.047	10.711	2.095	80.492	0.405	1.616	0.035	0.141	0.477	0.030	0.045	0.000	96.355
160_fig17_p4_16	0.071	10.952	2.104	80.326	0.400	1.665	0.013	0.177	0.477	0.041	0.101	0.001	96.586
160_fig17_p4_17	0.051	10.481	2.101	80.514	0.400	1.685	0.017	0.164	0.471	0.074	0.013	0.016	96.242
160_fig17_p4_18	0.068	11.238	2.057	80.670	0.385	1.666	0.007	0.179	0.476	0.052	0.092	0.016	97.164
160_fig17_p4_19	0.058	10.965	2.090	81.024	0.401	1.663	0.015	0.162	0.499	0.050	0.071	0.000	97.266

Table B2. (Continued)

SAMPLE	SiO_2	TiO_2	Al_2O_3	FeOt	MnO	MgO	CaO	CoO	V_2O_3	Cr_2O_3	ZnO	Nb_2O_5	TOTAL
160_figb_p1_13	0.041	14.215	1.813	77.584	0.441	1.644	0.017	0.176	0.492	0.010	0.101	0.009	96.810
160_figb_p1_14	0.043	11.893	2.007	79.788	0.398	1.580	0.012	0.190	0.474	0.040	0.125	0.000	96.808
160_figb_p1_15	0.073	11.804	1.963	79.667	0.373	1.472	0.033	0.154	0.500	0.021	0.074	0.000	96.407
160_figb_p1_16	0.083	11.341	2.044	80.490	0.376	1.490	0.019	0.144	0.503	0.053	0.034	0.006	96.858
160_figb_p1_17	0.063	10.940	1.988	80.080	0.405	1.512	0.010	0.140	0.517	0.067	0.107	0.000	96.109
160_figb_p1_18	0.054	11.539	2.031	80.277	0.395	1.527	0.015	0.159	0.496	0.029	0.060	0.013	96.865
160_figb_p1_19	0.081	11.103	2.014	79.710	0.419	1.511	0.016	0.142	0.503	0.041	0.044	0.049	95.904
160_figb_p1_20	0.051	11.553	2.010	80.337	0.391	1.486	0.016	0.155	0.513	0.016	0.076	0.006	96.890
160_figb_p1_21	0.050	10.685	1.992	79.659	0.403	1.505	0.018	0.171	0.513	0.045	0.053	0.000	95.371
160_cx_e_p1_16	0.047	15.687	1.741	76.304	0.544	1.808	0.012	0.129	0.385	0.081	0.084	0.000	97.030
160_cx_e_p1_17	0.044	11.718	2.042	79.193	0.503	1.546	0.015	0.154	0.503	0.052	0.144	0.009	96.197
160_cx_e_p1_18	0.061	10.924	2.076	79.884	0.460	1.547	0.020	0.152	0.486	0.069	0.038	0.018	95.998
160_cx_e_p1_19	0.071	10.585	2.032	80.337	0.475	1.648	0.016	0.181	0.463	0.057	0.080	0.012	96.209
160_cx_e_p1_20	0.053	10.613	2.044	80.418	0.472	1.561	0.014	0.171	0.535	0.063	0.115	0.003	96.352
160_cx_e_p1_21	0.049	10.281	2.087	80.076	0.478	1.550	0.010	0.179	0.501	0.035	0.065	0.037	95.622
160_cx_e_p1_22	0.057	10.771	2.063	79.699	0.499	1.545	0.008	0.158	0.492	0.056	0.096	0.000	95.711
160_cx_e_p1_23	0.047	10.412	2.051	79.711	0.486	1.522	0.003	0.191	0.535	0.041	0.000	0.000	95.291
160_cx_e_p1_24	0.046	10.959	2.041	80.269	0.449	1.502	0.013	0.149	0.494	0.021	0.000	0.000	96.211

Table B2. (Continued)

SAMPLE	SiO_2	TiO_2	Al_2O_3	FeOt	MnO	MgO	CaO	CoO	V_2O_3	Cr_2O_3	ZnO	Nb_2O_5	TOTAL
Cal-160_figf_p1_7	0.042	18.959	1.568	73.528	0.456	1.694	0.027	0.172	0.311	0.049	0.111	0.000	97.085
Cal-160_figf_p1_8	0.057	12.919	1.993	77.866	0.435	1.526	0.023	0.135	0.490	0.057	0.109	0.000	95.878
Cal-160_figf_p1_9	0.056	11.495	2.112	79.286	0.402	1.491	0.026	0.150	0.518	0.052	0.102	0.004	95.976
Cal-160_figf_p1_10	0.052	10.763	2.076	79.386	0.403	1.495	0.026	0.154	0.502	0.054	0.025	0.039	95.246
Cal-160_figf_p1_11	0.056	11.152	2.106	80.347	0.379	1.458	0.024	0.163	0.480	0.034	0.052	0.000	96.513
Cal-160_figf_p1_12	0.062	10.609	2.086	80.250	0.400	1.478	0.023	0.147	0.527	0.044	0.105	0.000	96.018
Cal-160_figf_p1_13	0.186	11.098	2.140	80.047	0.410	1.513	0.017	0.173	0.491	0.038	0.092	0.000	96.471
Cal-160_figf_p1_14	0.063	10.758	2.123	79.621	0.400	1.519	0.026	0.164	0.496	0.004	0.053	0.003	95.500
Cal-160_figf_p2_3	0.070	14.226	1.732	76.887	0.474	1.529	0.050	0.150	0.388	0.059	0.069	0.063	95.908
Cal-160_figf_p2_4	0.069	11.221	2.082	79.143	0.425	1.369	0.042	0.135	0.454	0.044	0.027	0.014	95.273
Cal-160_figf_p2_5	0.061	10.850	2.104	79.655	0.417	1.424	0.039	0.192	0.463	0.047	0.046	0.000	95.548
Cal-160_figf_p2_6	0.064	11.087	2.063	80.200	0.442	1.405	0.048	0.175	0.476	0.068	0.049	0.000	96.335
Cal-160_figf_p2_7	0.040	10.847	2.117	79.926	0.413	1.427	0.039	0.180	0.465	0.049	0.061	0.000	95.816
Cal-160_figf_p2_8	0.050	10.824	2.111	79.655	0.413	1.420	0.041	0.174	0.464	0.035	0.046	0.000	95.493

Table B2. (Continued)

SAMPLE	SiO_2	TiO_2	Al_2O_3	FeOt	MnO	MgO	CaO	CoO	V_2O_3	Cr_2O_3	ZnO	Nb_2O_5	TOTAL
Cal-160_figh_p1_9	0.055	15.259	1.774	75.675	0.472	1.520	0.033	0.140	0.443	0.025	0.015	0.014	95.665
Cal-160_figh_p1_10	0.039	13.157	1.933	77.587	0.460	1.620	0.029	0.153	0.542	0.045	0.103	0.000	95.963
Cal-160_figh_p1_11	0.060	11.943	2.019	78.573	0.425	1.522	0.032	0.150	0.508	0.024	0.069	0.000	95.612
Cal-160_figh_p1_12	0.065	11.125	2.083	79.816	0.416	1.496	0.024	0.149	0.508	0.052	0.046	0.000	96.056
Cal-160_figh_p1_13	0.051	10.430	2.103	79.776	0.416	1.461	0.020	0.168	0.525	0.021	0.075	0.027	95.361
Cal-160_figh_p1_14	0.048	10.226	2.108	80.232	0.392	1.466	0.024	0.173	0.513	0.033	0.111	0.000	95.606
Cal-160_figh_p1_15	0.059	10.446	2.132	79.698	0.423	1.444	0.022	0.166	0.516	0.061	0.069	0.000	95.317
Cal-160_figh_p1_16	0.047	10.310	2.114	79.853	0.401	1.494	0.008	0.176	0.521	0.019	0.134	0.003	95.364
Cal-160_figh_p1_17	0.065	10.414	2.096	80.117	0.409	1.475	0.025	0.172	0.541	0.029	0.096	0.117	95.849
Cal-160_figh_p1_18	0.060	10.447	2.110	80.731	0.403	1.432	0.031	0.174	0.543	0.053	0.078	0.011	96.368
Cal-160_figh_p1_19	0.043	10.483	2.068	79.783	0.410	1.455	0.008	0.155	0.508	0.060	0.020	0.015	95.298
Cal-160_figh_p1_20	0.055	10.417	2.105	79.989	0.416	1.455	0.027	0.145	0.553	0.037	0.043	0.010	95.554

B.6. References

Aragon, R, McCallister, RH, Harrison, HR (1984) Cation diffusion in titanomagnetites. Contributions to Mineralogy and Petrology 85(2), 174-185.

Barlow, RJ (1989) Statistics: a guide to the use of statistical methods in the physical sciences (Vol. 29). John Wiley & Sons.

Drouin, D, Couture, AR, Joly, D, Tastet, X, Aimez, V, Gauvin, R (2007) CASINO V2. 42—A Fast and Easy-to-use Modeling Tool for Scanning Electron Microscopy and Microanalysis Users. Scanning 29(3): 92-101. https://doi.org/10.1002/sca.20000

Hovington, P, Drouin, D, and Gauvin, R (1997) CASINO: A new Monte Carlo code in C language for electron beam interaction—Part I: Description of the program. Scanning 19(1), 1-14. https://doi.org/10.1002/sca.4950190101

Appendix C

Supplementary Material for Chapter 4

C.1. Pictures of mineral textures

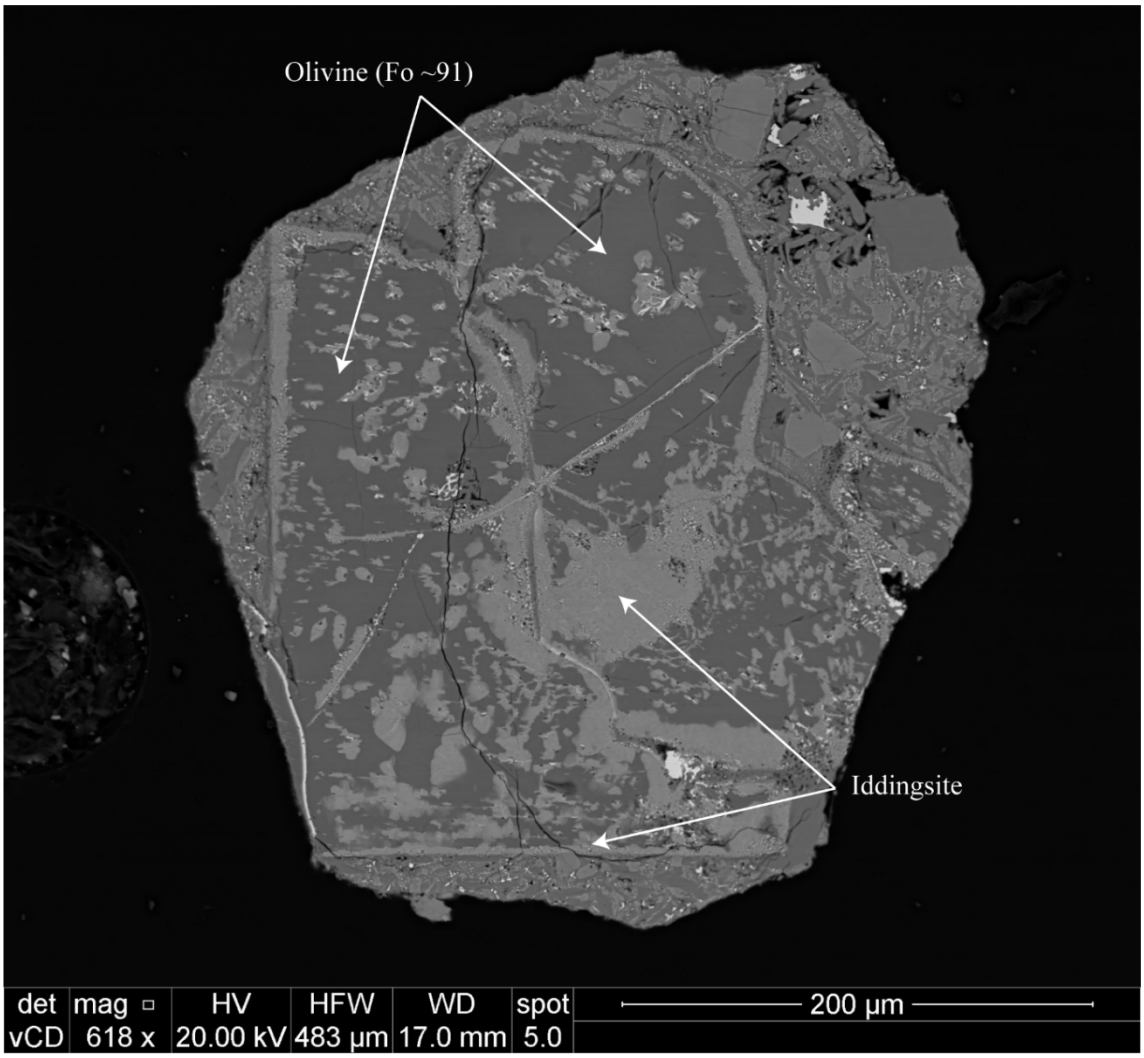

Figure C.1. *Backscatter image showing an olivine xenocryst surrounded by iddingsite alteration.*

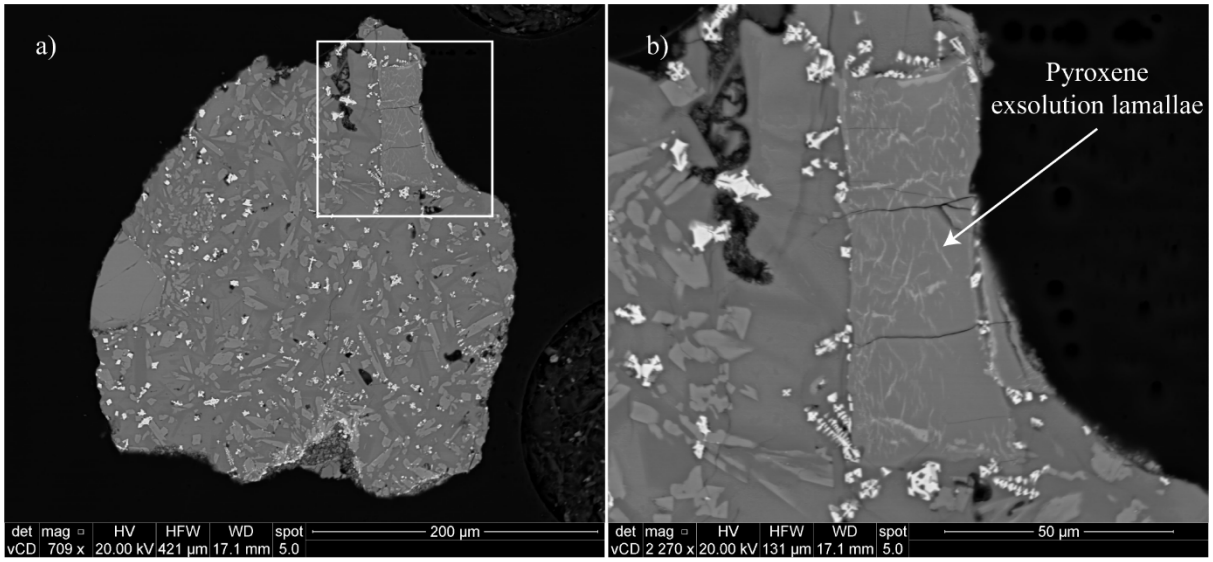

Figure C.2. *Backscatter image showing a portion of a xenolith including clinopyroxene with exsolution lamellae texture.*

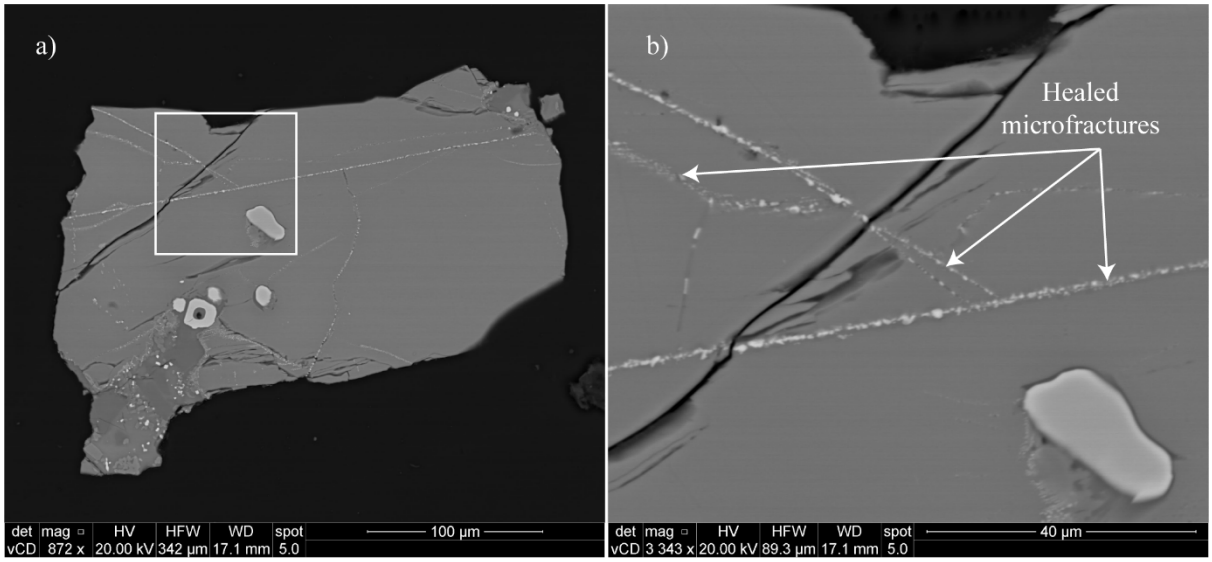

Figure C.3. *Backscatter image showing an orthopyroxene xenocryst with healed microfractures within.*

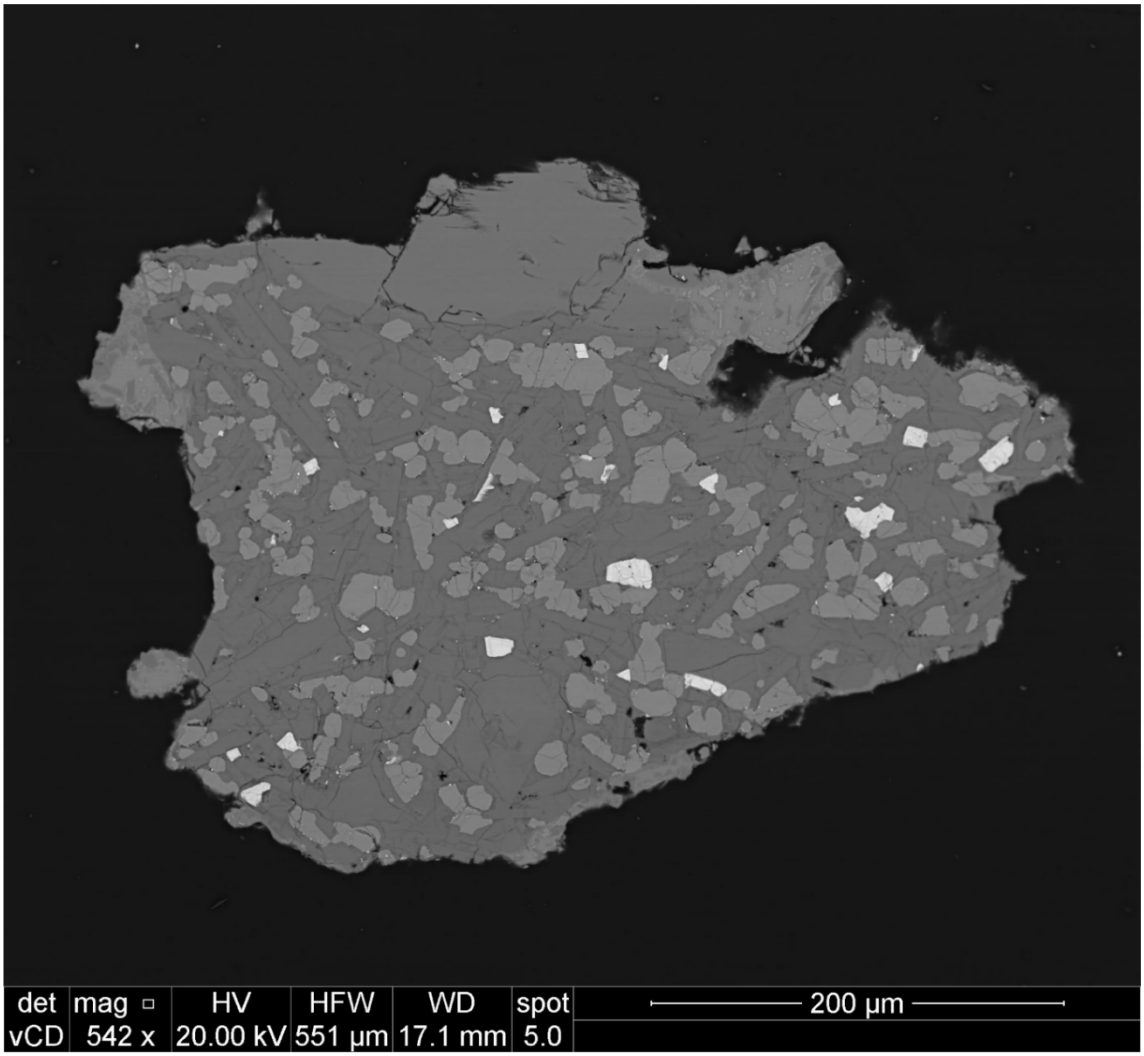

Figure C.4. *Backscatter image showing an orthopyroxene xenocryst with healed microfractures within.*

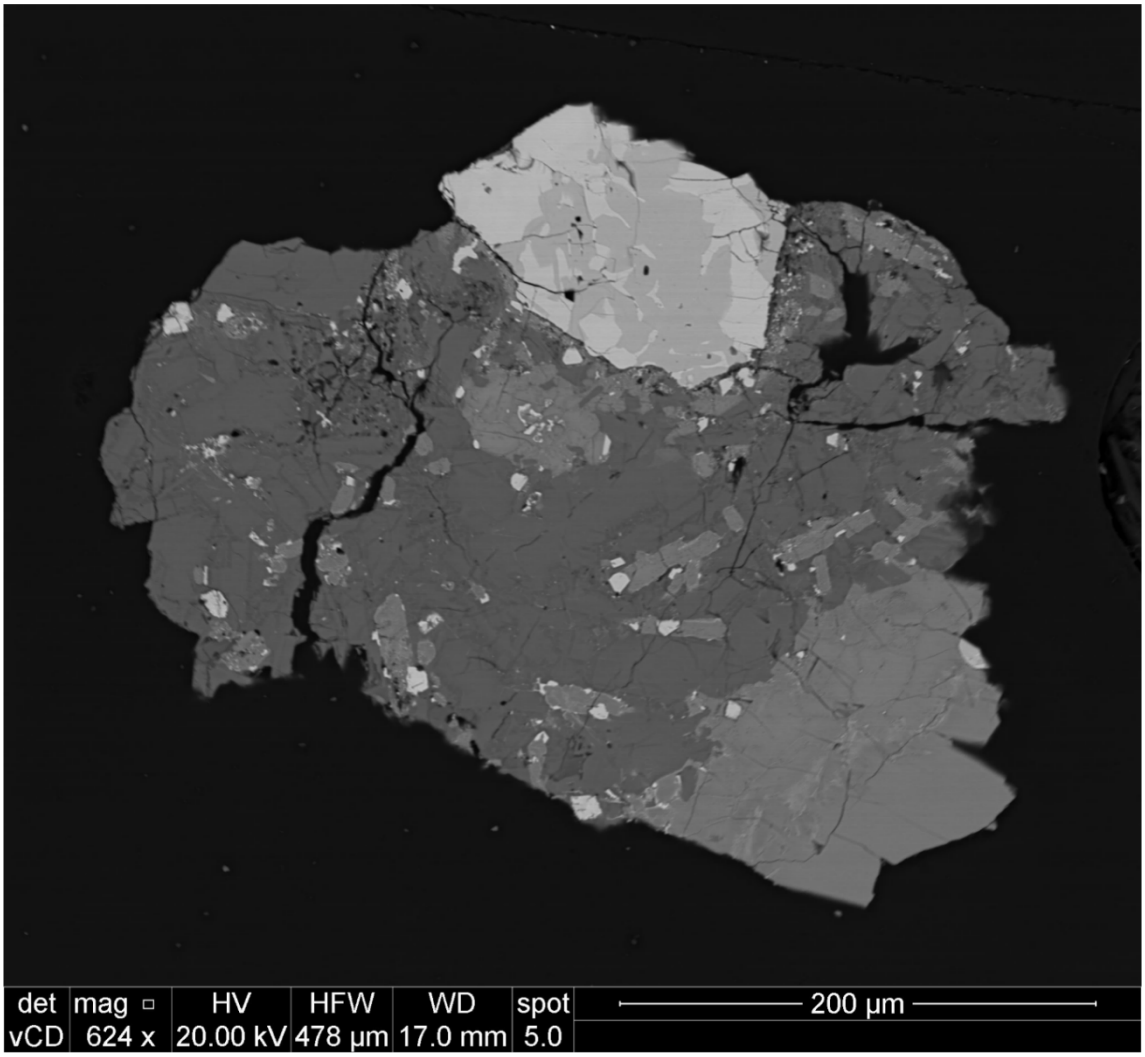

Figure C.5. *Backscatter image showing a portion of a xenolith.*

C.2. Rare earth elements

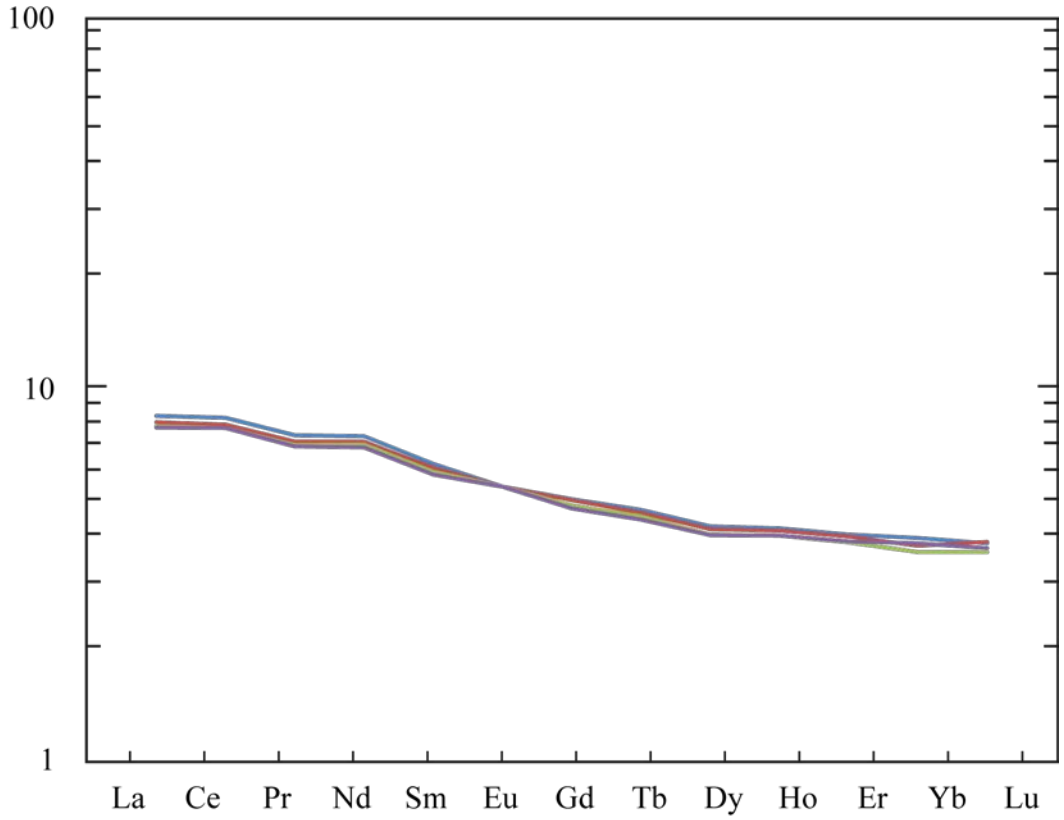

Figure C.6. Rare earth elements (REE) diagram showing a narrow range of La_N/Yb_N from 2.1 to 2.2. Values normalised to chondrite composition (Sun and McDonough, 1989).

C.3. Olivine-augite equilibrium

To test the equilibrium of in-contact olivine-augite phenocryst grains, we use the olivine-melt ($K_D^{Fe-Mg} = (X_{Fe}^{ol}\, X_{Mg}^{liq})/(X_{Mg}^{ol}\, X_{Fe}^{liq})$ = 0.3±0.05) and augite-melt (K_D^{Fe-Mg} = 0.25±0.09). Only if Mg/Fe^{2+} molar ratios are equivalent (including errors represented by dashed lines, Figure X5), we consider the pairs are in equilibrium.

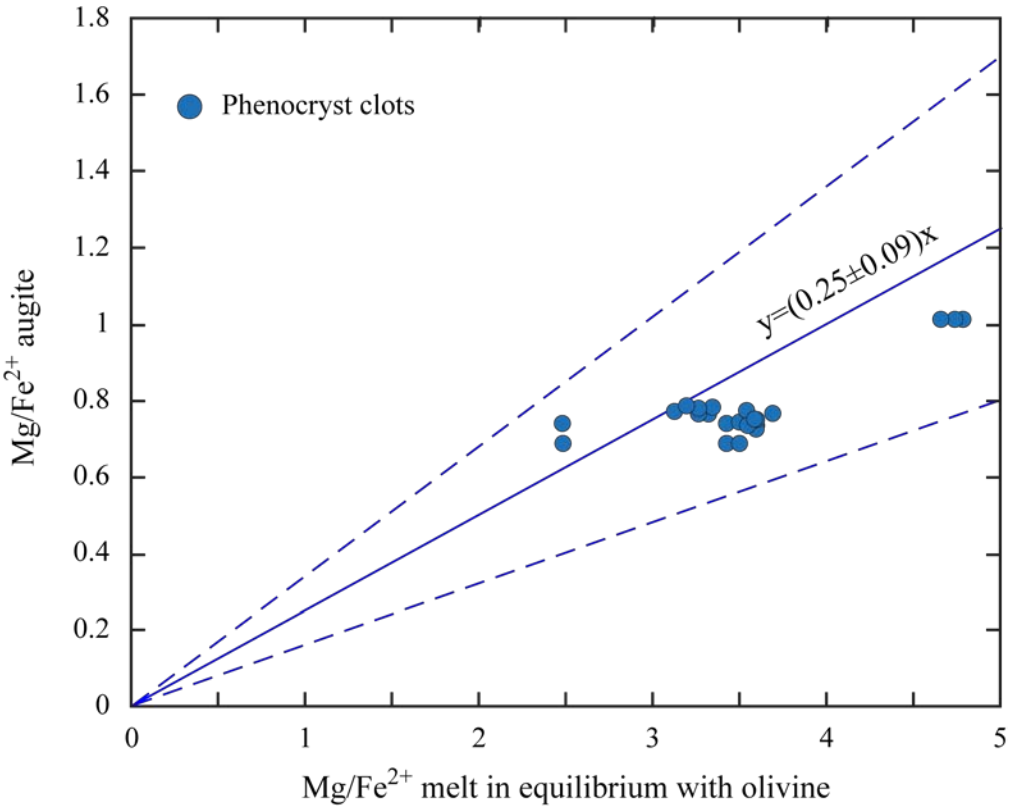

Figure C.7. *Augite-olivine equilibrium inferred from testing if a hypothesised melt composition (Mg/Fe^{2+}, in moles) is in equilibrium with both olivine and augite compositions. The solid line represents the augite-melt equilibrium composition (for a H_2O-saturated mafic melt) following Grove et al. (1997) equation for K_D and the dashed lines correspond to the reported uncertainties of K_D (Grove et al. 1997).*

C.4. Olivine-spinel equilibrium

Kamenetsky et al. (2001) suggested that a positive correlation between spinel Mg# (Mg# = Mg/(Mg+Fe^{2+}), in moles)and olivine forsterite content (Fo = (Mg/(Mg+Fe^{2+}))×100, in moles) reflects a local equilibrium between olivine and spinel inclusions within.

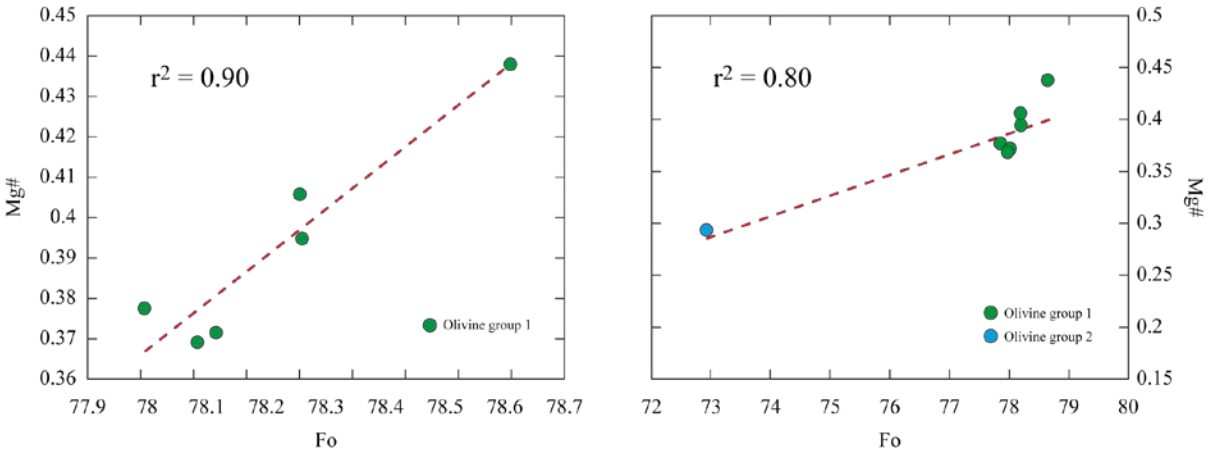

Figure C.8. *Relationships between host olivine Fo and spinel inclusions Mg#. The compositional trends are presented for olivine phenocrysts from groups 1 (FoX-Y) and 2 (FoZ-T) with their respective spinel inclusions.*

C.5. Details of calculations

Moore et al., 1998. The values of the constants used in equation A1 (equation 1, from Moore et al., 1998) are listed as follows:

$$2ln^{melt}X_{H_2O} = \frac{a'}{T} + \sum b'_i X_i \cdot \left(\frac{P}{T}\right) + c' \cdot log^{fluid}\left(f_{H_2O}\right) + d' \qquad (C1)$$

a’ = 2,565 (±362)

$b_{Al_2O_3}$ = -1.997 (±0.706)

$b_{Fe_{tot}}$ = -0.9275 (±0.394)

b_{Na_2O} = 2.736 (±0.871)

c’ = 1.171 (±0.069)

d’ = -14.21 (±0.54)

Kress and Carmichael, 1991. The values of the constants used in equation A2 (equation 7, from Kress and Carmichael, 1991) are listed as follows:

$$\log\left(\frac{XFe_2O_3}{XFeO}\right) = a \cdot \log(f_{O_2}) + \frac{b}{T} + c + \sum d_i \cdot X_i + e\left[1 - \left(\frac{T_0}{T}\right) - \log\left(\frac{T}{T_0}\right)\right] + f\left(\frac{P}{T}\right) + g\frac{(T - T_0)P}{T} + h\left(\frac{P^2}{T}\right) \qquad (C2)$$

a = 0.196

b = 11,492 (K)

c = -6.675

$d_{Al_2O_3}$ = -2.243

$d_{FeO_{tot}}$ = -1.828

d_{CaO} = 3.201

d_{Na_2O} = 5.854

d_{K_2O} = 6.215

f = $-7 \cdot 10^{-2}$ ($K \cdot bar^{-1}$)

g = $-1.5 \cdot 10^{-5}$ (bar^{-1})

h = $3.85 \cdot 10^{-7}$ ($K \cdot bar^{-2}$)

C.6. Mineral chemistry

Table C1. Compositions of olivine from the 1835 Osorno eruption (wt%).

SAMPLE	SiO_2	TiO_2	Al_2O_3	FeO	MnO	MgO	CaO	Cr_2O_3	NiO	TOTAL
Oso-144A_Fig2_Ol6_1	37.501	0.025	0.003	25.696	0.435	35.607	0.321	0.019	0.033	99.640
Oso-144A_Fig2_Ol6_2	37.763	0.022	0.011	25.817	0.443	35.392	0.303	0.021	0.044	99.816
Oso-144A_Fig2_Ol6_3	37.441	0.023	0.007	25.947	0.446	35.179	0.308	0.013	0.036	99.399
Oso-144A_Fig2_Ol6_4	37.806	0.028	0.011	25.078	0.411	36.225	0.293	0.019	0.040	99.912
Oso-144A_Fig2_Ol6_5	38.015	0.036	0.006	25.060	0.417	36.065	0.290	0.018	0.040	99.948
Oso-144A_Fig2_Ol6_6	37.806	0.026	0.004	25.186	0.420	35.870	0.339	0.022	0.036	99.709
Oso-144A_Fig2_Ol6_7	37.636	0.021	0.025	24.952	0.428	36.331	0.374	0.023	0.036	99.826
Oso-144A_Fig2_Ol6_8	37.978	0.025	0.010	25.623	0.430	35.795	0.330	0.022	0.038	100.251
Oso-144A_Fig2_Ol6_9	37.296	0.027	0.009	26.076	0.438	35.561	0.318	0.013	0.038	99.777
Oso-144A_Fig2_Ol6_10	37.560	0.037	0.015	25.106	0.435	35.744	0.388	0.028	0.042	99.354
Oso-144A_Fig2_Ol6_11	37.713	0.036	0.011	24.929	0.425	35.937	0.408	0.031	0.038	99.528
Oso-144A_Fig2_Ol6_12	38.385	0.014	0.005	21.031	0.353	39.434	0.210	0.021	0.077	99.529
Oso-144A_Fig2_Ol6_13	38.399	0.010	0.004	20.960	0.343	39.634	0.221	0.013	0.074	99.657
Oso-144A_Fig2_Ol6_14	38.857	0.008	-0.003	21.072	0.346	39.855	0.212	0.020	0.078	100.446
Oso-144A_Fig2_Ol6_15	37.471	0.023	0.003	26.811	0.463	34.450	0.312	0.006	0.029	99.570
Oso-144A_Fig2_Ol6_16	37.805	0.025	-0.001	26.416	0.455	34.838	0.298	0.009	0.030	99.874
Oso-144A_Fig2_Ol6_17	37.514	0.029	0.006	25.672	0.437	35.444	0.295	0.018	0.038	99.452

Table C1. (Continued)

SAMPLE	SiO_2	TiO_2	Al_2O_3	FeO	MnO	MgO	CaO	Cr_2O_3	NiO	TOTAL
Oso-164A_F3a_1	39.648	0.198	1.736	26.047	0.427	30.532	1.226	0.005	0.061	99.880
Oso-164A_F3a_2	38.515	0.020	0.002	24.774	0.405	35.972	0.199	0.008	0.075	99.970
Oso-164A_F3a_3	38.219	0.017	0.001	24.913	0.395	35.780	0.189	0.012	0.074	99.599
Oso-164A_F3a_4	38.001	0.018	0.000	24.778	0.394	35.894	0.186	0.008	0.066	99.344
Oso-164A_F3a_5	38.394	0.014	0.002	25.009	0.402	35.966	0.185	0.006	0.070	100.047
Oso-164A_F3a_6	38.686	0.014	0.002	24.600	0.398	35.912	0.181	0.009	0.067	99.870
Oso-164A_F3a_7	38.195	0.017	0.000	24.798	0.397	35.628	0.177	0.004	0.079	99.294
Oso-164A_F3a_8	37.430	0.015	0.000	24.776	0.392	35.694	0.175	0.011	0.074	98.567
Oso-164A_F3a_9	37.925	0.016	0.005	24.891	0.397	35.722	0.176	0.006	0.070	99.207
Oso-164A_F3a_10	38.429	0.010	0.000	24.976	0.397	35.810	0.175	0.007	0.073	99.878
Oso-164A_F3a_11	38.384	0.013	0.000	24.825	0.391	35.887	0.173	0.009	0.071	99.753
Oso-164A_F3a_12	37.624	0.018	0.000	24.901	0.395	35.699	0.172	0.005	0.066	98.880
Oso-164A_F3a_13	37.975	0.011	0.000	24.796	0.401	35.633	0.172	0.013	0.065	99.066
Oso-164A_F3a_14	37.959	0.020	0.000	24.866	0.402	35.660	0.172	0.008	0.073	99.159
Oso-164A_F3a_15	38.517	0.014	0.000	24.745	0.396	35.850	0.172	0.003	0.074	99.772
Oso-164A_F3a_16	37.694	0.011	0.000	24.869	0.396	35.564	0.171	0.009	0.076	98.789
Oso-164A_F3a_17	38.271	0.012	0.000	24.906	0.399	35.925	0.172	0.005	0.073	99.763
Oso-164A_F3a_18	37.835	0.015	0.000	25.013	0.399	35.644	0.171	0.007	0.072	99.155
Oso-164A_F3a_19	38.415	0.011	0.000	24.960	0.395	35.792	0.171	0.007	0.067	99.817
Oso-164A_F3a_20	38.011	0.010	0.000	24.954	0.402	35.906	0.171	0.008	0.070	99.531
Oso-164A_F3a_21	37.196	0.017	0.000	24.836	0.399	35.759	0.170	0.007	0.065	98.447
Oso-164A_F3a_22	38.207	0.009	0.002	24.808	0.399	35.965	0.169	0.010	0.061	99.632
Oso-164A_F3a_23	37.614	0.015	0.000	24.817	0.399	35.732	0.171	0.011	0.067	98.826

Table C1. (Continued)

SAMPLE	SiO_2	TiO_2	Al_2O_3	FeO	MnO	MgO	CaO	Cr_2O_3	NiO	TOTAL
Oso-164A_F3a_1	39.648	0.198	1.736	26.047	0.427	30.532	1.226	0.005	0.061	99.880
Oso-164A_F3a_2	38.515	0.020	0.002	24.774	0.405	35.972	0.199	0.008	0.075	99.970
Oso-164A_F3a_3	38.219	0.017	0.001	24.913	0.395	35.780	0.189	0.012	0.074	99.599
Oso-164A_F3a_4	38.001	0.018	0.000	24.778	0.394	35.894	0.186	0.008	0.066	99.344
Oso-164A_F3a_5	38.394	0.014	0.002	25.009	0.402	35.966	0.185	0.006	0.070	100.047
Oso-164A_F3a_6	38.686	0.014	0.002	24.600	0.398	35.912	0.181	0.009	0.067	99.870
Oso-164A_F3a_7	38.195	0.017	0.000	24.798	0.397	35.628	0.177	0.004	0.079	99.294
Oso-164A_F3a_8	37.430	0.015	0.000	24.776	0.392	35.694	0.175	0.011	0.074	98.567
Oso-164A_F3a_9	37.925	0.016	0.005	24.891	0.397	35.722	0.176	0.006	0.070	99.207
Oso-164A_F3a_10	38.429	0.010	0.000	24.976	0.397	35.810	0.175	0.007	0.073	99.878
Oso-164A_F3a_11	38.384	0.013	0.000	24.825	0.391	35.887	0.173	0.009	0.071	99.753
Oso-164A_F3a_12	37.624	0.018	0.000	24.901	0.395	35.699	0.172	0.005	0.066	98.880
Oso-164A_F3a_13	37.975	0.011	0.000	24.796	0.401	35.633	0.172	0.013	0.065	99.066
Oso-164A_F3a_14	37.959	0.020	0.000	24.866	0.402	35.660	0.172	0.008	0.073	99.159
Oso-164A_F3a_15	38.517	0.014	0.000	24.745	0.396	35.850	0.172	0.003	0.074	99.772
Oso-164A_F3a_16	37.694	0.011	0.000	24.869	0.396	35.564	0.171	0.009	0.076	98.789
Oso-164A_F3a_17	38.271	0.012	0.000	24.906	0.399	35.925	0.172	0.005	0.073	99.763
Oso-164A_F3a_18	37.835	0.015	0.000	25.013	0.399	35.644	0.171	0.007	0.072	99.155
Oso-164A_F3a_19	38.415	0.011	0.000	24.960	0.395	35.792	0.171	0.007	0.067	99.817
Oso-164A_F3a_20	38.011	0.010	0.000	24.954	0.402	35.906	0.171	0.008	0.070	99.531
Oso-164A_F3a_21	37.196	0.017	0.000	24.836	0.399	35.759	0.170	0.007	0.065	98.447
Oso-164A_F3a_22	38.207	0.009	0.002	24.808	0.399	35.965	0.169	0.010	0.061	99.632
Oso-164A_F3a_23	37.614	0.015	0.000	24.817	0.399	35.732	0.171	0.011	0.067	98.826

Table C1. (Continued)

SAMPLE	SiO_2	TiO_2	Al_2O_3	FeO	MnO	MgO	CaO	Cr_2O_3	NiO	TOTAL
Oso-164A_F3b_p2_1	38.258	0.041	0.097	24.857	0.393	35.414	0.262	0.006	0.068	99.397
Oso-164A_F3b_p2_2	38.254	0.032	0.002	24.702	0.408	35.725	0.219	0.009	0.067	99.419
Oso-164A_F3b_p2_3	38.029	0.026	0.000	24.910	0.394	35.792	0.209	0.007	0.069	99.432
Oso-164A_F3b_p2_4	37.814	0.023	0.000	24.895	0.398	35.625	0.200	0.011	0.075	99.038
Oso-164A_F3b_p2_5	38.037	0.019	0.000	24.960	0.402	35.736	0.193	0.011	0.076	99.434
Oso-164A_F3b_p2_6	37.751	0.014	0.000	24.917	0.401	35.679	0.192	0.010	0.075	99.035
Oso-164A_F3b_p2_7	37.815	0.018	0.000	25.033	0.405	35.813	0.187	0.014	0.079	99.363
Oso-164A_F3b_p2_8	38.436	0.047	0.252	25.002	0.400	34.790	0.331	0.008	0.062	99.328
Oso-164A_F3b_p2_9	37.375	0.026	0.006	24.609	0.397	35.419	0.221	0.008	0.075	98.136
Oso-164A_F3b_p2_10	38.032	0.022	0.005	25.066	0.398	35.864	0.210	0.012	0.072	99.682
Oso-164A_F3b_p2_11	37.468	0.022	0.000	24.962	0.406	35.864	0.201	0.010	0.076	99.004
Oso-164A_F3b_p2_12	38.076	0.023	0.000	25.071	0.401	36.031	0.197	0.008	0.069	99.872
Oso-164A_F3b_p2_13	37.335	0.019	0.000	24.804	0.394	35.207	0.191	0.007	0.070	98.025
Oso-164A_F3b_p2_14	37.967	0.015	0.000	25.067	0.403	35.747	0.186	0.009	0.073	99.465
Oso-164A_F3b_p2_15	38.249	0.019	0.000	24.940	0.406	35.940	0.184	0.009	0.079	99.824

Table C1. (Continued)

SAMPLE	SiO_2	TiO_2	Al_2O_3	FeO	MnO	MgO	CaO	Cr_2O_3	NiO	TOTAL
Oso-164A_F9a_p1_1	39.143	0.034	0.052	21.886	0.356	37.958	0.265	0.024	0.061	99.779
Oso-164A_F9a_p1_2	38.643	0.017	0.005	19.719	0.330	40.090	0.231	0.015	0.085	99.135
Oso-164A_F9a_p1_3	38.944	0.015	0.003	19.489	0.325	40.214	0.220	0.017	0.088	99.315
Oso-164A_F9a_p1_4	39.092	0.015	0.005	19.602	0.316	40.381	0.213	0.017	0.092	99.733
Oso-164A_F9a_p1_5	39.214	0.014	0.004	19.746	0.321	40.370	0.209	0.013	0.096	99.988
Oso-164A_F9a_p1_6	39.057	0.013	0.003	19.780	0.320	40.479	0.206	0.013	0.098	99.968
Oso-164A_F9a_p1_7	39.279	0.011	0.004	19.753	0.327	40.476	0.207	0.014	0.093	100.163
Oso-164A_F9a_p1_8	39.337	0.011	0.002	19.736	0.329	40.488	0.201	0.007	0.095	100.207
Oso-164A_F9a_p1_9	38.628	0.006	0.006	19.696	0.320	40.130	0.200	0.015	0.088	99.089
Oso-164A_F9a_p1_10	38.949	0.012	0.000	19.650	0.320	40.255	0.199	0.019	0.086	99.490
Oso-164A_F9a_p1_11	39.014	0.012	0.003	19.535	0.318	40.113	0.197	0.013	0.086	99.291
Oso-164A_F9a_p1_12	39.491	0.010	0.002	19.706	0.320	40.254	0.193	0.013	0.091	100.079
Oso-164A_F9a_p1_13	39.169	0.007	0.005	19.717	0.325	40.135	0.196	0.012	0.094	99.660
Oso-164A_F9a_p1_14	38.964	0.010	0.005	19.724	0.318	40.370	0.193	0.011	0.090	99.685
Oso-164A_F9a_p1_15	39.007	0.014	0.000	19.688	0.321	40.106	0.194	0.021	0.091	99.441
Oso-164A_F9a_p1_16	38.960	0.015	0.005	19.769	0.323	40.244	0.196	0.016	0.088	99.617
Oso-164A_F9a_p1_17	39.046	0.009	0.002	19.746	0.326	40.139	0.194	0.018	0.083	99.563
Oso-164A_F9a_p1_18	39.046	0.014	0.001	19.674	0.323	40.127	0.195	0.014	0.089	99.482
Oso-164A_F9a_p1_19	38.780	0.016	0.002	19.748	0.319	40.300	0.192	0.018	0.087	99.462
Oso-164A_F9a_p1_20	39.015	0.013	0.010	19.690	0.310	40.052	0.192	0.017	0.099	99.398
Oso-164A_F9a_p1_21	39.062	0.007	0.002	19.689	0.315	40.217	0.191	0.015	0.100	99.598
Oso-164A_F9a_p1_22	39.109	0.014	0.002	19.881	0.319	40.152	0.192	0.016	0.096	99.781

Table C1. (Continued)

SAMPLE	SiO_2	TiO_2	Al_2O_3	FeO	MnO	MgO	CaO	Cr_2O_3	NiO	TOTAL
Oso147A-Fig9b_p1_1	39.926	0.021	0.004	19.674	0.314	40.189	0.225	0.012	0.078	100.442
Oso147A-Fig9b_p1_2	40.048	0.017	0.003	19.633	0.325	40.151	0.218	0.016	0.090	100.501
Oso147A-Fig9b_p1_3	39.405	0.016	0.002	19.702	0.320	39.897	0.210	0.024	0.089	99.666
Oso147A-Fig9b_p1_4	39.387	0.010	0.001	19.577	0.320	39.968	0.208	0.016	0.079	99.564
Oso147A-Fig9b_p1_5	40.138	0.013	0.003	19.594	0.325	40.028	0.208	0.007	0.086	100.401
Oso147A-Fig9b_p1_6	39.314	0.011	0.000	19.652	0.320	39.970	0.202	0.016	0.102	99.586
Oso147A-Fig9b_p1_7	39.363	0.011	0.003	19.760	0.325	39.978	0.203	0.013	0.090	99.746
Oso147A-Fig9b_p1_8	39.295	0.011	0.000	19.745	0.321	40.007	0.198	0.005	0.086	99.668
Oso147A-Fig9b_p1_9	39.295	0.013	0.000	19.713	0.317	39.899	0.196	0.020	0.087	99.541
Oso147A-Fig9b_p1_10	39.161	0.009	0.000	19.633	0.316	39.830	0.198	0.014	0.089	99.250
Oso147A-Fig9b_p1_11	39.387	0.008	0.000	19.635	0.321	40.186	0.198	0.015	0.086	99.834
Oso147A-Fig9b_p1_12	39.016	0.008	0.000	19.650	0.314	39.728	0.195	0.009	0.086	99.005
Oso147A-Fig9b_p1_13	39.137	0.015	0.003	19.575	0.330	39.728	0.196	0.015	0.101	99.100
Oso147A-Fig9b_p1_14	39.282	0.015	0.000	19.605	0.311	39.721	0.193	0.019	0.097	99.243
Oso147A-Fig9b_p1_15	38.952	0.009	0.000	19.716	0.321	40.033	0.195	0.013	0.098	99.336
Oso147A-Fig9b_p1_16	39.110	0.008	0.000	19.836	0.324	40.017	0.194	0.012	0.092	99.593
Oso147A-Fig9b_p1_17	39.316	0.009	0.005	19.744	0.318	40.035	0.191	0.015	0.090	99.722
Oso147A-Fig9b_p1_18	39.364	0.015	0.000	19.703	0.318	39.999	0.193	0.015	0.084	99.690
Oso147A-Fig9b_p1_19	39.326	0.010	0.006	19.556	0.324	39.999	0.192	0.013	0.092	99.517

Table C1. (Continued)

SAMPLE	SiO_2	TiO_2	Al_2O_3	FeO	MnO	MgO	CaO	Cr_2O_3	NiO	TOTAL
Oso-164B_F1a_p1_1	38.726	0.030	0.011	21.554	0.370	38.146	0.257	0.023	0.061	99.178
Oso-164B_F1a_p1_2	39.300	0.020	0.006	20.345	0.335	39.342	0.235	0.017	0.088	99.688
Oso-164B_F1a_p1_3	38.982	0.015	0.002	19.757	0.327	39.546	0.223	0.014	0.088	98.954
Oso-164B_F1a_p1_4	39.478	0.021	0.000	19.808	0.326	39.804	0.216	0.017	0.092	99.760
Oso-164B_F1a_p1_5	38.903	0.015	0.001	19.904	0.323	39.858	0.212	0.016	0.089	99.319
Oso-164B_F1a_p1_6	39.209	0.011	0.002	19.925	0.325	39.984	0.208	0.018	0.088	99.768
Oso-164B_F1a_p1_7	39.211	0.013	0.002	19.875	0.327	40.058	0.210	0.012	0.090	99.798
Oso-164B_F1a_p1_8	39.750	0.015	0.001	19.918	0.328	39.952	0.205	0.015	0.092	100.277
Oso-164B_F1a_p1_9	39.475	0.006	0.001	19.866	0.324	39.896	0.204	0.015	0.092	99.878
Oso-164B_F1a_p1_10	39.191	0.014	0.005	19.930	0.320	39.814	0.201	0.017	0.088	99.580
Oso-164B_F1a_p1_11	39.332	0.010	0.000	19.999	0.322	39.971	0.202	0.020	0.094	99.950
Oso-164B_F1a_p1_12	39.810	0.011	0.006	19.935	0.315	40.085	0.198	0.012	0.089	100.463
Oso-164B_F1a_p1_13	39.327	0.010	0.001	19.942	0.332	39.802	0.199	0.017	0.090	99.720
Oso-164B_F1a_p1_14	39.526	0.013	0.000	19.925	0.330	39.800	0.198	0.010	0.084	99.886
Oso-164B_F1a_p1_15	38.877	0.008	0.000	19.909	0.320	39.840	0.198	0.014	0.087	99.252
Oso-164B_F1a_p1_16	39.580	0.013	0.001	19.753	0.322	39.828	0.197	0.022	0.080	99.796
Oso-164B_F1a_p1_17	39.533	0.012	0.000	19.710	0.328	39.663	0.197	0.014	0.096	99.552

Table C1. (Continued)

SAMPLE	SiO_2	TiO_2	Al_2O_3	FeO	MnO	MgO	CaO	Cr_2O_3	NiO	TOTAL
Oso-156A_F1b_p1_1	39.791	0.106	0.095	24.874	0.425	34.565	0.585	0.019	0.027	100.486
Oso-156A_F1b_p1_2	38.985	0.025	0.017	22.338	0.369	37.424	0.237	0.022	0.070	99.488
Oso-156A_F1b_p1_3	39.459	0.015	-0.002	20.179	0.334	39.562	0.220	0.013	0.076	99.856
Oso-156A_F1b_p1_4	39.708	0.019	0.005	19.892	0.322	40.188	0.214	0.014	0.082	100.444
Oso-156A_F1b_p1_5	39.665	0.015	0.001	19.655	0.325	39.998	0.209	0.016	0.084	99.968
Oso-156A_F1b_p1_6	39.225	0.016	0.003	19.694	0.329	40.033	0.206	0.010	0.091	99.608
Oso-156A_F1b_p1_7	39.756	0.009	0.000	19.808	0.322	40.131	0.202	0.015	0.097	100.340
Oso-156A_F1b_p1_8	39.620	0.010	0.005	19.820	0.320	40.226	0.201	0.018	0.094	100.315
Oso-156A_F1b_p1_9	39.482	0.013	-0.002	19.891	0.315	40.106	0.200	0.012	0.092	100.108
Oso-156A_F1b_p1_10	39.672	0.011	0.001	19.865	0.325	40.090	0.198	0.018	0.089	100.268
Oso-156A_F1b_p1_11	39.102	0.010	0.005	19.809	0.325	40.081	0.196	0.019	0.086	99.631
Oso-156A_F1b_p1_12	39.341	0.011	0.002	19.776	0.324	40.061	0.198	0.013	0.088	99.814
Oso-156A_F1b_p1_13	39.799	0.010	0.003	19.817	0.325	40.292	0.195	0.020	0.088	100.549
Oso-156A_F1b_p1_14	39.443	0.012	0.003	19.740	0.321	39.861	0.196	0.011	0.090	99.676
Oso-156A_F1b_p1_15	39.795	0.006	0.004	19.870	0.316	40.038	0.195	0.014	0.084	100.323
Oso-156A_F1b_p1_16	39.198	0.010	0.000	19.855	0.322	39.942	0.195	0.012	0.099	99.631
Oso-156A_F1b_p1_17	39.564	0.008	0.002	20.004	0.322	40.032	0.195	0.012	0.097	100.237

Table C1. (Continued)

SAMPLE	SiO_2	TiO_2	Al_2O_3	FeO	MnO	MgO	CaO	Cr_2O_3	NiO	TOTAL
Os-164_MI_Fig12_1	39.645	0.020	0.015	19.983	0.334	39.793	0.236	0.010	0.088	100.125
Os-164_MI_Fig12_2	39.821	0.021	0.016	19.985	0.330	40.081	0.224	0.016	0.090	100.583
Os-164_MI_Fig12_3	39.316	0.017	0.017	19.929	0.335	39.721	0.220	0.008	0.080	99.644
Os-164_MI_Fig12_4	39.671	0.016	0.016	19.799	0.315	39.868	0.212	0.018	0.079	99.995
Os-164_MI_Fig12_5	39.446	0.017	0.011	20.079	0.327	40.018	0.207	0.012	0.095	100.213
Os-164_MI_Fig12_6	39.630	0.013	0.013	19.985	0.325	40.184	0.206	0.014	0.090	100.460
Os-164_MI_Fig12_7	39.535	0.012	0.014	20.113	0.333	40.091	0.198	0.020	0.082	100.398
Os-164_MI_Fig12_8	39.548	0.013	0.013	20.027	0.325	39.992	0.198	0.007	0.084	100.206
Os-164_MI_Fig12_9	39.105	0.009	0.009	20.071	0.322	39.892	0.196	0.019	0.079	99.703
Os-164_MI_Fig12_10	39.133	0.001	0.010	20.074	0.331	39.915	0.196	0.021	0.076	99.756
Os-164_MI_Fig12_11	39.091	0.010	0.012	19.945	0.329	39.993	0.211	0.020	0.091	99.701
Os-164_MI_Fig13_a	39.412	0.011	0.017	19.756	0.328	40.420	0.191	0.009	0.094	100.239
Os-164_MI_Fig13_b	39.014	0.009	0.013	19.803	0.321	40.382	0.191	0.013	0.095	99.840
Os-164_MI_Fig23_1	39.089	0.020	0.042	20.057	0.339	40.014	0.262	0.021	0.080	99.925
Os-164_MI_Fig23_2	38.944	0.027	0.012	20.213	0.324	39.928	0.229	0.013	0.074	99.763
Os-164_MI_Fig23_3	39.537	0.021	0.012	20.002	0.333	39.961	0.210	0.020	0.084	100.182
Os-164_MI_Fig23_4	39.436	0.013	0.009	20.166	0.336	40.032	0.207	0.007	0.088	100.294
Os-164_MI_Fig23_5	39.386	0.014	0.011	20.109	0.326	39.959	0.212	0.011	0.078	100.107
Os-164_MI_Fig23_6	39.475	0.011	0.012	20.131	0.324	40.142	0.200	0.007	0.075	100.378
Os-164_MI_Fig23_7	39.678	0.013	0.008	20.110	0.328	40.160	0.192	0.007	0.077	100.574
Os-164_MI_Fig23_8	39.452	0.012	0.013	20.119	0.320	40.095	0.191	0.015	0.085	100.302
Os-164_MI_Fig23_9	39.492	0.009	0.009	20.114	0.329	40.137	0.197	0.013	0.071	100.371

Table C1. (Continued)

SAMPLE	SiO_2	TiO_2	Al_2O_3	FeO	MnO	MgO	CaO	Cr_2O_3	NiO	TOTAL
Os-164_MI_Fig23_10	39.438	0.009	0.010	20.236	0.338	40.033	0.191	0.014	0.084	100.352
Os-164_MI_Fig28_1	39.655	0.017	0.017	19.849	0.328	40.171	0.254	0.016	0.084	100.392
Os-164_MI_Fig28_2	39.569	0.017	0.014	19.799	0.340	40.348	0.237	0.004	0.103	100.431
Os-164_MI_Fig28_3	39.340	0.012	0.017	19.954	0.326	40.204	0.229	0.009	0.089	100.179
Os-164_MI_Fig28_4	39.679	0.010	0.009	19.870	0.326	40.019	0.233	0.019	0.096	100.261
Os-164_MI_Fig28_5	39.211	0.012	0.014	19.918	0.345	40.013	0.230	0.017	0.086	99.846
Os-164_MI_Fig28_6	39.876	0.016	0.012	19.936	0.332	40.111	0.232	0.008	0.090	100.613
Os-164_MI_Fig28_7	39.573	0.016	0.014	20.005	0.323	40.078	0.223	0.023	0.087	100.342
Os-164_MI_Fig28_8	39.791	0.009	0.012	20.020	0.327	40.272	0.224	0.018	0.090	100.763
Os-164_MI_Fig28_9	39.359	0.018	0.010	20.165	0.334	39.989	0.220	0.015	0.095	100.204
Os-164_MI_Fig39_a	39.314	0.007	0.012	19.698	0.315	40.371	0.202	0.019	0.094	100.032
Os-164_MI_Fig39_b	39.538	0.008	0.013	19.788	0.322	40.604	0.197	0.036	0.109	100.616
Os-164_MI_Fig39_c	39.074	0.005	0.016	19.534	0.315	40.331	0.209	0.005	0.102	99.590
Os-164_MI_Fig47_1	39.398	0.001	0.011	19.905	0.334	40.432	0.213	0.011	0.074	100.378
Os-164_MI_Fig47_2	39.243	0.011	0.008	20.113	0.328	40.348	0.210	0.012	0.085	100.358
Os-164_MI_Fig47_3	39.276	0.010	0.010	20.097	0.331	40.426	0.208	0.016	0.092	100.467
Os-164_MI_Fig47_4	38.795	0.010	0.011	20.091	0.335	40.092	0.211	0.010	0.089	99.643
Os-164_MI_Fig47_5	38.743	0.015	0.041	19.735	0.317	39.717	0.408	0.015	0.085	99.076
Os-164_MI_Fig47_6	39.610	0.013	0.014	20.214	0.339	40.478	0.202	0.019	0.082	100.969
Os-164_1_Fig9_1	40.474	0.031	0.340	19.691	0.331	39.293	0.346	0.011	0.094	100.611
Os-164_1_Fig9_2	40.038	0.012	0.015	19.448	0.319	39.933	0.231	0.010	0.108	100.113
Os-164_1_Fig9_3	40.165	0.009	0.015	19.404	0.308	39.938	0.220	0.009	0.090	100.157
Os-164_1_Fig9_4	39.806	0.006	0.006	19.401	0.314	39.866	0.215	0.013	0.106	99.733
Os-164_1_Fig9_5	39.813	0.017	0.014	19.451	0.316	40.145	0.215	0.018	0.099	100.088
Os-164_1_Fig9_6	39.709	0.013	0.013	19.635	0.325	39.813	0.212	0.006	0.098	99.823

Table C1. (Continued)

SAMPLE	SiO_2	TiO_2	Al_2O_3	FeO	MnO	MgO	CaO	Cr_2O_3	NiO	TOTAL
Os-164_Fig11_c1	39.808	0.002	0.007	20.152	0.327	39.868	0.207	0.011	0.099	100.480
Os-164_Fig11_c2	39.930	0.013	0.012	19.954	0.323	39.949	0.199	0.023	0.087	100.488
Os-164_Fig11_c3	40.039	0.012	0.010	19.778	0.329	40.415	0.191	0.017	0.083	100.874
Os-164_Fig11_c4	40.027	0.011	0.014	19.870	0.332	40.536	0.200	0.020	0.086	101.096
Os-164_ol_Fig39_c1	39.708	0.000	0.014	19.797	0.312	40.630	0.191	0.021	0.101	100.774
Os-164_ol_Fig39_c2	39.933	0.008	0.011	19.820	0.310	40.832	0.200	0.021	0.106	101.242
Os-164_Fig47_1	39.371	0.008	0.010	20.197	0.336	40.309	0.199	0.020	0.087	100.537
Os-164_Fig47_2	39.402	0.007	0.011	20.490	0.322	40.270	0.202	0.016	0.091	100.813
Os-164_Fig48_1	39.401	0.008	0.010	19.846	0.327	39.951	0.214	0.006	0.087	99.849
Os-164_Fig48_2	39.854	0.007	0.015	19.849	0.319	40.308	0.205	0.018	0.100	100.675
Os-164_Fig12_1	39.320	0.010	0.015	20.062	0.335	40.337	0.192	0.027	0.084	100.384
Os-164_Fig12_2	38.926	0.015	0.016	20.016	0.325	39.828	0.190	0.051	0.082	99.449
Os-164_Fig3_1	38.554	0.014	0.010	19.950	0.332	40.149	0.191	0.056	0.092	99.349
Os-164_Fig3_2	39.347	0.008	0.013	19.831	0.320	40.229	0.192	0.043	0.094	100.077
Os-164_Fig36_1	38.940	0.009	0.017	24.160	0.419	36.645	0.169	0.009	0.064	100.432
Os-164_Fig36_2	38.639	0.016	0.021	24.276	0.401	36.640	0.168	0.009	0.080	100.250
Os-164_Fig40_1	38.810	0.014	0.011	24.531	0.406	37.025	0.181	0.016	0.051	101.043
Os-164_Fig40_2	38.451	0.010	0.017	24.491	0.409	36.824	0.179	0.008	0.052	100.440

Table C2. Compositions of plagioclase from the 1835 Osorno eruption (wt%).

SAMPLE	SiO_2	TiO_2	Al_2O_3	FeO	MgO	CaO	SrO	BaO	Na_2O	K_2O	TOTAL
Os-144A_fig1_pl_1	52.416	0.055	30.410	0.797	0.169	13.567	0.089	0.005	4.051	0.103	101.662
Os-144A_fig1_pl_2	52.310	0.052	31.120	0.736	0.177	13.926	0.079	0.000	3.677	0.077	102.143
Os-144A_fig1_pl_3	49.456	0.039	32.356	0.636	0.129	15.603	0.097	0.001	2.744	0.041	101.103
Os-144A_fig1_pl_4	47.682	0.031	32.372	0.613	0.127	15.333	0.096	0.009	2.579	0.048	98.889
Os-144A_fig1_pl_5	48.814	0.033	33.485	0.603	0.116	12.905	0.096	0.004	2.725	0.088	98.870
Os-144A_fig1_pl_6	52.014	0.039	31.328	0.606	0.143	14.079	0.070	0.003	3.660	0.077	102.018
Os-144A_fig1_pl_7	50.249	0.036	31.419	0.621	0.142	14.757	0.089	0.002	3.295	0.072	100.684
Os-144A_fig1_pl_8	49.624	0.034	32.276	0.634	0.139	15.501	0.101	0.008	2.929	0.052	101.297
Os-144A_fig1_pl_12	50.550	0.040	31.833	0.612	0.141	15.057	0.085	0.010	3.287	0.065	101.679
Os-144A_fig1_pl_13	49.582	0.034	32.170	0.623	0.127	15.599	0.092	0.008	2.981	0.066	101.281
Os-144A_fig1_pl_14	49.865	0.034	32.328	0.618	0.130	15.224	0.070	0.000	2.862	0.056	101.186
Os-144A_fig1_pl_15	50.920	0.033	32.231	0.612	0.132	15.028	0.076	0.006	3.101	0.072	102.210
Os-144A_fig1_pl_16	51.335	0.032	31.032	0.616	0.122	14.355	0.067	0.006	3.561	0.077	101.203
Os-144A_fig1_pl_17	50.771	0.029	31.100	0.599	0.135	14.357	0.086	0.009	3.407	0.076	100.569
Os-144A_fig1_pl_18	51.810	0.036	30.749	0.610	0.129	13.994	0.087	0.003	3.772	0.080	101.269
Os-144A_fig1_pl_19	51.160	0.036	31.185	0.611	0.132	14.761	0.089	0.007	3.498	0.063	101.542
Os-144A_fig1_pl_20	51.610	0.033	31.620	0.597	0.137	14.843	0.089	0.002	3.351	0.069	102.349
Os-144A_fig1_pl_21	49.950	0.035	32.059	0.600	0.129	15.095	0.088	0.008	3.064	0.059	101.087
Os-144A_fig1_pl_22	49.453	0.030	32.276	0.607	0.128	15.205	0.095	0.000	2.751	0.047	100.591
Os-144A_fig1_pl_23	49.671	0.030	32.193	0.599	0.123	15.313	0.084	0.002	2.848	0.063	100.926
Os-144A_fig1_pl_24	49.986	0.037	31.633	0.609	0.129	14.929	0.083	0.000	3.122	0.062	100.590
Os-144A_fig1_pl_25	50.228	0.036	31.602	0.611	0.129	14.872	0.076	0.009	3.227	0.068	100.859
Os-144A_fig1_pl_26	50.448	0.034	31.078	0.616	0.131	14.218	0.070	0.001	3.434	0.072	100.101

Table C2. (Continued)

SAMPLE	SiO_2	TiO_2	Al_2O_3	FeO	MgO	CaO	SrO	BaO	Na_2O	K_2O	TOTAL
Os-144A_fig5_pl_1	51.990	0.060	30.039	0.767	0.171	13.666	0.080	0.010	4.009	0.084	100.877
Os-144A_fig5_pl_2	51.878	0.052	30.078	0.705	0.171	13.615	0.072	0.007	3.800	0.071	100.450
Os-144A_fig5_pl_3	50.758	0.051	31.241	0.715	0.163	14.401	0.085	0.002	3.409	0.070	100.895
Os-144A_fig5_pl_4	50.648	0.033	31.587	0.628	0.141	14.745	0.065	0.016	3.302	0.065	101.230
Os-144A_fig5_pl_5	51.052	0.042	30.218	0.603	0.138	13.723	0.076	0.012	3.566	0.077	99.506
Os-144A_fig5_pl_6	51.813	0.036	30.127	0.615	0.135	12.387	0.074	0.009	3.516	0.075	98.788
Os-144A_fig5_pl_7	50.677	0.043	31.218	0.609	0.146	14.310	0.074	0.003	3.330	0.068	100.478
Os-144A_fig5_pl_8	50.579	0.033	31.431	0.580	0.139	14.299	0.085	0.006	3.321	0.061	100.533
Os-144A_fig5_pl_9	46.351	0.024	33.931	0.555	0.108	17.274	0.070	0.000	1.775	0.021	100.109
Os-144A_fig5_pl_10	45.327	0.012	34.659	0.517	0.082	18.032	0.072	0.000	1.290	0.021	100.008
Os-144A_fig5_pl_11	45.376	0.010	35.154	0.494	0.071	18.453	0.081	0.004	1.318	0.017	100.978
Os-144A_fig5_pl_12	45.383	0.014	34.699	0.499	0.071	18.600	0.070	0.004	1.191	0.017	100.549
Os-144A_fig5_pl_13	45.368	0.010	34.962	0.466	0.067	18.278	0.071	0.002	1.234	0.016	100.475
Os-144A_fig5_pl_14	45.412	0.014	34.682	0.449	0.065	18.226	0.063	0.000	1.298	0.016	100.223
Os-144A_fig5_pl_15	45.346	0.008	34.418	0.461	0.070	18.069	0.075	0.006	1.330	0.020	99.803
Os-144A_fig5_pl_16	45.666	0.019	34.471	0.458	0.072	17.589	0.088	0.008	1.524	0.025	99.922
Os-144A_fig5_pl_17	46.183	0.016	34.722	0.469	0.079	17.694	0.081	0.000	1.541	0.025	100.809
Os-144A_fig5_pl_18	45.532	0.009	34.852	0.474	0.080	18.075	0.090	0.003	1.448	0.032	100.595
Os-144A_fig5_pl_19	45.343	0.017	34.689	0.471	0.074	17.981	0.112	0.004	1.452	0.019	100.161
Os-144A_fig5_pl_20	45.124	0.011	34.716	0.469	0.075	18.024	0.107	0.012	1.337	0.029	99.903
Os-144A_fig5_pl_21	45.113	0.012	34.295	0.470	0.074	18.103	0.083	0.011	1.348	0.027	99.536
Os-144A_fig5_pl_22	45.309	0.012	34.532	0.471	0.071	17.873	0.080	0.001	1.397	0.028	99.775
Os-144A_fig5_pl_23	45.212	0.011	34.480	0.469	0.073	18.096	0.057	0.000	1.312	0.017	99.726
Os-144A_fig5_pl_24	45.307	0.011	34.575	0.479	0.067	17.825	0.062	0.010	1.343	0.016	99.696
Os-144A_fig5_pl_25	45.093	0.018	34.548	0.487	0.077	18.032	0.088	0.011	1.369	0.030	99.753
Os-144A_fig5_pl_26	44.644	0.015	34.268	0.490	0.072	17.978	0.069	0.000	1.384	0.025	98.944
Os-144A_fig5_pl_27	46.373	0.032	33.360	0.648	0.131	17.132	0.075	0.000	1.682	0.049	99.481

Table C2. (Continued)

SAMPLE	SiO_2	TiO_2	Al_2O_3	FeO	MgO	CaO	SrO	BaO	Na_2O	K_2O	TOTAL
Os-144A_fig17_pl_1	52.662	0.079	28.392	0.941	0.191	12.879	0.087	0.010	4.239	0.110	99.589
Os-144A_fig17_pl_2	51.799	0.061	29.527	0.810	0.178	13.128	0.073	0.009	4.024	0.084	99.693
Os-144A_fig17_pl_3	51.173	0.052	29.918	0.759	0.166	13.526	0.081	0.000	3.831	0.088	99.593
Os-144A_fig17_pl_4	51.689	0.055	29.793	0.766	0.164	13.260	0.085	0.006	4.000	0.093	99.910
Os-144A_fig17_pl_5	51.317	0.046	30.231	0.704	0.173	13.466	0.086	0.004	3.787	0.083	99.895
Os-144A_fig17_pl_6	48.873	0.039	32.462	0.668	0.148	15.577	0.085	0.007	2.602	0.056	100.517
Os-144A_fig17_pl_7	48.284	0.041	32.234	0.672	0.142	15.894	0.099	0.006	2.624	0.053	100.049
Os-144A_fig17_pl_8	48.968	0.027	32.347	0.622	0.126	15.391	0.093	0.000	2.735	0.056	100.361
Os-144A_fig17_pl_9	48.775	0.035	32.859	0.618	0.123	16.118	0.086	0.008	2.422	0.041	101.085
Os-144A_fig17_pl_10	47.608	0.024	33.533	0.611	0.109	16.808	0.092	0.004	2.079	0.034	100.904
Os-144A_fig17_pl_14	46.917	0.031	32.939	0.687	0.147	17.068	0.089	0.004	2.040	0.022	99.944
Os-144A_fig17_pl_15	48.197	0.060	32.815	0.858	0.239	16.667	0.086	0.002	2.189	0.042	101.154
Os-144A_fig17_pl_16	46.740	0.029	33.033	0.652	0.117	16.681	0.084	0.003	2.043	0.051	99.433
Os-144A_fig17_pl_17	48.074	0.047	32.721	0.756	0.144	16.211	0.092	0.005	2.249	0.058	100.358
Os-144A_fig17_pl_18	47.555	0.027	33.012	0.653	0.122	16.358	0.090	0.010	2.293	0.038	100.159
Os-144A_fig17_pl_19	47.679	0.023	32.895	0.623	0.115	16.331	0.102	0.009	2.403	0.039	100.218
Os-144A_fig17_pl_20	49.481	0.027	32.651	0.616	0.118	15.345	0.081	0.005	2.858	0.054	101.236
Os-144A_fig17_pl_23	48.978	0.056	32.422	0.810	0.229	15.605	0.091	0.009	2.869	0.055	101.124
Os-144A_fig17_pl_24	48.282	0.034	32.131	0.606	0.124	15.200	0.089	0.000	2.871	0.044	99.375
Os-144A_fig17_pl_25	49.366	0.029	31.230	0.597	0.121	14.880	0.068	0.003	3.030	0.077	99.401
Os-144A_fig17_pl_26	49.565	0.036	31.769	0.623	0.144	14.950	0.081	0.009	3.042	0.070	100.287
Os-144A_fig17_pl_27	51.261	0.029	30.271	0.596	0.124	13.732	0.077	0.001	3.792	0.075	99.958
Os-144A_fig17_pl_28	51.917	0.044	30.706	0.585	0.144	13.554	0.087	0.006	3.838	0.082	100.964
Os-144A_fig17_pl_29	51.079	0.038	30.447	0.567	0.146	13.922	0.080	0.006	3.787	0.067	100.139
Os-144A_fig17_pl_39	54.358	0.054	28.473	0.989	0.166	11.508	0.049	0.008	3.945	0.204	99.753
Os-144A_fig17_pl_40	55.337	0.084	28.228	0.868	0.161	10.014	0.044	0.006	4.904	0.264	99.911

Table C2. (Continued)

SAMPLE	SiO_2	TiO_2	Al_2O_3	FeO	MgO	CaO	SrO	BaO	Na_2O	K_2O	TOTAL
Os-154A_fig12_pl_1	51.742	0.053	29.461	0.764	0.155	13.074	0.075	0.003	4.011	0.106	99.444
Os-154A_fig12_pl_2	51.338	0.050	30.896	0.772	0.161	14.512	0.094	0.000	2.397	0.066	100.276
Os-154A_fig12_pl_3	51.746	0.050	31.428	0.754	0.161	14.528	0.077	0.000	2.169	0.061	100.970
Os-154A_fig12_pl_4	50.344	0.031	31.033	0.653	0.130	14.470	0.080	0.002	3.405	0.058	100.205
Os-154A_fig12_pl_5	48.085	0.037	32.556	0.652	0.139	15.720	0.077	0.001	2.354	0.045	99.666
Os-154A_fig12_pl_6	49.803	0.034	32.733	0.651	0.144	15.824	0.069	0.000	1.106	0.050	100.410
Os-154A_fig12_pl_7	50.405	0.037	32.578	0.642	0.142	15.279	0.086	0.000	1.576	0.065	100.808
Os-154A_fig12_pl_8	49.617	0.035	31.745	0.646	0.140	14.725	0.082	0.009	2.390	0.060	99.448
Os-154A_fig12_pl_9	51.511	0.038	32.598	0.643	0.145	15.336	0.067	0.011	1.061	0.059	101.469
Os-154A_fig12_pl_10	49.903	0.040	31.883	0.632	0.144	15.292	0.083	0.002	1.646	0.067	99.692
Os-154A_fig12_pl_11	50.779	0.042	32.022	0.633	0.149	14.690	0.096	0.007	2.304	0.075	100.798
Os-154A_fig12_pl_12	51.018	0.039	31.136	0.614	0.139	14.476	0.076	0.006	1.863	0.065	99.432
Os-154A_fig12_pl_13	51.367	0.039	31.035	0.627	0.146	14.331	0.069	0.000	2.623	0.072	100.305
Os-154A_fig12_pl_14	50.644	0.042	31.098	0.605	0.137	14.532	0.085	0.000	2.251	0.065	99.458
Os-154A_fig12_pl_15	50.286	0.034	30.881	0.605	0.147	14.371	0.087	0.005	3.400	0.073	99.889
Os-154A_fig12_pl_16	50.760	0.036	31.221	0.600	0.131	14.620	0.071	0.004	3.520	0.069	101.032
Os-154A_fig12_pl_17	51.343	0.035	31.824	0.608	0.137	14.796	0.086	0.000	2.491	0.057	101.377
Os-154A_fig12_pl_18	50.484	0.029	32.473	0.591	0.124	15.600	0.097	0.000	1.728	0.048	101.171
Os-154A_fig12_pl_19	48.504	0.030	32.427	0.588	0.119	15.543	0.078	0.008	2.654	0.055	100.005
Os-154A_fig12_pl_20	49.534	0.028	32.288	0.579	0.123	15.271	0.072	0.000	2.463	0.059	100.413
Os-154A_fig12_pl_21	48.847	0.029	32.956	0.567	0.111	16.215	0.086	0.004	1.919	0.044	100.776
Os-154A_fig12_pl_22	47.998	0.027	33.010	0.558	0.101	16.355	0.078	0.004	2.315	0.035	100.481
Os-154A_fig12_pl_23	48.904	0.026	33.867	0.553	0.104	16.744	0.064	0.005	2.092	0.039	102.398
Os-154A_fig12_pl_24	48.210	0.021	33.967	0.543	0.086	16.921	0.087	0.004	1.892	0.037	101.769
Os-154A_fig12_pl_25	46.724	0.020	34.094	0.539	0.083	17.168	0.087	0.004	1.866	0.030	100.613
Os-154A_fig12_pl_26	47.327	0.020	34.858	0.531	0.089	17.496	0.110	0.000	1.394	0.031	101.852

Table C2. (Continued)

SAMPLE	SiO_2	TiO_2	Al_2O_3	FeO	MgO	CaO	SrO	BaO	Na_2O	K_2O	TOTAL
Os-164A_fig8a_pl_1	51.870	0.050	29.720	0.757	0.167	13.355	0.102	0.007	3.800	0.087	99.916
Os-164A_fig8a_pl_2	49.959	0.022	31.097	0.575	0.102	14.825	0.076	0.004	3.477	0.064	100.202
Os-164A_fig8a_pl_3	46.818	0.026	33.728	0.574	0.114	17.433	0.090	0.005	1.749	0.028	100.566
Os-164A_fig8a_pl_4	47.614	0.027	33.652	0.573	0.115	17.062	0.073	0.001	1.764	0.032	100.911
Os-164A_fig8a_pl_5	47.338	0.024	33.085	0.573	0.115	16.499	0.110	0.001	1.932	0.038	99.714
Os-164A_fig8a_pl_6	46.465	0.026	33.542	0.556	0.105	17.138	0.103	0.004	1.803	0.029	99.771
Os-164A_fig8a_pl_7	46.502	0.022	34.052	0.555	0.106	17.630	0.086	0.006	1.754	0.021	100.735
Os-164A_fig8a_pl_8	46.784	0.025	33.857	0.560	0.108	17.337	0.074	0.004	1.712	0.023	100.484
Os-164A_fig8a_pl_9	46.902	0.028	33.775	0.566	0.116	17.491	0.084	-0.004	1.660	0.027	100.644
Os-164A_fig8a_pl_10	46.931	0.028	33.635	0.558	0.112	17.200	0.081	0.008	1.927	0.030	100.510
Os-164A_fig8a_pl_11	46.952	0.022	33.586	0.559	0.106	17.427	0.088	0.000	1.880	0.034	100.654
Os-164A_fig8a_pl_12	46.691	0.023	33.590	0.554	0.109	17.702	0.078	0.004	1.917	0.026	100.695
Os-164A_fig8a_pl_13	47.136	0.023	33.723	0.555	0.112	17.097	0.100	0.009	1.928	0.027	100.710
Os-164A_fig8a_pl_14	47.252	0.025	33.372	0.548	0.113	17.534	0.083	0.007	1.984	0.030	100.946
Os-164A_Fig12_pl_1	52.277	0.064	29.870	0.847	0.192	13.782	0.080	0.000	3.826	0.078	101.015
Os-164A_Fig12_pl_2	50.628	0.042	31.146	0.720	0.163	14.585	0.069	0.000	3.372	0.066	100.787
Os-164A_Fig12_pl_3	49.681	0.043	31.088	0.696	0.160	14.643	0.091	0.006	3.162	0.043	99.614
Os-164A_Fig12_pl_4	49.802	0.046	30.752	0.686	0.167	14.752	0.079	0.004	3.170	0.047	99.505
Os-164A_Fig12_pl_5	46.849	0.030	33.270	0.583	0.113	16.673	0.072	0.007	1.979	0.034	99.610
Os-164A_Fig12_pl_6	46.907	0.021	33.503	0.566	0.102	17.051	0.055	0.004	1.949	0.026	100.183
Os-164A_Fig12_pl_7	47.794	0.019	33.432	0.565	0.112	16.938	0.071	0.004	1.960	0.036	100.930
Os-164A_Fig12_pl_8	47.431	0.024	33.224	0.554	0.111	16.741	0.081	0.008	1.952	0.025	100.151
Os-164A_Fig12_pl_9	47.034	0.022	33.777	0.557	0.106	17.072	0.096	0.000	1.918	0.040	100.614
Os-164A_Fig12_pl_10	47.221	0.018	33.697	0.561	0.111	17.424	0.084	0.000	1.872	0.019	100.999
Os-164A_Fig12_pl_11	46.953	0.023	33.366	0.558	0.118	17.351	0.090	0.007	1.982	0.028	100.475
Os-164A_Fig12_pl_12	48.420	0.020	33.369	0.554	0.125	16.734	0.067	0.001	2.111	0.021	101.423
Os-164A_Fig12_pl_13	48.314	0.024	33.299	0.562	0.120	16.830	0.077	0.000	2.175	0.039	101.438
Os-164A_Fig12_pl_14	47.505	0.027	32.962	0.561	0.122	16.276	0.074	0.015	2.278	0.038	99.860
Os-164A_Fig12_pl_15	48.191	0.022	33.350	0.557	0.117	16.893	0.082	0.004	2.085	0.036	101.338
Os-164A_Fig12_pl_16	48.247	0.025	33.507	0.554	0.119	16.864	0.064	0.000	2.082	0.025	101.482
Os-164A_Fig12_pl_17	47.259	0.022	33.592	0.561	0.112	16.986	0.083	0.004	2.088	0.034	100.741
Os-164A_Fig12_pl_18	47.066	0.018	33.677	0.545	0.106	17.290	0.075	0.004	1.908	0.028	100.716

Table C2. (Continued)

SAMPLE	SiO_2	TiO_2	Al_2O_3	FeO	MgO	CaO	SrO	BaO	Na_2O	K_2O	TOTAL
Os-164A_fig13_pl_1	53.142	0.209	27.361	1.671	0.416	11.589	0.078	0.009	4.640	0.172	99.286
Os-164A_fig13_pl_2	50.722	0.046	30.827	0.682	0.162	13.884	0.064	0.002	3.522	0.069	99.980
Os-164A_fig13_pl_3	48.713	0.034	32.921	0.589	0.129	15.781	0.095	0.001	2.348	0.046	100.658
Os-164A_fig13_pl_4	46.112	0.023	34.392	0.567	0.100	17.266	0.079	0.006	1.615	0.027	100.189
Os-164A_fig13_pl_5	45.913	0.022	34.058	0.572	0.097	17.631	0.091	0.002	1.630	0.022	100.037
Os-164A_fig13_pl_6	47.340	0.020	34.431	0.567	0.103	17.356	0.086	-0.004	1.766	0.032	101.697
Os-164A_fig13_pl_7	46.795	0.016	34.034	0.572	0.108	17.039	0.089	-0.005	1.921	0.033	100.602
Os-164A_fig13_pl_8	46.748	0.021	32.996	0.565	0.115	16.547	0.061	-0.004	2.095	0.027	99.171
Os-164A_fig13_pl_9	47.545	0.034	33.055	0.623	0.154	16.191	0.101	0.006	2.238	0.029	99.975
Os-164A_fig13_pl_10	48.846	0.024	33.031	0.573	0.131	16.219	0.086	0.001	2.515	0.046	101.472
Os-164A_fig13_pl_11	48.206	0.024	33.190	0.579	0.129	16.081	0.096	0.000	2.436	0.036	100.777
Os-164A_fig13_pl_12	47.611	0.039	32.688	0.699	0.236	16.541	0.084	0.004	2.256	0.034	100.192
Os-164A_fig13_pl_13	47.793	0.169	32.871	1.911	1.005	15.879	0.066	0.005	2.361	0.075	102.134
Os-164A_fig13_pl_14	47.207	0.021	33.868	0.561	0.115	16.899	0.068	0.005	2.061	0.030	100.834
Os-164A_fig13_pl_15	48.162	0.179	32.225	1.444	0.421	15.586	0.075	0.000	2.338	0.069	100.500
Os-144A_fig5_pl_microl_1	51.654	0.070	29.301	0.888	0.178	12.845	0.078	0.010	4.164	0.105	99.293
Os-144A_fig5_pl_microl_2	52.684	0.063	29.667	0.896	0.161	12.772	0.090	0.005	4.334	0.114	100.786
Os-144A_fig5_pl_microl_3	53.006	0.065	29.319	0.836	0.140	12.652	0.087	0.012	4.389	0.108	100.614
Os-144A_fig5_pl_microl_4	51.648	0.060	29.421	0.826	0.181	13.058	0.092	0.007	4.171	0.079	99.544
Os-164A_Fig12_pl_microl_2	50.959	0.047	31.122	0.735	0.161	14.511	0.089	0.012	3.532	0.070	101.237
Os-164A_Fig12_pl_microl_3	51.606	0.066	29.792	0.883	0.200	13.190	0.097	0.013	3.936	0.068	99.851

Table C3. Compositions of clinopyroxene from the 1835 Osorno eruption (wt%).

SAMPLE	SiO_2	TiO_2	Al_2O_3	FeO	MnO	MgO	CaO	Na_2O	K_2O	Cr_2O_3	NiO	TOTAL
Oso-144_Fig2_cx7_1	50.576	0.714	2.924	9.400	0.263	15.797	19.478	0.314	0.000	0.586	0.007	100.058
Oso-144_Fig2_cx7_2	52.732	0.413	1.440	10.425	0.339	18.109	16.745	0.228	0.000	0.326	0.005	100.761
Oso-144_Fig2_cx7_3	51.307	0.638	2.532	10.145	0.287	16.329	18.726	0.304	0.000	0.288	0.006	100.561
Oso-144_Fig4_cx3_1a	48.596	1.311	4.325	12.287	0.327	14.686	17.642	0.321	0.000	0.278	0.000	99.774
Oso-144_Fig4_cx3_2a	50.385	0.792	3.220	10.533	0.299	16.262	18.039	0.325	0.000	0.490	0.002	100.347
Oso-144_Fig4_cx3_3a	50.102	0.860	3.423	11.078	0.313	16.195	17.455	0.291	0.000	0.384	0.000	100.101
Oso-144_Fig8_cx2_1	50.276	0.860	3.345	10.946	0.282	15.170	19.252	0.347	0.000	0.170	0.004	100.651
Oso-144_Fig8_cx2_2	50.703	0.775	3.080	10.582	0.300	16.223	17.865	0.320	0.000	0.485	0.006	100.339
Oso-144_Fig8_cx2_3	50.752	0.738	3.053	9.159	0.245	15.773	19.716	0.316	0.000	0.707	0.009	100.469
Oso-144_Fig13_cx1_1	50.772	0.743	2.994	9.101	0.237	15.278	20.211	0.316	0.000	0.558	0.008	100.218
Oso-144_Fig13_cx1_2	50.435	0.867	3.224	10.476	0.268	14.872	19.717	0.331	0.000	0.151	0.007	100.348
Oso-144_Fig13_cx1_3	51.105	0.783	2.857	9.971	0.268	15.446	19.601	0.307	0.000	0.327	0.000	100.666
Oso-144_Fig15_cx12_1	52.082	0.419	2.724	8.035	0.226	17.025	19.578	0.318	0.000	0.546	0.013	100.964
Oso-144_Fig15_cx12_2	51.756	0.482	2.890	8.227	0.220	16.712	19.684	0.341	0.000	0.551	0.009	100.873
Oso-144_Fig15_cx12_3	51.830	0.450	2.720	8.119	0.220	16.839	19.667	0.329	0.000	0.527	0.006	100.708
Oso-144_Fig16_cx3_1	51.043	0.736	2.776	9.922	0.279	16.131	18.619	0.304	0.000	0.698	0.001	100.508
Oso-144_Fig16_cx3_2	49.584	1.187	2.991	12.956	0.360	14.520	18.276	0.319	0.000	0.029	0.000	100.222
Oso-144_Fig16_cx3_3	52.593	0.403	1.440	10.856	0.344	18.160	16.250	0.203	0.000	0.298	0.003	100.549

Table C4. Compositions of spinel from the 1835 Osorno eruption (wt%).

SAMPLE	SiO_2	TiO_2	Al_2O_3	FeO	MnO	MgO	CaO	Na_2O	K_2O	Cr_2O_3	NiO	TOTAL	SAMPLE
Os-164_1_fig11_2	0.078	3.428	14.810	45.771	0.352	8.121	0.018	23.419	0.098	0.749	0.037	0.102	96.312
Os-164_MI_fig26_a	0.103	2.613	16.319	43.561	0.327	8.655	0.027	25.049	0.070	0.689	0.074	0.097	96.869
Os-164_MI_fig26_b	0.112	2.621	16.399	43.745	0.341	8.567	0.026	25.003	0.097	0.697	0.067	0.091	97.059
Os-164_MI_fig39_1	0.150	2.043	19.198	41.279	0.319	9.256	0.020	23.567	0.108	0.624	0.081	0.097	95.976
Os-164_MI_fig39_2	0.134	1.621	19.553	40.230	0.331	9.338	0.035	25.451	0.107	0.624	0.063	0.068	96.783
Os-164_MI_fig48_a	0.092	3.210	15.758	44.894	0.352	8.533	0.025	23.524	0.100	0.813	0.083	0.090	96.771
Os-164_MI_fig48_b	0.106	3.340	15.683	44.910	0.344	8.507	0.018	23.460	0.085	0.778	0.055	0.099	96.682
Os-164_MI_fig47	0.174	3.620	14.488	46.791	0.328	8.060	0.010	22.656	0.089	0.775	0.077	0.087	96.489
Os-164_MI_fig37	0.093	3.108	16.611	43.090	0.326	8.692	0.017	23.884	0.111	0.733	0.075	0.102	96.125
Os-164_ol_fig3_a	0.087	2.324	16.383	42.462	0.335	8.571	0.067	25.766	0.077	0.633	0.107	0.086	96.190
Os-164_ol_fig3_b	0.083	2.455	16.372	42.330	0.342	8.431	0.042	25.706	0.082	0.619	0.085	0.079	95.931
Os-164_ol_fig12_1	0.074	2.813	16.285	45.455	0.352	7.849	0.015	23.089	0.087	0.712	0.050	0.083	96.217
Os-164_ol_fig12_2	0.052	2.747	16.439	44.767	0.344	8.414	0.017	22.900	0.086	0.707	0.065	0.101	95.944
Os-164_ol_fig36	0.103	2.626	12.093	55.606	0.355	6.050	0.009	18.912	0.076	0.801	0.101	0.115	96.846
Os-164_2_fig12	0.097	2.972	15.163	46.059	0.338	8.361	0.016	22.383	0.088	0.736	0.060	0.106	95.688

Table C5. Compositions of iddingsite from the 1835 Osorno eruption (wt%).

SAMPLE	FeO	SiO_2	MgO	NiO	CaO	Cr_2O_3	MnO	TiO_2	Al_2O_3	TOTAL
Os-164_idd_1	28.682	40.155	26.432	0.111	0.803	0.011	0.354	0.158	0.790	97.495
Os-164_idd_2	28.286	39.046	25.457	0.104	0.851	0.040	0.381	0.256	1.769	96.190
Os-164_idd_3	27.960	40.120	27.394	0.090	0.535	0.050	0.409	0.237	1.018	97.813
Os-164_idd_4	34.406	36.275	25.878	0.121	0.509	0.035	0.415	0.062	0.384	98.085
Os-164_idd_5	28.993	40.660	27.209	0.114	0.293	0.031	0.387	0.054	0.288	98.029

Table C6. Compositions of titanomagnetite from the 1835 Osorno eruption (wt%).

SAMPLE	SiO_2	TiO_2	Al_2O_3	FeO	MnO	MgO	CaO	CoO	V_2O_3	Cr_2O_3	NiO	ZnO	TOTAL
Os-164_Fig23a_1_7	0.081	17.301	3.377	72.494	0.422	1.968	0.035	0.135	0.829	0.129	0.000	0.085	96.855
Os-164_Fig23a_1_8	0.062	10.483	4.019	76.902	0.365	1.329	0.034	0.136	1.036	0.143	0.000	0.059	94.569
Os-164_Fig23a_1_9	0.072	10.450	3.985	77.204	0.384	1.327	0.030	0.150	1.086	0.152	0.001	0.019	94.862
Os-164_Fig23a_1_10	0.076	10.631	3.991	77.383	0.365	1.336	0.043	0.149	1.060	0.147	0.000	0.020	95.202
Os-164_Fig23a_1_11	0.062	10.856	3.938	76.904	0.360	1.347	0.031	0.132	0.981	0.117	0.000	0.024	94.752
Os-164_Fig23a_1_12	0.063	10.533	3.914	76.610	0.381	1.332	0.034	0.124	1.054	0.126	0.000	0.063	94.234
Os-164_Fig23a_1_13	0.063	10.135	3.953	77.255	0.390	1.389	0.034	0.151	1.041	0.091	0.000	0.057	94.560
Os-164_Fig23a_1_14	0.071	10.240	3.849	77.089	0.360	1.345	0.033	0.136	1.021	0.097	0.000	0.058	94.298
Os-164_Fig23a_2_7	0.077	16.845	3.449	71.157	0.440	1.806	0.042	0.129	0.945	0.221	0.000	0.000	95.110
Os-164_Fig23a_2_8	0.069	10.239	4.150	77.136	0.371	1.320	0.031	0.152	1.085	0.168	0.000	0.000	94.721
Os-164_Fig23a_2_9	0.080	10.457	4.047	77.332	0.356	1.315	0.033	0.158	1.073	0.153	0.000	0.000	95.004
Os-164_Fig23a_2_10	0.091	10.391	4.069	77.329	0.377	1.302	0.027	0.154	1.096	0.145	0.000	0.000	94.981
Os-164_Fig23a_2_11	0.081	10.097	4.021	77.337	0.375	1.332	0.039	0.140	1.060	0.091	0.000	0.000	94.573
Os-164_Fig23a_3_5	0.710	9.802	4.292	77.129	0.387	1.642	0.080	0.142	1.083	0.130	0.000	0.041	95.438
Os-164_Fig23c_1_4	0.077	12.095	3.872	75.756	0.379	1.485	0.030	0.153	1.107	0.153	0.013	0.022	95.142
Os-164_Fig23c_1_5	0.086	9.986	3.896	77.733	0.383	1.357	0.028	0.169	1.153	0.146	0.000	0.021	94.959
Os-164_Fig23c_1_6	0.075	10.003	3.877	77.581	0.370	1.324	0.033	0.166	1.128	0.123	0.000	0.008	94.688
Os-164_Fig23c_1_7	0.087	9.860	3.899	78.097	0.370	1.347	0.032	0.150	1.091	0.116	0.002	0.013	95.065
Os-164_Fig23c_1_8	1.199	9.736	3.852	77.276	0.365	1.875	0.055	0.178	1.077	0.105	0.000	0.042	95.759
Oso-164_Fig23b_6_4	0.966	5.135	4.855	79.288	0.412	1.433	0.075	0.181	1.342	0.218	0.000	0.033	93.938
Oso-164_Fig23b_6_5	0.061	5.009	4.763	80.275	0.367	1.054	0.055	0.177	1.316	0.211	0.000	0.026	93.314
Oso-164_Fig23b_6_6	0.079	5.023	4.842	80.044	0.369	1.092	0.056	0.162	1.337	0.222	0.023	0.012	93.260
Os-164_Fig23b_2_11	0.051	13.598	3.744	75.552	0.389	1.332	0.020	0.164	1.197	0.172	0.000	0.070	96.288
Os-164_Fig23b_2_12	0.054	13.644	3.745	74.644	0.397	1.303	0.014	0.156	1.202	0.179	0.017	0.000	95.354
Os-164_Fig23b_2_13	0.050	13.144	3.740	75.196	0.385	1.361	0.015	0.172	1.194	0.166	0.002	0.064	95.488
Os-164_Fig23b_2_14	0.126	13.412	3.680	75.496	0.375	1.338	0.040	0.168	1.186	0.169	0.008	0.004	96.003
Os-164_Fig23b_2_15	0.108	13.278	3.671	75.397	0.367	1.327	0.029	0.158	1.220	0.167	0.000	0.088	95.810
Os-164_Fig23b_2_16	0.046	13.586	3.656	75.358	0.362	1.348	0.020	0.156	1.230	0.150	0.009	0.083	96.003

Table C7. Compositions of ilmenite from the 1835 Osorno eruption (wt%).

SAMPLE	SiO_2	TiO_2	Al_2O_3	FeO	MnO	MgO	CaO	CoO	V_2O_3	Cr_2O_3	NiO	ZnO	TOTAL
Os-164_Fig23a_1_1	0.234	48.473	0.166	45.341	0.583	3.226	0.072	0.111	0.211	0.022	0.021	0.000	98.462
Os-164_Fig23a_1_2	0.128	49.115	0.137	45.510	0.550	3.185	0.067	0.070	0.196	0.024	0.000	0.000	98.982
Os-164_Fig23a_1_3	0.170	48.827	0.187	45.478	0.578	3.139	0.074	0.080	0.201	0.032	0.000	0.000	98.766
Os-164_Fig23a_1_4	0.241	48.312	0.183	45.482	0.563	3.231	0.057	0.090	0.185	0.017	0.005	0.000	98.364
Os-164_Fig23a_1_5	0.154	48.622	0.181	45.423	0.569	3.165	0.061	0.085	0.154	0.025	0.000	0.000	98.441
Os-164_Fig23a_1_6	0.074	48.741	0.210	45.320	0.607	3.280	0.065	0.107	0.158	0.043	0.000	0.000	98.604
Os-164_Fig23a_2_1	37.395	17.462	4.805	26.760	0.465	8.800	2.571	0.069	0.112	0.000	0.000	0.000	98.439
Os-164_Fig23a_2_2	0.216	49.434	0.171	45.104	0.573	3.259	0.086	0.120	0.154	0.043	0.000	0.000	99.160
Os-164_Fig23a_2_3	0.158	47.926	0.145	45.097	0.560	3.150	0.072	0.097	0.171	0.037	0.000	0.000	97.412
Os-164_Fig23a_2_4	0.116	50.102	0.156	45.815	0.574	3.014	0.063	0.112	0.196	0.007	0.000	0.000	100.155
Os-164_Fig23a_2_5	0.059	50.119	0.160	45.645	0.589	2.943	0.064	0.099	0.186	0.005	0.000	0.000	99.870
Os-164_Fig23a_2_6	0.046	50.209	0.189	45.520	0.616	2.972	0.060	0.082	0.138	0.000	0.000	0.000	99.834
Os-164_Fig23a_3_1	0.039	49.187	0.154	45.168	0.575	3.338	0.083	0.087	0.178	0.021	0.028	0.000	98.858
Os-164_Fig23a_3_2	0.041	48.604	0.165	45.499	0.552	3.394	0.077	0.100	0.158	0.040	0.000	0.000	98.628
Os-164_Fig23a_3_3	0.034	49.463	0.189	45.218	0.576	3.282	0.074	0.091	0.145	0.026	0.000	0.000	99.097

Table C7. (Continued)

SAMPLE	SiO_2	TiO_2	Al_2O_3	FeO	MnO	MgO	CaO	CoO	V_2O_3	Cr_2O_3	NiO	ZnO	TOTAL
Os-164_Fig23c_1_1	0.039	48.498	0.150	45.515	0.585	3.530	0.058	0.099	0.217	0.000	0.000	0.004	98.695
Os-164_Fig23c_1_2	0.057	47.961	0.142	45.519	0.597	3.423	0.041	0.084	0.217	0.031	0.000	0.000	98.072
Os-164_Fig23c_1_3	0.075	42.738	0.610	49.283	0.549	3.061	0.052	0.108	0.297	0.071	0.000	0.000	96.844
Oso-164_Fig23b_6_1	0.057	44.195	0.269	48.319	0.582	2.853	0.117	0.098	0.325	0.016	0.000	0.031	96.861
Oso-164_Fig23b_6_2	0.044	44.547	0.317	47.982	0.575	3.031	0.093	0.106	0.322	0.028	0.009	0.028	97.083
Os-164_Fig23b_2_1	0.039	49.996	0.188	45.105	0.564	3.023	0.046	0.081	0.167	0.024	0.000	0.000	99.231
Os-164_Fig23b_2_2	0.041	47.846	0.251	45.723	0.571	2.834	0.037	0.101	0.196	0.018	0.000	0.000	97.619
Os-164_Fig23b_2_3	0.046	48.333	0.257	45.916	0.566	2.771	0.031	0.094	0.191	0.027	0.000	0.022	98.254
Os-164_Fig23b_2_4	0.034	48.338	0.235	45.710	0.551	2.729	0.037	0.087	0.189	0.032	0.000	0.000	97.944
Os-164_Fig23b_2_5	0.058	48.660	0.232	45.868	0.546	2.708	0.042	0.078	0.147	0.021	0.000	0.000	98.359
Os-164_Fig23b_2_6	0.047	48.699	0.241	45.619	0.517	2.714	0.038	0.080	0.211	0.027	0.000	0.000	98.194
Os-164_Fig23b_2_7	0.035	49.814	0.187	45.526	0.572	2.729	0.044	0.074	0.154	0.000	0.000	0.000	99.136
Os-164_Fig23b_2_8	0.420	49.927	0.211	45.172	0.577	2.972	0.053	0.116	0.172	0.057	0.000	0.011	99.689
Os-164_Fig23b_2_9	0.133	49.901	0.168	45.037	0.564	2.889	0.060	0.086	0.134	0.001	0.000	0.000	98.974
Os-164_Fig23b_2_10	0.046	48.844	0.161	45.117	0.582	2.924	0.059	0.109	0.170	0.007	0.002	0.007	98.029

C.7. References

Grove, TL, Donnelly-Nolan, JM, Housh, T (1997) Magmatic processes that generated the rhyolite of Glass Mountain, Medicine Lake volcano, N. California. Contrib Mineral Petrol 127(3): 205-223.

Kamenetsky, VS, Crawford, AJ, Meffre, S (2001) Factors controlling chemistry of magmatic spinel: an empirical study of associated olivine, Cr-spinel and melt inclusions from primitive rocks. J Petrol 42(4): 655-671.

Kress, VC, Carmichael, IS (1991) The compressibility of silicate liquids containing Fe_2O_3 and the effect of composition, temperature, oxygen fugacity and pressure on their redox states. Contrib Mineral Petrol 108(1-2): 82-92

Moore, G, Vennemann, T, Carmichael, ISE (1998) An empirical model for the solubility of H_2O in magmas to 3 kilobars. Am Mineral 83(1-2): 36-42.

Sun, SS, McDonough, WS (1989) Chemical and isotopic systematics of oceanic basalts: implications for mantle composition and processes. Geological Society, London, Special Publications, 42(1), 313-345. https://doi.org/10.1144/GSL.SP.1989.042.01.19